


# ECIO 2020

European Conference on Integrated Optics

Paris-Saclay University, France

*Collected Manuscripts*

(c) Copyright 2020 The ECIO Board. All rights reserved.

# Contents


| ID | Author | Title |
|---|---|---|
| S1.1 | (Invited paper) Tetsuya Mizumoto | Application of Magneto-optic Material to Silicon Photonic Integrated Circuits |
| S1.2 | Mikhail Churaev1, Simon H¨onl2, | Hybrid silicon nitride-lithium niobate integrated platform for electro-optic conversion |
| S1.3 | Lukas Van Iseghem1,2, Umar Khan1 | Liquid crystal phase shifter integrated in a silicon photonics platform |
| S1.4 | A.A. Kashi1, J.J.G.M. van der To | Electro-Optic Slot Waveguide Phase Modulator in the IMOS platform(Student Paper) |
| S1.5 | Alicia Ruiz-Caridad1, *, Guillau | Erbium-doped oxide for optical gain on hybrid silicon photonics platforms (StudentPaper) |
| S1.6 | Jorge Parra1, Todora Angelova1, | Ultra-compact low-power hybrid VO2/Si waveguide switch (Student paper) |
| S2.1 | Alain Y. Takabayashi1, Hamed Sat | Broadband Compact Single-Pole Double-Throw Silicon Photonic MEMS Switch (Student Paper) |
| S2.2 | Iman Zand 1; 2 Xiangfeng Chen 1; | Application-specific Scaling in Programmable Photonic Circuits (Student Paper) |
| S2.3 | Maziyar Milanizadeh1, Elena Dami | Recursive MZI mesh for integral equation implementation (Student Paper) |
| S3.1 | Juan Fernández1,2, Joan Felip1, | Statistical analysis of passive components manufactured in a thick silicon nitride platform (Student Paper) |
| S3.2 | Maziyar Milanizadeh, Matteo Petr | Polarization insensitive tunable hitless filter for extended C band (Student Paper) |
| S3.3 | Pisu Jiang 1 and Krishna C. Balr | Building large scale photonic integrated circuits in suspended gallium arsenide: Passives |
| S3.4 | Madeleine Weigel1, Moritz Kleine | 3D Photonic Integration: Cascaded 1×1 3D Multi-mode Interference Couplers for Vertical Multi-layer Connections |
| S3.5 | Piotr. J Cegielski1, Stephan Suc | Silicon Nitride Waveguides and Spot Size Converters with < 1.76 dB Loss Over Broad Wavelength Range from 1010 nm to 1110 nm for OCT Applications |
| S4.1 | A. Moscoso-Mártir1*, J. Koch2, J | Silicon Photonics DWDM NLFT Soliton Transmitter Implementation and Link Budget Assessment |
| S4.2 | Danhao Ma1, Yiding Lin2, Ruitao | Tensile Strained Ge0.99 Si0.01 EA Modulator Arrays for Integrated Broadband Modulation |
| S5.1 | Hao Sun1 and Lawrence R. Chen1 | Discretely tunable optical delay lines using step-chirped subwavelength grating Bragg gratings (Student's paper) |
| S6.1 | John McCarthy 1;2, Mohamad Derna | Monolithically Integrated Tunable Comb Source using Gain Switched Slotted Fabry-P´erot Lasers (Student Paper) |
| S6.2 | P. Fanneau1, C. Besancon1, H. El | Heterogeneous integration of III-V materials on Silicon photonic platforms: In the quest for high power, single-longitudinal mode and widely tuneable on-chip laser diodes Student Paper |
| S7.1 | Aude Martin1, In`es Ghorbel1;2, | Generation of a compact oscillator using self-injected piezoelectric optomechanical crystal |
| S7.2 | Jianhao Zhang,1 Omar Ortiz,1 Xav | Subwavelength engineering for Brillouin gain optimization in silicon optomechanical waveguides |
| S8.1 | Dan Yi, Yaojing Zhang, Xinru Wu | Integrated Photonic Lantern for Speckle Spectroscopy Student Paper |

| | | |
|---|---|---|
| S8.2 | Lucas Deniel1, Erwan Weckenmann2 | Tunable optical dual-comb experiments using silicon Mach-Zehnder modulators(Student Paper) |
| S8.3 | Albert van Rees1, Cornelis A. A. | Realization of a Hybrid Integrated Diode laser for Visible Light Student Paper |
| S8.4 | Mahir Asif Mohammed1, F.A. de Bo | Highly Sensitive and Fast Responsive Photonic Integrated Relative Humidity Sensor using Porous SiO2 Cladding Student Paper |
| S8.5 | Luis Torrijos-Mor´an, Paula Mar | Real-time functionalization and biosensing in subwavelength grating bimodal waveguides(Student paper) |
| S9.1 | Junqiu Liu1, Hao Tian2, Erwan Lu | Monolithic piezoelectric control of soliton microcombs(Student Paper) |
| S9.2 | Anton Lukashchuk1, Johann Riemen | Microresonator Soliton based parallel FMCW LiDAR |
| S9.3 | Samuel Serna1,2,3, Hongtao Lin3, | A hybrid chalcogenide-on-silicon platform for non linear photonics |
| S10.1 | Samu-Pekka Ojanen1, Jukka Viheri | Widely Tunable 2.6 μm GaSbDiode Lasers UtilizingDiffraction Gratings or Silicon Photonics Reflectors (Student Paper) |
| S10.2 | Alberto Della Torre1, Milan Sino | Dispersion Trimming for Mid-Infrared Supercontinuum Generation in Silicon-Germanium on Silicon Wave guides (Student paper) |
| S10.3 | Miguel Montesinos-Ballester1, Qi | Optical modulation from 5 to 11 μm wavelength range using Ge-rich graded SiGe waveguides Student paper |
| S11.1 | L. Mercad´e1, L. L. Mart´ın1,2 | Frequency comb and microwave generation with a full phononic bandgap1D optomechanical crystal cavity (Student Paper) |
| S12.1 | Daniel Benedikovic1, Léopold Vir | Silicon-germanium p-i-n photodiodes with double heterojunction: high-speed operation at 10Gbps and beyond |
| S12.2 | Contestabile1, F. Bontempi1, and | 240 Gb/s (8×30 Gb/s) Directly Modulated Transmitter Monolithically Integrated on InPG. |
| S13.1 | Bozhang Dong1, Jianan Duan1, Hem | Study of hybrid silicon quantum dot frequency comb laser dynamic for 5G and datacom applications |
| S13.2 | Liwei Tang1,2, Shuai Shao1,2, Si | Frequency Modulated Continuous Wave Narrow Linewidth Laser Diode Based on Self-injection locking with External Micro-ring Resonator |
| S13.3 | S. Boust1,2, Y. Ibrahimi1, J.-F. | Single-mode and multi-mode DBR lasers using InP-Si3N4/SiO2 integration (Student paper) |
| S14.1 | Alexandre Maïnos 1, Stefano Paes | Near-optimal Sources of Single Photons in Silicon Quantum Photonics based on Intermodal Spontaneous Four-Wave-Mixing (Student) |
| S14.2 | Dorian Oser1, Florent Mazeas2, C | Silicon source providing multi-spectral photon pairs with high-quality entanglement |
| S14.3 | H. O. Çirkinoglu1, R. Santos2, K | Monolithically integrated differential phase shift transmitter for quantum key distribution |
| S15.1 | David González-Andrade1,*, José | Ultra-Broadband Passive Phase Shifter Using Anisotropic Subwavelength Metamaterials |
| S15.2 | José Manuel Luque-González1*, Al | Independent phase matching for TE and TM polarization in directional couplers with tilted subwavelength structures (Student Paper) |
| S15.3 | T. T. D. Dinh1, X. Le Roux1, J. | Dual-metamaterial silicon micro-ring resonators (Student Paper) |
| S15.4 | Yeyu Tong1, Xuetong Zhou1, Yi Wa | Bridging the Graded-Index Few-Mode Fibre with Photonic Integrated Circuits via Efficient Diffraction Waveguide Gratings (Student Paper) |
| S16.1 | Arab N1, Poette J1, Bastard L1, | Dual wavelength Y-junction glass integrated waveguides for mm-wavecarrier generation |
| S16.2 | Aref Rasoulzadeh Zali1, Steven K | Low Polarization Sensitive Semiconductor Optical Amplifier Co-Integrated with Passive Waveguides for Optical Datacom and Telecom Networks Student |

| | | |
|---|---|---|
| | | Paper |
| S16.3 | Qin Zou, Kamel Merghem,Badr-Eddi | Bifurcation and Chaotic Behavior of Feedback Semiconductor Lasers Operating in the Full Range of External Reflectivity |
| S16.4 | Julio Darío López1, Dan Zhao2,3, | Narrow-Linewidth DBR Laser Using Open-Access High-Precision Gratingin InP PIC Generic Foundry Platform |
| S16.5 | Mariangela Gioannini1, Lorenzo C | Design of hybrid lasers for silicon photonics: efficiency, optical feedback tolerance and laser dynamics |
| S16.6 | Junfei Xia,Qixiang Cheng,Tongyun | Design of III-V on Silicon OpticalSwitch based on Mach-ZehnderandSOA Switching Elements |
| S16.7 | E. Malysheva, A. Fiore, K.A. Wil | Manufacture-compliant InP-based metal cavity nanolaser designStudent Paper |
| S16.8 | Jack Mulcahy1,2, John McCarthy1, | Monolithically Integrated Wavelength Tunable Dual Comb Source usingGain Switching(Student Paper) |
| S16.9 | Juan Navarro-Arenas, 1Andrés F. | Perovskite Nanocrystals:an Active Material for Integrated Optics(Student Paper |
| S16.10 | Sander Reniers1, Kevin Williams1 | An Accurate Characterization Method for Polarization Converters on theIndium Phosphide Membrane on Silicon Platform(Student Paper) |
| S16.11 | Stanisław Stopiński, Krzysztof S | Hybrid Integration of aSingle-Frequency Ring Laser withaMicroelectronic Driver |
| S16.12 | ZhengruiTu1, Jianhao Zhang1, Joh | Prospect for compact on-chiplasing with hybriderbium-doped siliconintegration(Student Paper) |
| S17.1 | Chupao Lin 1,2, David Schaubroec | Low-loss single-mode waveguides operating at UV/violet wavelengths and fabricated with contactoptical lithography Student Paper |
| S17.2 | Jianhao Zhang,1Carlos Alonso-Ram | Ultra-wide band inter-mode four-wave mixingin sub-wavelength silicon waveguides |
| S17.3 | Pragati Aashna1and K Thyagarajan | Two-process frequency conversion under stimulated Raman adiabatic passage via a continuum of dark intermediate modes |
| S17.4 | BenedictoD1, DíasA2, Martín JC1, | Characterization of an Er3+/Yb3+Codoped Two CoreIntegrated Waveguide Femtosecond Laser written in a Phosphate Glass (Studentpaper) |
| S17.5 | J.-B. Dory1,2, J.-Y. Raty1,3,M. | Amorphous chalcogenide thin filmsfor nonlinear integrated optics in mid-infrared |
| S17.6 | Student Paper Glukhov I.A.,1,2 M | Polarization-selective defect mode suppression in a deterministic aperiodic photonic crystal through plasmon excitation in an embedded array of metallic nanoparticles |
| S17.7 | W.A.P.M. Hendriks, M. Dijkstra,C | High refractive index low-loss aluminium oxidewaveguides(Student Paper) |
| S17.8 | Zhengkai Jia1,Hua Yang2,Hui Wang | Quantum Well Intermixing of InP-Based AlInGaAs Quantum Wells Using IFVD Technique and the Mask Boundary Effect |
| S17.9 | I.V. Kondratyev1, M. Yu. Saygin1 | Robust Architecture for Programmable Universal Unitaries |
| S17.10 | S.M. Kostritskii1, Yu.N.Korkishk | Phase composition and electro-optic properties of channel proton-exchanged LiNbO3waveguides |
| S17.11 | Habib Mohamad1, Sylvain Blaize2, | The Aperiodic DM-FFF compared to the A-FMM: A Rigorous Method forthe Modeling of Guided Optical StructuresStudent Paper |
| S17.12 | Paramita Pal1, E. Kumi Barimah1, | Er3+doped Silica-on-Siliconusing fs-laserdopingprocess for Integrated Waveguide AmplifierPlatforms ‘Student Paper’ |
| S17.13 | Vincent Pelgrin1,2, Yuchen Wang2 | Kerr effect enhancement through hybrid integration of 2D materials on thesilicon platformStudent Paper |

| | | |
|---|---|---|
| S17.14 | R.Peyton1,2, D. Presti1,2, F. Vi | Multi Mode Interferometer plus simplified coherent coupling to design asmall footprint SOI power splitter |
| S17.15 | Dura Shahwar, Matteo Cherchi, Mi | Polarization splitter based on form birefringence for micron-scale Silicon photonics(Student Paper) |
| S17.16 | Kang WangUniversit´e Paris-Sacl | Valley-polarized beam propagation in metallic photonic graphene |
| S18.1 | A. Meighan, W. Yao, M. Wale, and | Microwave model for optimizing electro-optical modulation response of the Mach-Zehnder modulator |
| S18.2 | Alberto Tibaldi1;2, Mohammadamin | Modeling of plasmonic organic hybrid E/O modulators: towards a comprehensive 3D simulation framework |
| S18.3 | Aleksandra Paśnikowska, Stanisła | InP-based integrated OLT and ONU with cyclic AWG for WDM-PON Student Paper |
| S18.4 | C. Porzi1, F. Falconi2, L. Ansal | Fast Silicon Photonics Wavelength-Selective Phase Shifter |
| S18.5 | Christian Lafforgue 1, Mathias B | Strain-induced electro-optical effect in silicon Mach-Zehnder modulators (Student paper) |
| S18.6 | Ercan Karagöz1,2, Evren Öztekin1 | LiNbO3 V-Groove Fabrication for Optical Fibre Pigtailing (Student Paper) |
| S18.7 | Frederik Thiele1, Jan Philipp H¨ | Cryogenic operation of a polarisation cinverter and directional coupler in LiNbO3 for quantum circuits (student paper) |
| S18.8 | Mihai Kusko1, Rebeca Tudor1, Ste | Design of an Integrated Optical Circuit for Generation of Optical Vortex |
| S18.9 | N. Tessema, K. Prifti, A. Rasoul | Compact InP Wavelength Blocker based on a Single AWG and SOA gates for Metro Networks |
| S18.10 | Rahul D. Mishra1, Lalit Singh1, | Enhanced Optical Readout in Resistive Memory Through Plasmonic Amplification (Student Paper) |
| S18.11 | Reza Hosseini1,3, Shahryar Sabou | Side Mode Suppression Ratio Reduction in Mach-Zehnder Modulators Using Slow-Light Waveguides |
| S18.12 | Robinson Guzman1, Alberto Zarzue | Integrated Microwave Photonic Signal Generation System based on the External Modulation Technique |
| S18.13 | A. Brimont1, D. Zurita1, V. C. D | Optical fiber-to-chip assembly process for ultra-low loss photonic devices based on silicon nitride for space applications |
| S19.1 | G. Martina, M. Foina, F. Gardill | First results on an electro-optic visible multi-telescope beam combiner for next generation FIRST/SUBARU instruments |
| S19.2 | Hongsik Jung1 | Guided-Wave, Electro-Optic Electric-Field Sensors Utilizing Ti Diffused Lithium-Niobate (Ti:LiNbO3) Channel Waveguides |
| S19.3 | I.A. Krutov, M.Yu. Saygin, I.V. | Optimized low-loss integrated photonics silicon-nitride Y-branch splitter |
| S19.4 | J. Enrique V´azquez-Lozano, Alej | Chiroptical Applications Enabled by Integrated Photonic Waveguides (Student Paper) |
| S19.5 | Jerry Yeung1 and Markus Pollnau1 | Light-Intensity Distributions in Distributed-Feedback Resonators |
| S19.6 | Marcin Lelit1,2, Mateusz Słowiko | Silicon nitride passive photonic platform for applications at visible wavelengths: design, fabrication and characterization (Student Paper) |
| S19.7 | Mauricio Tosi1, Jeffry H. Martín | Fabrication of Silicon Nitride PIC by Laser Direct Writing |
| S19.8 | Maziyar Milanizadeh, Matteo Petr | FSR free coupled microring resonator filter on extended C-band in silicon photonics (Student Paper) |
| S19.9 | Nirmalendu Acharyya 1 Mohamed Ma | Self-referenced Sensing in Microring Resonators |
| S19.10 | N. Verellen1*, Q. Deng1,2, O. Ar | Enabling High-Resolution Fluorescence Microscopy and Detection using Integrated Photonics |
| S19.11 | Pedro-Andrei Krochin-Yepez1,2, U | CMOS Compatible Thermal Management Solutions for Silicon Photonic |

| | | |
|---|---|---|
| | | Optical Phased Arrays |
| S19.12 | Nevlacsil S.1, Muellner P.1, Mae | PECVD SiN photonic integrated circuit for swept source OCT at 840 nm (Student Paper) |

# Application of Magneto-optic Material to Silicon Photonic Integrated Circuits

*(Invited paper)*

**Tetsuya Mizumoto**[1], **Yuya Shoji**[2], **Daiki Kano**[1]
[1] Tokyo Institute of Technology
[2] Institute of Innovative Research, Tokyo Institute of Technology
*e-mail: tmizumot@pe.titech.ac.jp*

## ABSTRACT

Optical isolators are fabricated on a silicon waveguide platform by directly bonding a magneto-optic garnet. The fabricated devices exhibit performance characteristics of a 30 dB isolation, a 20-dB isolation bandwidth of 8 nm, and a temperature-insensitive backward isolation. As another application of magneto-optic garnet, an optical switch is also fabricated having a latching function.

**Keywords**: photonic integrated circuit, silicon photonics, magneto-optic garnet, optical isolator, optical switch

## 1. INTRODUCTION

Magneto-optic materials enable us to realize various functions in photonic circuits. The most distinctive application is optical nonreciprocal devices such as an isolator and a circulator, which are realized by breaking time symmetry by virtue of magneto-optic effects. Magneto-optic effects are controlled by a magnetic field applied. For instance, the rotation direction of polarization plane is reversed by reversing the direction of magnetostatic field applied axially to a Faraday rotator. A magnetostatic field applied transverse to the light propagation direction in a magneto-optic waveguide induces a phase shift of guided light wave. Light waves experience different phase shift by reversing the direction of applied magnetostatic field as well as the propagation direction. Such a feature can be used to switch the output port of a Mach-Zehnder interferometer (MZI).

In this article, we present the development of silicon waveguide optical isolators which utilize the magneto-optic phase shift dependent on the light propagation direction. As another application of magneto-optic material, we demonstrate the optical switch which has a latching function.

## 2. DIRECT BONDING

Rare earth iron garnets are the best candidate among several magneto-optic materials for the application to optical devices used in optical fiber communication wavelength bands because of large magneto-optic effect and low optical absorption. An issue of integrating a magneto-optic garnet on a silicon waveguide platform is the differences of material parameters. A single-crystalline garnet cannot be grown on silicon. In order to make a full use of a large first-order magneto-optic effect, we developed a direct bonding technique of a magneto-optic garnet on silicon.

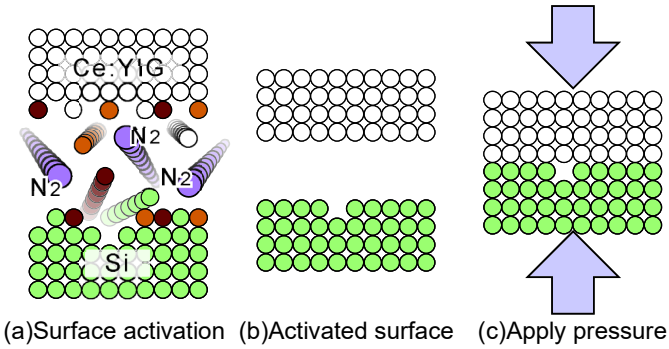



*Figure 1. Schematic illustration of surface activated direct bonding.*

A single-crystalline magneto-optic garnet, $CeY_2Fe_5O_{12}$ (Ce:YIG), was grown by an RF sputtering on a (111)-oriented $(GdCa)_3(GaMgZr)_5O_{12}$ (SGGG) substrate. The Ce:YIG wafer was directly bonded on silicon waveguides fabricated in the top silicon layer of an SOI wafer [1]. Figure 1 illustrates schematically the surface activated direct bonding process. The surfaces of Ce:YIG and silicon were activated by $N_2$ plasma exposure for 20 sec. Two wafers were contacted in a vacuum chamber at room temperature. The contacted sample was pressed with a pressure of 12 MPa at 200 °C for 90 min.

## 3. OPTICAL ISOLATOR

Using the magneto-optic phase shift in a MZI, we have realized a silicon waveguide optical isolator as shown in Fig. 2. The isolator was fabricated by directly bonding a 500-nm-thick single-crystalline Ce:YIG layer on a 450-nm-wide and 220-nm-thick silicon waveguide [2]. The Faraday rotation constant of Ce:YIG was –4500 °/cm at a wavelength of 1550 nm. The magnetic field required to saturate the magnetization of Ce:YIG layer in the film-plane was 50 Oe, which was favourable in the applications using a magneto-optic phase shift.

By applying a magnetostatic field in anti-parallel directions in two MZI arms, a phase difference is given between two arms. In the forward propagation, the phase difference brought about by the magneto-optic effect is set to be $-\pi/2$ by adjusting the magneto-optic interaction length. The magneto-optic phase difference is cancelled by a $\pi/2+2m\pi$ ($m$: integer) phase bias installed in the left arm. The phase bias, which is independent of light propagation direction, is realized by an optical path difference between two arms. Thus, light waves propagating in two arms interfere constructively in the output coupler. In the backward propagation, the magneto-optic phase difference changes its sign by virtue of a nonreciprocal nature of magneto-optic effect. Since the phase bias remains constant by reversing the propagation direction, the total phase difference between two arms amounts to $\pi$. Thus, light waves interfere destructively in the left coupler. No light is output at the central port of left coupler, which is an input port for the forward propagation.

We demonstrated an isolation of 30 dB in a fabricated device as shown in Fig. 2(b) [2]. The 20-dB isolation bandwidth was extended to 8 nm by adjusting the phase bias [3]. We also demonstrated temperature-insensitive backward isolation in a temperature range of 20-60 °C [4] by cancelling the temperature dependence of magneto-optic effect with that of phase bias.

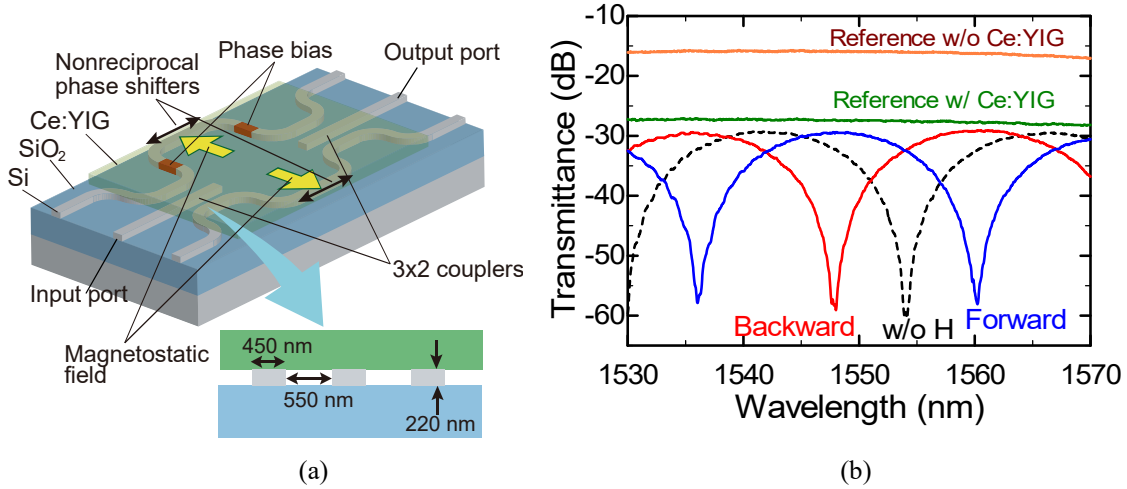



*Figure 2. (a) Device structure of silicon waveguide optical isolator and (b) its measured fiber-to-fiber transmittance [2].*

## 4. OPTICAL SWITCH

The sign of magneto-optic phase difference between two MZI arms is flipped by reversing the magnetization direction of Ce:YIG instead of reversing the propagation direction. When the magneto-optic phase difference becomes $+\pi/2$ and $-\pi/2$ with a $\pi/2+2m\pi$ ($m$: integer) phase bias installed in one of MZI arms, constructive interference occurs in the bar and cross ports, respectively, in a 2×2 MZI. Thus, the output port is switched between the two ports. The unique feature of this magneto-optic switch is that the switch state is maintained by holding a magnetostatic field generated by a tiny external magnet without any additional power consumption. The switch state is flipped by reversing the magnetization of the external magnet.

We fabricated the magneto-optic switch in a hydrogenated amorphous silicon (a-Si:H) waveguide prepared on the 500-nm-thick Ce:YIG single-crystalline layer [5]. Figure 3(a) shows the schematic of fabricated device. An MZI waveguide pattern was formed in an a-Si:H layer deposited on the Ce:YIG using plasma-enhanced chemical vapor deposition by $SF_6$ reactive ion etching [6]. The waveguide height and width were 240 and 600 nm, respectively. After depositing an 800-nm-thick $SiO_2$ over-cladding layer, 300-nm-thick FeCoB was deposited, using an RF facing-target sputtering method [7], as thin-film magnets with a 10-nm-thick Ru buffer layer over the MZI arms. After a 150-nm-thick $SiO_2$ cover layer was deposited, a 500-nm-thick and 30-μm-wide silver electrode was prepared to flow a pulse current that generated a magnetic field used for flipping the magnetization direction of FeCoB.

Figure 3(b) shows the temporal optical output change measured at the cross port of the switch. It is observed that the output changes from a high to a low level and vice versa by applying a 1-μs-wide pulse current to flip the FeCoB magnetization. The switch state is maintained after ceasing the current flow. This is attributed to that the

Ce:YIG magnetization is maintained to generate a magneto-optic phase shift by virtue of the FeCoB thin-film magneto.

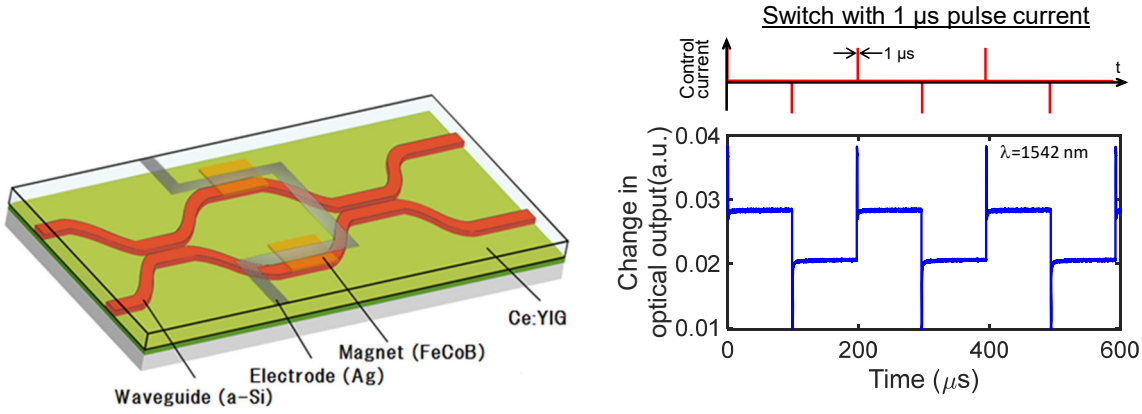



*Figure 3. Magneto-optic switch with a latching function. (a)Schematic device structure [3] and (b) measured temporal response.*

## 5. CONCLUSIONS

Silicon waveguide photonic devices are demonstrated that are based on a magneto-optic effect. By aligning the magnetization of a magneto-optic garnet cladding layer along the transverse direction to the light propagation, light waves propagating in a silicon waveguide experience a magneto-optic phase shift. The phase shift is dependent on the light propagation direction as well as the magnetization direction. Using the direction dependent magneto-optic phase shift, we demonstrated optical isolators with an isolation ratio of 30 dB, a 20-dB isolation bandwidth of 8 nm, and temperature-insensitive isolation performance in 20-60 ºC. Also, we demonstrated a magneto-optic switch with a latching function, in which an output port was switched by a pulse control current.

## ACKNOWLEDGEMENTS

This work was partly supported by JST/CREST #JPMJCR15N6, and JSPS KAKENHI #19H02190.

## REFERENCES

[1] R. Takei, K. Yoshida, and T. Mizumoto: Effect of wafer pre-cleaning and plasma irradiation to wafer surfaces for plasma-assisted surface activated bonding, *Jpn. J. Appl. Phys.*, vol. 49, 086204, Aug. 2010.

[2] Y. Shoji and T. Mizumoto: Magneto-optical nonreciprocal devices in silicon photonics, *Sci. Technol. Adv. Mater.*, vol. 15, 014602, Jan. 2014.

[3] Y. Shoji, Y. Shirato, and T. Mizumoto: Silicon Mach-Zehnder interferometer optical isolator having 8 nm bandwidth for over 20 dB isolation, *Jpn. J. Appl. Phys.*, vol. 53, 022202, 2014.

[4] K. Furuya, T. Nemoto, K. Kato, Y. Shoji, and T. Mizumoto: Athermal operation of a waveguide optical isolator based on canceling phase deviations in a Mach–Zehnder interferometer, *J. Lightwave Technol.*, vol. 34, pp. 1699–1705, April 2016.

[5] K. Okazeri, K. Muraoka, Y. Shoji, S. Nakagawa, N. Nishiyama, S. Arai, and T. Mizumoto: Self-holding magneto-optical switch integrated with thin-film magnet, *IEEE Photon. Technol. Lett.*, vol. 30, pp. 371–374, Jan. 2018.

[6] J. Kang, Y. Atsumi, M. Oda, T. Amemiya, N. Nishiyama, and S. Arai: Low-loss amorphous silicon multilayer waveguides vertically stacked on silicon-on-insulator substrate, *Jpn J. Appl. Phys.*, vol. 50, 120208, 2011.

[7] A. Hashimoto, K. Hirata, T. Matsuu, S. Saito, and S. Nakagawa: Crystal structure as an origin of high-anisotropy field of FeCoB films with Ru underlayer, *IEEE Trans. Magn.*, vol. 44, pp. 3899–3901, 2008.

# Hybrid silicon nitride-lithium niobate integrated platform for electro-optic conversion

Mikhail Churaev[1], Simon Hönl[2], Rui Ning Wang[1], Charles Möhl[2], Tianyi Liu[1], J. Connor Skehan[1], Johann Riemensberger[1], Daniele Caimi[2], Junqiu Liu[1], Paul Seidler[2], Tobias J. Kippenberg[1]
[1]*Swiss Federal Institute of Technology Lausanne (EPFL), CH-1015 Lausanne, Switzerland*
[2]*IBM Research - Zurich, CH-8803, Rüschlikon, Switzerland*
*e-mail: tobias.kippenberg@epfl.ch, pfs@zurich.ibm.com*

## ABSTRACT

We demonstrate the integration of a silicon nitride Damascene photonic platform with thin-film lithium niobate on insulator (LNOI) via direct wafer bonding. This process enables fabrication of hybrid microresonators exploiting second- and third-order nonlinearity with Q-factor of 1 million, as well as integrated travelling wave EO modulators.

**Keywords**: Lithium niobate, microresonators, electro-optic modulation, wafer bonding.

## INTRODUCTION

Electro-optic modulators are central to optical communications. To date, bulk modulators are primarily based on lithium niobate (LN). Over the past decade, a variety of alternative chip-scale integrated modulators have been developed. Examples include silicon modulators [1], InP modulators [2], plasmonic modulators [3], organic hybrid modulators [4], modulators based on 2D materials [5], and others. Recently, advances in fabrication of LN thin films and breakthroughs [REFS] in their processing have led to low-loss integrated LN modulators with low switching voltage and high bandwidth. Alternatively, it is possible to avoid etching of LN all together by combining a thin film of LN with a separate photonic platform providing strong confinement, such as integrated silicon or surface-ridge silicon nitride waveguides. Excellent performance with $V_\pi L$ of 3 V·cm has been reported in such hybrid devices [6], [7] – a value on par with etched thin-film LN modulators – despite having only a portion of the optical mode confined in LN. Currently, these hybrid technologies still exhibit considerable optical losses (more than 1dB/cm).

## LOW-LOSS INTEGRATION

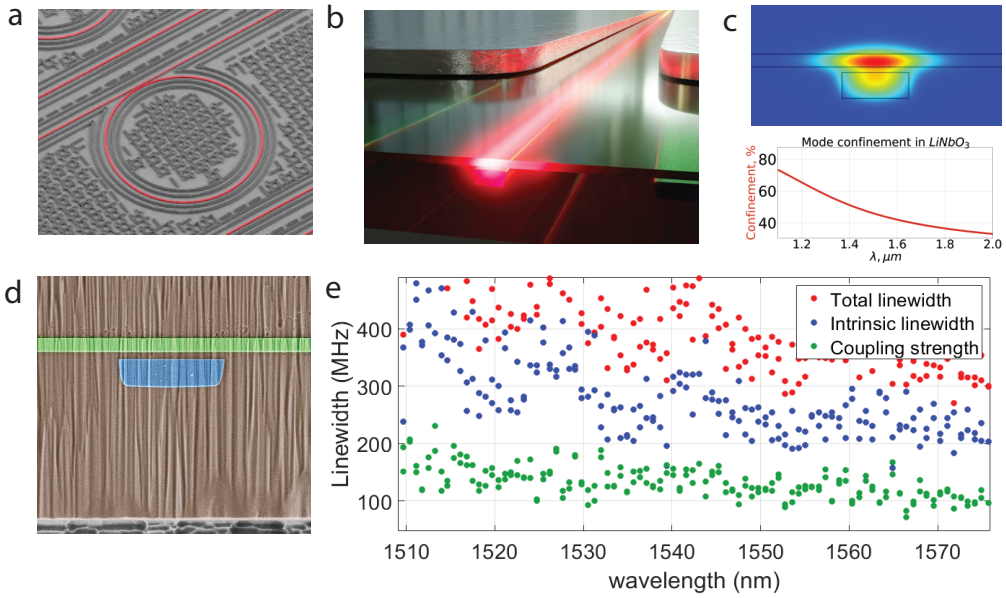



Figure 1. **Hybrid structure and characterization.** (a) SEM image of Photonic Damascene circuits (b) Artist's view on the hybrid structure (c) FEM simulations of mode profile and confinement in LN (d) SEM image of the bonded structure (e) Optical resonance linewidth characterization results

Our photonic Damascene process [8] enables the fabrication of ultralow-loss integrated photonic circuits with tight optical confinement. A photonic Damascene wafer is prepared with a thin $SiO_2$ dielectric interlayer via low-temperature PECVD, and subsequent chemical mechanical polishing (CMP). After CMP, the short-range rms roughness of the $SiO_2$ layer is reduced to 130 pm. The wafer is then bonded to a commercial LN-on-insulator wafer (NanoLN) using a thin $Al_2O_3$ interface layer. The LN substrate is then removed using a combination of mechanical lapping and wet etching of the silicon substrate. The buried oxide on top of the LN layer is subsequently removed with buffered hydrofluoric acid.

In order to confirm the low optical losses of the hybrid structure, one microresonator was characterized at an optical wavelength of 1550 nm (figure 1e). The ring resonator has radius of 225 $\mu$m, which corresponds to a free spectral range of approximately 100 GHz. The measured intrinsic linewidth of the resonances is 200 MHz, which corresponds to the Q-factor of $9.55\times10^5$ ($\approx$ 0.335 dB/cm optical losses). Moreover, the losses decrease at higher wavelength, opposite to the typical regime of pure $Si_3N_4$ microresonators. This dependency proves that the mode is shared between $Si_3N_4$ waveguide and the $LiNbO_3$ thin film. As depicted in Figure 1c, the optical mode shifts into the $Si_3N_4$ waveguide at higher wavelengths, which leads to a decrease in whispering-gallery losses in the LN thin film.

## ELECTRO-OPTIC MODULATION

To demonstrate the electro-optical response of the bonded structure, Nb electrodes are fabricated on chip-level using magnetron sputtering for the deposition of a 1 $\mu m$ thick Nb film which is then patterned into electrodes with reactive ion etching. The electrodes are placed with 11.5 $\mu m$ gap distance, which was chosen to prevent additional optical losses due to the mask misalignment. The total length of the fabricated travelling-wave phase modulators is 4 mm.

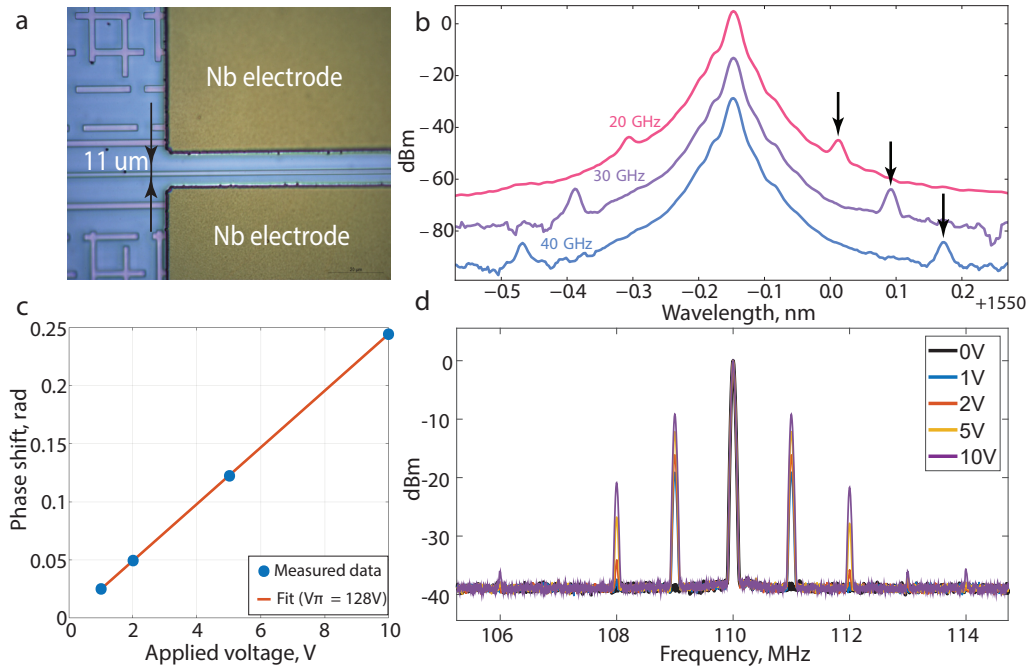



Figure 2. **Phase modulator experiments** (a) Nb electrode on-chip integration (b) OSA spectra for 20 GHz, 30 GHz, and 40 GHz modulation tones driven at 23 dBm power (c) Phase shift as a function of applied voltage (d) ESA spectra of low-frequency modulation sidebands for $V_\pi$ calculations

In order to estimate the $V_\pi$ value of the fabricated device, self-heterodyne measurements are performed at 110 MHz, frequency shifted using an AOM. The resulting beatnote from the sidebands is analyzed using an ESA (see figure 2c-d). By fitting the sideband amplitudes with a Bessel function expansion, $S_n \propto J_n(\phi)$, we are able to extract the amplitude of phase modulation $\phi$. By measuring the phase modulation amplitude at different driving voltages, we derive a $V_\pi$ value of 127 volts. We also observe direct modulation of the device with high RF frequencies up to 40 GHz (figure 2b).

## SUMMARY

In summary, we demonstrate just a few of the the potential benefits of combining an ultralow-loss photonic platform and an integrated LN thin film for electro-optical conversion. Our direct wafer bonding retains the low-loss optical propagation typical of $Si_3N_4$ integrated photonics, which is promising for future applications

in optical communications. The first phase modulator devices were fabricated and tested successfully at RF frequencies up to 40 GHz.

## ACKNOWLEDGMENT

We thank Ute Drechsler and Darius Urbonas for helpful discussions during fabrication. This work was supported by funding from the European Union Horizon 2020 Programme for Research and Innovation under grant agreement No. 722923 (Marie Curie ETN OMT), grant agreement No. 732894 (FET Proactive HOT), grant agreement No. 812818 (Marie Curie ETN MICROCOMB), and grant agreement No. 846737 (Marie Curie IF – CoSiLiS). This work was also supported by the Swiss National Science Foundation under grant agreement No. 176563 (BRIDGE).

## REFERENCES

[1] Xu, Q. *et al.*, "Micrometre-scale silicon electro-optic modulator" *Nature* 435, 325-327 (2005)

[2] Ogyso, Y.*et al.*, "Over 67 GHz Bandwidth and 1.5 V Vpi InP-Based Optical IQ Modulator With n-i-p-n Heterostructure" *J. Light. Technol.* 35, 1450–1455 (2017).

[3] Haffner, C. *et al*., "All-plasmonic Mach–Zehnder modulator enabling optical high-speed communication at the microscale" *Nat. Photonics*. 9, 525–528 (2015).

[4] Alloatti, L. *et al.*, "100 GHz silicon–organic hybrid modulator" *Light Sci. Appl.* 3, e173–e173 (2014).

[5] Liu, M. *et al.*, "A graphene-based broadband optical modulator," *Nature* 474, 64–67 (2011).

[6] Jin, S. *et al.*, "LiNbO3 Thin-Film Modulators Using Silicon Nitride Surface Ridge Waveguides" *IEEE Photonics Technol. Lett.* 28, 736–739 (2016).

[7] Chen, L. *et al.*, "Hybrid silicon and lithium niobate electro-optical ring modulator" *Optica* 1, 112 (2014).

[8] Pfeiffer, M. H. P. *et al.*, "Photonic Damascene process for integrated high-Q microresonator based nonlinear photonics" *Optica* 3, 20–25 (2016).

# Liquid crystal phase shifter integrated in a silicon photonics platform

Lukas Van Iseghem [1,2], Umar Khan [1,2], Pierre Edinger [3] , Carlos Errando-Herranz [3] ,
Alain Yuji Takabayashi [4], Hamed Sattari [4], Kristinn B. Gylfason [3],
Niels Quack [4], Jeroen Beeckman [2,5] and Wim Bogaerts [1,2]
[1]*Photonics Research Group, Ghent University-IMEC, Dept. of Information Technology, Ghent, Belgium*
[2]*Center of Nano and Biophotonics, Ghent, Belgium*
[3]*KTH Royal Institute of Technology, SE-100 44 Stockholm, Sweden.*
[4]*École Polytechnique Fédérale de Lausanne (EPFL), 1015 Lausanne, Switzerland.*
[5]*Liquid Crystal and Photonics, Ghent University, Dept. of Electronics and Information Systems, Ghent, Belgium*
*e-mail: lukas.vaniseghem@ugent.be*

## ABSTRACT

We demonstrate a compact phase shifter using liquid crystal actuation, integrated in an established silicon photonics platform. The devices are fabricated using IMEC's iSiPP50G platform with a simple post-processing, making this technology compatible with current fabrication possibilities. In this first device demonstration we measure 0.75$\pi$ phase shift for 10 V actuation over a 60 $\mu m$ length.

**Keywords**: compact phase shifter, liquid crystal, integrated silicon photonics, low loss.

## 1 INTRODUCTION

IMEC's iSiPP50G silicon photonics platform has become mature over the past few years, and it enables different possibilities to implement thermo-optic phase shifter and electro-optic modulators. [1] The key functional difference between a phase shifter and a modulator is the operation speed, and the trade-off with the strength of the effect. Carrier-based modulation is fairly weak and usually accompanied with a significant insertion loss, while thermal tuners have a stronger effect on the effective index, but are limited in speed and come with a high, constant power consumption. A compact phase shifter with short optical path length requires a strong effect, and are very useful when switching times are not critical to tune devices on a chip.

In this paper we explore the integration of liquid crystal(LC) phase shifters into the existing iSiPP50G platform as a mechanism for slow responding but strong phase shifts. One of the major drawbacks in earlier demonstrations of LC-based tuning was the necessity of a very high voltage to get the required effect [2]. Another demonstration uses a slot waveguide filled with liquid crystal[3], but coupling light into the slot proves to be problematic in itself and the slot waveguide has high optical propagation losses. The phase shift reported by the slot waveguide system is very promising because of the high optical overlap with the liquid crystal and the high electric field between the two actuated halves of the slot waveguides. So in this work we try to achieve a similar actuation effect using the LC as a waveguide cladding, keeping the light confined in a single waveguide core, but using a similar lateral actuation between the waveguide and a narrow bar of silicon on the side of the waveguide core. In addition, we do this without sacrificing any of the functionality in IMEC's platform, so we can combine the LC phase shifters with modulators and Germanium Photodetectors, and use the built-in metallization to contact the LC electrodes.

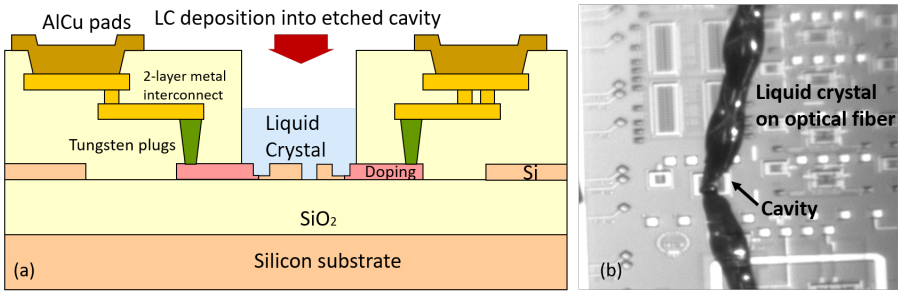



Figure 1. (a) Integration of liquid crystal in iSiPP50G platform (b) Experimental deposition of liquid crystal in etched cavity, using a motorized cleaved fiber as delivery mechanism

## 2 FABRICATION

The phase shifter has been implemented in the iSiPP50G plaform from IMEC, consisting of silicon with various doping levels and two levels of metal interconnects, as shown in Fig. 1a. One of the features of the

iSiPP50G is a local back-end opening step that exposes the top surface of the waveguide. We use these cavities for the liquid crystal. In a short post-processing buffered HF etch, the oxide next to the silicon waveguides is removed, so we can introduce the LC to the side of the waveguide. This post-processing is part of a process flow developed in the MORPHIC project to add MEMS functionality to the iSiPP50G. [4].

In this work, we present the results of a first exploratory attempt to fill such a cavity with liquid crystal. A tweezer is dipped in LC and stroked against an optical fiber. The LC covered fiber was positioned in such an etched cavity, making careful contact with the bottom at low speed to force a capillary flow of the LC into the cavity. To release the droplet from the feeding (depositing) fiber it is pulled up at higher speed, releasing a droplet of LC into the cavity, as shown in Fig. 1b.

## 3 OPERATION PRINCIPLE

Liquid Crystal (LC) is an an-isotropic material due to the high molecular aspect ratio. The permittivity (and consequently the refractive index) felt by electric field along the ”long direction” of the molecules is higher compared the two other axes. Using this mechanism one can tune the cladding of a waveguide. The modified cladding index leads to a change in the effective index of guided modes in the waveguide core, and this induces a phase delay/shift. LC molecules will align along electric field lines. This is shown in Fig. 2b, where a square wave of 500 Hz is applied, causing a quasi homogeneous electric field in the gap between the silicon structures. The square wave modulation is used to avoid the formation of an ionic charge layer at the edges, which means the average voltage should be zero [3], but the nematic LC molecules we use here still orient themselves along the field direction.

The iSiPP50G platform can connect the silicon device layer with metal contact pads via the 2-layer metal interconnect, tungsten plugs and doped silicon. This enables us to apply an electric field over the gap between two silicon ridges. In [3] this was used to create a strong field in a slot waveguide without resorting to a high voltage. But as slot waveguides have a considerable loss, we create a strong field on the side of the waveguide. The guided modes stays largely confined in the single mode waveguide (450 nm wide), improving the loss dramatically, while still having the possibility of reorienting the molecules without resorting to very high voltages. The smaller silicon electrode (220 nm wide) supports no guided modes at 1550 nm wavelength.

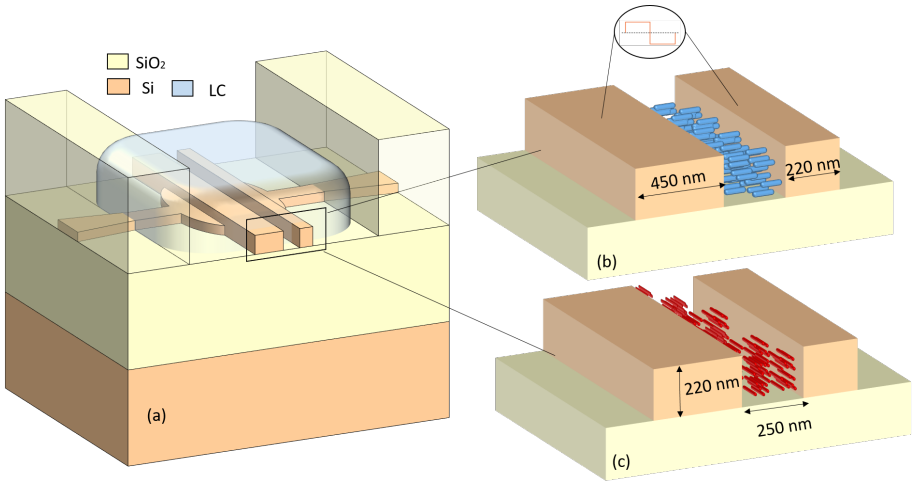



Figure 2. Operation principle of the phase shifter. (a) a shifter with an etched opening with a droplet of liquid crystal, accessed by silicon which is electrically connected to the oxide-clad back-end. (b) LC molecules oriented when a voltage is applied. (c) LC molecules relaxed along the waveguide when no voltage is applied.

Figure 2c shows the orientation of the molecules without an applied electric potential. Mechanical relaxation processes dominate in the liquid crystal, forcing it to align itself in the gap along the longitudinal direction of the waveguide. Note the gap of 250 nm between waveguide and electrode structures, making electric fields for reorientation possible at reasonable voltages.

## 4 MEASUREMENT AND RESULTS

The phase shifter is designed in an on-chip Mach-Zehnder interferometer (MZI) where one arm has no etched cavity, and the other has the LC phase shifter. In Fig. 3a it is shown a filled cavity can be identified using a visible light camera (the used LC has scattering and absorption loss in the visible wavelength range). The filled cavity blacks out of the camera image, making it distinguishable from the unfilled cavities. Once a liquid crystal drop is deposited in the cavity as discussed in the fabrication process, probes are placed in contact with the metal contact pads and the optical fibres are aligned to sweep the transmission in wavelength,

as shown in Fig. 3b. From the measured MZI responses, a phase shift could be determined as function of the applied voltage. These results are shown in Fig. 4. It can be noticed that the LC is not yet in saturation (fully reoriented), but due to the equipment limitations 10 V was the maximum in this experiment. In future measurements will go beyond this voltage to determine an actual $V_\pi \cdot L_\pi$ number.

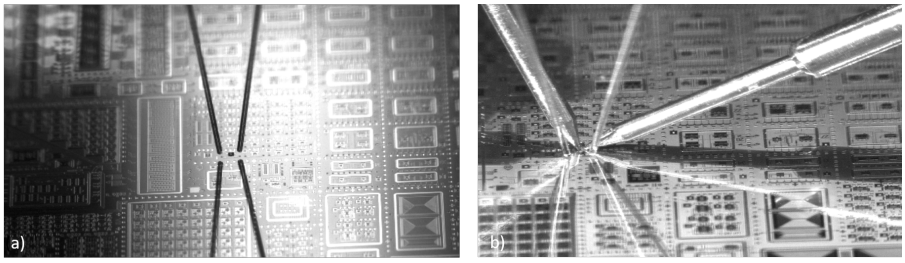



Figure 3. a) Camera picture of a cavity with deposited LC between two cleaved fibres.(b) Measurement setup, with electrical probes for the actuation and aligned optical fibers to vertical grating couplers to measure the MZI transmission spectrum.

For each measured spectra (Fig. 4a), a sine curve is fitted to determine the induced phase shift, which then gives us the response curve of the phase shifter, as shown in Fig. 4b. We see only the initial part of a sigmoid, and moving beyond 10 V we expect that the device will go in a more linear regime, as we have also observed in [3]. These early results are promising, giving almost $0.8\pi$ phase shift at 10 V.

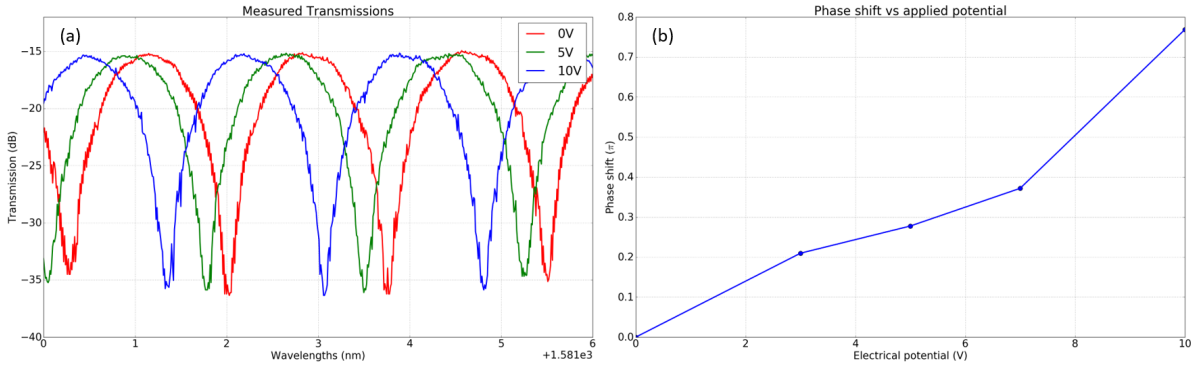



Figure 4. (a) Measured MZI responses for applied potentials of 0 V, 5 V and 10 V. (b) Phase shift for different applied voltages.

## 5 CONCLUSION

A first attempt to integrate a liquid crystal phase shifter in the iSiPP50G platform has been demonstrated and shows promising results. Future experiments will improve on this device by narrowing the gap, adding a second side electrode, and narrowing the core of the waveguide, which will push the mode more into the tunable liquid crystal cladding. Future measurements will move to voltages beyond 10 V and use a more controlled local deposition system for the liquid crystal. Optimal device parameters (such as gap, waveguide dimensions, electrode dimensions, etch depth, driving frequency, bias voltage, ...) can be determined in future measurements.

## ACKNOWLEDGMENT

This work was supported by the European Union through grants 780283 (MORPHIC) and 725555 (PhotonicSWARM). We would also like to thank Liesbeth Van Landschoot for performing the required Focused Ion Beam operations on devices.

## REFERENCES

[1] M. Pantouvaki, S. A. Srinivasan, Y. Ban, P. De Heyn, P. Verheyen, G. Lepage, H. Chen, J. De Coster, N. Golshani, S. Balakrishnan, P. Absil, and J. Van Campenhout, "Active Components for 50 Gb/s NRZ-OOK Optical Interconnects in a Silicon Photonics Platform," *Journal of Lightwave Technology*, vol. 35, no. 4, pp. 631–638, 2017.

[2] W. De Cort, J. Beeckman, T. Claes, K. Neyts, and R. Baets, "Wide tuning of silicon-on-insulator ring resonators with a liquid crystal cladding," *Optics Letters*, vol. 36, no. 19, p. 3876, 10 2011.

[3] Y. Xing, T. Ako, S. Member, J. P. George, S. Member, D. Korn, H. Yu, P. Verheyen, M. Pantouvaki, G. Lepage, P. Absil, A. Ruocco, C. Koos, J. Leuthold, K. Neyts, and J. Beeckman, "Digitally Controlled Phase Shifter Using an SOI Slot Waveguide With Liquid Crystal Infiltration," *Photon. Technol. Lett.*, vol. 27, no. 12, pp. 1269–1272, 6 2015.

[4] W. Bogaerts, H. Sattari, P. Edinger, Y. A. Takabayashi, I. Zand, X. Wang, A. Ribeiro, M. Jezzini, C. Errando-Herranz, G. Talli, K. Saurav, M. Garcia Porcel, P. Verheyen, B. Abasahl, F. Niklaus, N. Quack, K. B. Gylfason, P. O'Brien, and U. Khan, "MORPHIC : Programmable photonic circuits enabled by silicon photonic MEMS," *Proc. SPIE*, vol. 11285, pp. 11 285–1, 2020.

# Electro-Optic Slot Waveguide Phase Modulator in the IMOS platform

*(Student Paper)*

**A.A. Kashi[1], J.J.G.M. van der Tol[1], Y. Jiao[1] and K.Williams[1]**
[1] *Institute for Photonic Integration (IPI), Eindhoven University of Technology, the Netherlands*
*E-mail: A.Abbas.Kashi@tue.nl*

**ABSTRACT**

We present an electro-optic slot waveguide phase modulator on the InP membrane on Silicon (IMOS) platform. For the first time, it is developed and fabricated on an InP based membrane. Low-frequency characterization of this modulator shows that it can achieve $V_\pi L_\pi$ as low as 3 V.mm. Here, working principle, design and fabrication of this modulator is presented.

**Keywords**: Slot waveguide modulator, Electro-optic polymer, IMOS platform

## 1. INTRODUCTION

A high-speed modulator is an essential component for photonic integrated circuits (PICs) to enable high data rate communications. Many researchers around the world are trying to find a way to improve the efficiency and bandwidth of the modulators. One of the solutions to achieve such a high-speed modulator is to use a slot waveguide filled with electro-optic (EO) polymer, which can induce a phase shift in the optical signal when an electric field is applied. This type of modulator is called: electro-optic slot waveguide phase modulator and has already been introduced on silicon platforms.

Recent advances in silicon organic hybrid (SOH) modulators have shown the great potential of these devices to reach a very fast, on-off-keying (OOK) signals at a data rate beyond 100 Gbit/s, and energy-efficient, fJ/bit power consumption, phase modulators [1-3]. These modulators can achieve very high modulation efficiencies with low voltage-length products ($V_\pi L_\pi$). State-of-the-art SOH modulator shows $V_\pi L_\pi$ below 0.1 V.mm [2], which position it among the most efficient modulators. However, as it is depicted in Figure1, InP in comparison to Si features lower optical loss and higher carrier mobility at the same doping level. These properties enable InP based devices to achieve higher doping concentration levels to reduce the electrical resistance of the device while keeping the insertion loss low and mobility high. This eventually leads to wider modulation bandwidth and better the modulation efficiency [4].

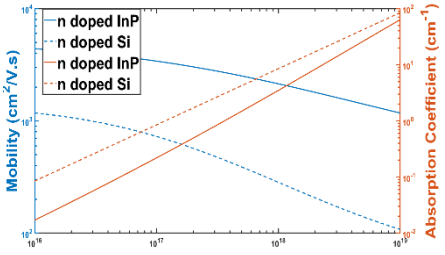



*Figure 1. (Right Y axis) Mobility of InP compare to Si as a function of doping concentration. InP mobility is near 10 times higher in high doping concentrations. (Left Y axis) Carrier absorption coefficient of InP compare to Si vs doping concentration. The carrier absorption coefficient of InP is nearly half of that of Si.*

InP membrane on Silicon substrate (IMOS) [5, 6] is a versatile platform to realize a slot waveguide modulator, since apart from utilizing the superior performance of InP materials, both passive and active components, such as lasers, can be fabricated in one optical layer, in contrast to silicon-based platforms. Furthermore, the high refractive index contrast of the IMOS platform leads to high mode confinement and reduced dimensions of components, compared to traditional substrate-based InP photonic integrated circuits (PICs).

In this paper, first the working principle of the slot waveguide modulators will be explained and then the design and fabrication of this device will be described. Finally, the low-frequency characterization of a fabricated device will be reported.

## 2. WORKING PRINCIPLE

In Figure 2 the design of the Mach-Zehnder interferometer (MZI) modulator, with slot waveguides phase shifters in the branches, is illustrated. The TE fundamental mode is coupled to the chip with a surface grating coupler. It is split in a symmetric 1x2 Multi-Mode Interferometer (MMI) over the two arms. There the light is converted to the mode of the slot waveguide. These waveguides confine the optical mode in the slot which contains

an EO polymer, see Figure 2 (c). Confinement in the slot leads to a high overlap of the optical mode with the EO polymer.

These polymers are able to induce a phase shift to the optical mode coming from refractive index change while applying an electric field, according to equation 1.

$$\Delta n = -1/2 \,.\, r_{33} . n^3 . V / w_{slot} . \Gamma \quad (1)$$

Where, $r_{33}, n, V, w_{slot}$ $and$ $\Gamma$ are the electro-optic coefficient of the polymer, effective refractive index, applied voltage, width of the slot and confinement factor of the optical mode in the slot, respectively.

In our MZI modulator, the InP slot waveguides are electrically contacted with a highly n-doped ($2\times10^{18}$) InP layer (30 nm) which is connected to the electric pads. These pads are placed 2µm away from the slot waveguide, to prevent unwanted losses due to overlap of the optical mode with the high optical loss metals. In the other hand, this distance has designed to have a reasonably low electrical resistance.

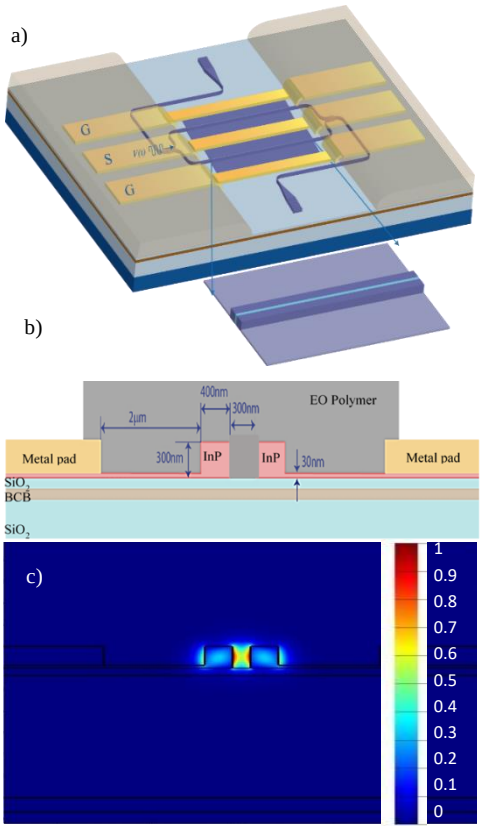



*Figure 2. (a) Illustration of the MZI device where the two arms are made of slot waveguides. Inset shows the magnified view of one of the arms. [6] (b) cross section of the MZI arm with dimensions. (c) Electric field distribution of the optical mode over the slot.*

## 3. DESIGN AND FABRICATION

The optical properties of the MZI are optimized with Finite-Difference Eigenmode (FDE) and Time-Domain (FDTD) solvers to reach low loss and high confinement of the light in the slot. The obtained optical loss of the optimized design is 0.014 dB/cm with the confinement factor (Γ) equal to 17%.

It is predicted to have an electro-optic coefficient ($r_{33}$) around 70 $pm/V$ in our slot. If it is assumed that the maximum voltage is limited to 4 V, from equation 1 it can be shown that a minimum electrode length of 670 µm is needed to have a π phase shift. These long electrodes are comparable to the wavelength of the radio frequency (RF) electrical signal required for driving this modulator. Therefore, a traveling-wave electrode design was considered to reduce RF reflection, loss and velocity mismatch. Electromagnetic field simulation software was used to design traveling-wave electrodes. Three parameters mainly influenced the electrode performance: electrode height, electrode width and distance of the electrode to the center of the slot. The performance of the device is the consequence of these three parameters together. A set of parameters was obtained to satisfy the desired RF properties. In Figure 3 (a), the Impedance of the line is shown to be around 30 Ohm for the frequency range between 10 to 100 GHz. Figure 3 (b) shows the RF loss in the frequency range. RF loss at maximum (100 GHz) reaches 75 dB/cm. In figure 3 (c), effective refractive index of the RF signal is indicated. In order to reduce velocity mismatch it is demanded to have a match between the electrical phase and optical group velocities. This imposes both effective refractive index of the RF and group effective refractive index of the optical mode, be equal. In our design, it is not possible to match these two values but it is tried to make them as close as possible ($n_{TE} = 2.04$ $and$ $n_{RF} = 3.2$ $at$ $100$ $GHz$). Figure 3 (d), illustrate the $S_{21}$ component of the transfer matrix for two different length of the electrode (100 µm and 250 µm). Due to simulation time costs it is not possible to simulate the whole 670 µm long electrode. Therefore, it is inferred from the trend, that around 40 GHz 3 dB modulation bandwidth can be expected for 670 um electrode length.

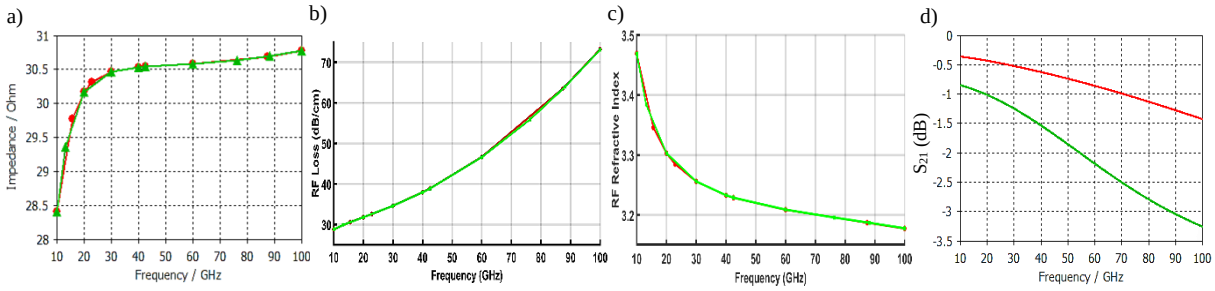



*Figure 3. (a) Optimized impedance of the transmission line vs frequency of the RF signal. (b) RF loss vs frequency of the RF signal. (c) Propagation constant vs frequency. (d) $S_{21}$ component of the transfer matrix of the transmission line for two different lengths of the optimized device arms. In all graphs, red curve is for 100 µm long electrode and green is for 250 µm long electrode.*

The MZI structures are patterned using electron beam lithography (EBL). Fabrication was done on an InP membrane bonded to a silicon substrate (IMOS) with BCB polymer [5]. The thickness of the InP membrane is 300 nm. The fabrication involves four EBL exposures. The first exposure is to define the markers of the pattern for alignment purposes. Then, the exposed pattern of the markers is etched in the semiconductor with an etch depth of 270 nm. In the second exposure, both waveguides and focusing grating couplers are defined and subsequently etched in the semiconductor (The etch depth is again 270 nm). At the third exposure, the 30 nm of the semiconductor remaining is removed from the slot areas and around the metal electrodes, to electrically isolate the structure. The last exposure is to define the metal contacts, which consists of 30 nm Ni / 50 nm Ge / 250 nm Au (Figure 4 (a)). The last step is to spin coat a layer of EO polymer on top of the fabricated sample. Figure 4 (b) shows that the EO polymer filled the narrow slot without leaving any voids.

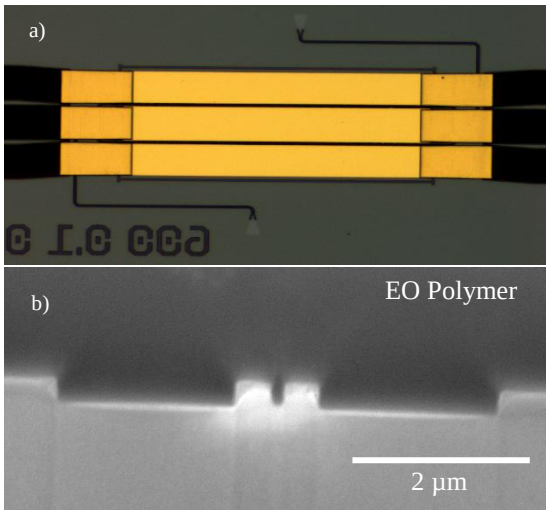



*Figure 2. (a) Fabricated MZI modulator on IMOS platform. (b) FIB cross section cut to check the adhesion properties of the EO polymer to InP surface. Dark gray color is EO polymer. It can be seen that EO polymer completely filled the narrow slot.*

## 4. LOW-FREQUENCY CHARACTERIZATION

EO polymer needs to be poled in order to obtain the electro-optic properties. Poling is a process in which polymeric chains are aligned in the direction of the applied electric field. As shown in Figure 5 (a), this process includes raising the temperature until the glass transition temperature (Tg) of the polymer and cool down slowly with an electric field applied.

After the EO polymer is poled it can induce phase shift if an electric field is applied.

Due to charge screening in the EO polymers, it is not possible to characterize the MZI performance in the DC regime, thus, a kHz-frequency measurement is used instead. In this measurement, a signal with a fixed voltage amplitude (4V) is applied to the electrode and the optical output signal for different bias voltages is recorded. In Figure 5 (b) a sinusoidal behavior of the device under different bias values is illustrated. From the figure it can be inferred the $V_\pi$ is around 3V for 1000 µm long device . Furthermore, from equation 1 the corresponding $r_{33}$ is around 63 $pm / V$.

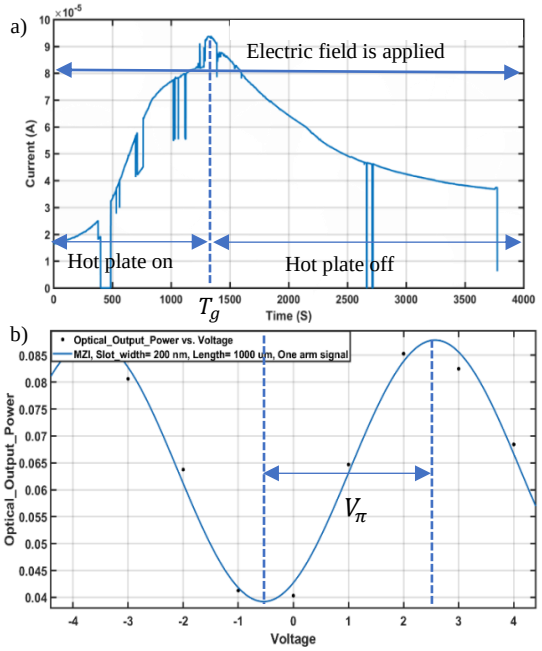



*Figure 3. (a) Poling current of the EO polymer vs time. Temperature is increased with the rate of 7.5 degree/min and after reaching the $T_g$, then left to cool down to ambient temperature while the electric field is applied to the slot. (b) Optical output power vs bias voltage. $V_\pi$ is the half of the voltage difference between two successive peaks.*

## 5. CONCLUSIONS

For the first time, an electro-optic slot waveguide phase modulator in the IMOS platform has been demonstrated. Low-frequency measurements showed we can achieve $V_\pi L_\pi$ equal to 3 V.mm. Currently, high frequency characterization is underway.

## REFERENCES


[1] Feng Qiu et al.: Plate-slot polymer waveguide modulator on silicon-on-insulator, OPTICS EXPRESS, 2018.

[2] Clemens Kieninger et al.: Ultra-high electro-optic activity demonstrated in a silicon-organic hybrid modulator, Optica, 2018

[3] Stefan Wolf et al.: Silicon-Organic Hybrid (SOH) Mach-Zehnder Modulators for 100 Gbit/s on-off Keying. scientific reports, 2018

[4] Naoki Sekine et al.: Investigation of optical loss and bandwidth of InP-organic hybrid optical modulator , Compound Semiconductor Week, 2019

[5] J. J. G. M. van der Tol, et al.: Indium Phosphide Integrated Photonics in Membranes, JSTQE Journal, 2018

[6] Millan Mejia, A. J. et al.: Fabrication technology of a slot waveguide modulator in InP Membranes on Silicon (IMOS) , 18th European Conference on Integrated Optics (ECIO), 2016

# Erbium-doped oxide for optical gain on hybrid silicon photonics platforms

*(Student Paper)*

**Alicia Ruiz-Caridad[1, *], Guillaume Marcaud[1,2], Jianhao Zhang[1], Christian Lafforgue[1], Joan Manel Ramirez[3], Elena Durán-Valdeiglesias[1], Ludovic Largeau[1], Thomas Maroutian[1], Sylvia Matzen[1], Stephane Collin[1], Carlos Alonso-Ramos[1], Guillaume Agnus[1], Sylvain Guerber[1,4], Charles Baudot[4], Frédéric Boeuf[4], Vladyslav Vakarin[1], Eric Cassan[1], Delphine Marris-Morini[1], Philippe Lecoeur[1], Laurent Vivien[1].**

*[1]Centre de Nanosciences et de Nanotechnologies, CNRS, Univ. Paris-Sud, Université Paris-Saclay, C2N - Palaiseau, 91120 Palaiseau, France*
*[2]Now in department of Applied Physics, Yale University, New Haven, CT, USA*
*[3] III-V lab, a joint lab from Nokia Bell Labs, Thales and CEA, 1 avenue Augustin Fresnel, 91767 Palaiseau Cedex*
*[4] TR&D STMicroelectronics SAS, Crolles, 38920, France*

*e-mail: alicia.ruiz-caridad@c2n.upsaclay.fr*

**ABSTRACT**
Increase of power consumption on integrated optical devices for photonic applications has encouraged material engineering to explore new materials and its properties. One of the main challenges on silicon photonics for optical applications is the hybrid integration of these materials due to the lattice mismatch imposed by silicon. In this regard, yttria-stabilized zirconia (YSZ) with a lattice parameter similar to silicon and several functional oxides has been widely studied [1]. Moreover, YSZ waveguides have demonstrated low propagation loss, and no two photon absorption (TPA). Furthermore, it is transparent from the ultraviolet to the near-infrared and exhibit good Kerr effect. It was recently demonstrated about 2 dB/cm propagation losses in waveguides etched on YSZ at a wavelength of 1380 nm [2]. In order to grow an active material as waveguide cladding, we doped YSZ with $Er^{3+}$ ions with a wavelength emission within the C-band of telecommunication window ($\lambda$=1530 nm). In our study, we have considered Er:YSZ cladding deposited by Pulsed Laser Deposition (PLD) on a hybrid $SiN_x$ waveguide. Moreover, we demonstrated guided emission for near-IR transitions of erbium ions under continuous-wave pump laser excitation at 1480 nm. Enhancement of $Er^{3+}$ ion output signal at 1530nm will be discussed and explored and preliminary optical gain will be presented.

**Keywords**: optical gain, integrated optics, silicon platform, rare-earth, oxides, hybrid integration.

## 1. INTRODUCTION

The demand of new materials for more efficient photonic devices for silicon photonics has challenged material engineering to explore new functional materials and its properties comprising superconductivity, magnetism, ferroelectricity, catalytic activity, resistive switching, electro-optic effects, piezoelectricity, or optical nonlinearities, among others [3]-[5]. Hybrid integration on silicon photonics platform demand to overcome lattice constraints imposed by silicon. In this regard, material engineering has proposed and widely studied epitaxial buffer layers for high-crystalline functional oxide grown on silicon to minimize interfaces light scattering and defect density [6]. Yttria-stabilized zirconia (YSZ) is a well-known oxide used as buffer layer of functional oxides. It is widely employed as electrolytes, gas sensors and fuel cells due to its thermal and chemical stability, hardness and mechanical durability. Within the photonics field, YSZ also show promising optical properties putting this buffer oxide under the scope for photonic applications on hybrid platforms [7]-[9]. Other oxides as $LiNbO_3$, $Al_2O_3$ and $Y_2O_3$ [10]-[13] have already demonstrated its optic potential as light sources and optical amplifiers when doped with rare-earth ions to develop new light sources and optical amplifiers. For this purpose, low phononic materials are required to avoid non-radiative effects after doping of the host with rare earth. In order to obtain a high efficient active material, high rare-earth ion doping level is required while avoiding quenching effects and maintaining high crystallinity of the host matrix. Among the rare-earth ions, erbium is preferred for its good solubility in YSZ, as well for its emissions in the near-infrared (near-IR) range of wavelengths, making this rare-earth a perfect candidate for the development of efficient light emitting functional oxides at C-band telecommunication.

To this end, we engineered a YSZ multilayer matrix with two different $Er^{3+}$ ion concentrations to provide a highly luminescent overlayer on top of low-loss SiNx waveguides. Firstly, we have designed the guiding structure at two different wavelengths corresponding to the probe at 1480 nm and to the optical signal according to the $Er^{3+}$ transition at 1530 nm, respectively. Secondly, we optimized $Er^{3+}$-doped layer thickness to provide a trade-off

between optical power confinement of the quasi-transverse electric (quasi-TE) mode in the passive photonic circuitry and its overlap with the active upper layer cladding. Experimentally, under a continuous-wave excitation at 980 nm wavelength and normal incidence excitation, we shown strong luminescence for the $Er^{3+}$ transition that corresponds with the C-band wavelengths harnessed for telecom applications in silicon photonics. Moreover, we also demonstrated guided emission for both visible and near-IR transitions of erbium ions under continuous-wave pump excitation at 1480 nm.

Recently, we demonstrated a propagation loss as low as 2 dB/cm at a wavelength of 1380 nm for YSZ waveguides [14]. In this study, we demonstrated light optical gain at 1.53 µm on a hybrid photonic platform. Firstly, we have grown by means of pulsed laser deposition (PLD) technique a layer Er:YSZ on a pasive silicon nitride (SiNx) buried on SiO2 and we characterized this layer optically by photoluminescence (PL) at 980nm. Secondly, we proved guided emission and optical enhancement for near-IR transitions of erbium ions under continuous-wave pump excitation at 1480 nm.

## 2. EXPERIMENTAL DETAILS

### 3.1. Growth

Pulsed laser deposition (PLD) by means of a KrF excimer laser pumping at 248-nm wavelength, a fluence of 3-J/cm², and at 5-Hz repetition rate was used. Oxide deposition was carried out at high-vacuum on a stainless-steel chamber. Laser alternatively ablates 8 mol %yttria-stabilized zirconia and metallic erbium with a purity higher than 97% by using rotating ceramic targets with an incident angle of 45°. Material is deposited on a substrate placed at 50 mm from the targets on a heated holder. Substrate is heated from room temperature to 800°C at a rate of 10°C/min at an initial pressure of $10^{-6}$Torr. During deposition, constant flux of oxygen is provided to the chamber and holder is then cooled under 300 Torr oxygen at a rate of 10 °C/min.

Wafers of chemical polished 1.4µm silicon dioxide ($SiO_2$) encapsulated silicon nitride ($SiN_x$) waveguides of 600nm height and 700nm width on a silicon platform (Fig. 1 (a)) have been developed following the STM requirements. By PLD, we deposited directly on wafer surface erbium-doped yttria-stabilized zirconia (Er:YSZ) thin films.

### 3.2. Optical characterization

We optically characterized Er:YSZ thin films by means of photoluminescence (PL) on a free-space optical bench using a normal incident scheme (Fig. 1 (b)). Continuous wave of Ti:Sapphire laser at a wavelength of 980-nm and power of 5-mW excites erbium ions perpendicular to the surface of the sample using a microscope objective (not guided PL). Emission and probe are perpendicularly collected by same microscope objective after excitation and focused by a convergent lens of 50-cm focal plane from the detector. Laser wavelength is filtered with a low-pass filter (1100-nm) and only erbium emission in near-IR is detected on a iHR320 spectrometer with a nitrogen-cooled-detector. Er:YSZ thin film photoluminescence (PL) emission profile shows an emission at 1530-nm wavelength corresponding to erbium ion transition $\mathbf{^4I_{13/2} \rightarrow {}^4I_{15/2}}$ (Fig. 1 (c)). A fix laser working at 1480nm **(Fig. 2 (d))**, cooperated with an external optical attenuator is applied as the pump source with a tunable range from 0 to 30dBm. A probe laser at 1530nm is combined with the fix laser though power splitter which output another output is guided into the integrated waveguide through grating coupler. The output power from the sample is directed to the optical spectrum analyser (OSA) for gain record. The characterization is repeated on waveguides with identical cross-section (400nm ×600nm), with different lengths. During the signal enhancement measurements, we observed amplified spontaneous emission and strong green up-conversion in the visible range of wavelengths. After data treatment, optical gain has been studied for three waveguides of different lengths.

## 3. CONCLUSIONS

In this work we have demonstrated a hybrid photonic platform composed by a low-loss $SiN_x$ waveguide cladded by an active Er:YSZ. We have deposited a thin film of Er:YSZ on $SiN_x$ waveguides. We performed optical characterizations by PL perpendicular to the erbium-doped oxide cladding proving emission on the near-IR wavelength corresponding to erbium transition at 1530 nm. We also measured in-plane guided emission of erbium ions on the near-IR wavelengths range by butt-guide-coupling. Finally, we observed optical gain on three different length waveguides.


## 4. ACKNOWLEDGEMENTS

This work has received the funding from the European Research Council (ERC) under the European Union's Horizon 2020 Research and Innovation Program (ERC POPSTAR – grant agreement No 647342) and ANR FOIST project.

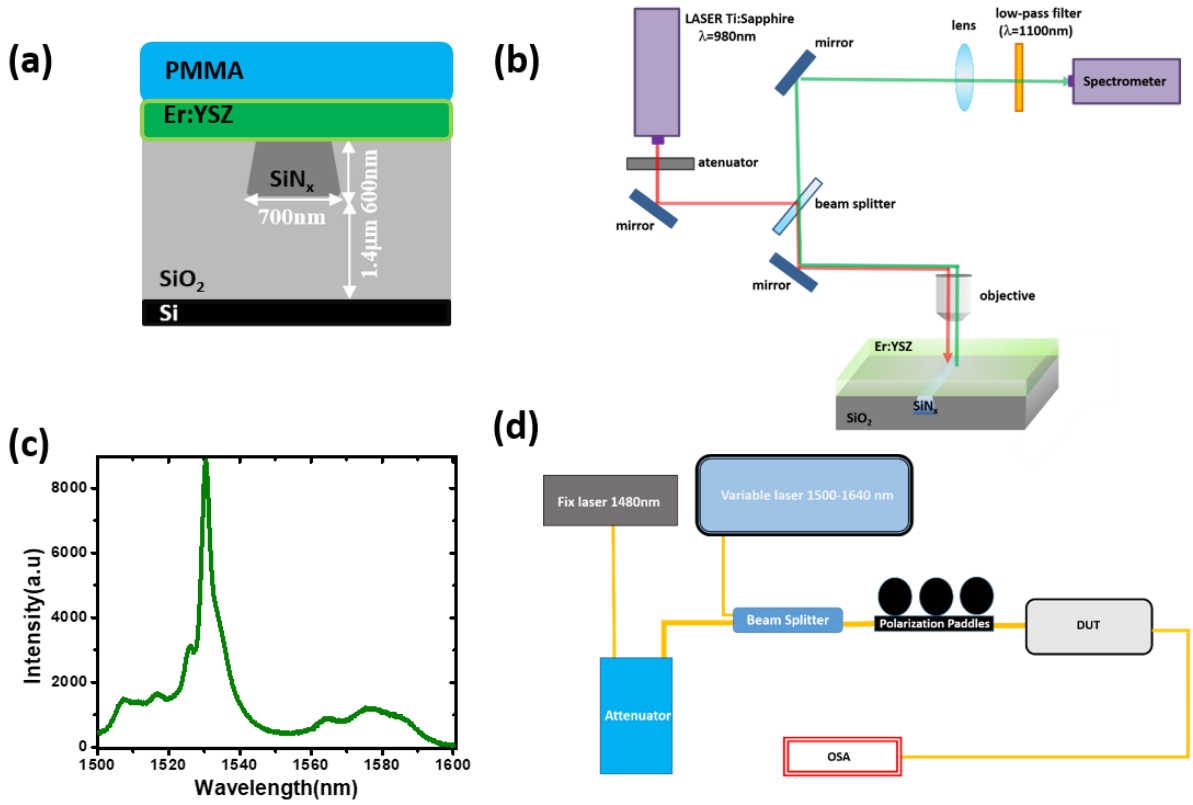



*Figure 1. (a) Cross-sectional schematics views of the hybrid waveguide. (b) PL profile of erbium* $^4I_{13/2} \rightarrow {}^4I_{15/2}$ *transition for Er:YSZ. (c) PL setup. (d) Gain measurement setup.*

## REFERENCES


[1] M. Dekkers et al., Ferroelectric properties of epitaxial Pb(Zr,Ti)$O_3$ thin films on silicon by control of crystal orientation. *Appl. physics letters*, vol. 951, p.012902, Jul. 2009.

[2] Marcaud, G., et al., High-quality crystalline yttria stabilized zirconia thin layer for photonic applications, Rev. Phys. Materials, vol. 2, sp. 035202 , Nov. 2018.

[3] F. Eltes et al., "Monolithic integration of Si/$BaTiO_3$ electro-optic modulators on a silicon photonics platform," *IEEPIEEE Photonics Conference (IPC)*, Reston, VA, 2018, pp. 1-2.

[4] B. Shen et al.,"Broadband couplers for hybrid silicon-chalcogenide glass photonic integrated circuits," *Opt. Express*, vol. 27, pp. 13781-13792, Apr. 2019.

[5] E. Hosseini et al., "CMOS-compatible 75mW erbium-doped distributed feedback laser," *Opt. Lett.*, vol. 39, pp. 3106-3109, May 2014.

[6] H.Y. Hwang, Y. Iwasa, M. Kawasaki, B. Keimer, N. Nagaosa and Y. Tokura,"Emergent phenomena at oxide interfaces," *Nat. Mater.*, vol. 11, pp. 103–113, Jan. 2012.

[7] S. Kim, S.H. Choi and W. Lu," Comprehensive Physical Model of Dynamic Resistive Switching in an Oxide Memristor," *ACS, Nano*, vol. 8, no.3, pp. 2369-2376, Febr. 2014.

[8] M. Ando, K. Kadono, M. Haruta, T. Sakaguchi and M. Miya, "Large third-order optical nonlinearities in transition-metal oxides," *Nature*, vol. 374, pp. 625-627, Apr. 1995.

[9] M. Lorenz et al., "The 2016 oxide electronic materials and oxide interfaces roadmap", *J. Phys. D*, vol. 49, no.43, pp. 9-24, Oct. 2016.

[10] S. Abel et al., "A strong electro-optically active lead-free ferroelectric integrated on silicon", *Nature Comm.*, vol. 4, p. 1671, Apr. 2013.

[11] S. Jun, Y.S. Kim, J. Lee, and Y.W. Kim, "Dielectric properties of strained (Ba, Sr) $TiO_3$ thin films epitaxially grown on Si with thin yttria-stabilized zirconia buffer layer", *Applied Physics Letters*, vol. 78, no. 17, pp. 2542-2544, Apr. 2001.

[12] S. Hashiguchi, E. Min, K. Sakuta K. and T. Kobayashi," YBaCuO thin-film growth on electro-optic LiNbO3 substrate with buffer layer" *Jpn. J. Appl. Phys.*, vol. 31, no. 1, pp. 780-785, Mar. 1992.

[13] R. Laishram,"Role of YSZ buffer layer and $PbTiO_3$ seed layer in the crystallization of PZT on $SiO_2$/Si substrate," *J. Phys. Chem. Solids*, vol. 104, pp. 8-12, May 2017.

[14] T. Wei et al., "Optical spectroscopy and population behavior between $^4$I11/2 and $^4$I13/2 levels of erbium doped germanate glass," *Opt. Mater. Express*, vol. 4, pp. 2150-2165, Sep. 2014.

# Ultra-compact low-power hybrid $VO_2$/Si waveguide switch

*(Student paper)*

Jorge Parra[1], Todora Angelova[1], Mariela Menghini[2,3], Pía Homm[2], Jean-Pierre Locquet[2], Pablo Sanchis[1,*]
[1]*Nanophotonics Technology Center, Universitat Politècnica de València, Camino de Vera s/n, 46022 Valencia, Spain*
[2]*Department of Physics and Astronomy, KU Leuven, Celestijnenlaan 200D, 3001 Leuven, Belgium*
[3]*IMDEA Nanociencia, Calle Faraday 9, E28049, Madrid, Spain*
*e-mail: pabsanki@ntc.upv.es*

## ABSTRACT

Phase change materials such as vanadium dioxide ($VO_2$) could enable new functionalities in the silicon photonics platform. Here, we propose a hybrid $VO_2$/Si waveguide switch enabled by a $SiO_2$ upper-cladding with an on-top microheater. The feasibility of fabricating this device is demonstrated by experimentally depositing a $SiO_2$ upper-cladding with plasma-enhanced chemical vapor deposition (PECVD). Results show power consumption of 260 μW and switching speed of 4.8 μs with an extinction ratio of around 20 dB for a 2-μm-long switch.

**Keywords**: vanadium dioxide, phase change material, microheater, switch, silicon photonics.

## 1 INTRODUCTION

Integration of CMOS-compatible materials with unique properties such as phase change materials in the silicon photonics platforms can enable new functionalities in photonic integrated circuits (PICs) [1]. Among the phase change materials, vanadium dioxide ($VO_2$) exhibit an insulator to metal transition (IMT) that can be triggered by different stimuli such as temperature, light or electric field [2]. Hybrid $VO_2$/Si devices using microheaters to induce the IMT has been demonstrated [3], [4]. However, the power consumption is still too high because the microheaters are not optimally located with respect to the $VO_2$/Si waveguide since they are laterally placed. By using an upper-cladding, the microheater could be placed on top of the hybrid waveguide and thus, the power consumption be drastically reduced.

In this work we design an optimum $VO_2$/Si switch with on-top microheater by using a $SiO_2$ upper-cladding. Furthermore, feasibility of using of using plasma-enhanced chemical vapor deposition (PECVD) for depositing $SiO_2$ without affecting the $VO_2$ properties is experimentally demonstrated.

## 2 SWITCH DESIGN

Fig. 1 depicts the proposed hybrid $VO_2$/Si waveguide switch comprising a silicon waveguide with a $VO_2$ patch on top. The hybrid waveguide switches between a low- and high- loss state when the $VO_2$ is in the insulating and the metallic phase, respectively. The IMT is triggered by placing a microheater on top of the hybrid waveguide. Typically, CMOS-compatible metals are used as heaters in PICs. Hence, the high loss induced by metals requires gaps of around one or two microns. In this case, a transparent conducting oxide such as indium tin oxide (ITO) is utilized. By using a low-loss ITO microheater, the gap between the waveguide and the heater can be reduced to hundreds of nanometres and thus, both power consumption and the switching speed could be improved [5].

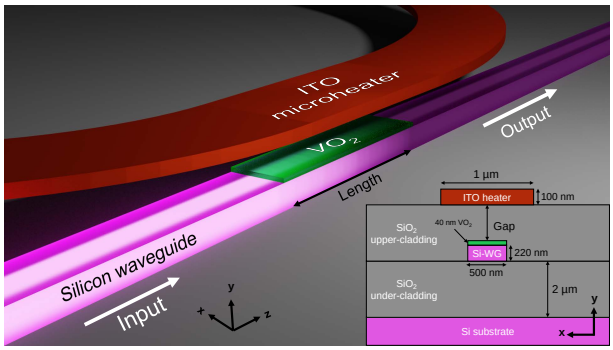
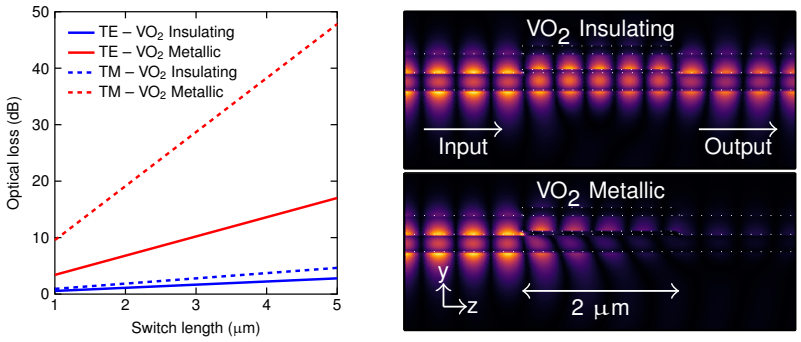



Figure 1: Illustration of the proposed hybrid $VO_2$/Si waveguide switch triggered by an on-top ITO microheater. The inset shows the cross-section of the structure used for simulations




(a) (b)

Figure 2: (a) Optical loss as a function of the switch length for a gap of 200 nm. Results are shown for both polarizations and $VO_2$ states at $\lambda$ = 1550 nm. (b) TM mode propagation, $|E_y|$, through a 2-μm-long switch for both $VO_2$ states and 200 nm gap.

The $VO_2$ IMT is fully achieved for temperatures of around 80 °C. Taking into account that the microheater temperature depends inversely with its length for a given power consumption, the latter could be decreased by shortening the $VO_2$/Si switch. Finite element method (FEM) simulations were carried out to obtain the temperature steady state and temporal response. Simulations were done considering values for the gap ranging between 200 nm and 2 μm. On one hand, the power consumption per unit length ranges between 130 and 270 μW μm$^{-1}$. Because of the low thermal conductivity of $SiO_2$, power consumptions lower than the milliwatt can be achieved if the switch length is in the order of microns. On the other hand, rise/fall times of the switch go from 4.8 to 16.6 μs. Therefore, small gaps are highly preferred since the power consumption and switching speed could be two- and three- fold improved, respectively.

The influence of the ITO heater optical loss was investigated by calculating the optical mode of the switch for TE and TM polarization and both $VO_2$ states. Optical modes were obtained by FEM and using refractive index values of $3.21 + j0.17$ and $2.15 + j2.79$ for $VO_2$ in the insulating and metallic states, respectively [6]. Due to the ultra-low optical loss of ITO, optical losses are ultimately determined by the $VO_2$. Therefore, gaps as low as 200 nm can be used. Fig. 2a shows optical loss as a function of the switch length for a 200 nm gap. For a 2-μm-long switch and TM polarization, optical losses of 1.86 and 19.13 dB for the insulating and metallic states could be attained, respectively, with a power consumption of 260 μW and a switching speed of 4.8 μs. The optical behaviour was confirmed by 3D finite-difference time-domain (3D-FDTD) simulations as depicted in Fig. 2b.

## 3 EXPERIMENTAL RESULTS

### 3.1 $VO_2$ Optical Properties with a $SiO_2$ PECVD cladding

Covering the $VO_2$ with a $SiO_2$ cladding by PECVD has been reported not to be possible because the IMT would be supressed, with the $VO_2$ layer stabilized to the metallic phase even at room temperature [7]. In the present work, however, we have been able to keep $VO_2$ properties after being covered by $SiO_2$ using PECVD.

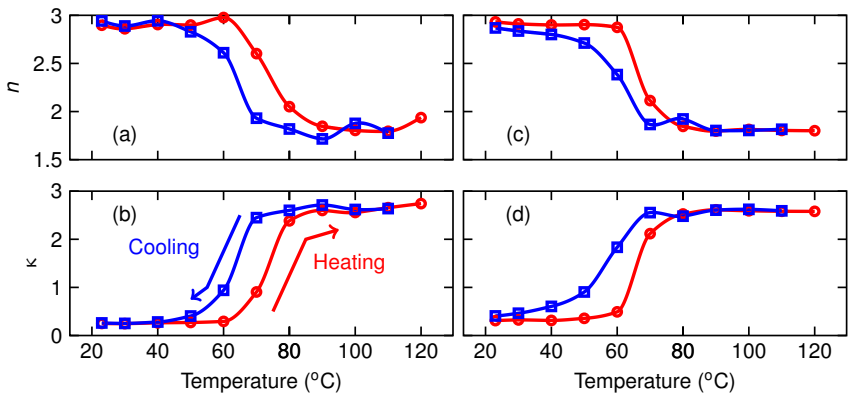
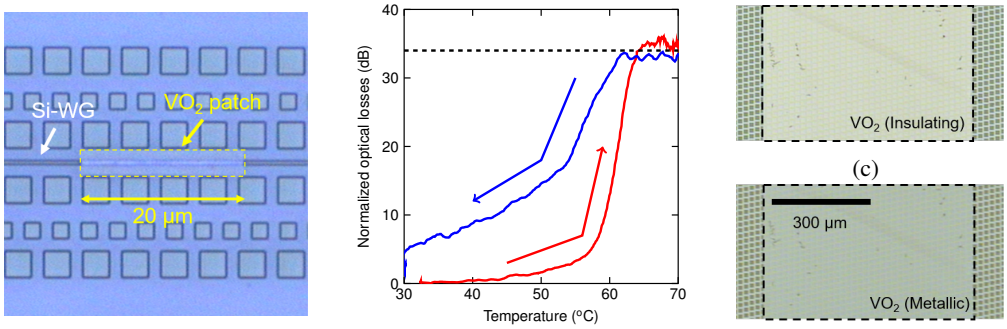



Figure 3: $VO_2$ complex refractive index, $n + j\kappa$, at $\lambda = 1550$ nm as a function of the temperature for: (a,b) air and (c,d) 700-nm-thick $SiO_2$ claddings.




(a) (b) (c) (d)

Figure 4: (a) Optical image of the hybrid $VO_2$/Si waveguide covered with 700 nm $SiO_2$ deposited by PECVD. (b) TE normalized losses as a function of the temperature. Dashed line stands for the noise floor of the photodetector. (c,d) Optical images of a $VO_2$ patch at (c) 30 ºC and (d) 80 ºC.

A 40-nm-thick $VO_2$ layer was grown by molecular beam epitaxy (MBE) on a silicon substrate. The sample was characterized by spectroscopic ellipsometry on a hot plate heated between room temperature and 120 ºC. Then, a 700-nm-thick $SiO_2$ cladding was deposited by PECVD and characterized using the same method. Fig. 3 show the obtained refractive index of the $VO_2$ layer with air and $SiO_2$ claddings as a function of the temperature. As it can be noticed, for both claddings, the $VO_2$ exhibits the IMT around 60 ºC with similar values on the refractive index.

### 3.2 On-chip Thermo-optic Tuning Performance of the Switch

The performance on-chip of the $VO_2$ covered with $SiO_2$ by PECVD was also investigated. The same thickness $VO_2$ and $SiO_2$ upper-claddings layers were deposited on silicon waveguides (Fig. 4a). The phase change of the $VO_2$ was achieved by heating the sample with a Peltier. Fig. 4b shows the normalized optical losses for TE polarization and a 20-µm-long switch. Similar IMT was obtained, though in this case, the induced optical losses in the metallic state were limited by the noise floor of the photodetector. Because of this, the IMT stops at around 65 ºC whereas in ellipsometry measurements stopped around 80 ºC. Finally, the IMT of $VO_2$ was also confirmed by observing a change in both color and transparency as shown in Figs. 4c and 4d.

## 4 CONCLUSIONS

In this work, an ultra-compact and ultra-low power absorption switch has been proposed by using a $VO_2$/Si waveguide. Both features are enabled by using a $SiO_2$ upper-cladding with a low-loss ITO microheater on top. Results show an extinction ratio of around 20 dB between the $VO_2$ insulating and metallic states for a 2-µm-long switch together with a power consumption of 260 µs and switching speed of few microseconds. Furthermore, the feasibility of using PECVD for depositing the $SiO_2$ upper-cladding has been experimentally on-chip demonstrated.

## ACKNOWLEDGMENTS

Funding from projects TEC2016-76849 (MINECO/FEDER, UE) and PROMETEO/2019/123 (Generalitat Valenciana) is acknowledged. Jorge Parra also acknowledges Ministerio de Ciencia, Innovación y Universidades for funding his predoctoral research grant (FPU17/04224).

## REFERENCES

[1] K. J. Miller, R. F. Haglund, and S. M. Weiss, "Optical phase change materials in integrated silicon photonic devices: review," *Optical Materials Express*, vol. 8, no. 8, p. 2415, 2018.

[2] K. Liu, S. Lee, S. Yang, O. Delaire, and J. Wu, "Recent progresses on physics and applications of vanadium dioxide," *Materials Today*, vol. 21, no. 8, pp. 875–896, 2018.

[3] I. Olivares, L. Sánchez, J. Parra, R. Larrea, A. Griol, M. Menghini, P. Homm, L.-W. Jang, B. van Bilzen, J. W. Seo, J.-P. Locquet, and P. Sanchis, "Optical switching in hybrid VO2/Si waveguides thermally triggered by lateral microheaters," *Optics Express*, vol. 26, no. 10, p. 12387, 2018.

[4] L. D. Sánchez, I. Olivares, J. Parra, M. Menghini, P. Homm, J.-P. Locquet, and P. Sanchis, "Experimental demonstration of a tunable transverse electric pass polarizer based on hybrid VO2/silicon technology," *Optics Letters*, vol. 43, no. 15, p. 3650, 2018.

[5] J. Parra, J. Hurtado, A. Griol, and P. Sanchis, "Ultra-low loss hybrid ITO/Si heater with optimized power consumption," *Submitted*.

[6] R. M. Briggs, I. M. Pryce, and H. A. Atwater, "Compact silicon photonic waveguide modulator based on the vanadium dioxide metal-insulator phase transition," *Optics Express*, vol. 18, no. 11, p. 11192, 2010.

[7] K. Shibuya, Y. Atsumi, T. Yoshida, Y. Sakakibara, M. Mori, and A. Sawa, "Silicon waveguide optical modulator driven by metal–insulator transition of vanadium dioxide cladding layer," *Optics Express*, vol. 27, no. 4, p. 4147, 2019.

# Broadband Compact Single-Pole Double-Throw Silicon Photonic MEMS Switch

*(Student Paper)*

**Alain Y. Takabayashi[1], Hamed Sattari[1], Pierre Edinger[2], Peter Verheyen[3], Kristinn B. Gylfason[2], Wim Bogaerts[4], Niels Quack[1]**

[1] École Polytechnique Fédérale de Lausanne (EPFL), CH-1015 Lausanne, Switzerland
[2] KTH Royal Institute of Technology, Malvinas väg 10, SE-100 44 Stockholm, Sweden
[3] IMEC, 3DSIP Department, Si Photonics Group, Leuven, Belgium
[4] Ghent University – IMEC, Department of Information Technology, Photonics Research Group, Technologiepark-Zwijnaarde 15, 9052 Ghent, Belgium
*e-mail: alain.takabayashi@epfl.ch*

## ABSTRACT

We demonstrate a photonic Single-Pole Double-Throw (SPDT) switch based on electrostatically actuated MEMS waveguides implemented in IMEC's ISiPP50G silicon photonics platform with custom MEMS release post-processing. An average Extinction Ratio (ER) > 23 dB is maintained over a 70 nm bandwidth with a peak ER of 25 dB at 1550 nm while an actuation voltage of 22 V is applied to the curved electrode electrostatic actuator of the device. A compact footprint of 30 µm × 60 µm and a low Insertion Loss (IL) allow for device integration in larger switch networks.

**Keywords**: Microelectromechanical Systems, Photonic Integrated Circuits, Silicon Photonics, Photonics

## 1. INTRODUCTION

An elementary, yet important function in Photonic Integrated Circuits (PIC) is the ability to actively switch and re-route optical signals on-chip. Switching in PICs is commonly implemented by exploiting the electro-optic, thermo-optic, or free carrier dispersion effect. However, since the magnitude of these effects is typically weak in silicon, conventional switches tend to occupy significant area or require bandwidth-limiting resonant photonic structures and exhibit significant power consumption, thereby prohibiting the scaling to very large PICs. In contrast, mechanically displacing waveguides is a physical mechanism for low-power and scalable approach for implementing photonic switches [1, 2]. Microelectromechanical systems (MEMS) technology provides a convenient means to obtain the desired mechanical translation. Previous demonstrations of large-scale silicon photonic MEMS switch networks exploiting multi-layer, out-of-plane actuated waveguides have shown scalability up to 240 × 240 in- and output ports [3].

Here we present an electrostatic, in-plane 1×2 silicon photonic MEMS switch with a Singe-Pole Double-Throw (SPDT) topology. The device is designed within IMEC's iSiPP50G silicon photonics platform and we make use of a custom post-processing step to provide freestanding MEMS waveguides [2]. This approach allows integration of the silicon photonic MEMS switch with a wealth of standard passive and active components such as low-loss waveguides, electrical wiring, modulators and high-speed detectors. Our device has a compact footprint and exhibits broadband behaviour making it suitable for inclusion in large-scale on-chip optical switch networks.

## 2. WORKING PRINCIPLE, DESIGN AND SIMULATION

SPDT switches are well known in the field of electronics for providing three states: (1) an OFF state, (2) input to a first output, and (3) input to a second output. Oberhammer et al. implemented a MEMS-based SPDT switch for electrical signals with three cantilevers moving in-plane under the influence of two curved electrodes, which provide an optimal force-to-size balance [4]. Here we introduce the photonic equivalent of the SPDT switch: as shown in Fig. 1a), the "single-pole" refers to the one physically movable input waveguide and the "double-throw" is represented by the two static output waveguides. The movable waveguide is anchored on its left side and is free to move in-plane under the influence of an applied actuation voltage to the top or bottom electrodes. Mechanical stoppers limit the maximum deflection of the input to prevent pull-in of the MEMS actuator. The anchors are designed to minimize optical losses when transiting from the suspended air-clad waveguide region to the fully oxide-clad region. The coupling regions on each waveguide (i.e., free ends) are adiabatically tapered to reduce coupling length and achieve broadband behaviour. In the OFF state, the input waveguide is separated by a 400 nm gap from either output waveguide and residual power coupling is equally split between the two outputs. After actuation, the gap between the input and the respective output decreases while the complementary gap increases,

thereby transferring power to one branch only. Optical simulations Fig. 1b) confirm efficient power transfer from the input to the first output while keeping the optical mode well confined.

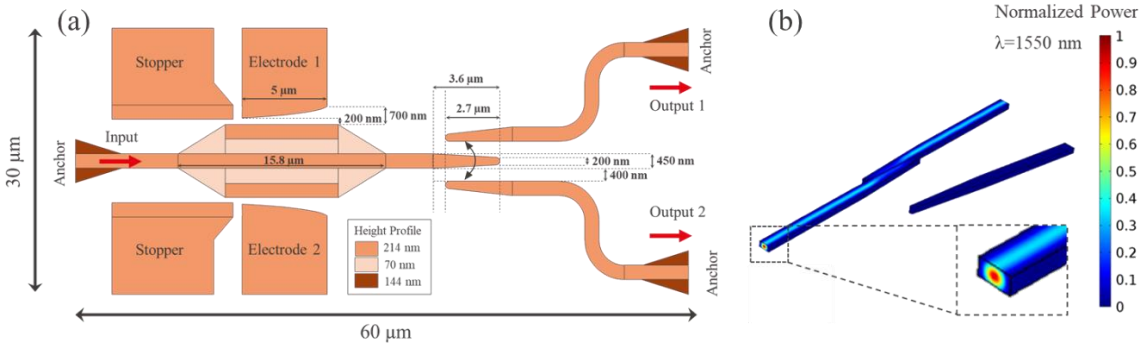



*Figure 1. a) Geometry of the MEMS-based photonic SPDT switch exhibiting a compact footprint (dimensions not to scale), and b) optical simulation showing efficient power transfer from the input waveguide to output 1.*

## 3. FABRICATION

The silicon photonics structures are fabricated in IMEC's iSiPP50G technology and the MEMS release process is performed at EPFL at the Center of MicroNanoTechnology (CMi). The release employs a previously demonstrated process sequence of protective alumina layer deposition, etch window opening, and vapour-phase HF sacrificial oxide etch [2]. An optical microscope image of the chip area showing the switch, the grating couplers serving as optical interfaces, the electrical metal wiring (to electrical contact pads outside of the visible area), as well as the opening in the alumina passivation is provided in Fig.1a). The metal ring, which partially obstructs the view of the underlying waveguide routing is implemented in the final top-metallization and is intended for a later sealing step of the MEMS not used here. Figure 2b) shows an SEM image of the final, released device with the suspended input waveguide well centred between the two output waveguides.

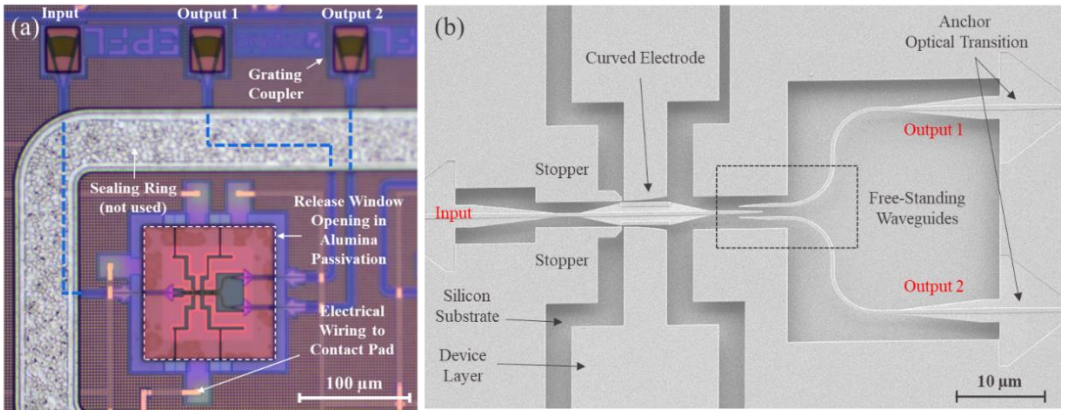



*Figure 2. a) Optical microscope image showing an overview of the device, including grating couplers, electrical wiring and MEMS release window opening. b) SEM image of the released optical SPDT switch, highlighting the freestanding silicon waveguides, curved electrostatic actuation electrodes, and mechanical stoppers.*

## 4. EXPERIMENT

Characterization is performed using a tuneable wavelength laser that is connected to a fibre array, which couples light into and out of the chip by means of the on-chip grating couplers shown in Fig. 2a). Power transmission to the two output ports is read using photodetectors and is recorded for a wavelength sweep from 1510 nm to 1580 nm. Electrical probe tips allow for the application of an actuation voltage in the range of 0 to 22 V to contact pads wired on-chip to either electrode 1 or electrode 2 to produce the desired actuation.

As shown in Fig. 3, when no actuation voltage is applied, passive power coupling is observed in both waveguides. The amount of coupled residual power can be designed by appropriate distance and direction of the coupling waveguides. Under ideal conditions, the power split should be even, however, we observe a difference of typically 3 dB in residual power coupled to the two output ports. We attribute this disparity to differences in the mechanical boundary conditions at the anchor points after release that cause the input waveguide to bend preferentially to output port 1 without any applied voltage. In addition, there may also be loss variations in the optical path between the two outputs related to the transitions or grating couplers. Such asymmetry also provides an explanation as to why the power transfer to the active port is not exactly the same for the two ON states. By

increasing the applied voltage on electrode 1 or 2, the input waveguide is electrostatically pulled towards the respective output port where most of the power is transferred through direct coupling. Removing the actuation voltage allows the input waveguide to return to its initial state and by applying an actuation voltage to the opposite electrode, the power transfer characteristic is reversed.

Measurements indicate excellent broadband behaviour, as indicated by an average ER > 23 dB that is maintained over almost the entire wavelength sweep of 70 nm for both actuation states. We observe an ER of 25 dB at 1550 nm, the central wavelength for which this device has been designed to operate. Simulations predict an IL of less than 0.1 dB, yet measurements of such low insertion loss proved not reliable with our measurement setup due to variations in the coupling of the fibre array to the grating couplers.

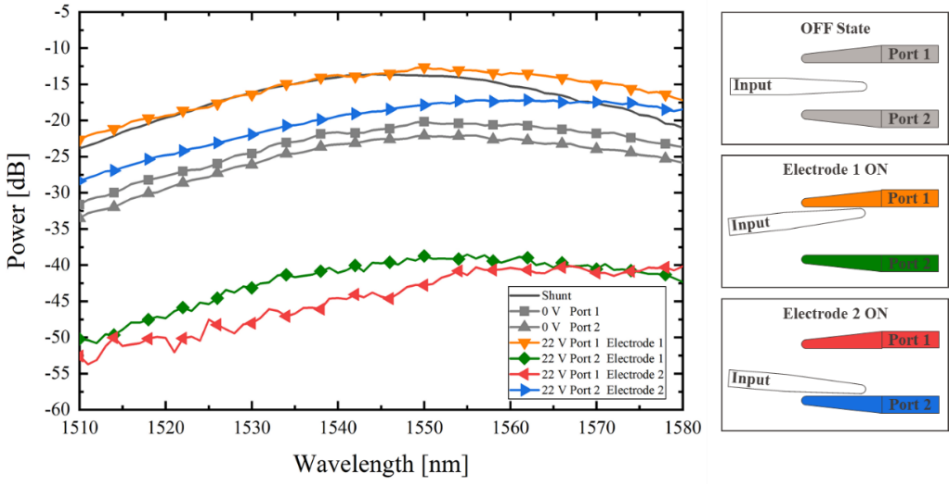



*Figure 3. Transmission spectrum of the Silicon Photonic MEMS Single-Pole Double-Throw switch for the respective OFF, and the two ON states, redirecting the light to either output 1 or output 2.*

## 5. CONCLUSION

We present the design, fabrication, and characterization of a novel SPDT Silicon Photonic MEMS switch in an established silicon photonics platform with custom MEMS post-processing. The device can transition between three distinct states by applying an actuation voltage of 22 V to generate an electrostatic force that induces mechanical modulation of the coupling behaviour between input and output waveguides. The device exhibits > 23 dB ER over a 70 nm bandwidth and an ER of 25 dB at the designed 1550 nm wavelength for both ON states. The IL, although not definitively quantifiable in the current experimental setup due to non-uniformity in the grating couplers is expected to be very low from simulations and initial qualitative measurements. As demonstrated, the unique SPDT topology allows this device to be used as a digital switch to completely redirect optical power from the input to either output port. This device could also potentially be used as an analog power coupler to vary the power distribution between the input and output ports by applying intermediate voltages between 0 and 22 V. Overall, the broadband and compact characteristics of our switch, combined with the high ER and low IL, make it a promising new component for large-scale on-chip photonic switch networks.

## ACKNOWLEDGEMENTS

This project has received funding from the European Union's Horizon 2020 research and innovation programme under grant agreement No. 780283 (MORPHIC – www.h2020morphic.eu). H. Sattari acknowledges funding from the Hasler Foundation under grant No. 17008.

## REFERENCES

[1] C. Errando-Herranz, A. Y. Takabayashi, P. Edinger, H. Sattari, K. B. Gylfason, and N. Quack, "MEMS for Photonic Integrated Circuits," IEEE Journal of Selected Topics in Quantum Electronics, vol. 26, no. 2, pp. 1–16, Mar. 2020, doi: 10.1109/JSTQE.2019.2943384.

[2] N. Quack et al., "MEMS-Enabled Silicon Photonic Integrated Devices and Circuits," IEEE Journal of Quantum Electronics, vol. 56, no. 1, pp. 1–10, Feb. 2020, doi: 10.1109/JQE.2019.2946841.

[3] T. J. Seok, K. Kwon, J. Henriksson, J. Luo, and M. C. Wu, "Wafer-scale silicon photonic switches beyond die size limit," Optica, OPTICA, vol. 6, no. 4, pp. 490–494, Apr. 2019, doi: 10.1364/OPTICA.6.000490.

[4] J. Oberhammer, M. Tang, A. Q. Liu, and G. Stemme, "Mechanically Tri-Stable In-Line Single-Pole-Double-Throw All-Metal Switch," in 19th IEEE International Conference on Micro Electro Mechanical Systems, 2006, pp. 898–901, doi: 10.1109/MEMSYS.2006.1627945.

# Application-specific Scaling in Programmable Photonic Circuits

*(Student Paper)*

Iman Zand [1,2] Xiangfeng Chen [1,2] Wim Bogaerts [1,2]
[1]*Photonics Research Group, Department of Information Technology, Ghent University-IMEC, 9052 Ghent, Belgium*
[2]*Center of Nano and Biophotonics, Ghent University, 9052 Ghent, Belgium*
*e-mail: wim.bogaerts@ugent.be*

## ABSTRACT

We performed a scaling analysis of programmable hexagonal two-dimensional (2D) waveguide meshes with different shapes. We show that the shape of the meshes can impose restrictions such as high path losses or large foot-prints for certain configurations and applications. We use the graph-based strategy to guide our application-specific scaling analysis. The design practices are discussed for implementing the programmable mesh for beam splitters and $N \times N$ switches. This will provide a guideline of the shape and size for the future programmable photonic circuits.

**Keywords**: programmable photonic circuits, scaling analysis, hexagonal waveguide meshes, beam splitters, switches, graph-based strategy

## 1 INTRODUCTION

Programmable photonic integrated circuits (PIC) [1], at their core, consist of a linear optical processor, which allows arbitrary linear transformations between optical ports. This can be implemented as a circuit mesh composed of tunable couplers and phase shifters, which can be 'programmed' to perform routing or filter functions. One of the important choices in the design of such programmable meshes is their size and shape; in fact, scaling of meshes can cause adverse parasitic effects, high loss, or large footprint of the photonic circuit [2]. Here, we explore how shape of such meshes influences their scaling and the programming of desired functions.

## 2 METHODOLOGY

We start from a mesh with hexagonal unit cells for our 2D meshes as proposed in [3] and organize the unit cells in a radial, square, or rectangular fashion, as shown in Fig. 1a. We add "whiskers" with an additional tunable coupler on all boundaries. In these designs, we assume that each cell has three phase shifters which are connected to the couplers through waveguides. The expansion parameters (i.e. how the mesh grows) for a radial, square, and rectangular mesh are $r$, $w$, and $(a, b)$, respectively.

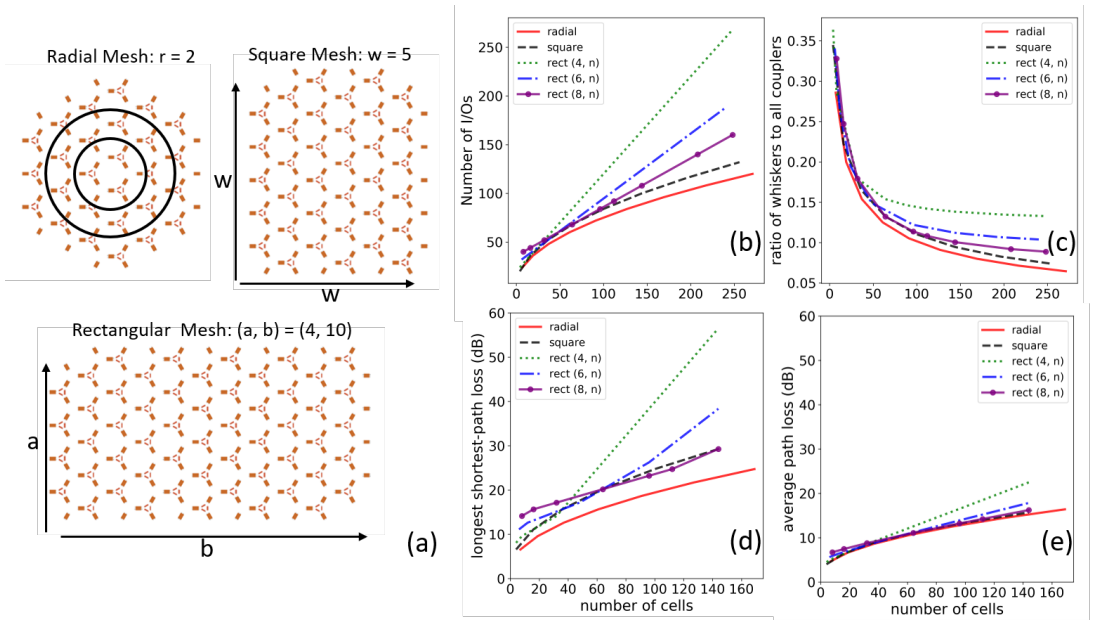



Figure 1. a) Schematic of the waveguide meshes using hexagonal topology and with radial, square, and rectangular shape. b) Number of ports, c) Ratio of the whiskers to all couplers (edge to area ratio), d) Loss of the longest shortest-path, e) Average path loss . Here, we have considered three types of the rectangular meshes with fixed number of rows ($b$=4, 6, 8).

## 3 MESH PROPERTIES

For the scaling analysis, we consider four mesh properties: (1) the number of I/O's, (2) the ratio of edge-to-area indicated by the number of whiskers divided by the number of couplers, (3) the loss of the longest shortest-path (i.e. the longest straight path between two ports on the edge, which is an important metric for routing performance), and (4) average loss of the mesh (Fig. 1(b-d). The loss calculations are based on recent results on silicon photonic MEMS devices from the MORPHIC project, estimated as 0.75 dB for the paths segment loss [4], [5]. smallest average distance of the ports from each other. As a result, it shows the lowest loss for the longest shortest path. Moreover, the radial mesh has a lower average path loss indicating a lower loss for multi routing. While the radial mesh scales better in terms of losses, it may impose restrictions for some applications, which will be discussed later. Meshes with a higher edge-to-area ratio have a worse scaling behavior.

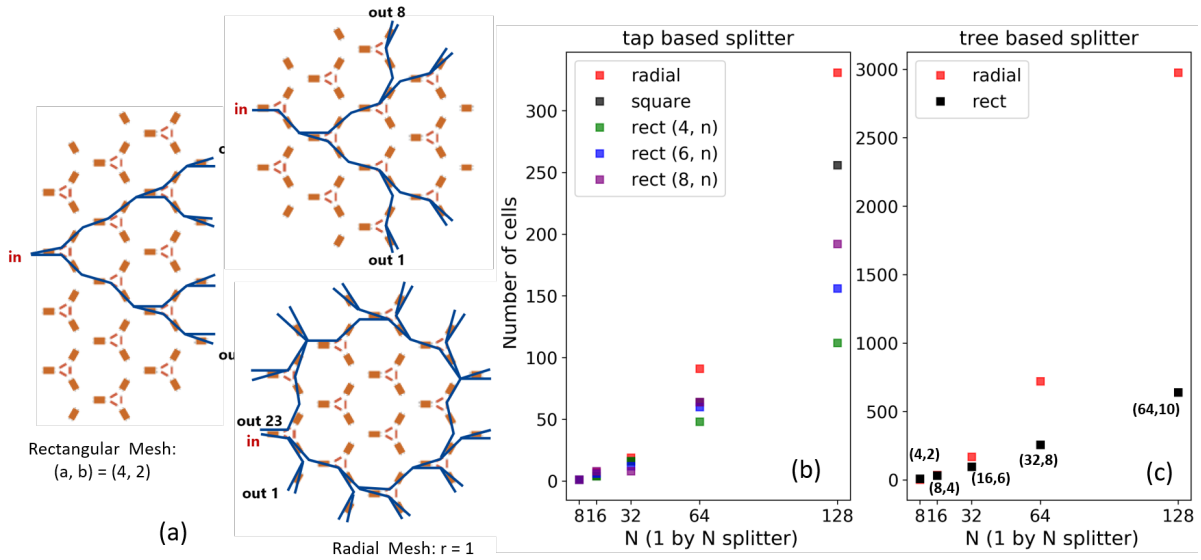



Figure 2. a) Schematics of a $1 \times 8$ tree-based beam splitter in rectangular and radial meshes; and, also, a $1 \times 23$ tap-based beam splitter in radial mesh ($r = 2$). The number of cells of different meshes required to b) configure tap-based $1 \times N$ beam splitters in radial, square, and three different rectangular meshes. c) tree-based $1 \times N$ beam splitters in radial and rectangular meshes with $(a, b) = (4, 2), (8, 4), (16, 6), (32, 8), (64, 10)$.

## 4 SCALING FOR DIFFERENT APPLICATIONS

### 4.1 Beam Splitters

One of the important functions in a programmable mesh is a splitter network for multicasting or the distribution network for an optical beam former. Here, *tap-based* and *tree-based* beam splitters have been studied in the meshes shown in Fig. 1a. Figure 2a shows a few examples of splitter implementations in radial and rectangular meshes. Tap-based splitters do not have balanced paths but can lead to a more compact mesh; a radial mesh with $r = 1$ can support a $1 \times 23$ tap-based beam splitter, while in a fully balanced tree it can only be programmed for a $1 \times 8$ splitter. For the different mesh shapes we calculated the required size of the mesh to implement a tap or tree-based splitter with different numbers of outputs. Comparing the results of tap-based splitters for different mesh shapes (Fig. 2b) shows that a steady increase of the mesh foot print for the tap-based splitter, and this effect is even more adverse for the tree-based splitter (Fig. 2c). Results show that using rectangular meshes provides better splitting performance compared to the radial meshes.

### 4.2 $N \times N$ Switching Circuits

The programmable mesh with a rectangular shape scales up in both directions $(a, b)$ to enable $N \times N$ switching. In Fig. 3, we provide an example graph representation [6] for such hexagonal mesh with $(a, b) = (8, 7)$. The degrees of freedom for the choice of input-output ports of a switch circuit is large. An $N \times N$ means that any input can be connected to any output on a one-to-one basis. It quickly becomes computationally expensive to route all these possible pair combinations. Thus, we assume that if a mesh can allocate $N$ input-output pairs in both full-parallel and full-diagonal assignment, it can probably allocate the full $N \times N$ switch circuit. For example, Fig. 3a-b shows simultaneous multi routing for 8 input-output pairs in parallel and in

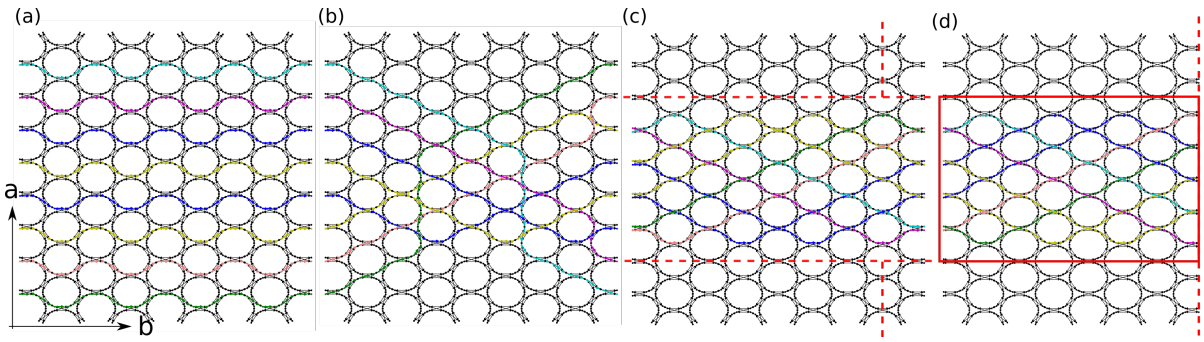



Figure 3. Graph-based routing in a rectangular-shaped meshes with $7 \times 8$ hexagonal cells. (a) Multi-routing finding the shortest paths routing for 8 input-output pairs in parallel and (b) in diagonal assignment. (b) shows a sparse use of 16 input-output ports (one per whisker) while (c) shows a dense use (two per whisker). The boundaries in dashed red lines shows the reduction in required mesh size, which is further improved in (d), representing the minimum mesh size to implement $8 \times 8$ switching

diagonal assignment, with a sparse assignment of inputs and outputs (one per whisker). We observe that every path will cross 7 other paths in Fig. 3b. so, as long as we reserve sufficient crossing couplers, we can reduce the cell number $a$ in vertical direction, as shown in Fig. 3c. For a given number of inputs/outputs, we use heuristic-based congestion negotiation algorithms to sweep the values of both $a$ and $b$. These simulations verify that the minimal size mesh for an $N \times N$ switch from left to right has boundary conditions as the mesh scales up: When $b$ is an odd number as in Fig. 3c, the East side is symmetric with the West side, whereas when $b$ is an even number as in Fig. 3d, the East side has more output ports than the West side. We choose the symmetrical configuration as the minimal requirement: solutions are found when $b \geq N - 1$ ( $b$ odd) and $a \geq N/2$. When $b$ is even, the conditions are $b \geq N - 2$ and $a \geq N/2$. If the mesh is smaller than these conditions, generic left-to-right switching is no longer guaranteed.

## 5 CONCLUSION

We performed a scaling analysis for 2D waveguide meshes with different shapes (based on hexagonal unit cells). Simulation results show that the shape of the meshes can considerably affect the loss scaling and restrict the implementation of application-specific functions such as beam splitters and $N \times N$ switches. This paper provides a design guideline for the future programmable photonic circuits.

## ACKNOWLEDGEMENTS

This work was funded by the EU through grant 780283 (MORPHIC) and 725555 (PhotonicSWARM)

## REFERENCES

[1] D. Pérez, I. Gasulla, and J. Capmany, "Programmable multifunctional integrated nanophotonics - Review Article," *De Gruyter - Nanophotonics 2018*, vol. 7, no. 8, pp. 1351–1371, 2018.

[2] I. Zand and W. Bogaerts, "Effects of Coupling and Phase Imperfections in Programmable Photonic Hexagonal Waveguide Meshes," *Photonics Research*, vol. 8, no. 2, 2019.

[3] D. Pérez, I. Gasulla, J. Capmany, and R. A. Soref, "Reconfigurable lattice mesh designs for programmable photonic processors," *Optics Express*, vol. 24, no. 11, p. 12093, 2016.

[4] W. Bogaerts, H. Sattari, P. Edinger, Y. A. Takabayashi, I. Zand, X. Wang, A. Ribeiro, M. Jezzini, C. Errando-Herranz, G. Talli, K. Saurav, M. Garcia Porcel, P. Verheyen, B. Abasahl, F. Niklaus, N. Quack, K. B. Gylfason, P. O'Brien, and U. Khan, "MORPHIC : Programmable photonic circuits enabled by silicon photonic MEMS," *Proc. SPIE*, vol. 11285, pp. 11 285–1, 2020.

[5] C. Errando-Herranz, A. Y. Takabayashi, P. Edinger, H. Sattari, K. B. Gylfason, and N. Quack, "MEMS for Photonic Integrated Circuits," *IEEE Journal of Selected Topics in Quantum Electronics*, vol. 26, no. 2, pp. 1–1, 2019.

[6] X. Chen and W. Bogaerts, "ME2.2 - A Graph-based Design and Programming Strategy for Reconfigurable Photonic Circuits," *2019 IEEE Photonics Society Summer Topical Meeting Series (SUM)*, pp. 1–2, 2019.

# Recursive MZI mesh for integral equation implementation

*(Student Paper)*

**Maziyar Milanizadeh[1], Elena Damiani[1], Tigers Jonuzi[1], Mario Junior Mencagli[2], Brian Edwards[3], David A.B. Miller[4], Nader Engheta[3], Andrea Melloni[1], Francesco Morichetti[1]**

[1]Dipartimento di Elettronica, Informazione e Bioingegneria - Politecnico di Milano, Milano, 20133 Italy.
[2]Dept. of Electrical and Computer Engineering - UNC at Charlotte, Charlotte, NC 28223, USA
[3]Department of ESE - University of Pennsylvania, Philadelphia, Pennsylvania, 19104, USA
[4]Ginzton Laboratory - Stanford University, Spilker Building, Stanford, CA 94305, USA
*mail: maziyar.milanizadeh@polimi.it*

**ABSTRACT**

In this work we present a photonic integrated circuit based on a mesh of Mach-Zehnder Interferometers (MZIs) acting as a programmable photonic equation solver. The working principle is demonstrated by numerical simulations showing all-optical solution of a Fredholm integral equation. A thermally actuated circuit is fabricated on a silicon platform demonstrating the feasibility and programmability of the proposed device concept. Circuit calibration has been experimentally demonstrated and validated by simulations.

**Keywords**: silicon photonics, reconfigurable PIC, Fredholm integral equations, optical analogue computing

## 1. INTRODUCTION

Lately, there has been an increasing interest in programmable photonic integrated circuits (PICs) that can be reconfigured during operation to perform different linear functions. For instance, meshes of Mach-Zehnder interferometers (MZIs) [1] have been successfully used in a wide range of applications, such as mode-division multiplexing and demultiplexing, imaging, beam steering, quantum information processing and deep learning.

In this work, we exploit programmable meshes of silicon MZIs to bring to photonics the concept of an equation solver that has been recently demonstrated in the microwave domain by using a suitably engineered metamaterial [2,3]. With respect to this pioneering demonstration, photonics offers the benefits of footprint reduction, higher scalability to more complex systems of equations, programmability and wider bandwidth. As a proof-of-concept demonstrator, we conceived a recursive photonic circuit made of a 3x3 mesh of silicon MZIs enclosed in an array of optical feedback loops, which can be thermally programmed to solve systems of Fredholm integral equations of the second kind with arbitrary unitary kernels.

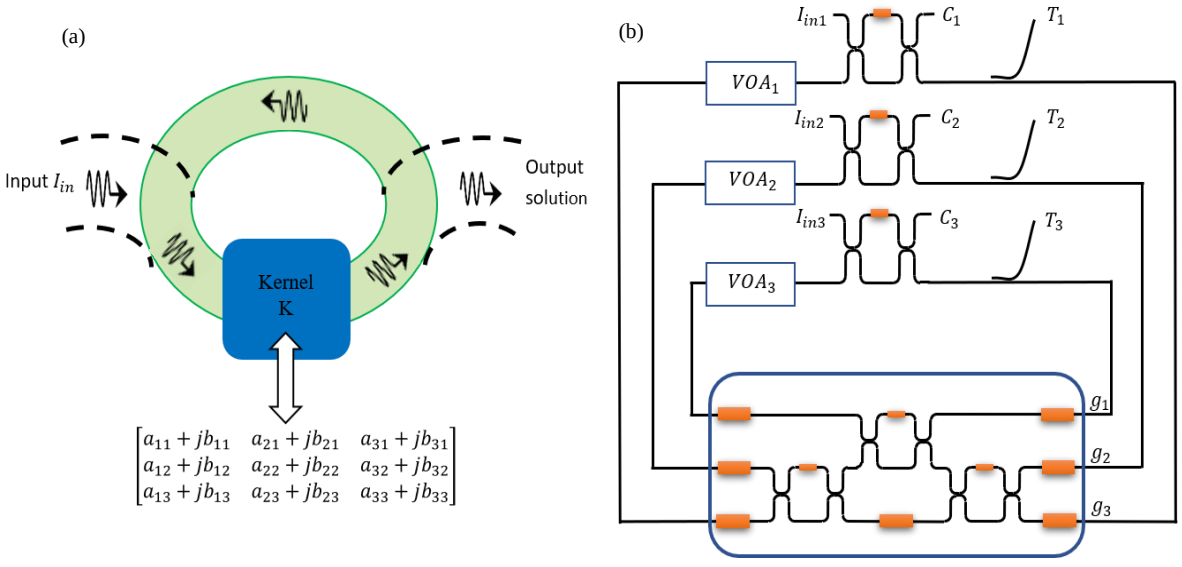



Figure 1: Programmable photonic equation solver: (a) schematic concept of the device and (b) circuit topology of the PIC. A mesh of tunable couplers implementing the programmable kernel K is enclosed in a feedback loop array of optical waveguides.

## 2. RECURSIVE MZI MESH

Figure 1 shows the schematic concept of the proposed equation solver PIC (a) together with its photonic circuit topology (b). A triangular mesh of MZI is used to implement a programmable kernel (K) and a feedback network of optical waveguides is used to make the light recirculate through the kernel. This scheme recalls the recursive solution of a Fredholm integral equation of second kind as expressed in equation (1):

$$g(x,t) = I_{in}(x,t) + \int K(x,y)\, g(y,t)\, dy. \quad (1)$$

where $I_{in}(x,t)$ is the vector containing the complex amplitudes of the optical field at the input ports and $g(x,t)$ are the optical fields at the beginning of the kernel. In the considered 3x3 mesh implementation, $x$ and $y$ take discrete integer values {1, 2, 3} labelling the corresponding waveguide loops. Each optical input $I_{in}(x,t)$ is coupled to the feedback loops by means of tunable couplers realized by using balanced MZIs. The kernel is composed of three MZIs each with two phase shifters for the implementation of amplitude- and phase-tunable couplers. Additional phase actuators are used to adjust the round-trip phase of each loop. Therefore, nine phase-shifters are enough to implement any unitary matrix of arbitrary complex amplitudes. Variable optical attenuators (VOAs) are also integrated in the feedback loops to either compensate for differential loss or to provide additional degrees of freedom for PIC tuning. It should be noted that, since the optical inputs need to be injected in the device through optical couplers, the optical response of the circuits approaches the integral equation (1) only when these coupling ratios are reasonably small (typically < 10%).

As an example, consider a kernel implementing a frequency domain Fourier-based tritter matrix [4] as expressed in equation (2):

$$K = \frac{1}{\sqrt{3}} \begin{bmatrix} e^{j\frac{2\pi}{3}} & e^{j\frac{4\pi}{3}} & e^{j2\pi} \\ e^{j\frac{4\pi}{3}} & e^{j\frac{8\pi}{3}} & e^{j4\pi} \\ e^{j2\pi} & e^{j4\pi} & e^{j6\pi} \end{bmatrix} \quad (2)$$

The solution *g(x,t)* of equation (1) is provided by the complex-amplitude distribution of optical waves at the input of the kernel or equivalently by their frequency domain expression *g(x,f)*. The information is then extracted by 10% taps. Figure 2 shows the comparison between the intensity (a) and phase (b) of *g(x,f)* as calculated by numerically solving equation (1) (solid lines) and by simulating the optical response of the PIC of Fig. 1b. In the considered case the optical inputs are set to $I_{in}(x,f) = [0\ \ 0\ \ 1]$ at any wavelength, the input tunable couplers are 10% and all the feedback loops share the same round trip phase. Due to the presence of three loops, the frequency domain response exhibits three resonance peaks, whose wavelength position is given by the phase terms of the kernel. By selecting a specific wavelength (e.g. λ = 1556.909 nm), the steady state solution to a CW input vector is found, as shown in Fig. 2c.

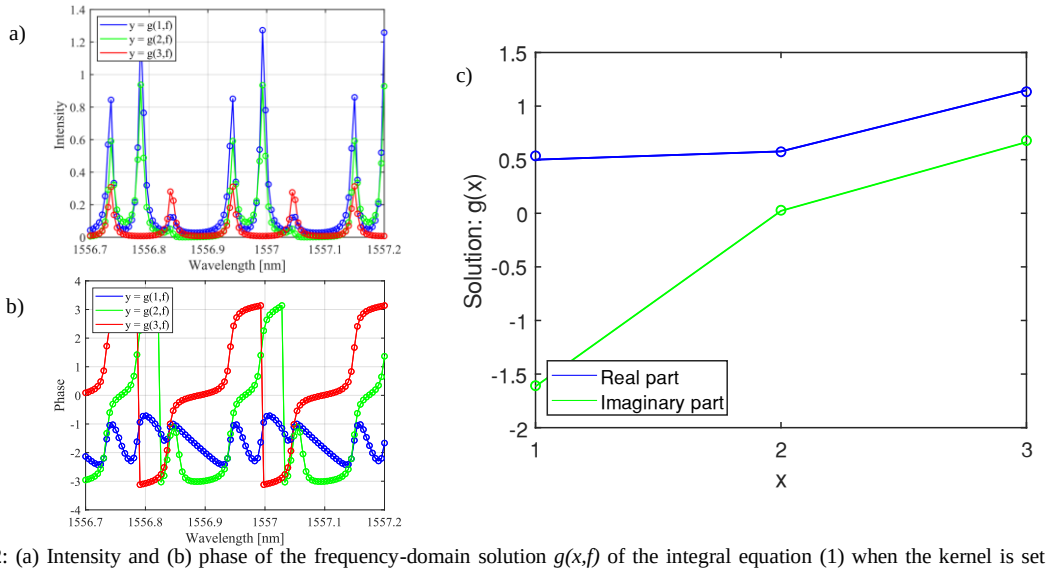



Figure 2: (a) Intensity and (b) phase of the frequency-domain solution *g(x,f)* of the integral equation (1) when the kernel is set to a Fourier-based tritter matrix, all the non-linearities considered. Comparison between the analytical solution (solid lines) and numerical simulation of the photonic equation solver (circles). (c) Comparison between the real (blue) and imaginary (green) part of the analytical solution (solid line) and of the numerical simulation of the photonic equation solver (circles) at a wavelength of 1556.909 nm.

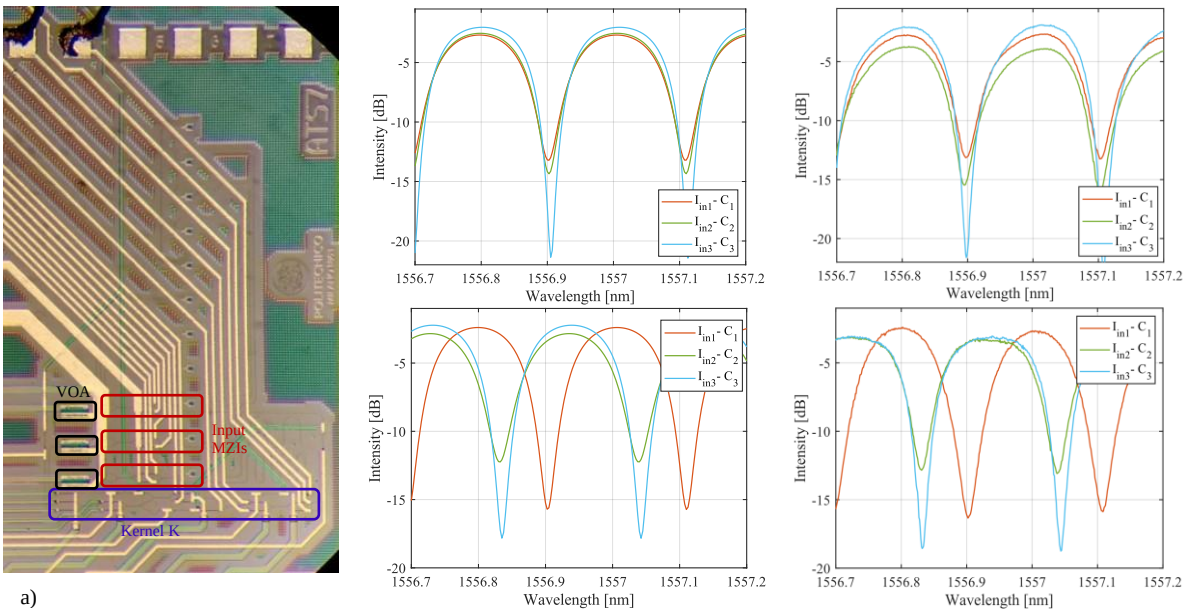
## 3. EXPERIMENTAL RESULTS AND KERNEL CALIBRATION

A proof-of-concept demonstrator of the programmable photonic equation solver was realized on a standard 220 nm silicon photonic platform (AMF, Singapore). The tunable couplers of the 3x3 programmable kernel, as well as those used to couple the optical inputs to the PIC, are realized by means of thermally tunable balanced MZIs. The feedback loops share the same physical length of 2786.869 $\mu$m, providing a free spectral range of 0.214 nm, and the overall device footprint is 1.1 x 1.48 mm$^2$. Figure 3a shows a top-view picture of the photonic chip assembled on an electronic printed circuit board (PCB) hosting the drivers of the thermal tuners.

Preliminary tests were carried out to demonstrate the possibility to program the kernels and bring the PIC to the desired working point. Targeting the implementation of the tritter matrix of equation (2), a specific algorithm

was developed to set the thermal tuners of the 3x3 mesh to the required phase shift. Implementing a three-way beamsplitter matrix means splitting equally the optical power at the three outputs, therefore, the upper interferometer of the mesh must be set at 67% split ratio while the other two MZIs should work as 50% splitters. The implemented calibration procedure implies a sequential injection of the light from the tunable MZIs ($I_{in1}$ - $I_{in3}$ ports) and the acquisition of the optical spectrum from the output ports ($C_1$ - $C_3$). Once the desired intensity response of the mesh is achieved, the phase response must be adjusted, also taking into consideration phase contribution given by fabrication tolerances. In order to have robust phase control, strategies to mitigate thermal crosstalk among thermal tuners can be also adopted [5].

Figure 3 shows the simulated (b) and measured (c) frequency domain response of the device when the 3x3 mesh operates as a three-way beamsplitter and all the feedback loops are set to resonate at the same frequency. Each curve in the plot corresponds to a different input ($I_i$) - output ($C_i$) pair. From this condition, the phases of the kernel elements can be adjusted by exploiting the feedback loops as integrated interferometers, mapping phase shifts to resonance wavelength shift. For instance, Fig. 3d shows the effect of an additional $2\pi/3$ shift in the elements $K_{11}$ and $K_{22}$, resulting in a wavelength shift of FSR/3, that is 0.071 nm. The agreement between the expected and the observed behaviour demonstrates the possibility of programming the mesh to any arbitrarily complex kernel.




a)

Figure 3: (a) Top view photograph of our bonded chip mounted on its specific PCB. (b) Optical simulation results of the spectrum collected at the MZIs port ($C_1$-$C_3$) when the mesh is configured (in amplitude) as a tritter matrix, so that the power is split equally in the three output waveguides. (c) Experimental results when the mesh represents the three-way beamsplitter matrix. See comparison with (b). (d) Optical simulation results of the spectrum collected at the MZIs port ($C_1$-$C_3$) port when the main diagonal phases of the tritter matrix are set. (e) Experimental results when also the main diagonal phases are considered. See comparison with (c).

## 4. CONCLUSION

We developed a programmable photonic integrated equation solver based on meshes of MZI. This concept is used to solve a Fourier-based tritter matrix and results are compared with analytical solutions. We presented precise calibration of the fabricated circuit to implement a desired transformation and results are validated by simulation. Experimental activities for implementation of specific integral equation are ongoing.

*M.J.M., B.E., D.A.B.M., and N.E. acknowledge the support from the US Air Force Office of Scientific Research (AFOSR) Multidisciplinary University Research Initiative (MURI) grant # FA9550-17-1-0002.*

## REFERENCES

[1] Miller, D. A. B. (2013). Self-configuring universal linear optical component. *Photonics Research*, *1*(1), 1-15.

[2] Estakhri, N. M., Edwards, B., & Engheta, N. (2019). Inverse-designed metastructures that solve equations. *Science*, *363*(6433), 1333-1338.

[3] Mencagli, M. J., Estakhri, N. M., Edwards, B., & Engheta, N. (2018, May). Solving Equations with Waves in Collections of Mach-Zehnder Interferometers. In *2018 Conference on Lasers and Electro-Optics (CLEO)* (pp. 1-2). IEEE.

[4] Miller, D. A. B. (2015). Perfect optics with imperfect components. *Optica*, *2*(8), 747-750.

[5] Milanizadeh, M., Aguiar, D., Melloni, A., & Morichetti, F. (2019). Cancelling thermal cross-talk effects in photonic integrated circuits. *Journal of Lightwave Technology*, *37*(4), 1325-1332.

# Statistical analysis of passive components manufactured in a thick silicon nitride platform

*(Student Paper)*

**Juan Fernández[1,2], Joan Felip[1], Jose Serrano[1], Raffaele Caroselli[1], Bernardo Gargallo[1], David Domenech[1], Pascual Muñoz[1,2]**

[1] VLC Photonics S.L., c/ Camino de Vera s/n – 46022, Valencia – Spain

[2] Universitat Politènica de València, c/ Camino de Vera s/n – 46022, Valencia – Spain

*e-mail: juan.fernandez@vlcphotonics.com*

## ABSTRACT

In this paper, the statistical analysis of the measurements of passive components manufactured in a thick silicon nitride platform is presented. The devices studied are Asymmetric Mach-Zehnder interferometers (AMZI) and 1x2 and 2x2 Multimode Interference Couplers (MMI). Components from four different Multi-Project-Wafer runs [1], have been designed, manufactured and tested. Each run yielded two wafers and two dies per wafer have been measured and reported. The Asymmetric Mach-Zehnder interferometers were used to evaluate the propagation parameters of the strip waveguides employed in the designs. These parameters are: the propagation losses, the modal effective index and the group index. The multimode interference couplers (MMI) have been employed to evaluate the fabrication tolerances. By collecting and evaluating this statistical data across multiple dies, wafers and runs we have concluded that the designs evaluated are robust and the manufacturing process is stable within the tolerances provided by the foundry. This is fundamental for high-volume, high-yield commercial applications for future market developments in thick silicon nitride platforms as quantum, comb generations, LIDAR systems, etc.

**Keywords**: thick silicon nitride, silicon nitride, yield, manufacturing.

## 1. INTRODUCTION

Photonic devices performance is very sensitive to geometrical variations in the mid/high index contrast platforms. These variations have a direct impact on the spectral response of the different building blocks and it requires an in-depth statistical analysis of the manufactured and tested devices. The increasing of photonic integrated market demands fabrication tolerant building blocks and an extensive yield analysis [2-3]. Thick silicon nitride is a promising technology due to its intrinsic properties as anomalous dispersion in C band, low loss for TE and TM polarizations, compactness, low bending radius and operation from visible to mid infrared band [4].

Different techniques are employed in the fabrication of photonic integrated circuits (PICs) to physically evaluate the geometrical definition of the waveguides composing the circuits. From Critical-Dimension Scanning Electron Microscopy (CD-SEM) in the lithography tools to post fabrication analysis with Atomic Forces Microscopy (AFM). In this work, the optical characterization of interferometric devices [5] is employed to derive the fabrication deviations in the waveguides of a thick silicon nitride platform.

## 2. MZI measurements

The Free Spectral Range (FSR) and the resonance wavelength of an AMZI are related to the effective and group index of the waveguides through the formulae:

$$\lambda_{res} = \frac{n_{eff0} \cdot \Delta L}{m}, \qquad FSR = \frac{\lambda_{res}^2}{n_g \cdot \Delta L}$$

Being $m$ the order of MZI resonance, $\lambda_{res}$ the central wavelength of the resonance, $n_{eff0}$ the effective index at this wavelength, $n_g$ the group index of the waveguide, $\Delta L$ the incremental length of the waveguide and $FSR$ the distance in nanometers between two adjacent resonances. With a combination of different order AMZIs the effective and group indices of their waveguides can be accurately obtained [5].

A test cell has been designed, manufactured and characterized in 4 different Multi Project Wafer runs in the Ligentec platform employing the PDK co-developed with VLC Photonics [1]. The standard test die has a size of 5x10 mm². Several 1x2 and 2x2 multimode interference couplers (MMIs) and AMZIs employing the 2x2 MMI couplers with FSRs of 8, 12 and 20 nm have been included in the test cell for every run. The measurements of

the MMIs show a broadband operation with low imbalance and the MZI devices show in some cases more than 40 dB of rejection ratio. In general, the performance of the components is in good agreement with the simulations.

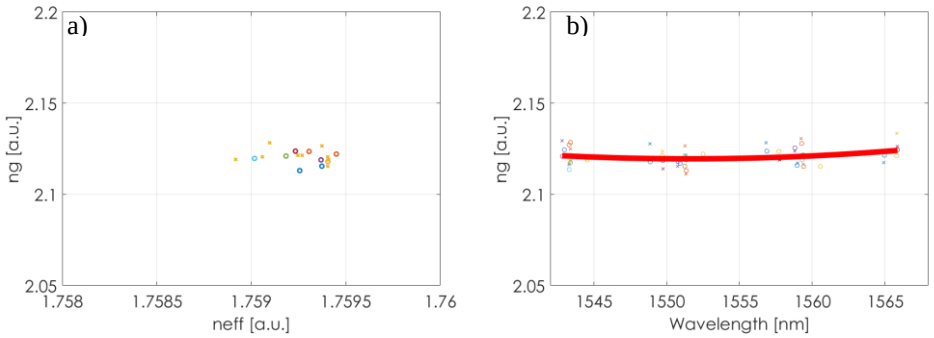



Figure 1. (a) $N_{eff}$ vs $n_g$ at 1550 nm, (b) $n_g$ vs wavelength measured

Figure 1-(a) shows the effective index versus group index at 1550 nm wavelength. The mean value of the effective index is 1.75925 ± 2.5e-4. In figure 1-(b), the group index versus wavelength is plotted. The mean value is 2.119 ± 9e-3. It can be observed that the group index variation is larger due to the fact that there are a small number of points in wavelength. This can be solved by having an AMZI device with a smaller FSR.

TABLE 1. Comparative of $n_g$, $n_{eff}$ and incremental length

| FSR | Sim. $n_g$ [a.u] | Sim. $n_{eff0}$ [a.u.] | $\Delta L$ [µm] | $m$ [a.u] | Meas. $n_g$ [a.u] | Meas. $n_{eff0}$ [µm] |
|---|---|---|---|---|---|---|
| 20 | 2.1166 | 1.7585 | 56.744 | 64 | [2.11-2.128] | [1.7589-1.7594] |
| 12 | 2.1166 | 1.7585 | 94.590 | 107 | [2.11-2.128] | [1.7589-1.7594] |
| 8 | 2.1166 | 1.7585 | 141.88 | 160-161 | [2.11-2.128] | [1.7589-1.7594] |

Table 1 includes a comparison of simulated and measured effective and group indices of the manufactured MZIs. The standard deviation of the measured values matches perfectly with the expected shift in the indices due to the fabrication tolerances according to the foundry process. A remarkable observation of the data is the shift of effective index in median of about 5e-4. To investigate this shift, an extensive set of simulations were performed sweeping over different waveguide widths and heights. A model for the effective and group indices has been developed to fit the indices as a function of waveguide widths and heights.

$$n_{eff}(1550nm) = 1.285 + 0.5099 \cdot w + 0.1472 \cdot h - 0.1883 \cdot w^2 + 0.04167$$
$$n_g(1550nm) = 1.964 + 0.2078 \cdot w + 0.1167 \cdot h - 0.0833 \cdot w^2 - 0.0833 \cdot w$$

From the model obtained, it can be derived that an increase in width of 50 nm or an increase in the height of 12 nm can explain this shift of the effective index.

### 2.1 MMI 1x2 and MMI 2x2

MMIs are fabrication tolerant devices when compared to other power splitters [6-10]. Figure 2 shows the response across eight wafers and sixteen dies from four different fabrication runs (two wafers per run, 4 dies measured per wafer) of the imbalance and the excess losses calculated from the transmission measurements.

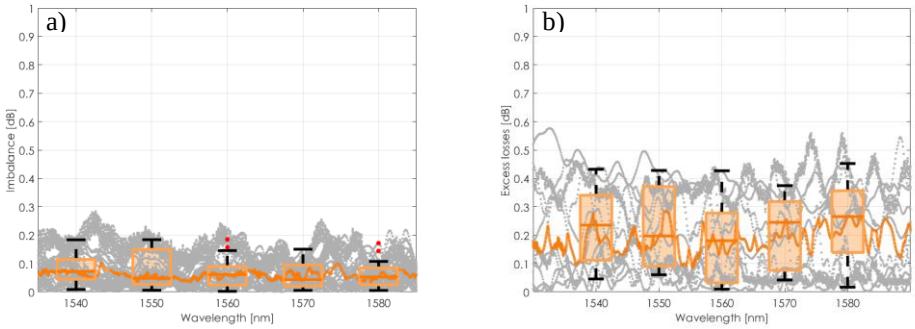



Figure 2. MMI 1x2 (a) imbalance and (b) excess losses

The median of imbalance, as shown in Fig. 2-(a), is below 0.1 dB and the median of the excess losses is kept below 0.3 dB as depicted in Fig. 2-(b) for the 60 nm wavelength range under study.

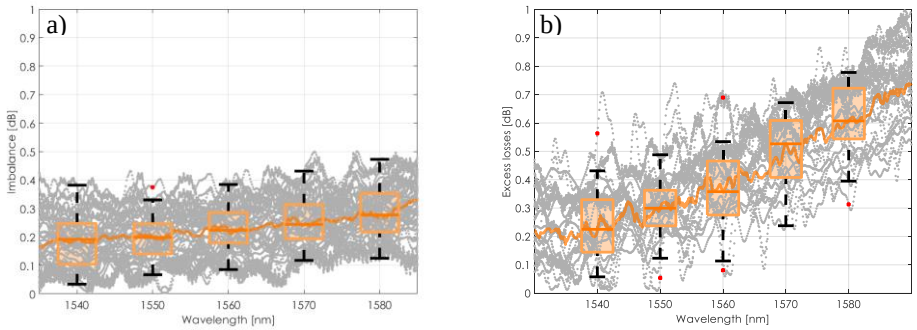



Figure 3. MMI 2x2 (a) imbalance and (b) excess losses

Figure 3 provides imbalance and excess losses versus wavelength for MMI 2x2. Interestingly, the imbalance median is below 0.3 dB in the wavelength range evaluated. The most striking observation is that the minimum of the excess losses is centered below 1530 nm. An analysis of the MMI simulations showed that a deviation of 50 nm in width could explain this shift in the minimum peak value of the excess losses that has to be around 1550 nm. With this information we have been able to conclude that if the MMI is shortened 2 microns in length, the excess losses response will improve at 1550 nm wavelength.

## 3. CONCLUSIONS

The statistical study of the basic building blocks measurements, designed and fabricated in a thick silicon nitride platform has been performed to evaluate the impact of the process variability in the components performance. A theoretical model for the effective and group index of the silicon nitride waveguides has been employed to correlate the measured data with the waveguide width and height deviations expected from the fabrication process. With the analysis of the measurement data of the 1x2 and 2x2 MMIS we have demonstrated the robustness of the designs against the variation tolerances of the fabrication platform. This statistical analysis can be employed to improve the design of the components.

## ACKNOWLEDGEMENTS

The authors acknowledge the fabrication of the silicon nitride dies to Ligentec S.A. Juan Fernandez acknowledges the financial support through project MINECO Doctorado Industrial DI_15-08031 and through the UPV Spin-off, VLC Photonics S.L.

## REFERENCES

[1] Ligente MPW runs: https://www.ligentec.com/ligentec-foundry/
[2] W. Bogaerts et al., “Layout-aware variability analysis, yield prediction, and optimization in photonic integrated circuits”. IEEE Journal of Selected Topics in Quantum Electronics, 25(5), 1-13 (2019).
[3] Lu, Zeqin, et al. "Performance prediction for silicon photonics integrated circuits with layout-dependent correlated manufacturing variability." Optics express 25.9 (2017): 9712-9733.
[4] P. Muñoz et. al., “Silicon nitride photonic integration platforms for visible, near-infrared and mid-infrared applications”, Sensors, 17(9), 2088 (2017).
[5] Y. Xing et. al. “Hierarchical model for spatial variations of integrated photonics” In 2018 IEEE 15th International Conference on Group IV Photonics (GFP) (pp. 1-2).
[6] Bachmann, Maurus, Pierre A. Besse, and Hans Melchior. "General self-imaging properties in N× N multimode interference couplers including phase relations." Applied optics 33.18: 3905-3911. (1994)
[7] Besse, P. A., Bachmann, M., Melchior, H., Soldano, L. B., & Smit, M. K. (1994). Optical bandwidth and fabrication tolerances of multimode interference couplers. Journal of Lightwave Technology, 12(6), 1004-1009.
[8] Soldano, L. B. et.al. “Optical multi-mode interference devices based on self-imaging: principles and applications” Journal of lightwave technology, 13(4), 615-627. (1995)
[9] Hanfoug, Rabah, et al. "Reduced reflections from multimode interference couplers." Electronics letters 42.8 (2006): 465-466.
[10] Gottesman, Y., E. V. K. Rao, and B. Dagens. "A novel design proposal to minimize reflections in deep-ridge multimode interference couplers." IEEE Photonics Technology Letters 12.12 (2000): 1662-1664.

# Polarization insensitive tunable hitless filter for extended C band

*(Student Paper)*

**Maziyar Milanizadeh, Matteo Petrini, Francesco Morichetti and Andrea Melloni**
Dipartimento di Elettronica, Informazione e Bioingegneria - Politecnico di Milano,
Milano, 20133 Italy

*e-mail: andrea.melloni@polimi.it*

## ABSTRACT

Controllable loss induced through variable optical attenuators integrated in microring resonators is exploited to implement a novel hitless tuning scheme for silicon photonic WDM filters. The proposed concept is demonstrated in a polarization insensitive architecture operating across the extended C-band.

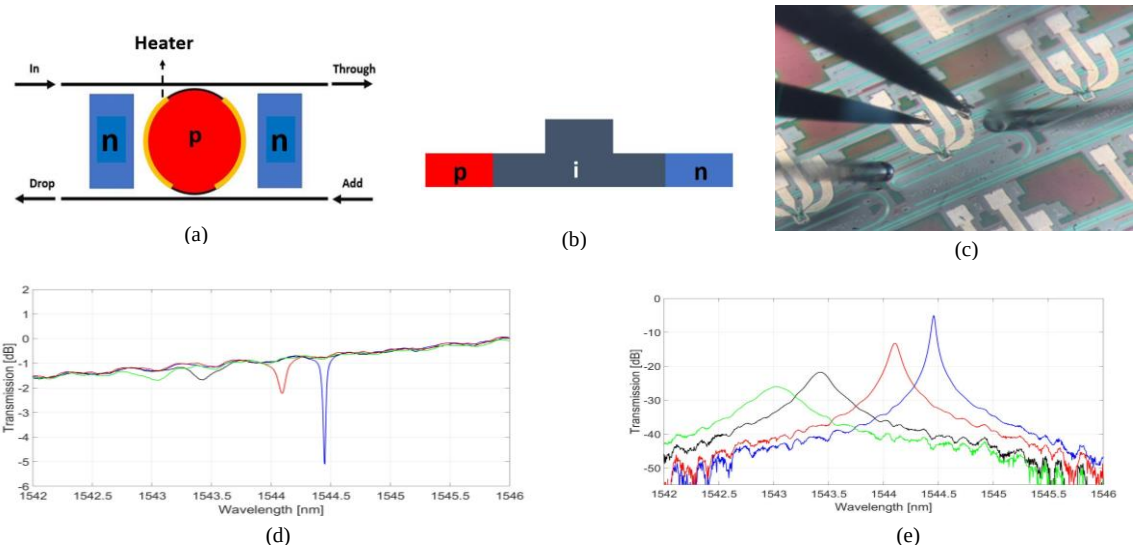
**Keywords**: Photonic Integrated Circuits, Silicon Photonics, Ring Resonators, Optical Add Drop, Hitless Filters.

## 1. INTRODUCTION

Tuneable optical filters are key functional building blocks of optical networks, where flexible allocation of WDM channels and dynamic channel routing between network nodes is required. Although silicon photonics is a promising platform for the realization of WDM filters, many issues have limited its use in real applications. Among all, the need for wide band filter tuneability (at least across the C telecom band), the possibility of implementing hitless tuning (that is without affecting other channels propagating in the same link) and the inherent polarization sensitivity of silicon waveguides have represented major limiting factors to their real implementation. Although several solutions have been proposed for the realization of silicon photonics hitlessly tuneable WDM filters [1], no one so far was demonstrated to solve all the above mentioned issues.

In this work we present a novel hitless tuning scheme for silicon photonic coupled-resonator WDM filters operating across the extended C-band. The proposed strategy exploits controllable loss induced through variable optical p-i-n attenuators integrated in the microring resonators, rather than tuneable couplers and/or selective detuning. These two techniques rely on phase shift applied to single parts of the system, which can lead to unwanted critical coupling issues, disrupting non resonant channels.

The proposed tuning concept is demonstrated in a 4$^{th}$ order filter, designed according to a new Vernier-based technique in order to provide wide FSR operation (> 100 nm) [2], which is integrated in a polarization diversity scheme guaranteeing polarization insensitive channel filtering.




(a) (b) (c) (d) (e)

Figure 1: (a) Scheme of a single microring resonator with integrated p-i-n junction, acting as VOA. (b) Cross section of the waveguide the ring resonator is made by. (c) Microscope photograph of the ring with VOA and heater under test. (d) Through port disconnection steps, the voltages applied to the p-n junction are 0 V (blue function), 1 V (red), 1.5 V (black), 2 V (green). (e) Drop port disconnection steps, same voltages as figure (c)

## 2. Disconnection Mechanism for Hitless Tuning

In this section we present a novel disconnection mechanism, in order to effectively perform hitless tuning. While tuning from a channel to another the filter has to be disconnected from the bus waveguide, to avoid any disturbance in the channels between the starting position and the target one.

Since selective detuning and tuneable couplers can lead to unwanted critical coupling, we are going to present an approach that relies on the dismantlement of the resonance peaks, decreasing directly the power flowing inside the rings. This is possible implementing a Variable Optical Attenuator (VOA) inside the microring resonators. If the losses inside the MRR structure are large enough, the entire incoming optical power is conveyed to the through port, leaving the filtering architecture disconnected.

From a design point of view, the VOAs are implemented through p-i-n junctions integrated in the waveguide, as it is shown in Figure 1 (a) and (b). To do so, p-doped and n-doped regions have been put alongside the rib-waveguide, which is intrinsic.

When a driving voltage above the threshold (typically about 0.7 V) is applied between the 'p' and 'n' electrodes of the VOA, free carriers are injected into the waveguide, leading to a desired increase of the MRR round trip loss, which is also associated with an unwanted variation of the waveguide refractive index (according to the Soref formulas [3]). This shift is partially induced by waveguide heating (leading to an increase of the refractive index and thus to a red shift of the MRR resonances) and by free-carrier injection (leading to a decrease of the refractive index and thus to a blue shift of the MRR resonances). The latter effect is typically dominant, so that a residual blue shift of the MRRs is observed during "uncompensated" disconnection of the filter. Figure 1 (d) and (e) show the effect of disconnection on the frequency response of the single ring filter itself (Through and Drop port).

The concept is now extended from the single ring to a fourth order MRR filter, with 40 GHz bandwidth. FSR larger than 100 nm is achieved exploiting innovative Vernier scheme, with non-integer coefficients [2,4]. This device has been realized in Silicon-on-Insulator platform with rib waveguides 500 nm by 220 nm in size by AMF. The hitless mechanism is achieved by integrating p-i-n junctions inside the two innermost rings (second and third one) to realize VOAs as indicated in figure 2 (a), (b) and (c). The complete hitless tuning from the channel with central wavelength of 1530nm to 1560nm with a truly disconnect state is shown in fig. 2 e). This demonstrates the hitless tunability across an extended C-band. The detrimental impact on neighbour channels of the p-n junction induced blue shift is thermally compensated during the disconnection and connection phases using the heaters integrated in the MRRs. Figure 2 (d) and (f) show the (dis)connection process of the filter with VOA and heaters automatically controlled by monitoring the drop port signals. Filter disconnection (> 35 dB isolation of the drop port transmission) is achieved with 0.95 V for VOA1 and 1.3 V for VOA2.

Thanks to the thermal compensation, the MRRs resonances remains within the bandwidth of the filter and the off-band rejection (for a 50 GHz spaced channel) is larger than 30 dB. Remarkably, negligible off band notches and

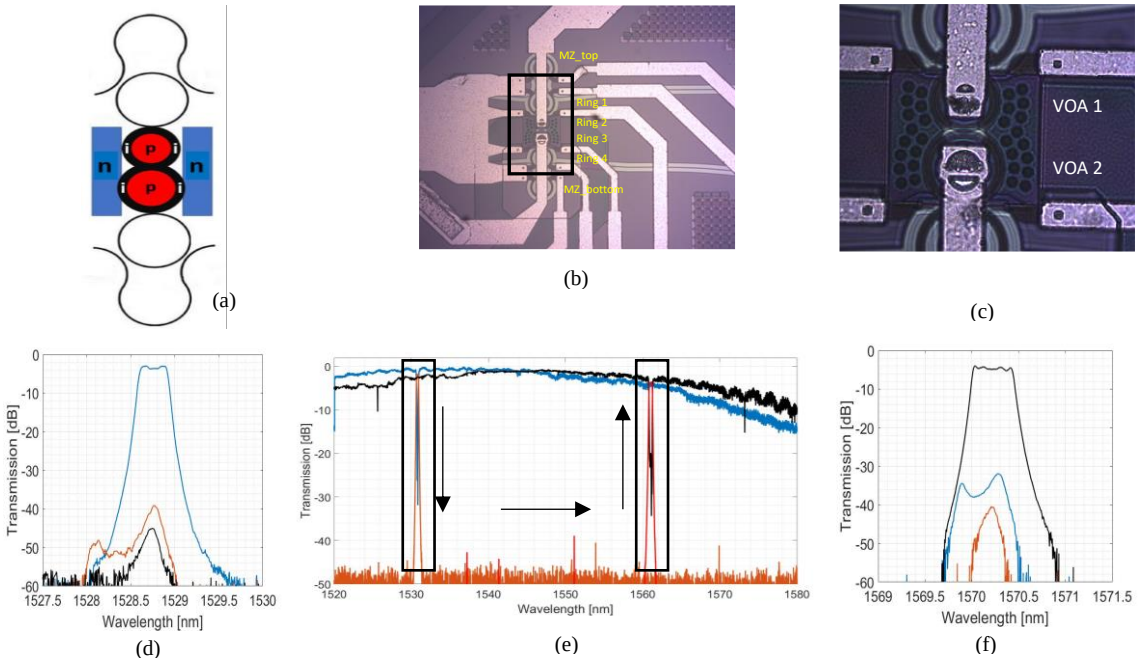



Figure 2: (a) Scheme of the 4th order MRR filter with integrated p-n junction, acting as VOA. (b) Microscope photograph of a 4th order TOADM filter with tunable MZI couplers in the first and fourth MRRs and integrating VOAs in the inner MRRs. Heaters, via holes and metal lines are clearly visible in the picture. (c) Detail of the rings with VOAs. (d) Detail of disconnection steps of 1530 nm channel (sequence: red, blue, black). (e) Tuning of two channels at the edges of the extended C-band (1530 nm and 1560 nm). (f) Detail of reconnection steps of 1560 nm channel (sequence: red, blue, yellow).

ripples appear in the through port filter response all over the extended C-band wavelength range even during operation, demonstrating the effectiveness of the proposed architecture. In the considered example, the most relevant notch is only 0.8 dB deep and 60 GHz as bandwidth, inducing an almost negligible impact on the performance of the whole system.

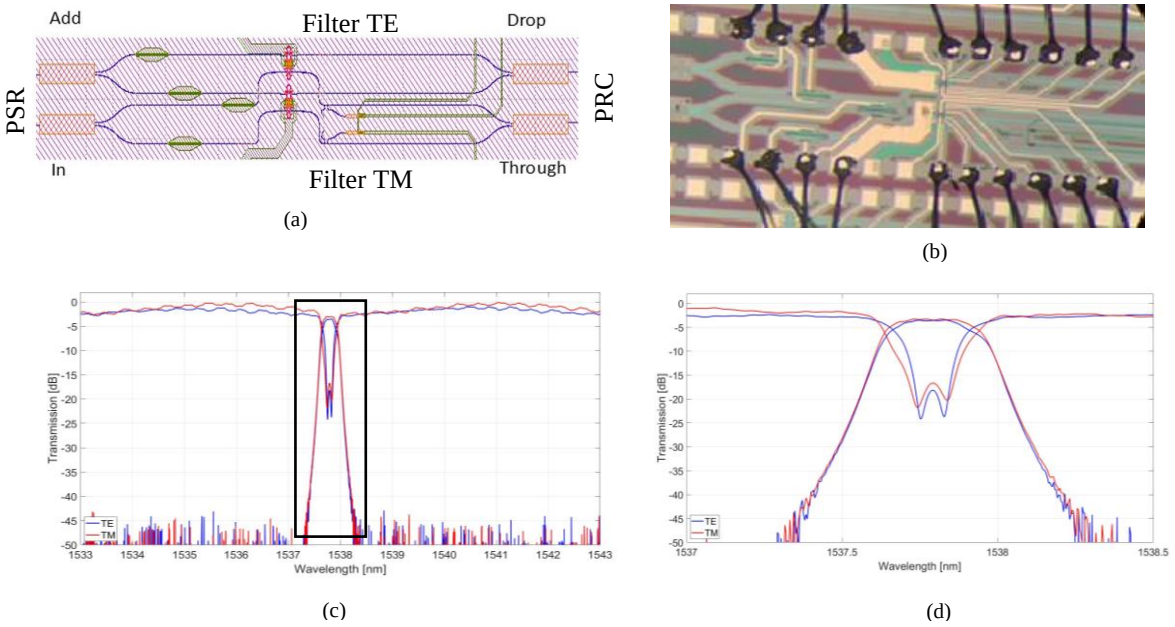
### 3. Polarization Diversity Scheme

Figure 3 shows the mask layout (a) and the top-view photograph (b) of the Polarization Diversity Filter. The Input and Add ports of the filter own a Polarization Splitter and Rotator (PSR, foundry proprietary design) that splits the incoming signal polarizations in two separate waveguides and rotates the TM polarization to have all the waveguides of the circuit operating in TE mode only.

To ease calibration operations, VOAs (implemented though a linear p-i-n junction) are integrated in both arms of the polarization diversity scheme. The two 4th order MRR filter are nominally identical and are individually controlled. At the output, a polarization rotator and combiner (PRC) is used to rotate from TE to TM the mode that was not rotated before, and then combine the two orthogonal modes at the output.

At first, the two filters of the polarization diversity scheme have been separately characterized. To this aim we controlled the polarization state of the input signal in order to calibrate the upper filter for operation on TM polarized input light and the lower filter on TE polarized input light.

Figure 3 (c) and (d) show the TE (blue) and TM (red) frequency response of the polarization diversity TOADM filter when both filters are tuned at a wavelength of 1537.8 nm, on a wavelength span of 4 nm around the considered channel.




(a) (b) (c) (d)

Figure 2: Mask layout (a) and photo (b) of the Polarization Diversity MRR Filter. (c) Tuned filter responses of Through and Drop ports with separated TE and TM polarized input signals. (d) Detail of the inband spectral responses.

The spectral behavior of the two filters are almost the same in terms of bandwidth (40GHz) and in band rejection (nearly 16 dB). Moreover, the FSR is higher than 50 nm and there are no side notches across the entire extended C-band. From the tuning point of view, the voltages applied to the heaters of the two different filters are very similar, which leads to a certain reproducibility of this kind of devices.

BER and other system testing with generic input polarization states are in progress.

### 4. CONCLUSION

Reported results demonstrate for the first time the feasibility of an architecture to achieve a polarization independent, hitless, tuneable filter operating over an extended C band of 50 nm in silicon photonics.

### REFERENCES


[1] Douglas Aguiar et al. “Automatic Tuning of Microring-Based Hitless Reconfigurable Add-Drop Filters”. Optical Society of America (2018)

[2] M.Milanizdeh et al. “FSR free coupled microring resonator filter on extended C-band in silicon photonics”, submitted to ECIO2020

[3] R. Soref and B. Bennet, “Electrooptical effects in silicon”, Journal of Quantum Electronics, 1987

[4] Chinda Chaichuay, Preecha P.Yupapin e Prajak Saeung. “The serially coupled multiple ring resonator filters and Vernier effect”.Optica Applicata XXXIX, No. 1 (2009).

# Building large scale photonic integrated circuits in suspended gallium arsenide: Passives

Pisu Jiang [1] and Krishna C. Balram [1]
[1] *QET Labs, University of Bristol, Woodland Road, Bristol BS8 1UB, UK*
*e-mail: krishna.coimbatorebalram@bristol.ac.uk*

## ABSTRACT

The spectacular success of silicon-based photonic integrated circuits (PICs) in the past decade naturally begs the question of whether similar fabrication procedures can be applied to other material platforms with more desirable optical properties. In this work [1], we demonstrate the individual passive components (grating couplers, waveguides, multi-mode interferometers and ring resonators) necessary for building large scale integrated circuits in suspended gallium arsenide (GaAs). Implementing PICs in suspended GaAs is a viable route towards achieving optimal system performance in areas with stringent device constraints like energy efficient transceivers for exascale systems, integrated electro-optic comb lasers, integrated quantum photonics, cryogenic photonics and electromechanical guided wave acousto-optics.

**Keywords**: Photonic integrated circuits, grating couplers, rib waveguides, ring resonators, waveguide couplers, multimode interferometers

## 1 INTRODUCTION

The scale, complexity and performance of silicon photonic integrated circuits (PICs) has revolutionized optical communications in the past decade [2]. Perhaps the most surprising aspect of this revolution is the fact that silicon does not possess many desirable optical properties (apart from a high refractive index) and the silicon photonics revolution was primarily driven by the availability of a foundry fabrication infrastructure [4]. On the other hand, there are a number of application areas in which silicon's lack of desirable optical properties proves a severe limitation to achieving system performance. These limitations include the absence of a direct bandgap, lack of a $\chi^{(2)}$ nonlinearity to build fast electro-optic devices and zero piezoelectric response which makes it challenging to design acousto-optic devices. As a representative example, one of the key challenges facing transceivers for exascale systems is avoiding the $\sim$ 3 dB penalty for coupling light from the III-V laser die to the silicon PIC. Other application areas where alternative material platforms are worth exploring are: cryogenic photonic circuits for interfacing superconducting digital circuits with the outside world and integrated acousto-optics, which requires a piezoelectric material for exciting acoustic waves [5].

Gallium arsenide (GaAs) presents a viable alternative to silicon for these applications as it possesses all the desirable optical properties that silicon lacks: a direct bandgap, a $\chi^{(2)}$ nonlinearity, and a (weak) piezoelectric coefficient [6]. More importantly, GaAs has a refractive index that is almost identical to silicon ($\lambda$ = 1.55 $\mu$m), making it easy to port a variety of optimised photonic designs and fabrication process flows between the platforms. In contrast to other electro-optic platforms like lithium niobate, it has a higher refractive index allowing compact component design, which is key to monolithic systems integration. GaAs also provides a natural route towards incorporating active gain media like quantum dots and wells, which are promising for applications in both classical and quantum photonics. Traditionally integrated photonics in GaAs has suffered from the low index contrast achievable between GaAs and the AlGaAs buffers which serve as waveguide cladding layers. The low index contrast leads to large mode sizes and bend radii which make photonic integration challenging [6]. In addition, the reduced optical power density (due to larger mode area) makes it difficult to adequately exploit the nonlinear coefficients for frequency conversion and EO modulator applications [8]. In recent years, there has been tremendous progress in the development of thin films of GaAs on low index media (particularly silicon oxide and nitride) by wafer bonding and a wide variety of devices showing impressive nonlinear performance have been demonstrated. On the other hand, wafer bonding is well-known to be a notoriously fickle process and it is challenging to get high device yields (a prerequisite for building PICs) in an academic cleanroom environment.

In this work, we show that a multi-step fabrication process, derived from a standard passive silicon photonics platform [7], can be applied to build large scale photonic integrated circuits in suspended GaAs. The suspension of the GaAs layer, achieved by selective etching of the underlying AlGaAs film, is necessary to achieve high refractive index contrast [9].

## 2 FABRICATION PROCESS

Figure 1 shows a schematic illustration of the main process steps for a grating coupler fabricated using this process. The process starts by patterning the grating coupler teeth and defining the outline of the waveguides and

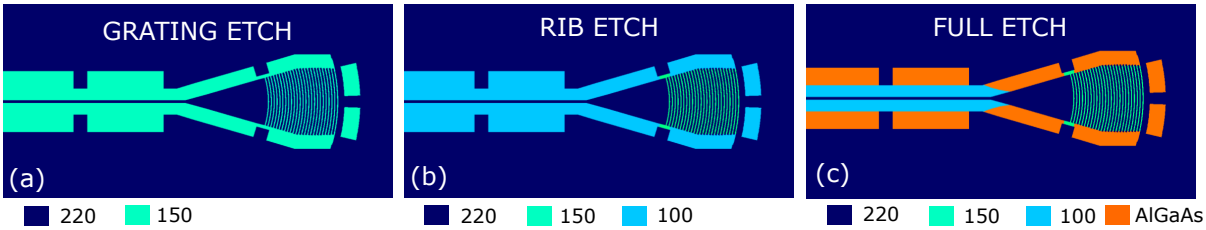



Figure 1. Illustrative schematic of the process flow for building a suspended waveguide platform in GaAs. The process follows the standard three step process used to fabricate passive silicon photonic devices. The GaAs thickness (in nm) in each region is indicated. (a) A 70 nm GRATING etch is used to define the grating coupler in GaAs. (b) The GaAs is etched a further 50 nm to define the rib waveguides (RIB etch). (c) Finally, a 100 nm FULL etch is carried out to reach the AlGaAs layer. The exposed AlGaAs layer is selectively etched away in weak HF acid and the sample is covered with $\sim 2\ \mu m$ $SiO_2$.

the tethers (GRATING etch) in GaAs (Fig. 1 (a)). The patterning is carried out using electron beam lithography with hydrogen silsesquioxane (HSQ) resist and the GaAs layer is etched using a standard $Ar/Cl_2$ chemistry with etch thickness monitored using an ellipsometer to ensure precise etch depths are achieved. This is followed by a RIB etch step (Fig. 1 (b)), where the GaAs layer is etched a further 50 nm to define the rib waveguides. The grating coupler region is protected with HSQ resist during this step. The two layers are registered with respect to each other using a set of alignment marks defined during the GRATING etch step. A FULL etch step is next carried out by etching the remaining 100 nm of the GaAs layer (+ 20 nm overetch) to access the AlGaAs buffer as shown in Fig.1(c). To suspend the GaAs layer, the AlGaAs buffer is selectively etched in dilute hydrofluoric acid (HF) solution. To remove any remnants of etch residue, the sample is cleaned in a dilute potassium hydroxide solution and flash dried using isopropanol [10]. After HF release, the suspended GaAs film is capped with $\sim 2\ \mu m$ of silicon oxide deposited using plasma enhanced chemical vapor deposition (PECVD). The oxide film is necessary for separating the metal electrodes (required for the electro-optic devices) from the GaAs layer. In addition, they provide mechanical rigidity to the suspended films by pinning them at the corners of the etch holes [1].

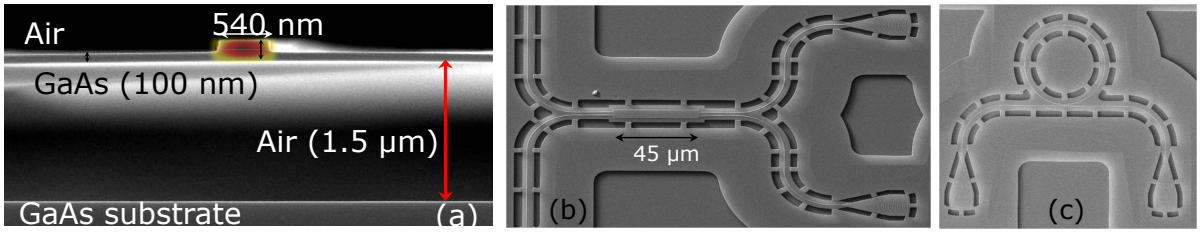



Figure 2. Representative devices fabricated in this platform: (a) Rib waveguides (b) 2x2 multimode interference (MMI) coupler and (c) Microring resonators (25 $\mu m$ radius). The suspended grating couplers used to provide optical access can be seen in (b) and (c).

A representative set of passive devices fabricated using this suspended GaAs platform is shown in Fig.2. These include suspended rib waveguides (Fig.2(a)), grating couplers (Fig.2(b,c)), on-chip waveguide splitters (multimode interference couplers shown in Fig.2(b)) and microring resonators (Fig.2(c)). As silicon photonics and before it silicon microelectronics have shown, once a set of robust building blocks have been demonstrated, circuits of arbitrary complexity can be synthesized by connecting these building blocks together in the desired order. The passive devices demonstrated here serve as a key building block for the development of active devices, in particular, efficient integrated electro-optic and acousto-optic modulators, which are currently under development.

## 3 DEVICE CHARACTERISATION

Fig.3 shows the measured device performance for various components fabricated in this suspended GaAs platform. Fig.3(a) shows that a suspended 2x2 MMI coupler can achieve on-chip splitting ratios very close to 50:50, with very low excess loss. Grating couplers (shown by the blue curve in Fig.3(a) show coupling loss 4 dB/ coupler. In contrast to traditional III-V PICs which have relied on edge coupling, grating couplers open the door to in-situ device testing by avoiding the need for chip cleaving. This is especially useful to maximise device yield as the scale and component density of PICs increases. Fig.3(b,c) show the measured transmission spectra of microring resonators fabricated in this platform. The quality factor of our rings is $\sim$ 15000. Based on the measured resonator $Q_{opt}$ and free spectral range (from Fig.3(b)), we estimate our current waveguide propagation loss to be $\sim$ 7 dB/cm. We believe the resonator is currently operating in the overcoupled regime, and hence the propagation loss estimate is an upper bound.

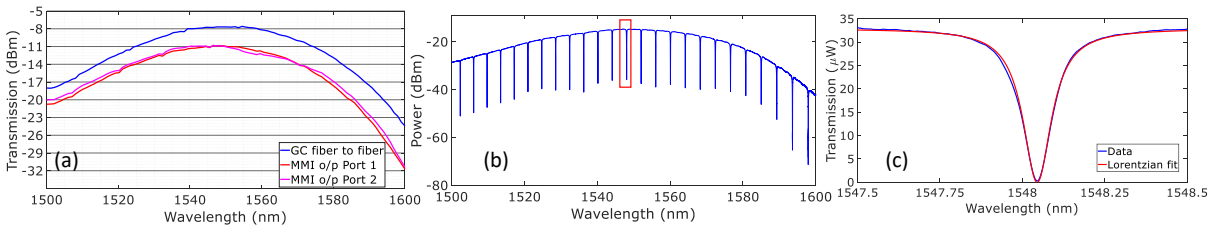



Figure 3. (a) Measured transmission spectrum through the two output ports (labelled 1 and 2 and indicated by the red and magenta curves) for a suspended MMI coupler. The reference fiber to fiber transmission spectrum, without the MMI, is shown in blue. (b) Measured transmission spectrum of the resonator showing a series of TE resonant modes ($P_{in}$ = -6 dBm). The TE polarisation is determined by the grating coupler. (c) Zoomed-in scan of one of the resonances, fitted with a Lorentzian lineshape, giving a measured $Q_{opt} \sim 15000$.

## 4 CONCLUSIONS AND FUTURE WORK

In this work, we have demonstrated that the complexity of the standard (passive) silicon photonics process can be readily transferred to more interesting optical materials, in particular GaAs. The similarity of the refractive indices of the two materials ensures that high device performance can be readily ensured without requiring extensive component re-design. Bringing the scale and complexity of silicon photonics to more interesting optical platforms will be revolutionary for device applications in wide-ranging areas from quantum photonics to cryogenic photonic circuits. Moving forward, we will extend this platform to demonstrate low-loss long spiral ($L_{wvg} \sim$ cm) waveguides, and active electro-optic and acousto-optic devices.

## ACKNOWLEDGMENTS

K.C.B. would like to thank Kartik Srinivasan for lending him the GaAs substrate used for carrying out this work. Sample fabrication was also carried out on GaAs substrates provided by the UK Engineering and Physical Sciences Research Council (EPSRC) National Epitaxy Facility in Sheffield, through a pump-prime grant. We would like to thank Ed Clarke, Imad Faruque, Edmund Harbord, George Kanellos, Laurent Kling, Andy Murray, Josh Silverstone, Joe Smith, Kartik Srinivasan, and Siyuan Yu for valuable discussions and suggestions. We would like to acknowledge funding support from the European Research Council (ERC-StG, SBS3-5 / 758843). Nanofabrication work was carried out on equipment funded by the EPSRC (EP/N015126/1).

## REFERENCES

[1] P. Jiang and K.C. Balram, "Suspended gallium arsenide platform for building large scale photonic integrated circuits: Passive devices," arXiv:1912.05301

[2] D. Thompson, A. Zilkie, J.E. Bowers, T. Komljenovic, G.T. Reed, L. Vivien et al., "Roadmap on silicon photonics," Journal of Optics 18(7), pp. 073003, 2016.

[3] A.H. Atabaki, S. Moazeni, F. Pavanello, H. Gevorgyan, J. Notaros, L. Alloatti et al., "Integrating photonics with silicon nanoelectronics for the next generation of systems on a chip," Nature 556(7701), pp.349, 2018.

[4] K. Giewont, K. Nummy, F.A. Anderson, J. Ayala, T. Barwicz, Y. Bian et al., "300-mm Monolithic Silicon Photonics Foundry Technology," IEEE J. Sel. Top. in Quant. Elec. 25(5), pp.1–11, 2019

[5] K.C. Balram, M.I. Davanco, J.D. Song and K. Srinivasan, "Coherent coupling between radiofrequency, optical and acoustic waves in piezo-optomechanical circuits," Nature Photonics 10(5), pp. 346, 2016.

[6] C. Dietrich, A. Fiore, M.G. Thompson, M. Kamp and S. Höfling,"GaAs integrated quantum photonics: Towards compact and multi-functional quantum photonic integrated circuits," Laser & Photonics Reviews 10(6), pp.870–894, 2016.

[7] C. Littlejohns, Y. Tran, H. Dan, S. Stankovic, X. Yan, G, Sharp et al. "Rapid device prototyping using the CORNERSTONE platform," Silicon Photonics XIV 10923, 2019.

[8] J. Wang, A. Santamato, P. Jiang, D. Bonneau, E. Engin, J.W. Silverstone et al., "Gallium arsenide (GaAs) quantum photonic waveguide circuits," Opt. Comm. 327, pp. 49–55, 2014

[9] T.H. Stievater, M.W. Pruessner, W.S. Rabinovich, D. Park, R. Mahon, D.A. Kozak et al.,"Suspended photonic waveguide devices," Appl. Opt. 54(31), pp.F164–F173, 2015.

[10] L. Midolo, T. Pregnolato, G. Kiršanskė and S. Stobbe, "Soft-mask fabrication of gallium arsenide nanomembranes for integrated quantum photonics, " Nanotechnology 26(48), pp.484002, 2015.

# 3D Photonic Integration: Cascaded 1x1 3D Multi-mode Interference Couplers for Vertical Multi-layer Connections

**Madeleine Weigel**[1], **Moritz Kleinert**[1], **Hauke Conradi**[1], **Anja Scheu**[1], **Martin Kresse**[1], **Crispin Zawadzki**[1], **David de Felipe**[1], **Norbert Keil**[1], **Martin Schell**[1]
[1] Fraunhofer Heinrich Hertz Insitute, Einsteinufer 37, 10587 Berlin, Germany
*e-mail: madeleine.weigel@hhi.fraunhofer.de*

## ABSTRACT

A vertical interconnection across four stacked polymer waveguide layers using 3D multi-mode interference couplers (3D MMIs) is presented. This system bridges a vertical distance of 21.6 µm with a minimum on-chip loss of 2.5 dB. The multi-layer connection is a basic element for novel applications, like large-scale optical switching matrices with a waveguide crossing-free architecture and a small footprint.

**Keywords**: 3D photonic integration, polymer waveguide, multi-layer waveguide system, vertical multi-mode interference coupler.

## 1. INTRODUCTION

By extending planar photonic integrated circuits (PICs) into the 3rd dimension, a new degree of freedom in their design arises. This leads to novel applications such as waveguide crossing-free large-scale switching matrices, multicore-fiber-PIC-interconnections and 3D optical phased arrays. Especially with regard to complex crossing-free optical switches, passive routing (Figure 1 (b)) over more than two layers is necessary for a small footprint. The crossing-free routing in Figure 1 is enabled by a multi-layer waveguide system for multiple parallel optical flows and vertical interconnects consisting of 1x1 3D MMIs [1]. 3D PICs with only two connected waveguide layers have already been demonstrated on HHI's polymer-based photonic integration platform PolyBoard as reported in [1] – [4]. The 1x1 3D MMIs were successfully fabricated with on-chip losses of 1 dB [1] for a vertical distance of 7.2 µm (centre-to-centre).

The polymer waveguide technology allows a reproducible, low-loss fabrication of 1x1 3D MMIs over several layers [1, 5]. Such a multi-layer connection for four waveguide layers is shown in Figure 1 (a). This structure is a basic element for a crossing-free routing, as shown in Figure 1 (b), inside a switching matrix. The light path covers a vertical distance of 21.6 µm. The system exhibits low on-chip losses of 2.5 dB.

Subsequently, the design of the multi-layer vertical interconnects is shown. Furthermore, the results of the characterization of such a fabricated device as shown in Figure 1 (a) are presented.

(a) (b)

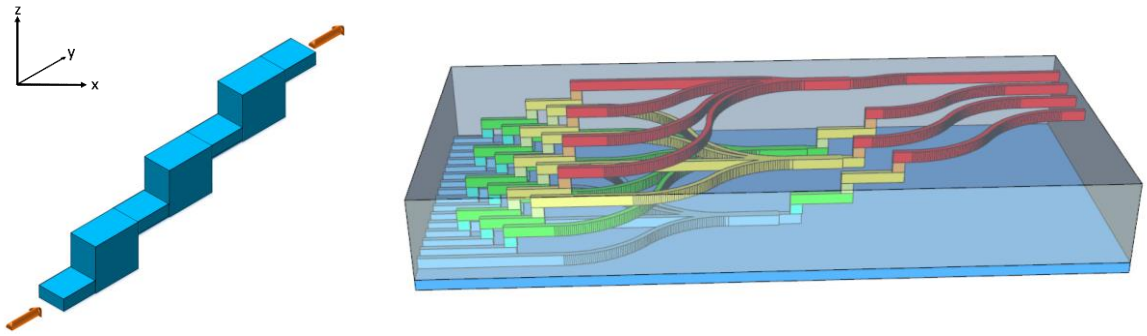



*Figure 1: 3D sketch of a multi-layer connection for four waveguide layers (a) and a 3D sketch of a concept of a crossing-free waveguide routing (b) for large-scale optical switching matrices.*

## 2. DESIGN AND SIMULATION

The design to connect four waveguide layers by three cascaded 1x1 3D MMIs is shown in Figure 1 (a). The basic building block is the 1x1 3D MMI in Figure 2 [1]. The single-mode input and output waveguides of a 1x1

3D MMI are connected by a multi-mode interference section. The light is transmitted from the single-mode waveguide with a height of 3.2 µm to a 10.4 µm high MMI section. The waveguides are channel waveguides based on a polymer core and a polymer cladding with an index contrast of $\Delta n$ = 0.03 at 1550 nm [2, 3]. In the MMI, a multi-mode field arises, resulting in self-interference. Based on the self-imaging theory, an image of the input field at the output waveguide is obtained for a fixed combination of length and height [6, 7]. This output field is similar in phase and intensity to the input field.

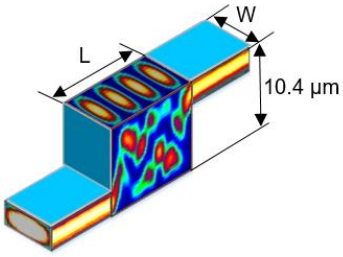



*Figure 2: 3D sketch of a vertical 1x1 3D MMI for connecting two vertical waveguide layers. The sketch shows the simulation results of the optical light field [1].*

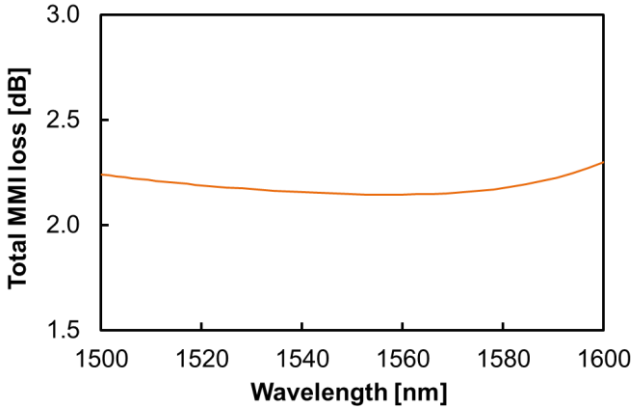



*Figure 3: Simulated MMI loss depending on the wavelength of a multi-layer connection for four vertical waveguide layers with fixed parameters of 1x1 3D MMIs (MMI length L = 173 µm, MMI width W = 1.4 µm and MMI height of 10.4 µm).*

To determine the expected intensity of the output field as a function of the wavelength, the multi-layer connection structure (Figure 1 (a)) with three connected 1x1 3D MMI was implemented in FIMMPROP. Starting point of the simulation is based on the successfully fabricated and characterized 1x1 3D MMIs with a MMI height of 10.4 µm, MMI length $L$ = 173 µm and MMI width $W$ = 1.4 µm [1]. In Figure 3 the total MMI losses for three cascaded 1x1 3D MMIs are shown depending on the wavelength for the given parameter set. As a result, the simulation yields a minimum total MMI loss of 2.1 dB at a wavelength of 1550 nm.

## 3. CHARACTERIZATION

Optical transmission measurements were conducted on a fabricated multi-layer connection of four waveguide layers based on three cascaded 1x1 3D MMIs. Figure 4 shows the wavelength dependent on-chip losses for such a device with a MMI length $L$ = 173 µm, a MMI width $W$ = 1.4 µm and a MMI height of 10.4 µm. The on-chip losses are normalized by the average transmission losses of straight reference waveguides per waveguide layer (approx. 2 dB). Figure 4 shows for the device a minimum on-chip loss of 2.5 dB at a wavelength of 1517 nm. The device was successfully fabricated with low additional loss (< 0.4 dB) compared to the simulation (Figure 3).

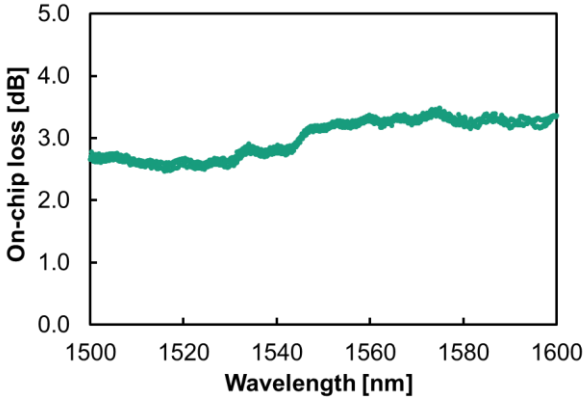



*Figure 4: Optical transmission measurement on a multi-layer connection of four vertical waveguide layers consisting of three cascaded 1x1 3D MMIs with a MMI height of 10.4 µm, MMI length L = 173 µm and a MMI width W = 1.4 µm. The losses of the device were normalized by the transmission loss through a straight reference waveguide (2 dB) without vertical interconnection.*

Figure 4 shows a shift of the wavelength with the minimum loss compared to the simulation results in Figure 3 to smaller wavelengths. Based on the self-imaging theory, this shift may be due to the variation of the parameters

MMI length or MMI height [6, 7]. For a closer look at the reason, the measurements were repeated on devices with different MMI lengths. Figure 5 shows the on-chip losses over the wavelength for different MMI lengths. It can be seen that for all lengths, regardless greater or smaller than 173 µm, the shift to shorter wavelengths occurs. Hence, the variation of the MMI height is the decisive parameter. Due to the offset to smaller wavelengths, it follows from the self-imaging theory that the MMI height is smaller than 10.4 µm [6, 7]. In Figure 6 the simulation results for different MMI heights for a multi-layer connection over four waveguide layers are shown. From Figure 6 it can be seen that at a MMI height of 9.8 µm, the minimal losses occur at 1518 nm. In comparison to the measurement results in Figure 4, a similarly large wavelength shift is observed. The effective MMI height per 1x1 3D MMI is hence 0.6 µm smaller than assumed. In addition, it can be seen that with a difference of 0.6 dB the measurement results are close to the simulation results. This shows that the height is a sensitive parameter for the wavelength dependence of the device, but does not have a major impact on the minimal losses on this short range.

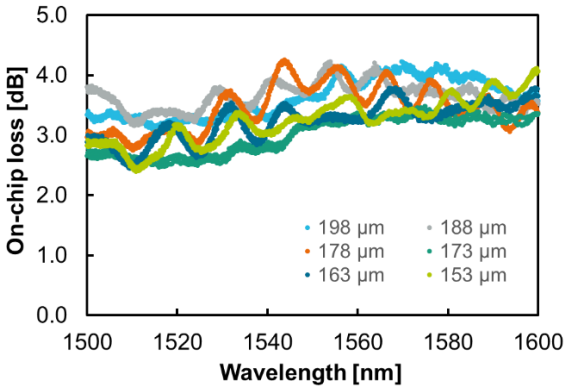



*Figure 5: Optical transmission measurements on multi-layer connections of four waveguide layers connected by three 1x1 3D MMIs with a fixed MMI height of 10.4 µm and a MMI width of 1.4 µm. The MMI lengths L varies for the different devices. The losses of the devices were normalized by the transmission loss of straight reference waveguide (2 dB) without vertical interconnection.*

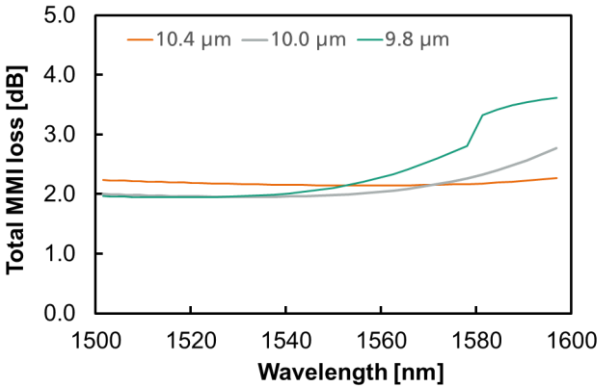



*Figure 6: Simulated MMI loss depending on the wavelength of a multi-layer connection for four vertical waveguide layers with fixed MMI length L = 173 µm and MMI width W = 1.4 µm for three different MMI heights: 10.4 µm (orange), 10.0 µm (grey) and 9.8 µm (green).*

## 4. CONCLUSION

A connection of four waveguide layers using three cascaded vertical 1x1 3D MMI couplers with a vertical distance of 21.6 µm was successfully fabricated on the HHI's PolyBoard platform. The multi-layer connection exhibited a minimum on-chip loss of 2.5 dB at a wavelength of 1517 nm. Furthermore, it was shown that the height of the MMI is a critical parameter with regard to the wavelength with the lowest losses. This multi-layer structure is a basic element for novel applications, such as complex waveguide crossing-free routing for optical switching matrices.

## ACKNOWLEDGEMENTS

*This work was partially funded through the project ICT-3PEAT by European Union's Horizon 2020 research and innovation programme under grant agreement No 780502.*

## REFERENCES

[1] M. Nuck, *et al.*: "Low-loss Vertical MMI Coupler for 3D Photonic Integration," *ECOC*, 2018, Tu3.C4.
[2] D. de Felipe, *et al.*: "Recent Development in Polymer-Based Photonic Components for Disruptive Capacity Upgarde in Data Centers," *Journal of Lightwave Technology*, Vol. 35, no.4, p. 683, 2017.
[3] M. Kleinert, *et al.*: "Photonic integrated devices and functions on hybrid polymer platform," *Photonics West*, 2017, paper 10098-45.
[4] M. Nuck, *et al.*: "3D Photonic Integrated 4x4 Multi-Mode Interference Coupler," *Photonics West*, 2019, paper 10921-47.
[5] J.-M. Lee, *et al.*: "Vertical Coupling of Polymeric Double-Layered Waveguides Using a Stepped MMI Coupler," *ETRI Journal*, Vol. 25, no. 2, p. 81, 2003.
[6] L.B. Soldano, *et al.*: "Optical Multi-Mode Interference Devices Based on Self-Imaging: Principles and Applications," *Journal of Lightwave Technology*, Vol. 13, no. 4, p. 615, 1995.
[7] J. Zhao, *et al.*: "Optimal design of multimode interference couplers using an improved self-imaging theory," *Optics Communications*, Vol. 281, p. 1576, 2008.

# Silicon Nitride Waveguides and Spot Size Converters with < 1.76 dB Loss Over Broad Wavelength Range from 1010 nm to 1110 nm for OCT Applications

**Piotr. J Cegielski[1], Stephan Suckow[1], Anna Lena Giesecke[1], Caroline Porschatis[1], Holger Lerch[1], Maik Lütticke[1], Bartos Chmielak[1], Max C. Lemme[1,2]**

[1]*AMO GmbH,*
*Otto-Blumenthal-Str. 25*
*52074 Aachen,*
[2]*Chair of Electronic Devices*
*RWTH-Aachen University,*
*Otto-Blumenthal-Str. 25*
*52074 Aachen,*
*e-mail: cegielski@amo.de*

## ABSTRACT

In this work the first spot size converters for edge coupling into the silicon nitride waveguide platform with coupling loss lower than 1.76 dB in the wavelength range from 1010 nm to 1110 nm are presented. The spot size converters consist of a SU-8 waveguide matching the mode field diameter of a single mode fiber. High quality end facets of SU-8 are prepared by carefully dicing through the SU-8 waveguides without edge polishing. The SU-8 waveguide mode is converted to the $Si_3N_4$ waveguide mode by an inverse taper. The $Si_3N_4$ taper tips are narrower than 200 nm, which is required to avoid reflections. They are fabricated using cost efficient i-line projection lithography with a nominal resolution of 500 nm. The $Si_3N_4$ waveguide propagation losses are as low as 0.4 dB/cm. Such low loss broadband photonic platform can find use in e.g. retinal optical coherence tomography. The measured coupling loss is comparable to the best available devices for longer wavelengths.

**Keywords**: silicon nitride, integrated photonics, spot size converters, edge coupling

## 1. INTRODUCTION

The silicon nitride waveguide platform is especially interesting for applications at visible and near infrared wavelengths such as optical coherence tomography (OCT) [1, 2], which requires broadband low loss photonic integrated circuits (PICs). Grating couplers, which are often used to couple light into PICs, are not well suited for broadband applications as their principle of operation is intrinsically wavelength dependent. The best grating couplers have been shown to reach a 3-dB bandwidth of 76 nm, and required bottom distributed Bragg reflectors, which are challenging and costly to fabricate [3]. A better performance in terms of bandwidth and loss can be achieved using edge coupling, which can also be less technically demanding. The height of $Si_3N_4$ waveguides is typically lower than 400 nm, meaning that matching the mode field to that of the single mode fibers (SMF) of several microns in diameter requires fabricating complicated 3D structures as spot-size converters. Finally, spot-size converters often make use of inverse tapers with narrow tips in order to avoid reflections. Since the waveguide dimensions are proportional to the wavelength, this is becoming more and more challenging as the wavelength of interest gets shorter and higher resolution lithography is required. Moreover, the optical quality of the facets has to be high, which often makes it necessary to polish the PICs after dicing them into separate chips.

Here, we present first spot size converters for a broad wavelength range from 1010 to 1110 nm, which is especially interesting for OCT applications such as retinal OCT [4]. Thanks to the use of SU-8 for matching to the SMF modes, our devices are efficient and straightforward in fabrication. Furthermore, we achieve sub-200 nm tip widths of $Si_3N4$ inverse tapers exclusively using i-line stepper lithography, which makes our devices low loss and cost-effective at the same time.

## 2. DESIGN

The spot size converters consist of SU-8 waveguides, which efficiently couple light from an SMF (mode field diameter of 6.5 µm), and a taper section converting the large SU-8 mode to the much smaller $Si_3N_4$ waveguide mode (Figure 1a). To maximize the efficiency of light coupling to the SU-8 its core dimensions are set to 7 µm × 7 µm, which matches well the mode of the SMF. The $Si_3N_4$ waveguide is 200 nm high and 700 nm wide and supports a single TE mode in the wavelength range of interest from 1010 nm to 1110 nm. The tip of the inverse $Si_3N_4$ taper is narrower than 200 nm in order to avoid reflections and maximize the converters efficiency. Since the refractive index contrast of $Si_3N_4$ (n = 2) and SU-8 (n = 1.56) is relatively low the taper has

to be long to efficiently convert the modes. If only the $Si_3N_4$ waveguide is tapered the maximum conversion efficiency reaches only 83 % even for tapers as long as 3.5 mm. In order to improve the conversion efficiency, the SU-8 is also tapered, enhancing efficiency to 85 % with a shorter taper of 2 mm (Figure 1b). Elongating the taper further results in a less significant increase of efficiency. Reaching lossless conversion would require at least a 4 mm long taper, which is impractical for the PIC design. Therefore, 2 mm was chosen as a tradeoff for the final devices.

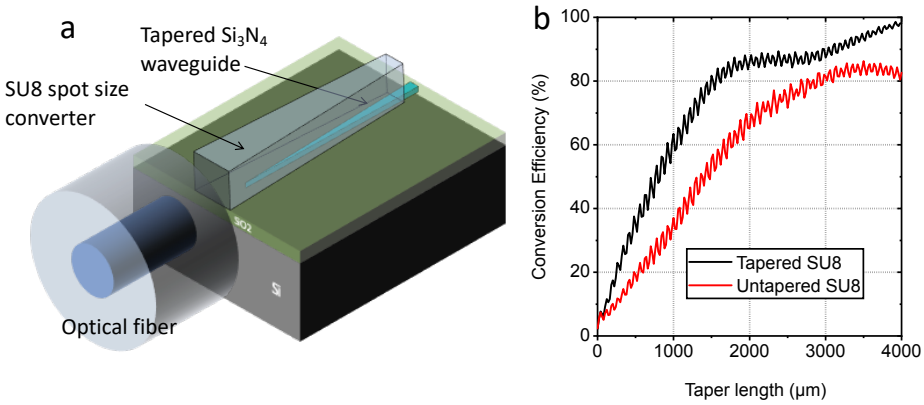



*Figure 1 a) A schematic of the SU-8 spot size converter b) Simulated mode conversion efficiency from the SU-8 spot size converter to the $Si_3N_4$ waveguide vs the $Si_3N_4$ taper length for tapered SU-8 (black) and untapered SU-8 (red).*

## 3. FABRICATION

PICs have been fabricated on 6" silicon substrates with 2.3 µm of thermally grown $SiO_2$. Then, 200 nm of $Si_3N_4$ has been deposited by low-pressure chemical vapor deposition (LPCVD) and the waveguides have been patterned using projection lithography (Canon FPA 3000 i5r i-line Stepper with 0.5 µm resolution) and dry etching. $Si_3N_4$ taper tips narrower than 200 nm have thus been obtained. Next, 1 µm of LTO cladding (low temperature oxide) has been deposited in an LPCVD furnace. In order to achieve a direct contact of SU-8 with $Si_3N_4$, cavities have been etched into the $SiO_2$ cladding using exactly the same layout as that of the SU-8 tapered waveguides. A combination of wet and dry etching lead to $Si_3N_4$ waveguides that were completely uncovered without damaging the $Si_3N_4$ surface (Figure 2a). Next, SU-8 waveguides have been fabricated from a 7 µm thick layer of SU-8 by i-line stepper lithography. This has been followed by dicing the wafers into individual chips. During this step, the SU-8 waveguides were also cut to reveal the facets of the spot size converters (Figure 2b). As the surface of the SU-8 facet was smooth directly after dicing, no extra polishing step was required.

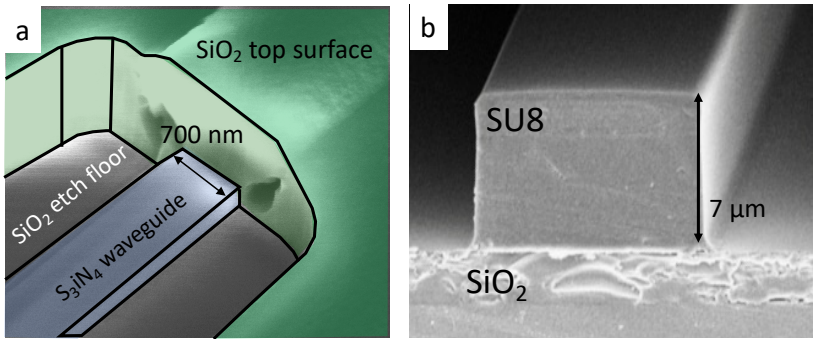



*Figure 2 a) SEM micrograph taken at a 35-degree angle of a cavity in $SiO_2$ etched to uncover the $Si_3N_4$ waveguide before SU-8 deposition. b) Diced SU-8 facet of a finished spot size converter.*

## 4. CHARACTERIZATION

The spot size converters and waveguides have been characterized with a continuously tunable laser (Toptica CTL) with a wavelength tuning range from $\lambda$ = 1010 nm to 1110 nm and a Newport 1918-IR power meter. Two cleaved single mode polarization maintaining SMF fibers (OptoSigma PM980) have been aligned with the spot size converters using X-Y-Z manual stages. In addition, an index matching liquid (Norland) has been used to reduce reflections from the end facets of both fibers and the SU-8 waveguides. Waveguide propagation and coupling losses have been measured using the cutback method [5] (Figure 3a). The slope of the linear fit of the transmission loss versus the $Si_3N_4$ waveguide length indicates the waveguide propagation loss, while the intercept with the Y-axis indicates the combined coupling loss of input and output spot size converters. A propagation loss

of only 0.3 - 0.4 dB/cm was observed. The measured coupling losses were lowest at λ = 1010 nm with a value of only 1.42 dB per coupler and were lower than 1.76 dB over the entire wavelength range, which is marked with a straight red line in Fig. 3b. The transmission spectrum of a spot size converter with 2 mm long taper shows oscillations with a free spectral range of approximately 6 nm and an amplitude of 0.5 dB (Figure 3b). In order to identify the source of these oscillations, spot-size converters with various lengths have been measured. They show a clear dependency of the free spectral range on the taper length. This indicates that the mode conversion is incomplete and that reflections from the end of the SU-8 taper are causing the oscillations. This indicates that losses can be further reduced by optimizing the design of the taper section of the device.

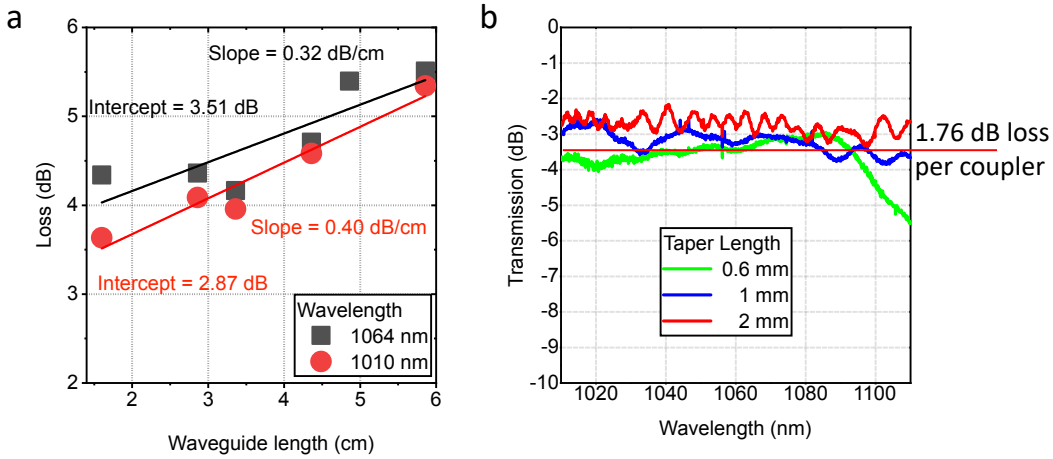



*Figure 3 a) Coupling loss and waveguide propagation loss measured by the cutback method. b) Transmission spectra through a pair of spot size converters. The waveguide loss of 0.175 dB of 5.5 mm long $Si_3N_4$ waveguide has been subtracted and the curves depict only the combined loss of input and output spot size converters.*

## 5. CONCLUSIONS

The presented spot size converters are the first devices of this kind for the wavelength range from λ = 1010 to 1110 nm. Their coupling loss of 1.76 dB is comparable with the best devices available for longer wavelengths (1.5 dB [6]). SU-8 has several advantages over inorganic materials: high quality facets obtained with simple dicing, ease of fabrication and the possibility of further improvements by utilizing multilayer SU-8 structures. All devices were fabricated exclusively using a conventional i-line stepper with a relatively low resolution of 500 nm, which eliminates the need for expensive deep UV or electron beam lithography. Hence, our broad band spot size converters complement the low loss silicon nitride waveguide platform, making it extremely useful for applications such as OCT or on chip spectroscopy.

## ACKNOWLEDGEMENTS

The authors acknowledge the financial support by the Federal Ministry of Education and Research of Germany in the framework of ElecTRIC (project number FKZ 13N14971), European Union's Horizon 2020 research and innovation programme under grant agreement No 861950, project POSEIDON and European Regional Development Fund (ERDF) in the framework of PerovsKET (project number EFRE 0801508, NW-2-2-018a).

## REFERENCES

[1] G. Yurtsever, N. Weiss, J. Kalkman, T. G. van Leeuwen, and R. Baets: Ultra-compact silicon photonic integrated interferometer for swept-source optical coherence tomography, *Opt. Lett.*, vol. 39, no. 17, p. 5228, 2014, doi: 10.1364/ol.39.005228.

[2] A. Rahim *et al.*: Open-Access Silicon Photonics Platforms in Europe, *IEEE J. Sel. Top. Quantum Electron.*, vol. 25, no. 5, pp. 1–18, Sep. 2019, doi: 10.1109/JSTQE.2019.2915949.

[3] J. Hong, A. M. Spring, F. Qiu, and S. Yokoyama: A high efficiency silicon nitride waveguide grating coupler with a multilayer bottom reflector, *Sci. Rep.*, vol. 9, no. 1, p. 12988, Dec. 2019, doi: 10.1038/s41598-019-49324-5.

[4] A. Unterhuber *et al.*: In vivo retinal optical coherence tomography at 1030 nm with enhanced penetration into the choroid, in *Optics InfoBase Conference Papers*, 2005, vol. 13, no. 9, p. 586103, doi: 10.1117/12.632961.

[5] T. G. Reed and P. A. Knights:*Silicon Photonics: an Introduction*. Chichester, West Sussex PO19 8SQ, England: John Wiley & Sons Ltd, 2004.

[6] Ligentec: Ligentec All Nitride Core Technology. [Online]. Available: https://www.ligentec.com/ligentec-an-technology/. [Accessed: 05-Feb-2020].

# Silicon Photonics DWDM NLFT Soliton Transmitter Implementation and Link Budget Assessment

**A. Moscoso-Mártir[1*], J. Koch[2], J. Müller[1], S. Sharif Azadeh[1,3], S. Pachnicke[2], J. Witzens[1]**
[1] Institute of Integrated Photonics, RWTH Aachen University, Alois-Riedler-Str. 4, 52074 Aachen, Germany
[2] Chair of Communications, Faculty of Engineering, Kiel University, Kaiserstraße 2, 24143 Kiel, Germany
[3] Now at NINT Department, Max Planck Institute of Microstructure Physics, 06120 Halle, Germany
*e-mail: amartir@iph.rwth-aachen.de*

## ABSTRACT

We analyze the implementation and capabilities of a silicon photonics transmitter capable of modulating and multiplexing groups of four solitons with different frequency and time spacing based on the nonlinear Fourier transform.

**Keywords**: Nonlinear optics, DWDM system, NLFT system, integrated optoelectronic circuits.

## 1. INTRODUCTION

The optical backbone infrastructure has to support the continuing demand for exponentially growing data throughput. A cost-effective solution to increase the channel capacity avoiding the deployment of new fibers consists in increasing the limits of useable power per fiber without incurring nonlinear penalties [1]. In transmission systems based on the nonlinear Fourier transform (NLFT), the nonlinear Kerr effect simply results in a change of the phase in the nonlinear spectrum that can be compensated at the receiver (Rx) end [2]. However, current systems present some limitations in their ability to create higher-order solitons for more efficient data transmission [3]. These limitations stem from the required computational complexity, high sampling rate and high bandwidth (BW). To overcome these, it has been proposed to shift the soliton merging from the electrical to the optical domain using a photonic integrated circuit (PIC) [4]. In this solution, first-order solitons are generated on individual optical carriers and are multiplexed later using a programmable architecture that allows a precise control over time and frequency spacing between the individual solitons with minimal spectral distortion [4]. Since only first-order solitons have to be generated and detected in the electrical domain, BW requirements on the electrical and optoelectronic components are significantly reduced. Moreover, it is possible to parallelize first-order soliton generation and detection, further reducing the digital signal processing (DSP) speed requirements.

In this paper, we present the realization of a silicon photonics (SiP) transmitter (Tx) that can modulate four first-order solitons and multiplex them with adjustable time-delays by means of a programmable delay network implemented with coupled (ring-)resonator optical waveguide (CROW) optical add-drop multiplexers (OADMs) [5]. Based on the modeled and measured characteristics of the fabricated PIC, and previous experience with fully functional wavelength division multiplexed (WDM) transceivers [6], a complete model for a system setup combining commercially available equipment and the proposed PIC is established and analyzed. A link budget is derived to obtain realistic power values for the multiplexed soliton pulses at the output of the PIC. This information is used to upgrade the simulation tool presented in [4] to model the link together with the fabricated chip, so that the features and programmability of the PIC can be investigated. Using this simulation tool, we have run different scenarios concerning pulse timing and explored the capabilities of the SiP DWDM NLFT soliton transmitter under development. Experimental system-level results available by the time of the conference will also be presented.

## 2. TRANSMITTER IMPLEMENTATION AND LINK BUDGET

The envisioned system as well as a micrograph of the recently delivered system chip fabricated in a multi-project wafer run at Advanced Micro Foundries (AMF) are shown in Fig. 1 and Fig. 2(a). A comb source from Pilot Photonics (Lyra-OCS-1000) is used to provide the carriers for the first-order solitons. The comb has an adjustable free spectral range (FSR) of 10 ± 4 GHz that can be used to adjust the soliton frequency spacing. Each line has a power of -6 dBm and a linewidth of 80 kHz. Four of these lines are filtered with an external 45 GHz passband optical filter with 2 dB insertion loss (IL). The selected carriers are amplified to 10 dBm with an EDFA with a noise figure (NF) of 5 dB, so that the total power injected in the PIC does not exceed 16 dBm to prevent permanent damage to the grating coupler (GC, IL = 3 dB) used as a coupling device. Inside the chip, four 2$^{nd}$-order CROW OADMs (IL = 1.6 dB, BW = 6.5 GHz) route carriers to one of the two input ports of two IQ Mach-Zehnder modulators (MZM), as shown in Fig. 2(a). The designed IQ-MZMs with slotted transmission lines and inter-phase-shifter cross-talk suppression [7,8] have 4.4 mm long phase shifters, a BW of 14 GHz optimized for the present application, a $V_\pi L$ of 2.45 V·cm and 4.5 dB IL. Operated with 1 $V_{pp}$ signals and biased to achieve full extinction during soliton shaping, they introduce an insertion loss and modulation penalty of 13.5 dB, defined as the

attenuation of the peak power after modulation. Afterwards, channels 1 and 2, that respectively carry the same information as channels 3 and 4, are delayed (IL = 3 dB) as a means to emulate four independent channels. All channels are multiplexed onto one out of two bus waveguides using four 4th-order CROW OADMs (IL = 2 dB, BW = 17.5 GHz) that are tuned to achieve equal peak power for all channels.

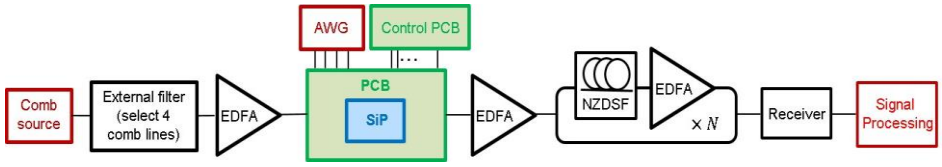



*Figure 1. Block diagram of investigated link.*

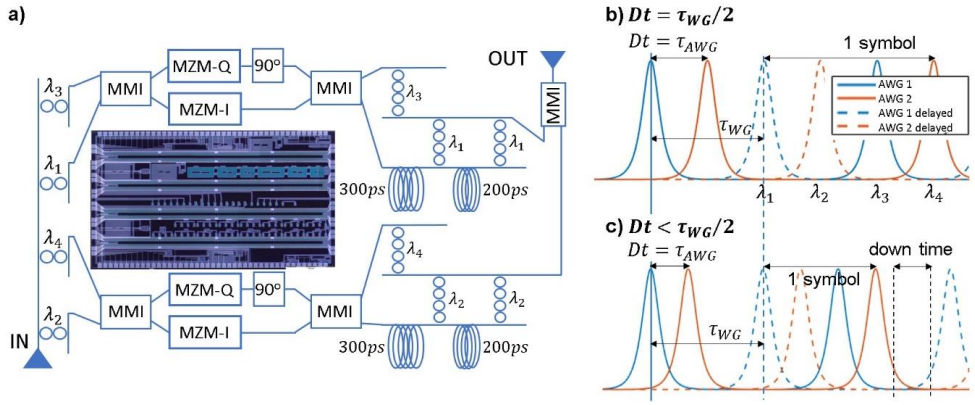



*Figure 2. (a) PIC block diagram and chip micrograph (inset). (b,c) Soliton pulse sequencing within the transmission window.*

A multimode interferometer coupler (MMI) finally serves to combine the two bus waveguides into one (IL = 3 dB), that is then routed off chip via a second GC. Merging via an MMI allows for pulses of even and odd channels to have partial spectral overlap without clipping of the spectra [4]. Including interconnection and monitor tap losses (1.5 dB), we obtain a soliton peak power of -20.6 dBm per channel. These power levels have to be reamplified with an EDFA to reach launch powers that fulfill the soliton condition, depending on soliton pulse width and the length of the used recirculating, amplified non-zero dispersion shifted fiber (NZDSF) loops [1].

In the implemented transmitter [Fig. 2(a)], neighboring channels (single increment in channel number also corresponds to closest spectral and time overlap inside the transmission window (TW), since $\lambda_1 < \lambda_2 < \lambda_3 < \lambda_4$ and $t_1 < t_2 < t_3 < t_4$) are sent to different IQ-MZMs to ensure fully independent data streams. This also ensures that channels multiplexed onto the same bus waveguide at the output of an IQ modulator also have sufficiently low spectral overlap to be routable by the OADMs with minimal cross-talk. The four optical channels are modulated with only a 4-channel arbitrary waveform generator (AWG). The delay $\tau_{WG}$ applied to channels 1 and 2 by on-chip delay loops can be selected to be either 300 ps or 300 ps + 200 ps. Together with the pulse repetition time at the output of the AWG (duration of a complete symbol, i.e., a 4-pulse TW) as well as the time delay between independent pulse trains applied to the two IQ-MZMs ($\tau_{AWG}$), this allows reprogramming of the pulse-to-pulse time delays (Dt). For example, this allows to explore pulse spacings Dt of 250 ps or 150 ps with pulse trains fully filling 1000 ps or 600 ps long TWs [Fig. 2(b)]. A 3rd configuration also modeled below consists in closer spaced pulses (Dt = 100 ps) only partially filling a 500 ps long TW also including a 100 ps down time [Fig. 2(c)].

## 3. SIMULATION SETUP AND RESULTS

For the simulations, blocks of 40,000 bits are QPSK modulated and split up into two channels. Using these symbols, soliton pulses are created with a characteristic pulse width ($T_0$) of 38 ps, a BW of 8.8 GHz (99% power) and a peak amplitude of 1 $V_{pp}$. These soliton pulses are then applied to the IQ-MZMs to modulate and multiplex the four channels. The relative carrier frequencies are set to $\Delta f$ = [-15 GHz, -5 GHz, 5 GHz, 15 GHz]. As mentioned above, soliton pulses have a peak power of -20.6 dBm at the output of the PIC, which needs to be amplified by an EDFA (NF = 5 dB) up to -0.3 dBm fulfilling the soliton condition. After amplification, the combined solitons are launched into N spans of 50 km NZDSF combined with an EDFA (NF = 5 dB), resulting in a 28 dB optical signal-to-noise ratio (OSNR) at the Rx after 3,750 km (OSNR accounting for 4 soliton pulses and noise in the entire TW). On the Rx side, the 4-pulse trains are wavelength demultiplexed and sent to four parallel coherent Rx. After demodulation, each soliton pulse is low-pass filtered, sampled and digitized. Finally, solitons are normalized and analyzed using the forward-backward method, followed by a blind phase search for phase recovery [4].

We have simulated the system to understand how the time spacing affects soliton integrity and demodulation. As seen in Fig. 3(a), it is possible to transmit groups of 4 solitons with Dt = 250 ps (8 Gbps) up to 2,000 km with

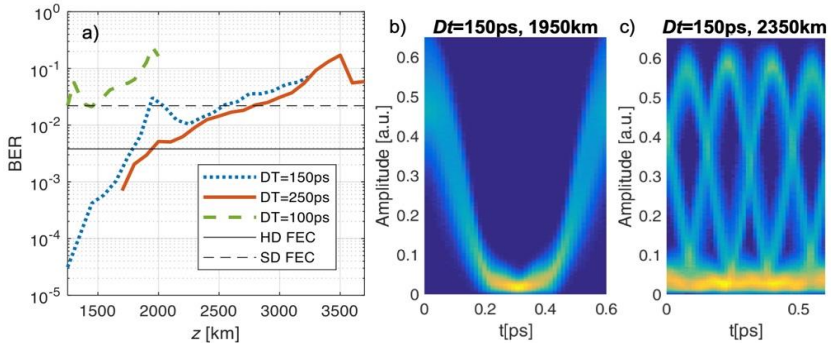



*Figure 3. (a) BER as a function of distance for different Dt. Soliton pulse eye diagrams for (b) Dt = 150 ps at 1,950 km and (c) Dt = 150 ps at 2,350 km.*

a BER below the hard-decision forward error correction (HD FEC) limit and up to 2,750 km below the soft-decision (SD) FEC limit. Similar results are obtained for a tighter soliton sequencing with Dt =150 ps (13.3 Gbps). Packing the solitons even closer clearly affects their integrity as can be seen for Dt = 100 ps. This shows that the four solitons can be packed together in a TW of width $4T_0$ with small penalty, but that higher compactification is detrimental. Ripples are seen in the BER curves at 1950 km for Dt = 150 ps and at 3500 km for Dt = 250 ps. In soliton merging, soliton pulses propagate together with different group velocities, changing their initial position within their TW. At specific distances they can partially or even completely overlap, as seen in Fig. 3(b). This makes it more difficult to recover them at the Rx even when compared with longer distances where they are again equally spaced [Fig. 3(c)], as a consequence of the partial spectral overlap of the soliton pulses [4] making wavelength demultiplexing imperfect. Changing the frequency spacing or the initial time domain separation as enabled by the Tx reconfigurability allows shifting these ripples away from a targeted transmission length. Hence, this problem can be avoided in a real transmission scenario. While data rates that are currently considered are still low, they will be increased once the system has been experimentally proven by increasing the number of solitons, using more complex modulation formats and reducing the width $T_0$ of the solitons. With the current chip, we could generate QPSK modulated solitons up to 20 Gbps. It is also possible to redesign the IQ-MZM to achieve higher BWs [8] and higher values of Vpp could be used to reduce the modulation penalty. Furthermore, data dependent time shifts on a small scale can be included to introduce amplitude modulation in the NLFT domain [1].

## 4. CONCLUSIONS

We have presented a SiP DWDM soliton Tx that has been characterized and is currently being used in experimental system tests. It can modulate four first-order solitons and multiplex them with different frequency and time spacing. Nonlinear link simulations have been run for different pulse-to-pulse spacing and fiber lengths. Simulation results show that solitons can be compactified together in a transmission window $4T_0$ and still allow to reach up to 2,500 km with a BER below the SD FEC limit. Furthermore, we have explored the evolution of soliton merging over distance, providing a solution to soliton overlap by shifting it out of the region of interest via Tx reconfiguration. There are multiple paths towards increasing the data rates we are presently working with that will be taken once the current configuration has been experimentally proven.

## REFERENCES


[1] S. K. Turitsyn, *et al.*: Nonlinear Fourier transform for optical data processing and transmission: advances and perspective, *Optica*, vol. 4, issue 3, pp. 307-322, 2017.

[2] S. Li, *et al.*: Optical signal processing in the discrete nonlinear frequency domain, *Proc. Opt. Fiber Commun. Conf. & Expo.*, San Diego, CA, USA, March 2018, paper W2A.40.

[3] J. Koch, *et al.*: Transmission of Higher Order Solitons created by Optical Multiplexing, *IEEE J. Lightw. Technol.*, vol. 37, issue 3, pp. 933-941, Feb. 2019.

[4] J. Koch, *et al.*: DWDM Soliton Transmission enabled by Integrated Photonics and Nonlinear Fourier Transform, *Proc. 20th ITG-Symposium on Photonic Networks*, pp. 52-54, May 2019.

[5] F. Xia *et al.*: Ultra-compact high order ring resonator filters using submicron silicon photonic wires for on-chip optical interconnects, *Opt. Expr.*, vol. 15, issue 19, pp. 11934-11941, 2007.

[6] A. Moscoso-Mártir, *et al.*: 8-channel WDM silicon photonics transceiver with SOA and semiconductor mode-locked laser, *Opt. Expr.*, vol. 26, pp. 25446-25459, 2018.

[7] F. Merget, *et al.*: Silicon photonics plasma-modulators with advanced transmission line design, *Opt. Expr.*, vol. 21, issue 17, pp. 19593-19607, 2013.

[8] S. S. Azadeh, *et al.*: Advances in silicon photonics segmented electrode Mach-Zehnder modulators and peaking enhanced resonant devices, *Photonics North*, Proc. SPIE 9288, Sep. 2014.

# Tensile Strained $Ge_{0.99}$ $Si_{0.01}$ EA Modulator Arrays for Integrated Broadband Modulation

**Danhao Ma[1], Yiding Lin[2], Ruitao Wen[3], Lionel Kimerling[1], Jurgen Michel[1]**
[1] Department of Materials Science and Engineering, Massachusetts Institute of Technology, USA
[2] School of Electrical and Electronic Engineering, Nanyang Technological University, Singapore, Singapore
[3]Department of Materials Science and Engineering, Southern University of Science and Technology, China
*e-mail: madanhao@mit.edu*

**ABSTRACT**

Electronic and photonic integrated circuits serve as a promising platform for telecommunications and sensing applications. A one-for-all tensile strained $Ge_{0.99}$ $Si_{0.01}$ modulator array design is proposed to cover a broad telecommunication band with multiple modulators designed and fabricated simultaneously in a single lithography and patterning flow. Modulators with the width from 0.5μm to 3μm demonstrated the absorption edge shift from 1533nm to 1566nm, relating to an array wavelength operation from 1526nm to 1575 nm, with an extinction ratio of 4.5dB at 3V reverse bias. This strain engineering innovation can be applied not only to Ge and GeSi materials, but also to III-V materials for light-emitting, photodetecting, wavelength filtering, and sensing applications. This approach allows electronic - photonic integrated systems to be developed with a simpler device layout, higher device yield, and lower fabrication cost.

**Keywords**: strain, germanium, waveguide device, modulator, integrated photonics, low-cost fabrication

## 1. INTRODUCTION

Electronic and photonic integrated circuits serve as a promising platform for telecommunications and sensing applications [1]. Electroabsorption modulators utilize the field-induced Franz-Keldysh effect, which allows fast modulation, small device footprint, and low power consumption [2-3]. Epitaxially grown GeSi films on Si substrates are a suitable materials platform for integrated modulator applications because of the Si CMOS compatibility and distinctive optoelectronic materials properties [3]. A modulator's operation wavelength adjustment and its system integration for broadband modulation are two major challenges of fabricating on-chip modulator arrays for telecommunication. In the case of an electro-absorption modulator, the optimization of the modulator material for a specific wavelength can be achieved by tuning the material composition or applying strain to the material since modulation is achieved near the direct bandedge.

The conventional strategy of inserting a modulator for a specific modulation wavelength involves specific materials engineering and device fabrication for each individual modulator [4-5]. In order to realize an integrated system with broadband modulation, multiple modulators have to be fabricated individually and assembled onto a chip. Each fabrication step adds cost to design and processing. Integrating more modulators for multiple operation wavelengths gives broader band coverage and higher optoelectronic data processing capacity. In this work, a one-for-all tensile strained $Ge_{0.99}Si_{0.01}$ modulator array design is proposed and demonstrated to cover a broad telecommunication band with multiple modulators designed and fabricated simultaneously in a single lithography and patterning flow [6]. A stressor layer applies a homogeneous strain to the modulator structures. By changing the modulator width, the strain in the modulator changes, tuning the $Ge_{0.99}Si_{0.01}$ bandgap and, therefore, the modulation operation wavelength. Thus, modulators made of the same material can operate at various wavelengths with the same stressor layer by simply changing in the dimension of the modulators.

## 2. MODULATORS ARRAY DESIGN WITH STRAIN ENGINEERING

The waveguide-integrated modulator contains three major optical parts, as shown in Fig 1a. The $Ge_{0.99}Si_{0.01}$ waveguide is placed on top of the Si waveguide with GeSi optical tapers on both ends for the light coupling in and out of the waveguide modulator. The electro-absorption optical modulation occurs in the $Ge_{0.99}Si_{0.01}$ waveguide. The height of Si and $Ge_{0.99}$ $Si_{0.01}$ waveguides are 250nm and 300 nm, respectively. The width of the modulator waveguide is a unique design parameter to vary the modulator materials bandgap as a response of the external stressor layer. The 0.6GPa tensile stressor layer is designed to be on the sides of the modulator waveguides in order to apply uniform and sufficient tensile stress across the short axis of the modulator waveguide. The electrical contacts are on top and bottom of the modulator with ground-signal-ground pads for high-speed modulation measurements, as shown in Fig 1b. As a demonstration of the concept, the $Ge_{0.99}Si_{0.01}$ modulators with waveguide widths of 500nm, 1μm, and 3μm are fabricated and tested.

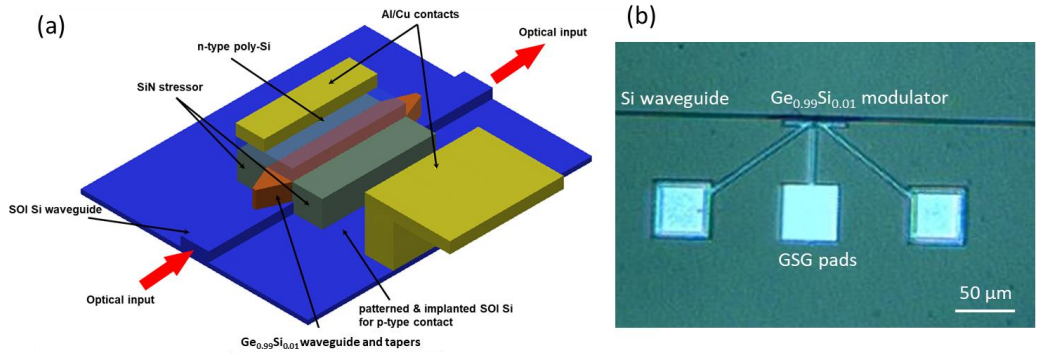



Figure 1. (a) individual $Ge_{0.99}Si_{0.01}$ waveguide modulator schematic, and (b) optical image of the modulator

A finite element model was developed to investigate the strain distribution in $Ge_{0.99}Si_{0.01}$ modulators array for broadband modulation. The simulation was based on solid mechanics theory. The stressor layer is made from silicon nitride with a tensile stress of 0.6 GPa. The strain distribution in 500nm, 1µm, and 3µm wide $Ge_{0.99}Si_{0.01}$ waveguide modulators are plotted in Fig 2. Uniform tensile strain of 0.39%, 0.33%, and 0.18% is obtained in waveguides with widths of 500nm, 1µm, and 3µm, respectively. A deformation potential theory based on quantum mechanics was applied to derive the effect of strain on the band structure of semiconductor materials. The electro-absorption modulator operation wavelength is related to its material band structure. Therefore, the correlation between the operation wavelength and modulator waveguide strain is established and plotted in Fig 2. The $Ge_{0.99}Si_{0.01}$ waveguide modulators with widths of 500nm, 1µm, and 3µm are simulated to have absorption edge at 1572 nm, 1563 nm, and 1542 nm, respectively.

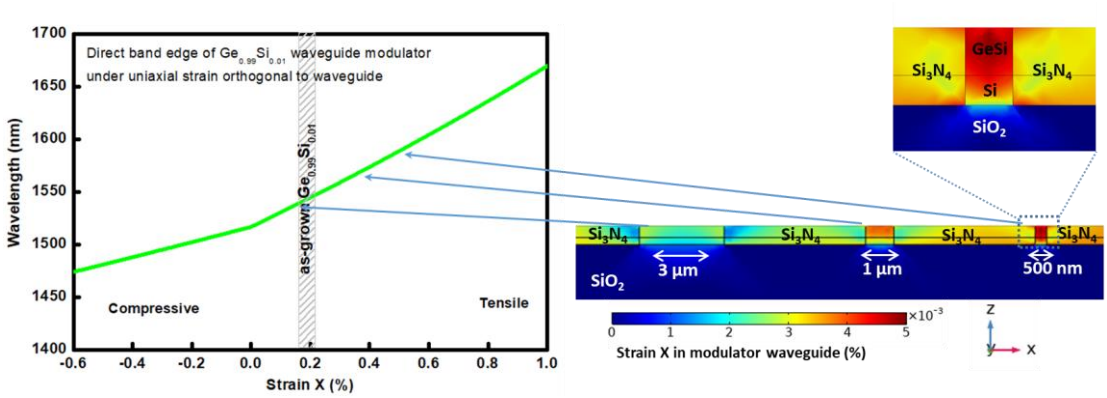



Figure 2. modulator absorption edge as a function of strain in $Ge_{0.99}$ $Si_{0.01}$ waveguide, along with strain distribution in the waveguides under 0.6GPa stressor layer

## 3. DEVICE FABRICATION AND EXPERIMENTAL RESULTS

The strained modulators array was fabricated in MIT Nano and the Substrate Engineering Lab Cleanroom Facilities. We started with 250nm Si on 3µm $SiO_2$ insulator wafers. The boron implantation was performed on patterned Si on the SOI wafer. $Ge_{0.99}Si_{0.01}$ was grown epitaxially and annealed cyclically on the p-type Si layer, followed by a poly Si layer growth on top of the $Ge_{0.99}Si_{0.01}$ layer. Phosphorous was implantated with subsequent thermal annealing to provide an n-type Si contact layer. $Ge_{0.99}Si_{0.01}$ waveguides of various dimensions were patterned and etched. A $Si_3N_4$ stressor layer was then deposited via multi-frequency plasma-enhanced chemical vapor deposition. Finally, trenches were opened for the metal contacts. Multiple waveguides are simultaneously fabricated in the same process flow to achieve the modulators array. The fabrication steps are CMOS-compatible and can be readily implemented into a foundry fabrication.

Optical transmission measurements with and without DC bias were performed to evaluate the device operation wavelength and modulator performance, as shown in Figure 3. The optical transmission spectra of three waveguide modulators with various widths show a shift of the absorption band-edge. A generalized Franz-Keldysh model was applied to fit the optical transition and exacted the direct band structure parameters. The direct bandgaps derived from the fitting are 0.792 eV, 0.797 eV, and 0.809 eV for 500nm, 1µm, and 3µm wide $Ge_{0.99}$ $Si_{0.01}$ waveguide modulators with the 0.6GPa tensile stressor layer. That corresponds to the wavelength of the absorption edge at 1566nm, 1555nm, and 1533nm, which are consistent with the values simulated from the device design. Since the modulation width of a single GeSi EA modulator is around 15 nm [3], the demonstrated wavelength

range for our modulator array ranges from 1526nm to 1575 nm. The optical transmission under reverse bias shows a device extinction ratio of 4.5dB at –3V. The modulators show an increase in insertion loss with waveguide width, that is believed to be due to the optical loss during the light coupling through the tapers, and optical absorption induced from the contacts. The device design can be further improved to reduce insertion loss and increase the extinction ratio.

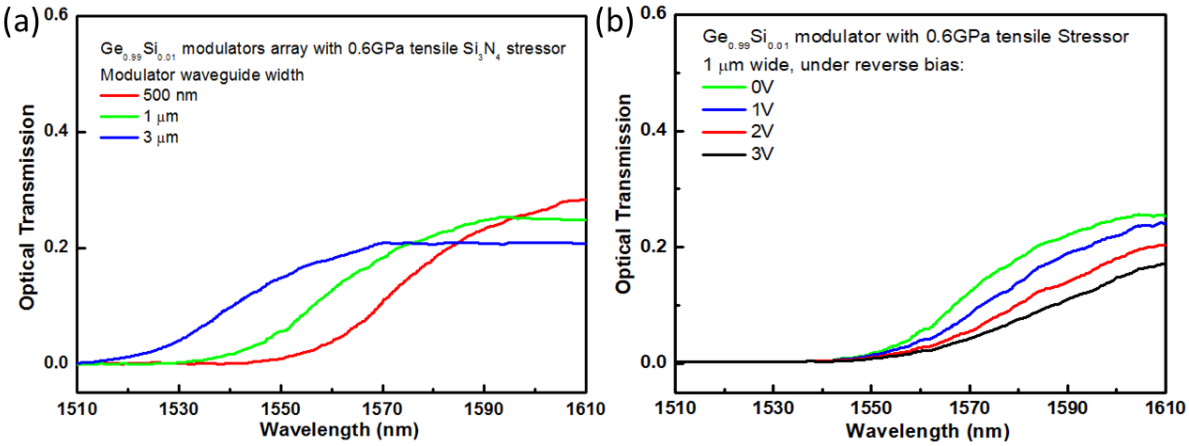



Figure 3. Optical transmission measurement of modulators array (a) without and (b) with reverse bias voltage.

## 4. CONCLUSIONS

In summary, a one-for-all tensile strained $Ge_{0.99}$ $Si_{0.01}$ modulator array design is proposed to cover a broad telecommunication band with multiple modulators designed and fabricated simultaneously in a single lithography and patterning flow. Modulator arrays with waveguide widths from 0.5μm to 3μm, show an wavelength operation from 1526nm to 1575 nm, with an extinction ratio of 4.5 dB at operation wavelength and 3V reverse bias. Variation in composition and strain can extend the operation range of the array significantly. This strain engineering innovation can be applied not only to Ge and GeSi materials, but also to III-V materials for light-emitting, photodetecting, wavelength filtering, and sensing applications. That allows the electronic and photonic integrated system be developed with a simpler device layout, higher device yield, and lower fabrication cost.

## ACKNOWLEDGEMENTS

This research was supported by Futurewei Inc. Y. Lin acknowledges the support from SMART (Singapore-MIT Alliance for Research and Technology) Graduate Fellowship.

## REFERENCES

[1] David Thomson, *et al*.: Roadmap on silicon photonics, *J. Opt*., vol. 18. 073003, 2016.
[2] Kazumi Wada, Lionel C. Kimerling: Photonics and Electronics with Germanium, *Wiley-VCH*, Chapter 9, pp. 191-217, 2015.
[3] Jifeng Liu, et al. : Waveguide-integrated, ultralow-energy GeSi electro-absorption modulators, *Nature Photon*, Vol. 2, pp. 433-437, 2008.
[4] Papichaya Chaisakul, *et al*.: 23 GHz Ge/SiGe multiple quantum well electro-absorption modulator, *Opt. Express*, vol. 20, pp. 3219-3224, 2012.
[5] S. Gupta, *et al*.: 50GHz Ge Waveguide Electro-Absorption Modulator Integrated in a 220nm SOI Photonics Platform, *Optical Fiber Communication Conference*, Tu2A.4, 2015.
[6] Danhao Ma, Yiding Lin, Jurgen Michel: Strained Germanium Silicon Modulators Array for Integrated High Speed Broadband Modulation, *PCT International Patent/US19/53353*, filed Sept. 27, 2019.

# Discretely tunable optical delay lines using step-chirped subwavelength grating Bragg gratings

*(Student's paper)*

**Hao Sun**[1] **and Lawrence R. Chen**[1]
[1] *Department of Electrical and Computer Engineering, McGill University, Montreal, QC H3A 0E9 Canada*
*e-mail: lawrence.chen@mcgill.ca*

## ABSTRACT

A discretely tunable optical delay line based on step-chirped subwavelength grating Bragg gratings is proposed and experimentally demonstrated. A total delay of 55 ps in steps of 9 ps is obtained over an operating bandwidth of 29 nm. The device is fabricated using electron beam lithography with a single etch in silicon on insulator.

**Keywords**: subwavelength grating, silicon photonics, time delay, Bragg grating

## 1. INTRODUCTION

Integrated optical delay lines are important for signal processing in optical communications and microwave photonics [1]-[4]. One conventional implementation of on-chip optical delay lines uses various lengths of waveguides interconnected by optical switches: the state of the switches is set to obtain different waveguide paths, and hence different delays. In this manner, discrete tuning of the delay can be obtained [1]. Another implementation involves cascading several optical ring resonators; by tuning the phase offset and the power coupling coefficient of the ring resonators, continuous tuning of the delay can be obtained [4]. Finally, continuous or discrete tuning can be obtained using chirped or step-chirped waveguide Bragg gratings (BGs) [5], [6].

Recently, subwavelength grating (SWG) waveguides with low loss and the flexibility in tailoring the effective index have attracted significant attention. Numerous SWG waveguide devices have been realized, including wideband couplers, ring resonator filters, and BG filters [7]. The effective index of the SWG waveguide can be tuned through its duty cycle; thus, SWG waveguides of the same length but different duty cycles will have different propagation delays. We exploited this feature to implement index-variable optical true time delay lines [8]. For SWG waveguides that are 8 mm in length, we observed a differential time delay of ~ 1.6 ps for a difference in duty cycle of 1%.

In this paper, we propose and experimentally demonstrate an integrated discretely tunable optical delay line using SWG waveguide-based step-chirped BGs in silicon-on-insulator (SOI). The step-chirped SWG BG comprises a serial array of ten SWG BGs whose Bragg wavelengths increase linearly with position. We observe a total time delay of up to 54 ps over a 29 nm bandwidth (1524 nm to 1553 nm), with eight discrete delay steps and an increment delay of ~ 9 ps.

## 2. Device design

The conventional configuration of the SWG waveguide and the simulated effective index are shown in Figs. 1 (a) and (c), respectively; the waveguide cross-section is illustrated in Fig. 1(e). Note that the period and width of the SWG waveguide is 245 nm and 400 nm. All of the effective indices are obtained using 3-D Finite Difference Time Domain (FDTD) simulations [9]. The effective index of the SWG waveguide can be modulated by positioning two loading segments on both sides of the conventional SWG waveguide as shown in Fig. 1 (b) [10]. The simulated effective index of the 'loaded' SWG waveguide for different gap distances as a function of

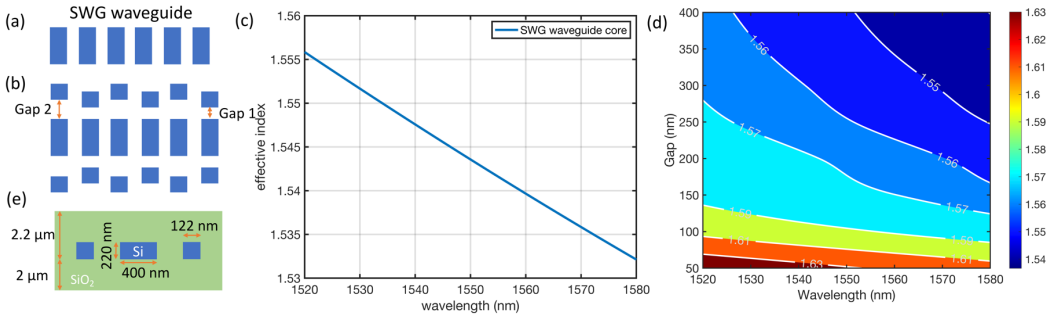



*Figure 1. (a) Configuration of the SWG waveguide; (b) configuration of the SWG BGs; (c) simulated effective index of the SWG waveguide in (a); (d) simulated effective index of the 'loaded' SWG waveguides; (e) Cross-sectional view of the SWG BG.*

TABLE 1. THE GAPs OF EACH BGs.

| (nm) | BG1 | BG2 | BG3 | BG4 | BG5 | BG6 | BG7 | BG8 | BG9 | BG10 |
|---|---|---|---|---|---|---|---|---|---|---|
| Gap 1 | 381 | 310 | 243 | 217 | 188 | 156 | 139 | 124 | 113 | 104 |
| Gap 2 | | 500 | 356 | 272 | 232 | 207 | 172 | 149 | 133 | 120 |

wavelength is shown in Fig. 1 (d). Since the effective index of the 'loaded' SWG waveguide can be 'mapped' to a gap distance, we can design a SWG BG with specific BG wavelength and bandwidth by picking out the suitable combination of gaps. The designed gaps of each SWG BGs in our step-chirped SWG BG are shown in Table 1. The slash in BG1 represents that no loading segments were used. Theoretically, by directly cascading ten SWG BGs, the designed step-chirped SWG BG can provide ten separate reflection bands with an incremental delay step of ~ 6 ps. The width of the square loading segments is 122 nm and the number of periods in each SWG BG is 1,000. The layout of the device includes two vertical grating couplers (VGCs) for input and output coupling and two tapers for the mode conversion between solid core and SWG waveguides.




*Figure 2. Layout of the step-chirped SWG BG; VGC: vertical grating coupler.*

## 3. Experimental Results and Analysis

Two experiments are conducted to measure the time delay response. First, the group delay is measured directly using an optical vector analyser (LUNA OVA 5000) as shown in Fig. 3 (a), where a circulator is introduced to measure the reflected signal from the chip. Second, a time-of-flight measurement is used to record the time delay for sinusoidally modulated carriers at different wavelengths, see Fig. 3 (b).

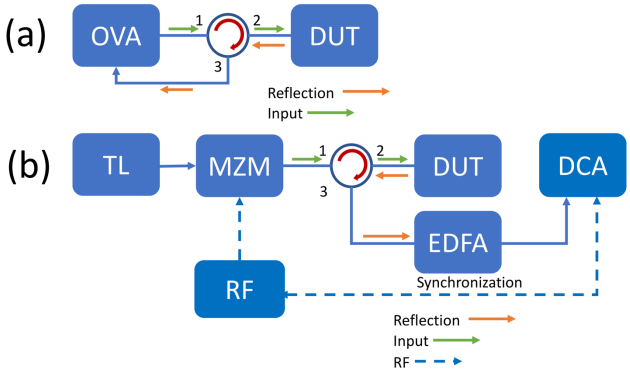



*Figure 3. Experimental setup: (a) the measurement of group delay; (b) the time-of-flight measurement; DUT: device under test; EDFA: Erbium-doped optical fiber amplifier; MZM: Mach-Zehnder modulator; TL: tunable laser; DCA: digital communications analyzer. OVA: optical vector analyzer.*

Fig. 4 (a) and (b) show the group delays in reflection measured using the OVA. Note that the opposite group delay response is obtained when the input and output ports are reversed. We obtain a total delay of up to 54 ps with an incremental delay of ~ 9 ps. The sinusoidal signals in Fig. 4(c) show clearly an increase in delay with increasing wavelength (we use a signal at 1527 nm as the reference). The time delay steps are given in Table 2.

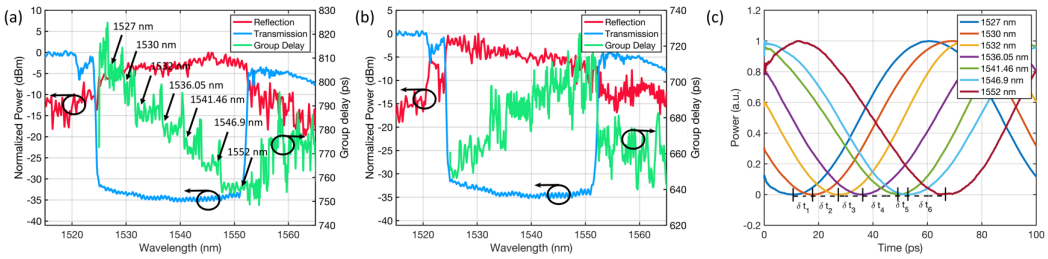



*Figure 4. (a) and (b) the measured group delays; (c) the time delay response characterized by DCA.*

In contrast to our intended design, we only observe 8 reflection bands. The bands used in the time-of-flight measurements are marked in Fig. 4 (a). According to Table 2, the steps are almost equal at shorter wavelengths; however, the variation is greater at longer wavelengths. The reason is that when we design SWG BGs with a longer BG wavelength, the difference between the two gaps becomes very small (e.g., ~20 nm) compared to the fabrication resolution (~ 60 nm). Moreover, a small misalignment of the loading segments will lead to an undesired effective index change, which can cause the shift of the BG wavelength or the expansion of the bandwidth.

TABLE 2. CORRESPONDING TIME DELAY STEPs OF FIG. 4 (C).

| Step | $\delta t_1$ | $\delta t_2$ | $\delta t_3$ | $\delta t_4$ | $\delta t_5$ | $\delta t_6$ |
|---|---|---|---|---|---|---|
| (ps) | 7 | 10 | 8 | 14 | 4 | 11 |

## 4. Summary and Discussion

We have designed and experimentally demonstrated an integrated discretely tunable optical delay line in SOI using step-chirped SWG BGs. We realized a total time delay of up to 54 ps over a 29 nm bandwidth; the incremental delay is ~ 9 ps. The device response can be tailored by changing the value of gaps of the loading segments; however, the number of SWG BGs that can be placed in the array is limited in part by fabrication resolution. More specifically, in order to increase the number of steps within a fixed operating bandwidth, more BGs need to be cascaded, and hence a smaller difference between the gaps in a BG is needed. On the other hand, when the number of steps is fixed, adjusting the gap distance of each BG can be used to tune the BG wavelength. A slight modification of the gaps can cause a relatively small shift of BG wavelength. Thus, the fabrication resolution determines the minimum tuning step of the BG wavelength. In order to optimize the performance of the step-chirped SWG BGs, we need to choose suitable gaps between SWG waveguide core and loading segments. Nevertheless, we believe that this provides a new means for tailoring the group delay response of SWG BG structures.

## ACKNOWLEDGEMENTS

We thank Prof. Jose Azana for providing LUNA OVA 5000, Saket Kaushal for the assistance in using LUNA OVA 5000, Yue Wang for the assistance in time delay measurement and Applied Nanotools Inc. for the fabrication.

## REFERENCES

[1] J. Xie, *et al.*: Seven-bit reconfigurable optical true time delay line based on silicon integration, *Opt. Express* 22, pp. 22707-22715, 2014.
[2] Z. Zou, *et al.*: Channel-spacing tunable silicon comb filter using two linearly chirped Bragg gratings, *Opt. Express* 22, pp. 19513-19522, 2014.
[3] M. Burla, *et al.*: On-chip CMOS compatible reconfigurable optical delay line with separate carrier tuning for microwave photonic signal processing, *Opt. Express* 19, pp. 21475-21484, 2011.
[4] Y. Liu, *et al.*: Ultra-low-loss Silicon Nitride optical beamforming network for wideband wireless applications, *IEEE J Sel Top Quantum Electron*, vol. 24, no. 4, pp. 1-10, 2018.
[5] M. Spasojevic and L. R. Chen: Discretely tunable optical delay lines using serial and step-chirped sidewall Bragg gratings in SOI, *Electron. Lett.*, vol. 49, no. 9, pp. 608 -610, 25 April 2013.
[6] W. Zhang and J. Yao: Silicon-Based Integrated Microwave Photonics, *IEEE J Quantum Electron*, vol. 52, no. 1, pp. 1-12, Jan 2016.
[7] P. Cheben, *et al.*: Subwavelength integrated photonics, *Nature* 560, pp. 565–572, 2018.
[8] J. Wang, *et al.*: Subwavelength grating enabled on-chip ultra-compact optical true time delay line, *Sci Rep* 6, pp. 30235, 2016.
[9] Lumerical Solutions, Inc., Available: http://www.lumerical.com.
[10] J. Čtyroký, *et al.*: Design of narrowband Bragg spectral filters in subwavelength grating metamaterial waveguides, *Opt. Express* 26, pp. 179-194, 2018.

# Monolithically Integrated Tunable Comb Source using Gain Switched Slotted Fabry-Pérot Lasers

*(Student Paper)*

John McCarthy [1,2], Mohamad Dernaika [3], Jack Mulcahy [1,2], Albert A. Ruth [4], Satheesh Chandran [4], Prince M. Anandarajah [5], Eamonn P. Martin [5], Justin K. Alexander [6], Frank H. Peters [1,2]

[1]*Tyndall National Institute, Lee Maltings, Cork, Ireland*

[2]*Physics Department, University College Cork, College Road, Cork, Ireland*

[3]*Rockley Photonics Ireland, Lee Mills House, Lee Maltings, Cork, Ireland*

[4]*Physics Department and Environmental Research Institute, University College Cork, Cork, Ireland*

[5]*School of Electronic Engineering, Dublin City University, Glasnevin, Dublin 9, Ireland*

[6]*Aeponyx, Montreal, QC, Canada*

*e-mail: john.mccarthy@tyndall.ie*

## ABSTRACT

A tunable comb generation photonic integrated circuit (PIC) is demonstrated by gain switching a three section device. The PIC consists of a slave laser section and master laser, where the master laser is made up of a gain and a slotted mirror section. The tunability of the master laser was demonstrated by varying the bias across the gain and slotted sections producing nine wavelengths (with a side mode suppression ratio (SMSR) greater than 30 dB) with a tuning range of 1555 nm - 1582 nm. Frequency combs were produced by injection locking the slave laser to the master laser and gain switching the slave laser by applying a high power radio frequency (RF) signal using a signal generator, an RF amplifier and a ground-signal (GS) probe. Combs were generated with line spacings ranging from 3 GHz - 9 GHz.

**Keywords**: Slotted Fabry-Pérot, gain switching, tunable wavelength, frequency comb, injection locking.

## 1 INTRODUCTION

Optical frequency comb sources (OFCS) show significant promise in many modern day applications such as spectroscopy [1], space-based instruments [2] and high speed telecommunications [3]. OFCS generate equally spaced spectral carriers. Due to their precise and stable frequency, they can potentially reduce/eliminate the use of guard bands between neighbouring wavelength division multiplexed (WDM) signals [4]. One method of generating frequency combs in a PIC (which is the method investigated in this paper) is by injection locking a slave laser with a single mode master laser and gain switching the slave laser by applying a high power radio frequency (RF) signal.

Injection locking using an external master laser has been demonstrated to reduce phase noise in gain switched lasers [5]. In this paper we demonstrate the integration of a master tunable Slotted Fabry-Pérot (SFP) laser with a gain switched slave Fabry-Pérot (FP) laser in order to reduce phase noise and reduce the output linewidths. These two lasers are monolithically integrated in a strongly coupled master/slave configuration [6], whereby the slave laser is optically phase-locked to the master laser. The single mode characteristics of the laser have been known to improve by on-chip optical phase locking, particularly with increasing the side mode suppression ratio (SMSR) [7]. The master laser is more heavily biased than the slave and so the two sections are operating in an asymmetric bias regime. So while no isolator exists between the lasers, the asymmetry of the operation has been shown to allow for injection locking [8]. The slave laser is then gain switched using a high power RF signal generator to generate the optical combs. The output of the slave laser is analyzed using an ANDO AQ6317B optical spectrum analyzer (OSA), which has a resolution of 0.02 nm, and so the number of comb lines and their spacing can be observed.

## 2 DEVICE DESIGN

The device itself is made up of three sections, consisting of a master section, a slotted section and a slave section. Slots etched between the three sections of the device allows for electrical isolation and therefore permit independent biasing [9]. The master gain region and slave laser have lengths of 800 $\mu$m and 400 $\mu$m respectively. The slotted section is 756 $\mu$m in length and has 8 slots with an interslot distance of 108 $\mu$m.

The lasing material used to fabricate this device consists of 5 compressively strained 6 nm wide AlGaInAs quantum wells on an n-doped InP substrate. The upper p-doped cladding consists of a 0.2 $\mu$m InGaAs cap layer, which is followed by 0.05 $\mu$m of InGaAsP, lattice matched to 1.62 $\mu$m of InP. The ridge and slot features were defined using standard lithographic techniques, with a ridge width of 2.5 $\mu$m and a height of 1.7 $\mu$m, and a slot

width of 0.88 $\mu$m, with the ridge etch stopping above the quantum wells. A ground-signal (GS) contact was added to the slave section to allow for the gain switching of the device, where the ground pad makes contact with the n-type substrate via a deep etch through the active region into the n-region.

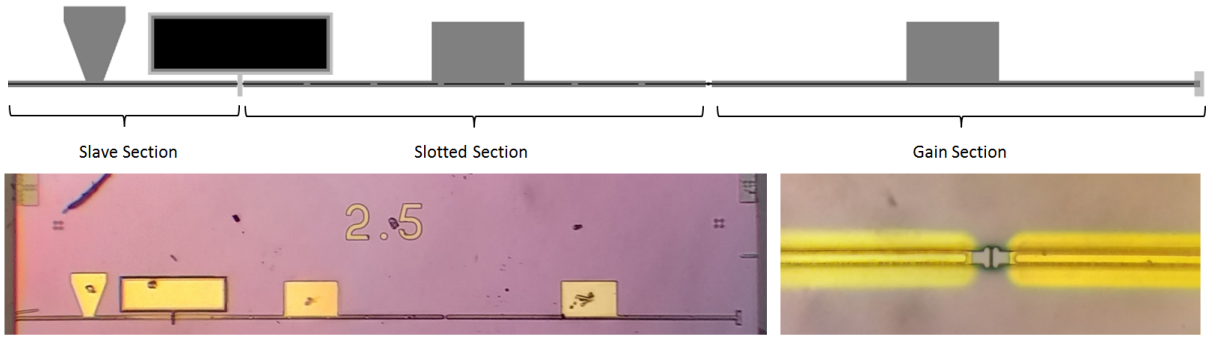



Figure 1. Schematic of device design (top). Microscope image of on chip device (bottom left) and slot (bottom right).

## 3 DEVICE CHARACTERISATION

Initially, the gain and slotted sections of the device were biased using currents ranging from 20 mA - 200 mA through the gain section and 20 mA - 100 mA through the slotted sections. At each interval the optical spectrum was recorded using the OSA and the SMSR and peak lasing wavelength was recorded; results plotted in Fig. 2. It was found that the master laser, made up of the gain and slotted sections, lased at a single mode (SMSR $>$ 30 dB) and had a tunable wavelength. From the plots attained, the master section produced multiple single mode regions within a wavelength range of 1555 nm - 1582 nm.

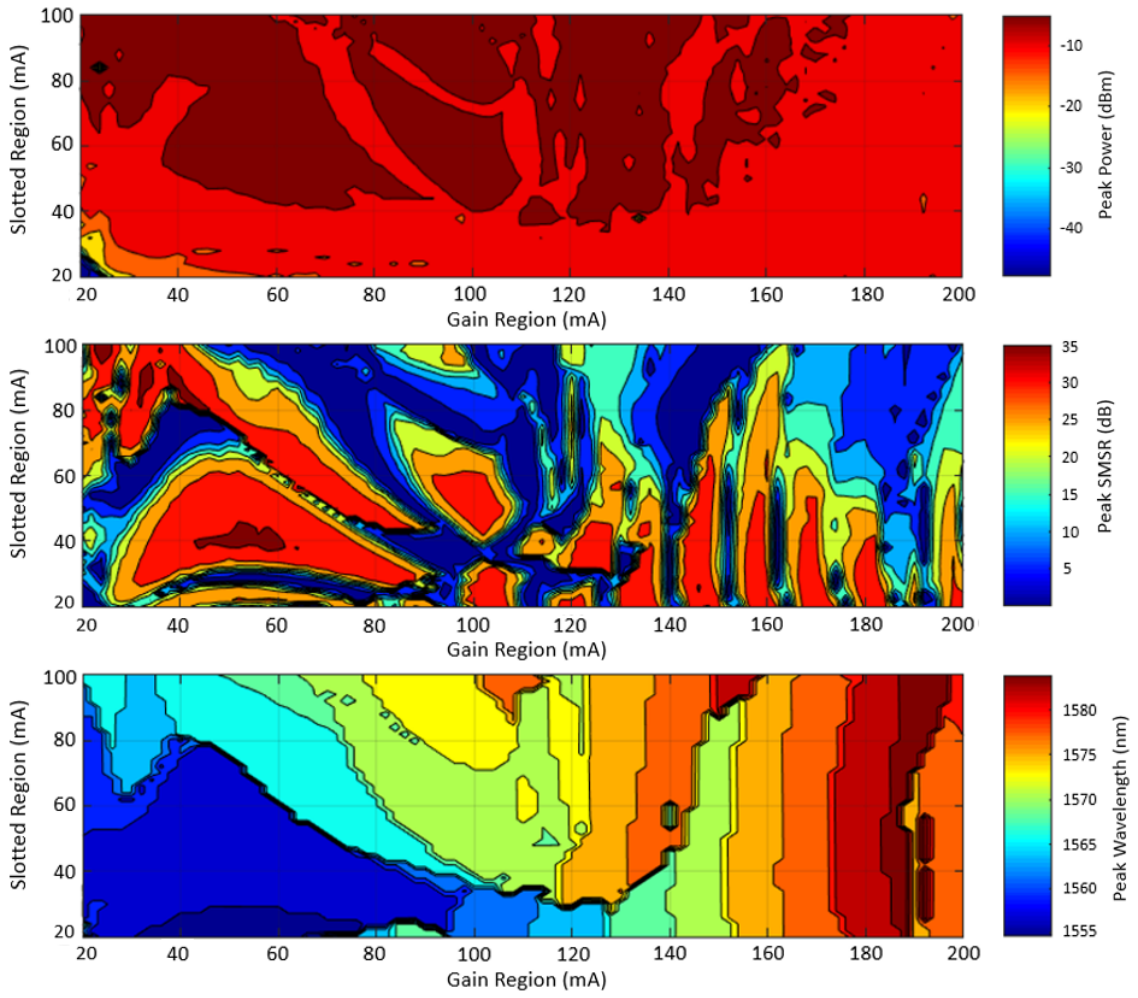



Figure 2. Power (top), SMSR (middle) and wavelength (bottom) of the master SFP while varying the current through the gain and slotted regions.

The slave section of the device was biased and the slave laser was injection locked to the master laser in order to reduce the phase noise. In order to injection lock the slave laser with the master laser, the master laser was biased so that it produced a single mode spectrum. The optimal biasing of the slave laser was found to be at a value approximately at its threshold current (25 mA - 32 mA).

Once injection locking was achieved, a strong RF signal was applied to the slave section to allow for gain switching to occur. Frequency combs were attained with line spacing between 3 GHz - 9 GHz. The best combs had a free spectral range of approximately 5.75 GHz, such as shown in Fig. 3. In Fig. 3 the comb spectrum was attained by biasing the gain, slotted and slave sections at 179 mA, 28 mA and 27 mA, respectively. We observe 8 comb lines within 4 dB of each other.

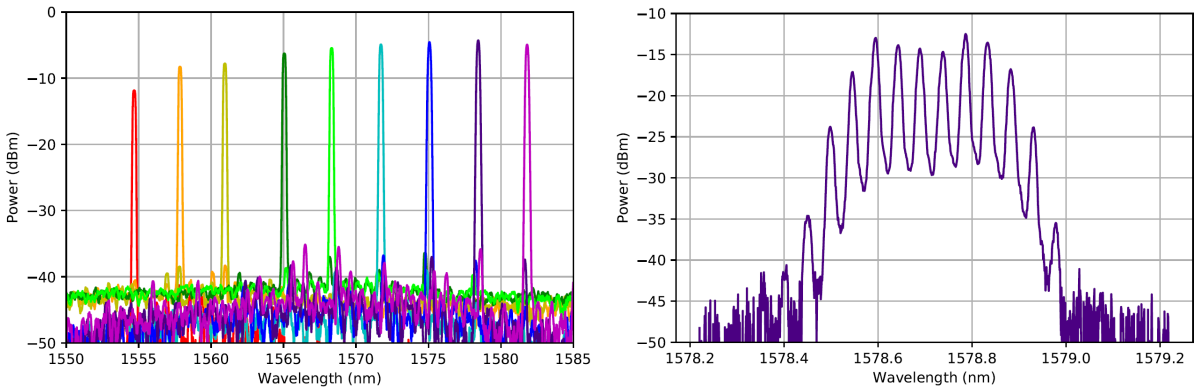



Figure 3. Different wavelengths attained by varying the bias across the gain and slotted section (left). Frequency comb generated at 1578.7 nm with a free spectral range of 5.75 GHz (right).

## 4 CONCLUSION

An optical frequency comb was obtained from the PIC by gain switching a slave laser that has been injection locked with a single mode master SFP. Due to the reflective defects caused by the slots, the master laser was shown to have a tunable wavelength, producing nine single mode wavelengths across a range of 27 nm. Combs were attained at each wavelength with line spacings ranging from 3 GHz - 9 GHz with optimal comb lines being produced by gain switching at an RF frequency of 5.75 GHz. This resulted in up to 8 comb lines being generated within 4 dB of each other.

## ACKNOWLEDGMENT

This work was supported by the Enterprise Ireland commercialisation fund CF-2017-0683A&B, and by Science Foundation Ireland under grants 12/RC/2276 (IPIC), SFI/13/IA/1960 and 14/TIDA/2415.

## REFERENCES

[1] I. Coddington, W. Swann, and N. Newbury, “Coherent multiheterodyne spectroscopy using stabilized optical frequency combs,” Phys. Rev. Lett. 100(1), 013902 (2008).

[2] X. Wang, S. Takahashi, K. Takamasu, and H. Matsumoto, “Space position measurement using long-path heterodyne interferometer with optical frequency comb,” Opt. Express 20(3), 2725-2732 (2012)

[3] A. Ellis and F. Gunning, “Spectral density enhancement using coherent WDM,” IEEE Photon. Technol. Lett. 17(2), 504-506 (2005).

[4] R. Zhou, P. M. Anandarajah, D. G. Pascual, J. O’Carroll, R. Phelan, B. Kelly, and L. P. Barry, “Monolithically integrated 2-section lasers for injection locked gain switched comb generation,” Optical Fiber Communications Conference and Exhibition (2014).

[5] L. P. Barry, P. Anandarajah, A. Kaszubowska, “Optical pulse generation at frequencies up to 20 GHz using external-injection seeding of a gain-switched commercial Fabry-Perot laser,” IEEE Photon. Technol. Lett. 13(9), 1014-1016 (2001).

[6] D. Byrne, Q. Lu, W. H. Guo, J. F. Donegan, B. Corbett, B. Roycroft, P. Lambkin, J. P. Engelstaedter, and F. Peters, “A facetless laser suitable for monolithic integration,” Optical Fiber Communication/National Fiber Optic Engineers Conference (2008).

[7] A. Tauke-Pedretti, G. A. Vawter, E. J. Skogen, G. Peake, M. Overberg, C. Alford, W. W. Chow, Z. S. Yang, D. Torres, and F. Cajas, “Mutual injection locking of monolithically integrated coupled-cavity DBR lasers,” IEEE Photon. Technol. Lett. 23(13), 908-910 (2011).

[8] A. H. Perrott, L. Caro, M. Dernaika, F. H. Peters, “A Comparison between off and On-Chip Injection Locking in a Photonic Integrated Circuit,” Photonics, 6, 103, (2019).

[9] D. C. Byrne, J. P. Engelstaedter, W. H. Guo, Q. Y. Lu, B. Corbett, B. Roycroft, J. O’Callaghan, F. H. Peters, and J. F. Donegan, “Discretely tunable semiconductor lasers suitable for photonic integration,” IEEE J. Sel. Topics Quantum Electron. 15(3), 482-487 (2009).

# Heterogeneous integration of III-V materials on Silicon photonic platforms: In the quest for high power, single-longitudinal mode and widely tuneable on-chip laser diodes

***Student Paper***

**P. Fanneau[1], C. Besancon[1], H. Elfaiki[1], T. Verolet[1], D. Neel[1], N. Vaissiere[1], S. Malhouitre[2], V. Muffato, C Jany[2], A. Shen[1], C. Caillaud[1], J. Decobert[1], D. Bitauld[1], S. Olivier[2], K. Hassan[2] and J. M. Ramirez[1]**

[1] III-V Lab, Avenue Augustin Fresnel, 1, Palaiseau 91767, France

[2] CEA LETI, Minatec, Grenoble, France

*e-mail: joan.ramirez@3-5lab.fr*

## ABSTRACT

On-chip light sources and amplifiers are meant to be key components for next generation datacentres and long haul telecommunications managing large amounts of data within the Terabyte and Zetabyte range. To successfully deploy them, high-power, narrow linewidth and widely tunable compact lasers are needed to allocate multiple parallel data channels with optimum performance and low energy consumption. In this perspective, we demonstrate compact heterogeneous tunable laser diodes integrated on a 200-mm silicon photonics platform. It provides 5 dBm of optical fiber-coupled power in a wafer-testing configuration with a current density threshold of 1.7 kA/cm$^2$ , a differential resistance below 6 Ω at the nominal bias point and a tunable range of 60 nm within the C-band of telecommunications. Moreover, the small device footprint of ~1 mm$^2$, the large scalability heterogeneous III-V-on-SOI integration and the maturity of the fabrication processes make these lasers a compelling solution for competitive future wavelength-division-multiplexing solutions.

**Keywords**: Heterogeneous integration, silicon photonics, lasers, optical links, datacentres, telecommunications.

## 1. INTRODUCTION

Over the last few years, optical communications have experienced an enormous transformation and great progress, driven by the continuous need to meet the requirements of the massive data exchange rates in nowadays datacentres or long haul communications underpinning the digital world [1]. Further than that, the imminent deployment of new applications and hyper-connected networking architectures such as the 5G network, the Internet of things or the laser detection and ranging (LIDAR) systems for autonomous vehicles will surely increase the need for efficient, high-bandwidth, low power consuming and densely packed optical systems. Mass-volume fabrication of compact systems with small form factors is often seen as an appealing solution to reach that goal [2]. In this regard, silicon photonics provides an ideal platform, as it enables high-level integration of photonic devices and circuits with competitive performance, allowing the emergence of Photonic Integrated Circuits (PICs) with complex and multifunctional architectures [3, 4].

The demonstration of compact on-chip lasers compatible with the silicon photonics technology has been one of the burning challenges motivating an intense research on heterogeneous integration [4]. High-speed monolithic modulators and sensitive photodetectors are nowadays readily available in most of the Si foundries [5], but lasers have been the missing enabling device for optical transceivers to become a reality in silicon photonics. Hybrid devices combining InP gain-chips with passive silicon photonics external cavity circuits in a butt-coupling configuration are often used as an alternative solution and they demonstrate performances well in line with the specifications of the system demands [6]. Although impressive progress has been done in that regard, alignment of the two chips remains complex. It often takes place in a lab environment using in-house alignment techniques and costly packaging processes. This overhead is acceptable for prototyping but it has prevented the main industrial stakeholders from a massive exploitation of these devices. Nevertheless, with the advent of the heterogeneous integration of III-V materials on top of mature silicon photonic front-end wafers, the interest for this technology has exploded due to the possibility to implement on-chip optical interconnects using large-scale CMOS processes, giving access to low-cost and highly performing solutions for such miniaturized lasers [3].

In this work, we present our recent advancement on widely tunable heterogeneous III-V-on-Si laser diodes for datacom and telecom applications. Devices have been fabricated in a 200-mm silicon photonics platform. Our lasers easily achieve 5 dBm of optical fiber-coupled power across the wafer with a threshold current density of 1.7 kA/cm$^2$, a differential resistance below 6 Ω and a wavelength tunability over 60 nm.

## 2. Widely tunable lasers

The tunable laser diodes studied in this work are formed by a III-V gain material containing multiple quantum wells and a passive external cavity entirely defined in the silicon wafer. Wafer bonding of unprocessed InP wafers on already processed Si photonics wafers followed by several etching steps and metallization is performed to define the heterogeneous III-V-on-Si lasers. Asymmetric cavity feedback is defined with Sagnac mirrors. A Vernier filter composed by two racetrack ring resonators containing thermal heaters is used to coarsely tune the laser emission wavelength according to the maximum free spectral range (FSR) of the filter. Fine wavelength tuning is obtained with an additional phase shifter located outside the Vernier filter. Vertical grating couplers are employed to enable rapid wafer testing of devices. Further details on the design and fabrication of such lasers can be found in ref. 3.

Figure 1(a) shows a representative static characteristic of a tunable laser diode, with a threshold current density value of 1.7 kA/cm$^2$, a maximum fiber-coupled optical power exceeding 3 mW (i. e. 5 dBm) and single-longitudinal mode emission with a side-mode suppression ratio (SMSR) exceeding 40 dBm. The multiple kinks observed correspond to mode hops between adjacent lasing modes. This is due to the temperature rise in the III-V part of the laser being higher than in the silicon, where the external Vernier filter is defined. This fact is represented in one of the insets of figure 1(a) (at the right-hand side), where two different lasing modes corresponding to a different laser injection current are superimposed, showing an evident wavelength red shift. In addition, the optical power-versus injected current density curve is represented with segments of different colours corresponding to each lasing mode. Figure (b) displays the typical Voltage-current density characteristic of the diode laser, with an onset voltage value of around 0.7 V and an almost linear behaviour of the leakage current. We observe a slope diminution from 4.5 kA/cm$^2$ on, followed by an irregular behaviour for injected current density values close to 6 kA/cm$^2$. This behaviour is attributed to the activation of non-negligible thermal effects and to charge accumulation within the laser diode. Figure 1 (c) shows the measured differential resistance evolution as a function of the injected current density. As can be seen, the differential resistance rapidly decreases until values below 6 Ω, in agreement with the onset of lasing, and then remains almost constant until 4.5 kA/cm$^2$. The measurement becomes noisy and slightly chaotic beyond this value, in agreement with the onset of thermal and charging effects in the laser diode.

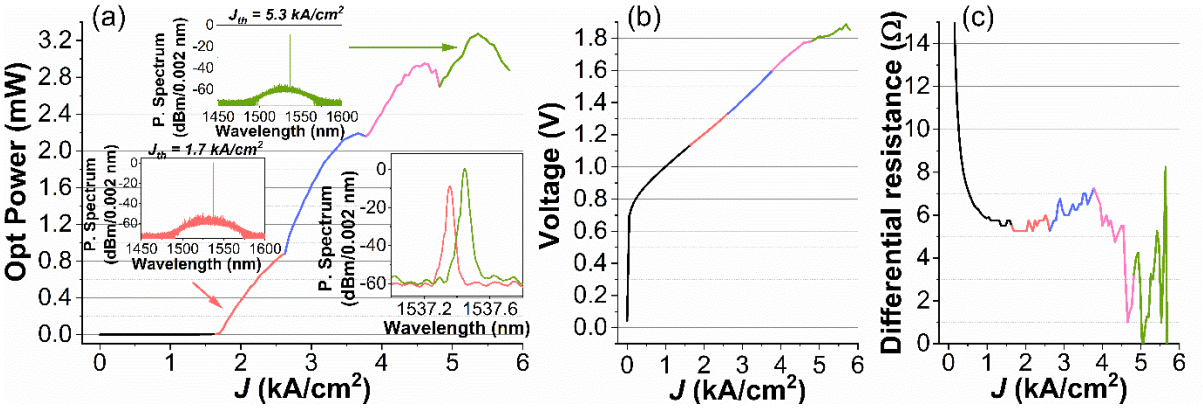



Figure 1. Static optoelectronic characteristic of an integrated tunable lasers. The current density range for different lasing modes is highlighted with different colours to ease the correspondence between the different curves: (a) Single-mode fibre-coupled optical power as a function of the injected current density in the laser. Insets on the left-hand side show the measured laser spectrum for low current density values after the threshold (magenta curve) and for high current density values close to the optical power saturation point (green curve). Right-hand inset compares the emission spectrum for the two spectra, showing different lasing modes. Votage-current density (b) and differential resistance-current density (c) curves of a tunable laser.

Figure 2(a) shows a representative tuneability map of a tunable laser diode. The y- and x-axes show the injected current in each of the two heaters that compose the Vernier filter. The measured lasing emission wavelength is represented by the colour bar, with values comprised between 1500 nm and 1560 nm, i. e a tuning range of 60 nm. As a criterion, only the measured spectra showing an SMSR > 40 dB are coloured, whereas the ones with SMSR < 40 dB have been depicted in black. To better illustrate the spectral tuneability of the laser diode, figure 2(b) shows the evolution of wavelength of emission as a function of the injected current in the heaters for the current density range indicated by the white cross in figure 2(a). A step-like behaviour is observed, corresponding to the coarse tuning of the external filter. It is worth noting that continuous wavelength tuning is achievable by combining the two heaters and the phase shifter.

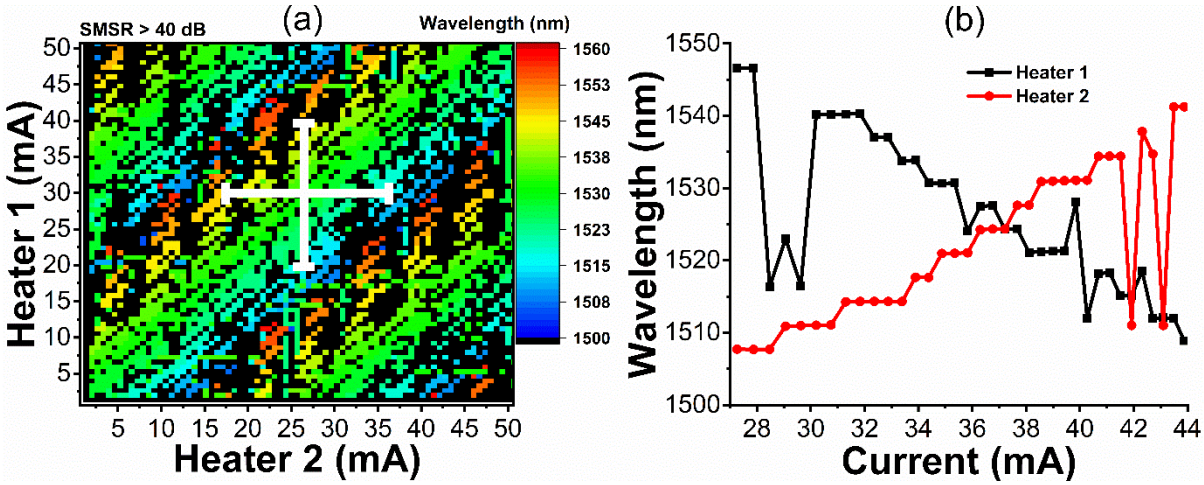



Figure 2. (a) Colour map of the spectral tunability of the integrated laser. (b) Evolution of the laser spectral wavelength as a function of the injected current in each of the thermal heaters comprising the Vernier filter. The curves correspond to the data marked with a white cross in figure (a).

## 3. CONCLUSIONS

In this work, we present our latest work on the demonstration of compact widely tuneable heterogeneous laser diodes on 200-mm Si platform. Devices show good optoelectronic properties, with a threshold current density of 1.7 kA/cm$^2$, a differential resistance below 6 Ω, maximum fiber-coupled optical power of 5 dBm, an SMSR > 40 dBm and a wavelength tuneability of 60 nm. The total device footprint is approximately 1 mm$^2$, including the external Si cavity. These results pave the way towards low-cost, energy-efficient and easily scalable compact lasers suitable for applications requiring high spectral efficiency and demanding optical power budget.

## REFERENCES

[1] E. Agrell, et al: Roadmap of optical communications, Journal of Optics, 18(6) 063002, 2016.
[2] J. J. Van der Tol et al: InP photonic integrated circuits on silicon. Silicon photonics, 99 189, 2018.
[3] J. M. Ramirez et al.: III-V-on-Silicon Integration : From Hybrid Devices to Heterogeneous Photonic Integrated Circuits, IEEE J. Sel. Top. Quantum Electron. 26(2) pp. 1-13, 2020.
[4] B. Szlag, et. al: Hybrid III-V/Silicon technology for laser integration aon a 200 mm fully CMOS-compatible silicon photonics platform, IEEE J. Sel. Top. Quantum Electron. 25(5) 8201210, 2019.
[5] T. Komljenovic, et al: Heterogeneous silicon photonic integrated circuits. J. LightWav. Technol. 34(1), 20-35 (2016).
[6] A. Lim et al: Review of silicon photonics foundry efforts. IEEE J. Sel. Top. Quantum Electron. 20(4), 405-416 (2013).
[7] Y. Gao, et al: High-Power, Narrow-Linewidth, Miniaturized Silicon Photonic Tuneable Laser with Accurate Frequency Control. J. LightWav. Technol. 2019.

# Generation of a compact oscillator using self-injected piezoelectric optomechanical crystal

Aude Martin[1], Inès Ghorbel[1,2], Maëlle Bénéfice[1], Rui Zhu[2], Sylvain Combrié[1], Rémy Braive[2,3], Alfredo De Rossi[1]

[1]*Thales Research and Technology, 1, avenue Augustin Fresnel, 91767 Palaiseau Cedex*
[2]*Centre de Nanosciences et de Nanotechnologies, CNRS, Université Paris-Sud, Université Paris-Saclay, C2N, 10, Boulevard Thomas Gobert, 91120 Palaiseau, France*
[3] *Université Paris Diderot, Sorbonne Paris Cité, 75207 Paris Cedex 13, France*

*e-mail: aude.martin@thalesgroup.com*

## ABSTRACT

We report on the demonstration, in ambient atmospheric conditions, of an optomechanical oscillator made of InGaP. Self-sustained oscillations directly at 3 GHz are achieved with a low optical power of 47 $mu$W and a linewidth narrowed down to 80 Hz. We report on injection locking experiments where the phase noise was reduced by 20 dB with 56 mV of input power. By introducing a delay, the phase noise could be also reduced by 20 dB via piezoelectric effect.

**Keywords**: Optomechanical oscillator, Photonic crystal cavity, Injection-locked oscillators, Phase noise

## 1 INTRODUCTION

Radar technologies rely on the development of ultra-stable oscillators to increase the sensitivity of detection systems. This sensitivity is linked to the phase noise of oscillators describing the spectral width of the modulated signal. A first challenge in this field lies in the direct generation of high-frequency microwave signals in the GHz domain and above, with ultralow phase noise. A second challenge lies in the implementation of miniaturized, compact, transportable and integrated oscillators, especially for potential on-board applications and on-chip signal processing.

In these applications, the frequency references are generally quartz oscillators. These provide an oscillation whose frequency can typically reach hundred megahertz with very good performance in terms of frequency stability and phase noise (-90 dBc/Hz for a carrier frequency of 100 MHz). To reach the gigahertz range, a crystal oscillator is followed by frequency multiplication steps that cause an intrinsic degradation of the noise performance of the synthesized oscillator. An alternative solution is to generate an oscillaton directly at high frequency based on optics. In fact, optics has several advantages: low transmission losses in the optical fiber, wide bandwidth of optoelectronic components, and high maturity of the components developed in the context of telecommunications. In this context, the optoelectronic oscillator was developed [1]. It relies on a long optical delay, giving high quality factors at high frequency and a phase noise of -100 dBc/Hz at 100 Hz for a carrier frequency of 10 GHz [2]. Although these types of oscillators have been integrated on-chip [3], losses limit the quality factor and strongly degrade the phase noise (-91 dBc/Hz at 1 MHz for a carrier frequency of 7 GHz). However, on-chip generation of temporal delays (up to several hundreds of ns)is required for the implementation of compact and efficient RF oscillators. Optomechanical crystals (OMC), which exploit the interaction between light and a moving cavity, and more specifically, phononic waveguides based on the slow propagation ( 3000m/s) of the RF signal in the acoustic domain should help build compact stable and high frequency oscillators.

## 2 FREE RUNNING OPTO-MECHANICAL OSCILLATOR

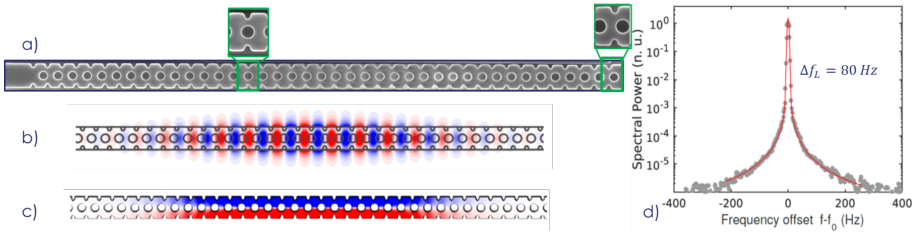



Figure 1. a) SEM picture of the fabricated structure in InGaP and modelling of the b) electromagnetic and c) displacement field of the bichromatic cavity. d) Fit of the normalized RF spectrum with the Voigt function.

The design of the one dimensional cavity ( Figure 1a) is based on the concept of the bichromatic lattice [4]. It consists of a suspended beam made of GaInP, patterned with a line of holes with fixed period $a$ and, on the sides, half-ellipses, with period $a' = 0.98a$. On one side, some holes and teeth are removed in order to couple light in the cavity and taper the loaded quality factor. This cavity sustains an optical mode (Figure 1b) and a high frequency mechanical breathing mode (Figure 1c) which are co-localized and are coupled together. The measured optical intrinsic quality factor, limited by fabrication disorder, is equal to $3.10^5$ and the fundamental mechanical breathing mode ocillates at 2.93 GHz. By probing the optical resonance with a tunable laser and analyzing the light coming back from the cavity, a lecture of the mechanical movement of the cavity is achieved. Moreover, an exchange of energy between the mechanical mode and the optical mode can compensate the losses of the mechanical mode leading to self sustained oscillations [5]. To obtain a mechanical spectrum (Figure 1d), the light coming from the cavity is analyzed with a photodiode and the generated electrical signal is sent to an Electric Spectrum Analyzer. We observe self-sustained oscillations with a threashold optical on-chip power of 47 $\mu W$ and a narrowing of the Lorentzian linewidth from 1.2 MHz to 80 Hz for an on-chip power of 53 $\mu W$ (Figure 1d)[6].

## 3 INJECTION LOCKING EXPERIMENT WITH LOW AC POWER

In the following work, the design of the OMC is slightly different and inspired from [7]. Light is injected in the sample via a taper and the OMC can be actuated thanks to capacitive gold electrodes (3a). The fundamental optical mode is at 1593.12 nm and its quality factor is equal to 160 000. The mechanical mode of interest is a beam wave mode (inset of Figure 3a) which frequency is equal to 21.5 MHz. The quality factor at room temperature and atmospheric pressure is equal to $1316 \pm 153$ (corresponding linewidth : $15 \pm 2$ kHz) .

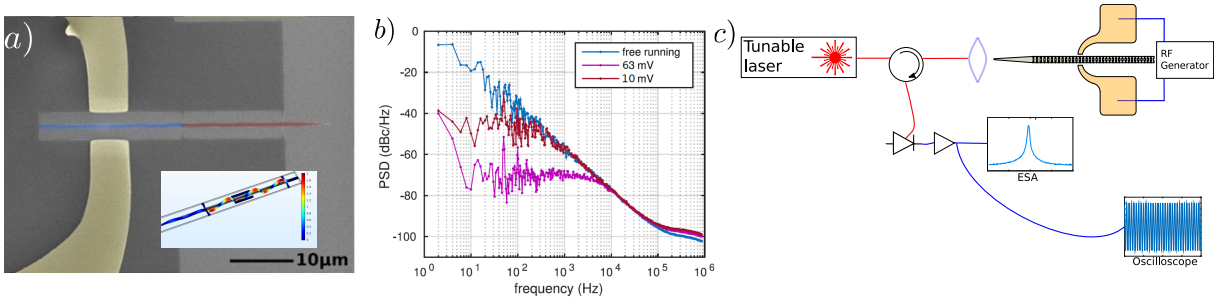



Figure 2. a) SEM image in false colors of the sample (OMC in blue, injection taper in red, gold electrodes in yellow with simulated displacement of the mode of interest with Finite Element Method implemented in Comsol (inset). b) Phase noise spectral density in a free running configuration or with injected RF signal at various input AC powers.

In the experiment shown in Figure 2c), we inject an AC voltage on the electrodes at a frequency of 21.5 MHz $\pm$ 10 kHz and analyze the short-term stability of the locked oscillator by measuring the phase noise. The phase noise is the power spectral density of the fluctuations of the phase of the RF signal. To compute it, the RF signal generated by the photodiode is transfered to the time domain with an oscilloscope and the time trace is numerically processed. In a similar experiment in [8], an improvement of the phase noise of 20 dB was obtained for a DC voltage of 50V and an AC voltage of 400 mV generated by a RF generator. Here, for a frequency offset ranging between -5 kHz and 5 kHz, the OMC is locked to the RF trigger and the mechanical frequency is tuned over 10 kHz. In this region, the phase noise is also locked to the phase noise of the RF generator and experiences an improvement of 20 dB with 53 mV and no DC input.

## 4 STABILIZATION OF THE OSCILLATION USING A FEEDBACK LOOP

The set-up used here is shown in Figure 3b). The back reflected light from this sample is injected into a fiber delay line of a few kilometers. The signal detected by the photodiode (PD) is injected on the electrodes to provide a feedback on the OMC. A feedback loop on a free running optomechanical oscillator was already proposed in the literature [9]. Here, we introduce a fiber delay which acts as a filter and decreases noise in the oscillator. The phase noise (Figure 3c) is measured and experiences an improvement of 20 dBc/Hz at 1kHz as the delay in the loop is increased compared to the case where there is no fiber delay in the feedback loop.

## 5 CONCLUSION

In this work, we have proposed a new design for optomechanical crystals and shown that this device can go into mechanical self-sustained oscillations. We have also achieved locking of an optomechanical oscillator to an external RF generator via the piezoelectric effect. Finally, we made a feedback loop on an optomechanical oscillator including a fiber delay and shown that a decrease of the phase noise of 20dB was possible. Future work is aimed at repeating this feedback loop experiment in the GHz range, integrating the delay thanks to a phononic waveguide and synchornizing several oscillators.

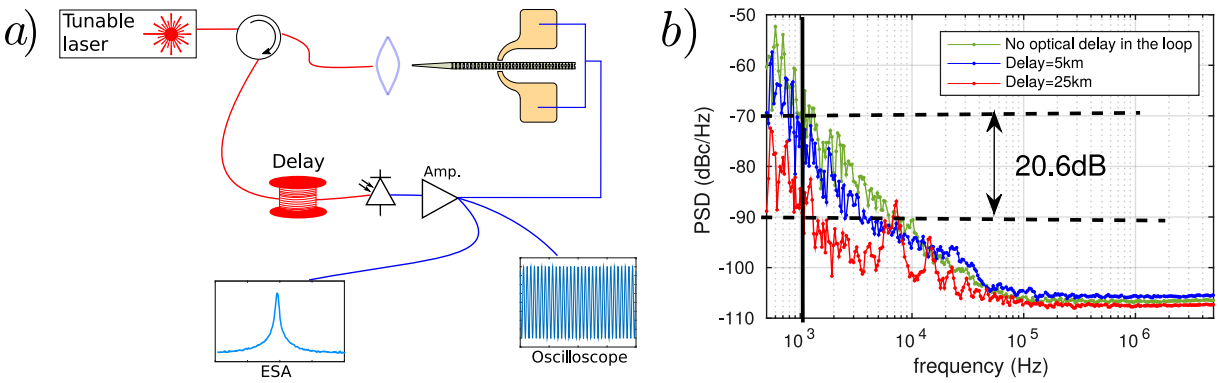



Figure 3. a) Set-up b) Phase noise measurements for different delay lengths.

## ACKNOWLEDGMENT

This work was supported by the European Union's Horizon 2020 research and innovation programme under Grant Agreement No. 732894 (FET Proactive HOT).

## REFERENCES

[1] X.Steve Yao and Lute Maleki, "Optoelectronic microwave oscillator" *J.Opt.Soc.Am.B*, **13**, 1725-1735 (1996)

[2] O. Lelièvre et al, "A model for designing ultralow noise single-and dual-loop 10-GHz optoelectronic oscillators" Journal of Lightwave Technology, **35**(20), 4366–4374 (2017).

[3] J. Tang et al "Integrated optoelectronic oscillator" *Opt. Express*, **26**, 12257-12265 (2018)

[4] Filippo Alpeggiani, Lucio Claudio Andreani, and Dario Gerace. "Effective bichromatic potential for ultra-high Q-factor photonic crystal slab cavities." *Applied Physics Letters*, 107(26):261110, December 2015.

[5] M. Aspelmeyer et al "Cavity optomechanics" *Reviews of Modern Physics*, **86**, Iss.4, 2014

[6] I. Ghorbel et al, "Optomechanical gigahertz oscillator made of a two photon absorption free piezoelectric III/V semiconductor". *APL Photonics*, 4(11):116103, 2019.

[7] R. Stockill et al, "Gallium Phosphide as a Piezoelectric Platform for Quantum Optomechanics," Phys. Rev. Lett., **123**, 163602 (2019).

[8] Bekker et al, "Injection locking of an electro-optomechanical device," Optica, **4**(10), 1196-1204 (2017).

[9] M. J. Storey et al, "Radiation pressure enhanced opto-acoustic oscillator", *2014 IEEE International conference on MEMS 1209-1212*

# Subwavelength engineering for Brillouin gain optimization in silicon optomechanical waveguides

**Jianhao Zhang,[1] Omar Ortiz,[1] Xavier Le-Roux,[1] Eric Cassan,[1] Laurent Vivien,[1] Delphine Marris-Morini,[1] Daniel Lanzillotti Kimura,[1] Carlos Alonso-Ramos[1]**

[1] Centre de Nanosciences et de Nanotechnologies, Université Paris-Saclay, Univ. Paris-Sud, CNRS, 91120, Palaiseau, France.

*e-mail: jianhao.zhang@c2n.upsaclay.fr*

## ABSTRACT

Brillouin optomechanics has recently emerged as a promising tool to implement new functionalities in silicon photonics, including high-performance opto-RF processing and non-reciprocal light propagation. One key challenge in this field is to maximize the photon-phonon interaction and the acoustic lifetime, simultaneously. Here, we propose a new strategy that exploits subwavelength engineering of the photonic and phononic modes in silicon membrane waveguides to maximize the Brillouin gain. The proposed optomechanical waveguide comprises a lattice of holes with a period in the subwavelength regime for near-infrared photons and GHz phonons. By properly designing the dimensions of the subwavelength periodic structuration, we tightly confine optical and acoustic modes, minimizing leakage losses and maximizing the Brillouin coupling. Our theoretical analysis predicts a high acoustic quality factor of up to 2000 and a remarkable Brillouin gain yielding 10000 $(\mathrm{W}\cdot\mathrm{m})^{-1}$. We believe that the proposed subwavelength-nanostructured waveguide holds a great potential for the engineering of Brillouin optomechanical interactions in silicon.

**Keywords**: Silicon photonics, optomechanics, nonlinear optics, subwavelength structures, Brillouin.

## INTRODUCTION

Brillouin scattering is a third order optical nonlinear process that results from light-sound coupling [1]. This effect has been widely explored in the context of laser physics, microwave-frequency acoustic excitation and precision spectroscopy, among others. The availability of materials co-confining phonons and photons in the same device [2-4] has enabled the demonstration of Brillouin scattering on chip [5-7], showing exceeding strengths over Kerr and Raman interactions. Over the past decade, there have been remarkable achievements in the control of on-chip Brillouin optomechanics using chalcogenide-based materials [5], gallium arsenide [2, 4, 8] and silicon [9]. Acoustic phonons with GHz frequencies in nanometric-scale waveguides have wavelengths close to one micron. Thus, they can strongly interact with in-phase lightwaves in the near-infrared [10-13]. This high-efficiency coupling enabled remarkably large Brillouin gain [14] and even Brillouin laser [15] in silicon. Silicon membranes have been identified as a promising solution to efficiently confine photons and phonons [9, 11, 15]. However, the phonon lifetime in silicon membranes may be limited by acoustic leakage, from the waveguide core to the lateral silicon slabs or silica substrate. This loss has been alleviated by inserting air gaps [14, 15] or by implementing phononic stop bands in the transversal dimension [16]. The former approach may result in reduced photon-phonon overlap because the expanded phonons distribution along the Si slab between the air gaps, limiting the gain to $1000\ (W\cdot m)^{-1}$ [14]. The latter provided higher calculated Brillouin gain of $1750\ (W\cdot m)^{-1}$ [16], but is limited in bandwidth, as only the phonons within the stop-band are confined. Here, we propose a new waveguide geometry that exploits geometrical subwavelength softening to minimize the lateral leakage of the acoustic modes and subwavelength index engineering to confine optical modes. By working well below the photonic and phononic bandgaps, the proposed subwavelength-lattice waveguide allows to simultaneously enhance the photon-phonon interaction and increase the quality factor of the acoustic mode, while overcoming the typical bandwidth limitations of phononic and phoxonic crystals. Our calculations show that the proposed waveguide may provide Brillouin gain as high as $10000\ (W\cdot m)^{-1}$.

## 1. PROPOSED GEOMETRY

As shown in Fig. 1 (a), the proposed membrane waveguide consists of a central strip and a lattice of lateral arms that anchor the waveguide core to the infinite silicon slab. The acoustic confinement in our structure is achieved by giant impedance mismatch between the air and the silicon core, instead of a phononic Bragg mirror, while the arm lattice with subwavelength period introduces a small acoustic dissipation. The strip has a width of $w_{wg} = 500$ nm and a thickness of $t_{wg} = 220$ nm, while the arms have a width of $w_{arms} = 2.5$ μm and a thickness of $t_{arms} = 50$ nm. Silicon waveguides with lateral subwavelength cladding have been used for mid-infrared optical propagation [17], and thermo-optical devices [18]. More recently, Si membranes with periodic arms in the cladding have also been studied for the optimization of Brillouin scattering [16]. However, the period of the arms

was substantially larger than the acoustic wavelength and the lateral acoustic confinement required the implementation of a Bragg corrugation in the transversal dimension. Here, we choose a period of $p = 240$ nm, well below the acoustic wavelength (1.07 μm in silicon, at 9GHz) and optical wavelength (640 nm in silicon, i.e. 1550 nm in vacuum).

As an example, the normalized intensity profile of the subwavelength optical mode, at 195THz, collected from plane I and II is shown in Figs 1 (b) and (c), respectively.

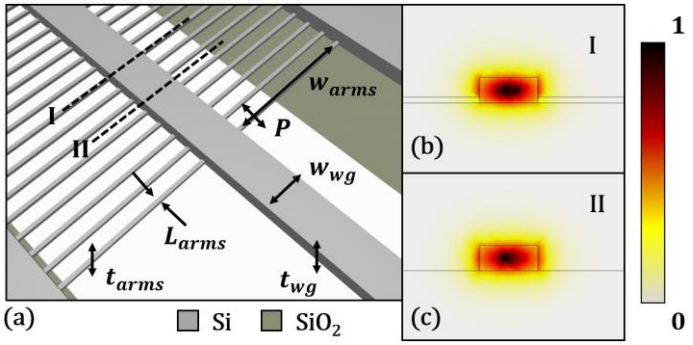



Fig. 1. (a) Schematic of the proposed subwavelength-lattice silicon waveguide. Optimized dimensions: $t_{arms} = 50nm$, $t_{wg} = 220nm$, $w_{wg} = 500nm$ and $p = 240nm$. $w_{arms} = 2.5um$ The Brillouin performance is studied as a function of the length of the arms, $L_{arms}$. Normalized intensity of the electric field collected at (b) plane I and (c) plane II, defined in schematic geometry in (a).

## 2. OVERVIEW OF OPTOMECHANICAL PERFORMANCE

Three cascaded unit cells of the proposed optomechanical waveguide are shown in the inset of Fig. 2, together with the distribution of the transverse acoustic mode (with frequency at 9 GHz), calculated using finite element methods (FEM) model. The maximum displacement occurs for the waveguide core along the arm direction (*x*) indicated by the black arrows. Flexural displacement takes place in the silicon arms. The high acoustic velocity (~9000m/s) results in an acoustic wavelength around 1 μm, which is on the same order as optical wavelength at telecom frequency. Thus, the lattice period of $p = 240$ nm, is well below half of the optical wavelength, suppressing diffraction effects that may arise from the periodicity. Hence, this periodic structure can be described as a subwavelength-lattice waveguide grating for the acoustic mode, doing an analogy with optical subwavelength grating waveguide membranes [17].

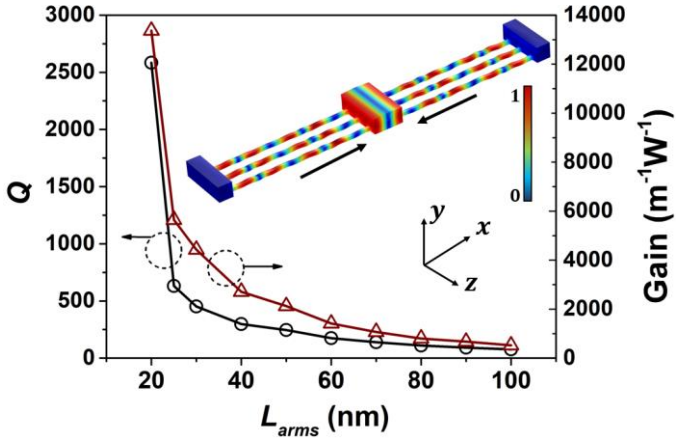



Fig. 2. (a) The quality factor of the acoustic mode and the overall Brillouin gain as a function of the length of silicon arms $L_{arms}$. Inset is the normalized displacement profile of the acoustic mode with a frequency of 9.1 GHz. The strain direction of the silicon core is shown by the thick, black arrows.

We have calculated the quality factor (*Q*) of the acoustic mode using FEM model, considering the loss from surrounding air, loss from the acoustic leakage to the infinite slab and the thermo-elastic loss. As shown in Fig. 2 (black line), *Q* changes nonlinearly with the length of the arms. A remarkable *Q* of up to 1200 can be obtained for an arm length of 25 nm.

The Brillouin gain can be calculated with an integrated optical force [9-13] distributed in the whole unit cell:

$$G = \frac{2\omega_p Q_A}{\tilde{m}_{eff}\Omega_A^2} S(f) \left| \frac{1}{p} \int f_d dv \right|^2. \quad (1)$$

In equation (1), $\omega_p$, $\Omega_A$ and are the angular frequencies of the optical and acoustic modes, respectively, $Q_A$ is the quality factor of the acoustic mode, $\tilde{m}_{eff}$ is the mass density per unit propagation length. $S(f)$ is the Lorentzian-shape spectrum of Brillouin gain and $S(\Omega_A/2\pi)$ indicate the maximum gain. The optical force density $f_d$ includes the optimized overlap between the optical and mechanical modes and is governed mainly by the radiation pressure

force and electrostriction calculated from photo-elastic tensors. The Brillouin gain, calculated as a function of the arm length, $l_{arms}$, is shown in Fig. 2 (red line). The Brillouin gain increases sharply when the arm length is below 30 nm. For an arm length of 20 nm the Brillouin gain can increase up to $10000\ (W \cdot m)^{-1}$. For an arm length of 50 nm, compatible with electron-beam lithography, the Brillouin gain is $2000\ (W \cdot m)^{-1}$. This gain value compares favorably with previously proposed silicon membranes with periodic silicon arms [14], while obviating the need for transversal Bragg phononic mirrors.

## 3. CONCLUSION

We proposed and analyzed a new strategy to optimize Brillouin scattering in silicon membrane waveguides. The proposed waveguide geometry confines mechanical and optical modes by subwavelength softening and subwavelength index engineering, respectively. By working well below the photonic and phononic bandgaps, this proposed subwavelength-lattice waveguide allows to simultaneously enlarge the photon-phonon interaction and increase the quality factor of the acoustic mode, obviating the typical bandwidth limitations of phononic and phoxonic crystals [16]. Our calculations show that the proposed waveguide may provide high acoustic quality factor up to 2000 and Brillouin gain up to 10000 $(W \cdot m)^{-1}$ in the most severe clean room fabrication conditions. These results confirm the possibility to simultaneously shape the propagation of acoustic and optical modes with silicon subwavelength structures. We believe these results will expedite the exploration in photon-phonon interaction based on subwavelength-lattice waveguides.

## 4. ACKNOWLEDGEMENTS

Agence Nationale de la Recherche (MIRSPEC ANR-17-CE09-0041, BRIGHT ANR-18-CE24-0023-01) is acknowledged for supporting this work.

## REFERENCES

[1] G. P. Agrawal, *Nonlinear Fiber Optics*., 5th ed., Rochester, New York, USA, 2013, pp. 1–21.
[2] M. Esmann, *et al.*: Brillouin scattering in hybrid optophononic Bragg micropillar resonators at 300 GHz, *Optica*, vol. 6, pp. 854-859. 2019.
[3] G. Arregui, *et al.*: Anderson photon-phonon colocalization in certain random superlattices, *Phys. Rev. Lett.*, vol. 122, p. 043903, 2019.
[4] F.R. Lamberti, *et al.*: Optomechanical properties of GaAs/AlAs micropillar resonators operating in the 18 GHz range, *Opt. Express*, vol. 25, pp. 24437-2447. 2017.
[5] R Pant, *et al.*: On-chip stimulated Brillouin scattering, *Opt. Exp.*, vo. 19, pp. 8285-8290, 2011.
[6] B. J. Eggleton, *et al.*: Brillouin integrated photonics, *Nat. Photon.*, vo. 13, pp. 664-677, 2019.
[7] A. H. Safavi-Naeini, *et al.*: Controlling phonons and photons at the wavelength scale: integrated photonics meets integrated phononics, *Optica*, vol. 6, pp. 213-231. 2019.
[8] F. Kargar, *et al.*: Direct observation of confined acoustic phonon polarization branches in free-standing semiconductor nanowires, *Nat. Comm.*, vol. 7, p. 13400. 2016.
[9] P. T. Rakich, *et al.*: Giant enhancement of stimulated Brillouin scattering in the subwavelength limit, *Phys. Rev. X*, vo. 2, p. 011008, 2012.
[10] W. Qiu, *et al.*: Stimulated Brillouin scattering in nanoscale silicon step-index waveguides: a general framework of selection rules and calculating SBS gain, *Opt. Exp.*, vo. 21, pp. 31402-31419, 2013.
[11] R. Van Laer, *et al.*: Interaction between light and highly confined hypersound in a silicon photonic nanowire, *Nat. Photon.*, vo. 9, pp. 199-203, 2015.
[12] C. J. Sarabalis, *et al.*: Guided acoustic and optical waves in silicon-on-insulator for Brillouin scattering and optomechanics, *APL Photonics*, vo. 1, p. 071301, 2016.
[13] C. Wolff, *et al.*: Stimulated Brillouin scattering in integrated photonic waveguides: Forces, scattering mechanisms and coupled-mode analysis, *Phys. Rev. A*, vo. 92, p. 013836, 2015.
[14] E. A. Kittlaus, *et al.*: Large Brillouin amplification in silicon, *Nat. Photon.*, vo. 10, pp. 463-468, 2015.
[15] N. T. Otterstrom, *et al.*: A silicon Brillouin laser, *Science*, vo. 360, pp. 1113-1116, 2016.
[16] M. K. Schmid, *et al.*: Suspended mid-infrared waveguides for stimulated Brillouin scattering, *Opt. Exp.*, vo. 27, pp. 4976-4989, 2019.
[17] J. S. Penades, *et al.*: Suspended silicon mid-infrared waveguide devices with subwavelength grating metamaterial cladding, *Opt. Exp.*, vo. 24, pp. 22909-22916, 2018.
[18] J. Zhang, S. He: Cladding-free efficiently tunable nanobeam cavity with nanotentacles, *Opt. Exp.*, vo. 25, pp. 12541-12551, 2017.

# Integrated Photonic Lantern for Speckle Spectroscopy

*Student Paper*

**Dan Yi, Yaojing Zhang, Xinru Wu and Hon Ki Tsang**
Department of Electronic Engineering, The Chinese University of Hong Kong, Shatin, NT, Hong Kong SAR
*e-mail:*hktsang@ee.cuhk.edu.hk

## ABSTRACT

We propose a high-resolution compact spectrometer based on a multimode waveguide with a planar photonic lantern. Four modes were launched into the multimode waveguide via asymmetric directional couplers and individually switched by four modulators. The mode field of the multimode waveguide was spatially sampled to four separate detectors. By measuring the 64 possible states (16 switch states × 4 modes), the spectrum of the optical signal can be recovered. Experimentally, we demonstrate a spectroscopy with a 0.3-nm resolution at a wavelength of 1560 nm using multimode waveguide length of 0.5 mm. The operation bandwidth can be increased by compressive sensing for sparse spectra reconstruction. We believe this work to be the first time for high spectral resolution measurement with only four integrated detectors. This work may lead to ultra-compact and sensitive compressive sensing systems.

**Keywords**: speckle spectroscopy, compressive sensing, and multi-mode waveguide.

## 1. INTRODUCTION

Spectrometers for biological and chemical sensing have been widely explored. Previous integrated spectrometers structures include integrated echelle gratings [1], arrayed waveguide gratings [2], digital planar holography [3], dispersive photonic crystal lattice [4], and resonant devices [5]. A common problem for these kinds of systems is their sensitivity to fabrication errors. Speckle spectrometers [6] were proposed as an alternative which is robust to fabrication errors. Example implementations of speckle spectrometers include on-chip random spectrometer [7], multimode fibre based spectrometer [8], and spiral waveguide spectrometer [9]. A spectral resolution of 0.75 nm was achieved for a 25μm radius on-chip random spectrometer. Multimode fibres based spectrometer achieved an ultra-high resolution of 1 pm using a multimode fibre with 100 m length. Spiral waveguides achieved 0.01nm resolution with equivalent waveguide length 4.8 mm. However, some problems still exist [6]. For on-chip speckle spectrometers, the number of spectral grains limits the number of independent spectral channels that can be retrieved. A large number of channels leads to low optical power for a specific channel. Thus, the sensitivity for weak signal is poor.

In this paper, we use the on-chip multimode waveguide along with planar photonic lantern [10] to build a spectrometer. Four modes were launched into the multimode waveguide. The strong scrambling and interference between four modes lead to high spectral resolution. By minimizing the insertion loss of ADC and photonic lantern, we efficiently guide the propagating light to four detectors. We also employed four modulators to act as switches to switch the interference at the four detectors. Thus 64 effective states (16 switch states x 4 detectors) could be achieved using only four detectors without the disadvantage of reducing the power by spreading it across a larger number of detectors.

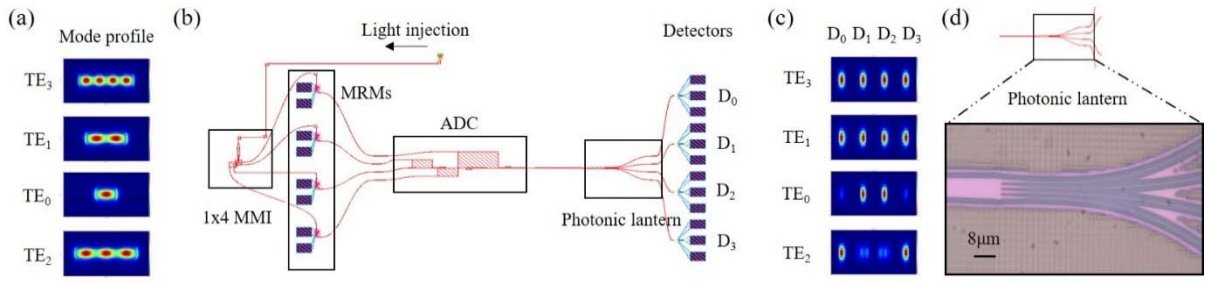



*Figure 1. (a) Mode profile for different higher TE mode in silicon waveguide. (b) Schematic of proposed configuration, the whole structure is composed of a 1 ×4 multimode interferometer (MMI), four Micro-ring modulators (MRMs), asymmetrical directional coupler (ADC), photonic lantern and four high-speed detectors. (c)Power intensity distribution on four detectors for each mode.(d) Zoom-in picture of photonic lantern*

## 2. DEVICE DESIGN AND EXPERIMENTAL SETUP.

The proposed configuration of the speckle spectrometer is shown in Fig. 1(b). Light was injected to the waveguide through a grating coupler and evenly divided into four paths by the 1×4 MMI. In each path, a MRM was used to switch the light before launching $TE_0$, $TE_1$, $TE_2$, $TE_3$ modes respectively in the multi-mode waveguide through the four asymmetric directional couplers (ADC) [11]. Since the coherence length is given by $L = c/n\Delta f$, and the linewidth of the laser is 50 MHz, effective index $n$ is 2.3, the coherence length is 2.6m that is much larger than the multimode waveguide length 0.5 mm. Thus the four modes are coherent and can interfere with each other. Different switch state produces different interference signatures sampled by detectors $D_0$, $D_1$, $D_2$, and $D_3$ after propagating through the photonic lantern. Simulated power patterns on photonic lantern for different modes were shown in Fig. 1(c), while the according mode profiles were shown in Fig. 1(a). The device was fabricated on IMEC MPW with fully etched silicon layer of 220 nm, 2μm buried oxide (BOX) and cladding of silicon oxide. Zoomed-in picture of fabricated photonic lantern was shown in Fig. 1(d). Width of multimode waveguide was increased from 1.7μm to 8μm through 350-μm taper while width of single-mode waveguide was reduced from 1.35μm to 0.45μm through 15-μm taper for photonic lantern.

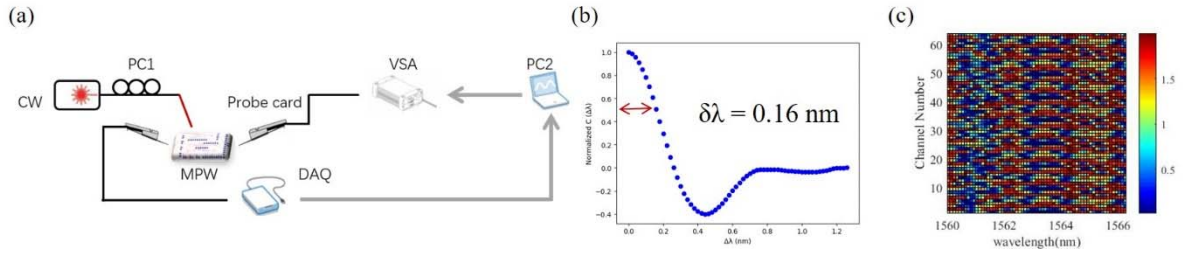



*Figure 2. (a) Schematic of experimental setup, CW: continuous wavelength laser, PC1: polarization controller, MPW: multi-project wafer, DAQ: data acquisition module, VSA: voltage source array, PC2: personal computer. (b) Normalized correlation of spectrometer. (c)The weighted matrix "T".*

Experimental setup is as shown in Fig.2 (a), CW laser was used as an optical source, and a polarization controller was used to launch TE mode in the waveguide. Four on-chip modulators were driven by voltage source array module while the four on-chip detectors were connected to a computer for receiving the detected powers. Thus the four modulators and four detectors could be controlled and monitored simultaneously.

With only four integrated detectors, the number of possible frequency channels can be retrieved is usually limited. Here we use the four modulators to act as switches and modify the received speckle pattern. For each mode, the modulator could be biased at '0' or '1' to change the intensity and phase of light filed. Therefore, there are $2^4$ (16) possible switch states per photodetector and 64 possible states from the four integrated photodetectors. With specific wavelength, the power received on four detectors is unique for each switch state as a result of spatial scramble and interference. Therefore, the 64 pixels of pattern could be collected and recorded as the column of calibration weight matrix 'T' as shown in Fig.2 (c).

Based on the recorded weight matrix 'T', resolution of the spectrometer could be quantified by the spectral correlation function of the intensity on the detectors as: $C(\Delta\lambda, x) = < I(\lambda, x)I(\lambda + \Delta\lambda, x) > / [< I(\lambda, x) >< I(\lambda + \Delta\lambda, x) >] - 1$, where $I(\lambda, x)$ denotes the intensity of wavelength λ for possible state $x$, $< \cdots$represent the average over λ. $I(\lambda, x)$ was measured by the four on-chip Germanium detectors. After calculation, C is normalized to 1 at $\Delta\lambda = 1$ while the half maximum δλ is calculated to be 0.16 nm as shown in Fig.2 (b). It's also important to consider the sensitivity of the system. To improve the sensitivity of the system, insertion loss of the whole system dominated by ADC and photonic lantern need to be minimized. Loss of ADC was measured to be less than 2.5 dB which can be further improved through designing while loss of photonic lantern was less than 3dB. To date, we only have four output detectors instead of 64 detectors here, the sensitivity was improved 16 times by employing four modulators.

## 3. EXPERIMENTAL RESULTS AND DISCUSSION.

After calibration, the probe spectrum was sent into the system, and intensity of 64 possible states were recorded as matrix 'D'. Then the probe spectrum can be retrieved by $S = T^{-1}D$ [9]. To mitigate the influence of phase noise caused by thermal crosstalk, equipment noise, and small vibration of the stage. Singular vector decomposition (SVD) was applied to the estimation of matrix T. Elements in the unitary matrix below noise level were truncated. After that, a nonlinear optimized algorithm [12] was used to minimize the $||D-TS||^2$ so as to restore the wavelength spectrum.

Since δλ was estimated to be 0.16 nm, we chose the spectral channel spacing to be slightly smaller that is 0.1 nm. Here, we choose the number of channels to be 64, so that the spectrum restored by direct matrix inverse and spectrum reconstructed by nonlinear optimization can be compared. The whole experiment was demonstrated from 1560 nm to 1566.4 nm.

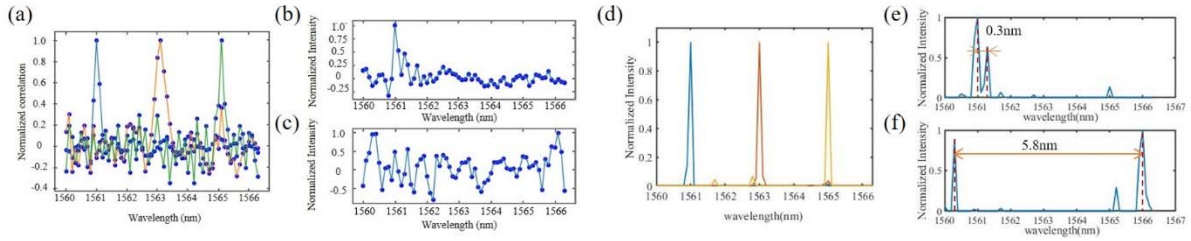



*Figure 3. (a)- (c) Reconstructed spectrum using direct matrix inverse. (d)-(f) Reconstructed spectrum using nonlinear optimization.*

Spectrum calculated by matrix inverse $S = T^{-1}D$ for single line and double lines were shown in Fig.3 (a)-(c), respectively. It can be shown that, small variations of detector intensity in spatial domain can lead to big noise in spectral domain. After SVD truncation and nonlinear optimization, the spectrum can be much clearer. As shown in Fig.3 (d), individual spectral lines can be retrieved accurately with linewidth less than 0.15 nm and extinction ratio ~500. To further test whether this system can retrieve double lines, we use a fibre-based coupler to form the double lines probe spectrum. And we found that double lines with distance as small as 0.3 nm could be successfully reconstructed while as far as 5.8nm could be reconstructed. To date, this method could be further exploited for larger spectrum range and multiple lines or continuous wavelength retrieve.

## 4. CONCLUSION

In summary, we have shown in this paper that a properly designed multiplexing system and planar photonic lantern can be used as a compact on chip spectrometer. The strong scrambling and interference enable high resolution to be achieved in a small footprint. In this paper, we demonstrate the use of a multimode waveguide which support the propagation of four modes with four MRMs and four integrated photodiodes to obtain 64 spectral grains. The input spectra were accurately reconstructed from the spatial intensity distributions of transmitted light. We demonstrated 0.3 nm resolution with 6.4 nm bandwidth around 1560nm. This could be further exploited for larger spectrum range and continuous wavelength retrieve.

## REFERENCES


[1] S. Janz, *et al.*:Planar waveguide echelle gratings in silica-on-silicon, *IEEE Photon. Technol. Lett.*, vol. 16. pp. 503-505, 2004.

[2] K. Okamoto, and H. Yamada:Arrayed-waveguide grating multiplexer with flat spectral response, *Opt. Lett.*, vol. 20. pp. 43-45, 1995.

[3] C. Peroz, *et al.*:Multiband wavelength demultiplexer based on digital planar holography for on-chip spectroscopy applications, *Opt. Lett.*, vol. 37. pp. 695-697, 2012.

[4] B. Momeni, *et al.*:Integrated photonic crystal spectrometers for sensing applications, *Opt. Commun.*, vol. 282. pp. 3168-3171, 2009.

[5] Z. Xia, *et al.*:High resolution on-chip spectroscopy based on miniaturized microdonut resonators, *Opt. Express*, vol. 19. pp. 12356-12364, 2011.

[6] H. Cao:Perspective on speckle spectrometers, *J Opt*, vol. 19. pp. 060402, 2017.

[7] B. Redding, *et al.*, presented at the 2013 Conference on Lasers & Electro-Optics Europe & International Quantum Electronics Conference CLEO EUROPE/IQEC, 2013.

[8] B. Redding, *et al.*:High-resolution and broadband all-fiber spectrometers, *Optica*, vol. 1. pp. 175-180, 2014.

[9] B. Redding, *et al.*:Evanescently coupled multimode spiral spectrometer, *Optica*, vol. 3. pp. 956-962, 2016.

[10] S. G. Leon-Saval, et al.:Multimode fiber devices with single-mode performance, Optics Letters, vol. 30. pp. 2545-2547, 2005.

[11] M. N. Weiss, and R. Srivastava:Spectral characteristics of asymmetric directional couplers in graded index channel waveguides analyzed by coupled-mode and normal-mode techniques, *Appl. Opt.*, vol. 34. pp. 1029-1040, 1995.

[12] B. Redding, *et al.*:Compact spectrometer based on a disordered photonic chip, *Nat. Photonics*, vol. 7. pp. 746-751, 2013.

# Tunable optical dual-comb experiments using silicon Mach-Zehnder modulators

*(Student Paper)*

**Lucas Deniel[1], Erwan Weckenmann[2], Diego Pérez Galacho[1,+], Laurent Bramerie[2], Carlos Alonso-Ramos[1], Fréderic Boeuf[3], Laurent Vivien[1], Christophe Peucheret[2], Delphine Marris-Morini[1]**

[1] Université Paris-Saclay, CNRS, Centre de Nanosciences et de Nanotechnologies, 91120 Palaiseau, France

[2] Univ Rennes, CNRS, FOTON - UMR 6082, F-22305 Lannion, France

[3] ST Microelectronics, 850 rue Jean Monnet, 38920 Crolles, France

[+] Now at ITEAM research institute, Universitat Politècnica de València, Camino de Vera s/n, 46022, Valencia, Spain

*e-mail: lucas.deniel@c2n.upsaclay.fr*

## ABSTRACT

Dual comb spectroscopy is a technique that simultaneously enables high signal-to-noise ratio and quasi-instantaneous measurements of optical spectra. It requires the generation of two mutually coherent optical frequency combs, and electro-optical modulation of a monochromatic carrier can be used for this purpose. By tuning the applied modulation frequency, it is possible to control the spacing between the lines of the electro-optical frequency combs (EOFCs), and by changing the input carrier frequency, it is possible to control the EOFCs absolute frequencies. On-chip EOFC generators are highly desirable to develop low-cost and low-weight dual-comb systems. In this context, silicon photonics is a promising technology, as it benefits from CMOS compatible fabrication process. In this work, a demonstration of dual-comb generation is performed, using two silicon Mach-Zehnder modulators. The tunablity of the obtained 5 main beat notes was studied for an input wavelength ranging from 1530 nm to 1570 nm, and for a driving modulation frequency between 1 GHz and 12 GHz.

**Keywords**: Dual-Comb, Silicon, Electro-optic, Modulators, Tunable.

## 1. INTRODUCTION

Optical frequency dual-comb experiments have raised a strong interest in the fields of spectroscopy and ranging [1-3], since these method enable high-speed and precise measurements of optical spectra. When two optical frequency combs with slightly different line spacings are combined and applied to a photodetector, the resulting beating products between the optical lines create a down-scaled image of the optical spectrum in the electrical radio-frequency (RF) domain. The generation of optical frequency combs (OFCs) can be achieved using mode-locked lasers, optical non-linearities in micro-resonators (microcombs), or by electro-optical RF modulation of a continuous wave (CW) laser beam. While in mode-locked laser based combs and in microcombs the OFC line spacing is linked to the cavity resonances, in the case of electro-optical frequency combs (EOFCs) the spacing between optical lines (or repetition rate) is determined by the frequency of the applied modulating signal. In addition, the EOFC central frequency is defined by the input laser source, and the generation of new lines is not limited by optical dispersion as for microcombs. Therefore, EOFCs are tunable, both in line spacing and in absolute frequency position, making them advantageous for dual-comb generation.

Integrated photonics allows the development of novel low-weight and small-footprint dual-comb generators for remote spectroscopy and ranging applications [4]. Being compatible with complementary metal-oxide semiconductors (CMOS) technology fabrication process and facilities, the silicon on insulator (SOI) platform is a suitable platform that permits a combination of photonic circuits with electronics [5].

This work presents an optical dual-comb experiment, where two EOFCs are generated using silicon Mach-Zehnder modulators (Si MZMs) based on free-carrier plasma dispersion effect, and an external acousto-optic modulator (AOM). The dual comb tunability is studied in terms of central wavelength and repetition rate.

## 2. MODULATOR DESIGN

The silicon Mach-Zehnder modulators used for the experimental demonstration were fabricated on STMicroelectronics 300-mm SOI technological platform [6]. A 4-mm long PN junction acting as a high-speed depletion based phase-shifter is embedded in each arm of a Mach-Zehnder structure, as shown in Fig. 1. Both PN

junctions are nested together: by connecting the N regions to the same electrical potential, the MZM is working in a single-drive push-pull operation. Electrical traveling wave electrodes are contacting the PN junction through highly doped regions, in order to reduce the access resistance. The rib waveguides are 300-nm high and 400-nm wide and the slab thickness is 50 nm.

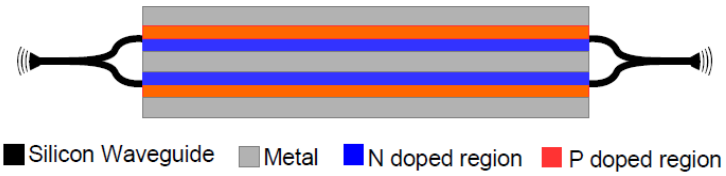



*Figure 1. Schematic top view of the silicon single-drive push-pull operating MZM.*

The estimated attenuation factor in the phase-shifter is 1.24 dB/mm at 0-V bias, according to a numerical simulation based on Soref model. Static measurements of the MZM efficiency showed a half-wave voltage of $V_\pi$ = 8 V, and a small signal electro-optical bandwidth of 18 GHz was measured for a -6 V bias of both diodes.

## 3. THE DUAL-COMB EXPERIMENTS

### 3.1 Principle and experimental generation.

The principle of dual-EOFC measurements consists in applying different RF signals with closely spaced frequencies $f_{RF}$ and $f_{RF} + \Delta f_{RF}$ to each MZM, as shown in Fig. 2, to simultaneously produce and combine two EOFCs with slightly different frequency spacings. In the resulting optical spectrum, lines of the first comb are found at frequencies $f_1 + n \times f_{RF}$, where $f_1$ is the input carrier frequency for the first comb, and n is the comb line order, while lines of the second comb are found at frequencies $f_2 + n \times (f_{RF} + \Delta f_{RF})$, where $f_2$ is the input carrier frequency for the second comb. As a result, a line pair can be found for a given order n, and produces a beat note at the frequency $(f_2 - f_1) + n \times \Delta f_{RF}$ after photodetection.

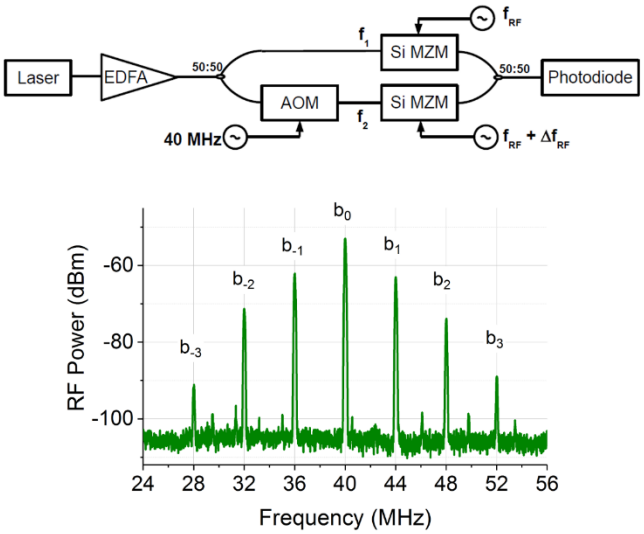



*Figure 2. (a) Schematic of the experimental setup used for the dual-comb generation. A tunable external cavity laser emits a light beam at a 1.55 µm wavelength. After being amplified by the EDFA, the light beam is split in two paths. In one path, an AOM shifts the laser frequency from $f_1$ to $f_2$=$f_1$ + 40 MHz. Two EOFCs are then generated from the silicon MZMs, by applying 8-Vpp RF signals at $f_{RF}$ and $f_{RF} + \Delta f_{RF}$ frequencies, respectively, to them. Both EOFCs are finally combined and applied to a high-speed photodiode. EDFA: erbium doped fiber amplifier, AOM: acousto-optic modulator, Si MZM: silicon Mach-Zehnder modulator. (b) Beat notes experimentally measured on an electrical spectrum analyzer after photodetection, labelled with the letter b, numbered from -3 to +3.*

As a first experimental demonstration, a dual comb is generated by applying two 22-dBm (8-$V_{PP}$) RF signals with frequencies $f_{RF}$ = 500 MHz and $f_{RF} + \Delta f_{RF}$ = 504 MHz to the silicon MZMs. The input carrier frequency of one MZM is shifted by 40 MHz by using an acousto-optic modulator, in order to distinguish beat notes originating from the $n^{th}$ order line pair from beat notes originating from the $-n^{th}$ order line pair. The obtained spectrum is displayed in Fig. 2(b). The retrieved electrical spectrum shows 7 beat notes labelled from $b_{-3}$ to $b_3$.

### 3.2 Study of the tunability

One of the main benefits of EOFCs is the possibility to tune the central frequency by changing the input laser wavelength, as well as tuning the line frequency spacings, by changing the modulating signal frequency. To study the comb tunability in absolute frequency, the external cavity laser source wavelength is swept from 1530 nm to 1570 nm, and the RF power of beat notes $b_{-2}$ to $b_2$ is measured at each step of 2.5 nm, as shown in Fig. 3(a). For this experiment, the modulation frequencies are fixed at 10 GHz and 10.004 GHz, and the applied RF input power is 25 dBm (11.2 $V_{PP}$) on each modulator. The dots correspond to the measurements while the continuous lines correspond to quadratic fits. Interestingly a similar evolution with the wavelength is seen for every beat-note, which is due to the grating couplers transmission. It can be noted that the accessible measurement range is limited by the bandwidth of the EDFA.

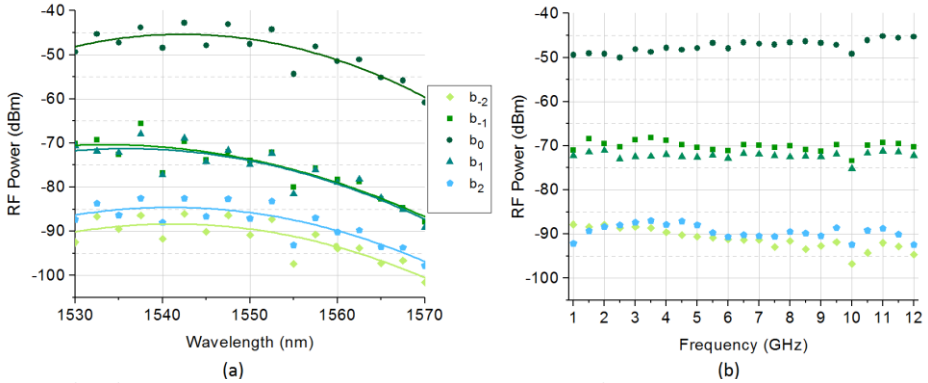



*Figure 3. (a) RF power of the five main beat notes while the input wavelength is swept from 1530 nm to 1570 nm. The symbols correspond to the measurements while the continuous curves are quadratic fits. (b) RF power of the five main beat notes while the modulation frequency $f_{RF}$ is swept between 1 and 12 GHz, the difference between both modulation frequency $\Delta f_{RF}$ being kept constant at 4 MHz.*

The tunability in modulation frequency is then studied around a fixed wavelength of 1550 nm. The modulation frequency $f_{RF}$ is swept between 1 and 12 GHz (Fig. 3 (b)), while the slight difference between both driving signals frequency is kept constant at 4 MHz. The highest frequency (12 GHz) is imposed by the driving RF amplifiers bandwidth.

The RF power applied to each MZM is set to 24 dBm (10 $V_{PP}$). All beat notes appear steady over the scanned range, which is compatible with a modulator electro-optical bandwidth of 18 GHz. These results prove the suitability of Si MZMs for EOFC-based dual comb applications.

## 4. CONCLUSIONS

Dual-comb experiments are reported, using EOFC generated from two silicon single-drive push-pull MZMs. 7 beat notes were observed in the electrical spectrum after photodetection. The dual-comb tunability in wavelength is tested between 1530 nm and 1570 nm, and is limited only by the bandwidth of the grating couplers and of the EDFA. Finally, a measurement of the 5 main beat notes is reported for a modulation frequency spanning from 1 GHz to 12 GHz, showing a good stability over this range. These results pave the way towards the use of silicon MZMs as low-weight and low-cost EOFC generators for flexible dual-comb applications.

## ACKNOWLEDGEMENTS

This work has been partially funded by the Agence Nationale de la Recherche (ANR- 17-CE09-0041 MIRSPEC and ANR-18-CE39-0009 OBIWAM).

## REFERENCES

[1] I. Coddington, *et al.*: Dual-comb spectroscopy, *Optica*, vol. 3. pp. 414-426, April 2016.
[2] N. Picqué, *et al.*: Frequency comb spectroscopy. *Nat. Photonics*, vol. 13. pp. 146-157, Feb. 2019.
[3] Z. Zhu, *et al.*: Dual-Comb Ranging. *Engineering*, vol. 4(6). pp. 772-778, Dec. 2018.
[4] A. Dutt, *et al.*: On-chip dual-comb source for spectroscopy. *Sci. Adv.*, vol. 4 (3). pp. e1701858, March 2018.
[5] C. Weimann, *et al.*: Silicon photonic integrated circuit for fast and precise dual-comb distance metrology. *Opt. Express*, vol. 25(24). pp. 30091-30104, Nov. 2017.
[6] C. Baudot *et al.*: Daphne silicon photonics technological platform for research and development on WDM applications, *in Proc. SPIE 9891*, 2016, 98911D.

# Realization of a Hybrid Integrated Diode laser for Visible Light

*Student Paper*

**Albert van Rees[1*], Cornelis A. A. Franken[1], Youwen Fan[1], Dimitri Geskus[2], Ronald Dekker[2], Douwe H. Geuzebroek[2], Carsten Fallnich[3], Peter J. M. van der Slot[1], and Klaus-J. Boller[1]**

[1] *Laser Physics and Nonlinear Optics, Faculty of Science and Technology, MESA+ Institute of Nanotechnology, University of Twente, Enschede, The Netherlands*

[2] *Lionix International BV, Enschede, The Netherlands*

[3] *Institute of Applied Physics, University of Münster, Münster, Germany*

**e-mail: a.vanrees@utwente.nl*

## ABSTRACT

Hybrid integration of a semiconductor amplifier with a feedback circuit containing ring resonators has been widely demonstrated in the infrared. Such lasers provide ultra-narrowband and single-mode oscillation, which can be tuned over a large spectral range, and easily integrated in a photonic circuit. Contrary to this, applications in the visible spectral range, such as precision metrology with optical clocks, rely on bulk optics lasers, which are susceptible to acoustic noise as they cannot be integrated on a chip. To realize hybrid integrated lasers in the visible range, where scattering losses are typically higher than in the infrared, it is required to design a feedback circuit based on low-loss waveguides. Here, we present the first design and realization of a hybrid integrated diode laser in the visible, by integrating an AlGaInP based amplifier with a $Si_3N_4$ based feedback circuit. Our experimental results show that the laser can be tuned over a 11 nm wide interval around the central wavelength of 685 nm and that it delivers a single wavelength output power of up to 4.8 mW. This result is of great importance for the development of on-chip narrowband and tuneable light sources in the visible range.

**Keywords**: semiconductor laser, hybrid integration, visible light, silicon nitride, low-loss waveguides

## 1. INTRODUCTION

Over the last years, several photonic platforms have emerged for the visible range [1]. These platforms allow integration of bulk optical components in a small form factor, which provides stability and a reduction in size, weight and costs. Photonic integration in the visible range is of high interest for applications in bio-photonics [2] and metrology, but also for portable atomic clocks [3] or quantum computing with trapped ions [4]. Even though photonic integration platforms are well-developed, they still require the use of external lasers.

In the infrared, hybrid integrated lasers, by integration of a semiconductor amplifier with a low-loss feedback circuit have been demonstrated. These lasers provide single wavelength operation with sub-100-Hz intrinsic linewidths, and can be tuned over a large wavelength range [5]. This concept has been demonstrated for telecom application around 1550 nm and, with a few exceptions, at other infrared wavelengths, for example at 850 nm [6] and 1 µm [7]. Further extension towards the visible range is difficult, because absorption and scattering hinder low-loss feedback from a dielectric circuit, which is essential in constructing a hybrid laser.

Here, we design a hybrid laser for wavelengths around 685 nm, based on weakly guiding and low-loss $Si_3N_4$ waveguides and show, for the first time, operation in the visible range.

## 2. HYBRID LASER DESIGN

A schematic of the chip design is shown in Fig. 1 (a). The laser comprises an AlGaInP based amplifier, which is hybrid integrated with a $Si_3N_4$ based feedback circuit. One mirror of the laser cavity is formed by a high-reflective (HR) coating on the amplifier chip, while the other mirror is formed by the feedback circuit. The function of the feedback circuit is i) to provide frequency selective feedback to restrict oscillation to a single cavity mode, and ii) to extend the cavity length with low losses to extend the photon lifetime, which reduces the laser's intrinsic linewidth.

Key in this design for the visible range is a proper waveguide cross section, which provides low propagation losses. For this feedback circuit we use the TriPleX™ platform due to its wide transparency range, which extends down to 400 nm wavelength [8]. The platform also enables lateral tapering of the waveguides at the facet, which we used to minimize coupling losses with the gain chip and for efficient single-mode fibre output coupling. To reduce scattering losses, we exploit the weak mode confinement of a 2 µm wide and 25 nm thick single stripe $Si_3N_4$ buried in a $SiO_2$ cladding. As a consequence of the weak mode confinement, the minimum bend radius is 1200 µm for negligible bend losses. Therefore, microring resonator (MRR) radii are chosen as 1200 and 1205 µm, for MRR1 and MRR2, respectively. The slight difference in radii allows the sequential ring resonators to function as a Vernier filter to select a single cavity mode within the gain bandwidth of the amplifier. To tune the microring

resonances, heaters are placed on top of the microring resonators to work as thermoelectric phase shifters. Similarly, a so-called phase section is present to tune the optical length of the laser cavity.

To enable stable operation of the laser, the amplifier chip, feedback chip and output fibre are hybrid integrated. All tuneable elements are wire bonded to electrical contacts, which allows control by external current sources and power supplies.

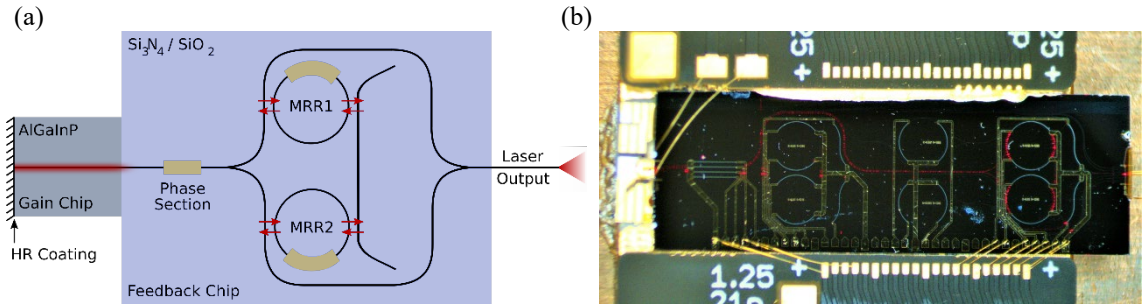



*Figure 1. a) Schematic overview of the hybrid laser comprising a gain chip and a feedback circuit based on two high-Q microring resonators (MRR1 and MRR2). Thermoelectric phase shifters are indicated in yellow. b) Photo of the laser during operation. A pair of microring resonators (on the right hand side of the feedback chip) provides frequency selective feedback. Due to the resonant build-up of light in the resonators and weak scattering of light in the waveguides, the red colour of the light is clearly visible.*

Figure 1 (b) shows a photo of the final assembly of the hybrid laser, where the laser is turned on by supplying current to the amplifier. In the shown case, the pair of ring resonators located on the right hand side of the feedback chip provides the frequency selective feedback to the amplifier. Due to the resonant build-up of light in these resonators and due to weak scattering of the light in the waveguides, these rings are brightly lit with the red colour of the laser light. Fig. 1 (b) confirms, for the first time, the operation of a hybrid diode laser in the visible spectral range.

## 3. EXPERIMENTAL RESULTS

Figure 2 gives an overview of the laser's output power and tuning characteristics. The fibre-coupled output power as measured vs. the pump current of the amplifier is shown Fig. 2 (a), and Fig. 2(b) shows the overall spectral coverage. The power was measured by connecting the output fibre of the laser with a 50/50 coupler and a photodiode power sensor and by correcting the output power with the losses through the coupler. During such measurement, while increasing the pump current, the laser's carrier was kept at a temperature of 20° C. Only the heater on the phase section was optimized for maximum output power (MRR heaters not actuated). We determined the threshold current at 46 mA. Above this value, the output power increases approximately linearly. Deviations from the linear trend can be attributed to mode hops, due to the index changes in the semiconductor material when the current and, consequently, the internal diode temperature would increase. For the maximum specified pump current of 90 mA, the output power is found to be 4.80 mW. Estimating the chip-to-fibre coupling losses as approximately -1 dB, an on-chip optical power of about 6 mW is available for further on-chip processing in fully integrated applications. For this setting, we also measured the spectral characteristics of the light output with an optical spectrum analyser (OSA, ANDO AQ6317, resolution bandwidth of 0.01 nm) and found single-mode oscillation within the resolution limit.

Figure 2 (b) shows several superimposed laser spectra, as measured with the OSA, while the electrical power supplied to the heater of MRR1 was varied in steps of 25 mW. For each measurement, the phase section was optimized under inspection with the OSA in order to obtain a single-mode operation. From these spectra, we observe that the laser wavelength can be tuned over 11 nm around 685 nm, which corresponds to the gain bandwidth of the amplifier as indicated by the black dotted lines in Fig. 2 (b). The gain bandwidth was measured before hybrid integration via recording the spectrum of amplified spontaneous emission of the solitary amplifier chip. As expected, the highest output power was measured near then peak of the gain spectrum. These measurements also show that the laser wavelength can be controlled by setting the ring resonators, which confirms that the laser indeed operates based on feedback from the $Si_3N_4$ circuit.

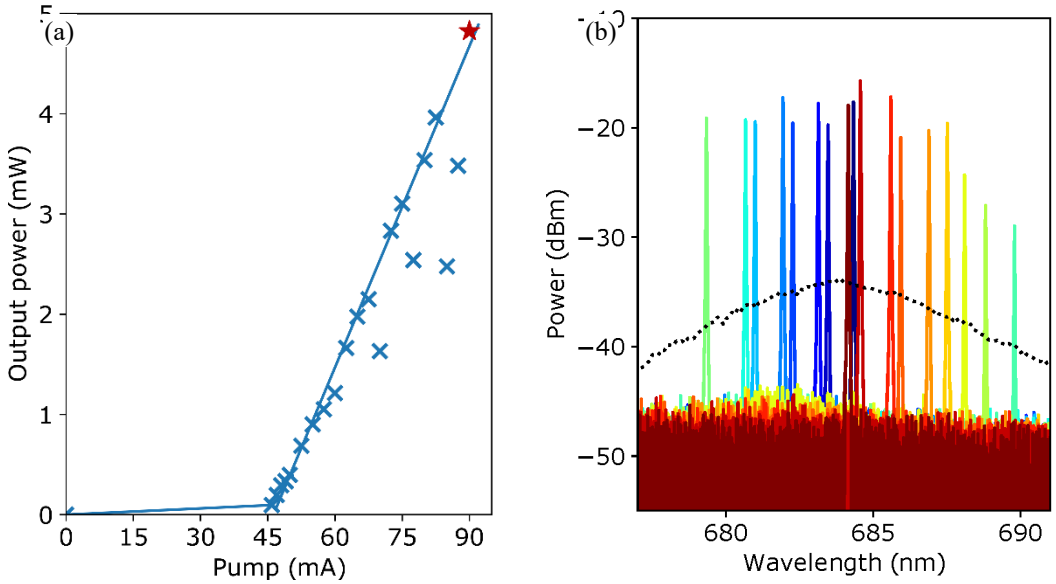



Figure 2. a) Measured fibre-coupled output power of the laser as function of the pump current to the amplifier. The maximum measured power of 4.80 mW (6 mW on chip) is indicated with a star. Comparison with a straight line drawn through the data points of maximum power indicates an approximately linear increase of the output with pump current. b) Superimposed laser spectra as measured with an OSA (resolution bandwidth 0.01 nm), showing an 11 nm wide tuning range of the hybrid laser around 685 nm. In order to obtain these spectra, MRR1 was heated between 0 and 400 mW in steps op 25 mW, while the pump current was set to 75 mA. The dotted black line shows the amplified spontaneous emission (ASE) of the solitary amplifier chip recorded before hybrid integration .

## 4. CONCLUSIONS

We realized, for the first time, a hybrid integrated diode laser for the visible range. To provide frequency selective feedback with very low losses, a $Si_3N_4$ based feedback circuit has been designed. $Si_3N_4$ based waveguides provide negligible absorption losses in the visible range, while the weak mode confinement of the optimized waveguide cross section reduces sidewall scattering losses. The demonstrated tuning range of the hybrid laser spans an 11 nm wide interval around 685 nm. A maximum output power of 4.8 mW has been measured at the maximum gain current of 90 mA. This demonstration in the visible range can form a breakthrough for applications which require tuneable and narrowband light sources on a chip. Further extension of this concept towards lower wavelength appears feasible, given the excellent transparency of the $Si_3N_4$ platform down to 400 nm.

## ACKNOWLEDGEMENTS

This research is funded by the European Union's Horizon 2020 research and innovation programme under grant agreement No. 688519 (PIX4LIFE).

## REFERENCES

[1] M. A. G. Porcel *et al.*: Silicon nitride photonic integration for visible light applications, *Opt. Laser Technol.*, **112**, 299 (2019).

[2] J.-C. Tinguely, Ø. I. Helle, and B. S. Ahluwalia: Silicon nitride waveguide platform for fluorescence microscopy of living cells, *Opt. Express* **25**, 27678 (2017).

[3] N. Poli *et al.*: A transportable strontium optical lattice clock, *Appl. Phys. B* **117**, 1107 (2014).

[4] F. Schmidt-Kaler *et al.*: Realization of the Cirac-Zoller controlled-NOT quantum gate, *Nature* **422**, 408 (2003)

[5] Y. Fan *et al.*: Ultra-narrow linewidth hybrid integrated semiconductor laser, *Arxiv.org*, 1910.08141 (2019).

[6] E. P. Haglund *et al.*: Silicon-Integrated Hybrid-Cavity 850-nm VCSELs by Adhesive Bonding: Impact of Bonding Interface Thickness on Laser Performance, *IEEE J. Sel. Top. Quantum Electron.* **23**, 1700109 (2017).

[7] K. Numata and J. Camp: Precision laser development for interferometric space missions NGO, SGO, and GRACE Follow-On, *J. Phys. Conf. Ser.* **363**, 012054 (2012).

[8] C. G. H. Roeloffzen *et al.*, Low-Loss Si3N4 TriPleX Optical Waveguides: Technology and Applications Overview, *IEEE J. Sel. Top. Quantum Electron.* **24**, 4400321 (2018).

# Highly Sensitive and Fast Responsive Photonic Integrated Relative Humidity Sensor using Porous $SiO_2$ Cladding

*Student Paper*

**Mahir Asif Mohammed[1], F.A. de Bot[1], Oded Raz[1]**
[1] *Electro-Optical Communications Group, Dept. of Electrical Engineering, Eindhoven University of Technology, Eindhoven*
*e-mail: O.Raz@tue.nl*

## ABSTRACT

Silicon dioxide ($SiO_2$) surface is known to be hydrophilic in nature. By increasing the porosity of $SiO_2$ thin layers, one can realize a much larger surface area to trap a significantly larger amount of water. Exploiting these effects, a micro-ring resonator (MRR) based photonic integrated relative humidity sensor with a porous $SiO_2$ cladding is demonstrated. The MRR easily tracks a 30 – 70 % relative humidity change (with a respective 3 nm resonance shift) and a linear operation region is observed between 30 – 55 %. Time-resolved humidity measurements indicated the highly sensitive and fast responsive nature of this sensor compared to a commonly used electronics-based sensor.

**Keywords**: Humidity, sensor, photonic, integrated optics, micro-ring resonator.

## 1. INTRODUCTION

Measurement and accurate control of humidity are much needed in agriculture, food storage, medical, drug production and process industries such as semiconductors and automotive [1]. Such a sensor implemented with optical and photonic integrated devices can potentially offer advantages like small form-factor, lightweight, high sensitivity and immunity to electromagnetic interference [2]. Materials such as $CoCl_2$, polyvinyl alcohol, sol-gel silica that naturally adsorbs water from ambient conditions have been used as a cladding material for realizing photonic relative humidity sensors [2]–[4]. In this work, a new technique for realizing a photonic integrated relative humidity sensor is demonstrated using porous silicon oxide ($SiO_2$) which has been previously studied for its water adsorption property at the surface [5]. The porous cladding layer results in increased surface areas and hence increased trapped water content yielding higher sensitivity [6]. Using these two effects, a novel photonic relative humidity sensor is demonstrated that presents high sensitivity (>75pm/%) and fast response (<2 sec) properties. This demonstrated technique offers a pathway towards highly sensitive photonic integrated relative humidity sensor using low-cost foundry friendly material that is also suitable for flexible substrates due to low-temperature deposition conditions.

## 2. DEVICE FABRICATION

For probing the changes within the cladding layer due to water absorption, a highly sensitive micro-ring resonator (MRR) was used that was fabricated using hydrogenated amorphous silicon (a-Si:H). The a-Si:H layer of 210 nm thickness was deposited at 80 °C by inductively coupled plasma-enhanced chemical vapor deposition (ICP-PECVD) technique [7]. The MRR radius was 25 µm and consists of *a*-Si:H waveguide that is 480 nm in width by 210 nm in height. The $SiO_2$ cladding was deposited using an ICP-PECVD system with a deposition temperature of 80 °C. The thickness of the deposited $SiO_2$ cladding was 300 ± 5 nm. And the refractive index determined using spectroscopic ellipsometry measurement was n=1.388 ± 0.015 at 1550 nm indicating the porous nature of the material.

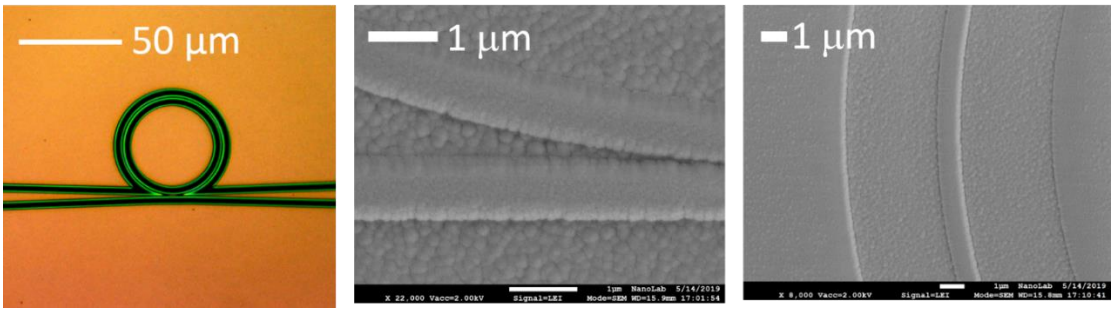



*Figure 1. The optical microscope image of the fabricated a-Si:H MRR (left) scanning electron microscope (SEM) image of the MRR waveguide sections with porous $SiO_2$ cladding (middle and right).*

## 3. RESULTS AND DISCUSSION

The fabricated device was tested in a humidity-controlled chamber with relative humidity conditions varying between approximately 30 - 70 %. In the following figure, the MRR response shift with respect to relative humidity conditions is reported. It is clearly shown that the MRR without cladding was minimally responding to the changes in the relative humidity. While the device with approximately 300 nm thick $SiO_2$ cladding was responding very well to changes in relative humidity. Between 30 – 55 % the changes are seen to be linear, while the resonance shift tends to be saturated until the increase of the relative humidity up to 70%. It is important to note that, the redshift of the resonance was observed, which indicates an increase of the effective refractive index as a result of water loading within the porous network. During this experiment, the temperature changed between 24.9 to 25.6 °C, which is not expected to affect the resonance much since the device sensitivity to temperature was determined to be 79.5 pm/°C.

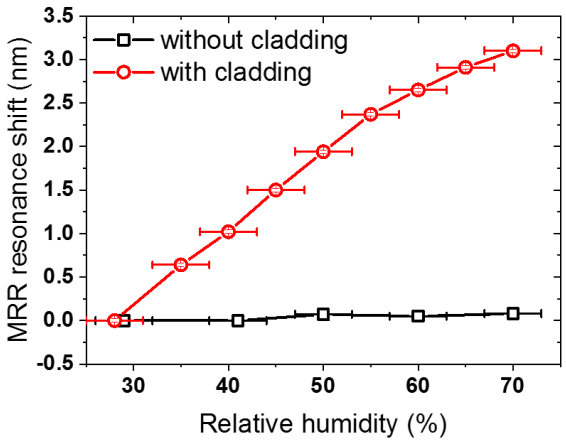



*Figure 2. MRR resonance shift with respect relative humidity for MRR with and without porous $SiO_2$ cladding.*

The sensitivity of the device was examined with a commercially available electronics-based relative humidity sensor, DHT22 as the humidifier was abruptly turned 'ON' and 'OFF' (Figure 3). The DHT22 sensor was interfaced with an Arduino Uno to act as a real-time relative humidity and temperature logger. Data were collected every 2 seconds.

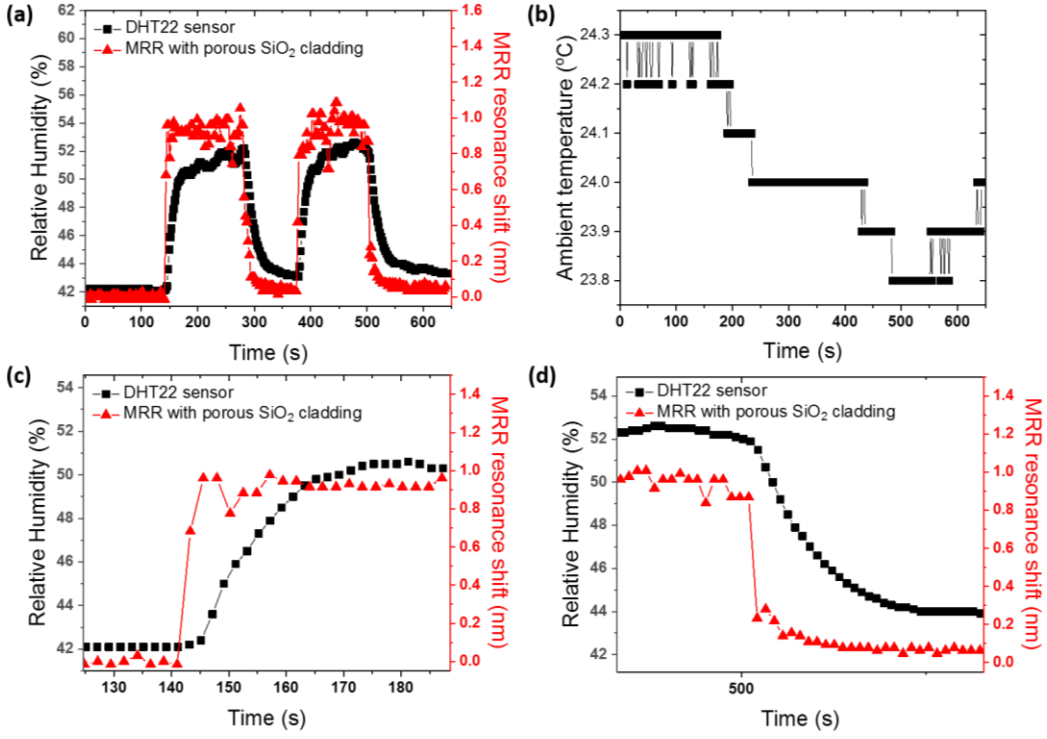



*Figure 3. (a) Dynamic response comparison between the MRR with porous $SiO_2$ cladding and DHT22. (b) Recorded ambient temperature during the experiment. (c) The rise time and (d) the fall time comparison between the MRR with porous $SiO_2$ cladding and DHT22.*

The MRR cladded device showed a stable response initially just as the DHT22. Turning 'ON' and 'OFF' the humidifier triggered both devices. As the relative humidity was changed by 10%, the MRR response red-shifted by approximately 1 nm as shown in Figure 2. During the experiment, the ambient temperature was quite stable as shown in Figure 3 (b). It is worth noting that the MRR device holder temperature was TEC controlled. Therefore, temperature affecting the photonic device response can be considered negligible. Careful inspection of the rise time and fall time for both devices clearly indicate that the MRR is very fast in responding to the changes in the relative humidity compared to DHT22. Also, MRR with porous $SiO_2$ cladding tends to saturate faster compared to DHT22. In addition, it was also found that the sensor can be used to probe alcohol based substances in the ambient. In Figure 4(left), the test setup is shown with the photonic chip and DHT22 sensor. Few drops of 2-propanol are left to evaporate nearby as shown in the figure. While the DHT22 response remained fairly constant, the response of the porous $SiO_2$ cladded MRR shifted every time 2-proponol drop was placed until it completely evaporated. This was reproduced several times as shown in Figure 4(right).

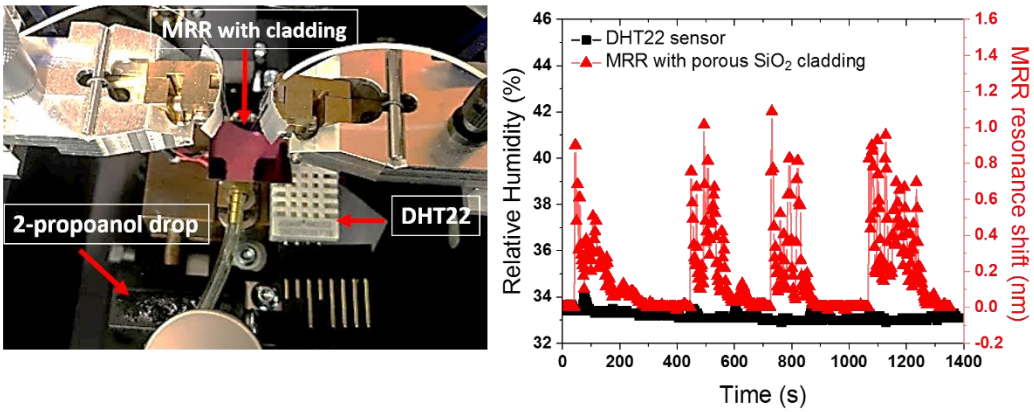



*Figure 4. Sensitivity to 2-propanol presence, the verticle coupling setup with 2-propanol drop (left) and the measured response (right).*

## 4. Conclusions

Porous $SiO_2$ attracts water from ambient humid conditions [5], [6]. By cladding a micro-ring resonator with this material, it is possible to sense the changes in the ambient relative humidity. It was found that the response change of the device to the relative humidity device is linear between 30 - 55 % according to the measurements. However, the most important attribute is perhaps the highly sensitive and fast-responding nature of this device, compared to a commonly used electronics-based sensor. Therefore, this technique can be suitable for application areas where small changes in humidity conditions are needed to be identified in a fast manner. Finally, the technique can be suitable for sensing other substances in the ambient as well. However, this needs further elaborate research work to understand the complete scope of this sensing material.


## ACKNOWLEDGEMENTS

We thank Dr. Aaron Albores Mejia for arranging the access to the humidity control chamber and facilitating the measurements at Effect Photonics B.V.


## REFERENCES


[1] S. Sikarwar and B. C. Yadav, "Opto-electronic humidity sensor: A review," *Sensors Actuators, A Phys.*, vol. 233, pp. 54–70, 2015.

[2] B. Bhola, P. Nosovitskiy, H. Mahalingam, and W. H. Steier, "Sol-gel-based integrated optical microring resonator humidity sensor," *IEEE Sens. J.*, vol. 9, no. 7, pp. 740–747, 2009.

[3] S. Muto, H. Sato, and T. Hosaka, "Optical humidity sensor using fluorescent plastic fiber and its application to breathing-condition monitor," *Jpn. J. Appl. Phys.*, vol. 33, no. 10R, pp. 606–604, 1994.

[4] A. Gastón, F. Pérez, and J. Sevilla, "Optical fiber relative-humidity sensor with polyvinyl alcohol film," *Appl. Opt.*, vol. 43, no. 21, pp. 4127–4132, 2004.

[5] D. B. Asay and S. H. Kim, "Evolution of the adsorbed water layer structure on silicon oxide at room temperature," *J. Phys. Chem. B*, vol. 109, no. 35, pp. 16760–16763, 2005.

[6] B. Torun, C. Kunze, C. Zhang, T. D. Kühne, and G. Grundmeier, "Study of water adsorption and capillary bridge formation for SiO2 nanoparticle layers by means of a combined in situ FT-IR reflection spectroscopy and QCM-D set-up," *Phys. Chem. Chem. Phys.*, vol. 16, no. 16, pp. 7377–7384, 2014.

[7] M. A. Mohammed, J. Melskens, R. Stabile, W. M. M. Kessels, and O. Raz, "Light-Induced Reversible Optical Properties of Hydrogenated Amorphous Silicon : A Promising Optically Programmable Photonic Material," *Phys. Status Solidi A*, vol. 215, no. 12, p. 1700754, 2018.

# Real-time functionalization and biosensing in subwavelength grating bimodal waveguides

*(Student paper)*

Luis Torrijos-Morán, Paula Martínez-Pérez and Jaime García-Rupérez
*Nanophotonics Technology Center, Universitat Politècnica de València, Camino de Vera s/n, 46022 Valencia, Spain*
*e-mail: luitorm2@ntc-upv.es*

## ABSTRACT

In this paper, we present for the first time experimental results of biosensing processes by using subwavelength grating bimodal waveguides as a refractive index sensors. We demonstrate the detection of 10ppm concentration of Bovine Serum Albumin (BSA) with a 190pm wavelength shift after a functionalization of the sensor surface with a layer of protein A/G in a continuous flowing system. Real-time data of each step is obtained, validating these kind of novel and highly sensitive SWG sensors for biosensing purposes.

**Keywords**: Subwavelength grating structures, bimodal waveguides, refractive-index biosensors, BSA detection, integrated photonic devices.

## 1 INTRODUCTION AND DESIGN

Subwavelength grating (SWG) waveguides have emerged as a promising alternative for a new kind of photonic devices with enhanced properties [1]. They are composed by a periodic dielectric repetition of a certain lattice in the propagation direction, whose period is relatively smaller than the effective wavelength of light. As a consequence, light propagates through these structures as if it were an homogeneous medium, but with the main advantage of a higher light-matter interaction of the field with the cladding [2], [3]. On the other hand, a new type of evanescent sensors based on bimodal waveguides [4], [5] have been demonstrated for biosensing applications. The underlying concept of these bimodal sensors stems from exciting two modes of the same polarization, the fundamental one acting as reference and the higher order mode acting as a sensing signal. At the end, a change in the cladding refractive index (RI) will be translated into a relative variation in the accumulated phase shift between both modes.

In previous work, we have experimentally demonstrated the use SWG structures as bimodal waveguides for highly sensitive RI sensing [6], [7], encompassing both ideas described above. Here, we present new experimental measurements including the biofunctionalization and the recognition of BSA by a SWG bimodal sensor, which validates for the first time the use of these devices as biosensors. The proposed design is depicted in Fig. 1a, where a displaced single-mode input waveguide excites the first two modes (even and odd parities in the y-axis direction) of the same transverse-electric (TE) polarization. Similarly, the power of both modes will be transferred into the fundamental mode of the output single-mode waveguide, thus creating an interference pattern in the transmission spectrum. Due to some dispersion properties of the modes propagating for these SWG structures [6], high spectral shifts are obtained for a change in the RI of the cladding. The design parameters are a=280nm, $w_i$=180nm, $w_e$=1400nm, d=350nm, with N=480 elements of the SWG bimodal region and accessed in and out with a single-mode waveguide of 450nm width. Figure 1b shows some scanning electron microscope (SEM) images of the fabricated sensor, using electron beam lithography, of 134.4 microns length on a silicon-on-insulator (SOI) wafer of 220nm height that has been used in the following biosensing experiments.

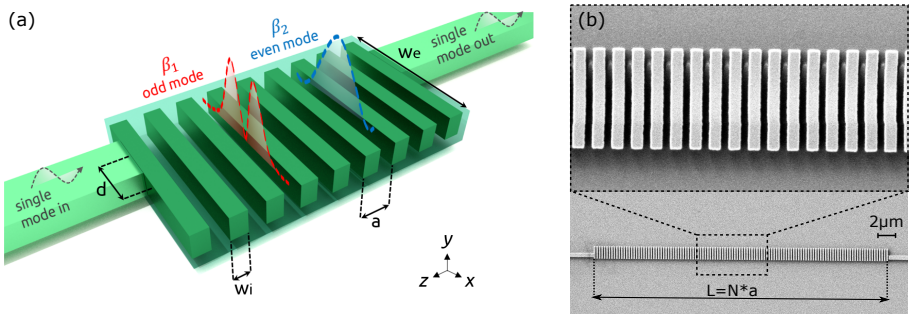



Figure 1. a) Skecth of the proposed design and its design parameters, composed by the single-mode input and output waveguides and the bimodal region of SWG elements. The fundamental mode (even mode) is depicted in blue while the first order mode (odd mode) is colored in red. b) SEM images of the fabricated sensor for the experimental validation, a complete structure and a detail of the SWG elements are shown.

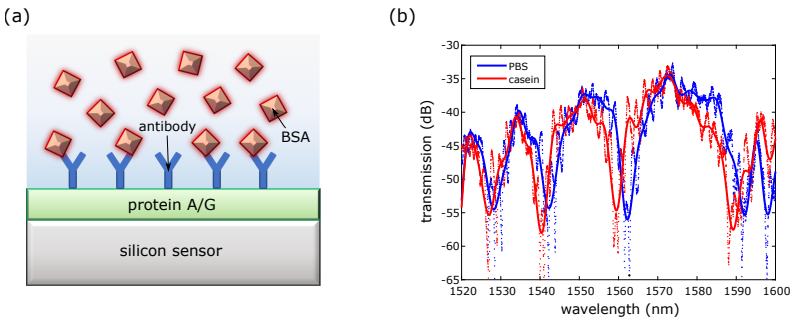



Figure 2. a) Sketch of the biofunctionalization and detection processes carried out in the experiments. In green the layer of protein A/G is depicted, in blue the antibody receptors and in red the targets molecules of BSA. b) Transmission spectra of a SWG bimodal waveguide of N=480 elements of a=280nm, $w_i$=180nm, $w_e$=1400nm and d=350nm. The spectra for PBS and casein as surrounding media are depicted in blue and red, respectively.

## 2 BIOSENSING RESULTS

The whole chip has been placed over a sample holder for the optical characterization. To this matter, a coherent TE polarized light from a tunable laser has been vertically coupled into the chip by using grating couplers. At the output, light was collected by an optical power meter that was previously synchronized with the laser. In addition, a methacrylate cell was disposed over the sensor in order to flow different analytes over time. The entire biosensing process is depicted in Fig. 2a, formed by a functionalization stage of protein A/G on the silicon surface of the sensor and casein as a blocking solution. Over the protein layer, the antibody will be flowed as the receptor molecule with the aim of detecting the target analyte of BSA at the end. Figure 2b shows the transmission spectra of the sensor over two different solutions, in Phosphate Buffered Saline (PBS) and casein, which are the baselines of the protein A/G and the BSA, respectively. As it can be seen, there is an increment in the cladding RI between PBS and casein that is translated into a negative wavelength shift, as it was predicted in [7]. Moreover, four different peaks are available as a consequence of the destructive interferences produced by both modes for wavelengths around 1520nm, 1540nm, 1560nm and 1590nm. Therefore, four different detection signals on each peak will be processed afterwards, where the most sensitive are the ones placed at higher wavelengths.

The optical setup was able to record around four spectra per minute. Over each one, a lorentzian fitting of the mentioned peaks was carried out. The detection signals are based on the minimun of these fitting peaks, therefore showing a point every fifteen seconds. The concentrations of the dilutions are 10$\mu$g/ml of protein A/G, 1$mg$/ml of casein, 50$\mu$g/ml of Antibody and 10$\mu$g/ml of BSA. Figure 3a shows the functionalization process of the protein A/G layer that has been placed on the sensor surface. It can be seen how there is absolute wavelength shift that remains after certain minutes of flowing protein A/G. In Fig. 3b and c we can see the change of baseline between PBS and casein, and the deposition of the antibody on the sensor surface. Finally BSA was flowed in Fig. 3d, showing an optical detection between 190pm and 320pm, of optical wavelength shift.

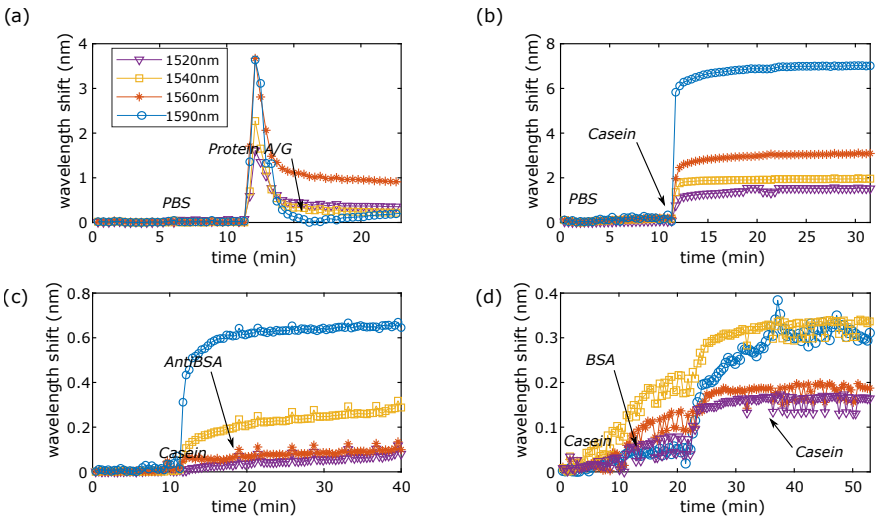



Figure 3. Optical measurements of PBS and protein A/G (a), PBS and casein (b), casein and antibody (c) and casein and BSA (d). The flowing rate was 20$\mu$g/ml in all the measurements.

## 3 CONCLUSIONS

To conclude, real-time optical measurements of a functionalization and biosensing experiment using bimodal SWG waveguides is presented. More in detail, a 10ppm of BSA is detected for the first time in these kind of structures, which validates SWG bimodal waveguides as biosensors. Future optimization of the measurements and biosensing studies will be carried out to further evaluate the limits of these SWG sensors in the area of integrated biophotonics.

## 4 ACKNOWLEDGMENTS

The authors acknowledge the funding from the Generalitat Valencia through project AVANTI/2019/123 and grant ACIF/2019/009.

## REFERENCES

[1] Pavel Cheben, Robert Halir, Jens H. Schmid, Harry A. Atwater, and David R. Smith. Subwavelength integrated photonics. *Nature*, 560(7720):565–572, 2018.

[2] Robert Halir, Przemek J. Bock, Pavel Cheben, Alejandro Ortega-Moñux, Carlos Alonso-Ramos, Jens H. Schmid, Jean Lapointe, Dan Xia Xu, J. Gonzalo Wangüemert-Pérez, Íñigo Molina-Fernández, and Siegfried Janz. Waveguide sub-wavelength structures: A review of principles and applications. *Laser and Photonics Reviews*, 9(1):25–49, 2015.

[3] J. Gonzalo Wangüemert-Pérez, Abdelfettah Hadij-ElHouati, Alejandro Sánchez-Postigo, Jonas Leuermann, Dan Xia Xu, Pavel Cheben, Alejandro Ortega-Moñux, Robert Halir, and Íñigo Molina-Fernández. Subwavelength structures for silicon photonics biosensing. *Optics and Laser Technology*, 109:437–448, 2019.

[4] Kirill E. Zinoviev, Ana Belén González-Guerrero, Carlos Domínguez, and Laura M. Lechuga. Integrated bimodal waveguide interferometric biosensor for label-free analysis. *Journal of Lightwave Technology*, 29(13):1926–1930, 2011.

[5] Daphné Duval, Ana Belén González-Guerrero, Stefania Dante, Johann Osmond, Rosa Monge, Luis J. Fernández, Kirill E. Zinoviev, Carlos Domínguez, and Laura M. Lechuga. Nanophotonic lab-on-a-chip platforms including novel bimodal interferometers, microfluidics and grating couplers. *Lab on a Chip*, 12(11):1987–1994, 2012.

[6] Luis Torrijos-Morán and Jaime García-Rupérez. High Sensitivity Optical Sensing Based on Modal Interferences in One-Dimensional Photonic Crystals. *Proceedings*, 4(1):20, 2018.

[7] Luis Torrijos-Morán and Jaime García-Rupérez. Single-channel bimodal interferometric sensor using subwavelength structures. *Optics Express*, 27(6):8168–8179, 2019.

# Monolithic piezoelectric control of soliton microcombs

*(Student Paper)*

Junqiu Liu[1], Hao Tian[2], Erwan Lucas[1], Arslan S. Raja[1], Grigory Lihachev[1],
Rui Ning Wang[1], Jijun He[1], Tianyi Liu[1], Miles H. Anderson[1], Wenle Weng[1],
Sunil A. Bhave[2], and Tobias J. Kippenberg[1]
[1]*Institute of Physics, Swiss Federal Institute of Technology Lausanne (EPFL), CH-1015 Lausanne, Switzerland*
[2]*OxideMEMS Lab, Purdue University, 47907 West Lafayette, IN, USA*
*e-mail: junqiu.liu@epfl.ch*

## ABSTRACT

High-speed laser frequency actuation is critical in all applications employing single frequency lasers or frequency combs, and is prerequisite for phase locking, laser stabilization and stability transfer among multiple optical carriers. Here, we demonstrate such capability for initiation, tuning and stabilization of soliton microcombs, by monolithically integrating piezoelectric AlN actuators on ultralow-loss $Si_3N_4$ photonic circuits. The integrated AlN actuators feature bi-directional tuning with high linearity, operate with only 300 nW power and exhibit flat actuation response up to megahertz frequencies, significantly exceeding bulk piezo tuning bandwidth. This capability can be used to demonstrate soliton-based source for parallel continuous-wave frequency-modulated LiDAR, via synchronously tuning laser and microresonator. Our approach endows soliton microcombs with integrated, ultralow-power-consumption, and fast actuation, significantly expanding the repertoire of technological applications.

**Keywords**: frequency comb, integrated photonics, microresonator, silicon nitride, MEMS.

## INTRODUCTION

In recent years there has been major progress in soliton microcombs which constitute chip-scale, broadband, high-repetition-rate coherent frequency combs. Silicon nitride ($Si_3N_4$) [1], [2] has emerged as a leading platform for integrated soliton microcomb generation, based on which several system-level applications have been demonstrated. For many applications of frequency combs, the ability to achieve megahertz locking-bandwidth of comb teeth (i.e. the repetition rate), is critical. This includes e.g. optical frequency synthesis, low-noise microwave generation via frequency division, or dual-comb spectroscopy. While femtosecond laser combs have developed a wide range of high-bandwidth actuators within the laser cavity, measurement-based feedback of chip-based soliton microcombs still relies on off-chip, bulk AOM or EOM that actuate on the pump laser. There have been limited solutions for optical modulation on $Si_3N_4$ waveguides, e.g. based on electro-absorptive graphene and ferroelectric lead-zirconate-titanate (PZT) [3], [4], [5]. However these methods have not been able to maintain or achieve simultaneously ultralow optical loss ($\sim$ 1 dB/m) in $Si_3N_4$ waveguides. Therefore, currently employed integrated actuation techniques for soliton microcombs rely primarily on metallic heaters [6], [7], which have only kilohertz actuation bandwidth. In addition, heaters exhibit uni-directional tuning, and typically consume electrical power exceeding 30 mW, comparable to the threshold optical power for soliton formation in state-of-art integrated devices [8], [9], [10], and are not compatible with cryogenic operation.

## RESULTS

Here we overcome the challenges mentioned above, and demonstrate integrated piezoelectric actuators based on aluminium nitride (AlN), a commercial MEMS technology to build microwave filters and oscillators. The AlN actuators are monolithically integrated on ultralow-loss $Si_3N_4$ waveguides fabricated using the photonic Damascene reflow process [11]. In this hybrid structure, the $Si_3N_4$ microresonators feature a preserved, intrinsic quality factor ($Q_0$) exceeding $15 \times 10^6$, similar to previous reported value in bare $Si_3N_4$ microresonators [11]. Figure 1(a) shows the microscope image of the fabricated device, and the schematic of soliton microcomb generation in this device. A frequency-fixed or narrow-band tunable CW laser is coupled into the $Si_3N_4$ microresonator, and soliton is initiated by inducing and tuning the strain in the $Si_3N_4$ waveguide. Such strain is generated by applying a voltage and deforming the AlN actuator by the inverse piezoelectric effect. Figure 1(b) shows the low-speed (DC) tuning curve, and the average linear tuning coefficient at DC is $\delta\nu/\delta V = 15.7$ MHz/V. Note that, this resonance tuning is *bi-directional*, determined by the sign of the applied voltage, in contrast to the thermal tuning using heaters which is uni-directional.

We next demonstrate that the AlN actuator enables voltage-controlled soliton initiation, switching, and tuning. Figure 1(c) shows the recorded effective laser-resonance detuning and soliton detuning using a vector network analyser. The resonance is initially forward-tuned to the laser (0 V $\rightarrow$ 71 V), and subsequently generates

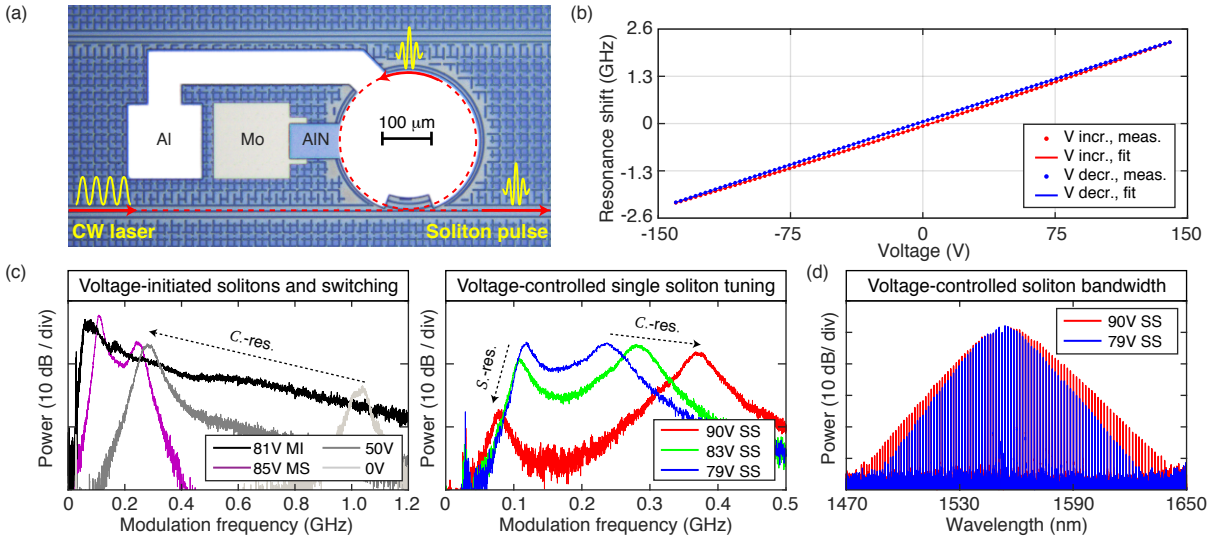



Figure 1. (a) Microscope image of the sample, and schematic of soliton generation this device. (b) Resonance shift versus applied voltage of a $TE_{00}$ resonance at 1556 nm. (c) Soliton detuning control via AlN actuation. (d) Different soliton states with different voltage applied on the AlN actuator.

a primary comb (PC, 71 V), modulation instability (MI, 81 V), and finally a multi-soliton state (MS, 85 V). Next, the AlN voltage is reduced such that the backward tuning enables switching to the single soliton state (SS, 79 V). The soliton detuning, as well as the spectral bandwidth, is further increased by increasing the voltage (90 V), as shown in Fig. 1(d). Because the AlN actuator is an excellent capacitor, the current to operate the AlN actuators at high voltage is measured as $\sim 2$ nA, corresponding to less than 300 nW power consumption at 150 V voltage.

Finally, we show that the AlN actuator allows fast modulation of the microresonator, and can be utilized to stabilize the soliton repetition rate. As the soliton repetition rate, $\nu_{\mathrm{rep}} = 191$ GHz, is not directly measurable, we utilize an electro-optic frequency comb (EO comb) of 14.6974 GHz line spacing, and measure the beat signal between the first line of the soliton microcomb and the 13th line of the EO comb. The schematic is shown in Fig. 2(a). Both combs, the microcomb and EO comb, are generated with the same pump laser. The measured beat signal is further compared to a reference microwave signal of 60.0 MHz, and the error signal is applied directly on the AlN actuator, such that the actuation on the microresonator stabilizes the soliton repetition rate to the EO comb line spacing. Figure 2(b, c) compares the measured phase noise of the beat signal between the first line of the soliton microcomb and the 13th line of the EO comb, in the cases of free-running and locked states. The locking bandwidth, determined by the merging point of two phase noise curves, is 600 kHz. It is important to emphasize that this is a record bandwidth for piezoelectric optical frequency actuators, compared to conventional lasers where the piezo response is typically limited to few kHz (similar to integrated heaters of few kHz bandwidth).

As an application, the AlN actuator can be a key component for a soliton-based, parallel, frequency-modulated continuous-wave (FMCW) LiDAR [12]. This is realized by using the AlN actuation on the microresonator, such that the microresonator resonance $\nu_{\mathrm{c}}$ is *modulated synchronously* to the pump frequency $\nu_{\mathrm{L}}$. This results in transferring the pump frequency chirp to all soliton comb teeth. Combined with diffractive optics that disperses multiple frequency lines, this approach to FMCW LiDAR allows high-speed parallel acquisition of both velocity and position in each pixel. The experimental details and results are found in Ref. [13]

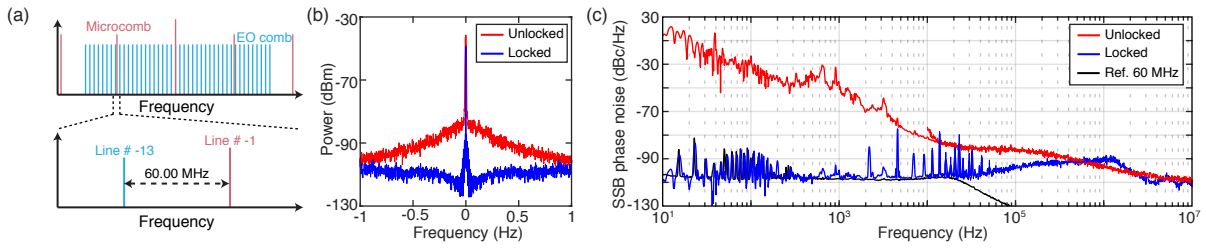



Figure 2. (a) Schematic of soliton repetition rate stabilization using an EO comb with 14.6974 GHz line spacing. (b) Measured beatnote signal of the first line of the soliton microcomb and the 13th line of the EO comb, in the cases of locked and unlocked (free-running) states. (c) Measured phase noise of the beat signal.

## CONCLUSION

In conclusion, we demonstrate integrated piezoelectric control of soliton microcombs, by monolithically integrating AlN actuators on ultralow-loss $Si_3N_4$ waveguides. This novel capability not only benefits existing applications, but also allows synchronous scanning of the pump laser and photonic microresonator, as required for massively parallel FMCW LiDAR. While polycrystalline AlN is used in our current work, the operation voltage can be reduced by more than $\times 2$ using scandium-doped AlN. By future co-integration of CMOS electronic circuitry on a closeby die, compactly packaged soliton microcombs with rapid electronic actuation is attainable.

The full results of this work are available in Ref. [13].


## FUNDING INFORMATION

This work was supported by Contract HR0011-15-C-055 (DODOS) from the Defense Advanced Research Projects Agency (DARPA), Microsystems Technology Office (MTO), by the Air Force Office of Scientific Research, Air Force Material Command, USAF under Award No. FA9550-15-1-0099, and by Swiss National Science Foundation under grant agreement No. 176563. (BRIDGE).

## ACKNOWLEDGMENT

We thank Johann Riemensberger, Anton Lukashchuk and Maxim Karpov for the fruitful discussion. E.L. acknowledge the support from the European Space Technology Centre with ESA Contract No. 4000116145/ 16/ NL/ MH/ GM. The $Si_3N_4$ microresonator samples were fabricated in the EPFL center of MicroNanoTechnology (CMi), and Birck Nanotechnology Center at Purdue University.


## REFERENCES


[1] D. J. Moss *et al*, Nature Photonics 7, 597 (2013).

[2] A. L. Gaeta *et al*, Nature Photonics 13, 158 (2019).

[3] N. Hosseini *et al*, Opt. Express 23, 14018 (2015).

[4] K. Alexander *et al*, Nature Communications 9, 3444 (2018).

[5] W. Jin *et al*, Opt. Express 26, 3174 (2018).

[6] C. Joshi *et al*, Opt. Lett. 41, 2565 (2016).

[7] X. Xue *et al*, Opt. Express 24, 687 (2016).

[8] B. Stern *et al*, Nature 562, 401 (2018).

[9] A. S. Raja, *et al*, Nature Communications 10, 680 (2019).

[10] B. Shen *et al*, arXiv 1911.02636.

[11] J. Liu *et al*, Optica 5, 1347 (2018).

[12] J. Riemensberger *et al*, arXiv 1912.11374 (2019).

[13] J. Liu *et al*, arXiv 1912.08686 (2019).

# Microresonator Soliton based parallel FMCW LiDAR

Anton Lukashchuk [1], Johann Riemensberger [1], Maxim Karpov [1], Erwan Lucas [1], Wenle Weng [1], Junqiu Liu [1], Tobias Kippenberg [1]

[1] *Institute of Physics (IPHYS), Swiss Federal Institute of Technology in Lausanne (EPFL), CH-1015 Lausanne, Switzerland*

*e-mail: tobias.kippenberg@epfl.ch*

## ABSTRACT

We demonstrate an architecture for massively parallel frequency-modulated continuous wave (FMCW) laser ranging (LiDAR) by transferring linear chirps of a single narrow linewidth laser onto all soliton comb teeth though generation of a dissipative Kerr soliton in an integrated $Si_3N_4$ microresonator. Furthermore, we introduce a novel approach using dual soliton microcombs. We show a parallel distance measurement with 24 channels requiring only a single FMCW pump laser and coherent receiver for read-out.

**Keywords**: LiDAR, FMCW, microresonator, frequency combs, Dissipative Kerr Solitons.

Coherent laser ranging [1], i.e. laser ranging that relies on a phase sensitive detection is a technique of growing interest in the long range 3D LiDAR application market due to its resilience to interference and sunlight glare [2], [3], the possibility to achieve shot-noise limited detection signal-to-noise without the use of single-photon detection and direct measurement of distance *and* velocity in each pixel. Its principle, depicted in Figure 1 b), is based on mapping the optical time-of-flight to frequency via linear frequency chirping [4], [5] of the laser and delayed detection of the return light. The target velocity is detected by extracting the common Doppler shift from several interleaved linear chirp ramps of different pitch. Yet, despite the inherent advantages of coherent ranging, the LiDAR application field is still dominated by simple time-of-flight systems, which is mainly related to the challenge of constructing narrow linewidth and frequency-agile lasers, which can be precisely chirped [6], precluding implementations based on laser-arrays.

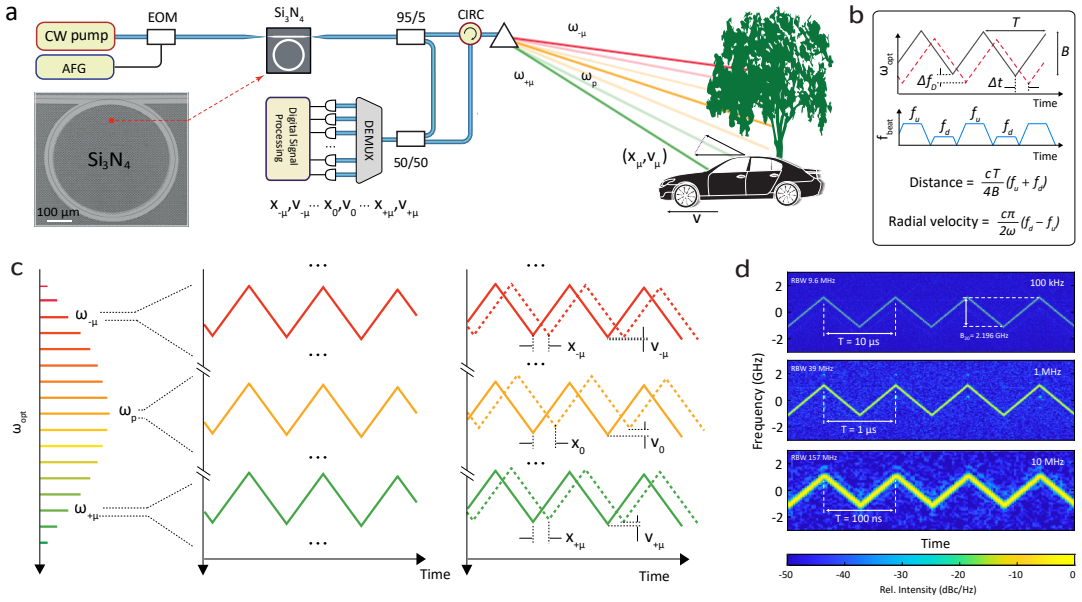



Figure 1. **Massively parallel LiDAR architecture based on soliton microcombs** (a) Sketch of the proof-of-concept parallel FMCW LiDAR experiment. (b) RF spectrum of the sideband at 194.4 THz ($\mu = +14$) with the flywheel rotating at 228 Hz. (c) Time-frequency maps of the retrieved LiDAR signals for multiple channels (A) $\mu = +2$, (B) $\mu = +8$, (C) $\mu = +14$ for the static and rotating flywheel. (d) Results for distance (9.65m in SMF28 fiber, 35 cm in free space) and velocity measurements over the 30 channel span highlighting the capability to measure cm-level distance and velocities. The effective sampling rate of the measurement is 3 Mpixels/s at a 100 kHz chirp modulation frequency.

Here we present an architecture for massively parallel FMCW LiDAR using only a single narrow linewidth, well controlled frequency-agile laser. We use this laser to drive a dissipative Kerr soliton [7] in an integrated $Si_3N_4$ microresonator, which is fabricated with the photonic damascene process [8] and multiplex its chirp onto all the generated frequency comb sidebands $|\mu| > 0$. These sidebands can be spatially separated using cheap diffractive optics and telecom equipment (WDM). *Each sideband* can *simultaneously and independently* measure the distance and velocity of a target object (cf. Fig. 1 a). Spectral separation prevents self interference of the coherent carrier, while spatial separation and CW operation greatly reduces the peak and average optical

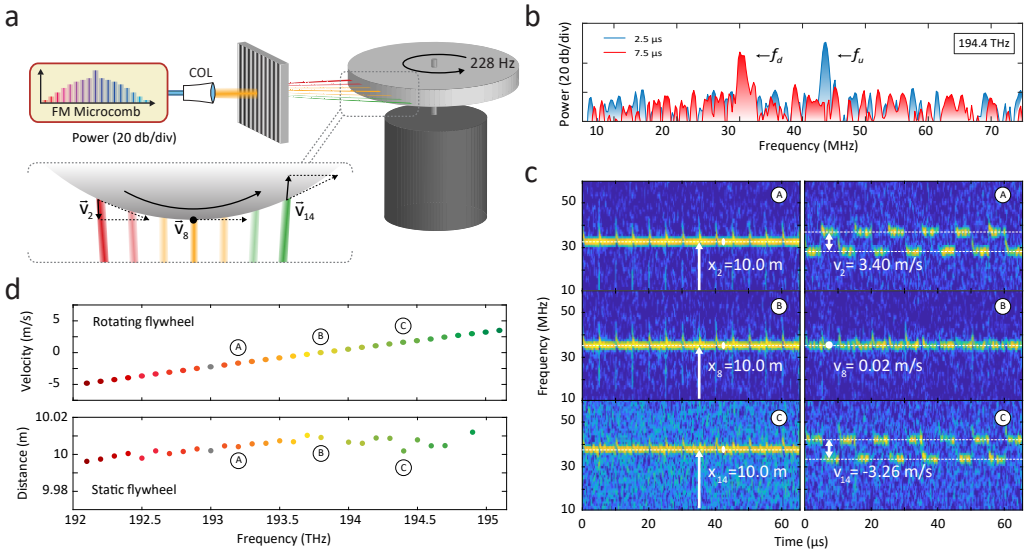



Figure 2. **Proof-of-concept demonstration of parallel LiDAR based on soliton microcomb** (a) Sketch of the proof-of-concept parallel FMCW LiDAR experiment. (b) RF spectrum of the sideband at 194.4 THz ($\mu = +14$) with the flywheel rotating at 228 Hz. (c) Time-frequency maps of the retrieved LiDAR signals for multiple channels (A) $\mu = +2$, (B) $\mu = +8$, (C) $\mu = +14$ for the static and rotating flywheel. (d) Results for distance (9.65 m in SMF28 fiber, 35 cm in free space) and velocity measurements over the 30 channel span highlighting the capability to measure cm-level distance and velocities.

power on target and prevents eye and camera damage. Tuning the laser within the frequency range of stable soliton generation faithfully transfers the linear chirps to all the sidebands up to frequency excursion bandwidths $B \approx 2$ GHz and modulation frequencies $1/T = 10$ MHz (cf. Fig. 1 c,d). Despite Raman self-frequency shift [9] and modal interactions [10], the sideband nonlinearity, defined as the RMS deviation between the frequency modulation pattern and a symmetric triangle remains below 5 MHz at 100 kHz modulation frequency and 2 GHz frequency excursion for all channels.

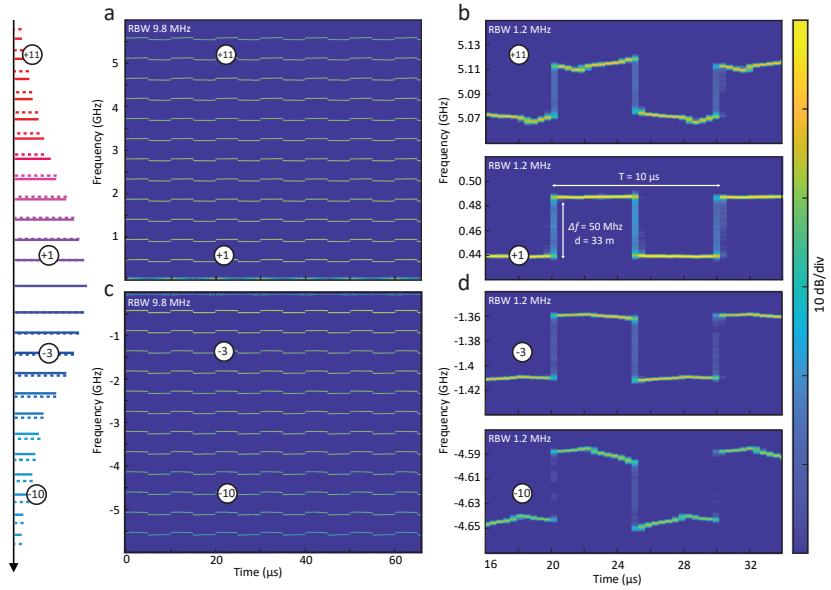



Figure 3. **Dual-comb coherent LiDAR distance measurement** (a,b) Time-frequency maps of the retrieved LiDAR signals with 100 kHz modulation rate performing parallel distance measurement of the arm of Mach-Zehnder interferometer of the signal and LO combs (fiber delay) for multiple optical channels of (a) positive and (b) negative frequencies. (a) features ($\mu = +1$, $\mu = +12$) channels, (b) - ($\mu = -1$, $\mu = -12$) channels. (c,d) Zoomed (a) and (b) featuring $\mu = +11$, $\mu = +1$, $\mu = -3$ and $\mu = -10$ channels. Difference in $f_{up}$ and $f_{down}$ of 50 MHz determines 33 m distance of the fiber delay between the signal and LO combs.

As proof-of-concept experimental demonstration, we perform a FMCW LiDAR experiment with the soliton microcomb source. We generate more than 30 individual channels, limited by the amplification bandwidth of our EDFA and spatially disperse the light with a transmission grating along the circumference of a small aluminum flywheel mounted on a fast DC motor. A schematic drawing of the experiment is depicted in Figure 3 a). The LiDAR source is amplified with a gain-flattened EFDA, which limits the usable channels number to 30 within the telecom C-band. The effective sampling rate of the LiDAR source is 3 Mpixels/s at a 100 kHz

chirp modulation frequency, with capability to achieve beyond 150 Mpixels/s. Hence, our proposed scheme, inherently compatible with nanophotonic gratings and phased arrays [11], marks an promising new approach for high-frame rate 3D coherent imaging systems.

We further extend this technology and present a novel architecture for DKS based dual-comb coherent LiDAR. By merging the concepts of parallel FMCW LiDAR and multi-heterodyne detection, we implement massively parallel FMCW operation with only a single narrow linewidth FMCW laser source and a single coherent photoreceiver. The experimental setup of the dual-comb parallel FMCW LiDAR would be a little modified from the one depicted in Fig. 1. Second $Si_3N_4$ microresonator ring featuring a slight difference in repetition rate ($\Delta f_{rep}$ = 465 MHz) is added and pumped from the same laser by a chirped beam. Then every single optical channel would be mapped to its frequency window with range equal to difference in repetition rates (465 MHz in our case). Thus one can get rid of optical wavelength division multiplexing system and array of photodiodes, having instead one high bandwidth coherent receiver.

In the proof-of-concept experiment we demonstrate the measurement of the 33 m fiber delay in Mach-Zehnder interferometer between the signal and LO. We utilize 12 'positive', i.e. $\mu > 0$ and 12 'negative', i.e. $\mu < 0$, frequency channels. Parallel acquisition of 24 channels features equivalent same time delays (Fig. 3) mapped to 50 MHz frequency difference between $f_{up}$ and $f_{down}$ beat frequencies. Here the frequency modulation rate is 100 kHz and frequency excursion is 0.75 GHz resulting in distance delay equal to 33 m. Nonlinear behavior of the higher channels (Fig. 3 $\mu = +11$, $\mu = -10$) as in the case of a single comb is related to the Raman self frequncy shift [9] and can be minimized by optimizing the input power and laser-cavity detuning of the two microresonators. In summary, the present scheme allows the cost effective simultaneous detection of up to 50 coherent LiDAR channels further improving the sampling speed, is compatible with heterogeneous photonic integration and naturally aligns with modern optical phased array technology.

## ACKNOWLEDGMENTS

This work was supported by funding from the Swiss National Science Foundation under grant agreement No. 165933. This material is based upon work supported by the Air Force Office of Scientific Research (AFOSR), Air Force Material Command, USAF under Award No. FA9550-15-1-0250. J.R. and W.W. acknowledge support from the EUs H2020 research and innovation program under Marie-Sklodowska-Curie IF grant agreement No. 846737 (CoSiLiS) and No. 753749 (SOLISYNTH), respectively.

### REFERENCES

[1] H. Bostick, A carbon dioxide laser radar system. *IEEE Journal of Quantum Electronics* 3, 232–232 (1967).

[2] C. Urmson, *et al.* Autonomous driving in urban environments: Boss and the urban challenge. *Journal of Field Robotics* 25, 425–466 (2008).

[3] B. Behroozpour *et al.*, Lidar system architectures and circuits. *IEEE Communications Magazine*, 55, 135–142 (2017).

[4] R. I. MacDonald, Frequency domain optical reflectometer. *Applied Optics* 20, 1840 (1981).

[5] D. Uttam, & B. Culshaw, Precision time domain reflectometry in optical fiber systems using a frequency modulated continuous wave ranging technique. *IEEE Journal of Lightwave Technology* 3, 971–977 (1985).

[6] P. A. Roos *et al.*, Ultrabroadband optical chirp linearization for precision metrology applications. *Optics Letters* 34, 3692 (2009).

[7] T. J. Kippenberg *et al.*, Dissipative Kerr solitons in optical microresonators. *Science* 361, eaan8083 (2018).

[8] M. H. P. Pfeiffer *et al.*, Photonic Damascene process for low-loss, high-confinement silicon nitride waveguides, IEEE Journal of selected topics in quantum electronics 24, 4, 2018

[9] M. Karpov, *et al.* Raman self-frequency shift of dissipative Kerr solitons in an optical microresonator. *Physical Review Letters* 116, 1–5 (2016.

[10] X. Yi *et al.*, Theory and measurement of the soliton self-frequency shift and efficiency in optical microcavities *Optics Letters* 41, 3722 (2016).

[11] Sun, J., *et al.* Large-scale nanophotonic phased array. *Nature* 493, 195–199 (2013).

# A hybrid chalcogenide-on-silicon platform for nonlinear photonics

**Samuel Serna[1,2,3], Hongtao Lin[3], Carlos Alonso-Ramos[2], Xavier Le Roux[2], Kathleen A. Richardson[4], Eric Cassan[2], Nicolas Dubreuil[5,6], Juejun Hu[3], and Laurent Vivien[2]**

[1] Department of Physics, Bridgewater State University, Bridgewater, Massachusetts 02325, USA
[2] Université Paris-Saclay, CNRS, Centre de Nanosciences et de Nanotechnologies, 91120, Palaiseau, France
[3] Department of Materials Science and Engineering, Massachusetts Institute of Technology, Cambridge, Massachusetts 02139, USA
[4]College of Optics and Photonics-CREOL, University of Central Florida, Orlando, Florida 32816, USA
[5] Laboratoire Charles Fabry, Institut d'Optique Graduate School, CNRS, Université Paris Saclay, 2 Avenue Augustin Fresnel, 91127 Palaiseau cedex, France6
[6]LP2N, Institut d'Optique Graduate School, CNRS, Univ. Bordeaux, 33400 Talence, France
*e-mail:* ssernaotalvaro@bridgew.edu;safes@mit.edu

## ABSTRACT

We demonstrate a highly nonlinear hybrid waveguide platform based on infiltration of $As_2S_3$ chalcogenide glass into silicon slot waveguides. The nonlinear properties of the hybrid waveguides have been precisely quantified via a bidirectional top-hat D-scan method, enabling a direct comparison between properties measured using different device geometries. We experimentally report hybrid $As_2S_3$-Si slot waveguides with a two-photon absorption (TPA) figure of merit exceeding 2 at near infrared wavelengths. These waveguides allow for nonlinear phase shifts greater than π with minimal overall losses. These results pave the way for efficient and robust ultrafast all-optical devices and circuits in large-scale silicon photonics technology.

**Keywords**: nonlinear optics, chalcogenide glass, silicon photonics, waveguides.

## 1. INTRODUCTION

There has been a strong interest in silicon photonics in the last years due to its compatibility with the CMOS technology and its relatively low cost [1]. However, as a nonlinear optical signal processing platform silicon is disadvantaged by high nonlinear losses due to two photon absorption (TPA) at telecom wavelengths [2]. To overcome this limitation, TPA-free alternative platforms such as silicon nitride and high index silica (Hydex) have been explored [3]. But the nonlinear parameter ($\mathrm{Re}\{\gamma\}$) in these platforms is very low compared to silicon. Another route is the heterogeneous integration of SOI waveguides with a low nonlinear loss material such as a nonlinear polymer. In particular, slot geometries have been proposed where light is confined within a gap between semiconductor rails therefore taking advantage of the high permittivity contrast between Si and the lower index material filling the slot [4].

Here, we demonstrate experimentally complete filling of nano-slots in silicon waveguides with $As_2S_3$ glass using a simple thermal reflow process. We also validate enhancement of third order nonlinearities and nonlinear figure of merit in these hybrid slot waveguides using a bidirectional D-Scan measurement method [5], showing the possibility of engineering effective nonlinearities in complex hybrid photonic circuits. Besides, we show experimentally that it is possible to have different effective non-linearities by changing the slot sizes. Our results illustrate the potential for the development of dispersion engineered slotted structures for efficient ultra-fast all-optical nonlinear photonics in chip-scale platforms.

## 2. SIMULATION RESULTS

To investigate the impact of hybrid waveguide design on the nonlinear parameters, we calculated and plot in Fig. 1 the confinement factor in the $As_2S_3$ cladding (left axis) and the inverse of the effective mode area (right axis), which is proportional to the effective third order nonlinear susceptibility ($\gamma_{wg}$) as defined in Ref. [6]. These simulations serve as a guideline for investigating realistic slot width values for nonlinear applications.

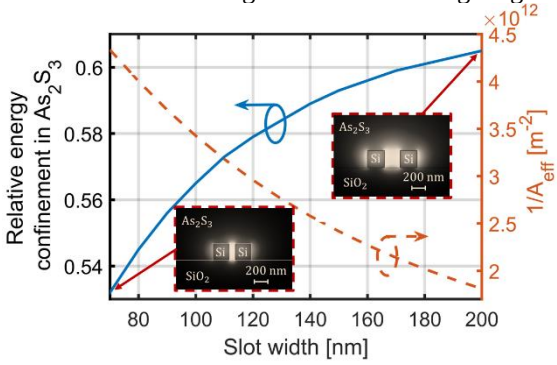



*Fig. 1. Simulated modal confinement factor (left axis) and inverse of the effective mode area (right axis) of hybrid As2 S3- Silicon waveguides as a function of slot width. Insets: TE- polarized modal profile.*

## 3. SAMPLE FABRICATION

The devices were fabricated on SOI wafers (Soitec) with a 220 nm-thick silicon layer over 2 μm of buried $SiO_2$. Device structures (slots) were defined in ZEP-520A resist (Zeon Chemical Co.) by 80 kV e-beam lithography Nanobeam NB-4 system. The writing fields were set to $50 \times 50\ \mu m^2$ for a beam current of 0.5 nA and a beam step size of 2 nm. The resist patterns were then transferred to the Si layer by an inductively coupled plasma (ICP) reactive ion etching process using $SF_6$ and $C_4F_8$ gases. Following this, thin films of $As_2S_3$ were prepared using single-source thermal evaporation. The film deposition was performed using a custom-designed system (PVD Products, Inc.) following previously established protocols [7]. The devices were then annealed for 1 min at $250^{\circ}C$ in an inert gas atmosphere. The annealing step reduced viscosity of $As_2S_3$ at elevated temperatures to facilitate the viscous flow of the glass. Since $As_2S_3$ wets Si waveguide surfaces, the glass could spontaneously fill the slots completely without leaving voids or other loss-inducing defects [8]. Fig. 2 (a) shows a SEM injection coupler 3 μm wide separated by 3 μm etched silicon in both sides covered with 1 μm $As_2S_3$ layer. Fig. 2 (b) is a slot waveguide, with squared silicon rails of 220 nm, fully covered with the chalcogenide material, the slot width of 70 nm is the smaller than the one used in this study, demonstrating the ability to fill larger slot widths.

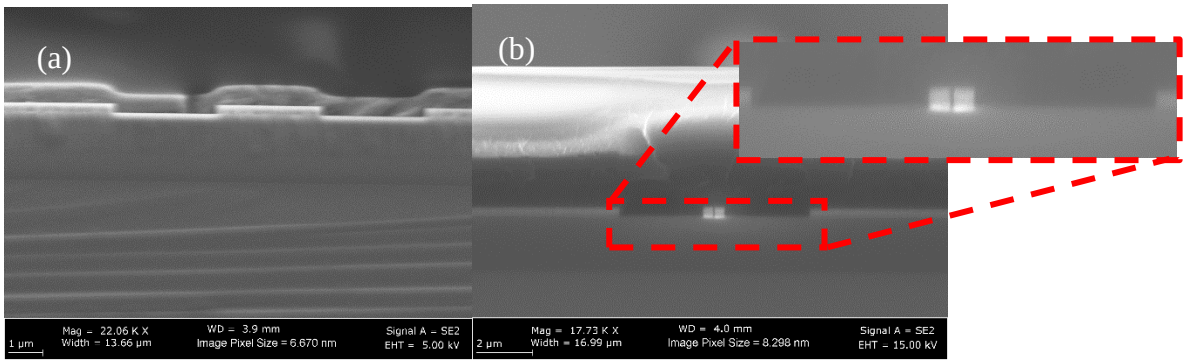



*Fig. 2. (a) SOI multimode injection waveguide covered with a layer of chalcogenide glass. (b) 70 nm slot waveguide filled with the chalcogenide glass after annealing.*

## 4. EXPERIMENTAL SET-UP

For the experimental characterization of the nonlinear effective susceptibilities, we have used a bidirectional top-hat D-Scan technique [5]. This allowed the measurement of the coupling coefficients, as well as the direct quantification of the sign and magnitude of the real and imaginary third order nonlinear susceptibilities. More details about the technique and the used set-up, shown in Fig. 3, will be presented during the conference.

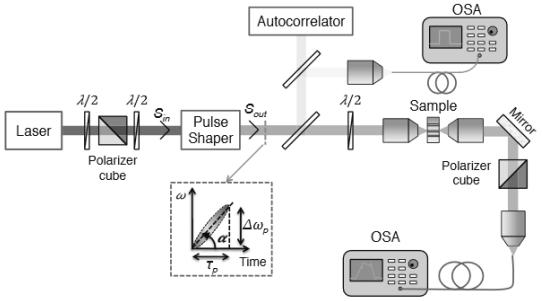



*Fig. 3. Experimental set-up where femtosecond pulses of an Er-doped amplifier fiber laser are sent into a grating-based pulse shaper prior to their injection into the sample by means of a microscope objective [9].*

## 5. RESULTS AND DISCUSSION

We present in Fig. 4 (a) the magnitude of the effective third order nonlinear susceptibilities in the hybrid structures. For larger slots, the real $\gamma$ is smaller but the imaginary part decreases faster as the confinement in the slot regions is larger. Ending up in a larger TPA figure of merit. After performing the different scan measurements on the different hybrid waveguides, we demonstrated this trend experimentally (Fig 4 (b)). Compared to silicon (gray bar), the hybrid slot waveguides exhibit a fourfold improvement in terms of the $FOM_{TPA}$. More importantly, the observed trends show that $FOM_{TPA}$ of all the slot waveguides measured are larger than unity (violet-colored-dashed line in Fig. 4 (b)). These devices thus meet a critical criterion for efficient nonlinear integrated photonics. Specifically, the power required to reach a $\pi$ phase shift for the fabricated device with a 160 nm slot width and a 0.73 mm effective length is on the order of 45 W, the power levels already used in the past with the same chalcogenide glass composition[10]. Moreover, the slot waveguide configuration further enables precise tailoring of the dispersion characteristics and enhancement of light–matter interactions with slow light.

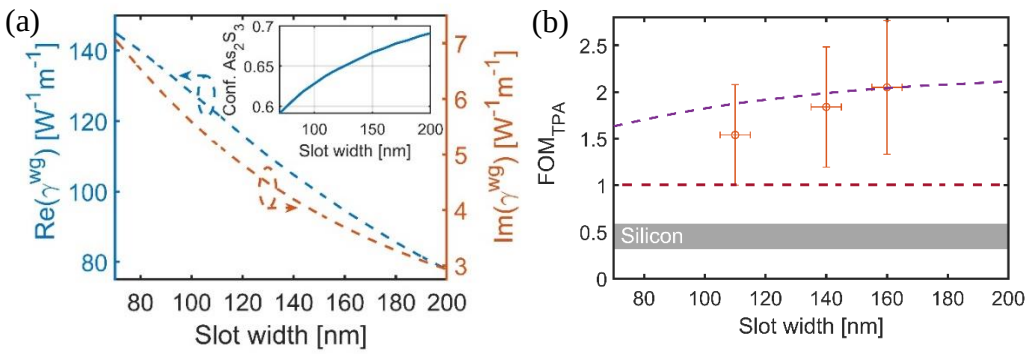



*Fig. 4. (a) Real and imaginary susceptibilities as a function of the slot width. Inset: Confinement factor inside the slot. (b) Simulation and experimental TPA figure of merit for the three different characterized waveguides. The milestone of $FOMT_{TPA}$=1 is highlighted [11].*

TABLE 1. DIFFERENT EXPERIMENTALLY STUDIED PARAMETERS IN HYBRID SLOT WAVEGUIDES.

| Slot size [nm] | Prop. $L^{slot}$ [mm] | $L_{eff}^{slot}$ [mm] | Re($\gamma^{slot}$) [W$^{-1}$ m$^{-1}$] | FOM$_{TPA}^{wg}$ – |
|---|---|---|---|---|
| 0 | – | – | 159 ± 16 | 0.7 ± 0.1 |
| 110 ± 10 | 1.65 | 1.37 | 120 ± 20 | 1.5 ± 0.5 |
| 140 ± 10 | 0.45 | 0.42 | 105 ± 18 | 1.8 ± 0.6 |
| 160 ± 10 | 0.85 | 0.73 | 95 ± 15 | 2.1 ± 0.7 |

[a]Slot width=0 nm is given as a reference and corresponds to a single mode strip waveguide covered with chalcogenide.

## 6. CONCLUSION

In conclusion, we demonstrated the improvement of non-linear properties in hybrid silicon slot waveguides filled with $As_2S_3$ chalcogenide glass. We have shown that the slot width is a critical design parameter that governs the linear propagation losses, the confinement factor in the slot region, and the figure of merit $FOM_{TPA}$. We further conclude that larger slot widths are beneficial as they combine lower linear propagation losses and a larger $FOM_{TPA}$, although they require longer structures as the effective area is larger. Our result opens new opportunities for engineering effective nonlinearities in integrated photonic devices and is useful for realizing novel nonlinear functionalities such as stimulated Brillouin scattering (SBS) [12] and the Kerr effect induced spectral broadening in a silicon-based platform.

## ACKNOWLEDGEMENTS

The authors thank the support from the grants: H2020 European Research Council (647342); National Science Foundation (1506605); Agence Nationale de la Recherche (MIR-SPEC). The presenting author thanks the travel support from Bridgewater State University.

## REFERENCES

[1] L. Vivien and L. Pavesi, Handbook of silicon photonics (Taylor & Francis, 2016).
[2] A. Liu, R. Jones, L. Liao, D. Samara-Rubio, D. Rubin, O. Cohen, R. Nicolaescu, and M. Paniccia, Nature 427, 615 (2004).
[3] J. Leuthold, C. Koos, and W. Freude, Nat. photonics 4, 535 (2010).
[4] V. R. Almeida, Q. Xu, C. A. Barrios, and M. Lipson, Opt. letters 29, 1209 (2004).
[5] S. Serna and N. Dubreuil, Opt. Lett. 42, 3072-3075 (2017).
[6] T. Vallaitis, S. Bogatscher, L. Alloatti, P. Dumon, R. Baets, M. L. Scimeca, I. Biaggio, F. Diederich, C. Koos, W. Freude et al., Opt. express 17, 17357 (2009).
[7] Q. Du, Z. Luo, H. Zhong, Y. Zhang, Y. Huang, T. Du, W. Zhang, T. Gu, and J. Hu, Photonics Res. 6, 506 (2018).
[8] J. Hu, N.-N. Feng, N. Carlie, L. Petit, A. Agarwal, K. Richardson, and L. Kimerling, Opt. express 18, 1469 (2010).
[9] S. Serna, J. Oden, M. Hanna, C. Caer, X. Le Roux, C. Sauvan, P. Delaye, E. Cassan, and N. Dubreuil, Opt. Express 23, 29964-29977 (2015).
[10] M. R. Lamont, B. Luther-Davies, D.-Y. Choi, S. Madden, and B. J.Eggleton,Opt. Express16, 14938 (2008).
[11] S. Serna, H. Lin, C. Alonso-Ramos, C. Lafforgue, X. Le Roux, K. A. Richardson, E. Cassan, N. Dubreuil, J. Hu, and L. Vivien, Opt. Lett. 44, 5009-5012 (2019).
[12] B. J. Eggleton, C. G. Poulton, and R. Pant, Adv. Opt. Photonics 5, 536 (2013).

# Widely Tunable 2.6 µm GaSb Diode Lasers Utilizing Diffraction Gratings or Silicon Photonics Reflectors

*(Student Paper)*

**Samu-Pekka Ojanen[1], Jukka Viheriälä[1], Matteo Cherchi[2], Nouman Zia[1], Eero Koivusalo[1], Pentti Karioja[3] and Mircea Guina[1]**

[1] Optoelectronics Research Centre, Physics Unit, Tampere University, FI-33720 Tampere, Finland

[2] VTT Technical Research Centre of Finland, FI-02044 Espoo, Finland

[3] VTT Technical Research Centre of Finland, FI-90570 Oulu, Finland

*e-mail: samu-pekka.ojanen@tuni.fi*

## ABSTRACT

We present two tunable extended cavity laser configurations emitting around 2.6 µm. The gain is provided by a type-I GaSb-based quantum well heterostructure. To demonstrate the high power and broad tuning capabilities of the gain material, an extended cavity laser based on feedback via a diffraction grating is demonstrated. Tuning range of 154 nm, with an average output power of ~10 mW at 2.63 µm, corresponding to a peak power of ~100 mW, is demonstrated. For a more compact and integrable configuration, we demonstrate an extended cavity laser utilizing silicon photonics resonators, where the feedback and tuning is obtained via Vernier effect between two microring resonators. Here, a tuning range of ~70 nm, with an average output power of ~1 mW at 2.55 µm, corresponding to a peak power of ~10 mW, are demonstrated.

**Keywords**: tunable lasers, mid-IR laser, silicon photonics, photonic integration, extended cavity diode lasers

## 1. INTRODUCTION

The development of a light source for gas sensing in the wavelength region of 2-3.5 µm has captured increasing attention, because many important environmental gases, like $H_2S$, $C_2H_4$, $CH_4$, CO, $CO_2$, $N_2O$, and $H_2O$, have strong absorption in this wavelength region [1]. Tunable extended cavity lasers, which combine a semiconductor gain chip and an external tuning mechanism, are attractive for gas sensing and spectroscopy applications, since they are able to achieve wide tunability and narrow linewidth simultaneously. In contrast, monolithic diode lasers often have to make a compromise between these two characteristics.

Hybrid integrated III-V/SOI lasers are able to achieve continuous tuning and narrow linewidth in a compact and cost-effective architecture, making them optimal for gas sensing and spectroscopy applications. However, so far such integrated lasers have been limited to around 2.35 µm wavelength, exhibiting mW-level peak powers near room temperature (RT) operation [2]. To address a wider range of environmental gases there is a need to extend the wavelength range towards 3 µm, ideally using gain elements based on GaSb-based type-I quantum well (QW) heterostructures. However, non-radiative recombination processes limit the output power of such sources, especially at wavelengths beyond 2.3 µm. For example, state-of-the-art superluminescent diodes (SLDs) at 2 µm exhibit continuous wave (CW) output powers as high as 150 mW at RT [3], while SLDs at 2.55 µm require pulsed operation, and exhibit only mW-level average output power [4].

Here, we demonstrate two extended cavity laser configurations, one utilizing a diffraction grating for feedback and tuning (Littrow laser), and one utilizing a thermally tunable silicon reflector chip, exploiting the Vernier effect between two microring resonators (MRRs) (Vernier laser). In both lasers, the gain is provided by a GaSb-based single-transverse-mode reflective semiconductor amplifier (RSOA) chip with a wide gain peak around 2.6 µm.

## 2. GAIN CHIP AND CAVITY CONFIGURATIONS

The epitaxial structure of the RSOA chip was similar to the SLDs we have reported earlier [4]. The RSOA employed a "J-shape" ridge waveguide (RWG), where the front facet is tilted at 7° to reduce back reflections, and the rear facet is kept straight to provide maximum reflection. The bending radius of the waveguide was large enough to lead to negligible bending losses. The RSOA chip was mounted p-side up in the Littrow laser, and p-side down in the Vernier laser. The front facet had an anti-reflection coating (ARC) to maximize output coupling, while the rear facet was either as-cleaved (p-side up chip) or had an $Al_2O_3$ protective layer (p-side down chip), providing ~30% reflection in both cases. In order to minimize the heating effects, the chips were driven in pulsed operation with a pulse width of 1 µs, and a duty cycle of 10% at 20°C. The average output power of the chips as a function of injection current amplitude is shown in Fig. 1 (a), and the amplified spontaneous emission (ASE) spectrum is shown in Fig. 1 (b).

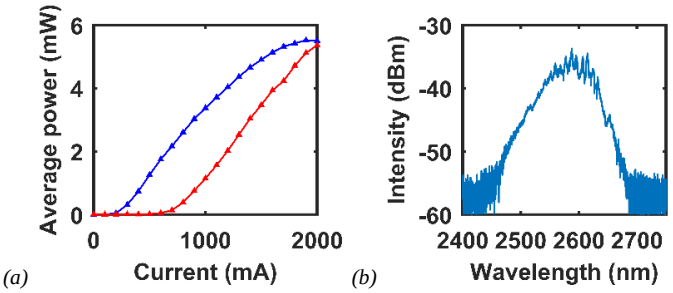



*Figure 1. (a) Average power as a function of injection current pulse amplitude for the p-up chip (red), and the p-down chip (blue), and (b) the ASE spectrum of the RSOA chips.*

Fig. 2 shows a schematic of the Littrow laser. The front facet of the RSOA is coupled with a lens to an external diffraction grating, which provides feedback at the first diffraction wavelength. Tunability was achieved by rotating the grating with a linear motor. The output signal was gathered from the rear facet of the RSOA with a multimode fiber.

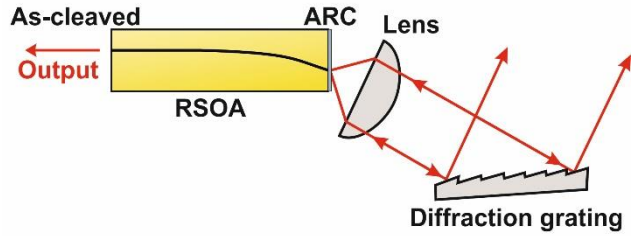



*Figure 2. Schematic of the Littrow laser cavity.*

Fig. 3 shows a schematic of the Vernier laser. The RSOA was edge-coupled to the SiPh chip, which had an ARC on both facets to minimize parasitic reflections. The SiPh chip consisted of two MRRs (MRR1 and MRR2) with slightly different free spectral ranges (FSRs), which leads to Vernier effect, where only certain wavelengths are transmitted strongly, while other wavelengths are suppressed (spaced by a FSR of ~42 nm). Wavelength tuning is achieved with two resistive heaters (heater 1 and heater 2) that were integrated next to the MRRs. By applying voltage to the heaters, the temperature change inflicts a change of the effective refractive index of the MRRs, which moves the location of the reflected peaks. Because the SiPh chip was originally designed to be used as the out-coupler, it has a 72:28 multimode interference (MMI) coupler at the output waveguide, which transmits 28% of the Vernier signal, and reflects 72% back to the RSOA.

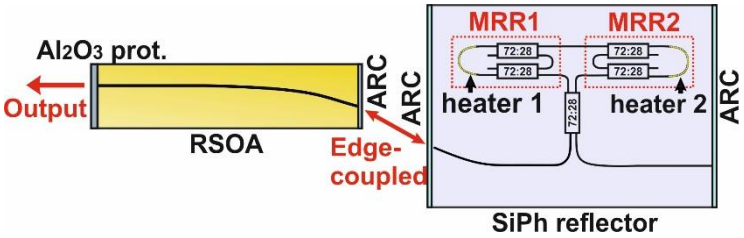



*Figure 3. Schematic of the Vernier laser cavity.*

## 3. MEASUREMENT RESULTS

The Littrow laser was driven with 700 mA pulses, and the emission wavelength was measured with a Fourier transform infrared (FTIR) spectrometer, while the grating was scanned with the linear motor. The emission wavelength as a function of linear motor position is shown in Fig. 4. The laser was tunable from 2513 nm to 2667 nm, corresponding to a tuning range of 154 nm. The full width at half maximum of the spectra were <0.2 nm, and the side-mode suppression ratio was >20 dB (both limited by the FTIR) over the whole scanning range. By driving the laser up to 1500 mA injection current, an average output power of ~10 mW was measured at 2628 nm. This corresponds to a peak power of ~100 mW.

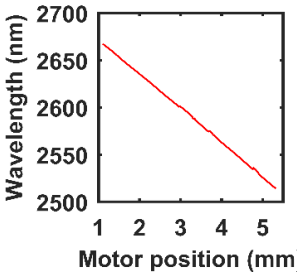



*Figure 4. Emission wavelength of the Littrow laser as a function of the position of the linear motor.*

The average output power of the Vernier laser at 2.55 µm as a function of injection current pulse amplitude is shown in Fig. 5 (a). The laser reaches an average power of ~1 mW, corresponding to ~10 mW of peak power. This is the highest power reported for hybrid lasers in the 2.5-2.7 µm wavelength range. The Vernier laser was then driven with 2000 mA pulses, and the emission wavelength was measured as a function of power driven to heaters 1 and 2. The result is shown in Fig. 5 (b). The laser is able to attain almost all wavelengths between 2550 nm and 2620 nm, corresponding to a tuning range of ~70 nm. This is limited by the FSR of the Vernier reflector, which is much smaller than the gain bandwidth of the RSOA. In addition, the laser exhibits fairly strong side maxima, which is evident in the emission spectrum shown in Fig. 5 (c). This is related to the fact that the reflectance peaks adjacent to the maximum reflectance have too high reflectivity.

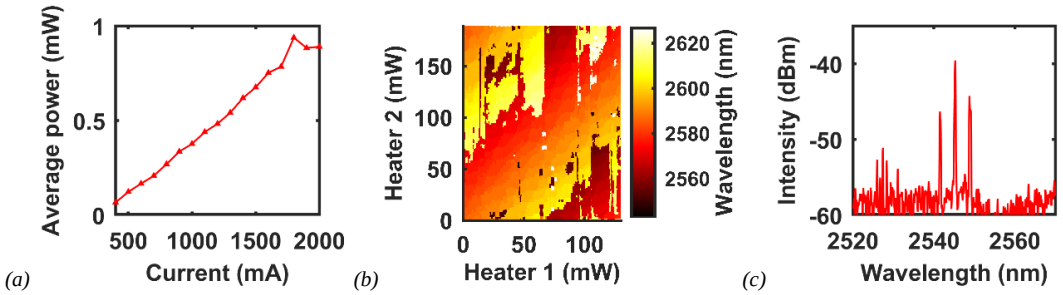



*Figure 4. (a) Average power at 2.55 µm as a function of injection current pulse amplitude, (b) the emission wavelength as a function of power applied to the heaters, and (c) the emission spectrum of the Vernier laser at 2.55 µm.*

## 4. CONCLUSIONS

We have demonstrated two tunable GaSb-based extended cavity lasers in the 2.5-2.7 µm wavelength region. The Littrow laser showed a wide tuning range of 154 nm, and a high average output power of ~10 mW (100 mW peak power), while the Vernier laser showed a tuning range of ~70 nm, and an average power of 1 mW (10 mW peak power). In future, we will test SiPh chips with 100% reflectance, lower losses, wider FSR, and higher spectral purity, in an effort to suppress the side modes, as well as increase the tuning range and the output power of the Vernier laser.

## ACKNOWLEDGEMENTS

Authors wish to thank M.Sc. Jarno Reuna for preparation of AR/HR coatings, and Ms. Mariia Bister for fabrication of the devices. S.-P. Ojanen would like to thank Vaisala Oyj for funding of the Ph. D. program. The research was funded by EU H2020 project MIREGAS (Grant Agreement 644192), and Business Finland project RAPSI (decision 1613/31/2018). The work is part of Academy of Finland flagship program PREIN (decision 320168).

## REFERENCES

[1] I. E. Gordon, *et al.*: The HITRAN2016 molecular spectroscopic database, *J. Quant. Spectrosc. Radiat. Transfer*, vol. 203(Supplement C), pp. 3-69, Dec. 2017.

[2] R. Wang, *et al.*: Widely tunable 2.3 µm III-V-on-silicon Vernier lasers for broadband spectroscopic sensing, *Photon. Res.*, vol. 6, pp. 858-866, Aug. 2018.

[3] N. Zia, *et al.*: High-power single mode GaSb-based 2 µm superluminescent diode with double-pass gain, *Appl. Phys. Lett.*, vol. 115, pp. 231106, Dec. 2019.

[4] N. Zia, *et al.*: GaSb superluminescent diodes with broadband emission at 2.55 µm, *Appl. Phys. Lett.*, vol. 112, pp. 051106, Jan. 2018.

# Dispersion Trimming for Mid-Infrared Supercontinuum Generation in Silicon-Germanium on Silicon Waveguides

*(Student paper)*

**Alberto Della Torre[1], Milan Sinobad[1,2], Rémi Armand[1], Barry Luther-Davies[3], Pan Ma[3], Stephen Madden[3], Sukanta Debbarma[3], Khu Vu[3], David J. Moss[4], Arnan Mitchell[2], Jean-Michel Hartmann[5], Jean-Marc Fedeli[5], Christelle Monat[1], Christian Grillet[1]**

[1] Université de Lyon, Institut des Nanotechnologies de Lyon (INL), 69131 Ecully, France
[2] School of Engineering, RMIT University, Melbourne, VIC 3001, Australia
[3] Laser Physics Center, Australian National University, Canberra, ACT 0100, Australia
[4] Centre for Microphotonics, Swinburne University of Technology, Hawthorn, VIC 3122, Australia
[5] Université Grenoble Alpes, CEA-Leti, 38054 Grenoble Cedex 9, France
*e-mail: alberto.della-torre@ec-lyon.fr*

## ABSTRACT

We report octave spanning mid-infrared supercontinuum generation in a highly nonlinear silicon germanium-on-silicon ridge waveguide. We show that, by adding a chalcogenide cladding, it is possible to trim *a posteriori* the waveguide's dispersion profile which, in turn, governs the properties of the generated supercontinuum. In particular, we experimentally show that a shift from anomalous to normal dispersion takes place when a 1.26 μm thick cladding layer of $Ge_{11.5}As_{24}Se_{64.5}$ is added. Finally, we show that the group velocity dispersion of the waveguide can be precisely controlled by changing the thickness of the cladding layer. This demonstrates that the heterogeneous integration of materials can be used as a post-processing technique to precisely control the supercontinuum properties.

**Keywords**: Supercontinuum generation; nonlinear optics; integrated optics; mid-infrared; dispersion trimming**.**

## 1. INTRODUCTION

On-chip mid-infrared (mid-IR, between 3 μm and 20 μm) supercontinuum (SC) generation is a technological challenge that is promising to have a strong impact in many different fields such as bio imaging, environmental sensors and security [1-5]. The prediction of great nonlinear properties, wide transparency window from 3 to 15 μm and CMOS compatibility of germanium have attracted a growing interest toward germanium-based platforms [6,7]. An octave spanning supercontinuum generation up to 8.5 μm has been already demonstrated by our group in a SiGe on Si waveguide [8-10]. The bandwidth and the coherence properties of the generated SC are mainly determined by the waveguide's dispersion profile. In general, the dispersive properties are set at the design stage and cannot be adjusted once the device has been fabricated. However, fabrication inaccuracies, surface roughness, surface contamination and the presence of defects may lead to a deviation from the targeted dispersion profile. Therefore, post-process mechanisms to post-trim the waveguide dispersion depending on the actual structure produced by fabrication are of great interest.

Here we demonstrate mid-IR supercontinuum generation in a SiGe and in a hybrid chalcogenide/SiGe waveguide with shifted dispersion. We show that it is possible to fine tune the dispersion profile *a posteriori* by changing the chalcogenide cladding thickness, introducing a simple post-processing tool to control the supercontinuum dynamics and its properties.

## 2. SUPERCONTINUUM GENERATION AND DISPERSION TRIMMING

### 2.1 Supercontinuum generation

A 7 cm long 3.75 x 2.7 $\mu m^2$ cross-section $Si_{0.6}Ge_{0.4}$/Si waveguide (Fig. 1a) was coated with a 1.26 μm thick layer of chalcogenide $Ge_{11.5}As_{24}Se_{64.5}$ (Fig. 1b). Numerical simulations show that the group velocity dispersion shifts from anomalous (air clad, Fig. 2a top) to normal (chalcogenide clad, Fig. 2b top) when the coating layer is added. The waveguide, operating in TE single mode, was pumped before and after the deposition of the chalcogenide layer with ~200 fs pulses at 4 μm (air clad) and 4.15 μm (chalcogenide clad) delivered from a MIROPA-fs optical parametric amplifier with 63 MHz repetition rate. Fig. 2a (bottom) and 2b (bottom) shows the experimental (and theoretical) SC generated out of the air clad and chalcogenide clad waveguide respectively. In the former case the resulting SC, spanning from 2.63 up to 6.18 μm, shows asymmetric profile and uneven amplitude across the spectrum, both typical of SC generation in the anomalous dispersion regime. In the latter case a narrower and smoother spectrum (with a -30 dB bandwidth extending from 3.1 to 5.5 μm), typical of SC generation in normal

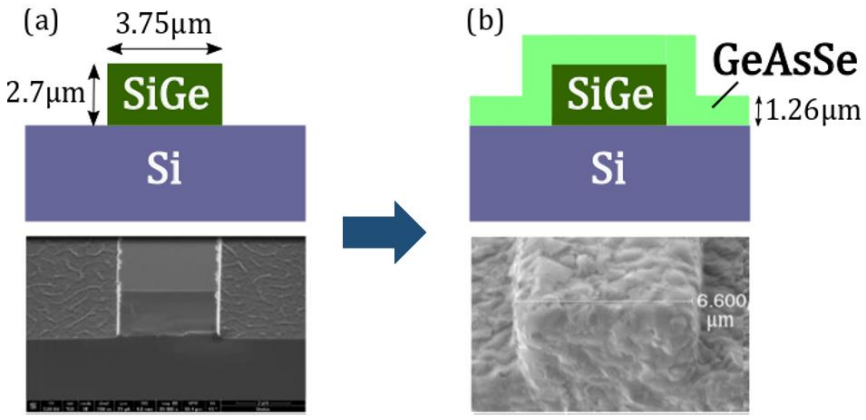



*Figure 1. Schematic (top) and Scanning Electron Microscope image (bottom) of the air clad (a) and the chalcogenide clad (b) waveguide.*

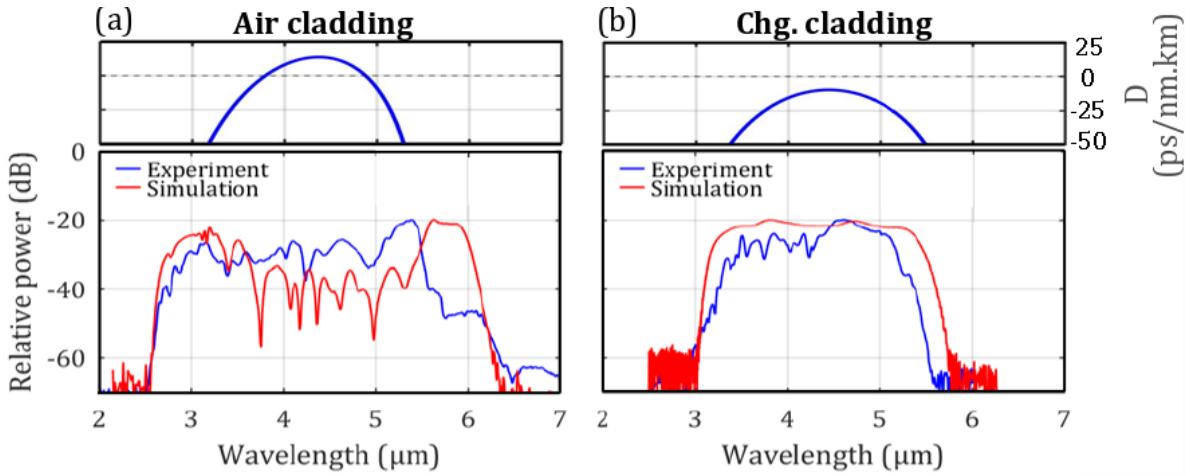



*Figure 2. Calculated group velocity dispersion for air clad (a top) and chalcogenide clad (b top) waveguide with the same 3.75 x 2.7 µm2 core cross-section. Experimental (blue) and simulated (red) spectra out of the air cladded (a bottom) and chalcogenide cladded (b bottom) waveguide. The waveguides were pumped by 200 fs pulses at 4 and 4.15 µm respectively with 2.35 kW coupled peak power.*

dispersion regime, was obtained. The SC generation process was simulated by numerically solving the nonlinear Schrödinger equation, obtaining a good agreement with experiments.

### 2.2 Dispersion trimming

We have experimentally demonstrated that the addition of a chalcogenide layer on top of a SiGe/Si waveguide leads to a change in the dispersion, shifting, in our particular example, from an anomalous to normal dispersion. In order to clarify the impact of the chalcogenide thickness on the dispersion GVD profile, we have numerically calculated the dispersion curve for four different thicknesses, from 0.25 to 1.26 µm (Fig. 3). As the chalcogenide thickness increases, the overall dispersion gradually decreases, eventually reaching normal values for thicknesses higher than 500 nm. Moreover, the dispersion profiles converge as the thickness approaches 1 µm, in agreement with the confinement of the mode in the waveguide core. Along with the dispersion shift, a variation of the zero dispersion wavelengths and a flattening of the profile take place. As a flat profile of the dispersion is generally targeted for SC generation, both in the anomalous and in the normal dispersion regime, the possibility of controlling the dispersion profile and the position of the zero-dispersion wavelengths by simply changing the thickness of the chalcogenide layer (with a reasonable resolution of around 100 nm) is a convenient post-process dispersion engineering tool.

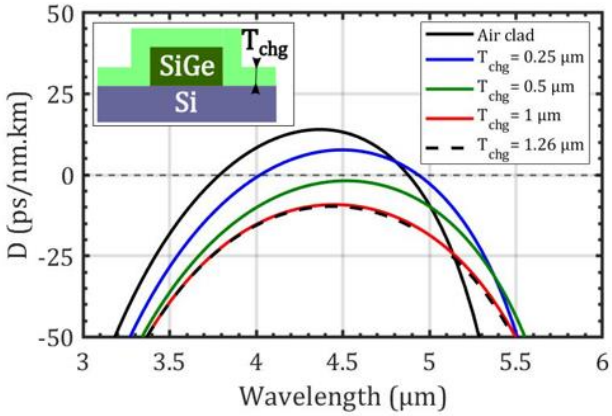



*Figure 3. Calculated group velocity dispersion for different thicknesses of the chalcogenide layer. The dashed black line indicates the zero dispersion. The inset show a schematic of the waveguide (adapted from [11]).*

## 3. CONCLUSIONS

In summary, we report the addition of a top chalcogenide layer as a simple post-processing technique to fine tune the dispersion profile of a nonlinear SiGe on Si waveguide for integrated SC generation. We experimentally show that, by adding a chalcogenide top layer to a ridge waveguide, anomalous-to-normal dispersion shift takes place and we numerically study the impact of the chalcogenide layer thickness on the group velocity dispersion.

## ACKNOWLEDGEMENTS

We acknowledge the support of the International Associated Laboratory in Photonics between France and Australia (LIA ALPhFA), the Agence Nationale de la Recherche (MIRSICOMB, ANR-17-CE24-0028) and the European Research Council (ERC) under the European Union's Horizon 2020 program (GRAPHICS 648546).

## REFERENCES

[1] R. Soref: Mid-infrared photonics in silicon and germanium, *Nature Photonics*, vol. 4. pp. 495-497, 2010.

[2] N. K. Hon, R. Soref and B. Jalali: The third-order nonlinear optical coefficients of Si, Ge, and $Si_{1-x}Ge_x$ in the midwave and longwave infrared, *J. Appl. Phys.*, vol. 110. pp. 011301, 2011.

[3] G. Z. Mashanovich, *et al.*: Germanium Mid-Infrared Photonic Devices, *J. Light. Technol.*, vol. 35. pp. 624–630, 2017.

[4] K. Hammani, *et al.*: Towards nonlinear conversion from mid- to near-infrared wavelengths using Silicon Germanium waveguides, *Opt. Lett.*, vol. 40. pp. 4118-4121, 2015.

[5] M. A. Ettabib, *et al.*: Broadband telecom to mid-infrared supercontinuum generation in a dispersion-engineered Silicon Germanium waveguide, *Opt. Lett.*, vol. 40. pp. 4118-4121, 2015.

[6] J. M. Ramirez, *et al.*: Low-loss Ge-rich $Si_{0.2}Ge_{0.8}$ waveguides for mid-infrared photonics, *Opt. Lett.*, vol. 42. pp. 105-108, 2017.

[7] J. M. Ramirez, *et al.*: Graded SiGe waveguides with broadband low-loss propagation in the mid infrared, *Opt. Express*, vol. 26. pp. 870-877, 2018.

[8] L. Carletti, *et al.*: Nonlinear optical response of low loss silicon germanium waveguides in the mid-infrared, *Opt. Express*, vol. 23. pp. 8261-8271, 2015.

[9] L. Carletti, *et al.*: Mid-infrared nonlinear optical response of Si-Ge waveguides with ultra-short optical pulses, *Opt. Express*, vol. 23. pp. 32202-32214, 2015.

[10] M. Sinobad, *et al.*: Mid-infrared octave spanning supercontinuum generation to 8.5μm in silicon-germanium waveguides, *Optica*, vol. 5. pp. 360, 2018.

[11] M. Sinobad, *et al.*: Dispersion trimming for mid-infrared supercontinuum generation in a hybrid chalcogenide/silicon-germanium waveguide, *J. Opt. Soc. Am. B*, vol. 36. pp. 98–104, 2019.

# Optical modulation from 5 to 11 µm wavelength range using Ge-rich graded SiGe waveguides

*Student paper*

**Miguel Montesinos-Ballester[1], Qiankun Liu[1], Carlos Alonso-Ramos[1], Xavier Le Roux[1], Lucas Deniel[1], David Bouville[1], Jacopo Frigerio[2], Andrea Ballabio[2], Laurent Vivien[1], Giovanni Isella[2], and Delphine Marris-Morini[1]**

[1] Université Paris-Saclay, Univ. Paris-Sud, CNRS, Centre de Nanosciences et de Nanotechnologies, 91120, Palaiseau, France

[2] L-NESS, Dipartimento di Fisica, Politecnico di Milano, Polo di Como, Via Anzani 42, 22100 Como, Italy

*e-mail: miguel.montesinos@u-psud.fr*

## ABSTRACT

The mid-infrared (mid-IR) wavelength range host unique vibrational and rotational resonances of a large number of molecules. The spectrum fingerprint can be used to detect the molecular compositions in a non-intrusive way. To analyse simultaneously as many molecules as possible in the same device, wide operational bandwidth is a must. This work reports the first demonstration of optical modulation in mid-IR photonic circuit reaching wavelengths larger than 8 µm, showing wide optical modulation from 5.5 to 11 µm wavelength range. This experimental demonstration confirms current free-carrier absorption theoretical models, paving the way towards efficient, high-performance, electrically-driven integrated optical modulators. Those devices are expected to have a strong impact in many applications, as they can be used to greatly enhance the detection sensitivity by synchronous detection.

**Keywords**: mid-infrared, modulation, Silicon, Germanium, photonic integrated circuits

## 1. INTRODUCTION

A large variety of molecules, such as alkanes or greenhouse gasses, presents vibrational and rotational resonances in the mid-infrared (mid-IR) wavelength range, i.e. from 2 to 20 µm. The fingerprint brings the possibility to detect in a non-intrusive way the molecular composition, which has a substantial interest for a broad variety of high impact applications [1-3]. Photonic integrated circuits (PICs) operating in such wavelength range are thus expected to have a major impact, as they provide great advantages in terms of compactness, robustness, reliability and cost.

Among the different proposed solutions to develop a mid-IR platform [4-9], Germanium (Ge)-based circuits are a promising candidate, as it performs a wide transparency window (up to 15 µm wavelength) and is compatible with large-scale, high-performance CMOS fabrication processes [10-15]. The operational bandwidth of the developed platform determines the amount of substances that can be simultaneously detected in a single device. In that regard, a Ge-rich graded SiGe platform operating in a wide mid-IR range has been proposed. Even though a whole set of passive devices have already been developed [16-19], active devices still must be achieved. As a first step, all-optical modulation is reported from 5 to 11 µm wavelength. This experimental result confirms current theoretical models [20], which is essential for the design of electrically-driven integrated optical modulators.

## 2. RESULTS

### 2.1 Fabrication

The Ge-rich graded SiGe platform under study has been previously reported in [15]. It relies on a 11 µm-thick graded SiGe layer epitaxially grown on Si substrate, in which the Ge concentration linearly increases from 0 up to 79%, followed by a 2 µm-thick $Si_{0.2}Ge_{0.8}$ layer (Fig. 1). Low-energy plasma-enhanced chemical vapor deposition is used to grow the $Si_{1-x}Ge_x$ material. This structure allows a smooth transition from pure Si to Ge-rich material while minimizing the threading dislocation density due to lattice mismatch. Since the refractive index increases linearly with the Ge content in the SiGe alloy, the mode is confined in the upper part of the epitaxial layer. A 1.5 cm-long rib waveguide has been fabricated with an etching depth of 3.8 µm and a width of 7 µm. To ensure low-loss butt-coupling in and out of the PIC, a 50 µm wide and 1 mm long waveguide is placed at the input/output sample facets, followed by 2 mm long linear transition to the 7µm wide waveguide.

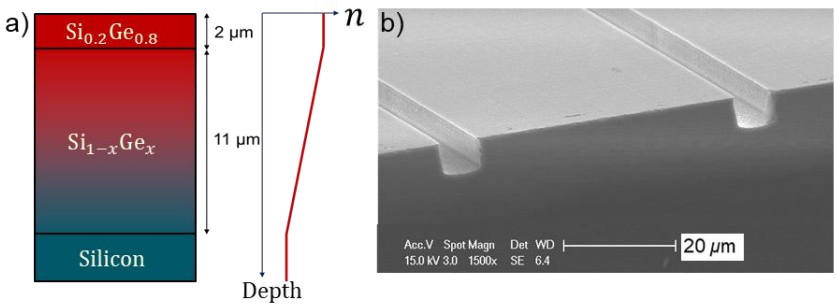



Figure 1. a) Graded-index platform scheme and representation of the refractive index (n) linear-increase as a function of the platform depth. b) SEM pictures of the sample facet in where the 50-µm-wide input (output) waveguide is shown

### 2.2 Optical modulation

To evaluate the effect of the free-carriers in the mid-IR beam absorption, a beam at 1.33 µm wavelength is coupled into the waveguide and modulated by a manual-actuating shutter. A mid-IR beam is also coupled into the sample at the same time, and collected in an external Mercury Cadmium Telluride detector. As the pump signal is absorbed in the waveguide, it generates free-carriers that are responsible for absorption of the mid-IR propagating mode, thus transferring the modulation from 1.33 µm to longer wavelengths in the mid-IR. This plasma dispersion effect is clearly seen in Fig. 2(a) at 11 µm wavelength. A modeling of the free carrier absorption for 3 different pump powers is carried out. A good agreement between experimental modulation depth (MD) and the theoretical modelling is shown in Fig. 2(b). This first experimental demonstration of optical modulation in a mid-IR PIC, carried out in long wave infrared (LWIR) regime (up to 11 µm), confirms theoretical free-carrier electro-absorption predictions [24].

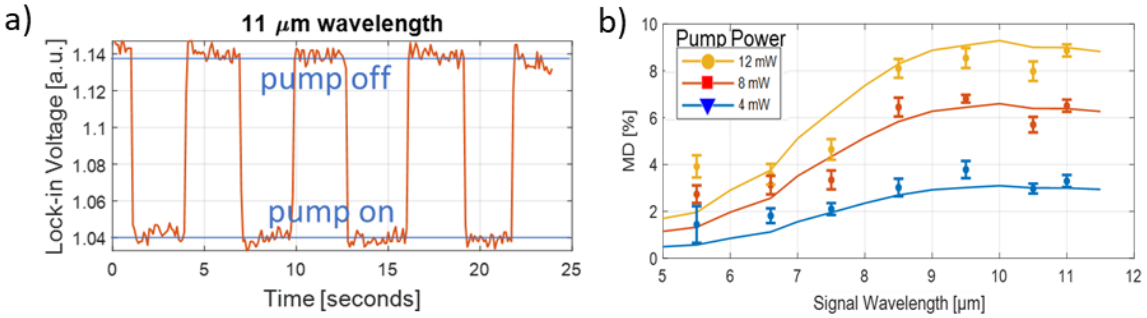



Figure 1. a) All-optical modulation at 11 µm wavelength is reported using a 12 mW-pump beam at 1.33 µm wavelength. The voltage at the lock-in amplifier, that is proportional to the mid-IR beam power is reported as a function of time, while the NIR pump is mechanically switched on or off using an external shutter. b) Modulation Depth (MD) as a function of the signal wavelength, for different NIR pump powers (wavelength of 1.33 µm). Experimental data (dots) show a good agreement with the modelling (solid lines). The error bars in the experimental data correspond to the variation of the measured modulation depth, when repeating the measurement 10 times.

## 3. CONCLUSIONS

We report the first experimental demonstration of optical modulation by plasma dispersion effect in the LWIR regime, up to 11 µm using Ge-rich SiGe waveguides. This results experimentally confirms current free-carrier absorption theoretical models, which is an important step towards the implementation of electrically-driven, high-efficient integrated mid-IR modulators. The development of such devices will have a high impact in many applications, as they can be used, for example, in synchronous detection systems, greatly enhancing the detection sensitivity. These results confirm the huge potential of Ge-based photonic circuits as a promising platform for the integration of mid-IR photonics functions, as it could benefit from low loss waveguides, compact photonics structures, together with the integration of active devices. The realization of complete functional systems in the MIR and LWIR paves the way for a plethora of applications, from mid-IR spectroscopy, sensing, to free-space telecommunications.

## ACKNOWLEDGEMENTS

This work was supported by the European Research Council (ERC) under the European Union's Horizon 2020 (No 639107 - INsPIRE). The fabrication of the device has been performed in the Platforme de Micro-Nano-

Technologie/C2N, which is partially funded by the "Conseil Général de l'Essonne". This work was partly supported by the french RENATECH network.

**REFERENCES**

[1] R. Soref: Mid-infrared photonics in silicon and germanium, *Nat. Photonics*, vol. 4. pp. 495–497, 2010.
[2] A. P. Michel, D. J. Miller, L. Tao, L. Stanton, M. A. Zondlo: Long-Path Quantum Cascade Laser-Based Sensor for Methane Measurements, *J. Atmos. Oceanic Technol*., vol. 33. pp. 2373-2384, 2016.
[3] Y. -C. Chang, *et al*.: Cocaine detection by a mid-infrared waveguide integrated with a microfluidic chip, *Lab Chip*, vol. 12. pp. 3020–3023, 2012.
[4] G. Z. Mashanovich, *et al*..: Low loss silicon waveguides for the mid-infrered, *Optics Express*, vol. 19. pp. 7112–7119, 2011.
[5] S. A. Miller, *et al*.: Low-loss silicon platform for broadband mid-infrared photonics, *Optica*, vol. 4. pp. 707–712, 2017.
[6] L. He, Y. Guo, *et al*.: Loss reduction of silicon-on-insulator waveguides for deep mid-infrared applications, *Opt. Lett.*, vol. 42. pp. 3454–3457, 2017.
[7] Z. Cheng, X. Chen, C. Y. Wong, K. Xu, H. K. Tsang: Mid-infrared suspended membrane waveguide and ring resonator on silicon-on-insulator, *IEEE Photonics J*., vol. 4. pp. 1510–1519, 2012.
[8] J. S. Penadés, *et al.*: Suspended silicon waveguides for long-wave infrared wavelengths, *Opt. Lett.*, vol. 43. pp. 795–798, 2018.
[9] T. Baehr-Jones, *et al*.: Silicon-on-sapphire integrated waveguides for the mid-infrared, *Opt. Express* 18. pp. 12127–12135, 2010.
[10] Y. C. Chang, V. Paeder, L. Hvozdara, J. M. Hartmann, H. P. Herzig: Low-loss germanium strip waveguides on silicon for the mid-infrared, *Opt. Lett*., vol. 37. pp. 2883–2885, 2012.
[11] M. Nedeljkovic, *et al.*: Germanium-on-silicon waveguides operating at mid-infrared wavelengths up to 8.5 µm, *Opt. Express,* vol. 25. pp. 27431, 2017.
[12] K. Gallacher, *et al.*: Low loss Ge-on-Si waveguides operating in the 8–14 µm atmospheric transmission window, *Opt. Express*, vol. 26. pp. 25667-2567, 2018.
[13] M. Brun, *et al.*: Low loss SiGe graded index waveguides for mid-IR applications, *Opt. Express,* vol. 22. pp. 508–518, 2014.
[14] M. Sinobad, *et al.*: Mid-infrared octave spanning supercontinuum generation to 8.5 µm in silicon-germanium waveguides, *Optica*, vol. 5, pp. 360-366, 2018.
[15] J.-M. Ramirez, *et al.:* Graded SiGe waveguides with broadband low-loss propagation in the mid infrared, *Opt. Express*, vol. 26. pp. 870–877, 2018.
[16] Q. Liu, *et al*.: On-chip Bragg grating waveguides and Fabry-Perot resonators for long-wave infrared operation up to 8.4 µm, *Opt. Express*, vol. 26, pp. 34366-34372, 2018.
[17] J. M. Ramirez, *et al*.: Broadband integrated racetrack ring resonators for long-wave infrared photonics, *Opt. Lett*., vol. 44, pp. 407-410, 2019.
[18] V. Vakarin, *et al*.: Ultra-wideband Ge-rich silicon germanium mid-infrared polarization rotator with mode hybridization flattening, *Opt. Express*, vol. 27. pp. 9838, 2019.
[19] M. Montesinos-Ballster, *et al.:* On-chip Fourier-transform spectrometer based on spatial heterodyning tuned by thermo-optic effect, *Sci. Rep.*, vol. 9. pp. 14633, 2019.
[20] M. Nedeljkovic, R. Soref, G. Z. Mashanovich: Predictions of Free-Carrier Electroabsorption and Electrorefraction in Germanium, *IEEE Photon. J.*, vol. 7. pp. 1-14, 2015.

# Frequency comb and microwave generation with a full phononic bandgap 1D optomechanical crystal cavity

*(Student Paper)*

L. Mercadé [1], L. L. Martín [1,2], A. Griol [1], D. Navarro-Urrios [2], A. Martínez [1]
[1]*Nanophotonics Technology Center, Universitat Politècnica de València, Camino de Vera s/n, 46022 Valencia, Spain*
[2]*Departamento de Física, Facultad de Ciencias, Universidad de la Laguna*
[3] *MIND-IN2UB, Departament d'Enginyeria Electrònica i Biomèdica, Facultat de Física, Universitat de Barcelona, Martí i Franquès 1, 08028 Barcelona, Spain*
*e-mail: laumermo@ntc.upv.es*

## ABSTRACT

In this work we show that a silicon optomechanical crystal cavity can be used as an optoelectronic oscillator when driven to the phonon lasing condition with a blue-detuned laser. The optomechanical cavity is designed to have a breathing like mode vibrating at $\Omega_m/2\pi$ =3.897 GHz in a full phononic bandgap. Our measurements show that the first harmonic displays a phase noise of -100 dBc/Hz at 100 kHz. Stronger blue-detuned driving leads eventually to the formation of an optomechanical frequency comb, with lines spaced by the mechanical frequency. The measured phase noise grows up with the harmonic number, as in classical harmonic mixing. We present real-time measurements of the comb waveform and show that it can be adjusted to a theoretical model recently presented. Our results suggest that silicon optomechanical cavities can play a role in integrated microwave photonics.

**Keywords**: optomechanical crystal cavity, phononic bandgap , optoelectronic oscillator, frequency comb.

## 1 INTRODUCTION

Cavity optomechanics studies the interaction between light and sound waves simultaneously confined in a cavity [1], [2]. In an optomechanical cavity (OMC), confined mechanical waves can coherently modulate an optical signal at MHz and even GHz frequencies via optomechanical interaction. Thus, OMCs could become relevant in microwave photonics, a discipline addressing the manipulation of microwave signals in the optical domain [3]. Furthermore, since OMCs are nonlinear elements, multiple harmonics of the fundamental mechanical vibrations can be overimposed on the optical signal [4], a phenomenon that has been interpreted theoretically as an optomechanical frequency comb (OFC) [5].

Here, we first demonstrate an OMC on a silicon nanobeam having a breathing-like mechanical mode vibrating close to 4 GHz with a high $g_0$ and placed in a full phononic bandgap [6]. Then, via blue-detuned laser pumping we demonstrate phonon lasing of this fundamental mechanical mode. Stronger pumping of the cavity leads to the observation of a series of harmonics forming an OFC in both the optical and RF spectrum. We measure the phase noise of the generated microwave tone and show that the OMC can be used as an optoelectronic oscillator. In addition, the phase noise of the harmonics degrades with the harmonic number as in standard harmonic mixing. We also perform real-time measurements of the temporal traces using a GHz-bandwidth oscilloscope and show that they are in good agreement with a theoretical model of an OFC. Our work paves the way for the use of silicon OMCs as ultracompact and ultraweight elements for microwave photonics.

## 2 OPTOMECHANICAL FREQUENCY COMB

The optomechanical cavity that we exploit here consist in a suspended silicon nanobeam with one-dimensional (1D) periodicity. The key idea is to have OM mirrors (that prevent leakage of both photons and phonons) on each nanobeam side whilst optical and mechanical resonant modes are confined in the central region, also having a good overlap between them. Our structure results of an optical mode at $\lambda_r$ =(1522.3±0.3) nm with an optical quality factor of $Q_o = 5 \times 10^3$, presented in Fig. 1(a), and a mechanical mode at $\Omega_m/2\pi$ =3.897 GHz with an optomechanical coupling rate of $g_0/2\pi = (660 \pm 70)$ kHz, depicted in Fig. 1(b). In addition, we have design our structure in order to have a full phononic bandgap in order to reduce the phonon leakage. Because of fabrication imperfections, the fabricated structures tend to be a bit different from the nominal ones. Thus, in order to ensure that our mechanical mode is confined in this full phononic bandgap, we simulated, in Fig. 1(c), the phononic band diagram from the profile extracted from a Scanning Electron Microscopy (SEM) image, which is shown (see Fig. 1(d)). Here, we can see that we have this phononic bandgap were our experimental mechanical mode lies.

The mechanical mode can be driven to the phonon lasing regime under proper conditions (see Section 3). When driving the OMC with a blue-detuned laser with respect to the optical resonance at even higher power,

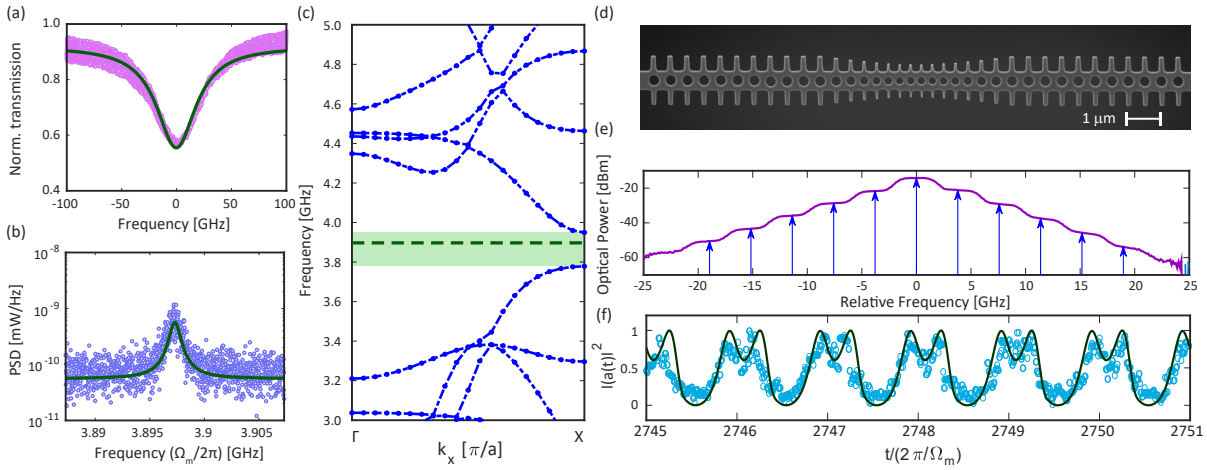



Figure 1. (a) Optical experimental resonance trace (purple) and Lorenztian fit (dark line). (b) Power spectral density of the mechanical resonance confined in the total bandgap. (c) Phononic band diagram for the real profile mirror unit cell extracted from the SEM image, including the experimental measured frequency of the mechanical mode (dashed line). (d) SEM image of the fabricated OM cavity. (e) Recorded optical spectrum in purple showing a set of peaks corresponding to different harmonics represented in blue at the expected position. (f) Comparison of the experimental (dots) and the theoretical (solid line) temporal OM-generated OFC traces.

higher-order harmonics can be observed in the detected signal. This closely resembles an optical frequency comb (OFC) of OM nature, which has been recently analyzed theoretically in [5]. We measured up to the fifth harmonic, which can be seen in the optical spectrum of the generated OFC in Fig. 1(e). In addition, we can also study the optical traces of the generated OM comb in the time domain where the dynamics generation can be described by a set of coupled equations describing the time evolution of the optical and mechanical mode amplitude [5]. The comparison between the acquired experimental traces and the theoretical model are presented in Fig. 1(f), showing a good agreement.

## 3 OPTOELECTRONIC OSCILLATOR

High-quality microwave sources, which are required for a number of applications, are typically made by applying frequency multiplication to an electronic source. This requires a cascade of frequency-doubling stages, which means that the power of the final signal is greatly reduced. Recently, different techniques to produce microwave tones via optical means have been proposed resulting in optoelectronic oscillators (OEO). Amongst the different techniques to build an OEO, we propose an OEO obtained from an OM cavity when pumped with a blue-detuned laser source. We made this experiment with the cavity proposed in the last section and we measured the resulting noise figure, as in Fig. 2(a), where we reach the comb regime. For the first harmonic shown in Fig. 2(b), the noise figure becomes as low as (-100±1) dBc/Hz at 100 kHz, which is a remarkable good value for an OEO oscillating at GHz frequencies. This performance is on par with some commercial mid-range devices, such as the Agilent N5183AMXG that displays a phase noise of -102 dBc/Hz at 100 kHz offset for a 10 GHz frequency [7]. We have also measured the phase noise of the different harmonics, as shown in Fig. 2(c). An RF spectra showing the first five harmonics is also depicted in Fig. 2(d). In principle, the harmonic mixing process will result in an added phase noise of $20 \times log(m)$ with respect to that of the first harmonic. It can be seen that the previous rule is well satisfied in our device.

## 4 CONCLUSIONS

In summary, we have demonstrated a new silicon-chip OMC implemented with a large OM coupling rate for a GHz mode within a full phononic bandgap. This OM cavity can perform as an ultracompact OEO at a microwave frequency around 4 GHz. Notice that our device is a free-running or open-loop OEO: the device generates an RF tone and there is no any feedback loop to improve the frequency stabilization. Operation at cryogenic temperatures would improve the phase noise [8] as a result of the enhancement of the mechanical Q factor because of the full phononic bandgap. In addition, the preliminary demonstration of the OFC paves the way towards synthesis of microwave signals beyond the generation of pure cw tones. The main advantages of the OMC approach for microwave signal processing are its extreme compactness and low weight, highly desirable in space and satellite applications, and its compatibility with silicon electronics and photonics technology.

## ACKNOWLEDGMENT

The authors thank the funding support by the European Commission (PHENOMEN H2020-EU-713450); Programa de Ayudas de Investigación y Desarrolo (PAID-01-16) de la Universitat Politècnica de València;

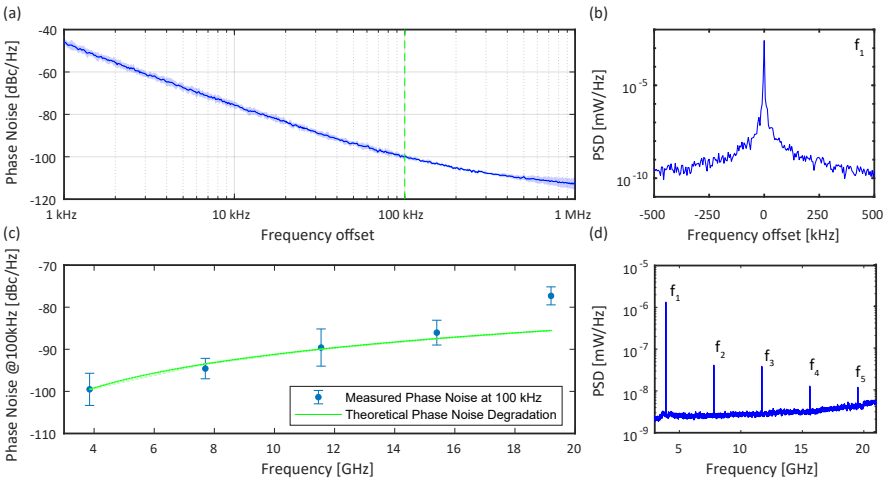



Figure 2. (a) Mean phase noise of the generated microwave tones in blue and its standard deviation represented by the shadowed area. The noise figure at 100 kHz is (-100±1) dBc/Hz for the first harmonic. (b) Linear scale of the first harmonic centered at 3.87 GHz. (c) Phase noise of the different harmonics of the OFC with the theoretical phase noise degradation of $20 \times log(m)$ with respect to that of the 1st harmonic. (d) RF spectra of the generated OFC showing the different obtained harmonics.

Ministerio de Ciencia, Innovación y Universidades (PGC2018-094490-B-C22, PRX18/00126) and Generalitat Valenciana (PROMETEO/2019/123, PPC /2018 /002, IDIFEDER/2018/033)

## REFERENCES

[1] Y. Pennec, V. Laude, N. Papanikolaou, B. Djafari-Rouhani, M. Oudich, S. El Jallal, J. C. Beugnot, J. M. Escalante, and A. Martínez, "Modeling light-sound interaction in nanoscale cavities and waveguides," Nanophotonics, vol. 3, pp. 413–440, 2014.

[2] M. Aspelmeyer, T. J. Kippenberg and F. Marquardt, "Cavity optomechanics," Rev. Mod. Phys., vol. 86, pp. 1391–1452, 2014.

[3] J. Capmany and D. Novak, "Microwave photonics combines two worlds," Nat. Photonics, vol. 1, pp. 319–330, 2007.

[4] M. Hossein-Zadeh and K. J. Vahala, "Photonic RF Down-Converter Based on Optomechanical Oscillation," IEEE Photonics Tech. L., vol. 20, pp. 234-236, 2008.

[5] M. A. Miri, G. D'Aguanno and A. Alu, "Optomechanical frequency combs," New J. Phys., vol. 20, 043013, 2018.

[6] L. Mercadé, L. L. Martín, A. Griol, D. Navarro-Urrios and A. Martinez, "Microwave generation and frequency comb in a silicon optomechanical cavity with a full phononic bandgap," arXiv:1912.06692 [physics.optics]

[7] https://www.keysight.com/us/en/assets/7018-08250/data-sheets/5989-7572.pdf

[8] M. Hossein-Zadeh and K. J. Vahala, "An Optomechanical Oscillator on a Silicon Chip," IEEE J. Sel. Top. Quant., vol. 16, pp. 276–287, 2010.

# Silicon-germanium p-i-n photodiodes with double heterojunction: high-speed operation at 10 Gbps and beyond

**Daniel Benedikovic[1], Léopold Virot[2], Guy Aubin[1], Jean-Michel Hartmann[2], Farah Amar[1], Bertrand Szelag[2], Xavier Le Roux[1], Carlos Alonso-Ramos[1], Paul Crozat[1], Éric Cassan[1], Delphine Marris-Morini[1], Charles Baudot[3], Frédéric Boeuf[3], Jean-Marc Fédéli[2], Christophe Kopp[2], and Laurent Vivien[1]**

[1]Universite Paris-Saclay, CNRS, Centre de Nanosciences et de Nanotechnologies, 91120, Palaiseau, France

[2]University Grenoble, Alpes and CEA, LETI, Grenoble, France

[3]STMicroelectronics, Silicon Technology Development, Crolles, France

*e-mail: daniel.benedikovic@c2n.upsaclay.fr*

**ABSTRACT**

We present recent results on high-speed waveguide p-i-n photodetectors with lateral hetero-structured Silicon-Germanium-Silicon (Si-Ge-Si) junctions monolithically integrated on Silicon-on-Insulator substrates. Optical photodetectors leverage a unique integration strategy, combining butt-waveguide-coupling and lateral Si-Ge-Si p-i-n hetero-junctions. Fabrication is then easier, more robust and fully compatible with available Si-foundry processes. Under a low-voltage operation, 1 µm wide devices have dark currents of at most 150 nA, high responsivity of 1.2 A/W, and -3dB cut-off frequency of 12 GHz. Furthermore, an errorless detection is experimentally achieved for a conventional 10 Gbps data rate, with power sensitivity down to -13.9 dBm with a bit-error-rate (BER) of $10^{-9}$. Moreover, under avalanche operation, a 0.8 µm wide p-i-n diode offers attractive improvements in opto-electrical performances. In particular, initial results show that device responsivity is enhanced from 0.42 A/W up to 2.79 A/W thanks to an avalanche multiplication gain of 6.7. The cut-off frequency remains larger than 17 GHz with a gain of 10.6, resulting in a gain-bandwidth product greater than 180 GHz. These promising results also yield error-free communication at $10^{-9}$ with 28 Gbps signal, providing power sensitivities down to -12.7 dBm at $10^{-9}$ BER. These results make hetero-structured p-i-n photodetectors appealing choice for high-bit-rate systems in integrated silicon nanophotonics.

**Keywords**: germanium photodiodes, silicon-on-insulator platform, high-speed optical communications

## 1. INTRODUCTION

Germanium (Ge) photodetectors (PDs) integrated on silicon (Si) waveguides are key devices in group-IV nanophotonics, including emerging areas such as sensing, interconnects, or communications, to name a few. Leveraging the maturity of Si-foundry processes and epitaxial Ge integration, group-IV PDs are presently well-mastered building blocks and their performances are rather good [1]. A large number of homo- [2-4] and hetero-junction [5-9] p-i-n devices have been proposed, fabricated, and demonstrated over the years. Si-Ge-Si p-i-n diodes benefit from a much better control over the intrinsic Ge region, a simpler and robust fabrication and improved opto-electrical performances compared to full-Ge PD architectures. Despite those promises, regular p-i-n diodes provide only a limited responsivity, suffer from a modest power sensitivity and require additional circuit electronics for use in transmission systems. As an alternative, avalanche photodiodes (APDs) with an internal multiplication gain can advantageously be used to meet the emerging demands for improved performances in Si nanophotonics [10-14]. Recently, different Si-Ge APD structures were designed and elaborated, tackling low-voltage operation at 10 Gbps [11-13] and 25 Gbps [14] bit rates, respectively.

In this work, we present recent results on waveguide-integrated p-i-n PDs with lateral Si-Ge-Si hetero-junctions operated under low-bias ("*p-i-n regime*") and high-bias ("*avalanche regime*") conditions, respectively. Cross-sectional schematics of the Si-Ge-Si PD investigated here are shown in Fig. 1(a). PDs were fabricated within CEA LETI's facilities on 200 mm wafers with industrial-scale manufacturing tools Details on design, fabrication, and comprehensive opto-electronic characterization steps can be found in Refs. [7-9].

## 2. P-I-N REGIME

Figure 1(b) shows the photo-responsivity versus applied reverse voltage for PDs with 1 µm wide intrinsic Ge regions and different lengths. Responsivities of 0.19 A/W and 1.2 A/W were assessed at -0.5V for the shortest and the longest designs from current-voltage measurements. Corresponding dark-currents were 7 nA to 150 nA, respectively. Beyond -0.5V, the responsivity remains neatly flat without any observable bias dependency. Indeed, the strong built-in electric field is already present at low-biases. This shows that PDs with Si-Ge-Si hetero-junction are able to sweep out a major part of photo-generated carries within their lifetime [8].

Figure 1(c) presents frequency responses of 1 µm wide and 40 µm long PDs, probed at different reverse biases. The -3dB cut-off frequencies at 0V, -1V, and -2V biases were equal to 1 GHz, 7 GHz, and 12 GHz, respectively. PD bandwidth is always small at 0V due to a comparatively long transit time of carriers and the weak built-in electric field. By contrast, higher bias voltage considerably improves bandwidth characteristics. This agrees well with the improved device responsivities at non-zero reverse voltages. Bandwidth properties of PDs with different

lengths were examined as well [7,8]. The bandwidth of Si-Ge-Si PDs with the same intrinsic Ge width and various lengths remained unchanged. This suggests that the PD frequency response is not limited by RC-delay. The main limiting factor of the frequency response is instead the transit time of carriers. Indeed, the PD bandwidth was shown to be inversely proportional to the width of the intrinsic Ge region [7]. As a result, narrower PDs yield faster frequency responses (well beyond 50 GHz), at the expense of responsivities, which are lower, then (typically less than the 1.2 A/W value demonstrated above) [9]. the inset of Fig. 1(c) shows clearly open eye diagram retrieved at a transmission bit rate of 10 Gbps. The device was probed at -1V bias.

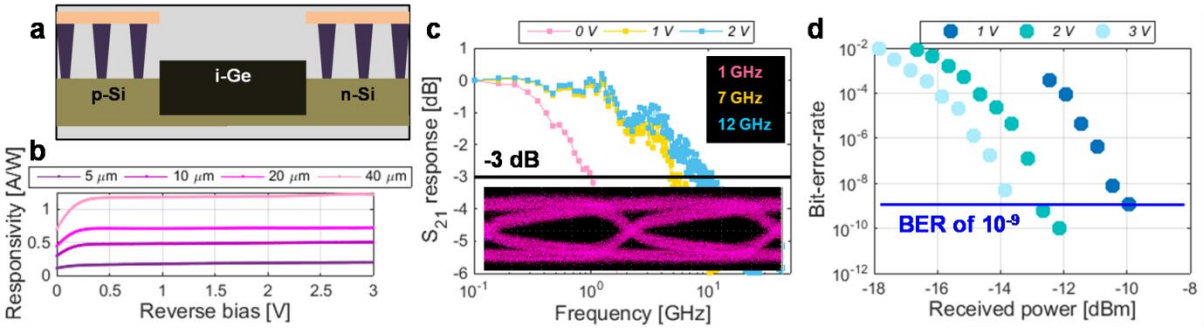



***Figure 1. 1 μm wide and 40 μm long PD at low-bias operation.*** *(a) Transversal schematic of a p-i-n PD with a lateral Si-Ge-Si hetero-junction. (b) Responsivity-voltage characteristic for Si-Ge-Si PDs with different intrinsic Ge lengths. (c) RF traces of $S_{21}$ parameter probed at different biases. Inset: 10 Gbps eye diagram aperture at -1 V bias. (d) BER versus received power for a 10 Gbps signal and different reverse biases.*

Figure 1(d) shows the bit-error-rate (BER) versus received optical power measured with a pseudo-random binary sequence at 10 Gbps bit rate and different biases. PD sensitivities of -10 dBm, -12.8 dBm, and -13.9 dBm were achieved at a BER level of $10^{-9}$. In addition, the energy consumption of hetero-structured Si-Ge-Si PDs, biased at low-voltages and operated with 10 Gbps signals, remained reasonably low, typically with a few tens of fJ/bit [9]. This makes Si-Ge-Si diodes good candidates for use in energy-efficient Si-based optical interconnects.

## 3. AVALANCHE REGIME

Simple p-i-n diodes operated at low-biases typically provide low electrical output levels. This can be overcome by biasing PDs at higher voltages in order to initiate an impact ionization process [1]. This is responsible for an avalanche multiplication effect, which consequently amplifies the generated current and yields improved device performances. To this end, hetero-structured Si-Ge-Si PD with 0.8 µm wide and 40 µm long intrinsic Ge region was considered for an avalanche operation. Figure 2(a) shows a gain-voltage curve, as determined from current-voltage tests (inset of Fig. 2(a)) and the ratios of net-light currents. They were assessed at a wavelength of 1.55 µm and an input power of -9.25 dBm. Low-bias PD responsivities at 0V and -0.5V were 0.42 A/W and 0.74 A/W. The multiplication gain of 6.7 significantly enhances the responsivity up to 2.79 A/W near the avalanche breakdown. The dark-current is still lower than 1 µA at low-bias voltages. It increases progressively with reverse bias up to 600 µA.

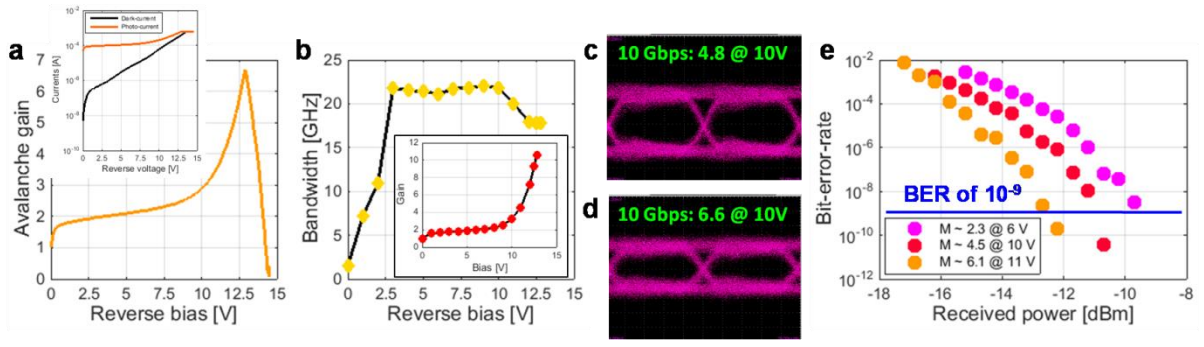



***Figure 2. 0.8 μm wide and 40 μm long PD under avalanche operation.*** *(a) Gain-voltage characteristic. Inset: Current-voltage plot for dark- and photo-currents. Photo-current was generated with an optical power -9.25 dBm at 1.55 μm wavelength. (b) Measured -3dB bandwidth versus reverse bias, with an optical power of -17.5 dBm. Inset: Corresponding gain-voltage characteristic. Eye diagram apertures at 10 Gbps and -10 V bias with gains of (c) 4.8 and (d) 6.6. (e) BER versus received power for a 28 Gbps signal at different biases.*

Figure 2(b) summarizes the bandwidth properties of hetero-structured Si-Ge-Si p-i-n APD, coming from small-signal radio-frequency testing. Bandwidth properties were examined at a wavelength of 1.55 µm and an optical input power of -17.5 dBm. The evolution of the avalanche multiplication gain with the reverse bias is shown in the inset of Fig. 2(b). Cut-off frequencies increases a lot with voltage within the low-bias range (up to -3V), from 1.5 GHz to 22 GHz, step-by-step reaching a high drift velocity. Then, the -3dB bandwidth remains nearly flat up to -10 V, as the photo-generated carriers reached their saturation velocity. Beyond -10V, the cut-off frequency

decreases down to 17.8 GHz due to an avalanche built-up time that sets restriction on the device operation speed. In this region, the avalanche gain increases exponentially up to a 10.6 peak. As a result, a gain-bandwidth product greater than 180 GHz was determined. Figures 2(c) and 2(d) show eye diagram apertures for PD working at 10 Gbps and -10V bias, with avalanche gains of 4.8 and 6.6, respectively. Both eye apertures are clearly open under these conditions of avalanche regime without observable degradation in the rise and fall times. Indeed, relative eye closure was observed for device operated with a higher gain (see Fig. 2(d)). This indicates that the studied PD approaches the bandwidth-limited operation regime.

Last, but not least, the potential of hetero-structured Si-Ge-Si APD for high-speed communication links was assessed experimentally through BER measurements. Figure 2(e) shows BER versus received optical power for an 0.8 μm wide and 40 μm long PD operated at 28 Gbps under different avalanche conditions at different biases (-6V; -10V; and -11V), for which multiplication gains were 2.3, 4.5, and 6.1, respectively. Optical power sensitivities of -9.7 dBm, -11 dBm, and -12.7 dBm were associated with those avalanche conditions.

## 4. CONCLUSIONS

We described recent results on high-speed p-i-n photodetectors with lateral Si-Ge-Si hetero-junctions. Under a low-voltage operation, devices afford low dark current, high responsivity, and fast response, which in turn, enables a bit-error-free operation at 10 Gbps data rate, with power sensitivities down to -13.9 dBm. Additionally, under an avalanche operation, photodetectors provided improved opto-electrical performances. Device responsivity was enhanced from 0.42 A/W to 2.79 A/W thanks to an internal avalanche gain of 6.7. A device response as high as 17 GHz with a gain of 10.6 was achieved, yielding a gain-bandwidth product greater than 180 GHz. These achievements opened up a route for an errorless signal detection at 28 Gbps data rate and a sensitivity as low as -12.7 dBm. These state-of-the-art results definitely extend opportunities for high-speed detection in integrated optoelectronic chips based on mature group-IV nanophotonic technology.

## ACKNOWLEDGEMENTS

This work was founded by the European Research Council (ERC) under the European Union's Horizon 2020 Research and Innovation Program (ERC POPSTAR - grant agreement 647342).

## REFERENCES

[1] J. Michel, et al.: High-performance Ge-on-Si photodetectors, Nat. Photonics **4**, 527-534 (2010).
[2] L. Vivien, et al: Zero-bias 40 Gbit/s germanium waveguide photodetector on silicon, Opt. Express **20**, 1096-1101 (2012).
[3] G. Li, et al.: Improving CMOS-compatible Germanium photodetectors, Opt. Express **20**, 18145-15155 (2012).
[4] H. Pan, et al: High-speed receiver based on waveguide germanium photodetector wire bonded to 90 nm SOI CMOS amplifier, Opt. Express **20**, 18145-18155 (2012).
[5] Y. Zhang, et al.: A high-responsivity photodetector absent metal-germanium direct contact, Opt. Express **22**, 11367-11375 (2014).
[6] H. Chen, et al.: -1 V 67 GHz bandwidth Si-contacted germanium waveguide p-i-n photodetector for optical links at 56 Gbps and beyond, Opt. Express **24**, 4622-4631 (2016).
[7] L. Virot, et al.: Integrated waveguide PIN photodiodes exploiting lateral Si/Ge/Si heterojunction, Opt. Express **16**, 19487-19496 (2017).
[8] D. Benedikovic, et al.: 25 Gbps low-voltage hetero-structured silicon-germanium waveguide pin photodetectors for monolithic on-chip nanophotonic architectures, Photon. Res. **7**, 437-444 (2019).
[9] D. Benedikovic, et al.: Comprehensive Study on Chip-Integrated Germanium Pin Photodetectors for Energy-Efficient Silicon Interconnects, IEEE J. Quantum. Electron. **56**, 8400409 (2020).
[10] Y. Kang, et al.: Monolithic germanium/silicon avalanche photodiodes with 340 GHz gain-bandwidth product, Nat. Photonics **3**, 59-63 (2009).
[11] S. Assefa, et al.: Reinventing germanium avalanche photodetector for nanophotonic on-chip optical interconnects, Nature **464**, 80-84 (2010).
[12] L. Virot, et al.: Germanium avalanche receiver for low power interconnects, Nat. Communications **5**, 4957 (2014).
[13] H. T. Chen, et al: High sensitivity 10Gb/s Si photonic receiver based on a low-voltage waveguide-coupled Ge avalanche photodetector, Opt. Express **23**, 815-822 (2015).
[14] X. Zheng, et al: Silicon-germanium avalanche photodiodes with direct control of electric field in charge multiplication region, Optica **6**, 772-777 (2019).

# 240 Gb/s (8×30 Gb/s) Directly Modulated Transmitter Monolithically Integrated on InP

**G. Contestabile[1], F. Bontempi[1], and N. Andriolli[1*]**
[1] Scuola Superiore Sant'Anna, Via Moruzzi 1, 56124 Pisa, Italy
[*] now with National Research Council of Italy - Institute of Electronics, Computer and Telecommunication Engineering (CNR-IEIIT), Via Caruso 16, 56122 Pisa, Italy
*e-mail: giampiero.contestabile@santannapisa.it*

## ABSTRACT

We report a high-speed integrated 8-channel transmitter fabricated using a generic InP integration platform. The photonic integrated circuits (PICs) include tunable directly modulated DFB lasers emitting in the C-band, monitoring photodetectors, MMI couplers and output spot size converters. The directly modulated lasers, designed in order to fit within a 100 GHz grid, show a maximum 3-dB small signal bandwidth of 21 GHz and a tunability range of about 4 nm. Operation up to 30 Gb/s per channel is reported for 200+ Gb/s applications.

**Keywords**: Photonic Integrated Circuits (PICs), Monolithic integrated circuits, High speed transmitters, Distributed feedback lasers.

## 1. INTRODUCTION

Multi-wavelength transmitters are useful in several applications in short- to long-haul optical digital transmission, including data center networks, access networks and mobile backhaul [1, 2]. They are also requested in microwave photonics, where dense and parallel transmitter integration is envisioned for broadband wireless access networks, sensor networks, radar, satellite communications, instrumentation, warfare systems, and also beamforming [3-7]. Indeed, compact integrated high-speed parallel transmission solutions are beneficial in different scenarios: namely, for directly connecting arrayed antennas, in order to enable the steering of the received signals at the receiver side, in hybrid fiber radio systems, where wavelength division multiplexed (WDM) systems can help in deploying cost effective network solutions.

In this framework, a number of properly coupled directly modulated lasers (DMLs) allows to realize a simplified yet effective transmitter architecture, suitable in several application fields. The monolithic integration of multiple modulated sources on the same chip has the advantage to enable very compact devices also leading to component cost reduction.

In this contribution, we report our recent results on directly modulated transmitter PICs fabricated with a generic foundry model. In particular, we report the characterization of an 8-channel transmitter working up to 30 Gb/s per channel useful for short reach 200+ Gb/s applications.

## 2. 8-CHANNEL MULTI-WAVELENGTH TRANSMITTER

The PIC has been fabricated with a generic integration technology [8] exploiting the InP platform at Fraunhofer HHI. It has been realized in a subsequent multi-project wafer run with respect to the one used for the devices reported in [9]. Here, the foundry improved the ohmic p-contact formation. This, as we report in the following, substantially improved the frequency response of the laser.

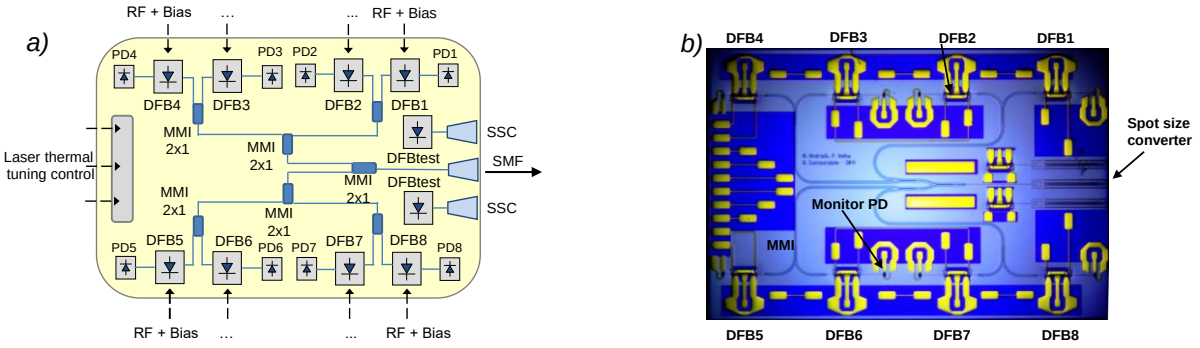



*Figure 1. (a) Schematic diagram of the PIC; (b) microscope picture of the fabricated eight-channel transmitter. Footprint: 6×4 mm$^2$.*

A picture of the 8-channel integrated multi-wavelength transmitter is reported in Fig. 1 together with its schematic diagram. Eight directly modulated DFB lasers are butt-coupled on both sides to passive waveguides so that one output of each laser is terminated onto an integrated monitoring photodetector (PD), and the other one is

connected to the 2×1 coupling MMI. Cascaded MMI-based couplers combine all the laser signals. The single output waveguide terminates into a spot size converter (SSC), that widens the waveguide mode to maximize the overlap with a standard single mode fiber. The SSC is adiabatic in order to minimize distortion and loss. The output facet is anti-reflection coated to minimize reflections, considering also that the SSC is orthogonal to the output facet. A number of additional electrical contacts are present on the chip surface so as to help in wire bonding and mounting the chip. The overall circuit footprint is 6×4 $mm^2$.

Each DML is a complex-coupled distributed feedback laser, which incorporates a twin waveguide formed by active InGaAsP multi-quantum wells and a quaternary bulk layer, and is 200 μm long [10]. The emission wavelength can be selected between 1530 and 1570 nm. An integrated heater allows an output wavelength tuning of about 4 nm.

While in [9] we demonstrated that high-frequency printed circuit boards (PCBs) can be used to operate the integrated transmitter with an ad-hoc mounting scheme and the wire bonding of the electrical contacts, all characterizations reported in this paper have been performed channel-by-channel using a 40 GHz ground-signal-ground microprobe as the PCB lines and the wire bonds limited the modulation bandwidth of the lasers. For this purpose, the chips have been mounted on a metal chuck by means of a thermally and electrically conductive epoxy resin. The temperature, controlled through a thermo-electric cooler (TEC) below the metal chuck, was stabilized at 25 °C. Spectra of the 8 lasers, after they have been thermally tuned on a 100 GHz (0.8 nm) grid in the spectral region 1554-1560 nm, are collected in Fig. 2 (left side), as recorded by a high resolution heterodyne spectrum analyzer with 40 MHz resolution (channel power is not an absolute value). Side mode suppression ratio (SMSR) is in excess of 55 dB for all lasers. The nominal output power from each DFB is estimated to be 4 dBm as per foundry specification, whereas the measured output power from the chip is in the range -10 to -12 dBm for each laser. This gives a 14-16 dB total insertion loss comprising the cascade of MMIs, the propagation across the chip, and the fiber coupling. The frequency response of the DMLs has been measured through a 50 GHz Network Analyzer using an external 32 GHz pin photodiode after an automatic calibration procedure for the electrical path. All the lasers have a similar frequency response with a bandwidth in the range 17-18 GHz at a current bias of 110 mA (i.e., the operating current used for the BER measurements reported in the following). A comparison of laser bandwidths for the transmitter reported in [9] and the most recent fabrication reported in this paper is shown in Fig. 2 (right side) for similar current values. An improvement of bandwidth at 3-dB of about 5 GHz can be appreciated.

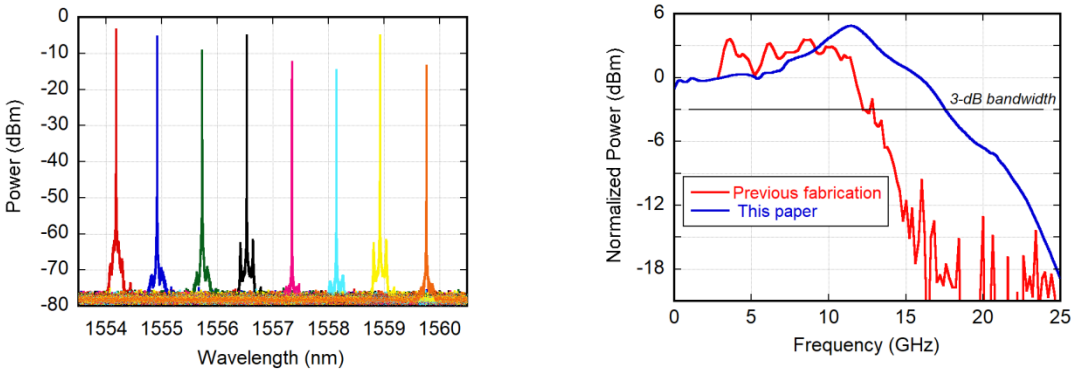



*Figure 2. Left side: Emission spectra of the eight lasers as recorded by a high resolution (40 MHz) optical spectrum analyzer. Wavelength spacing is 0.8 nm (100 GHz). Channel power is not an absolute value. Right side: Comparison of DFB normalized modulation response for a sample laser reported in [9] and a sample laser in the eight-channel transmitter presented in this paper (Bias current is 110 mA in both cases).*

To test the digital response of the transmitter we used the setup sketched in Fig. 3: a bias-tee was used to provide both the bias current and the $2^{31}$-1 non-return-to-zero (NRZ) modulated pseudo-random-bit-sequence (PRBS) generated by the pattern generator at different data rates and amplified to around 3.3 V peak-to-peak ($V_{pp}$). These values allow to maximize the extinction ratio and at the same time optimize the eye diagram shape. The bias and $V_{pp}$ working points were then slightly adjusted channel by channel and at varying the bitrates.

A standard single mode fiber (SMF) has been attached to a three axis micropositioner stage with optical power feedback control to guarantee optimal alignment throughout the transmission experiment. The emitted signal collected into the fiber is then sent into an amplified optical receiver made by an erbium doped fiber amplifier (EDFA), a 2 nm band pass filter (BPF), an optical attenuator (OA) and a 32 GHz amplified photoreceiver. The received electrical signal was then analyzed by an electrical sampling scope with a 56 GHz optical head and by an error detector.

Fig. 3 also reports the BER for all the 8 channels at 28 and 30 Gb/s, i.e., the maximum operating bitrates where all the channels were running error-free (namely, with BER<$10^{-9}$). Two sample eye diagrams are also reported in the upper part of the figure showing clear eye data opening at both frequencies. With respect to [9], where error-free operation was recorded up to 20 Gb/s, a 10 Gb/s capacity gain per channel can be appreciated.

Power sensitivity (at a BER=$10^{-9}$) is in the range -5.8 to -3 dBm for the 28 Gb/s channels, while it is in the range -3.6 to -1.5 dBm for the 30 Gb/s ones.

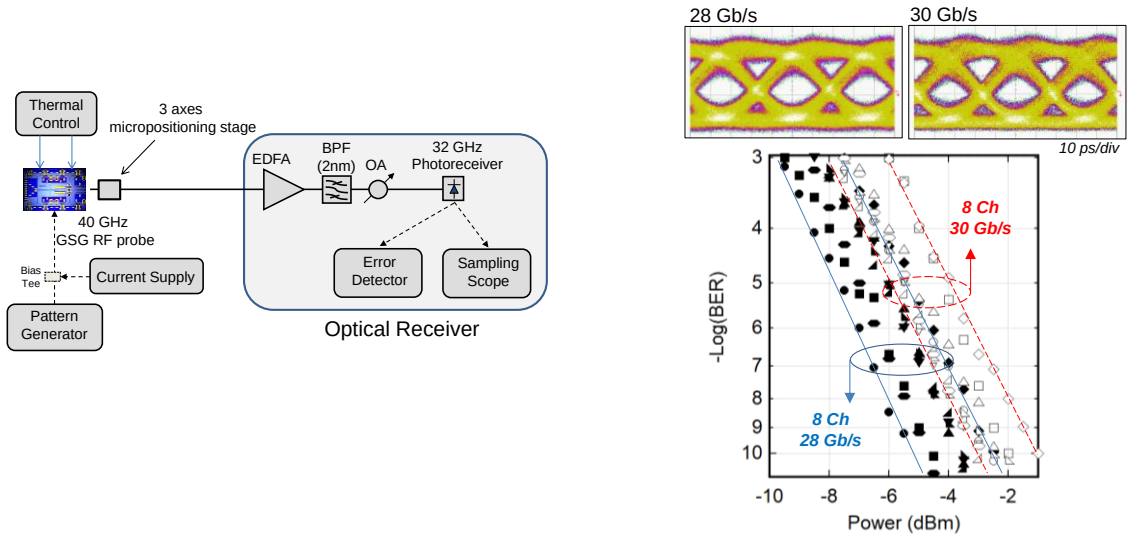



*Figure 3. Left side: Experimental setup for the BER measurements. Right side: Sample 28 and 30 Gb/s eye diagrams recorded with a 56 GHz sampling head and collection of all the eight BER curves as a function of the received power at 28 and 30 Gb/s.*

## 3. CONCLUSIONS

We have reported the characterization of a multi-wavelength integrated transmitters fabricated in an InP generic integration platform encompassing tunable DMLs, monitor PDs, and MMIs for signal multiplexing. The 8-channel-transmitter has 8 emitting carriers in C-band, ranging from 1554.2 to 1558.8 nm on a 100 GHz grid and a small signal modulation response of the DMLs of 17-18 GHz, allowing for error-free BER in back to back up to 30 Gb/s.

## ACKNOWLEDGEMENTS

The authors would like to acknowledge Dr. M. Baier and Dr. F. Soares of the Fraunhofer Institute for Telecommunication, Heinrich Hertz Institut, Berlin for the PIC fabrications.

## REFERENCES

[1] K. Lawniczuk, M. J. Wale, P. Szczepański, R. Piramidowicz, M. K. Smit and X. J. M. Leijtens, "Photonic multiwavelength transmitters with DBR laser array for optical access networks," *in OFC/NFOEC 2013 Tech. Dig*.

[2] CWDM4 MSA Group, "100G CWDM4 MSA Technical Specifications Revision 1.1," Nov. 2015.

[3] J. G. Andrews, S. Buzzi, W. Choi, S. V. Hanly, A. Lozano, A. C. K. Soong and J. C. Zhang, "What Will 5G Be?," *IEEE Journal on Selected Areas in Communications*, vol. 32, pp. 1065-1082 (2014)

[4] V. J. Urick, F. Bucholtz, J. D. McKinney, P. S. Devgan, A. L. Campillo, J. L. Dexter, and K. J. Williams "Long-Haul Analog Photonics," *Journal of Lightwave Technology*, vol. 29, pp. 1182-1205 (2011)

[5] A. J. Seeds and K. J. Williams, "Microwave Photonics," *Journal of Lightwave Technology*, vol. 24, pp. 4628-4641 (2006)

[6] J. Yao, "Microwave Photonics," *Journal of Lightwave Technology*, vol. 27, pp. 314-335 (2009)

[7] J. Capmany and D. Novak, "Microwave photonics combines two worlds," *Nature Photonics*, vol.1, pp. 319-330 (2007)

[8] M. Smit et al. "An introduction to InP-based generic integration technology," *Semiconductor Science and Technology*, vol. 29, p. 083001-1/41 (2014).

[9] N. Andriolli, P. Velha, M. Chiesa, A. Trifiletti, G. Contestabile, "A Directly Modulated Multiwavelength Transmitter Monolithically Integrated on InP," *IEEE Journal of Selected Topics in Quantum Electronics*, vol. 24, (2018)

[10] M. F. Baier, F.M- Soares, T. Gaertner, M. Moehrle, N. Grote, and C. Meuer, "50 Gbit/s PAM-4 Transmission using a Directly Modulated Laser made on Generic InP Integration Platform," *International Conference on Indium Phosphide & Related Materials (IPRM) 2015*, Santa Barbara, CA (USA) 2015, paper We2O7.3.

# Study of hybrid silicon quantum dot frequency comb laser dynamic for 5G and datacom applications

Bozhang Dong[1], Jianan Duan[1], Heming Huang[1], Geza Kurczveil[2], Di Liang[2], and Frédéric Grillot[1,3]
[1]*LTCI, Télécom Paris, Institut Polytechnique de Paris, 19 Place Marguerite Perey, 91120 Palaiseau, France*
[2]*Hewlett Packard Labs, 1501 Page Mill Rd, Palo Alto, CA 94304, USA*
[3]*Center for High Technology Materials, University of New-Mexico, Albuquerque, New-Mexico, 87106, USA*
*e-mail: bozhang.dong@telecom-paris.fr*

## ABSTRACT

This work reports on the high performance of a 1.3 $\mu$m hybrid quantum dot frequency comb laser. The material parameters such as gain, differential gain, and linewidth enhancement factor are studied and linked to the comb dynamics. In particular, results show that a larger linewidth enhancement factor is more beneficial for comb operation; moreover, we demonstrate that, by employing optical injection, both the 3-dB bandwidth and the flatness of the whole optical frequency comb is improved. Such novel findings give promising guidelines for the development of high-speed dense wavelength division multiplexing photonic integrated circuits in upcoming 5G telecommunications and datacom applications.

**Keywords**: frequency comb, quantum dot, silicon photonics, optical injection, linewidth enhancement factor.

## 1 INTRODUCTION

Broadband optical light sources play a key role in the rapid development of wavelength-division multiplexing (WDM) technologies, which are solutions of high transmission capacity to meet the huge demand in the upcoming 5G telecommunication industry, next generation of data centers and LiDAR system applied to self-driving cars [1]. In contrast to the multiple single-wavelength lasers configuration, the multi-wavelength light source such as the optical frequency combs (OFCs) is therefore a competitive candidate for performing WDM functions, owning to the possibility to achieve a large number channels with equidistant free spectral range (FSR), which is able to support the huge demand in transmission capacity [2]; on the other hand, its reduced device footprint is also advantageous for photonic integrated circuits (PICs) applications. Quantum dot (QD) lasers have been found to be efficient solution to OFCs owning to straightforward comb generation, large gain bandwidth, narrow spectral linewidth, low relative intensity noise (RIN) and high temperature stability [3], [4]; hybrid semiconductor comb lasers fabricated on silicon substrate are developed as well to meet the requirement of low-cost and energy-efficient integrated photonic component for PICs. In this paper, we report on the improved performance of 1.3 $\mu$m hybrid QD comb lasers. To do so, we analyze the linewidth enhancement factor ($\alpha_H$-factor) driven the coupling between gain and refractive index as well as the response of the comb laser to optical injection. The $\alpha_H$-factor is known as a vital parameter influencing semiconductor laser performance. Then presented results show that the higher the reverse voltage applied on the saturable absorber (SA), the larger the $\alpha_H$-factor, hence the stronger the frequency comb dynamics. With the view of improving the OFCs performance, we also demonstrate that optical injection (OI) is more beneficial to further enlarge the bandwidth and optimize the whole comb flatness.

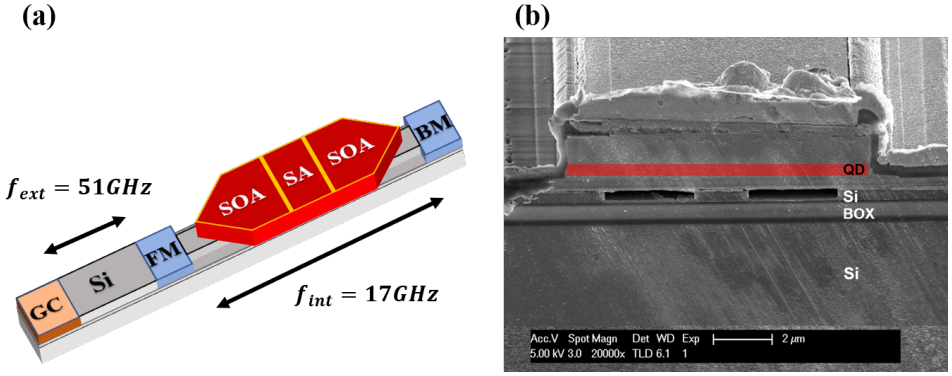



Figure 1. (a) Schematic diagram of the hybrid-silicon QD comb laser under study. SOA, semiconductor optical amplifier; SA, saturable absorber; FM, front mirror; BM, back mirror; GC, grating coupler. (b) SEM image of the cross section of the device. QD, quantum dot active region.

## 2 ANALYSIS OF DEVICE

### 2.1 Description of device

The schematic diagram and the SEM image of the hybrid-silicon QD comb laser is shown in Figure 1(a) and (b), respectively. The device under study consists of a 2.3-mm-long internal cavity (repetition rate at 17 GHz), where a 1200-$\mu$m-long semiconductor optical amplifier (SOA) and a 120-$\mu$m-long SA at the center are bonded. The two facets of the cavity are then combined with a front mirror (FM) and a back mirror (BM) at $\sim$50% and $\sim$100% power reflectivities, respectively. Outside the FM is followed by a 0.75-mm-long (repetition rate at 51 GHz) external cavity, which is applied to output a 102 GHz FSR on frequency comb behavior; and the light would eventually be coupled out by a $\sim$10% coupling efficiency grating coupler (GC). Varying the reverse voltage applied on the SA contributes to generate the comb dynamics, whereas the mode converters are applied to transfer the optical mode between the active hybrid waveguide and the passive Si waveguide. The full laser epitaxial structure and more detailed descriptions about the generation of 102 GHz repetition rate can be found elsewhere [5], [6].

### 2.2 Results discussions

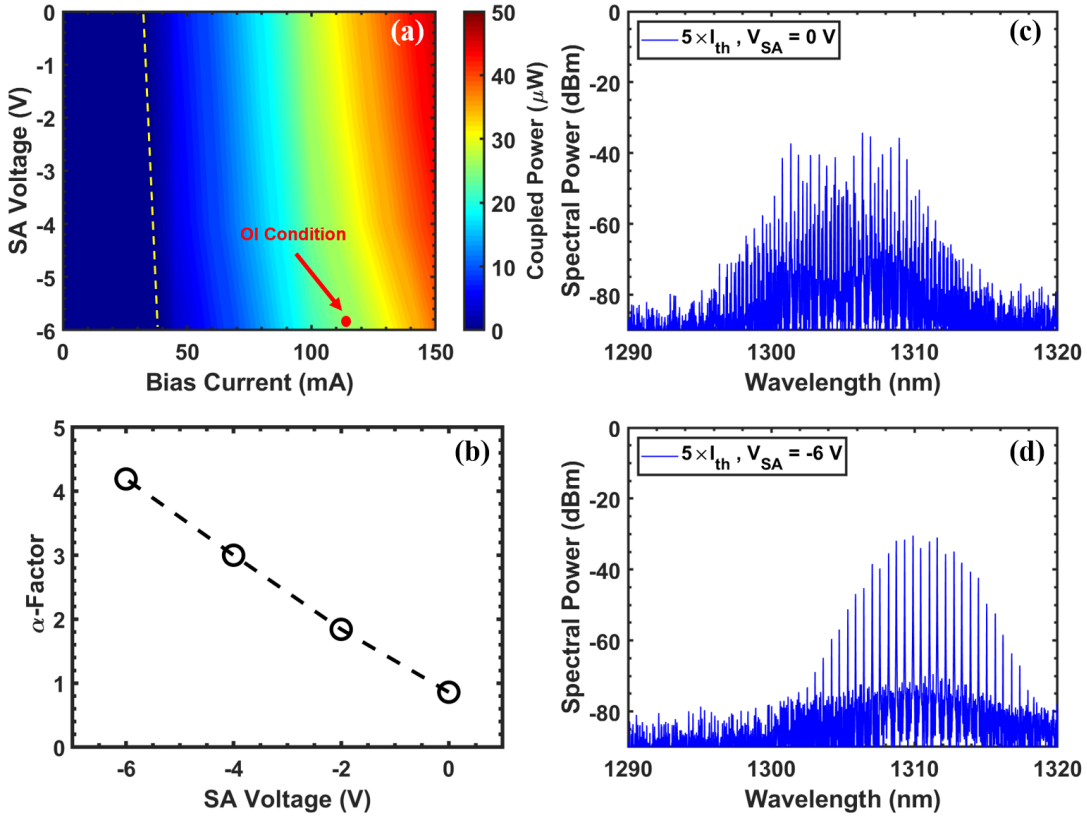



Figure 2. (a) Mapping of the coupled power under different reverse voltages on SA and bias current conditions. The yellow dashed line represents the evolution of the laser threshold with the reverse voltage. The red bullet corresponds to the device operation conditions applied in the optical injection, which is introduced in this paper hereafter. (b) $\alpha_H$-factor at threshold as a function of reverse voltages on SA. Optical spectrum at $5\times I_{th}$ with reverse voltage on SA at (c) 0 V and (d) -6 V.

Figure 2(a) depicts the mapping of light - current characterization as a function of the reverse voltage on SA of the comb laser under study. Let us note that the device temperature is carefully monitored and kept constant at room temperature (293K) throughout the experiment. The evolution of threshold current $I_{th}$, which is marked by the yellow dashed line, indicates that a higher reverse voltage on SA decreases the output power and increases the threshold. For instance, $I_{th}$ is found to slightly increase from 32 to 38 mA as the reverse voltage is varied from 0 V to -6 V, which is introduced by the higher internal loss from the increasing absorption in SA.

Not only the threshold and output power, but also the $\alpha_H$-factor is found to vary from different reverse voltage applied on SA. In this section, the extraction of the LEF is performed from the amplified spontaneous emission (ASE) [7]. With the view of ensuring a better precision of the LEF extraction, we used a CW current source to get smooth optical modes, which would then be captured by a 20 pm high resolution optical spectrum

analyzer (OSA); on the other hand, the modal wavelength red-shift above threshold caused by thermal effects is then totally subtracted from the wavelength blue-shift below threshold. Both the operations leads to an accurate extraction of the LEF from below to threshold.

The extracted $\alpha_H$-factors at threshold as a function of the reverse voltage on SA are shown in Figure 2(b). The values of $\alpha_H$-factor are found to increase from 0.9 to 4.2 with the reverse voltage from 0 V to -6 V due to the increase of modal differential wavelength and the decrease of the differential gain. It should be noted that a larger $\alpha_H$-factor is found to optimize the frequency comb dynamics, which can be clearly seen in Figure 2(c) and (d). This enlargement of comb bandwidth through four-wave mixing is attributed to the homogeneous broadening introduced by the spatial overlap among the quantum dots [8]. Nevertheless, let us stress that the increase of the comb bandwidth is limited because the dispersion for high frequency active mode is bigger. By the way, let us stress that the device under study does not output any pulse (no mode-locking) but rather operates under continuous-wave (CW) which is desired for WDM applications, as such devices are likely to have better reliability from the lower instantaneous power.

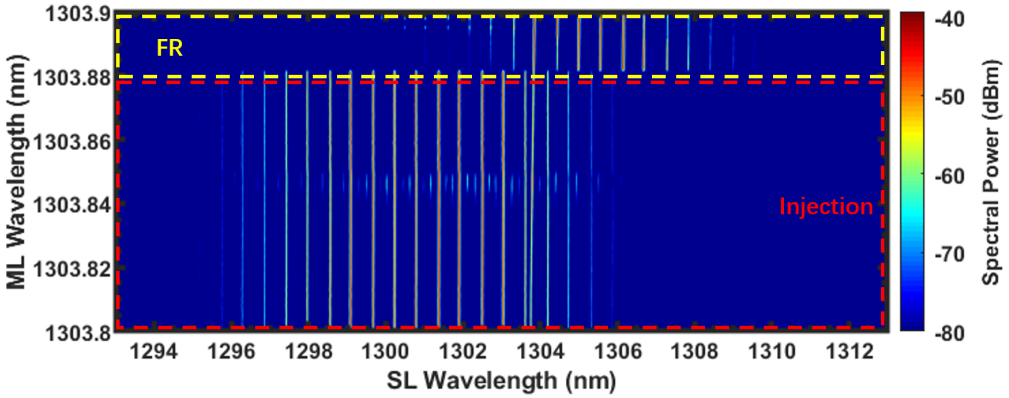



Figure 3. Evolution of the optical spectra of the slave comb laser as a function of the injected wavelength, device is biased at $3\times I_{th}$ with -6V applied on SA. Optical spectra at free running state are highlighted in the yellow dashed area (FR) and that under optical injection are in the red dashed area (Injection). ML, master laser; SL, slave laser.

With the view of improving the comb dynamics, we also investigated the effects of the OI as a way to process optical frequency comb by isolating and amplifying individual comb modes. The OI is applied when the device operates at $3\times I_{th}$ with -6 V applied on SA (conditions marked by red bullet in Figure 2(a)), and the injection strength is estimated to be below -12 dB. Let us stress that the $\alpha_H$-factor is therefore considered as a constant and not being influenced by the injected field due to such low injection strength. Figure 3 displays the evolution of optical spectra of the slave comb laser by varying the injection wavelength of master laser, where the optical spectra at free running state (without OI) are marked by the yellow dashed area (FR) and that under OI are highlighted in the red dashed area (injection). Under the intramodal injection at the peak of 1303.8 nm, a stable blue-shift of the comb spectrum as well as a broadening of comb bandwidth are observed. In our case, the full bandwidth of the comb laser broadens from 5.7 nm (11 lines above noise floor) to 10.7 nm (20 lines above noise floor), and its 3-dB bandwidth enlarges from 1.1 nm (3 lines) to 4 nm (8 lines). Such findings bring novel insights in the optimization of frequency comb dynamics.

## 3 CONCLUSIONS

To summarize, this investigates the role of optical injection on the high-performance of a frequency comb laser. We link the comb dynamic to the material properties such as that driven by the $\alpha_H$-factor. Therefore, a larger $\alpha_H$-factor occurs at higher reverse voltage on SA which in principle contributes to strengthen the comb laser performance. Intramodal OI is also proved to enhance the bandwidth and flatness of the comb spectrum. Those novel findings are very encouraging for the future integrated technologies required for 5G telecommunications and supercomputer applications.

## REFERENCES


[1] H. Ito et al., Opt. Express, Vol. 26, No. 20 (2018).

[2] H. Hu et al., Nat. Photon., vol. 12 (2018).

[3] Z. G. Lu et al., Opt. Express, vol. 26, 2160-2167 (2018).

[4] H. Huang et al., APL Photonics, Vol. 5, 016103 (2020).

[5] G. Kurczveil et al., IEEE Photon. Technol. Lett. Vol. 30, No. 1 (2018).

[6] B. Dong et al., Opt. Lett., Vol. 44, No. 23 (2019).

[7] J. Duan et al., Photonics Res., Vol. 7, No. 11 (2019).

[8] F. Grillot et al., IEEE J. Quantum Electron. Vol. 45, 872 (2009).

# Frequency Modulated Continuous Wave Narrow Linewidth Laser Diode Based on Self-injection locking with External Micro-ring Resonator

**Liwei Tang[1,2], Shuai Shao[1,2], Sigang Yang[1,2], Hongwei Chen[1,2], Minghua Chen[1,2]**
[1] Department of Electronic Engineering, Tsinghua University, Beijing, 100084, China
[2] Beijng National Research Center for Information Science and Technology (BNRist), Beijing, 100084, China
*e-mail: chenmh@tsinghua.edu.cn*

## ABSTRACT

A chip-scale frequency modulated continuous wave (FMCW) laser is implemented by coupling the distributed feedback (DFB) laser to an external high-Q micro-ring resonator based on $Si_3N_4$ waveguide. By self-injection locked, the laser realizes continuous tuning and frequency modulated without mode hopping. The lasering frequency is tracing the resonant frequency of the micro-ring which is tuned by thermo-optic (TO) effect. The laser shows a DC frequency tuning range of 9.1 GHz with a low noise of 3.7 kHz linewidth. Dynamic time-frequency domain analysis of the frequency modulation is also demonstrated, which has a potential application for light detection and ranging (LIDAR).

**Keywords**: Integrated optics, semiconductor laser, frequency sweep

## 1. INTRODUCTION

Coherent optical communication, optical coherence tomography (OCT), LIDAR, etc., have a rapidly rising demand for the FMCW laser source. Wideband tunable FP laser has been proposed by introducing the Vernier effect, while its mode hopping limits the modulation accuracy and bandwidth [1]. In this paper, a DFB laser packaged with micro-ring resonator based on $Si_3N_4$ waveguide is demonstrated, showing a continuous frequency modulation with narrow linewidth. The micro-ring resonator fabricated with low-loss $Si_3N_4$ waveguide featuring a Q (quality factor) value of $2 \times 10^5$, realizing a linewidth of 3.7 kHz. Resonant wavelength is tuned by the voltage applied to the electrode which is used to heating the waveguide. Based on the TO effect, the static tuning range is up to 9.1 GHz around 1547.1 nm and the modulation bandwidth is 0.9 GHz in 1 ms enabling the LIDAR based on FMCW.

## 2. PRINCIPLE and EXPERIMENT

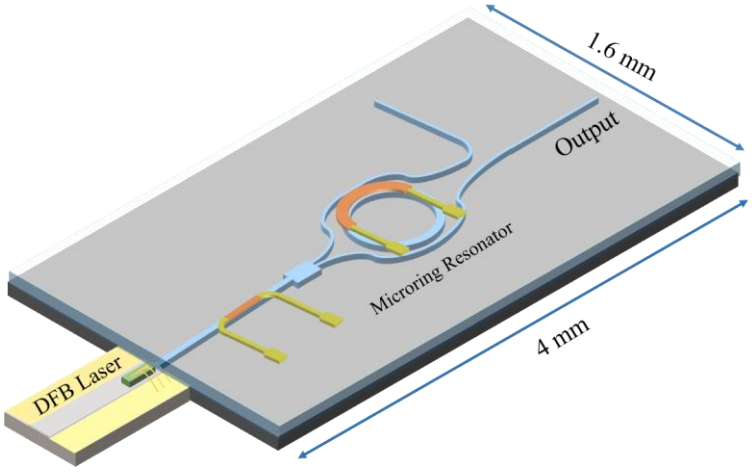



*Figure 1. Diagram of the FMCM laser. The DFB laser is coupled to a micro-ring based on $Si_3N_4$ waveguide where the blue line represent the waveguide, the red and yellow line represent the heating resistor and electrode.*

The optical source consists of commercial DFB laser diode (LD) and the extern micro-ring resonator which is shown in Fig. 1. In static operation, the micro-ring resonator can be regarded as a filter and mirror which reflects the selective wavelength and injects it into the DFB laser while outputting the filtered light. The efficiency of self-injection decided by the ration of Q of the laser and external cavity. The suppression of the linewidth is described by equation 1 derived for the reduction of close-in phase noise of the laser [2].

$$\eta = \frac{\Delta\nu_0}{\Delta\nu} = 1 + \sqrt{\frac{P_r}{P}(1+\alpha^2)}\,\frac{Q}{Q_{LD}} \tag{1}$$

where $\Delta\nu_0$, $\Delta\nu$ represent the linewidth after and before the injection respectively, $Q, Q_{LD}$ represent the quality factor of the micro-ring resonator and LD respectively. The device is fabricated based on low-loss Si3N4 waveguide bringing about a micro-ring Q attaining $2 \times 10^5$. Bring the injection power $P_r/P = 0.3$ and linewidth enhancement factor $\alpha = 2.5$ into equation 1, $\eta$ is estimated to be 1000 showing that the linewidth would be narrowed by 3 orders of magnitude. By altering the voltage on the two pairs of electrodes and the laser's operation temperature, the laser will meet the self-injection equilibrium condition and enter the self-injection locking mode. The principle of laser tuning can be simply explained by filtered optical feedback (FOF) theory [3], since it offers a description of the laser dynamics via two tuning parameters, viz. the centre frequency of micro-ring resonator and its spectra linewidth. This theory draws a conclusion that the detuning frequency of the laser is linear with the tuning frequency of the filter. The process of frequency modulation relies on the TO effect of the waveguide where the heating power on the micro-ring is linear with the detuning resonant frequency enabling a linear sweeping by applying a proper voltage on the electrodes. The results of the static tuning and dynamic frequency modualtion are experimentally demonstrated below.

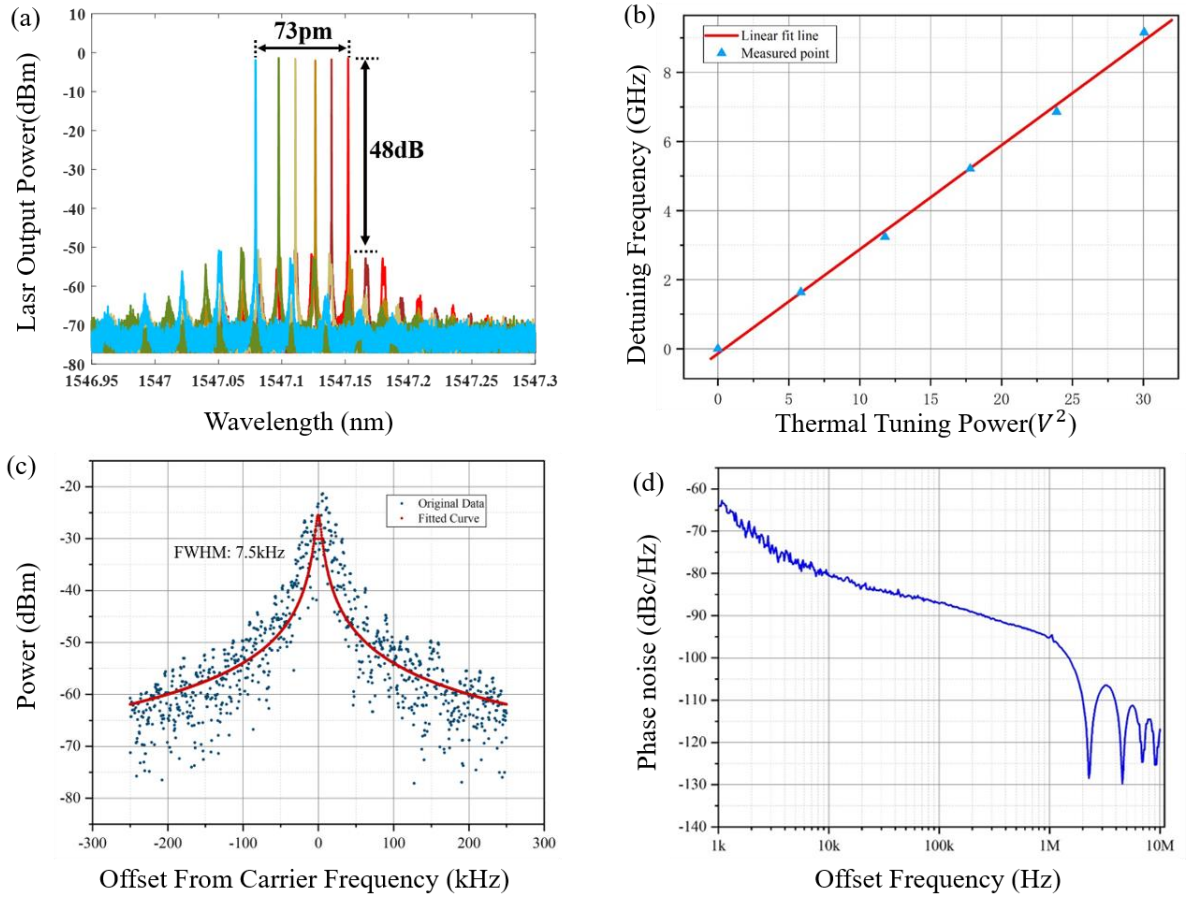



*Figure 2. Measurement of the static frequency tuning of the laser. (a)Static frequency tuning with narrow linewidth. (b) Proportional relationship between tuning frequency and thermal power where the red line is a proportional fit of the measured point (blue point). (c) Beat note of 10 km self-heterodyne interferometer with 200 MHz offset by acousto-optic modulator (AOM). The full width at half maximum of the curve is estimated to be 7.5 kHz, so the single laser linewidth is 3.7 kHz. (d) Phase noise of the beat note by 100 m unbalanced MZI.*

The DFB laser coupled with external micro-ring resonator is in 14-pin standard butterfly package for practical application. Thermoelectric cooler (TEC) packaged together is applied to maintain a constant temperature. Two electrodes are deposited on the chip for tuning the external roundtrip time and the resonant frequency based on the TO effect. The two-dimensional voltage tuning component allows the laser enter the self-injection locking state after going through the chaotic state and the mode-locked state. Figure 2 shows the self-injection locking state with narrow linewidth and static frequency tuning. By changing the voltage applied on the micro-ring from 8.7 to 9.7 V, 10 GHz frequency tuning was achieved. The linewidth measured by 10 km delayed self-heterodyne interferometer (DSHI) is around 4 kHz among the whole tuning range [4]. The linearity of the detuning frequency

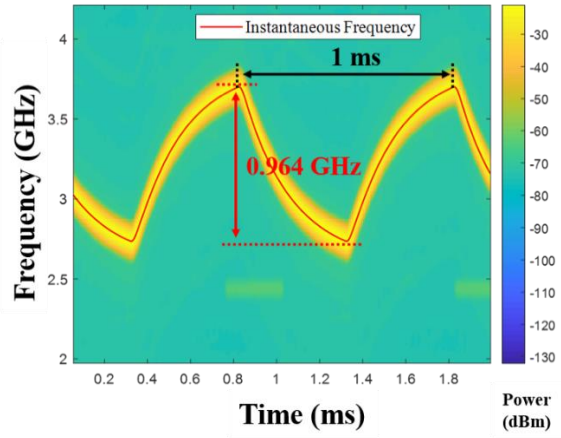



*Figure 3. Time-frequency analysis of the beat note by reference laser and FMCW laser.*

and the thermal tuning power is well fitted in Fig.2 (b), which make it possible for linear frequency sweeping. In addition, noise analysis is applied using an unbalanced Mach-Zehnder Interferometer (MZI) with a path imbalance (delay line) of 100m. The measured noise spectrum for the laser and the detection noise floor is plotted in Fig .2(d) where the noise shows -65 dBc/Hz at 1 kHz. Frequency modulating is demonstrated in Fig.3 . The continuous static frequency tuning has achieved 10 GHz, making it possible for the FMCW bandwidth to reach 10G. Based on the fact that the thermal power is proportional to the tuning frequency, the square of the voltage applied to the micro-ring is linear with time expecting a linear frequency modulation. Beat note of the FMCW laser and the reference laser is analysed by the time-frequency algorithm to obtain the time-frequency diagram. The frequency modulation based on the thermo-optic has a bandwidth of 0.964 GHz/ms and introduces the linear distortion as shown in Fig. 3.

## 3. CONCLUSIONS

A frequency sweep laser based on self-injection is proposed. The static tuning range is up to 73pm with 3.7kHz linewidth. Frequency sweeping by TO effect can achieve 0.96GHz/ms and 0.91GHz/25us by PZT driving. The time-frequency domain analysis of the two methods are also compared. The designed laser are in 14-pin butterfly package can be applied in FMCW Lidar.

## ACKNOWLEDGEMENTS

This work is supported by National Key R&D Program of China under Grant 2018YFB2201802 and National Natural Science Foundation of China (NSFC) under Grant 61771285.

## REFERENCES

[1] Li Y, Zhang Y, Chen H, et al. Tunable Self-Injected Fabry–Perot Laser Diode Coupled to an External High-Q Si 3 N 4/SiO 2 Microring Resonator[J]. Journal of Lightwave Technology, 2018, 36(16): 3269-3274.

[2] Hinkley E D, Freed C. Direct observation of the Lorentzian line shape as limited by quantum phase noise in a laser above threshold[J]. Physical Review Letters, 1969, 23(6): 277.

[3] Unlocking dynamical diversity: optical feedback effects on semiconductor lasers[M]. John Wiley & Sons, 2005.

[4] Bennetts S, McDonald G D, Hardman K S, et al. External cavity diode lasers with 5kHz linewidth and 200nm tuning range at 1.55 μm and methods for linewidth measurement[J]. Optics express, 2014, 22(9): 10642-10654.

# Single-mode and multi-mode DBR lasers using InP-$Si_3N_4$/$SiO_2$ integration

*(Student paper)*

**S. Boust[1,2], Y. Ibrahimi[1], J.-F. Paret[1], A. Garreau[1], K. Mekhazni[1], C. Fortin[1], F. Duport[1], M. Vallet[2], J.-M. Fedeli[3], F. van Dijk[1]**

[1] III-V Lab, a joint lab between Nokia Bell Labs, Thales Research and Technology and CEA-LETI, 1 Avenue Augustin Fresnel, 91767 Palaiseau, France

[2] Univ. Rennes, CNRS, Institut FOTON – UMR 6082, 35000 Rennes, France

[3] CEA-LETI Univ. Grenoble Alpes, 38000 Grenoble, France

*e-mail: sylvain.boust@3-5lab.fr*

## ABSTRACT

We propose to highlight the versatility of the integration of InP and $Si_3N_4$ platforms by presenting two hybrid lasers. Our first laser reaches a narrow optical linewidth of 5.6 kHz at 1546 nm, with a continuous tuning range of 12.7 GHz and a 65 dB side-mode suppression ratio. Then, we report preliminary work on another integrated multimode laser which presents 48 optical lines in a 10 dB bandwidth, spaced 1.19 GHz apart. Such integrated sources present low consumption, compact and affordable solutions for LiDAR, coherent communication transmissions or spectroscopy.

**Keywords**: Distributed Bragg reflector lasers, hybrid lasers, narrow linewidth, comb source

## 1. INTRODUCTION

The integration of lasers is a key leverage for a growing number of applications. Telecommunications, LiDAR, or microwave generation take profit of low cost, compactness and power saving integrated sources. However solutions based on monolithic InP integration are limited by their cavity length due to the propagation losses. They are not adapted to narrow linewidth single mode laser or low repetition rate mode-locked laser fabrication.

One possibility to integrate high-performance lasers is to extend the III-V gain chip cavity by butt-coupling a passive chip with low propagation losses [1]-[4]. We report here two hybrid lasers composed of an InP Reflective Semiconductor Optical Amplifier (R-SOA) with a silicon nitride ($Si_3N_4$) Bragg grating. Thanks to the maturity of the silicon platform, the propagation losses of the $Si_3N_4$ waveguides are very low. Consequently, the cavity length can be adapted to the targeted application. We emphasize in this abstract the flexibility of this hybridization. After describing the key fabrication steps of low loss $Si_3N_4$ waveguide, we present a single mode laser made of a short passive cavity and a narrow Bragg filter. Then, we will demonstrate a multimode laser composed of a longer passive cavity with a broad Bragg filter.

## 2. FABRICATION OF LOW LOSS PASSIVE WAVEGUIDES

The passive chip process begins by a 8-µm thermal oxidation of the 200-mm diameter silicon substrate. Then the stoichiometric $Si_3N_4$ 90-nm thin film is deposited by low pressure chemical vapour deposition (LPCVD). We define the waveguide by Deep Ultra Violet (DUV) lithography with a width of 2.9 µm. These dimensions of the waveguide enable a low confinement of the propagating mode over the core of the waveguide, leading to the lowest propagation losses and avoiding nonlinearity in the passive waveguide. It implies to monitor carefully the quality of the $Si_3N_4$ and the $SiO_2$. Thus we apply to the wafer a 3-hour annealing at 1200°C in oxygen atmosphere. It is a key step to purify the wafer from hydrogen. Next we encapsulate the waveguides with a $SiO_2$ thermally grown on a silicon wafer. Finally, clean optical facets are formed by deep etching down to the silicon. To turn the large wafer on several tens of chips, it is partially sawed by its rear side to release the chips.

We finally measure very low losses around 2 dB/m, which is a typical value in the top foundries [5]. Such performances easily open the road to very long cavity.

## 3. NARROW LINEWIDTH SINGLE MODE DBR

Our narrow linewidth single-mode DBR laser is using the design already presented in [3] for which we reduced the waveguide losses and improved the mode matching with the R-SOA. The R-SOA, built in our laboratory, is based on a SIBH structure, with an asymmetric optical confinement. This 1 mm-long component provides a gain centred on 1.55 µm strong enough (around 20 dB) to compensate the losses form a long external butt-coupled cavity.

To close the cavity, we choose to butt-couple a $Si_3N_4$ Bragg grating, which doesn't require a thermal control unlike ring filters with Vernier effect. The bandwidth has to be narrow enough to insure the single mode operation. Thus, we designed a high order Bragg grating allowing a low contrast effective refractive index, despite fabrication constraints. Every 5.797 µm, we increase the waveguide width from 2.9 µm to 3.7 µm to construct a 264x400 nm tooth. With a circulator, we measure its reflectivity spectrum (Fig. 2). The FWHM bandwidth is about 17.5 GHz (140 pm).

By using a dynamical alignment setup, we butt-coupled the two components to obtain the hybrid laser. Computing the overlap between the modes of two components gives a minimal loss estimate of 0.7 dB. By monitoring the optical power and the spectrum during a current sweep (not shown here), we noted a 55 mA threshold and a maximal output power of 6 mW in the fiber, which corresponds to 15 mW at the on-chip output port. During the current sweep, the R-SOA is slightly heating, thus the wavelength laser steadily increases until the laser undergoes mode hopping since the Bragg filter bandwidth is constant. We measure a typical laser spectrum before a mode hopping in Fig. 2, which permits to easily see the side modes and measure a 17.5 GHz FSR, and a 65 dB side-mode suppression ratio (SMSR). In the same time, we record a continuous tuning range of 12.7 GHz (102 pm), which is suitable with LiDAR applications.

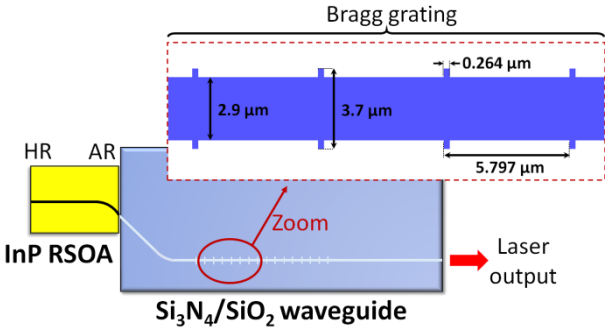



*Figure 1. Schematic of the hybrid cavity. The 21th order Bragg grating is made of regular tooth aside the $Si_3N_4/SiO_2$ waveguide.*

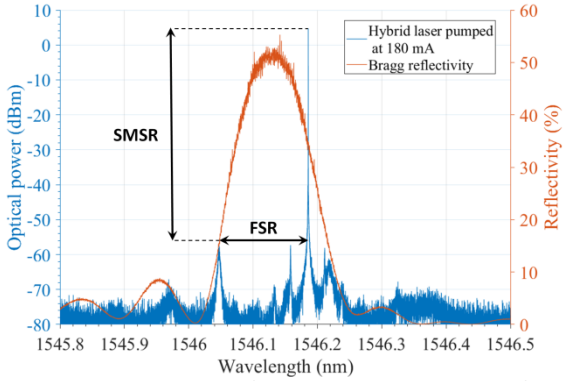



*Figure 2. Optical spectrum of a hybrid laser (blue) and of the Bragg reflexion (orange). The side peaks located at 1546.16 nm and 1546.21 nm are measurement artifacts due to APEX optical spectrum analyzer.*

By using a self delayed heterodyne setup, we measure the frequency noise of our hybrid laser. We deduce a 5.6 kHz lorentzian linewidth, which we compare with others works in Table 1. One should note that our cavity optical length (around 9 mm) is smaller than competitors, leading to a larger linewidth (see Table 1). For our next components, we plan to increase the cavity length and expect to reduce the linewidth below 1 kHz.

TABLE 1. Linewidth comparison for different configurations

| **Sructure** | **$L_{Bragg}$** | **$P_{out}$ (mW)** | **Linewidth (kHz)** | **References** |
|---|---|---|---|---|
| Bragg III-V + $Si_3N_4$ | 6.5 mm | 6 | 5.6 | Our work |
| Bragg III-V/Si | 15 mm, | 37 | 1 | Huang et al. OPTICA 2019 [6] |
| Bragg III-V/Si | 20 mm | 24 | 0.32 | Xiang et al. OL 2019 [1] |
| Ring III-V + $Si_3N_4$ | not applicable | 13 | 0.29 | Fan et al. CLEO 2017 [2] |
| Ring III-V/Si | not applicable | 3 | 0.22 | Tran et al. JSTQE 2019 [7] |
| Ring III-V + PLC ($SiO_2$) | not applicable | 10 | 2.7 | Verdier et al. ECOC 2017 [4] |

## 4. MULTIMODE DBR

The objective of this demonstration based on the same technological platforms is to realize a mode-locked laser with repetition rate in the microwave range. As in the previous experiment, we use the same R-SOA, but here we add in the $Si_3N_4$ chip a 77 mm delay before a broad Bragg grating at the end (Fig. 3) to fabricate a multimode laser. To reduce the constraints for the lithography process, we choose to create the Bragg grating by using $3\lambda/(4n_{eff})$ long-teeth instead of the standard $\lambda/(4n_{eff})$ length ($n_{eff}$ is the effective refractive index of the mode). Its performance is slightly deteriorated, but as shown in Fig.4, our 1.5 mm-long Bragg grating has still a 95 GHz FWHM-bandwidth.

When aligning the R-SOA and the passive chip, we obtain a very multimode laser. Within a 10 dB bandwidth (measured to 436 pm), we count 48 optical lines which results in an optical comb with a 1.19 GHz repetition rate. It corresponds to an effective optical cavity length of 12.6 cm.

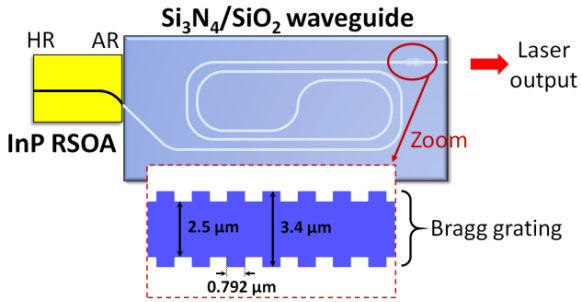



*Figure 3. Schematic of the multimode hybrid cavity.*

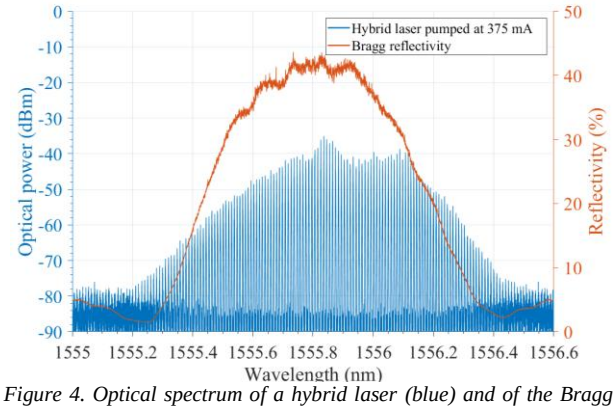



*Figure 4. Optical spectrum of a hybrid laser (blue) and of the Bragg reflexion (orange).*

The next step of this study will be to investigate the coherence of the peaks and the possibilities of passive or active mode-locking. It is a promising configuration, since it has very few elements and no saturable absorber. Furthermore, it can be tuned by adjusting the cavity length and working on the Bragg filter so as to obtain a specific repetition rate. Moreover it's worth pointing out this work is one of the very few that proposes a mode-locked laser by using the $Si_3N_4$ platform. Others integrated solutions are based either on monolithic or III-V/Si solutions [8], [9].

## 5. CONCLUSIONS

We demonstrated the flexibility of the hybridization between the InP and $Si_3N_4$ platforms. The striking advantage of this concept is to use the low losses of $Si_3N_4$ (2 dB/m in our devices), which enable the increasing of the cavity lengths. The main challenge is to control the coupling between the two components. We presented a single mode laser based on the butt coupling between a R-SOA and narrow Bragg grating, which presents 5.6 kHz linewidth. We demonstrated preliminary works on a multimode laser, which can become a compact and an affordable solution to mobile spectroscopic analysis and microwave signal generation.

## ACKNOWLEDGEMENTS

This work has been achieved with the support of the Direction Générale pour l'Armement (DGA). The authors thank the European Defense Agency (EDA) for the support to this work in the context of the project entitled "Photonic integrated circuits for multiband RF transceiver in arrayed systems (PICTURE)" funded by France and Italy and coordinated by Leonardo S.p.a. in the frame of the Project n° B-1487-IAP1-GP of the European Defense Agency. The authors thank the staff of the LETI silicon platform that managed to fabricate such passive devices with thick layers.

## REFERENCES

[1] C. Xiang, P. A. Morton, and J. E. Bowers: "Ultra-narrow linewidth laser based on a semiconductor gain chip and extended $Si_3N_4$ Bragg grating," *Optics Letters*, vol. 44. pp. 3825-3828, 2019.

[2] Y. Fan, *et al.*: "290 Hz intrinsic linewidth from an integrated optical chip-based widely tunable InP-$Si_3N_4$ hybrid laser." *Conference on Lasers and Electro-Optics (CLEO). IEEE*, 2017.

[3] P. Primiani, *et al.*: "Silicon Nitride Bragg Grating With Joule Thermal Tuning for External Cavity Lasers." *IEEE Photonics Technology Letters*, vol. 31. pp. 983-986, 2019.

[4] A. Verdier, *et al.*: "Wideband material for Low linewidth Widely Tunable Laser and Reach Extender for Optical Access Networks." *Conference on Lasers and Electro-Optics (CLEO). IEEE*, 2017.

[5] J. F. Bauters, *et al.*: "Planar waveguides with less than 0.1 dB/m propagation loss fabricated with wafer bonding." *Optics Express*, vol. 19. pp 24090-24101, 2011.

[6] D. Huang, *et al.*: "High-power sub-kHz linewidth lasers fully integrated on silicon." *Optica*, vol. 6. pp. 745-752, 2019.

[7] M. A. Tran, *et al.*: "Ring-resonator based widely-tunable narrow-linewidth Si/InP integrated lasers." *IEEE Journal of Selected Topics in Quantum Electronics*, vol. 26. pp. 1-14, 2019.

[8] S. Cheung, *et al.*: "1-GHz monolithically integrated hybrid mode-locked InP laser." *IEEE Photonics Technology Letters*, vol. 22. pp. 1793-1795, 2010.

[9] Z. Wang, *et al.*: "A III-V-on-Si ultra-dense comb laser." *Light: Science & Applications*, vol. 6. e16260, 2017.

# Near-optimal Sources of Single Photons in Silicon Quantum Photonics based on Intermodal Spontaneous Four-Wave-Mixing

*(Student)*

Alexandre Maïnos [1], Stefano Paesani [1], Massimo Borghi [2], Stefano Signorini [3], Lorenzo Pavesi [3], Anthony Laing [1]

[1]*Quantum Engineering Technology Labs, H. H. Wills Physics Laboratory and Department of Electrical and Electronic Engineering, University of Bristol, Bristol BS81FD, UK*

[2]*SM Optics S.R.L., Research Programs, Via John Fitzgerald Kennedy 2, 20871 Vimercate, Italy*

[3]*Department of Physics, University of Trento, Via Sommarive 14, 38123 Trento, Italy*

*e-mail: a.mainos@bristol.ac.uk*

## ABSTRACT

We report on a scalable near-unity purity and highly indistinguishable single photon source with high heralding efficiency integrated in a CMOS-compatible SOI platform. This source exploits the dual-mode pump-delayed excitation scheme [1] in a dispersion-engineered multi-mode waveguide through non-degenerate spontaneous four-wave-mixing. We experimentally demonstrate a spectral purity of $0.9904 \pm 0.0006$, a mutual indistinguishability of $0.987 \pm 0.002$ and an intrinsic heralding efficiency of $> 90\%$. We finally measure a heralded two-photon quantum interference with an unprecedented visibility of $0.96 \pm 0.02$ on chip. These results enable scaling quantum information processing with integrated photonics.

**Keywords**: Quantum, Photonics, Pure, Source, Intermodal, Spontaneous-four-wave-mixing

## 1 INTRODUCTION

Integrated photonics is considered as one of the most promising platforms for quantum information processing (QIP). A suitable hardware platform enabling quantum applications at scale required to outperform classical computers would necessitate the integration of millions of components, operating individually at a high fidelity [2]. Photonic QIP relies essentially upon three fundamental building blocks: generating, controlling and measuring quantum states [3] where the former has been the subject of extensive research in the fabrication of both deterministic and spontaneous single photon sources.

Solid-state sources such as quantum dots have attracted much interest for near-deterministic single photon generation. Nevertheless, their low-loss integration into photonic circuits at scale still remains impractical due to inefficient coupling to waveguides and low indistinguishability between different quantum emitters.

Spontaneous photon sources in silicon quantum photonic chips, based on spontaneous four-wave-mixing (SFWM), benefit from small footprints and mass-manufacturability, crucial for large-scale integration. However, SFWM in single-mode waveguides and ring cavities suffer from limited purity and heralding efficiency. Here, we report on a CMOS-compatible silicon photonics photon source based on intermodal SFWM in a multi-mode waveguide. By designing the waveguide dimensions, we engineer the phase matching conditions to obtain a near-ideal integrated spontaneous photon source. Our device is the first photon source that simultaneously meet all requirements for large-scale photonic quantum computing architectures [4].

## 2 DESIGN OF THE SOURCE

SFWM relies on both energy conservation and momentum conservation. When this process occurs in a single-mode waveguide, phase matching conditions are usually satisfied broadly around the pump, leaving energy conservation to dominate the photon generation process. This induces strong spectral anticorrelations in the joint spectral amplitude (JSA) that can only be suppressed by using spectral filtering drastically degrading heralding efficiency [5].

Here, we design a single photon source that uses intermodal SFWM in a spiralled multi-mode (MM) silicon waveguide to circumvent the low purity and low heralding efficiency issues encountered in the standard single-mode waveguide. To do so, we inject a coherent pulsed pump laser centred at 1550 nm initially propagated in the lowest order transverse magnetic (TM) mode and excite both TM0 and TM1 mode (see Figure 1A). A single photon in each mode is annihilated to create a signal and an idler photon, occupying TM0 and TM1 respectively [6]. The MM waveguide is engineered in such way that the dispersion relations avert any frequency conversion apart from two discrete sidebands away from the pump centre wavelength and with a bandwidth similar to that of the pump pulse. However, even though the two non-degenerate pump pulses diverge from each other due to different group velocities, their nonlinear interaction in the waveguide leaves residual correlations which can be eliminated by adding a temporal delay between the fast and the slow TM mode as illustrated in Figure 1A. The signal and idler photons initially in TM0 and TM1 are finally split up deterministically into two separate spatial modes via mode converters.

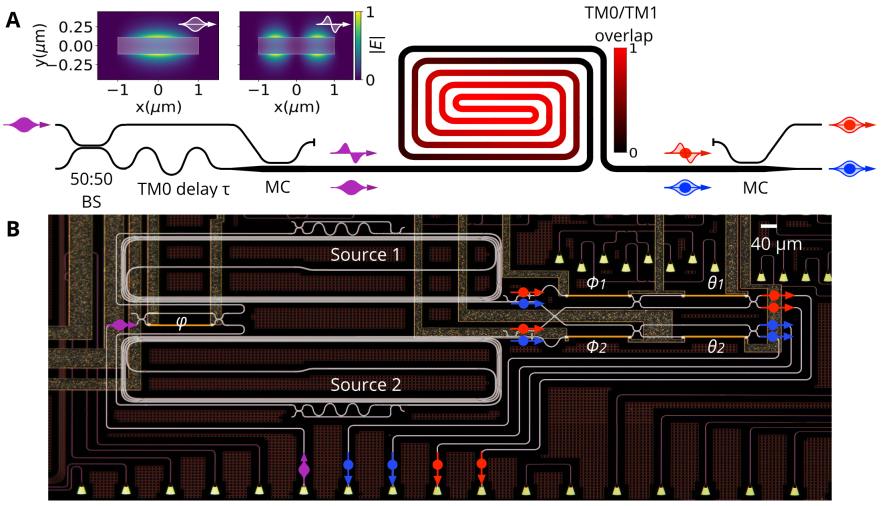



Figure 1. **Design of the multi-mode source. A.** Schematic of the source. **B.** Microscope image of the two sources device for characterising the source indistinguishability via two-photon RHOM interference and reconstruction of the generated entanglement via quantum state tomography.

## 3 RESULTS

In order to characterise the performance of the device, we integrate a reconfigurable silicon photonic circuit that enables the preparation of arbitrary two-qubit quantum states and performs reverse Hong-Ou-Mandel (RHOM) interference between two sources [7]. The intensity of the laser pumping each source is controlled by a Mach-Zehnder interferometer (MZI), driven by a phase $\varphi$. Moreover, arbitrary unitary operations are applied onto the signal (idler) photon via a phase-shifter $\phi_1$ ($\phi_2$) and an MZI via a phase $\theta_1$ ($\theta_2$) (see Figure 1B).

We carry out all measurements under the low-squeezing regime to keep the multi-photon noise negligible. The input pump power is then maintained at 0.5 mW (off-chip power), corresponding to a heralded second-order correlation function $g_h^{(2)}(0) = 0.0056$ and to a coincidence rate of 15 kHz. Broad-band off-chip filters are used to reject the pump but do not affect the photon spectral amplitudes given that their bandwidth is much broader than the photon spectra, resulting in a high intrinsic heralding efficiency of 91%.The remaining inefficiency is due to linear and non-linear losses in the multi-mode waveguide.

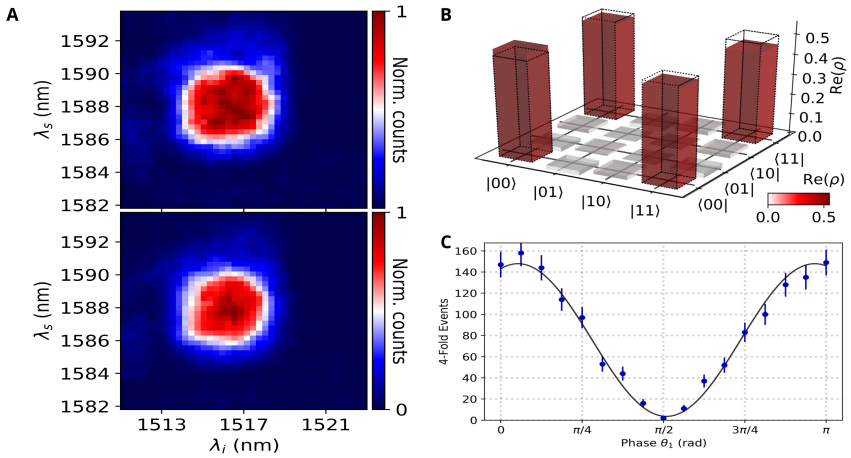



Figure 2. **Performance of the multiple sources. A.** Individual JSI distributions of two sources, showing an indistinguishability of 0.985. **B.** Density matrix of the generated two-qubit entangled state reconstructed from a quantum state tomography. The ideal maximally entangled Bell state $|\Phi_+\rangle = (|00\rangle + |11\rangle)/\sqrt{2}$ is depicted by the transparent bars. **C.** Heralded Hong-Ou-Mandel interference results. Points represent the raw number of four-photon events measured for an integration time of 4 hours for multiple values of phase $\theta$ of the MZI.

We characterise the source indistinguishability using three methods. The first consists of measuring the joint spectral intensity (JSI) of individual sources and calculating their mutual overlap (see Figure 2A). A second estimate relies on RHOM interference between two sources: the visibility measured by sweeping the phases $\phi_1 = \phi_2 = \phi$ provides a direct estimate of source indistinguishability [8]. The last consists of preparing a maximally entangled state and reconstructing its density matrix via quantum state tomography: the fidelity with

the ideal Bell state is estimated at 98.9% (see Figure 2B). All three methods provide consistent estimates of indistinguishability of $> 98\%$.

The purity of the single photons generated within the source is first evaluated using the JSIs. A first version of the design without any temporal delay between the two pump pulses yields a purity of 93.1%, then dramatically enhanced to 99.0% when the delay is applied. We perform a second estimate of purity by measuring the unheralded second-order correlation function and observe a thermal statistics signature with $g_u^{(2)}(0) = 1.973$, corresponding to 97.3% purity [9]. Finally, we implement HOM interferences [10] between signal photons and herald them by idler detections. HOM visibility comprises every source of noise among interfering photons. This quantity constitutes an essential figure of merit for determining the stochastic noise in quantum computing architectures and allows quantifying the computational complexity of multi-photon experiments in QSA. We resolve the resulting HOM fringe (see Figure 2C) of this four-fold experiment by scanning the reflectivity of the reconfigurable beam-splitter and obtain a raw visibility of 96.2%.

## CONCLUSION

We have presented a near-ideal single photon source that combines non-degenerate SFWM with a dual-mode pump-delayed strategy to tailor the nonlinear interaction of both TM0 and TM1 pump pulses. As a result, a substantial improvement in the purity, indistinguishability and heralding efficiency of the photons generated through that process has been observed. The results establish a significant leap towards the mass-manufacturability of ideal single photon sources. While error rates estimated from the observed HOM visibility remain below the fault-tolerant threshold for quantum error-correction in photonic quantum computing architectures [4], our analysis show promise to reach such threshold with minor changes onto our source design. For example, we estimate that improving the quality of the pump laser and using a fabrication process of a 4 nm uniformity, HOM visibilities of $> 0.999$ could be achieved. These results represent a milestone in the prospect of large-scale quantum information processing with integrated photonics.

## ACKNOWLEDGMENT

We acknowledge support from the Engineering and Physical Sciences Research Council (EPSRC) Hub in Quantum Computing and Simulation (EP/T001062/1), European Commission QUCHIP (H2020-FETPROACT-3-2014: quantum simulation), and the European Research Council (ERC). LP and SS has been supported by European Union's Horizon 2020 research and innovation programme under grant agreement No 820405. Fellowship support from EPSRC is acknowledged by A.L. (EP/N003470/1).

## REFERENCES

[1] B. Fang, O. Cohen, J. B. Moreno, and V. O. Lorenz: State engineering of photon pairs produced through dual-pump spontaneous four-wave mixing, Opt. Express 21, 2707-2717, 2013.

[2] S. Paesani, *et al.*: Generation and sampling of quantum states of light in a silicon chip. Nature Physics 15.9: 925-929, 2019.

[3] J. Silverstone, D. Bonneau, J. L. O'Brien, and M. G. Thompson: Silicon quantum photonics, IEEE Journal of Selected Topics in Quantum Electronics 22, 390-402, 2016.

[4] M. Gimeno-Segovia, P. Shadbolt, D. E. Browne, and T. Rudolph: From three-photon Greenberger-Horne-Zeilinger states to ballistic universal quantum computation. Physical review letters, 115(2), 020502, 2015.

[5] E. Meyer-Scott, *et al.*: Limits on the heralding efficiencies and spectral purities of spectrally filtered single photons from photon-pair sources. Physical Review A 95.6: 061803, 2017.

[6] S. Signorini, *et al.*: Intermodal four-wave mixing in silicon waveguides, Photon. Res. 6, 805-814, 2018.

[7] J. W. Silverstone, *et al.*: On-chip quantum interference between silicon photon-pair sources. Nature Photonics 8.2: 104, 2014.

[8] S. Paesani: Large-scale integrated quantum photonics: development and applications (Doctoral dissertation, University of Bristol), 2019.

[9] A. Christ, K. Laiho, A. Eckstein, K. N. Cassemiro and C. Silberhorn: Probing multimode squeezing with correlation functions. New Journal of Physics 13.3: 033027, 2011.

[10] C. K. Hong, Z. Y. Ou and L. Mandel: Measurement of subpicosecond time intervals between two photons by interference. Physical review letters, 59(18), 2044, 1987.

# Silicon source providing multi-spectral photon pairs with high-quality entanglement

Dorian Oser[1], Florent Mazeas[2], Carlos Alonso-Ramos[1], Xavier Le Roux[1],
Laurent Vivien[1], Sébastien Tanzilli[2], Éric Cassan[1], Laurent Labonté[2]
[1]*Centre de Nanosciences et de Nanotechnologies, CNRS, Universié Paris-Sud, Université Paris-Saclay, C2N, Palaiseau, France*
[2]*Université Côte d'Azur, CNRS, Institut de physique de Nice, France*
*e-mail: dorian.oser@c2n.upsaclay.fr*

## ABSTRACT

The silicon photonic platform has the ability of generating and manipulating individual quantum states on single chips. However, a major challenge is the on-chip rejection of the pump without affecting the pairs generated by the non-linear processes. We report the integration on a single substrate a photon-pair generator with a pump-rejection filter. It allowed us to generate photon pairs with near-perfect entanglement on 11 pairs of wavelength channels simultaneously, while achieving 85 dB of rejection of the pump. The frequency comb generated was at telecom wavelengths and compatible with the ITU channels spacing.

**Keywords**: ring resonator, photonics, SFWM, multimode, Bragg filters.

## 1 INTRODUCTION

Entanglement is becoming a resource for the quantum networks which requires a large number entangled photons. The Silicon-on-Insulator (SOI) platform provide industry ready photonic circuit that can be tailored for quantum application. Photon pairs can be produced on SOI thanks to ring resonators. They enhances the nonlinear effect of the Silicon by forming a cavity. Thanks to spontaneous four wave mixing (SFWM), signal/idler pairs are generated in the ring, where we showed high visibility and brightness for multiple pairs simultaneously [1]. However, SFWM has the disadvantage of requiring a pump close to the generated photon pairs in terms of wavelength. This makes the pump rejection challenging as it must be applied (>100 dB) on a relatively small bandwidth (∼10 nm). His has been demonstrated using active devices [2], [3] but at the cost of a high complexity, due to the control of all the filters which also brings large coincidence rate losses.

We use instead cascaded Bragg filter to rejection the pump. Such filters avoid saturation by rejecting in a higher order mode the pump and then scattering it with a single mode waveguide. This breaks the coherency between filters. Such strategies allowed us to achieve large rejection of 80 dB [4].

## 2 SAMPLE & EXPERIMENT

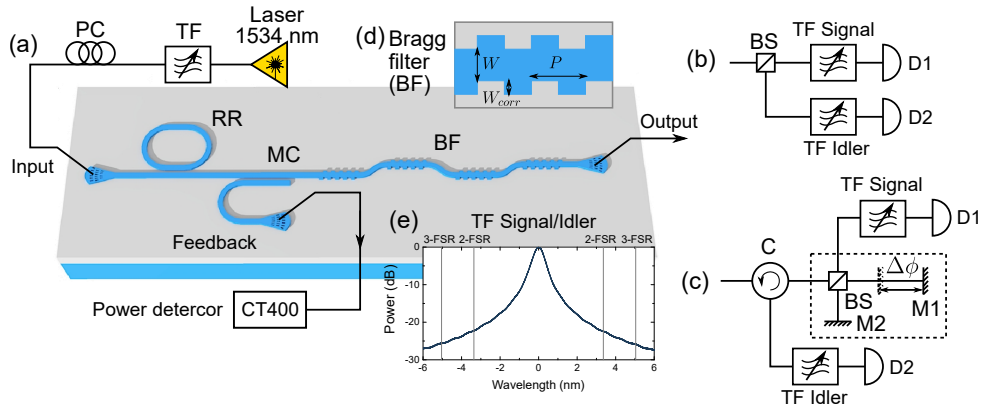



Figure 1. Schematics of the experimental setup. (a) Input laser with filter rejecting the amplified spontaneous emission (anti-ASE) and a polarization controller (PC). The light is injected in the ring resonator (RR), and then propagate to a modal directional coupler (MC) and through the stop-band filter (BF). The output of the chip is connected to either, (b) coincidence configuration with a beam splitter and bandpass filters (BP) to demultiplex signal and idler photon, or to (c) the entanglement qualification in a folded-Franson configuration. (d) Schematic top-view of the filter geometry. (e) Spectrum of the signal and idler filters which exhibit 22 dB and 25 dB rejection for the 2-FSR and 3-FSR configurations, respectively.

A ring resonator was combined with a cascaded filter on a single chip of silicon. This structure can generate pair of photons on all of the ring resonances and can be aligned to the telecom grid channel by carefully

choosing the ring free spectral range. The sample was made on SOI with a silicon layer thickness of 220 nm. Electron beam lithography was used to print the pattern. This structure only require a single step of lithographic for fabrication and no active tuning. All filter sections are naturally aligned by the fabrication process, using the cascaded filters strategy (figure 1d) [4].

The sample was pumped with a tunable laser which is cleaned from the amplified spontaneous emission. The ring resonator (RR) has $Q$-factor of 30 000 which converts the pump into an frequency comb of entangled-photon pairs, see figure 1. Then the Bragg filter (BF) cleans the comb from the pump (-85 dB attenuation). The pump rejection filter has a 3-dB bandwidth of 5.5 nm which does not allow to access the closest resonances (1-FSR) from the pumped resonance. A modal coupler is placed between the ring and the filter to collect the rejected light [5]. This allowed us to make sure that we are pumping the cavity at the right wavelength and control the alignment of the input fiber. The generated comb is demultiplexed and the pairs are sent to a coincidence measurement (figure 1b) to ensure the quantum nature of the light. Then they are sent to a two-photon interference measurement experiment (figure 1c), to measurement the entanglement between the pairs.

## 3 RESULTS

Entanglement is analyzed using a folded Franson arrangement consisting of a single unbalanced fiber Michelson interferometer. The integrated filter combined with a ring yields a rate of 480 pairs per seconds in the first available resonance (2-FSR from the pumped resonance). These photons are sent in the interferometer where the phase is changed. This reveals the two photon interferences as a sinusoidal oscillation of the coincidence rate. By fitting the oscillations with $\sim N_0(1 - V\cos(2\varphi))$, we can extract the visibility $V$. The closer it is to one, the more entangled the pair is.

We proceeded to test the entanglement over 11 pairs of resonances over 40 nm. We measured an raw visibility higher than >90 % (Fig. 2) for all the quantum channel tested with a high internal rate of >2 MHz. This was achieved by adding only a 20dB-crosstalk de-multiplexing after the chip, see figure 1e. On top of the integrated filter which uses multi-mode effects to break the coherence between filters.

This all passive system was made by a single lithographic step with large dimensions (>75 nm), which can be fabricated using industrial deep-UV lithography. Thanks to its simplicity and low loss [4], it does not increase the fabrication process while keeping the rate of generated pairs high. Moreover, there are already many de-multiplexing strategies on-chip, it is not a limitation.

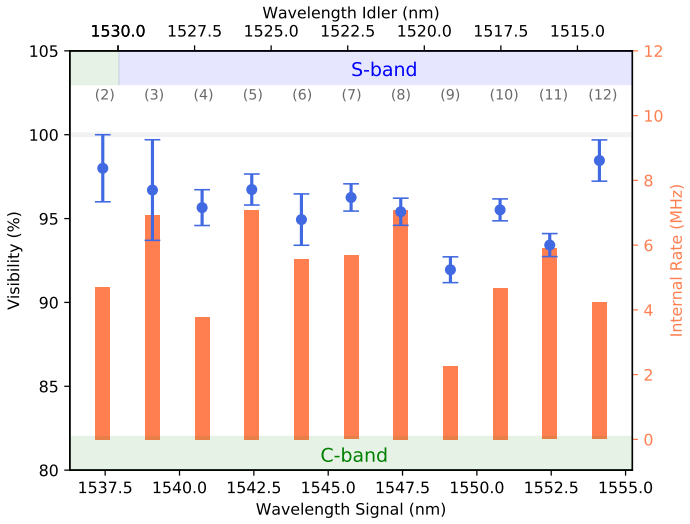



Figure 2. Raw visibilities and internal rate plotted as a function of the signal and idler wavelengths. For sake of clarity, we associate signal and idler wavelengths to their corresponding telecom band. The visibility was fitted using a time coincidence window of 200 ps centered around the maximum of the central coincidence peak.

## 4 CONCLUSION

We have demonstrated that using a new strategy of cascaded filters, we could make a source of entangled pairs of photons. This all-passive photon-pair source is an important step towards the integrated resource of telecom entangled photons. The low loss [4] and simplicity of the proposed approach allows the implementation of photon-pair sources with a high generation rate, based on a single lithography step. The pair generated yield a near unity visibility. This system directly can be used on quantum key distribution network to as a cheap source of entangled photon pair.

## REFERENCES


[1] F. Mazeas, *et al.*, High-quality photonic entanglement for wavelength-multiplexed quantum communication based on a silicon chip, Opt. Ex. **24**, 28731-28738 (2016).

[2] M. Piekarek, *et al.*, High-extinction ratio integrated photonic filters for silicon quantum photonics, Opt. Lett. **42**, 815-818 (2017)

[3] J. R. Ong, *et al.*, Ultra-high-contrast and tunable-bandwidth filter using cascaded high-order silicon microring filters. IEEE Phot. Tech. Lett., **25**, 1543-1546. (2013)

[4] D. Oser, *et al.*, Coherency-Broken Bragg Filters: Overcoming On-Chip Rejection Limitations., Laser Photonics Rev. 13.8 (2019)

[5] J. Wang, *et al.*, Broadband and fabrication-tolerant on-chip scalable mode-division multiplexing based on mode-evolution counter-tapered couplers, Opt. lett. **40**, 1956–1959 (2015).

# Monolithically integrated differential phase shift transmitter for quantum key distribution

**H. O. Çirkinoglu[1], R. Santos[2], K.Williams[1], X. Leijtens[1]**
[1] Eindhoven University of Technology, 5612 AZ, Eindhoven, The Netherlands
[2] SMART Photonics, Eindhoven, The Netherlands
*e-mail: h.o.cirkinoglu@tue.nl*

## ABSTRACT

An integrated differential phase shift QKD transmitter, which consist of a distributed Bragg reflector laser, a phase modulator, and Mach-Zehnder modulator sections for pulse carving and optical attenuation has been designed and fabricated. Initial characterization shows single mode operation of the laser with a linewidth around 2 MHz, and an achievable optical attenuation of more than 60 dB.

**Keywords**: Photonic Integrated Circuits, Quantum Key Distribution

## 1.INTRODUCTION

Quantum communication offers theoretically secure sharing of information through exploitation of the probabilistic nature of quantum physics [1]. Secure sharing of encryption keys can be guaranteed through quantum key distribution (QKD), without making any assumptions on how much computational power an eavesdropper might have [2]. Even though many successful quantum key distribution applications have been demonstrated [3, 4], many of them rely on bulk optics. Photonic integration offers realization of different optical functionalities on a single photonic chip; providing a platform for manufacturing scalable, robust, and mass-producible components for quantum key distribution applications. [5, 6]. Over more than three decades, there have been a number of protocols proposed for quantum key distribution, including BB84 [7], differential-phase shift (DPS) [8], and coherent-one-way (COW) [9]. In this work, we present an integrated DPS QKD transmitter, targeting the generation of weak pulses of phase-encoded optical coherent states. The fabrication of the chip is carried out through the generic platform of Smart Photonics [10, 11] as a part of the European Quantum Flagship project UNIQORN [12]. The fabricated transmitter consists of a distributed Bragg reflector (DBR) laser, an electro-refraction modulator to control the phase between pulses, a Mach-Zehnder Pulse carver to erase transition effects, and variable optical attenuator (VOA) stages to achieve the required signal levels. The security of the quantum channel is potentially compromised by the imperfect modulation of amplitude and phase of the transmitted signal [13]. We present the characterization results of the components of the chip, some of which were previously reported in [14]. We measured the laser spectrum and the laser linewidth, the dynamic response and the extinction ratio of the pulse carver, as well as the characteristics of the variable optical attenuator.

## 2.DIFFERENTIAL PHASE SHIFT QUANTUM KEY DISTRIBUTION

In DPS QKD using coherent light [15], the sender Alice prepares a pulse train of weak coherent states with average photon number of less than one, where the phase of each state is encoded randomly between $\{0, \pi\}$. The receiver Bob divides the received signal into two paths, and recombines them using a delay interferometer (DI) with a delay time equal to the time between each consecutive pulses. The DI is followed by photon detectors at its two outputs. The phase information at a time instance is retrieved based on which detector detects a photon. After transmission and detection, Bob reveals the information of the time instances at which a photon is detected. From this information, Alice can deduce what bit string Bob has. Compared to the well-known BB84 protocol, DPS QKD is advantageous due to the simplicity of detection, and utilization of each detected photon without the need of basis choice or sifting [16].

## 3.TRANSMITTER CHIP

The realized transmitter employs a light source consisting of a DBR laser [17] for light generation, an electro-refractive phase modulator section for phase encoding of the signal, and a Mach-Zehnder modulator (MZM) with electro-refractive modulators (ERM) in each of the interferometer arms for pulse carving. Multimode interference devices are used for splitting and combining of the signals. The transmitter is designed to be capable of switching between the classical and the quantum signal regime. In order to attain the required signal attenuation, the source is followed by a variable optical attenuator (VOA) function. For this, the circuit employs a cascade of three tunable Mach-Zehnder interferometers that can be tuned to each achieve up to 20 dB suppression. A schematic of the circuit, and a microscope image of the chip is shown in Fig. 1. The characterization results of the fabricated chips are presented below.

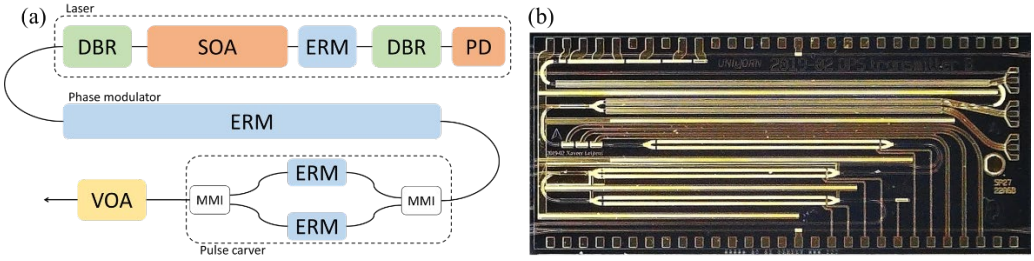



*Figure 1. (a) The schematic of the DPS QKD transmitter chip, (b) Microscope image of the fabricated chip.*

The DBR laser operates with a threshold current ($I_{th}$) of 28 mA at 22.1 ºC, comparable to values for previously fabricated lasers with the same design [17]. The power of the light collected using a lensed fiber from an output waveguide after the pulse carver section is at around 0.5 mW for the SOA bias current of 100 mA.

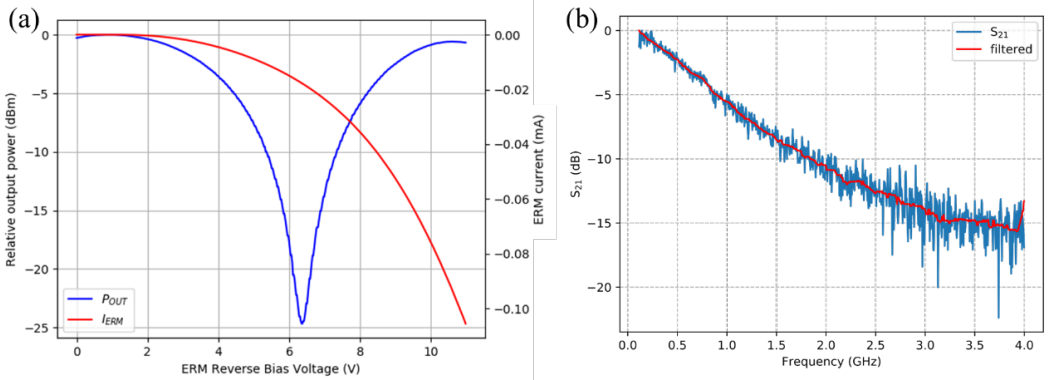



*Figure 2. (a) The relative transmission of the first stage attenuator based on electro-refraction. (b) The dynamic response of the pulse carver*

The attenuation of the output signal with the Mach-Zehnder-based VOA is evaluated. The output optical power, and the photo-current generated in the 2-mm-long active modulator section is recorded while varying the applied reverse bias voltage to one of the arms of the interferometer. The second arm is kept at a constant bias voltage. The response is given in Fig. 2(a). The figure shows a good extinction ratio of 24.6 dB, and a reverse bias voltage of 5.4 V is needed for π phase shift. The additional attenuation at 9.7 V bias voltage is at around 0.6 dB. The small signal response of the MZM pulse carver is measured using Agilent N4373C lightwave component analyser. The corresponding scattering parameter ($S_{21}$) is recorded for different speeds of the modulation signal applied to the MZM pulse carver. The resulting transmission characteristics (shown in blue), along with the trace (shown in red) obtained by applying a median filter to the acquired data is shown in Fig. 2(b), indicating a 3-dB cut-off point of around 590 MHz.

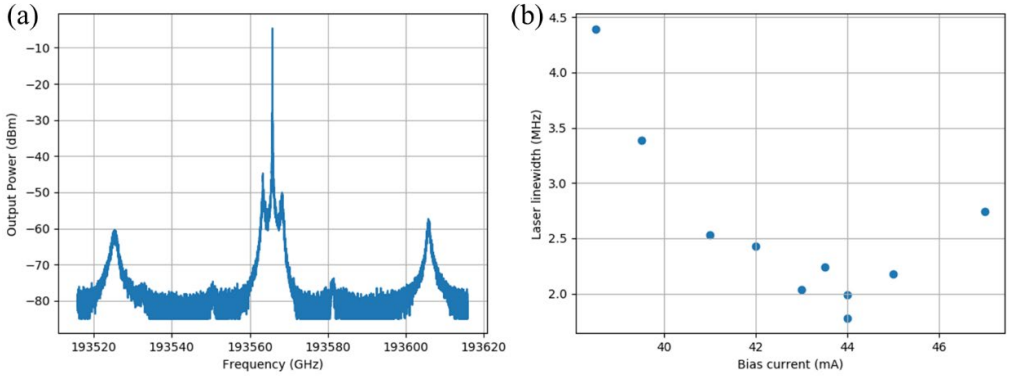



*Figure 3. (a) Optical spectrum of the DBR laser (b) Linewidth measurement results for different bias current values*

The optical spectrum, recorded by APEX 2041A spectrum analyzer with a resolution of 20 MHz is depicted in Fig. 3(a). The laser operating at 44 mA drive current results in a single mode emission around 1550 nm with >55 dB side-mode-suppression ratio. Two neighboring peaks around the main mode result from a relaxation oscillation frequency of around 3 GHz. The linewidth measurements for various bias current values are acquired using OEWaves OE4000 phase noise and linewidth measurement system, and are given in Fig. 3(b). The measurements display an intrinsic laser linewidth of ~2MHz around 44 mA bias current. For 1 GHz modulation of the signal, a linewidth of 2 MHz corresponds to 0.2% of the receiver interferometer free-spectral-range, which results in a quantum bit error rate of <0.5% [13].

## 4.DISCUSSION

The tests carried out so far aimed to anticipate the suitability of the transmitter chip in a DPS QKD scheme, through the analysis of the performances of its individual components. Based on the data given in Fig 2(a), we expect to be able to achieve an attenuation of the signal by > 60 dB, with a three-stage MZM. The frequency response of the pulse carver indicate that the modulation rate of around 0.6 GHz is achievable. Generation of weak coherent states requires attenuation of the optical signal to a level of <1 photons per pulse, while maintaining a good optical signal-to-noise ratio. In our device, where the light source is integrated together with rest of the circuit, the signal suffers from a flat frequency noise, which originates from amplified spontaneous emission at the laser active region. Furthermore, the unguided stray light originating from spontaneous emission remains independent from the applied attenuation, decreasing the signal-to noise ratio as signal power is reduced. Our further planned investigations include the analysis of the transmitted signal in terms of single photon characteristics, followed by the verification of the transmitter in a DPS QKD testbed. In order to drive all required signals simultaneously for the desired operation, the samples will be wire-bonded and connectorized.

## ACKNOWLEDGEMENTS

This work has received funding from the European Union's Horizon 2020 research and innovation programme through the Quantum-Flagship project UNIQORN under grant agreement No 820474. Nazca Design was used to generate the mask layout in this work.

## REFERENCES

1. H.K. Lo, M. Curty, and K. Tamaki, "Secure quantum key distribution," Nature Photonics, vol. 8, 595-604, 2014.
2. V. Scarani, H. Bechmann-Pasquinucci, N.J. Cerf, M. Dušek, N. Lütkenhaus, and M. Peev, "The security of practical quantum key distribution," Reviews of Modern Physics, vol. 81, 1301-1350, 2009.
3. H. Takesue, E. Diamanti, T. Honjo, C. Langrock, M.M. Fejer, K. Inoue, and Y. Yamamoto, "Differential phase shift quantum key distribution experiment over 105 km fibre," New Journal of Physics, vol. 7, 232, 2005.
4. M. B. Costa e Silva, Q. Xu, S. Agnolini, P. Gallion, and F.J. Mendieta. "Homodyne detection for quantum key distribution: an alternative to photon counting in BB84 protocol" in Proceedings of SPIE Photonics North, vol. 6343, 63431R, 2006.
5. P. Sibson, C. Erven, M. Godfrey, S. Miki, T. Yamashita, M. Fujiwara, M. Sasaki, H. Terai, M.G. Tanner, C.M. Natarajan, R.H. Hadfield, J.L. O'Brien, and M.G. Thompson, "Chip-based quantum key distribution," Nature Communications, vol. 8, 13984, 2017.
6. P. Sibson, J.E. Kennard, S. Stanisic, C. Erven, J.L. O'Brian, and M.G. Thompson, "Integrated silicon photonics for high-speed quantum key distribution," Optica, vol. 4, 172-177, 2017.
7. C.H. Bennett, and G. Brassard, "Quantum public key distribution system," IBM Technical Disclosure Bulletin, vol. 28, 3153-3163, 1985.
8. K. Inoue, E. Waks, and Y. Yamamoto, "Differential phase shift quantum key distribution," Physical Review Letters, vol. 89, 037902, 2002.
9. D. Stucki, N. Brunner, N. Gisin, V. Scarani, and H. Zbinden, "Fast and simple one-way quantum key distribution," Applied Physics Letters, vol. 87, 194108, 2005.
10. Smit, Meint, et al, "An introduction to InP-based generic integration technology," Semiconductor Science and Technology, vol. 29.8, 083001, 2014.
11. "Smart Photonics", http://smartphotonics.nl.
12. "UNIQORN Project", http://quantum-uniqorn.eu.
13. T. Honjo, T. Inoue, and K. Inoue, "Influence of light source linewidth in differential-phase-shift quantum key distribution systems," Optics Communications, vol. 284, 5856-5859, 2011.
14. H.O. Çirkinoglu, R. Santos, K. Williams, and X. Leijtens, "An InP-based integrated modulated coherent state source for differential phase shift quantum key distribution," accepted for publication in 24th Annual Symposium of the IEEE Photonics Benelux Chapter, November 21-22, 2019, Amsterdam, Netherlands.
15. K. Inoue, E. Waks, and Y. Yamamoto. "Differential-phase-shift quantum key distribution using coherent light." Physical Review A vol. 68.2, 022317, 2003.
16. B. Schrenk, M. Hentschel, and H. Hübel. "Single-Laser Differential Phase Shift Transmitter for Small Form-Factor Quantum Key Distribution Optics." Optical Fiber Communications Conference and Exposition (OFC), IEEE, 1-3, 2018.
17. D. Zhao, "High-precision Distributed Bragg Reflectors in a Generic Photonics Integration Platform". PhD thesis, Eindhoven University of Technology, Eindhoven, The Netherlands, 2018. ISBN 978-90-386-4627-5.

# Ultra-Broadband Passive Phase Shifter Using Anisotropic Subwavelength Metamaterials

**David González-Andrade[1,*], José Manuel Luque-González[2], J. Gonzalo Wangüemert-Pérez[2], Alejandro Ortega-Moñux[2], Pavel Cheben[3], Íñigo Molina-Fernández[2,4], Aitor V. Velasco[1]**

[1] Instituto de Óptica Daza de Valdés, Consejo Superior de Investigaciones Científicas (CSIC), Madrid 28006, Spain

[2] Departamento de Ingeniería de Comunicaciones, ETSI Telecomunicación, Universidad de Málaga, Málaga 29071, Spain

[3] National Research Council Canada, 1200 Montreal Road, Bldg. M50, Ottawa K1A 0R6, Canada

[4] Bionand Center for Nanomedicine and Biotechnology, Parque Tecnológico de Andalucía, Málaga 29590, Spain

*e-mail: david.gonzalez@csic.es*

## ABSTRACT

Optical phase shifters are a cornerstone constituent in most photonic integrated circuits aimed at high-end applications. However, most progress has focused on active phase shifters in recent years, while passive phase shifters have barely evolved. Here, we propose a new type of ultra-broadband passive phase shifter that exploits anisotropy and dispersion engineering in subwavelength metamaterial waveguides. Floquet-Bloch simulations of our proposed device predict a phase shift error below ±1.7° over an outstanding 400 nm bandwidth (1.35 – 1.75 μm). The subwavelength engineered PS was fabricated on an SOI platform and our measurements show a four-fold reduction in the phase variation compared to other conventional phase shifters based on tapered waveguides.

**Keywords**: phase shifter, silicon-on-insulator, subwavelength grating, metamaterial, ultra-broadband.

## 1. INTRODUCTION

Silicon-on-insulator (SOI) has become a ubiquitous platform for the development of several cutting-edge applications, including telecom and datacom, sensing, quantum computing, and microwave and terahertz photonics [1]-[3], to name a few. The SOI platform benefits from the compatibility with already-existing CMOS facilities that enables mass production of photonic integrated circuits (PICs) in a cost-effective way. Additionally, the high refractive index contrast between the silicon core waveguide and the silicon dioxide ($SiO_2$) layer results in a dense integration of photonic devices on a single chip, which facilitates the miniaturization of complex photonic systems.

Most PICs rely on fundamental building blocks like beam splitters [4], filters [5] and (de)multiplexers [6]. Optical phase shifters (PSs) are another essential constituent in photonic systems to induce a specific phase shift between different signals. In the last years, research efforts have mainly focused on the development of active phase shifters (PSs), especially for the implementation of optical modulators and switches. These devices are typically based on thermo-optic [7] or free carrier plasma dispersion [8] effects that enable to dynamically tune the phase shift between signals by means of an active control element. Conversely, passive PSs have barely evolved and are usually replaced by active PSs to compensate for possible fabrication errors or to adjust the phase response at a particular wavelength. However, passive PSs are attracting increasing attention for a wide range of applications such as mode-division multiplexing (MDM), optical 90° hybrids, beam splitting for different mode orders and for arbitrary power ratios [9]-[11].

In this work, we present an ultra-broadband passive 90° PS exploiting dispersion and anisotropy engineering in subwavelength grating (SWG) metamaterial waveguides. Our Floquet-Bloch simulations predict a phase error as low as ±1.7° over an outstanding 400 nm bandwidth (1.35 – 1.75 μm) for transverse electric (TE) polarization. The device was fabricated and a phase slope of only 16°/μm was measured within a 145 nm wavelength range (1.495 – 1.64 μm), limited by the laser source of our setup. This is a remarkable four-fold reduction compared to the 64°/μm measured for a conventional PS based on tapered waveguides.

## 2. DESIGN

The proposed PS is based on two parallel SWG waveguides of the same length as schematically shown in Fig. 1(a). SWG structures are an alternating disposition of different materials with a pitch below half the wavelength, which behave as a diffraction-less anisotropic medium [12]. For the design, we considered an SOI material platform based on 220-nm-thick Si waveguides and $SiO_2$ buried oxide (BOX) and upper cladding layers. The width of both waveguides must be wide enough to hold paraxiality condition [13] and, at the same time, to improve tolerances to width deviations, i.e. the variation of the effective index with respect to changes in width is lower than for narrow waveguides. In this way, the phase shift induced between two wide SWG waveguides can be simplified to [14]:

$$\Delta\Phi(\lambda) \approx \frac{\pi\lambda n_{xx}}{4n_{zz}^2}\left(\frac{1}{W_{e,B}^2}-\frac{1}{W_{e,A}^2}\right)L_{PS}, \quad (1)$$

where $\lambda$ is the free-space wavelength, $W_e$ is the effective width, $L_{PS}$ is the length of the SWG waveguides, and $n_{xx}$ and $n_{zz}$ are the refractive indexes of the 2D equivalent anisotropic medium in the $x$ and $z$ directions, respectively.

By judiciously selecting the pitch ($\Lambda$) and the duty cycle (DC) of the SWG waveguides, the term $n_{xx}/n_{zz}^2$ can be engineered to be inversely proportional to $\lambda$, thus yielding an almost flat phase shift response. To this end, we selected widths of $W_A = 1.8$ µm and $W_B = 1.6$ µm, a pitch value of 200 nm and a duty cycle of 50% to ensure a minimum feature size of 100 nm. Moreover, SWG tapers of $L_T = 3$ µm were included to perform an adiabatic transition between the non-periodic waveguides ($W_I = 500$ nm) and wide SWG waveguides. Taking into account that the phase shift introduced by SWG tapers is approximately 20°, the length of the phase shifting section is only $L_{PS} = 16.8$ µm to achieve a total 90° phase shift at the design wavelength of 1.55 µm.

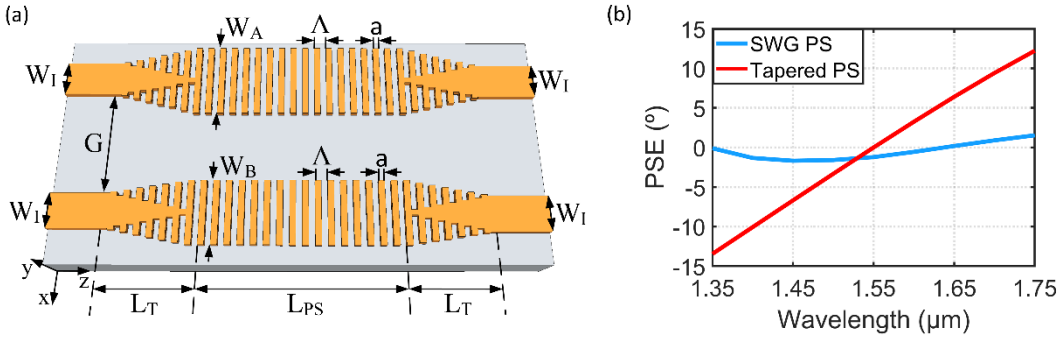



*Figure 1. (a) Schematic of the proposed phase shifter based on SWG metamaterial waveguides. (b) Simulated phase shift error as a function of the wavelength for the SWG PS (blue curve) compared to a conventional PS based on two tapers in back-to-back configuration and a straight waveguide (red curve).*

To assess the performance of the designed 90° PSs, we define the phase shift error (PSE) as the deviation from the target 90° phase shift. Figure 1(b) shows the PSE as a function of the wavelength for our SWG PS (represented with the blue curve) and a conventional PS based on two tapers in back-to-back configuration and a straight waveguide (in red). It should be noted that the tapered PS is also designed to perform a 90º phase shift. A small PSE of only ±1.7° is attained for the proposed SWG PS over an ultra-broad bandwidth of 400 nm (1.35 – 1.75 µm), whereas the conventional PS yields a PSE of ±13.5° within the same wavelength range.

## 3. EXPERIMENTAL RESULTS

Both SWG and tapered PSs were fabricated on a 220-nm-thick SOI platform with 2-µm-thick BOX using electron beam (e-beam) lithography and a reactive ion etching (RIE) process. Scanning electron microscope (SEM) of the fabricated devices are shown in Figs. 2(a) and 2(b), respectively. After taking SEM images, the circuit was covered with a 2.2-µm-thick $SiO_2$ upper cladding.

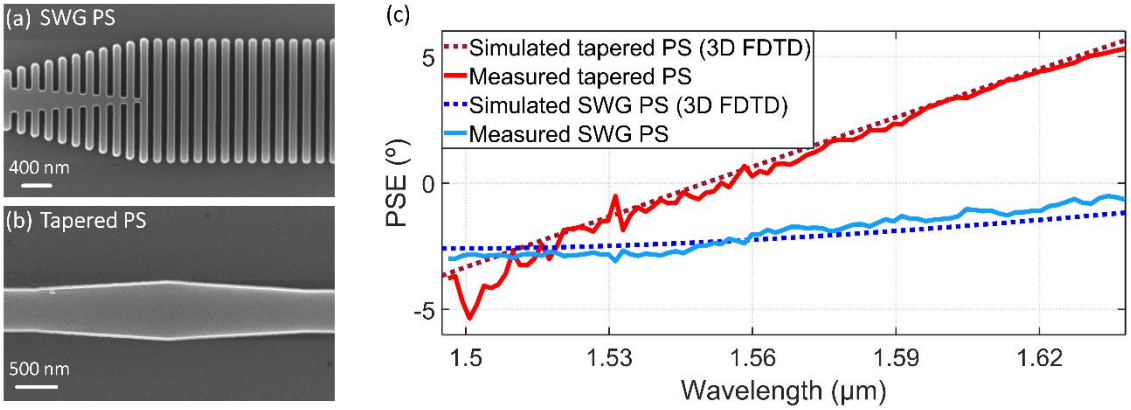



*Figure 2. Scanning electron microscope images of the upper arm of (a) our proposed SWG PS and (b) the tapered PS. (c) Measured phase shift error as a function of the wavelength for the SWG PS (blue) and the tapered PS (red). 3D FDTD simulation results are included (dotted lines) for comparison.*

To experimentally characterize the fabricated PSs, we used Mach-Zehnder interferometer (MZI) consisting of two SWG multimode interference (MMI) couplers and 14 PSs connected in series. The intensity signal measured at the MZI output is modulated with a period depending on the optical path delay between the arms of the MZI,

i.e. based on the phase shift response of the PSs. We developed a circuit model to simulate the MZI and estimate the phase error introduced by fabrication deviations. These errors were subtracted from the measured phase shift response, which was obtained by solving the matrix system posed by the MZI test structure when transmission matrices are considered [14].

Figure 2(c) shows that the measured wavelength dependence of tapered and SWG PSs (solid curves) are in very good agreement with our 3D finite difference time domain (FDTD) simulation results (dotted curves). The proposed SWG PS provides a phase slope as small as 16°/μm, whereas the tapered PS based on conventional (non-periodic) waveguides yields a phase slope of 64°/μm. This is a four-fold enhancement in terms of bandwidth within the measured wavelength range of 145 nm (1.495 – 1.64 μm).

## 4. CONCLUSIONS

In conclusion, we report on the experimental demonstration of an ultra-broadband PS based on waveguides of equal length. Limitations posed by conventional PSs based on non-periodic waveguides are overcome by exploiting the additional degrees of freedom provided by SWG metamaterial waveguides. Our proposed SWG PS leverages inherent anisotropy properties of SWG waveguides in combination with dispersion engineering to achieve a simulated phase shift error of only ±1.7° over an unprecedented 400 nm bandwidth. The device was fabricated and the concept of flattening the phase response was verified, showing a four-fold reduction compared to the tapered PS over the measured 145 nm bandwidth (1.495 – 1.64 μm). The proposed SWG PS opens new venues for the implementation of PICs targeting cutting-edge applications like quantum photonics and MDM.

## ACKNOWLEDGEMENTS

This work has been funded in part by the Spanish Ministry of Science, Innovation and Universities (MICINN) under grants RTI2018-097957-B-C33, TEC2015-71127-C2-1-R (FPI BES-2016-077798), CDTI SNEO-20181232 (Alcyon Photonics S.L.), and TEC2016-80718-R; the Spanish Ministry of Education, Culture and Sport (MECD) (FPU16/06762); and the Community of Madrid – FEDER funds (S2018/NMT-4326). This project has received funding from the Horizon 2020 research and innovation program under the Marie Sklodowska-Curie No. 734331.

## REFERENCES

[1] J. G. Wangüemert-Pérez, *et al.*: Subwavelength structures for silicon photonics biosensing, *Opt. Laser Technol.*, vol. 109. pp. 437-448, Jan. 2019.

[2] N. C. Harris, *et al.*: Large-scale quantum photonic circuits in silicon, *Nanophotonics*, vol. 5. pp. 456-468, March 2016.

[3] D. Marpaung, *et al.*: Integrated microwave photonics, *Nat. Photonics*, vol. 13. pp. 80-90, Jan. 2019.

[4] D. González-Andrade, *et al.*: Polarization- and wavelength-agnostic nanophotonic beam splitter, *Sci. Rep.*, vol. 9. pp. 3604, Mar. 2019.

[5] D. Oser, *et al.*: Coherency-broken Bragg filters: overcoming on-chip rejection limitations, *Laser Photon. Rev.*, vol. 13. pp. 1800226, Jul. 2019.

[6] P. J. Bock, *et al.*: Demonstration of a curved sidewall grating demultiplexer on silicon, *Opt. Express*, vol. 20. pp. 19882-19892, Aug. 2012.

[7] G. Cocorullo, *et al.*: Temperature dependence of the thermo-optic coefficient in crystalline silicon between room temperature and 550 K at the wavelength of 1523 nm, *Appl. Phys. Lett.*, vol. 74. pp. 3338-3340, Apr. 1999.

[8] R. A. Soref, *et al.*: Electrooptical effects in silicon, *IEEE J. Quantum Electron.*, vol. 23. pp. 123-129, Jan. 1987.

[9] D. González-Andrade, *et al.*: Ultra-broadband mode converter and multiplexer based on sub-wavelength structures, *IEEE Photonics J.*, vol. 10. pp. 2201010, Apr. 2018.

[10] M. Cherchi, *et al.*: Unconstrained splitting ratios in compact double-MMI couplers, *Opt. Express*, vol. 22. pp. 9245-9253, Apr. 2014.

[11] F. Ren, *et al.*: Variable-ratio mode-insensitive 1×2 power splitter based on MMI couplers and phase shifters, *IEEE Photonics J.*, vol. 10. pp. 7104912, Sep. 2018.

[12] P. Cheben, *et al.*: Subwavelength integrated photonics, *Nature*, vol. 560. pp. 565-572, Aug. 2018.

[13] L. B. Soldano, *et al.*: Optical multi-mode interference devices based on self-imaging: principles and applications, *J. Lightwave Technol.*, vol. 13. pp. 615-627, Apr. 1995.

[14] D. González-Andrade, *et al.*: Ultra-broadband nanophotonic phase shifter based on subwavelength metamaterial waveguides, *Photon. Res.*, doc. ID 373223 (posted 24 December 2019, in press).

# Independent phase matching for TE and TM polarization in directional couplers with tilted subwavelength structures

*(Student Paper)*

**José Manuel Luque-González[1*], Alaine Herrero-Bermello[2†], Alejandro Ortega-Moñux[1], Marina Sánchez-Rodríguez[1], Aitor V. Velasco[2], Jens H. Schmid[3], Pavel Cheben[3], Íñigo Molina-Fernández[1,4], Robert Halir[1,4]**
[1]Universidad de Málaga, Dpto. de Ingeniería de Comunicaciones, ETSI Telecomunicación, Campus de Teatinos s/n, 29071 Málaga, Spain
[2]Institute of Optics, Spanish National Research Council, 28006 Madrid, Spain
[3]National Research Council Canada, 1200 Montreal Road, Bldg. M50, Ottawa K1A 0R6, Canada
[4]Bionand Center for Nanomedicine and Biotechnology, Parque Tecnológico de Andalucía, 29590 Málaga, Spain
*e-mail: jmlg@ic.uma.es*
*†Currently with Alcyon Photonics S.L., Madrid 28006, España*

## ABSTRACT

Tilted subwavelength gratings (SWGs) are promising structures for birefringence control and polarization management in integrated photonic waveguides. Here we show how tilted SWGs can be used to design a directional coupler based polarization beam splitter which is symmetric for TM polarization but asymmetric for TE polarization. Using this approach, we develop a polarization beam splitter with calculated insertion loss below 1 dB and an extinction ratio better than 20 dB over a bandwidth of 86 nm. The fabricated device shows negligible insertion loss and an extinction ratio over 15 dB over a bandwidth of 72 nm.

**Keywords**: Photonic integrated devices, polarization management, subwavelength gratings.

## 1. INTRODUCTION

Polarization beam splitters (PBS) are key building blocks in high index contrast platforms as silicon-on-insulator. Among different approaches to implement PBS, directional couplers are typically used. In an asymmetric configuration, that is, when the two parallel waveguides of the directional coupler have substantially different propagation constants, only light of one polarization couples to the cross port, while the other polarization remains in the input waveguide [see Fig. 1(a)]. To achieve the required asymmetry, different solutions have been explored, such as adding different materials [2], or using multiple etch steps [3]. However, the existing methods often complicate device fabrication or result in long devices. Another promising approach to break the waveguide symmetry, which can be implemented with a single etch step, is the utilization of subwavelength grating (SWG) waveguides [4-5]. The SWG structures enable the lithographic definition of optical metamaterials which can be engineered to gain control over material anisotropy [5-6]. Specifically, recently demonstrated tilted SWG structures provide control over TE (in-plane) polarization while TM (out-of-plane) polarization remains virtually unaltered [7-8]. Therefore, SWGs are promising structures to break the coupler symmetry using a standard fabrication process.

Here we present a directional coupler with one arm comprising a tilted SWG waveguide while the other arm is a conventional SWG waveguide [See Fig. 1]. The TM polarized mode is only minimally affected by the tilt of the silicon blocks [7], so that for this polarization both waveguides have similar optical properties, and the phase matching condition is fulfilled. However, for TE polarization the symmetry is effectively broken and there is no phase matching. Our 3D-FDTD simulations predict an extinction ratio (ER) better than 20 dB over a bandwidth of 86 nm with negligible insertion loss (IL). The device has been fabricated in a 220 nm SOI platform, yielding an ER above 15 dB over a 72 nm bandwidth with subdecibel losses. Our device offers the advantage of control over the polarization properties enabled by tilted SWGs, opening a new method to design polarization diversity devices.

## 2. DESIGN OF THE POLARIZATION BEAM SPLITTER DIRECTIONAL COUPLER

The design of this directional coupler based PBS (DC-PBS) is carried out in the following two steps. First, we break the symmetry of the device for TE polarization by tilting the segments of the SWG waveguide in the upper arm of the directional coupler. Second, we optimize the device for the TM polarization by adding a silicon strip between the two waveguides.

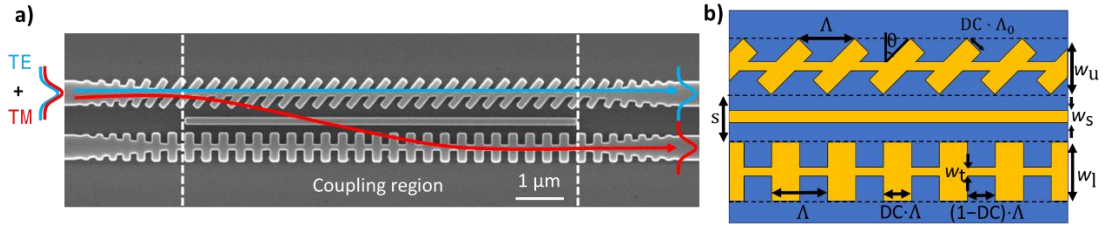



*Figure 1. (a) Scanning Electron Microscope image of the polarization beam splitter directional coupler (before $SiO_2$ cladding deposition). The segments of the upper waveguide are tilted to independently control the phase matching conditions for TE and TM polarization. (b) Schematic of the coupling region.*

### 2.1 Breaking the phase matching condition for the TE polarization

To demonstrate the principle of operation, we study a simplified geometry comprising two parallel SWG waveguides, brought into proximity to allow some power exchange. Referring to Fig. 1(b), the two SWG waveguides are $w_u = w_l = 0.6$ μm wide, with a nominal period $\Lambda_0 = 275$ nm, a 50% duty cycle and a tip width $w_t = 100$ nm. To illustrate how the tilt of the subwavelength segments optically decouples the two waveguides for TE polarization while permitting phase matching for TM polarization, we simulate the propagation of the fundamental TE and TM mode along the structures shown in Fig. 2(a) ($\theta = 0^o$) and Fig. 2(b) ($\theta = 40^o$). We observe that the tilt effectively suppresses power transfer for the TE polarized mode while the behavior for the TM polarized mode remains virtually unchanged. In Fig. 3(a) we show the insertion loss and extinction ratio of the structure for $\theta = 40^o$, calculated as: $\mathrm{IL}^{\mathrm{TE}} = \frac{P_{BAR}^{TE}}{P_{IN}^{TE}}$, $\mathrm{IL}^{\mathrm{TM}} = \frac{P_{CROSS}^{TM}}{P_{IN}^{TM}}$, $\mathrm{ER}^{\mathrm{TE}} = \frac{P_{CROSS}^{TE}}{P_{BAR}^{TE}}$, $\mathrm{ER}^{\mathrm{TM}} = \frac{P_{BAR}^{TM}}{P_{CROSS}^{TM}}$.

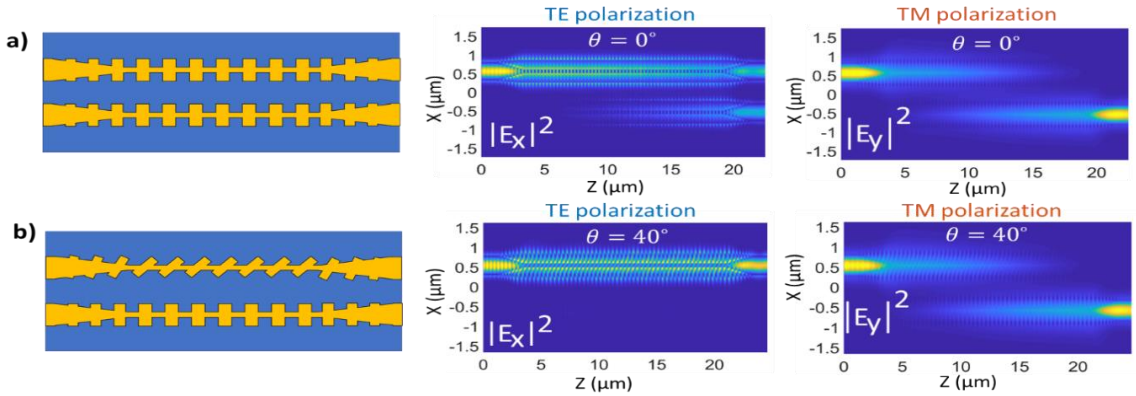



*Figure 2. (a) Schematics of the proposed DC-PBS for a tilt angle of θ=0º and 3D-FDTD simulations of the main component E- field propagation for TE and TM polarizations. (b) Schematic representation of the DC-PBS for a tilt angle of θ=40 º and 3D-FDTD simulations of the main component E- field propagation for the TE and TM polarizations.*

### 2.2 Optimizing the device behavior for the TM polarization

Once the index symmetry is broken for TE polarization, we optimize the device behavior for the TM polarization. This optimization process is done by adding a central silicon strip between the two waveguides [See Fig. 1]. Intuitively, this silicon strip allows to independently control the even supermode, while only slightly affecting the odd supermode. This behavior can be estimated by calculating the coupling length of the devices given by $L_\pi^{TM}(\lambda) = \lambda/[2(n_1^{TM}(\lambda) - n_2^{TM}(\lambda))]$ where $n_{1,2}^{TM}$ are the effective indices of the even and the odd TM polarized supermodes. Figure 3(b) show the calculated coupling length as a function of the wavelength, revealing that the central silicon strip not only reduces the device length but also flattens the wavelength response. In Fig. 3(a) we show the improvement in the device performance when the 150 nm wide silicon strip is added. The optimized design yields an ER more than 20 dB over an 86 nm bandwidth with negligible insertion loss.

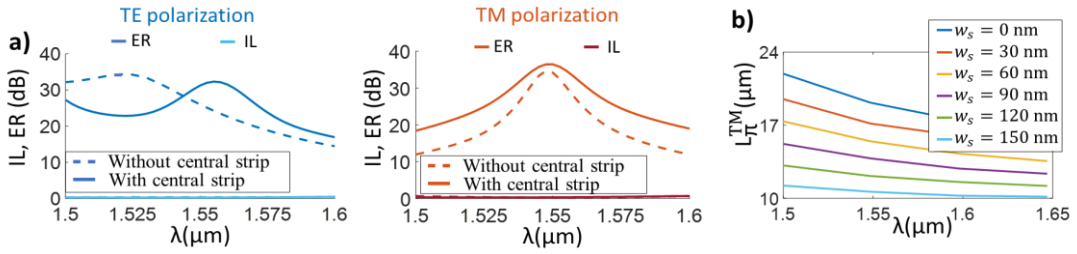



*Figure 3. (a) Insertion Loss and Extinction Ratio, for TE and TM polarizations, of the tilted SWG directional coupler with and without the central silicon strip. (b) TM polarization coupling length for the proposed tilted SWG DC-PBS for different silicon strip widths.*

## 3. EXPERIMENTAL RESULTS

The device has been fabricated using e-beam lithography on a 220-nm SOI wafer, with a 2-μm-thick buried oxide (BOX) and a 2.2-μm-thick $SiO_2$ upper cladding. Fig. 4(a) shows the measured insertion loss and extinction ratio of the fabricated device. For long wavelengths, the device performance is limited by the extinction ratio of the TE polarization. However, increasing the duty cycle from 50% to 60% enhances the modal confinement for TE polarization, thereby suppressing the coupling to the TE port, while only slightly changing the phase matching condition for TM polarization [see Fig. 4(b)].

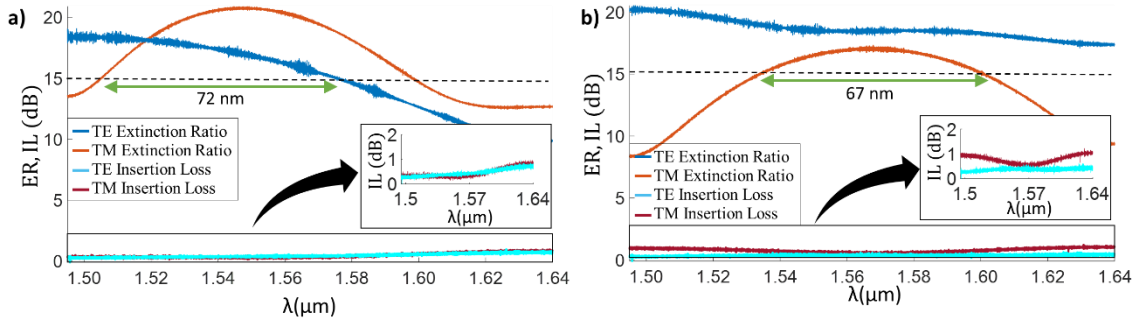



*Figure 4. (a) Measured extinction ratio and insertion loss for the nominal device. The IL is below 1 dB and ER is higher than 15 dB over a bandwidth of 72 nm (b) Measured extinction ratio and insertion loss for a +10% duty cycle biased device. The IL is below1 dB and the ER is >15 dB over a bandwidth of 67 nm.*

## 4. CONCLUSIONS

In this work we leverage the capability of tilted SWG waveguides to independently control the phase matching condition for TE and TM polarizations in a directional coupler. Based on this principle, we design a directional coupler based polarization beam splitter with measured polarization extinction ratio of >15 dB over a 72 nm bandwidth and a negligible insertion loss. The proposed strategy of controlling the symmetry of the DC-PBS presents an example of the excellent potential that tilted SWGs provide to the optical designer for polarization management control in integrated photonic devices.

## ACKNOWLEDGEMENTS

Ministerio de Economía y Competitividad MINECO (TEC2016-80718-R), Ministerio de Educación, Cultura y Deporte MECD (FPU16/06762), Fondo Europeo de Desarrollo Regional-FEDER, Proyecto I+D+i en el marco del Programa Operativo FEDER Andalucía 2014-2020 (UMA18-FEDERJA-219), Universidad de Málaga and Alcyon Photonics (8.06/5.59.5045).

## REFERENCES

[1] J. Wang, D. Liang, Y. Tang, D. Dai, and J. E. Bowers. Realization of an ultra-short silicon polarization beam splitter with an asymmetrical bent directional coupler., *Opt. Lett.* **38**, 4 (2013).

[2] T. Zhang, X. Yin, L. Chen, and X. Li. Ultra-compact polarization beam splitter utilizing a graphene-based asymmetrical directional coupler., *Opt. Lett.* **41**, 356 (2016).

[3] Y. Tian, J. Qiu, C. Liu, S. Tian, Z. Huang, and J. Wu. Compact polarization beam splitter with a high extinction ratio over S+ C+ L band., *Opt. Express* **27**, 999 (2019).

[4] R. Halir, A. Ortega-Moñux, D. Benedikovic, G. Z. Mashanovich, J. G. Wangüemert-Perez, J. H. Schmid, Í. Molina-Fernández, and P. Cheben. Subwavelength-grating metamaterial structures for silicon photonic devices., *Proc. IEEE* **106**, 2144 (2018).

[5] P. Cheben, R. Halir, J. H. Schmid, H. A. Atwater, and D. R. Smith. Subwavelength integrated photonics., Nature **560**, 565 (2018).

[6] Xu, H., Dai, D., Shi, Y., Ultra-Broadband and Ultra-Compact On-Chip Silicon Polarization Beam Splitter by Using Hetero-Anisotropic Metamaterials. *Laser & Photonics Reviews*, **13**, 1800349 (2019).

[7] J. M. Luque-González, A. Herrero-Bermello, A. Ortega-Moñux, Í. Molina-Fernández, A. V. Velasco, P. Cheben, J. H. Schmid, S. Wang, and R. Halir. Tilted subwavelength gratings: controlling anisotropy in metamaterial nanophotonic waveguides., *Opt. Lett.* **43**, 4691 (2018).

[8] A. Herrero-Bermello, J. M. Luque-González, A. V. Velasco, A. Ortega-Moñux, P. Cheben, and R. Halir. Design of a Broadband Polarization Splitter Based on Anisotropy-Engineered Tilted Subwavelength Gratings., *IEEE Photonics* J. **11**, 1 (2019).

# Dual-metamaterial silicon micro-ring resonators

*(Student Paper)*

**T. T. D. Dinh[1], X. Le Roux[1], J. Zhang[1], M. Montesinos[1], C. Lafforgue[1,2], D. Benedikovic[1], P. Cheben[3,4], E. Cassan[1], D. Marris-Morini[1], L. Vivien[1], and C. Alonso-Ramos[1]**

[1] Universite Paris-Saclay, Univ. Paris-Sud, CNRS, Centre de Nanosciences et de Nanotechnologies, 91120, Palaiseau, France

[2] École Normale Supérieure Paris-Saclay, Université Paris-Saclay, 94230 Cachan, France

[3] National Research Council Canada, ON K1A0R6 Ottawa, Canada

[4] Center for Research in Photonics, University of Ottawa, Ottawa K1N6N5, Canada

*e-mail: Dinh.Thi-Thuy-Duong@c2n.upsaclay.fr*

## ABSTRACT

Subwavelength metamaterial engineering has opened exciting prospects for controlling and manipulating light in silicon photonic waveguides. Most state-of-the-art subwavelength photonic waveguides rely on periodic nanostructuration of the core or the cladding, but not both. Here, we present a new waveguide geometry that exploits metamaterial engineering of the core and the cladding, independently. By implementing two metamaterials, this step-index geometry provides unique flexibility in the design of the waveguide index contrast. The proposed approach opens additional degrees of freedom to shape single-mode condition and to control modal confinement in the vertical and horizontal directions. Hence, the proposed dual-metamaterial waveguide geometry has a great potential for applications requiring optimized light-matter interactions such as sensing, hybrid integration or nonlinear wavelength conversion. As a proof-of-concept, we experimentally demonstrate dual-metamaterial micro-ring resonators in the 220-nm-thick Si technology with quality factors in excess of 50000 near 1550 nm wavelength.

**Keywords**: silicon photonics, subwavelength, light-matter interactions, sensing.

## 1. INTRODUCTION

Periodically patterning silicon with a pitch small enough to suppress diffraction effects has proven to be a simple and powerful tool to control the propagation of light in photonic waveguides [1-3]. Since the first demonstration of Si waveguide with subwavelength grating core [1], a great number of SWG-assisted devices have been proposed and demonstrated to achieve state-of-the-art performance [2,3]. Subwavelength grating (swg) waveguides are promising to shape modal light confinement, which could be instrumental for applications requiring tight control of light matter interactions like sensing, hybrid integration of active materials or nonlinear wavelength conversion. Most state-of-the-art swg waveguides rely on metamaterial engineering of the core [4-8] or the cladding [9,10], but not both. In these geometries, the index of the cladding or the core is fixed, thereby limiting the flexibility in controlling the modal confinement. In waveguides with a subwavelength metamaterial cladding only, the evanescent field is limited by the tight confinement in the central silicon strip. On the other hand, in waveguides with a subwavelength metamaterial core, the maximum waveguide width is set by single-mode operation. Then, the minimum effective metamaterial that can be implemented is restricted by leakage to the substrate, limiting the maximum evanescent field [11]. Subwavelength waveguides interleaving shifted silicon strips have been recently proposed that implement different metamaterials in the core and the cladding. However, the same silicon strips define the core and cladding geometry, limiting the flexibility in the design of the index contrast. Here, we propose and experimentally demonstrate a new waveguide geometry that implements different subwavelength metamaterials in the core and the cladding. This strategy enables flexible control of the synthesized metamaterial indices in the core and the cladding, independently, thereby relaxing the requirements for single-mode condition. Then, comparatively wider waveguides still afford single-mode operation, which alleviates restrictions in minimum effective metamaterial index. As a first demonstration of the potential of this approach, we have fabricated silicon micro-ring resonators implemented with single-mode dual-metamaterial waveguides with thickness of 220 nm and core width as large as 900 nm. The ring resonators exhibit measured quality factors in excess of 50000 and extinction ratio larger than 15 dB near 1550 nm wavelength. These results compare favorably with previously reported silicon resonators based on subwavelength nano-structuration, that showed quality factors on the order of 10000 [7,13].

## 2. WAVEGUIDE DESIGN

The geometry of the proposed dual-metamaterial waveguide is schematically shown in Fig. 1(a). The holes in the core and cladding have the same longitudinal and transversal periods of $\Lambda_L = 200$ nm and $\Lambda_T = 450$ nm,

respectively. The holes in the waveguide core have a length of $L_{core} = 100$ nm and a width of $W_{core} = 100$ nm, while the holes in the cladding have a length of $L_{cladding} = 100$ nm and a width of $W_{cladding} = 250$ nm. The silicon layer thickness is 220 nm. In each longitudinal period the waveguide comprises two holes in the core and 14 holes at each side of the cladding. We have considered silica as under- and upper-cladding materials.

The transverse-electric (TE) polarized modes typically have a strong field near the vertical waveguide walls, where the sidewall roughness is. This may result in high propagation loss. To avoid this issue, we choose to work with the transverse-magnetic (TM) polarized mode. We have calculated the electric field distribution of the fundamental TM mode near 1550 nm wavelength using three-dimensional finite difference time domain (3D-FDTD) simulations. The electric field distribution at the planes $\alpha$ and $\beta$ (described in Fig. 1(a)) are shown in Figs. 1(b) and (c), respectively. The TM mode has an effective index of ~1.9, and carries more than 70% of the electric field intensity outside the silicon.

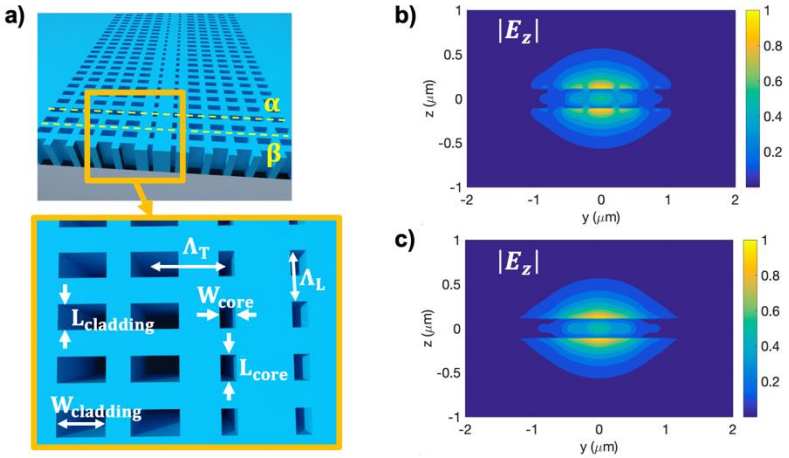



*Figure 1. a) Schematic view of the proposed dual-metamaterial waveguide. Electric field distributions of the fundamental TM mode near 1550 nm wavelength for a waveguide with $L_{core}$=100 nm, $W_{core}$=100 nm, $L_{cladding}$=100 nm and $W_{cladding}$ = 200 nm, along b) the plane α and c) the plane β, as marked in panel a).*

To study the single mode condition in the proposed waveguide we used the two-dimensional metamaterial waveguide model, as illustrated in Fig. 2(a). The metamaterials in the core and cladding are substituted by their equivalent effective index ($n_A = 3.36$, $n_B = 3.19$). We calculated the effective index for the fundamental and first order TM modes at 1550 nm wavelength as a function of the waveguide width, W. As shown in Fig. 2(b), the waveguide is single mode for a waveguide width below 1 μm. For comparison, the single-mode limit for conventional strip waveguide is near 500 nm. For a waveguide with subwavelength metamaterial core the single mode limit is near 600 nm.

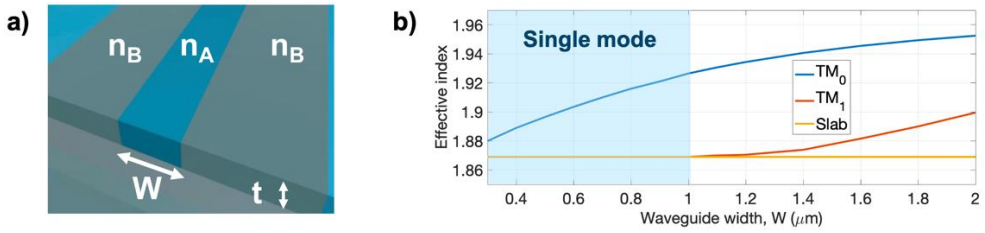



*Figure 2. a) Schematic two-dimensional model of the dual-metamaterial waveguide. The subwavelength metamaterial structures in the core and cladding are modelled by their equivalent refractive indices, $n_A$ and $n_B$. b) Effective index of the fundamental ($TM_0$) and first order ($TM_1$) order TM modes, calculated as a function of the waveguide width, W. The blue region indicates width satisfying the single-mode condition.*

## 3. EXPERIMENTAL DEMONSTRATION

To demonstrate the feasibility of the proposed approach, we have fabricated and experimentally characterized several ring resonators, implemented in the 220-nm-thick silicon platform with buried oxide (BOX) layer of 3 μm. The patterns were defined using electron-beam lithography and dry etching. Fabricated rings are cladded with PMMA to symmetrize the structure. The bus waveguide and the ring resonator are implemented with the dual-metamaterial waveguide with $L_{core} = 100$ nm, $W_{core} = 100$ nm, $L_{cladding} = 100$ nm and $W_{cladding} = 200$ nm. The micro-rings have a radius of 80 μm.

Figure 2(a) shows a scanning electron microscope image of one of the fabricated rings. The transmittance spectra for a ring resonator with a gap of 800 nm is shown in Fig. 2(b). From the lower envelope of the resonances, it can be concluded that the critical coupling is achieved near 1580 nm wavelength. In the critical coupling region,

the extinction ratio is ~25 dB and the quality factor (Q) is ~23000, as shown in Fig. 3(c). At shorter wavelengths, the ring is in the under-coupling regime, with a higher Q of ~55000 dB and an extinction ratio exceeding 15 dB.

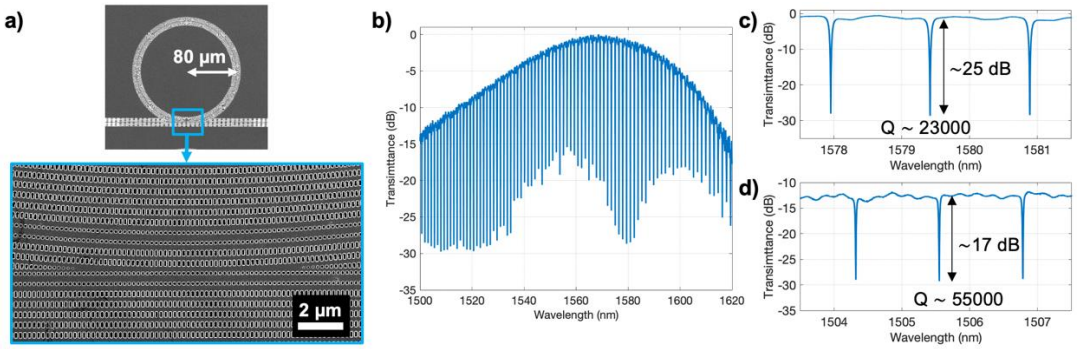



Figure 3. a) Scanning electron microscope image of fabricated ring. b) Transmittance spectrum of the ring resonator for TM polarization. Detail of the ring transmittance in c) critical coupling and d) under-coupling regimes.

## 4. CONCLUSIONS

We have proposed and experimentally demonstrated a new kind of waveguide geometry that implements two different metamaterials in the core and the cladding. This dual-metamaterial geometry provides new degrees of freedom to engineer the single-mode condition and the vertical and lateral field confinements. By judiciously designing the synthesized metamaterial indices in the core and cladding, we ensure single-mode operation for a waveguide width as large as 1 µm. Our 3D-FDTD simulations showed that for the fundamental TM mode of a waveguide with a width of 900 nm (within the single-mode regime), more than 70% of the electric field intensity propagates outside the silicon. To experimentally validate the feasibility of the proposed approach, we have fabricated dual-metamaterial ring resonators, exhibiting high quality factors exceeding 50000, among the highest values reported for silicon subwavelength ring resonators [7,13]. We believe that these results open a new route for the implementation of advanced modal confinement engineering in silicon photonic devices.

## ACKNOWLEDGEMENTS

Agence Nationale de la Recherche (MIRSPEC ANR-17-CE09-0041, BRIGHT ANR-18-CE24-0023-01).

## REFERENCES

[1] P.J. Bock, *et al.*: Subwavelength grating periodic structures in silicon-oninsulator: a new type of microphotonic waveguide, *Opt. Express*, vol. 18, pp. 20251-20262, 2010.
[2] R. Halir, *et al.*: Waveguide sub-wavelength structures: a review of principles and applications, *Laser Photonics Rev.*, vol. 8, pp. 25-49, 2015.
[3] P. Cheben, *et al.*: Subwavelength integrated photonics, *Nature*, vol. 560, pp. 565-572, 2018.
[4] J.G. Wangüemert-Pérez, *et al.*: Evanescent field waveguide sensing with subwavelength grating structures in silicon-on-insulator, *Opt. Lett.*, vol. 39, pp. 4442-4445, 2014.
[5] V. Donzella, *et al.*: Design and fabrication of SOI micro-ring resonators based on sub-wavelength grating waveguides, *Opt. Express*, vol. 23, pp. 4791-4803, 2015.
[6] H. Yan, *et al.*: Unique surface sensing property and enhanced sensitivity in microring resonator biosensors based on subwavelength grating waveguides, *Opt. Express*, vol. 24, pp. 29724-29733, 2016.
[7] D. Benedikovic, *et al.*: Sub-wavelength silicon grating metamaterial ring resonators, *in Proc. GFP 2017*, Berlin, Germany, Aug. 2017.
[8] E. Luan, *et al.*: Enhanced sensitivity of subwavelength multibox waveguide microring resonator label-free biosensors, *IEEE J. Sel. Top. Quantum Electron.*, vol. 25, pp. 7300211-1-7300211-11, 2018.
[9] J. Soler Penadés, *et al.*: Suspended SOI waveguide with sub-wavelength grating cladding for mid-infrared, *Opt. Lett.*, vol. 39, pp. 5661-5664, 2014.
[10] W. Zhou, *et al.*: Fully suspended slot waveguides for high refractive index sensitivity, *Opt. Lett.*, vol. 42, pp. 1245-1248, 2017.
[11] J.D. Sarmiento-Merenguel, *et al.*: Controlling leakage losses in subwavelength grating silicon metamaterial waveguides, *Opt. Lett.*, vol. 41, pp. 3443-3446, 2016.
[12] B. Taurel, *et al.*: Sub-wavelength grating interdigitated combs as photonic waveguides, *Opt. Lett.*, vol. 44, pp. 3869-3872, 2019.
[13] J.G. Wangüemert-Pérez, *et al.*: Subwavelength structures for silicon photonics biosensing, *Opt. Laser Technol.*, vol. 109, pp. 437-448, 2019.

# Bridging the Graded-Index Few-Mode Fibre with Photonic Integrated Circuits via Efficient Diffraction Waveguide Gratings

*(Student Paper)*

**Yeyu Tong[1], Xuetong Zhou[1], Yi Wang[1], Chi-Wai Chow[2] and Hon Ki Tsang[1*]**
[1] Department of Electronic Engineering, The Chinese University of Hong Kong, Shatin, Hong Kong, P.R. China
[2]Department of Photonics, National Chiao Tung University, Hsinchu, Taiwan
*e-mail: hktsang@ee.cuhk.edu.hk*

## ABSTRACT

Spatial-division multiplexing (SDM) employing few-mode fibres (FMF) has attracted much interest for increasing the capacity of optical fibre communication systems. Graded-index few-mode fibres (GI-FMF) have low modal differential group delay (DGD), allowing extended transmission distance and bandwidth. In this paper, we describe novel efficient waveguide grating couplers fabricated on the silicon photonic platform for selectively launching different modes in the GI-FMF. The waveguide grating couplers may be integrated with transceivers for implementing mode division multiplexing in the fibre communications. The single-polarization diffraction waveguide gratings is measured to have coupling efficiencies into the $LP_{01}$ mode and $LP_{11}$ mode of – 2.8 dB and – 3.88 dB, respectively. The measured 3-dB bandwidth of the two modes are 61.2 nm and 59.0 nm. A two-dimensional grating based on the effective medium theory (EMT) is also demonstrated, supporting totally four optical channels including the two orthogonal polarizations of the $LP_{01}$ mode and $LP_{11}$ mode. The obtained peak coupling efficiency is – 4.89 dB for $LP_{01}$ mode and – 5.71 dB for $LP_{11}$ mode. The 3-dB bandwidth of the two modes are 23.2 nm and 21.6 nm, respectively.

**Keywords**: Integrated optics, silicon photonics, diffraction gratings, spatial-division multiplexing.

## 1. INTRODUCTION

The continuing exponential growth of data traffic into and out of the data centres is driving the development of higher transmission capacity optical interconnects. The transmission capacity of standard single-mode fibre (SMF) has already approached the theoretical limit from Shannon's information theory and nonlinear fibre effects [1]. Spatial-division multiplexing (SDM) employing few-mode fibre (FMF) has thus attracted much interest to enable further capacity growth with the potential cost and space savings associated with using a single integrated transmitter for launching mode division multiplexing (MDM) signals in the FMF. Graded-index FMF has the benefit of a low modal differential group delay (DGD), which affects the time delay between the received SDM channels after FMF transmission. Assuming mode mixing in the fibre, any time delay has to be compensated by an equalizing filter with a finite number of taps, a smaller time delay is always preferred for implementable multiple-input multiple-output (MIMO) digital signal processing (DSP) [2].

As an alternative to the fibre photonic lantern and the 3-dimensional (3D) optical waveguides by laser inscription, integrated multimode waveguide grating couplers based on the silicon-on-insulator (SOI) platform offers the advantages of low cost, monolithic integration of multiple channel MDM transmitters and receivers and mass-production scalability [3], [4]. Optical signal processing employing the photonic integrated circuits such as mode unscrambling for high-speed optical communications have been previously explored [5]. In this work, we report efficient mode multiplexers for graded-index FMF (GI-FMF) based on waveguide gratings with record coupling efficiencies. The single-polarization grating coupler has a peak experimental coupling efficiency of – 2.8 dB for $LP_{01}$ mode, and – 3.88 dB for $LP_{11}$ mode. The 3-dB bandwidth are 61.2 nm and 59.0 nm, respectively. A two-dimensional grating based on the effective medium theory (EMT) is also demonstrated to support the two orthogonal polarizations of the $LP_{01}$ mode and $LP_{11}$ mode. The obtained peak coupling efficiency is – 4.89 dB for $LP_{01}$ mode and – 5.87 dB for $LP_{11}$ mode. The 3-dB bandwidth are 23.2 nm and 21.6 nm, respectively.

## 2. DESIGN AND SIMULATION

The *OFS* two-mode GI-FMF in our experiment has a mode field diameter (MFD) of 11.0 μm. The DGD between the $LP_{01}$ mode and the $LP_{11}$ mode is less than ± 0.2 ps/m, while it is about 2.1 ps/m for the OFS step index FMF. The SOI wafer has a top silicon layer with a thickness of 220 nm. Buried-oxide layer has a thickness of 2 μm. Transverse-electric (TE) modes in the SOI waveguides, $TE_0$ and $TE_1$ can selectively excite the $LP_{01}$ mode and $LP_{11}$ mode in the GI-FMF via a single grating structure as illustrated in Figs. 1(a) and 1(b), which is possible as their effective refractive indexes are similar in the wide slab waveguide and grating region. To enhance the grating directionality, a 160-nm poly-silicon layer is deposited on the whole silicon wafer as the grating teeth [6], [7]. 230

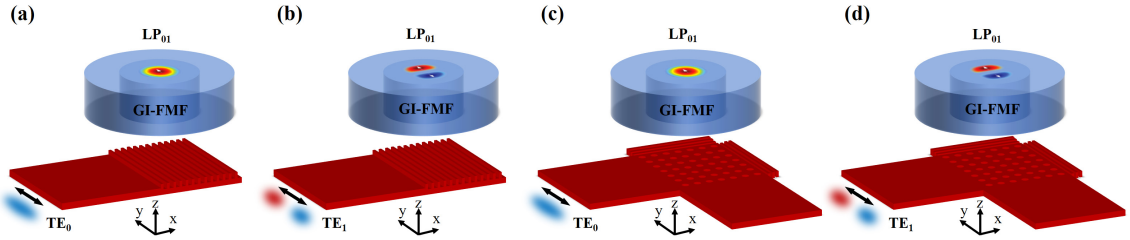



*Fig. 1. (a) and (b) Schematics of the single-polarization two-mode grating coupler, which has 380-nm thick grating teeth and 150-nm grating slits. (c) and (d) Schematics of the two-dimensional grating coupler, which has 220-nm thick grating teeth and 70-nm shallow-etched sub-wavelength holes. The grating design is symmetric for the two orthogonal polarizations.*

nm etching process is performed reaching 70 nm into the bottom crystalline silicon for the grating slits. For the two-dimensional grating coupler, a symmetric grating design can be employed so that totally four optical channels can be excited in the two-mode GI-FMFs as shown in Figs. 1(c) and 1(d). In the dual polarization two-dimensional grating coupler, the poly-silicon overlay was not used in order to keep grating strength low for efficient coupling across the diameter of the GI-FMF. Instead, the grating teeth have a thickness of 220 nm and the 70-nm shallow etched sub-wavelength holes are employed as the lower index sections. The square-shaped holes used in the 2-D FDTD simulation are converted to the round-shaped holes in fabrication as the latter can be fabricated using the standard deep-ultraviolet (DUV) photolithography with less stringent requirements [8]. Three rectangular slabs with a width of 190 nm and a spacing of 240 nm are utilized as the grating end reflector.

The grating coupler was optimized by genetic optimization algorithm with 2D-FDTD simulations [9]. For the two-dimensional grating, EMT is used and only the performance of the mode $TE_0$ is considered in the optimization process, as the mode $TE_1$ has similar effective refractive index and the grating region is symmetric for two orthogonal polarizations [10]. On-chip mode multiplexing of the $TE_0$ and $TE_1$ is realized by the asymmetric directional couplers (ADCs) which has a coupling gap of 200 nm [11]. The single-mode input waveguide has a width of 450 nm and the multimode bus waveguide has a width of 962 nm. The multimode waveguide connects with the grating that has a width of about 13.2 μm after a 360-μm linear taper.

Fig. 2(a) shows the structural width of the grating teeth and slits of the optimized single-polarization grating coupler. The minimum feature size is 181 nm for robust fabrication by 193-nm DUV lithography. The corresponding coupling efficiencies including the $LP_{01}$ mode and $LP_{11}$ mode are shown in Fig. 2(b) obtained by 3-D FDTD simulation. The single-polarization grating coupler has a peak experimental coupling efficiency of – 2.30 dB at 1557.14 nm for $LP_{01}$ mode, and – 2.96 dB at 1555.10 nm for $LP_{11}$ mode. The 3-dB bandwidth is 67.4 nm and 65.3 nm, respectively. Grating period of the two-dimensional grating is shown in Fig. 2(c). All the 70-nm shallow etched holes have the same diameter of 328 nm for ease of fabrication. Simulation performance of the grating is shown in Fig. 2(d). The obtained peak coupling efficiency is – 3.20 dB at 1538.78 nm for $LP_{01}$ mode and – 4.01 dB at 1536.73 nm for $LP_{11}$ mode. The 3-dB bandwidth of the two modes are similar of about 28.5 nm.

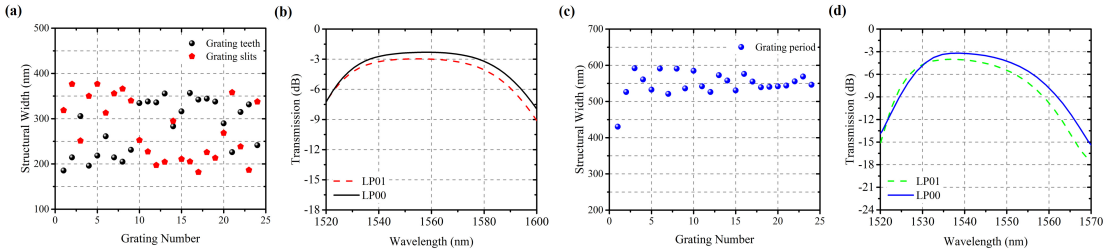



*Fig. 2. (a) Structural width of the teeth and slits of the single-polarization grating coupler. (b) Coupling efficiencies of the single-polarization grating coupler with GI-FMF obtained by 3D-FDTD simulation. (c) Width of the grating period of the two-dimensional grating coupler, the shallow-etch holes have the diameter of 328 nm. (d) Coupling efficiencies of the two-dimensional grating coupler with GI-FMF obtained by 3D-FDTD simulation. Performance of the other orthogonal polarization is the same.*

## 3. EXPERIMENTAL RESULTS

The silicon photonic chip was fabricated in a multi-project wafer (MPW) run at *IMEC*. Fig. 3(a) shows the microscopic image of the photonic integrated circuits including the input single-mode grating coupler, ADCs, linear waveguide taper and the diffraction gratings for GI-FMF. The input single-mode grating coupler is based on 10° off-vertical coupling. On-chip mode multiplexing of the $TE_0$ and $TE_1$ is realized by ADCs which has an experimental crosstalk lower than – 15 dB from 1520 nm to 1620 nm. A peak coupling efficiency of – 2.8 dB for $LP_{01}$ mode is measured at 1552.0 nm for the single-polarization waveguide grating as depicted by Fig. 3(b). The $LP_{11}$ mode has a peak efficiency of – 3.88 dB at 1539.4 nm. The 3-dB bandwidth of the two modes are 61.2 nm and 59.0 nm, respectively. Fig. 3(c) shows the measured coupling efficiencies of the two-dimensional grating for

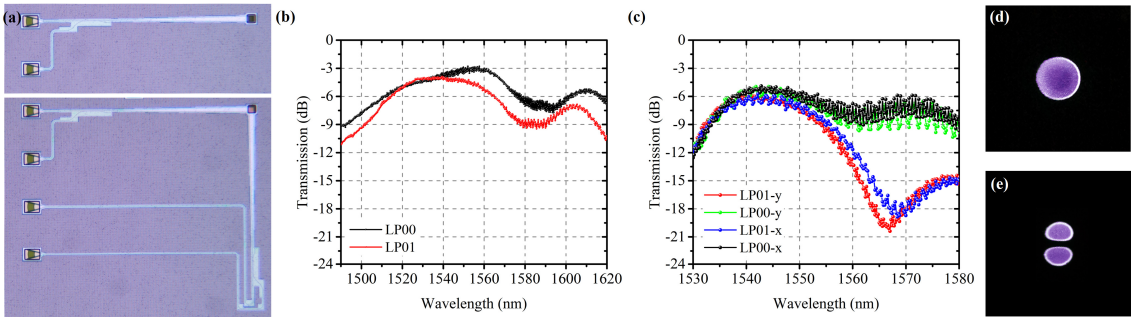



*Fig. 3. (a) Microscopic image of the photonic integrated circuits consisting of the input single-mode grating coupler, ADCs, linear waveguide taper and the single-polarization or two-dimensional few-mode grating coupler. (b) Experimental coupling efficiencies of the single-polarization grating coupler for GI-FMF. (c) Experimental coupling efficiencies of the two-dimensional grating coupler for GI-FMF including two orthogonal polarizations. (d) and (e) Mode field profiles of the GI-FMF captured by an infrared camera with a 40× lens when $LP_{01}$ mode and $LP_{11}$ mode are excited by the waveguide gratings.*

launching the two polarizations of the $LP_{01}$ mode and $LP_{11}$ modes. The obtained peak coupling efficiencies are – 4.89 dB and – 4.96 dB for $LP_{01}$ mode. $LP_{11}$ mode has peak coupling efficiencies of – 5.87 dB and – 5.71 dB. The 3-dB bandwidth are 23.2 nm and 21.6 nm, respectively. Mode field profiles of the GI-FMF captured by an infrared camera with a 40× lens, are presented in Figs. 3(d) and 3(e), demonstrating the selective launch of $LP_{01}$ mode and $LP_{11}$ modes via the diffraction waveguide gratings.

## 4. CONCLUSIONS

We propose novel diffraction waveguide gratings on SOI for a two-mode GI-FMF, which has a low DGD of less than ± 0.2 ps/m for future high-speed data transmission. The experimental coupling efficiency of the single-polarization waveguide grating is – 2.8 dB for the $LP_{01}$ mode, and – 3.88 dB for the $LP_{11}$ mode. The 3-dB bandwidth of the two modes are 61.2 nm and 59.0 nm, respectively. A two-dimensional waveguide grating which supports two orthogonal polarizations of the $LP_{01}$ mode and $LP_{11}$ mode is also demonstrated with peak coupling efficiency of – 4.89 dB for $LP_{01}$ mode and – 5.71 dB for $LP_{11}$ mode. The 3-dB bandwidth are 23.2 nm and 21.6 nm respectively. The multimode waveguide gratings couplers for GI-FMF can enable the integration of transceivers with four data channels per wavelength in the future SDM networks.

## ACKNOWLEDGEMENTS

This work was funded by Hong Kong Research Grants Council General Research Fund 14212816. The authors thank IMEC for device fabrication and Synopsys for support of the PICs layout software.

## REFERENCES

[1] D. J. Richardson, "Filling the Light Pipe," *Science*, vol. 330, no. 6002, pp. 327–328, Oct. 2010.
[2] R. Ryf et al., "Mode-Division Multiplexing Over 96 km of Few-Mode Fiber Using Coherent 6 × 6 MIMO Processing," *J. Lightwave Technol.*, vol. 30, no. 4, pp. 521–531, Feb. 2012.
[3] A. M. J. Koonen, et al., "Silicon Photonic Integrated Mode Multiplexer and Demultiplexer," *IEEE Photonics Technol. Lett.*, vol. 24, no. 21, pp. 1961–1964, Nov. 2012.
[4] Y. Ding, H. Ou, J. Xu, M. Xiong, and C. Peucheret, "On-chip mode multiplexer based on a single grating coupler," in *IEEE Photonics Conference* 2012, pp. 707–708.
[5] A. Annoni et al., "Unscrambling light—automatically undoing strong mixing between modes," *Light: Science & Applications*, vol. 6, no. 12, p. e17110, Dec. 2017.
[6] G. Roelkens et al., "High efficiency diffractive grating couplers for interfacing a single mode optical fiber with a nanophotonic silicon-on-insulator waveguide circuit," *Appl. Phys. Lett.*, vol. 92, no. 13, p. 131101.
[7] D. Vermeulen et al., "High-efficiency fiber-to-chip grating couplers realized using an advanced CMOS-compatible Silicon-On-Insulator platform," *Opt. Express*, vol. 18, no. 17, pp. 18278–18283, Aug. 2010.
[8] R. Halir, P. Cheben, S. Janz, D.-X. Xu, Í. Molina-Fernández, and J. G. Wangüemert-Pérez, "Waveguide grating coupler with subwavelength microstructures," *Opt. Lett.*, vol. 34, no. 9, pp. 1408–1410, May 2009.
[9] Y. Tong, W. Zhou, and H. K. Tsang, "Efficient perfectly vertical grating coupler for multi-core fibers fabricated with 193-nm DUV lithography," *Opt. Lett.*, vol. 43, no. 23, pp. 5709–5712, Dec. 2018.
[10] Y. Tong, et al., "Efficient Mode Multiplexer for Few-Mode Fibers Using Integrated Silicon-on-Insulator Waveguide Grating Coupler," *IEEE Journal of Quantum Electronics*, vol. 56, no. 1, pp. 1–7, Feb. 2020.
[11] D. Daoxin, W. Jian, and S. Yaocheng, "Silicon mode (de)multiplexer enabling high capacity photonic networks-on-chip with a single-wavelength-carrier light," *Opt. Lett.*, vol. 38, no. 9, pp. 1422–1424, 2013.

# Dual wavelength Y-junction glass integrated waveguides for mm-wave carrier generation

Arab N [1], Poette J [1], Bastard L [1], Broquin J-E [1]
[1] *Univ. Grenoble Alpes, CNRS, Grenoble INP, IMEP-LAHC, 38000 Grenoble, France*
*e-mail: julien.poette@grenoble-inp.fr*

## ABSTRACT

This paper presents the use of co-integrated lasers on glass for the generation of radio-frequency carriers by optical heterodyning. By using the ion exchange glass platform, two DFB lasers and a power combiner have been fabricated on a single substrate. Thanks to the excellent thermal stability of these lasers, a drift of the beating signal frequency as low as 5 MHz has been measured without any thermal regulation. These performances represent an improvement by several orders of magnitude when compared to heterodyned semiconductor lasers technology and have the potential to generate mm-wave carrier frequencies up to a few THz.

**Keywords**: glass integrated optics, DFB laser, waveguide, frequency generation, heterodyning, frequency drift.

## 1 INTRODUCTION

The generation of radio-frequency carriers, in the millimeter and sub-terahertz range is required for different applications such as radar, spectroscopy or communication systems. Optical systems offer interesting solutions to reach this frequency range that is difficult to access by electrical means. Different devices and architectures have been developed over the last decades. Among them, heterodyning using semiconductor lasers offers very high beating frequencies but with intrinsic large linewidths due to the low coherence of the lasers employed. Consequently, they require additionnal features like injection locking in order to reach the tenth of kiloHertz [1]. Additionally, in order to access large tunabilities or accordabilities over large ranges which restrict the use of electrical and optical feedback system, optical solutions are usually impaired by a large frequency drift [2], thus limiting the performance of the global system.

We propose here the use of two DFB lasers co-integrated on a glass substrate with the ion-exchange technology. Indeed, the Erbium-doped glass material presents a slower dynamic and allows a larger photon lifetime compared with semiconductor technology, which have a positive impact on laser linewidths and noise. Our integrated device contains two DFB lasers and a Y-junction coupler. Since properties of the heterodyned signal such as power, noise, linewidth and drift are similar whatever the carrier frequency [3], we have targeted a generated frequency of 5 GHz, compatible with our electrical characterization equipment. However, a similar device with minor design modifications would allow reaching carrier frequencies from 3 GHz to 3 THz. This article is organized as follows. The lasers description and fabrication are first presented. The heterodyne electrical signal obtained from the structure is then described and discussed. Finally, results of transmission experiments with standard communication protocoles are exposed to prove the performances of such sources as a carrier generator.

## 2 DESIGN AND FABRICATION

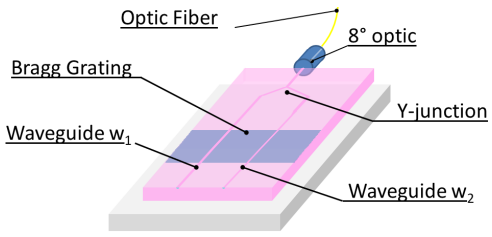



Figure 1. Design of the proposed dual-frequency laser.

The whole device has been fabricated on a co-doped Erbium-Ytterbium Phosphate glass (IOG-1 Schott$^{TM}$) using the process described in [4]. A schematic of the structure is presented on figure 1. The waveguides needed for the different elements have been manufactured using a silver/sodium ion-exchange. Two laser cavities are then formed by two waveguides covered by a single 2 cm long Bragg grating etched at the surface of the glass wafer. The grating of period $\Lambda$=510 nm is defined by a standard holographic process in a photoresist followed by a Reactive Ion Etching step. It has been chosen to adjust the effective refractive index $n_{eff}$ in each laser

cavity by adapting each waveguides' width through their diffusion aperture size. Indeed, each laser produces a wavelength $\lambda_i$ corresponding to $\lambda_i = 2.n_{eff}(w_i).\Lambda$.

This allows having different lasing wavelengths while using the same Bragg grating with an identical period $\Lambda$ for both waveguides. The beating frequency $f_b$ obtained by heterodyning the two lasers is given by: $f_b = c.\frac{\lambda_2 - \lambda_1}{\lambda_1.\lambda_2}$. A modification of the lasing wavelengths through the adjustement of the waveguide width allows generating a beating frequency as high as 300 GHz, while keeping all other technological parameters constant. An individual laser has been fabricated using the same process. Its threshold is close to 150 mW pump power and its efficiency is 10%. Its optical linewidth has been measured using an auto-heterodyne setup having a 25 km path difference. A value of $\leq$2 kHz, has been extracted from a Voigt fit of this measurement[5].

## 3 HETERODYNE SIGNAL CHARACTERIZATION

The device used for high-frequency carrier generation has been designed with two waveguide aperture widths of 9.3 and 9.4 $\mu$m in order to generate a frequency close to 5 GHz. The signal emitted by the two lasers are combined by the Y-jonction coupler and are then collected using a 8° angled facet optical fiber, to avoid any back-reflection from the interface. The detection by a photodiode then produces the desired electrical carrier. To pump the device, a 1550/980 pigtailed multiplexer is employed so both lasers are fed using the same pump diode and the counter-propagating laser signals are collected through the 1550nm branch of the multiplexer. Finally, the generated RF-signal is produced by a rapid PIN photodiode.

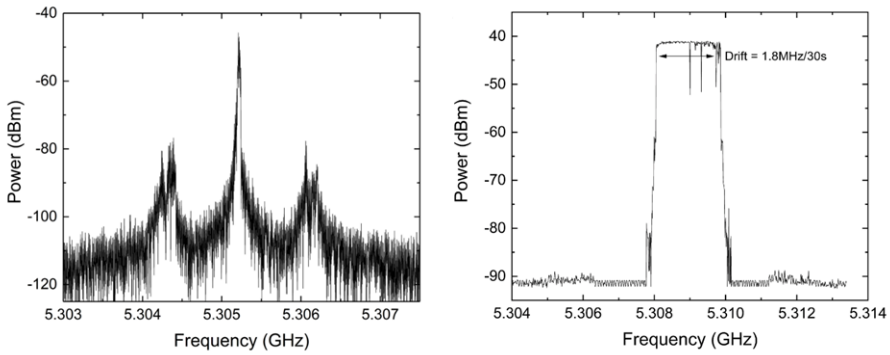



Figure 2. Electrical spectrum of the heterodyne signal at 5.3GHz : 50 ms measurement (left) and 30s Max Hold (right).

Figure 2-left shows the spectrum measured using an acquisition time of 50 ms. The extracted linewidth is 1.8 kHz, assuming a Lorentzian profile of the central feature. Note that the sidebands centered 800 kHz away from the carrier correspond to an increased noise of the lasers close to their relaxation frequencies (this feature also appears when measuring single lasers). Figure 2-right represents the result from a max-hold measurement of the beating spectrum over an acquisition time of 30 s. The total drift observed is 1.8 MHz, the lowest observed in the literature for free running heterodyne lasers in this frequency range and more than ten times lower than the values reported for free running semiconductor lasers [6]

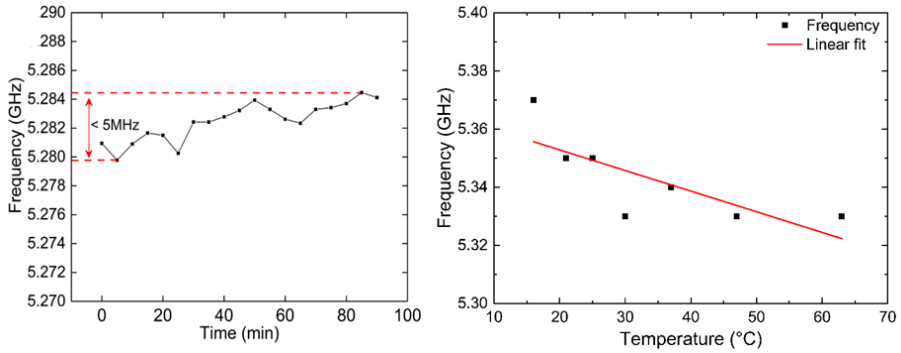



Figure 3. Impact of temperature variation on the frequency generated.

In order to qualify the long term stability of our system, we have measured the beating frequency over a period of 90 min, while the system was not being actively thermally stabilized. The result of this experiment is shown on the figure 3-left. A total variation smaller than 5 MHz has been measured. One explanation for the slow frequency drift observed in this experiment may be a change of the ambient temperature. In order to test this hypothesis, we have determined the thermal sensitivity of the beating frequency by actively changing the

temperature of the device. Figure3-Right shows the evolution of the emitted frequency with the temperature of the device. A linear fit of this variation leads to an average of 0.6 MHz/°C.

## 4 DATA TRANSMISSION EXPERIMENTS

To demonstrate the capability of our solution to provide electrical carriers suitable for telecommunication applications, we used our device as a frequency carrier generator for a radio-over-fiber communication system. The optical signal from our device is modulated with data, so that a dual band modulation is performed. This signal is then detected by a rapid photodiode and analyzed with a Vector Signal Analyzer.

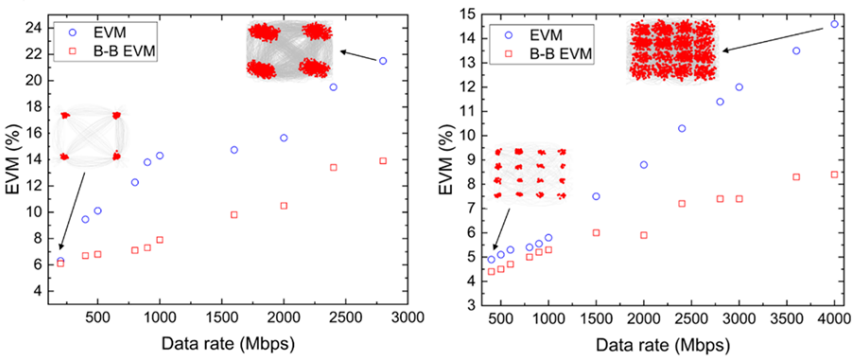



Figure 4. EVM measurements for different bitrates using QPSK (Left) and 16QAM (right) modulation formats. Back-to-back measurements are shown in red.

Figure 4 shows the demodulated signal transmitted by our system for Binary Phase Shift Keying (left) from 0.2 to 2.8 Gbps data rates, and for 16-Quadrature Amplitude Modulation from 0.4 to 4 GHz modulating an electrical subcarrier, applied on the optical modulator. The back-to-back reference measurement given consist in direct demodulations of the electrical signal applied to the optical modulator,thus including no electro-optical conversion. Once again, no electrical amplifier has been inserted in the transmission link. Based on the IEEE communication standards at 60 GHz, such results would allow the use of an equivalent frequency generator operating at 60 GHz for all bit rates tested using the BPSK modulation and for bit rates up to 2 GBps for both modualtion formats, despite the high back-to back values. The values are partially limited by the bandwidth available in our experiment has the generated carrier is only 5 GHz. An electrical amplifier may be inserted after detection to compensate for additional conversion losses in a standard 60 GHz communication system.

## 5 CONCLUSION

In conclusion, we have presented an integrated device based on a photonics on glass platform producing two wavelengths with controlled and stable spacing. The optical signal from this device has been detected using a rapid photodiode and analyzed, showing a very small linewidth of 1.8 kHz and a frequency drift of 1.8MHz, ten times smaller than values reported for similar devices using semiconductor lasers. The device has then successfully been used in transmission experiments using advanced modulation formats such as 16 QAM, where it validated IEEE communication standards at 60 GHz up to 2,5 GBps bit rates.

## ACKNOWLEDGMENT

This work was supported by the European Union Horizon H2020 research and innovation program under the Marie Sklodowska-Curie grant agreement No 642355 FIWIN5G.

## REFERENCES

[1] G. Carpintero, S. Hisatake, D. de Felipe, and al., "Wireless Data Transmission at Terahertz Carrier Waves Generated from a Hybrid InP-Polymer Dual Tunable DBR Laser Photonic Integrated Circuit", Scientific Reports 8, 3018 (2018).

[2] Haifeng Shao, Shahram Keyvaninia, Mathias Vanwolleghem, Guillaume Ducournau, Xiaoqing Jiang, Geert Morthier, Jean-François Lampin and Gunther Roelkens, "Heterogeneously integrated III–V/silicon dual-mode distributed feedback laser array for terahertz generation," Optics Letters, vol. 39, no. 22, pp. 6403-6406, 2014.

[3] N. Arab, L. Bastard, J. Poëtte, J-E. Broquin, and B. Cabon, "Thermal coupling impact on an MMW carrier generated using two free-running DFB lasers on glass," Opt. Lett. 43, 5500-5503 (2018).

[4] N. Arab, L. Bastard, D. Bucci, E. Ghibaudo, J-E. Broquin and J. Poëtte, "Integrated Optics DFB Lasers On Glass For High Radio-Frequency Generation", 2018 International Topical Meeting on Microwave Photonics (MWP). IEEE, 2018. p. 1-4.

[5] N. Arab, L. Bastard and J. Poëtte, "Co-integration of two DFB lasers on glass for millimeter-wave generation", Integrated Optics: Devices, Materials, and Technologies XXI. International Society for Optics and Photonics, 2017. p. 1010605.

[6] V. Lecocq and al., "Industrial integration of high coherence tunable single frequency semiconductor lasers based on VECSEL technology for scientific instrumentation in NIR and MIR," Proc. SPIE 10087, 2017.

# Low Polarization Sensitive Semiconductor Optical Amplifier Co-Integrated with Passive Waveguides for Optical Datacom and Telecom Networks

*Student Paper*

**Aref Rasoulzadeh Zali[1], Steven Kleijn[2], Luc Augustin[2], Ripalta Stabile[1], Nicola Calabretta[1]**
[1] IPI-ECO research institute, Eindhoven University of Technology, Eindhoven, the Netherlands
[2] Smart Photonics, High Tech Campus, Eindhoven, the Netherlands
*E-mail: a.rasoulzadehzali@tue.nl*

## ABSTRACT

For device application in Datacom and Telecom networks, low polarization sensitive (PS) SOAs with easy fabrication process co-integrated with passive photonic circuits are highly essential. In this work, a low polarization sensitive SOA based on a bulk active layer is designed, fabricated and characterized. The results of the present work focus on the investigation of low polarization ridge waveguides with bulk active layer. In the proposed structure, the SOA is integrated with other passive waveguides, therefore exhibiting its potential application to be integrated in a photonic integrated circuit. The low polarization sensitivity of bulk SOA is proven for a wide range of input power (-25 dBm to 10 dBm) and wavelength for network-device applications. Characterizations of an SOA with length of 1.5mm co-integrated with 2.3 and 0.8 mm passive waveguides indicate 17 dB net gain with a polarization dependent gain (PDG) between 0.3dB and 3dB at 1588nm wavelength and 125 mA bias current for different input optical powers.

**Keywords**: Semiconductor optical amplifiers, low polarization sensitivity, Bulk, and polarization dependent gain.

## 1. INTRODUCTION

Semiconductor optical amplifiers (SOAs) integrated with passive devices are attractive for optical Datacom and Telecom systems due to their high gain with small footprint and broad bandwidth operation. Polarization insensitive operation of the SOAs is essential in enabling transparent operation in all optical communication networks operating in broadband communication wavelength range. Approaches to achieve polarization insensitive (PI) SOAs have already been demonstrated with strained multi-quantum well (MQW) [1] and strained-bulk buried and ridge waveguide (WG) structures [2-5]. However, the realization of high gain PI MQW SOA has so far required growing technologies where high precision is needed to engineer the energy bands (for a desired wavelength emission band) [1]. Researchers have also realized SOAs based on bulk active layers but with buried waveguide structure [2],[3]. However, here tapering and window regions are required to improve the coupling loss and facet reflectivity [3], making co-integration with integrated passive circuits even harder.

In this paper we report bulk ridge-type PI SOA for 1.55µm wavelength co-integrated with passive waveguides. The designed size of the bulk active region renders them polarization insensitive over large current and wavelength ranges, while relaxing the fabrication process based on simple single-step grown unstrained active layers. This will also improve the SOAs reliability. Experimental results of SOAs co-integrated with passive waveguides show low PI operation and 17 dB net gain at different bias currents and input optical powers.

## 2. Structure, Design and Fabrication

To achieve low PDG SOA, a layer stack was grown consisting of an unstrained core of Q1.55 InGaAsP surrounded by a Q1.25 cladding, with a total InGaAsP thickness of 500 nm. The thickness of the cladding and core layers are optimized thereby the confinement factors of TE- and TM-polarization are almost the same which allows to achieve low PDG SOA. The SOA was then fabricated following the standard generic integration platform process offered by SMART Photonics B.V. [6]. An active layer structure is grown using metalorganic chemical vapour deposition (MOCVD) which is patterned and etched to leave the active layer structure where needed. The islands are regrown with a Q1.25 waveguiding layer, after which high resolution lithography and dry-etching is applied to pattern the waveguides. A passivating dielectric layer is deposited as well as a planarizing polymer, prior to metallization. To reduce facet reflections, a dielectric AR coating is deposited. A schematic of the fabricated structure is shown in Figure 1.

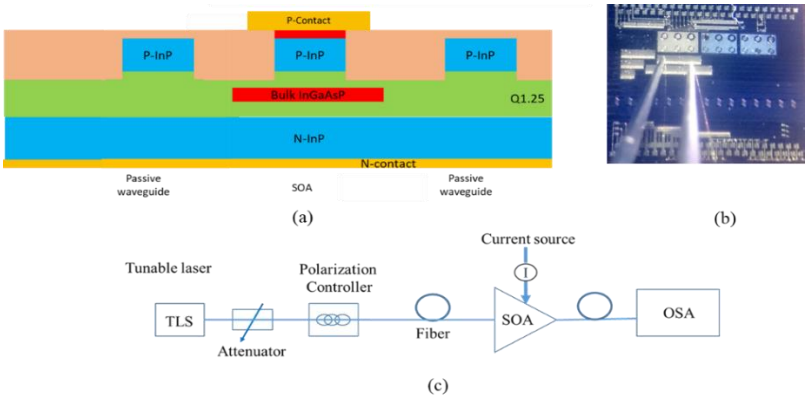



*Figure 1: (a) Cross-sectional view of the low PDG bulk SOA co-integrated with butt-coupled waveguides. The SOA consists of a bulk InGaAsP active core embedded in the 500 nm thick InGaAsP (Q1.25) waveguide. (b) The fabricated chip. And (c) the measurement setup.*

## 3. Characterization of low polarization sensitive bulk SOA

The low polarization sensitive bulk SOA have been assessed using the set-up shown in Fig. 1(c). Optical spectra of the amplified spontaneous emission (ASE) of a 1.5 mm long SOA for bias currents varying from 40 to 120 mA are shown in Fig. 2(a). Due to the band-filling effect, an increasing of the bias current results in a blue shift. The wavelength corresponding to the peak power shifts from 1621 nm to 1585 nm, for 20 mA and 125 mA, respectively. Additionally, the ASE peak power increases from -64 dBm to -36 dBm as well. Above 125 mA bias current, the gain of the SOA equals the total losses (including AR facets), which in turn makes it start lasing. This can be avoided by optimizing the AR coating further. Hence, at this step, the highest possible bias current used for the SOA is 125 mA.

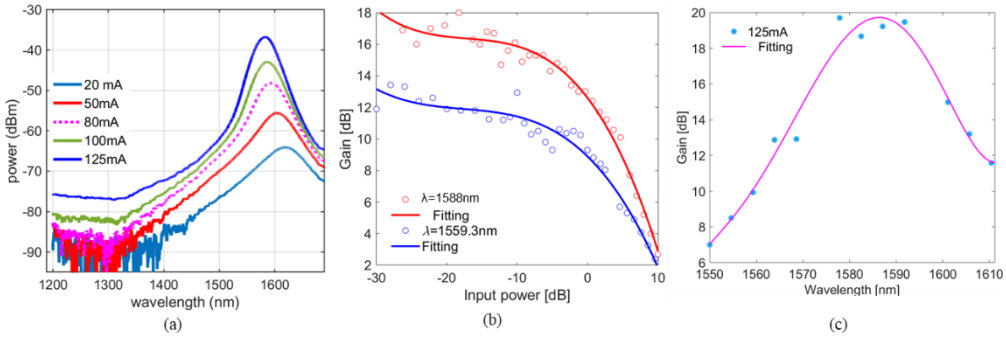



*Figure 2. Amplified spontaneous emission collected at the output facet of the ridge-bulk SOA for currents of 20, 50, 80, 100, and 125 mA at temperature of 20 ℃. Fig. 2(b) Chip gain (the highest value of gain considering different polarization) versus input power for the ridge-bulk SOA at bias current of 125 mA and for two wavelength: 1588nm and 1559.3 nm.*

To characterize the gain and polarization performance of the ridge-bulk SOA versus the input power, a tunable laser is connected to the input of the SOA using a tapered fiber via a polarization controller. The output optical spectrum is collected at the output facet of the SOA using a tapered fiber. We record the spectrum for different input powers varying from -20 dBm to 15 dBm. The bias current of the SOA is set to 125 mA. We change the polarization states to measure the highest (the best case) and lowest (the worst case) gain of the SOA, respectively. Fig. 2(b) shows the SOA gain at two different wavelengths: 1588nm (the wavelength corresponding to the peak power of ASE for 125mA bias current) and 1559.3nm which is different from the peak wavelength. As shown the gain at 1559.3 nm is 12 dB whereas the gain of the SOA at 1588nm is 17 dB. Figure 2(c) shows the gain spectrum of the SOA at bias current of 125mA. The peak gain is around 1580nm and the SOA has at least 10dB gain in the broadband interval of 1550nm to 1610nm.

The polarization sensitivity of the chip gain is defined as the absolute value of the difference of the chip gain for the linear TE and TM polarization $\left|\mathrm{TE}_{\mathrm{gain}}-\mathrm{TM}_{\mathrm{gain}}\right|=\left|\Gamma_{\mathrm{TE}}g_{\mathrm{mat,TE}}-\Gamma_{\mathrm{TM}}g_{\mathrm{mat,TM}}\right|$ which $g_{\mathrm{mat,TE/TM}}$ stands for material gain of bulk active layer. Based on the designed layer stack (c.f. Fig. 1(a)), same confinement factor for both polarization is achievable. Since the material gain for both polarization are almost equal, one could expect the low polarization sensitive SOA. Fig. 3 (a) and (b) shows the absolute magnitude of the polarization dependent

gain (PDG) versus the input power for the two different wavelength of interests, 1588nm and 1559.3nm. As depicted in the figures below, by increasing the input power at a fixed current (125 mA) the PDG also decreases. This result is in agreement with theoretical simulation of other types of buried hetero-structure based SOAs [2]. Comparison of the two figures suggests that the overall PDG is lower for wavelength of 1559.3 nm compared to 1588nm of half dB. This originates from the fact that the corresponding gain (c.f. Fig. 2(b)) is 4dB lower for 1559.3nm wavelength compared to the peak wavelength.

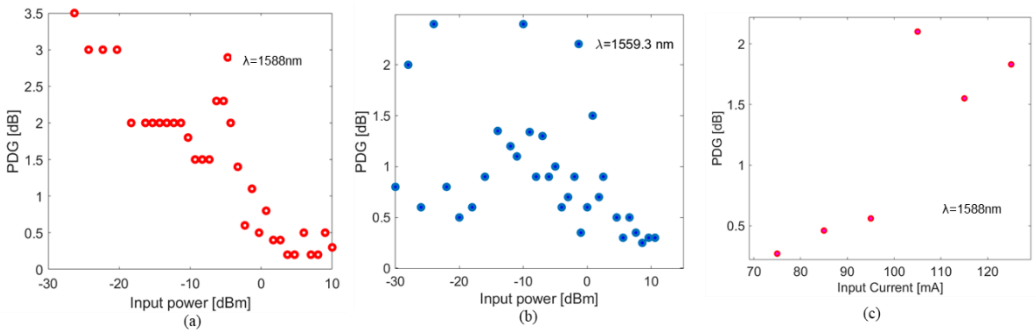



*Figure 3. Polarization dependent gain (PDG) of the proposed ridge-bulk SOA vs. input power varying from -25dBm to 10 dBm at bias current of 125 mA versus input power for a wavelength of a) 1588nm and b) 1559.3 nm. (c) PDG vs. bias current for assumed input power and wavelength of -22dBm at 1588nm, respectively.*

Moreover, Fig. 3(c) shows the PDG dependence of bulk SOA versus the bias current. Generally speaking by increasing the bias current the SOA gain increases and the PDG increases correspondingly. The PDG is less than 1dB for bias currents lower than 100m. However, at 105mA it increasers abruptly to 2.1 dB and then decreases to 1.5 dB at 110mA. Further theoretical investigation which we will consider in future is needed to understand more about its behaviour.

## 4. CONCLUSIONS

A low polarization sensitive ridge waveguide bulk SOA co-integrated with passive waveguide is realized with easy fabrication process and demonstrated. The SOA module exhibits polarization dependent gain in the range from 3 dB to 0.3 dB as function of the input power. Moreover, it exhibits a large gain of 17 dB for input bias current of 125 mA. Results also show that SOA has even lower polarization sensitivity for wavelengths away from the peak of ASE, though its gain decreases to 12 dB. The proposed bulk ridge-type PI SOA is well suited for integration with passive waveguides which allows to utilize these active components in more sophisticated circuits such as wavelength selective switches (WSS) where the integration of actives (which act as gain element or booster or gate) and passive components (arrayed waveguide gratings which act as multiplexers and de-multiplexers) on-chip are needed.

## ACKNOWLEDGEMENTS

This work has been supported by the European ICT project QAMeleon, contract No. 780354, an initiative of the Photonics Public Private Partnership (PPP), funded under Horizon 2020.

## REFERENCES

[1] Itoh, Masayuki, et al. “Amplifying Characteristics or 1.55-µm Polarization-Insensitive SOAs with MQW and Strained-Bulk Active Layers for Device Application.” *Journal of lightwave technology* 24.3, p.1478, 2006.

[2] Michie, C., et al. “Polarization-insensitive SOAs using strained bulk active regions.” *Journal of lightwave technology* 24.11, pp-3920-3927, 2006.

[3] Morito, K., et al., “High-output-power polarization-insensitive semiconductor optical amplifier.” Journal of Lightwave Technology, 21(1), pp-176-181, 2003.

[4] Holtmann, Ch, et al. “Polarization independent bulk active region semiconductor optical amplifiers for 1.3 µm wavelengths.” *IEEE Photonics Technology Letters* 8.3, pp-343-345, 1996.

[5] Holtmann, Ch, et al. “Polarization Insensitive Bulk Ridge-type Semiconductor Optical Amplifiers at 1.3 µm Wavelength.” *Optical amplifiers and their applications*. Optical Society of America, 1993.

[6] Augustin, Luc M., et al. “InP-based generic foundry platform for photonic integrated circuits.” *IEEE journal or selected topics in quantum electronics* 24.1, pp-1-10, 2017.

# Bifurcation and Chaotic Behavior of Feedback Semiconductor Lasers Operating in the Full Range of External Reflectivity

**Qin Zou, Kamel Merghem, Badr-Eddine Benkelfat, Musharrat Shabnam**

Samovar, CNRS, Télécom SudParis, Institut Polytechnique de Paris,
19 place Marguerite Perey, 91120 Palaiseau, France
*e-mail: qin.zou@telecom-sudparis.eu*

## ABSTRACT

We investigate the properties of a semiconductor laser with arbitrary levels of external optical feedback, by means of an iterative travelling-wave (ITW) model. Bifurcation diagrams and the corresponding Lyapunov exponent are used to describe the behavior of the feedback laser as the external feedback reflectivity increases from 0 to 1. Similarities and differences between the ITW model and the Lang-Kobayashi (LK) model are also reviewed. To determine the critical value of the external reflectivity, beyond which the LK model would no longer be valid, we propose a criterion based on the iterates of the phase maps for both the compound-cavity modes (ITW model) and the external-cavity modes (LK model). Preliminary results show that this critical value may correspond to the so-called «$r_\infty$-value», which is defined as the onset value of the first chaotic region.

**Keywords**: Semiconductor lasers; External optical feedback; Lang-Kobayashi model; Iterative travelling-wave model; Bifurcations and deterministic chaos; Lyapunov exponent.

## 1. INTRODUCTION

A semiconductor laser with delayed optical feedback builds an ideal system for analysing and exploring typical phenomena observed in a nonlinear time-delayed system, such as bifurcations, periodic oscillations, onsets of instability, and chaotic itinerancy. In order to describe adequately these phenomena, often occurring in the moderate- or strong-feedback regime of operation, an iterative travelling-wave (ITW) model was developed [1]. Here we summarize briefly our recent work on building, with this model, the bifurcation route of a feedback laser with the whole interval [0, 1] of external reflectivity (regimes I-V [1]) and present some preliminary results.

## 2. ITERATIVE TRAVELLING−WAVE MODEL

Consider the configuration of Figure 1. A single-longitudinal-mode laser diode is in resonance with an external Fabry-Perot cavity. We assume that $r_1$, $r_2$, and $r_3$ are all real and dispersionless. For this three-mirror-coupled system, multiple round trips inside the external cavity should be in general taken into account for an arbitrary feedback level, namely for any value of $r_3$ between 0 and 1.

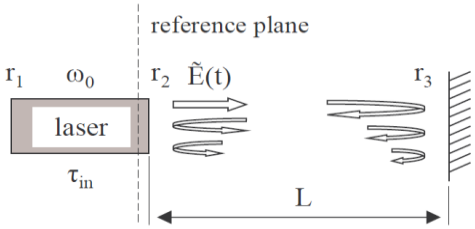



*Figure 1. Schematic of a single-mode laser diode with external optical feedback. $\omega_0$: emission (angular) frequency of the solitary laser; $\tau_{in}$: internal round-trip time; $r_1$: reflection coefficient of the rear facet of the laser; $r_2$: reflection coefficient of the front facet of the laser; $r_3$: reflection coefficient of the external mirror; $\tilde{E}(t)$: right-moving electrical field; L: length of external cavity assumed empty.*

### 2.1 Steady-state solutions

It has been shown [1] that the right-moving electrical field $\tilde{E}(t)$, which is calculated at steps of the internal round-trip time $\tau_{in}$ (in seconds), satisfies the following iterative equation:

$$\tilde{E}(t+\tau_{in}) = \frac{1}{r_2^2} exp\left\{\frac{\tau_{in} G_N}{2}(1+i\alpha)[N(t)-N_{th}]\right\} \times [\tilde{E}(t) - (1-r_2^2)\sum_{m=0}^{M}(-r_2 r_3)^m \tilde{E}(t-m\tau) exp(-im\Delta_0)] \quad (1)$$

In this equation, $G_N$ (in $s^{-1}m^3$) is the differential gain; $\alpha$ is the linewidth enhancement factor; $N(t)$ (in $m^{-3}$) is the carrier density and $N_{th}$ its threshold; $\tau$ (in seconds) is the external round-trip time and $\Delta_0$ (in radian, $\Delta_0 = \omega_0\tau$) is denoted as the initial feedback phase which is associated with the emission (angular) frequency $\omega_0$ of the solitary laser operating just above threshold.

By inserting $\tilde{E}(t) = \tilde{E}_0(t)exp(i\omega t)$ into Equation (1) and considering steady-state solutions for a feedback-induced compound-cavity mode, we obtain the following expressions for the excess gain $\delta G$ (in $s^{-1}$) and the feedback phase $\Delta$ (in radian, $\Delta = \omega\tau$, with $\omega$: possible emission frequency):

$$\delta G = \frac{-1}{\tau_{in}} ln \frac{(1-D)^2+E^2}{r_2^4} \tag{2}$$

$$tg\left(b_2 - \Delta\frac{\tau_{in}}{\tau}\right) + \frac{E}{1-D} = 0 \tag{3}$$

In these two equations, $D$ (dimensionless), $E$ (dimensionless), and $b_2$ (in radian) are written respectively as:

$$D = (1 - r_2^2)\sum_{m=0}^{M}(-r_2 r_3)^m cos[m(\Delta_0 + \Delta)] \tag{4}$$

$$E = (1 - r_2^2)\sum_{m=0}^{M}(-r_2 r_3)^m sin[m(\Delta_0 + \Delta)] \tag{5}$$

$$b_2 = \frac{-\alpha}{2} ln \frac{(1-D)^2+E^2}{r_2^4} \tag{6}$$

## 2.2 Bifurcation diagram

In Figure 2, is illustrated an example of the accumulation points of the iterates, whose values are calculated from the transcendental phase equation, Equation (3), for the full variation range (from 0 to 1) of $r_3$. The reflection coefficient of the front facet is taken as $r_2 = 0.65$ (HR-coated facet). The other parameter values are: $r_1 = \sqrt{0.3}$ (as-cleaved facet), $\alpha = 5$, $\tau_{in} = 9 \times 10^{-12}$ (s), $\tau = 9 \times 10^{-10}$ (s), and $M = 50$ (round-trip number).

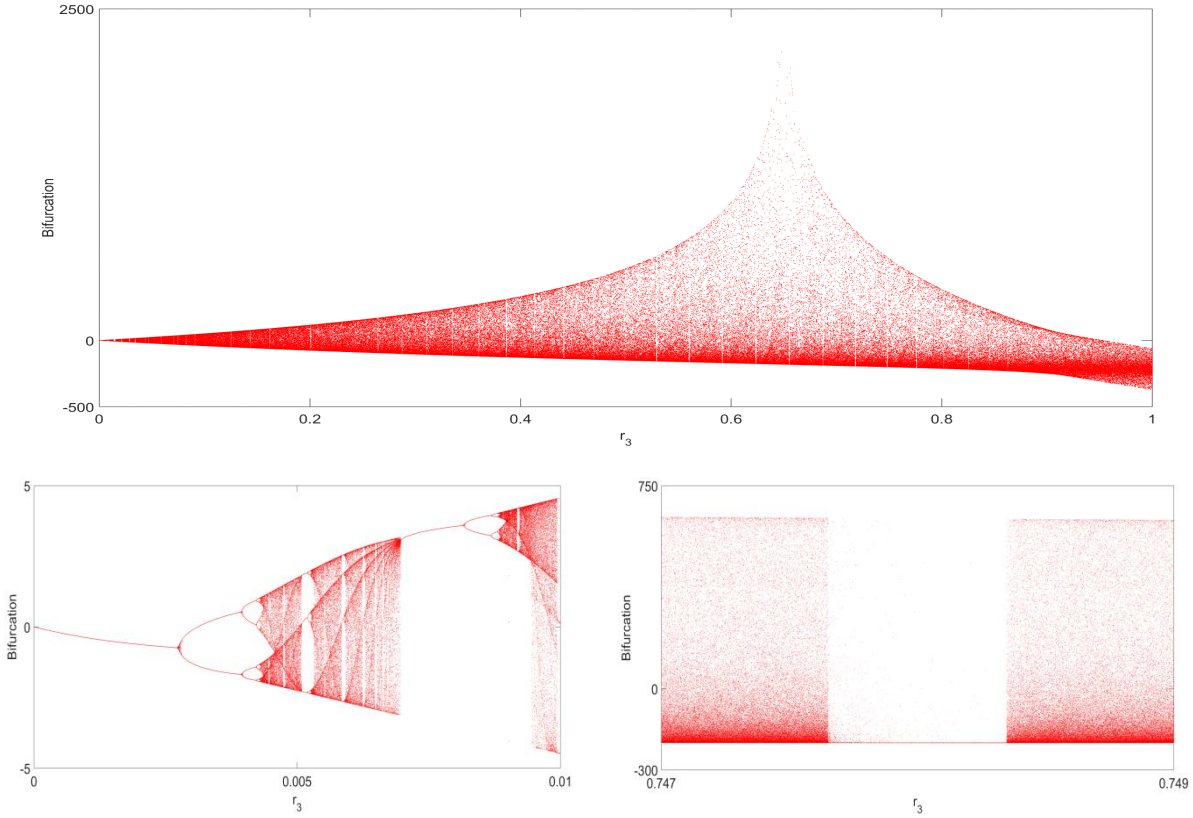



*Figure 2. Bifurcation diagram over the whole interval [0,1] of $r_3$, where the chaotic regime is interrupted by $r_3$-windows (upper); Zoom on the region corresponding to small values of $r_3$ (moderate-feedback regime, where the LK model may still be valid) (bottom-left); A narrow window between two adjacent chaotic regions in the strong-feedback regime (where the use of the LK model is no longer justifiable). This behavior confirms previous experimental observations: in the moderate- or strong-feedback regime, the system could be re-stabilized and as a result stable single-mode operation could be expected with $r_3$ close to 1 (bottom-right).*

## 3. COMPARISON BETWEEN THE ITW MODEL AND THE LK MODEL

In a previous study [2], we showed that in the weak-feedback regime ($r_3 \ll 1$, regime I), the two models are identical if (and only if) $\Delta_0 = 0$, and that any stationary solution to Equation (1) will lead to the following equation for both two models:

$$\frac{G_N}{2}(1+i\alpha)(N_s - N_{th}) + \gamma exp(-i\Delta) - i\omega = 0 \tag{7}$$

where $N_s$ is the steady-state carrier density and $\gamma$ (in $s^{-1}$) is the feedback rate which is defined as usual: $\gamma = (1-r_2^2)r_3 r_2^{-1}\tau_{in}^{-1}$. Equation (3) will then reduce to the widely-employed phase condition [3]:

$$\Delta = -\gamma\tau(\alpha \cdot cos\Delta + sin\Delta) \tag{8}$$

More generally, to determine the limit of the LK model, we compare the iterates of the phase maps obtained respectively from Equations (3) and (8). Figure 3 illustrates the difference between these two iterates, for the value of $r_3$ varying from 0 to 0.0045 (moderate-feedback regime). This figure suggests a critical value of about 0.002984 for $r_3$. This value might be (at least is very close to) the onset value ($r_\infty$-value) of the first chaotic region, at which the number of fixed points becomes infinite and the Lyapunov exponent is also equal to zero.

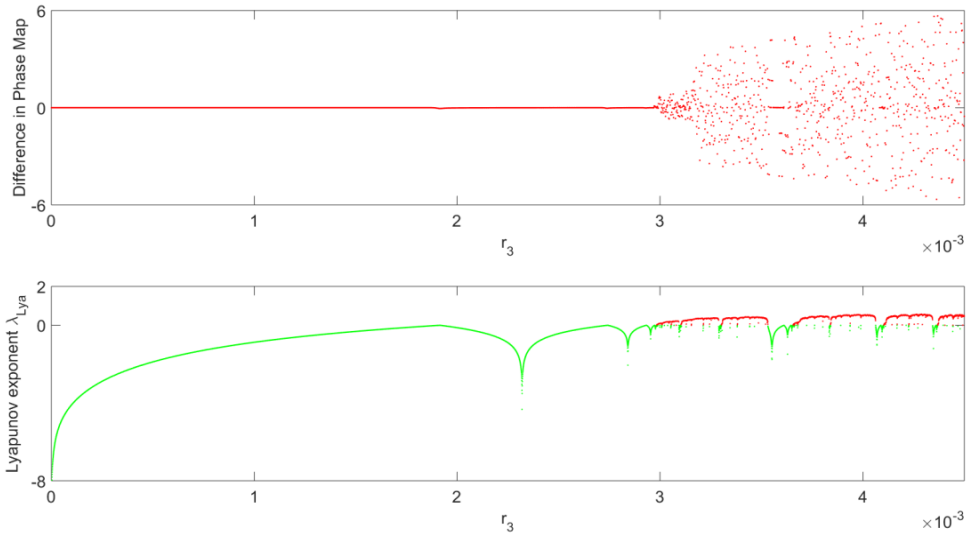



*Figure 3. Difference in phase map between the ITW model and the LK model (upper); Lyapunov exponent $\lambda_{Lya}$ calculated from Equation (3). A bifurcation takes place at $\lambda_{Lya} = 0$. Chaotic behavior corresponds to $\lambda_{Lya} > 0$ (red dots) (bottom).*

## 4. CONCLUSIONS

The iterates of the phase map and the Lyapunov exponent determine without ambiguity a state of a feedback laser and provide therefore a clear description of its behavior in each of the five feedback regimes so far classified, such as super-stable states, bifurcation points, periodic and chaotic regions, and re-(in)stabilization onsets. Stable single-mode operation could be expected in the strong-feedback regime due to the opening of reflectivity-windows inside the chaotic regions. The reflectivity value corresponding to the onset of the first chaotic region may be considered as the critical value for identifying the limit of the Lang-Kobayashi model. Future work will include an experimental investigation of a laser operating in the strong-feedback regime.


## ACKNOWLEDGEMENTS

Qin Zou would like to acknowledge Yaneck Gottesman (Télécom SudParis) for interesting discussions.


## REFERENCES


[1] L. N. Langley, K. A. Shore, J. Mørk: Dynamical and noise properties of laser diodes subject to strong optical feedback, *Optics Letters*, vol. 19, No. 24, pp. 2137-2139, 1994.

[2] Q. Zou: Steady-state behavior of semiconductor laser diodes subject to arbitrary levels of external optical feedback, *Optics and Photonics Journal*, vol. 3, No. 1, pp. 128-134, 2013.

[3] R. Lang, K. Kobayashi: External optical feedback effects on semiconductor injection laser properties, *IEEE Journal of Quantum Electronics*, vol. 16, No. 3, pp. 347-355, 1980.

# Narrow-Linewidth DBR Laser Using Open-Access High-Precision Grating in InP PIC Generic Foundry Platform

**Julio Darío López[1], Dan Zhao[2,3], Mu-Chieh Lo[4,*], Robinson Guzmán[1], Xaveer Leijtens[2], and Guillermo Carpintero[1]**

[1]Universidad Carlos III de Madrid, Leganés, Spain
[2]Technische Universiteit Eindhoven, Eindhoven, Netherlands
[3]now with ASML, Veldhoven, Netherlands
[4]University College London, London, UK
*e-mail: m.lo@ucl.ac.uk

## Abstract

- We present DBR lasers using DUV lithography in a generic InP-based photonic integration platform (SMART Photonics).
- The DBR lasers exhibit side mode suppression ratio (SMSR) > 45 dB and laser linewidths (LW) < 100 kHz.

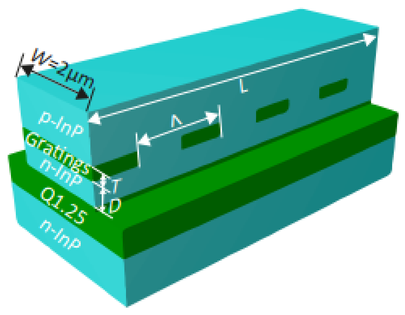
## Motivations

- CW lasers in PIC with narrow linewidth and high SMSR are key components for coherent transmission.

- Digital supermode (DG) DBR lasers:
  - 200 kHz LW and 40 dB SMSR [1].
- Sampled-grating (SG) DBR lasers:
  - 300 kHz LW and 40 dB SMSR [2].
- SGDBR laser with intra-cavity spectral filter and SOA:
  - 70 kHz LW and 50 dB SMSR [3].

- Simple and open-access DBRs are needed.

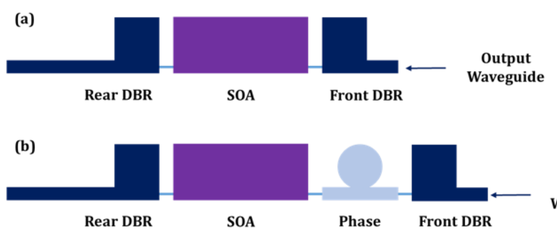
## Grating

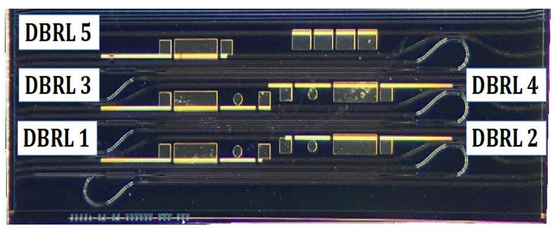



Schematic of DBR.
Zhao, D. (2018). High-precision distributed Bragg reflectors in a generic photonic integration platform. Eindhoven: Technische Universiteit Eindhoven.

- Grating structure patterned by deep ultraviolet (DUV) scanner featuring advantages of both e-beam and holographic lithography [4]
- Such a grating can be integrated with other active and passive building blocks in the platform to create a composite building block, e.g., distributed Bragg grating (DBR) laser.

## DBR Laser

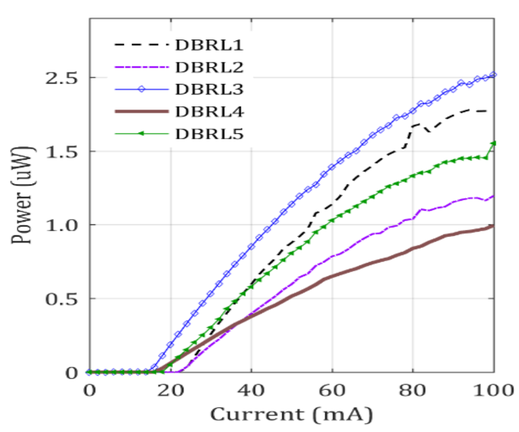


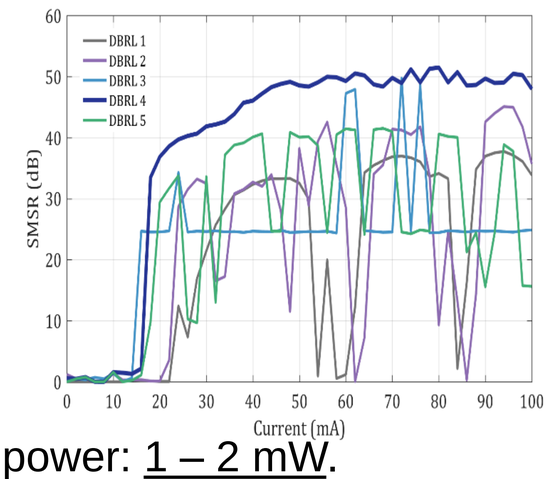




| | DBRL1 | DBRL2 | DBRL3 | DBRL4 | DBRL5 | |
|---|---|---|---|---|---|---|
| Front DBR | 30 | 50 | 100 | 200 | 50 | μm |
| Rear DBR | 600 | 600 | 600 | 600 | 600 | μm |
| Grating Pitch | 237 | 237 | 237 | 237 | 237 | nm |
| SOA (gain) | 370 | 370 | 370 | 370 | 370 | μm |
| EOPM (phase) | 300 | 300 | 300 | 300 | - | μm |
| DBRL Length | 1.39 | 1.41 | 1.46 | 1.56 | 1.08 | mm |

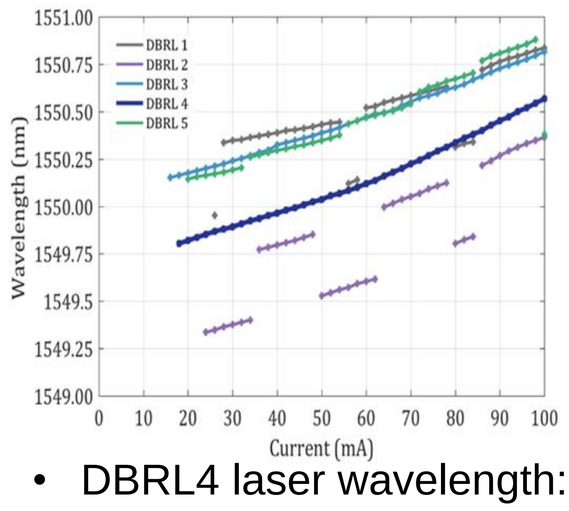
- 5 test DBR lasers made in SMART photonics technology.
- Microscope image of DBR lasers (PIC size: 4.6 mm x 1.6 mm) and the section lengths.

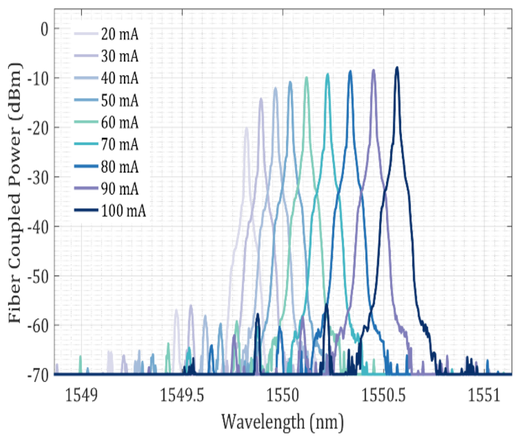
## Characterization Results



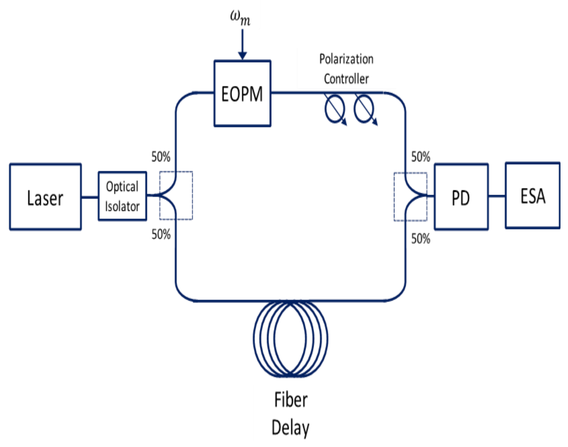



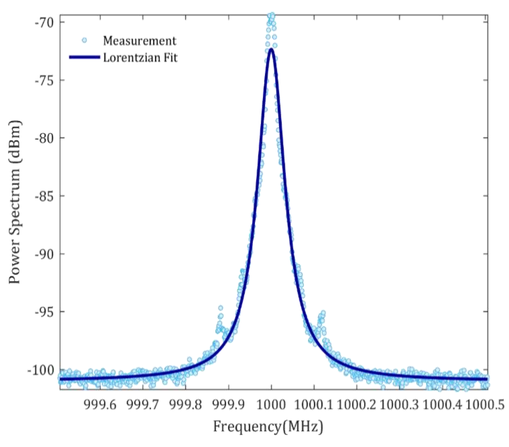

- Maximum fiber-coupled power: 1 – 2 mW.
- Threshold currents: 14 – 22 mA.
- DBRL4: 40 – 50 dB SMSR.
- Other lasers: multimode and mode hopping observed.




- DBRL4 laser wavelength:
  - < 1 nm tuning range: 1549.8 – 1550.6 nm for 20 – 100 mA.
  - ~ 0.0091 nm/mA.
- Other lasers: multimode and mode hopping observed.




- LW measured using delayed self-heterodyne method.
- 6.8-km optical fiber -> 35-μs time delay -> 10-kHz resolution.
- Measurement: full width at half maximum (FWHM) beat-note LW of 200 kHz (Lorentzian) -> Laser LW ~100 kHz.

## Conclusions

- Simple DBR lasers using DUV-defined gratings in generic foundry approach have been demonstrated:
- SMSR > 45 dB and laser LW < 100 kHz.
- insufficient output power, wavelength tuning range and multimode/mode hopping need to be improved.
- Open-access technology enables monolithic integration of DBR, SOA, and passive components for forming composite lasers with narrower LW [5].

European Union's Horizon 2020 Marie Skłodowska-Curie grant agreement No.642355 and No.713694. Spanish Ministerio de Economía y Competitividad through Programa Estatal de Investigación, Desarrollo e Innovación Orientada a los Retos de la Sociedad (grant iTWIT, TEC2016-76997-C3-3-R).

[1] S. Davies et al., "Narrow linewidth, high power, high operating temperature digital supermode distributed bragg reflector laser," ECOC, (2013), p. Th.1.B.3.
[2] M. Larson et al., "Narrow linewidth high power thermally tuned sampled-grating distributed bragg reflector laser," OFC, (2013), p.OTh3I.4.
[3] M. Larson et al., "Narrow linewidth sampled-grating distributed bragg reflector laser with enhanced side-mode suppression," OFC, (2015), p. M2D.1.
[4] D. Zhao et al, "Design of uniform and non-uniform DBR gratings using transfermatrix method," IEEE Photonics Benelux Chapter, (2015), pp. 87–90.
[5] S. Andreou, K. A. Williams, and E. A. Bente, "Monolithically integrated InP-based DBR lasers with an intra-cavity ring resonator," Optics Express 27, 26281–26294 (2019).

# Design of hybrid lasers for silicon photonics: efficiency, optical feedback tolerance and laser dynamics

**Mariangela Gioannini[1], Lorenzo Columbo[1], Antonino Bologna[1], Marco Novarese[1], Sebastian Romero-García[2], Dominic Siriani[2], Jock Bovington[2]**
[1] Department of Electronics and Telecommunication, Politecnico di Torino (Italy)
[2] Cisco Systems, San Jose, CA, (US)
*e-mail: mariangela.gioannini@polito.it*

## ABSTRACT

*We present the design and the simulation of the dynamics of hybrid lasers based on a reflective SOA edge-coupled to a silicon photonics integrated reflector realized with waveguide rings. We design the laser for high efficiency and tolerance to spurious optical feedback and we compare the best designs in SiN and SOI platforms. By simulating the laser dynamics with a Time Domain Travelling Wave approach we show that the hybrid solitary laser (ie: without feedback) can operate in various regimes from CW to self-pulsing. These regimes are triggered by the linewidth enhancement factor of the SOA and can be controlled by a phase control section. The tolerance to the optical feedback is also further enhanced by the damping of the relaxation oscillations filtered by the narrowband reflector.*

***Keywords**: hybrid laser, silicon photonics, optical feedback tolerance*

## 1. INTRODUCTION

It is well known that the integration of the laser source in a silicon photonics (SiPh) platform is one of the most challenging issues because the laser must be low cost, reliable, efficient, stable and robust against spurious optical back reflections coming from the rest of the SiPh circuit or from the output connectors. The technology closest to industrial commercialization is the hybrid integration technique consisting of flip-chip butt-coupling of a III-V gain chip with a SiPh mirror [1].

In this work we present the design of a hybrid laser realized via the edge-coupling of a commercial III-V MQW HR/AR reflective SOA (RSOA) with an integrated mirror implemented in a silicon nitride (SiN) platform as sketched in Fig.1. The SiN mirror forms an external cavity that can be designed to optimize the laser wall-plug efficiency (WPE), the tolerance to an external optical feedback [2], and the laser optical linewidth [3]. We show here that a trade-off between laser efficiency and feedback tolerance can be found with a proper selection of the mirror parameters [2], and we compare this design with a similar one in a Silicon-On-Isolator (SOI) platform. We also study the dynamics of these hybrid lasers both as solitary lasers and in the presence of spurious external optical feedback. As a final result, we demonstrate that the designed SiN hybrid laser can give an ultra-high tolerance to the external optical feedback thanks to the narrow bandwidth reflection coefficient of the SiPh mirror.

## 2. DESIGN

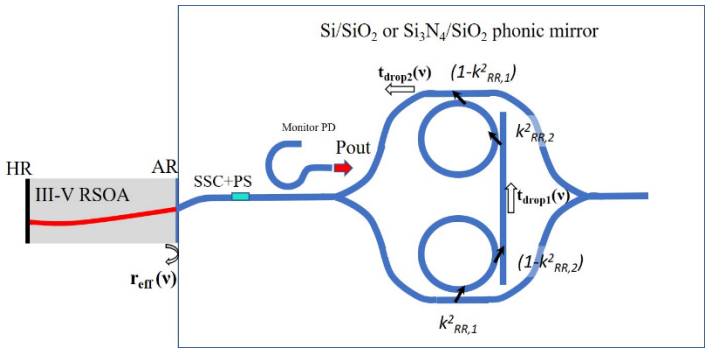



*Figure 1: Sketch of the hybrid external-cavity laser structure. The mirror is based on a Mach Zehnder Interferometer (MZI) loaded by two rings providing a narrowband complex reflectivity $r_{eff}(v)$ and a Vernier tuning of about 150 nm. The symbols are: PS = phase control sections, $k^2_{RR1,2}$ = power coupling coefficient of the two ring resonators in the critical coupling configuration ($k_{RR1,2}$), $t_{drop1,2}$ = drop port transmission coefficients of the two ring resonators, SSC = spot size converter. The output power $P_{out}$ is collected by the coupler with output coupling coefficient $T_{c,out}$.*

Starting from a simple model based on textbook rate-equations and an effective Lang-Kobayashi (LK) approach [2], we demonstrated that by increasing the mirror cavity effective length ($L_{eff}$) the laser in a SiN platform is more tolerant to optical feedback (compared to an equivalent FP laser) thanks to the increase of the cavity round trip time. In Fig. 2 we plot, as function of the ring coupling coefficients ($k_{RR,1}$=$k_{RR,2}$) and the output coupler transmission coefficient $T_{c,out}$, the calculated WPE at fixed output power $P_{out}$=20mW (Fig. 2a), the corresponding

SiPh mirror $L_{eff}$ and the resulting critical feedback level as predicted by the effective LK approach [2]. The RSOA is a commercial device, and we design the laser considering RSOA parameters extracted from measurements. In this work the design procedure of [2] for the SiN platform is extended also to the SOI platform by including the non-linear loss due to two-photon absorption (TPA) and free carrier absorption (FCA) in silicon straight waveguides and rings. TPA and FCA parameters are extracted from measurements. Fig.2(a) shows that high WPE of more than 19% can be reached in both platforms, even including silicon TPA and FCA of SOI waveguides. This is due to the design procedure that searches for the best design parameters to optimize the WPE and due to the high differential gain of the III-V gain material. On the contrary, Fig. 2(b) and (c) demonstrate that the choice of the platform significantly impacts on the $L_{eff}$ and hence the maximum tolerated feedback ($R_{ext,max}$). In the SiN platform $L_{eff}$ can be long because of large ring radii (>95 μm) and negligible non-linear loss. Fig. 2c also quantifies the impact of silicon non-linear loss on $R_{ext,max}$ showing that the high $R_{ext,max}$ achivable in SiN is significantly reduced in Si because of the TPA and FCA.

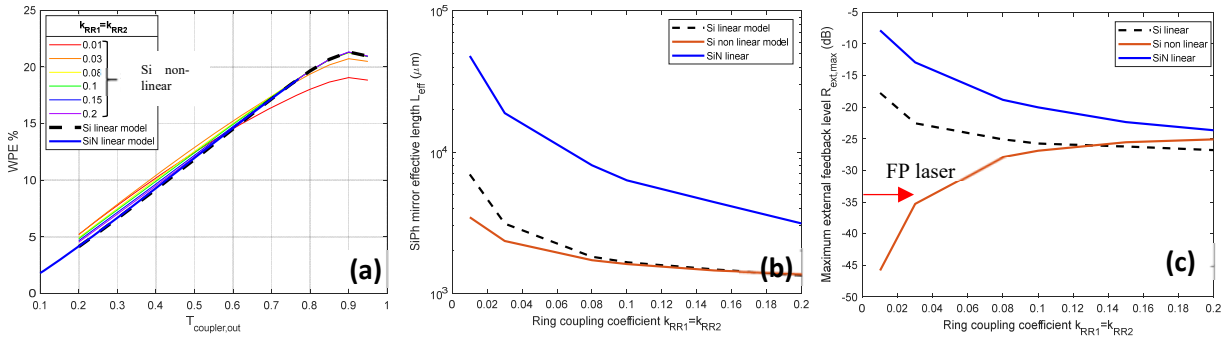



*Figure2:(a) Laser WPE at Pout=20mW as function of the design parameters and platform (SiN or SOI); (b) SiPh mirror effective length and (c) maximum tolerated external feedback as function of the ring coupling coefficients $k_{RR1,2}$. In (b) and (c) $T_{c,out}$ is fixed at 72%. The red arrow indicates the $R_{ext,max}$ of an equivalent Fabry-Perot laser.*

From this analysis we learned that the SiN design is more tolerant to the optical feedback thanks to the possibility of designing both long $L_{eff}$ maintaining sufficiently large tuning range. However the question is now if the narrowband $r_{eff}(\nu)$ of the mirror can play an additional role in increasing further the tolerance to the feedback by damping the relaxation oscillation of the laser. To answer this question, we have studied the laser dynamics.

## 3. LASER DYNAMICS

To study the dynamics of the hybrid solitary laser and to validate the design presented above, we have simulated the laser structure in Fig.1 with a Time Domain Travelling Wave (TDTW) simulator including polarization dynamics and hence the gain dispersion and the linewidth enhancement factor (LEF) of the SOA. The advantage of this approach is the inclusion of the dynamic competition between the lasing mode and the other cavity longitudinal modes. The TDTW model can also investigate the role of the narrowband SiPh mirror in the dynamics of the solitary laser and in the ultra-high tolerance to the optical external feedback.

Via TDTW numerical simulations we first found that the various operation regimes of the solitary laser (ie: stable single mode, self-pulsing, chaotic etc..) are triggered by the LEF and can be controlled by the phase control section PS. As shown in Fig. 3a, the lasing mode of the SiN laser of Fig. 1 can be tuned via the PS section to operate at the reflectivity peak (marked with "TW0 case" in Fig.3a) or detuned with respect to it ("TW1 case" in Fig.3a) where $dr_{eff}(\nu)/d\nu$ is positive and maximum. The TDTW simulations showed that when LEF is small (e.g. LEF=1) the TW0 solution is stable but, for higher LEF (e.g LEF=3), it becomes unstable evolving toward a pulsing regime (Fig.3b) sustained by the beating of two cavity longitudinal modes. On the contrary, the TW1 solution is always stable even for large LEF (Fig.3c). In the TW0 case, any noise can shift the lasing mode to the high frequency side of the reflectivity peak with a consequent significant reduction of the $r_{eff}(\nu)$ seen by the laser. This leads to the consequent increase of the carrier density and, in the case of large LEF, this further pushes the lasing mode to higher frequencies until a point of stable operation is reached. This stable operation is usually self-pulsing caused by the beating of two other cavity longitudinal modes emerging from the $(\nu-\nu_0)<0$ side. On the contrary, in the TW1 case, a negative feedback control is installed: if the lasing mode shifts to smaller/higher frequency due to the noise, the effective reflectivity reduces/increases leading to an increase/reduction of the carrier density that pushes the lasing mode back to the stable TW1 position.

This TW1 solution turns out to be very stable also in the presence of external optical feedback. In Fig. 3d we report the stability of the TW1 solution in the presence of an external feedback for different SiN laser designs with Tcout=72% and various ring coupling coefficients. The green symbols indicate a stable TDTW solution whereas the red symbols are unstable TDTW solutions triggered by the photon-photon resonance with other cavity longitudinal modes. We observed an improved stability with respect to the solution predicted by the effective LK

approach. In Fig.3e we compare the intensity modulation response of the solitary laser as predicted by a standard rate-equation model with spectrally flat $r_{eff}(v)$ and the one calculated with the TDTW approach including the narrowband $r_{eff}(v)$ with bandwidth narrower than the laser relaxation oscillation frequency. The peak of the relaxation resonance is significantly damped by the narrowband mirror and therefore the increased damping improves the $R_{ext,\,max}$ further with respect to the LK prediction. The drawback is however the turn-on of the photon-photon resonance appearing as second peak of the IM response. The PPR is indeed the cause of the red unstable TDTW solution in Fig. 3d.

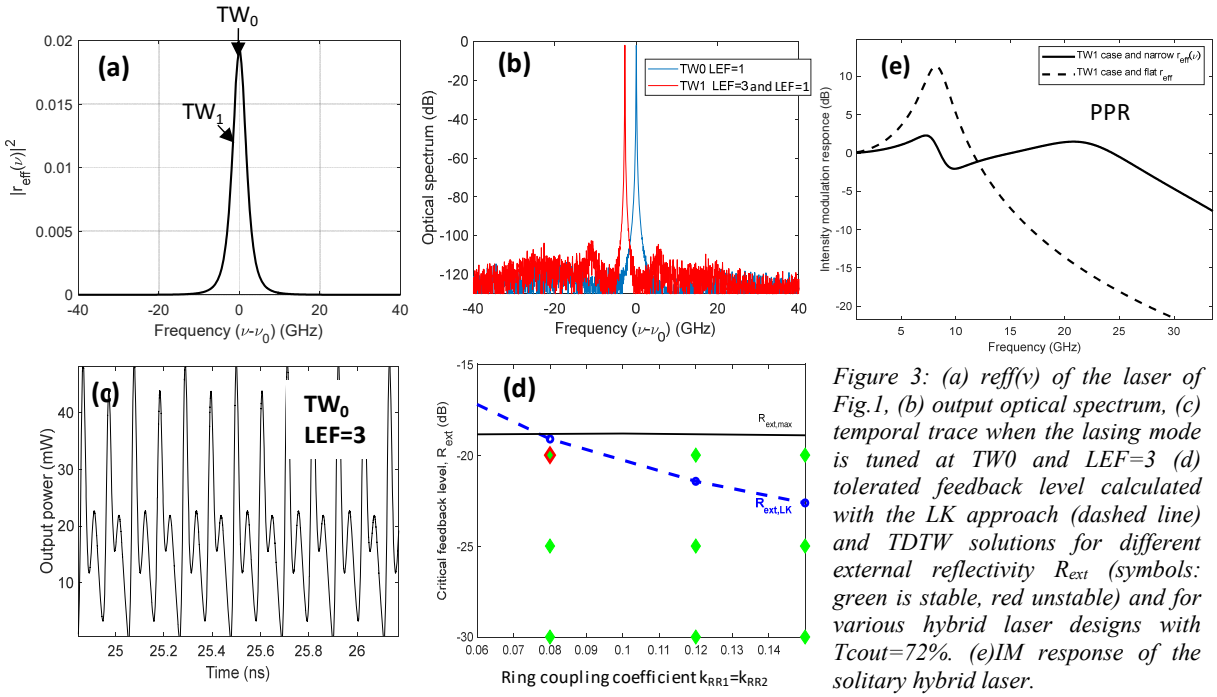



*Figure 3: (a) reff(v) of the laser of Fig.1, (b) output optical spectrum, (c) temporal trace when the lasing mode is tuned at TW0 and LEF=3 (d) tolerated feedback level calculated with the LK approach (dashed line) and TDTW solutions for different external reflectivity $R_{ext}$ (symbols: green is stable, red unstable) and for various hybrid laser designs with Tcout=72%. (e)IM response of the solitary hybrid laser.*

## CONCLUSIONS

We have presented the design of a hybrid laser based on RSOA and SiPh mirror. We have compared the laser performance in terms of efficiency and tolerance to the optical feedback for both SiN and SOI platforms demonstrating that both platforms can provide good WPE, but the TPA and FCA of silicon waveguides and rings significantly reduce the tolerance to spurious optical feedback. Studying the laser dynamics we have shown that the tolerance to spurious back reflections of the hybrid laser is significantly increased not only thanks to the long effective length of the SiPh mirror but also due to the very narrow bandwidth of the SiPh reflector that can damp significantly the laser relaxation oscillations that trigger the laser instability in the presence of spurious back reflection. This analysis demonstrates the potential of these structures for realizing lasers for a silicon photonics platform.

## REFERENCES


[1] Hang Guan et al. "Widely-tunable, narrow-linewidth III-V/silicon hybrid external-cavity laser for coherent communication," Opt. Express 26, 7920-7933 (2018)

[2] L. Columbo, J. Bovington, S. Romero-Garcia, D. F. Siriani and M. Gioannini, "Efficient and Optical Feedback Tolerant Hybrid Laser Design for Silicon Photonics Applications," in *IEEE Journal of Selected Topics in Quantum Electronics*, vol. 26, no. 2, pp. 1-10, March-April 2020

[3] Y. Fan et al., "Spectral linewidth analysis of semiconductor hybrid lasers
with feedback from an external waveguide resonator circuit," Opt. Express, vol.25, no. 26, pp. 32, 2017.

# Design of III-V on Silicon Optical Switch based on Mach-Zehnder and SOA Switching Elements

**Junfei Xia, Qixiang Cheng*, Tongyun Li, Richard V. Penty**

Centre for Photonic Systems, Electrical Engineering Division, Department of Engineering, University of Cambridge, 9 JJ Thomson Avenue, Cambridge CB3 0FA, UK.
**e-mail: qc233@eng.cam.ac.uk*

**ABSTRACT**

This paper proposes a novel lossless photonic switch based on III-V semiconductor optical amplifiers (SOAs) combined with silicon photonics in a heterogenerous integration scheme. An 8×8 device implemented using dilated Banyan topology achieves a 17dB input power dynamic range (IPDR) with power penalties of less than 1dB. Silicon-based thermo-optic (T-O) Mach-Zehnder (MZ) switching elements are used to manipulate light, whilst SOAs are placed in the middle to switch in tandem with the MZs to provide gain and crosstalk suppression. A 64×64 Clos switch built from the 8×8 blocks exhibits a 10dB IPDR with power penalties of less than 1dB.

**Keywords**: Integrated optical devices; silicon photonics; optical switching

## 1. INTRODUCTION

The exponential growth of network traffic in data centres places high scalable, low power consumption and low latency demands on optical interconnects. Photonic switches can act as an alternative to support growing bandwidth requirements as a result of the increasing scaling trend and high bandwidth density at both switch and link level [1]. To realise dynamic and reconfigurable networks, compatible, robust, fast and flexible optical switches are therefore required.

Optical space switches based on micro-electromechanical systems (MEMS) represent the most mature and commercial technologies; however, their rigorous calibration introduces significant complexity that is ultimately reflected in the cost per port [2]. To ensure low cost for eventual data-center adoption, integrated technologies are favoured [1]. Indium phosphide (InP) and silicon based integration technologies have been widely explored with significant advancement being achieved in the last decade. A few thousands of components have been monolithically integrated on the InP platform for a lossless SOA-based 16×16 port count switch [3] and a space-and-wavelength switch with 64×64 connectivity [4]. However, further scale-up may be bounded by the relatively large footprint of InP devices [5]. On the other hand, silicon photonics attracts attention as it offers the benefits of small footprint, energy efficiency, and CMOS manufacturing compatibility. While this type of technology has been demonstrated with very large-scale integrations with over a hundred port counts for optical switching circuits [5], the ultimate limitation is revealed as the intrinsic passive loss [1]. Currently, new research opportunities have been identified to accomplish gain integration into the silicon platform, via hybrid or heterogenous integration schemes. Whereas initial demonstrations of gain-integrated silicon switches tend to apply a hybrid integration approach where III-V dies are flip-chip bounded on top of a silicon carrier [6], this method requires a very precise alignment process and also has reflection issues at interfaces. In addition, it lacks flexibility in the switch design as the etched silicon cavity can be either placed at the front-end or back-end of the device. Heterogenous integration via wafer or die bonding techniques, however, provides a more powerful way for implementing gain in Si Photonic optical switches.

In this paper, we design an 8×8 III-V on silicon switching building block using a dilated Banyan topology and perform physical-layer simulations. An adiabatic coupler is deployed to couple the light from the underlying silicon waveguide to the SOA, which provides an optical gain to compensate the passive losses in silicon. A Clos topology is then applied to achieve a 64×64 switch fabric. Simulation results indicate that this new 8×8 gain-integrated silicon switch exhibits a very wide (IPDR) with power penalty less than 1dB and the 64×64 Clos silicon switch still achieves a reasonably wide IPDR of 1dB penalty.

## 2. 8×8 GAIN-INTEGRATED SILICON BUILDING BLOCK FOR A 64×64 CLOS SWITCH FABRIC

Figure 1(a) shows a schematic of heterogeneous integration of a III-V multiple quantum well (MQW) SOA on silicon. Optical signals couple from the underlying silicon waveguide to the upper layer where III-V SOAs are bonded via an adiabatic coupling taper [7]. At the end of the SOA section, the amplified signals couple back into the silicon waveguide via a second taper.

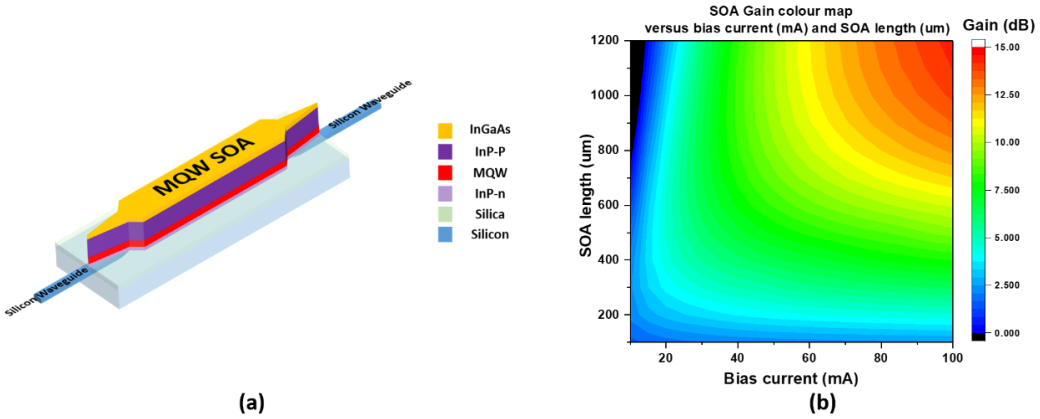



*Figure 1. (a) The configuration of the heterogeneous integration of III-V on silicon SOA with double adiabatic coupling taper ; (b) SOA gain colour-map versus SOA length and bias current at -5dBm switch on-chip input power.*

This heterogeneous integration introduces optical gain by the integrated SOA elements. However, the confinement factors of MQW and separated confinement heterostructure (SCH) are 0.035 and 0.15, respectively [8], which are lower relative to a typical stand-alone III-V based SOA (0.06 and 0.56) [12]. The optical gain as a function of SOA length and bias current is thus investigated using the VPI simulator [12] to determine the optimal design of the SOA block in the 8×8 integrated switch. The colour map in Figure 1(b) shows optical gain at device lengths from 100μm to 1200μm and bias currents from 10mA to 100mA at -5dBm input optical power. A 900μm long SOA is selected as it has a sufficient gain to compensate for the total loss of an optical path while with limited excess noise. In this simulation, we consider a worst-case scenario for silicon-based thermo-optic MZ switches, where the target length of the MZ phase shifter is 1mm and silicon waveguide loss is 1.5dB/cm [9]. An MZ switching elements has loss of less than 1dB and crosstalk of -20dB in our simulation although current engineered MZ switch has lower 1dB loss and crosstalk as low as -28dB [9]. In addition, Silicon waveguide crossing induces a 0.05dB loss and crosstalk of -40dB [10].

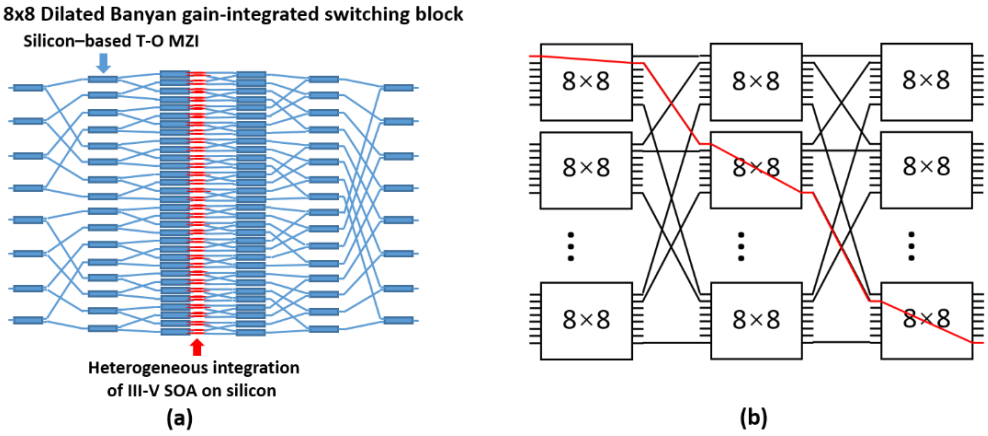



*Figure 2. (a) Schematic of 8x8 dilated Banyan gain-integrated silicon switch, Blue blocks indicate silicon-based T-O MZ silicon switches and the red shapes represent heterogeneous integration of SOAs on silicon (b) Schematic of 64x64 Clos Switch built by 8x8 designed building blocks, the red line represents an arbitrary switch path via three Clos stages.*

An 8×8 dilated topology is therefore chosen to suppress the crosstalk from the MZ switch units. Dilated Banyan architecture as a strictly non-blocking switch fabric [11] is implemented in this design which provides simple physical arrangement, logical equivalence and decreased waveguide crossings. Figure 2(a) describes the switching element in this design, where the binary dilated arrangement in this architecture provides a good isolation between adjacent paths for below -60dB crosstalk. In addition, an array of SOA elements bonded in the middle stage can compensate the insertion loss for every path and further suppress the crosstalk with an additional -30dB extinction ratio by providing strong absorption in the OFF state. Therefore, by using the proposed 8×8 switch building block, a 64×64 Clos switch fabric can be achieved.

## 3. 8×8 GAIN INTEGRATED BUILDING BLOCK AND 64×64 CLOS SILICON SWITCH PERFORMANCE

To assess the performance of the 8×8 switching building block and 64×64 Clos silicon switch, the component-level loss is initially estimated to determine the on-chip gain required for the SOAs . The 900μm-long SOA biased

with 40mA provides 11.0 dB optical gain, as shown in Figure 3(a), where on-chip power decreases because of passive silicon waveguide, waveguide bends and crossings, and MZ switch losses. The input power is set as -4.7dBm resulting in an output power -6.3dBm. In this work, the performance of silicon switch is simulated with parameters fitted from references and the design shuffle network crossing and bend numbers. A 10Gb/s non-return to zero (NRZ) modulated optical signal at 1550nm is transmitted as an input of the device. The worst-case loss and crosstalk are considered in the model, and the influence of 4 different bias levels is investigated. Figure 3(b) depicts the power penalty at a bit error rate (BER) of $10^{-9}$ versus input optical power. A 0.2dB power penalty floor and 17dB IPDR with a penalty less than 1dB are achieved when bias current is set to 50mA.

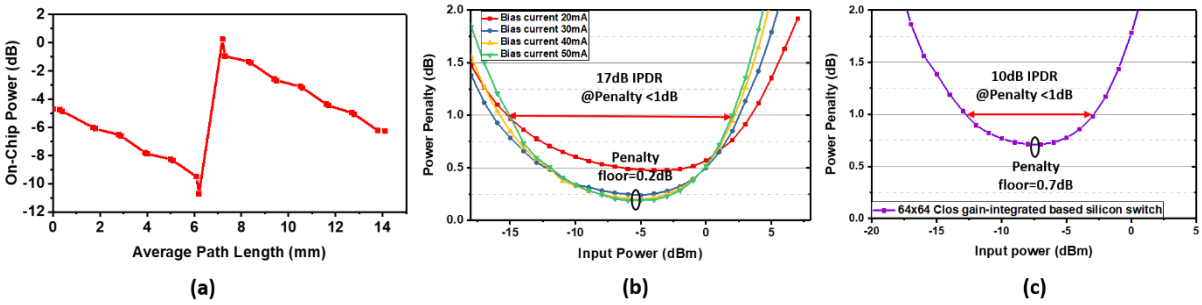



*Figure 3. (a) On-chip power as a function of switch path length in average for 8x8 dilated Banyan heterogeneous integrated silicon switch; (b) Power penalty at BER of $10^{-9}$ versus switch on-chip input power for 8x8 gain-integrated silicon switch; c) Power penalty at BER $10^{-9}$ versus switch on-chip input power for 8x8 dilated Banyan silicon switch;*

The component-level 2.2dB average loss induced by waveguide crossings and bending from 64×64 Clos shuffle networks are considered in this model. Simulation results for the 64×64 switch, where three Clos cascading stages include identical 900μm SOAs biased at 50mA, are shown in Figure 3(c). An IPDR of 10dB with power penalty less than 1dB is achieved.

## 4. CONCLUSION

This paper describes our recent work on a new gain-integrated 8×8 silicon switch design. Evanescently coupled SOAs elements and silicon-based T-O MZ switch units are used and assembled in dilated Banyan topology providing a strong suppression. This paper for the first time proposes and assesses the design of a 8×8 gain-integrated silicon switch building block, showing a 0.2dB power penalty floor at $10^{-9}$ BER and a 17dB IPDR for 1dB penalty. A 64×64 Clos switch is subsequently modelled exhibiting a 0.7dB penalty floor and 10dB IPDR with power penalty less than 1dB.

## ACKNOWLEDGEMENTS

The author would like to acknowledge funding from Cambridge Trust Scholarship.

## REFERENCES

[1] Cheng, Q. et al., "Photonic switching in high performance datacenters [Invited]," *Opt. Express* 26, 16022-16043 (2018)
[2] Kim, J., et al.: 1100 x 1100 port MEMS-based optical cross-connect with 4-dB maximum loss, *IEEE Photonics Technology Letters*., vol.15.pp 1537-1539, 2003
[3] Wang, H., et al. "Demonstration of a lossless monolithic 16 x16 QW SOA switch." *2009 35th European Conference on Optical Communication*. Vol. 2009. IEEE, 2009.
[4] Cheng, Q. et al., "The feasibility of building a 64× 64 port count SOA-based optical switch." *2015 International Conference on Photonics in Switching (PS)*. IEEE, 2015.
[5] Cheng, Q. et al. "Recent advances in optical technologies for data centers: a review." *Optica* 5.11 (2018): 1354-1370.
[6] Matsumoto, T., et al. "In-line optical amplification for silicon photonics platform by flip-chip bonded InP-SOAs." *2018 Optical Fiber Communications Conference and Exposition (OFC)*. IEEE, 2018.
[7] Kaspar, Peter, et al. "Hybrid III-V/silicon SOA in optical network based on advanced modulation formats." *IEEE Photonics Technology Letters* 27.22 (2015): 2383-2386.
[8] Stanković, Stevan, et al. "Hybrid III-V/Silicon laser based on DVS-BCB bonding." *Annual Symposium of the IEEE/LEOS Benelux Chapter, 2008*. IEEE-LEOS, 2008.
[9] Dupuis, Nicolas, et al. "Impact of topology on the scalability of Mach–Zehnder-based multistage silicon photonic switch networks." *Journal of Lightwave Technology* 36.3 (2017): 763-772.
[10] Zhang, Yang, et al. "Ultralow-loss silicon waveguide crossing using Bloch modes in index-engineered cascaded multimode-interference couplers." *Optics letters* 38.18 (2013): 3608-3611.
[11] Lu, Zeqin, et al. "High-performance silicon photonic tri-state switch based on balanced nested Mach-Zehnder interferometer." *Scientific reports* 7.1 (2017): 1-7.
[12] [Online]. Available: http://www.vpiphotonics.com

# Manufacture-compliant InP-based metal cavity nanolaser design

*Student Paper*

**E. Malysheva, A. Fiore, K.A.Williams, V.Dolores-Calzadilla**
Institute for Photonic Integration, Eindhoven University of Technology, Eindhoven, The Netherlands
*e-mail:* e.malysheva@tue.nl

## ABSTRACT

Nanolaser cavity structures are very sensitive to fabrication non-idealities. One of the important aspects is the cavity sidewalls non-verticality, produced with reactive ion etching, which have an impact on total optical losses. In this work the influence of etching slopes on the lasing performance is studied, and novel nanolaser cavity design on InP Membrane on Silicon platform with increased etching slopes tolerance is proposed. For cavity with width 800 nm and length 1000 nm threshold gain remains less than 1000 $cm^{-1}$ for etching slopes up to 2 degrees.

**Keywords**: photonic integrated circuits, photonic nanolasers, nanophotonics.

## 1. INTRODUCTION

Nanoscale light sources (e.g.nanolasers and nanoLEDs) with high emission efficiency are an active area of study, as they can operate efficiently at low powers [1], GHz speeds [2], and be densely integrated [3]. This made nanolasers ideal candidate for short-distance communication devices in integrated neuromorphic photonics [4]. Since the first demonstration of electrically pumped metallic nanolaser [5], significant improvements in this area were achieved by different groups, e.g. lasing on higher temperatures [6] and waveguide coupling [3]. However, currently continuous wave operation was achieved for metal-dielectric cavity nanolaser on room temperature without exact output power reporting [7]. The fabrication technology remains a challenge to achieve high-quality factor cavities that can lase, especially when waveguide coupling needs to be considered for future spike-based neuromorphic circuit architectures [4]. One of the main reasons for quality factor degradation is the nanopillar facets inclination, caused by etching process. In this work, we analyze numerically optical properties of metal-dielectric cavities with introduced etching slopes non-idealities, and propose novel cavity design on InP Membranes On Silicon (IMOS) integrated platform, which allow double-side processing technique, increasing fabrication flexibility, and compatibility with nanophotonic waveguides [3].

## 2. NANOLASER DESIGN

Nanolasers are particularly prone to mask erosion during fabrication and the subsequent off-vertical facets and sidewalls. There are three main sources of optical performance degradation caused by non-vertacality. The first source is caused by effective increase of nanolaser width in active medium layer, changing propagation loss and confinement factor. The second change corresponds to the front and end facets reflectivity reduction, the associated increase in the scattering loss and coupling to higher order modes. Finally, due to the nanopillar shape change, optical mode will be coupled more efficiently to highly doped bottom InGaAs contact layer. Since coupling to the bottom layer will increase propagation losses, in order to minimize bottom layer coupling contribution we propose a novel pillar/ridge based metal cavity design, which can be fabricated on the IMOS platform (Fig. 1, right). In this design cavity is flipped, which can be achieved by means adhesive bonding to a silicon substrate using Benzo-Cyclo-Butene (BCB) [8]. Partially removed contact layer would allow for reduced propagation losses and also for direct optical characterization of the cavities from the top.

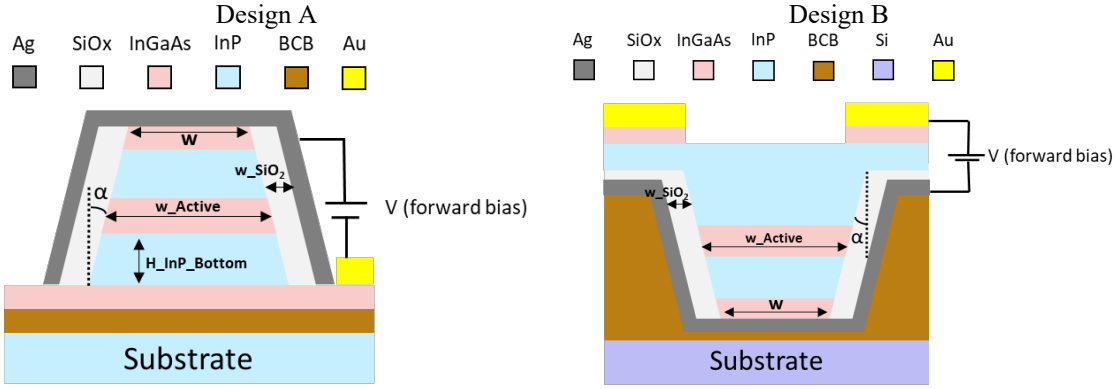



*Figure 1. Metal-dielectric cavity InP-based nanolaser structure. Left: classical metal cavity nanolaser design [3,5,6]. Right: flipped metal cavity InP-membrane nanolaser design.*

## 3. MODE PROPAGATION PROPERTIES

The fabrication process of metal-dielectric cavity nanostructures requires the etching of semiconductor nanopillar structures with a height larger than 1 μm [3]. Such etch depth is usually done via inductive coupled plasma (ICP) reactive-ion etching (RIE) which introduces a slope during the etching which results typically in increasing nanopillar's cross-section area from top to bottom. This effect causes the active medium volume increase, in comparison with an ideal cavity. To investigate how this affects the cavity's optical properties, mode analysis was done using Lumerical software [9]. Active medium was assumed to be transparent at 1.55 μm wavelength. To investigate the effects of the etching slopes on the laser cavity for different designs, mode analysis was done for different inclination angles α and cavity widths *w* (Fig. 2).

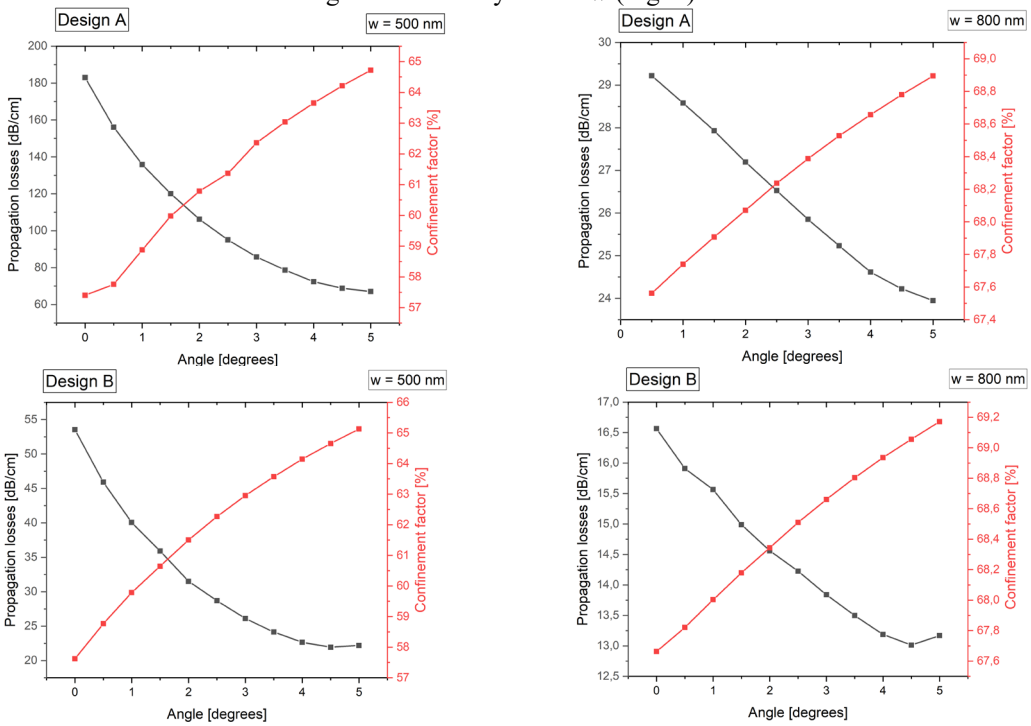



*Figure 2. Propagation losses and confinement factor change as a function of facets inclination angle. Left: semiconductor nanopillar width w = 500 nm, Right: w = 800 nm, Up: Design A, Down: Design B.*

Due to the optical mode coupling to bottom p-InGaAs layer, for the Design A, optical losses will be significantly higher, in comparison with the flipped cavity (design B). Here the main influence for the change in propagation losses and confinement factor with angle is the active medium volume, as compared with an ideal cavity. This effect is less significant for wider cavities, due to the smaller active medium area change.

## 4. FACET REFLECTIVITY

Another crucial effect due to tilted facets is the change in effective facet reflectivity. Due to the tilted reflective surface, the mode is less efficiently coupled back to the fundamental mode upon reflection, and scattering losses are increasing. To investigate this effect numerically, 2D finite-difference time-domain (FDTD) simulations were performed in Lumerical. We calculated the effective reflectivity as a ratio of the optical power which is coupled back to the fundamental TE mode after the reflection to incident fundamental mode. Thus, calculated reflectivity is taking into account metal absorption, high order modes coupling and scattering losses (Fig. 3).

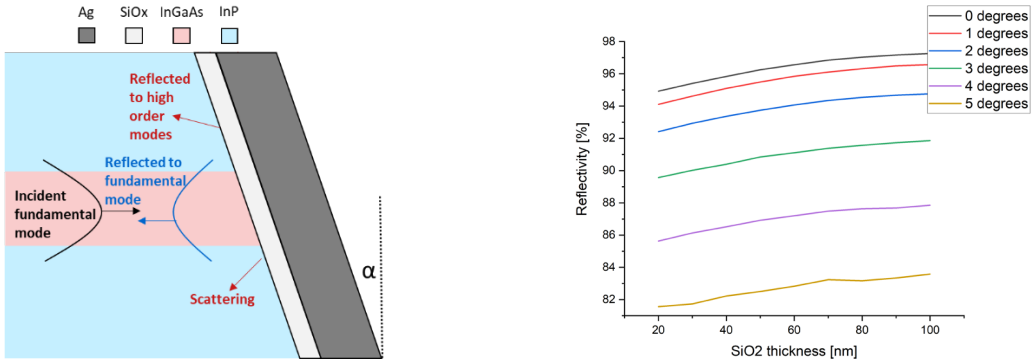



*Figure 3. Left: facet reflection scheme in metal-dielectric cavity; Right: nanocavity facet's reflectivity as a function of $SiO_2$ insulation thickness for different facets inclination angle α.*

For all the simulated angles, the reflectivity change in the same range for a given dielectric thickness range, so absorption losses in the metal are assumed to be constant with facet tilt. Thus, the mode coupling efficiency and scattering losses are giving the highest impact on reflectivity drop. Finally, summing up all the losses contributions, we can calculate the required gain to overcome the introduced losses as following [10]:

$$g_{th}\Gamma = a + \frac{1}{2L}\ln(\frac{1}{R_1R_2})$$

, where $g_{th}$ is the threshold gain, $\Gamma$ – confinement factor, $a$ - propagation loss, $L$ is a cavity length, $R_1$ and $R_2$ are the facets reflectivity. The calculated threshold gain for different cavity widths is presented on on Fig. 4.

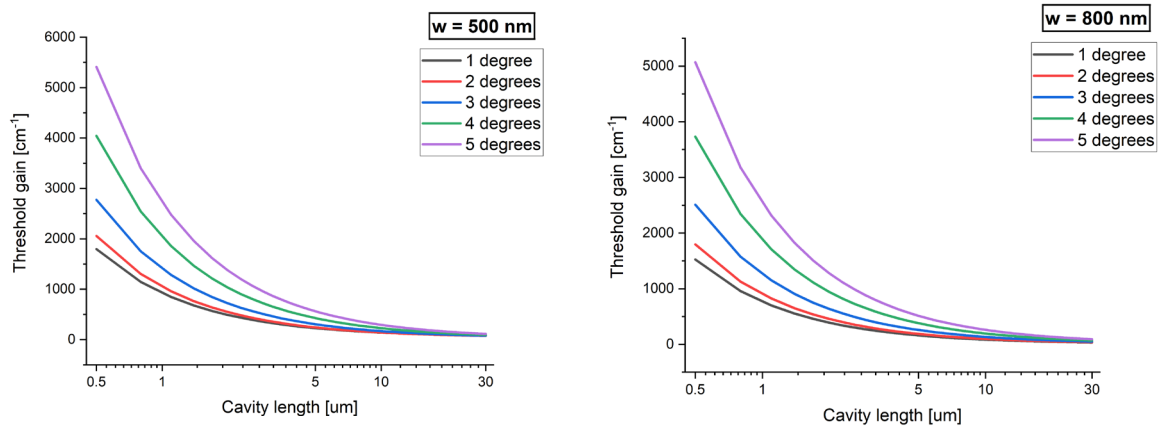



*Figure 4. Nanolaser's calculated threshold gain as a function of cavity length (logarithmic scale) for different inclination angles. Left: semiconductor nanopillar width w = 500 nm, Right: w = 800 nm.*

Considering a cavity width w = 500 nm and cavity length L = 1 µm, the threshold gain increases from 722 $cm^{-1}$ for an ideal cavity to 2482 $cm^{-1}$ for 5 degrees sidewall slopes. As it is shown on Fig. 4, the impact of etching slopes non-verticality becomes negligible for longer cavities, as reflection losses contribution become smaller over against propagation losses. For a wider cavity (w = 800 nm), the threshold gain initially is lower due to the smaller propagation loss, however for cavity length L > 10 µm this effect is insignificant.

## 5. CONCLUSIONS

The effect of etching slopes in the laser cavity was numerically investigated, both in the transversal and longitudinal directions which affect the propagation loss and reflectivity, respectively. Despite the increase in mirror reflection loss, the reduction in propagation loss and improvement in confinement almost compensate it for small angles and large cavity lengths. The proposed flipped cavity design showed smaller propagation losses, and due to the fabrication on IMOS platform can be potentially compatible with nanophotonic waveguide.


## ACKNOWLEDGEMENTS

This work was supported by European Commission, project ChipAI, with Grant 828841-ChipAI-H2020-FETOPEN-2018-2020.


## REFERENCES


[1] K. Ding, *et al.:* Modulation bandwidth and energy efficiency of metallic cavity semiconductor nanolasers with inclusion of noise effects*, Laser & Photonics Reviews*, 9, pp. 488-497, 2015.

[2] A. N. Chi-Yu, *et al:* Theory of high-speed nanolasers and nanoLEDs, *Opt. Express 20*, pp. 450-470, 2012.

[3] V. Dolores-Calzadilla, *et al.:* Waveguide-coupled nanopillar metal-cavity light-emitting diodes on silicon, *Nature communications* vol. 8 p. 14323, 2017.

[4] P.R. Prucnal, *et al.:* Recent progress in semiconductor excitable lasers for photonic spike processing, *Advances in Optics and Photonics* 8, 228, 2016.

[5] M. T. Hill, *et al.:* Lasing in metallic-coated nanocavities, *Nature Photonics*, vol. 1, pp. 589-594, 2007.

[6] C.-Y Fang., *et al.:* Lasing action in low-resistance nanolasers based on tunnel junctions, *Optics Letters*, 44(15), 3669, 2019.

[7] K. Ding, *et al.:* Record performance of electrical injection sub-wavelength metallic-cavity semiconductor lasers at room temperature. *Opt. Express* 21, 4728–4733, 2013.

[8] L. Shen *et al.:* Double-sided processing for membrane-based photonic integration, presented at the 18th Eur. Conf. Integrated Opt., Warsaw, Poland, 2016.

[9] Lumerical Inc. http://www.lumerical.com/

[10] Larry A. Coldren, *et al.:* Diode Lasers and Photonic Integrated Circuits, *2nd ed. Hoboken,* Wiley, 2012.

# Monolithically Integrated Wavelength Tunable Dual Comb Source using Gain Switching

*(Student Paper)*

Jack Mulcahy [1,2], John McCarthy[1,2], Mohamad Dernaika [3], Albert A. Ruth [4], Satheesh Chandran [4], Prince M. Anandarajah [5], Eamonn P. Martin [5], Justin K. Alexander [6] & Frank H. Peters [1,2]

[1]*Tyndall National Institute, Lee Maltings, Cork, Ireland*

[2]*Physics Department, University College Cork, Cork, Ireland*

[3]*Rockley Photonics Ireland, Lee Mills House, Lee Maltings, Cork, Ireland*

[4]*Physics Department & Environmental Research Institute, University College Cork, Cork, Ireland*

[5]*School of Electronic Engineering, Dublin City University, Glasnevin, Dublin 9, Ireland*

[6]*Aeponyx, Montreal, QC, Canada*

*e-mail: jack.mulcahy@tyndall.ie*

## ABSTRACT

A monolithically integrated dual output optical comb source is demonstrated by gain switching two separate injection locked Fabry Pérot lasers. The device consists of the two slave lasers and a master laser separated by a multi-mode interference coupler. Wavelength tunability has been demonstrated by varying the electrical bias of the master laser, which consists of three electrically isolated sections. Combs were generated and recorded for multiple wavelengths from each slave laser.

**Keywords**: optical frequency combs, photonic integrated circuit (PIC), pits mirror, injection locking, gain switching

## 1 INTRODUCTION

Optical frequency combs (OFCs) are very relevant in the fields of optical sensing, metrology and optical communications [1]. In telecommunications, optical combs provide a spectrally efficient means to generate multiple coherent channels which can facilitate highly spectrally efficient terabit per second (Tbps) communications systems [2]. Many methods exist for generating OFCs, one of which entails flexible OFC generation achieved by gain switching an injection locked laser diode [3]. With this approach, highly coherent and stable combs can be generated with the additional benefit of tunability.

Gain switching is a form of direct modulation wherein a high power radio frequency (RF) signal capable of switching the laser on and off is applied, causing the gain parameter of the laser to oscillate between positive and negative. The RF frequency applied directly relates to the spacing of the comb lines generated by this effect. Directly modulated lasers however suffer from added phase modulation known as chirp, which is measured as an increase in laser linewidth [4]. In this device such effects are mitigated through the on-chip injection locking of the gain switched laser. The use of injection locking from a single mode master laser into a simple Fabry Pérot (FP) slave laser has been previously shown to reduce linewidth and chirp in gain switched lasers [5].

In this paper we demonstrate a monolithically integrated dual optical comb source formed by a tunable master laser injecting into two FP slave lasers. Optical frequency combs are formed from the two injection locked slaves using a high power RF signal generator and the output of the slaves is analyzed (using an Ando AQ6317B with a resolution of $0.02\,\mathrm{nm}$) in order to resolve the comb lines.

## 2 DEVICE DESIGN

The dual comb device consists of two slave lasers, referred to in Fig. 1 as slave 1 and slave 2, and a master laser composed of three electrically isolated sections labeled Pit 1, Pit 2, and Gain. Pit 1 and Pit 2 act as single mode reflectors for Gain; the gain section of the laser. To produce single mode lasing, Pit 1 and Pit 2 are populated with small circular perturbations etched through the waveguide as shown in the scanning electron microscope (SEM) image on the right in Fig. 1.

These etched "pits" provide additional optical feedback along the laser cavity in place of traditionally cleaved facet reflectors, which results in further wavelength selectivity and high side mode suppression ratio (SMSR) ($>30\,\mathrm{dB}$). This wavelength selectivity is dictated via the pit spacing [6]. Both pitted sections in the device consist of three clusters of three pits. In Pit 1 the clusters are $108\,\mu\mathrm{m}$ apart and the pits within these clusters are $9\,\mu\mathrm{m}$ apart. In Pit 2 the clusters are $96\,\mu\mathrm{m}$ apart and the pits within these clusters are $9\,\mu\mathrm{m}$ apart. Sections Pit 1 and Pit 2 are separated by the Gain section, an electrically isolated waveguide of length $550\,\mu\mathrm{m}$. The master laser emission is then injected into the slave lasers via a 1x2 multi-mode interference coupler (MMI) of length $116\,\mu\mathrm{m}$ and width $10\,\mu\mathrm{m}$. The FP slave lasers are approximately $500\,\mu\mathrm{m}$ in length. Both slave lasers have one cleaved facet and one deep etched facet, which also serves to isolate the slave lasers from the MMI section.

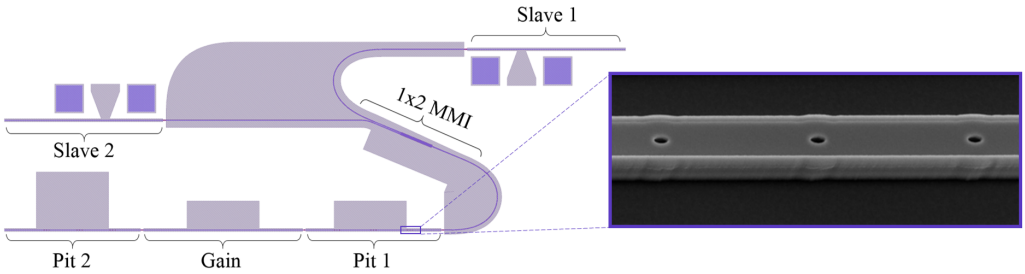
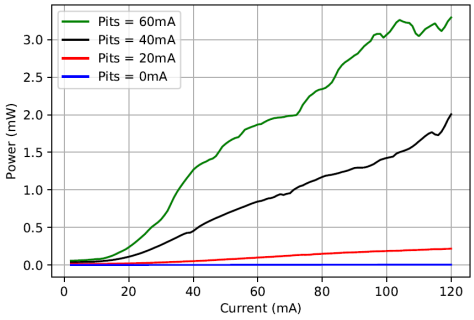



Figure 1: On the left, a schematic view of the device design showing labeled sections. Pit 1 and Pit 2 consist of clusters of three deeply etched pits as shown in the SEM image on the right.

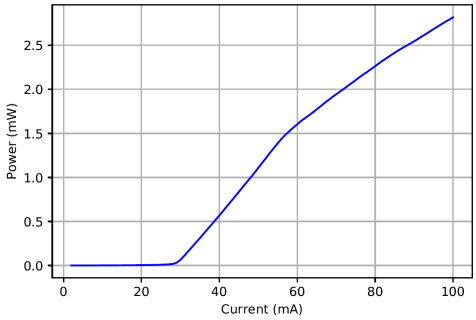
The device was fabricated on commercially available lasing material consisting of 5 compressively strained AlGaInAs quantum wells of width 6 nm, on an n-doped InP substrate. The upper p-doped cladding consists of a 0.2 µm InGaAs cap layer, followed by 0.05 µm of InGaAsP, lattice matched to 1.62 µm of InP. Standard lithographic techniques were used to define the ridge, with a ridge width of 2.5 µm, and height of 1.7 µm. Electrical isolation between different sections was achieved via narrow shallow etches, commonly referred to as slots with a width of 1 µm. These shallow ridge etches end above the quantum wells. A separate etch through the quantum wells was performed so as to provide access to the n region to form ground-signal (GS) contacts, to allow high-speed modulation of the slave section bias to facilitate gain switching.

## 3 DEVICE TESTING

### 3.1 DC Characterization



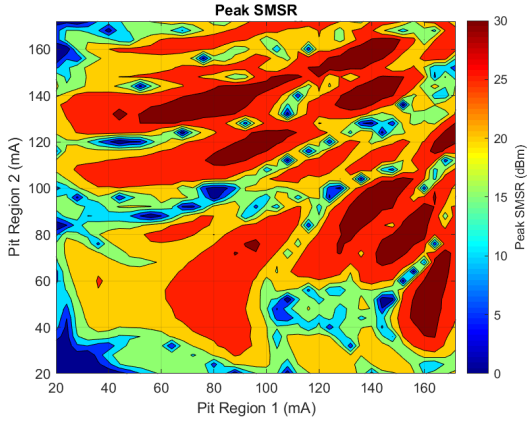

(a) LI curve of master laser with varying bias on sections Pit 1 and Pit 2.



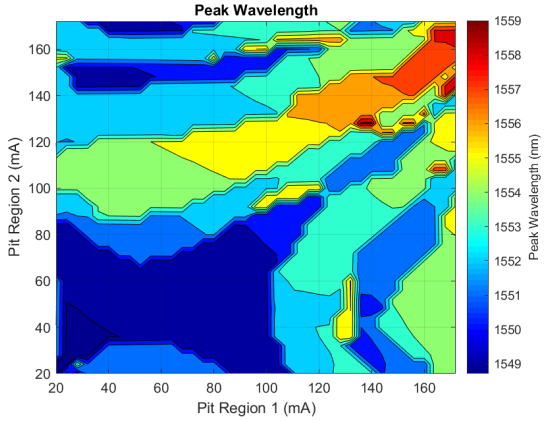

(b) LI curve of slave laser.

Figure 2: Light-current (LI) curves of component lasers of the device.

The DC characteristics of the device were first examined. The device was mounted on a temperature controlled chuck at 20 °C, and a lensed optical fiber was used to couple light from the device. To test the LI output of the master laser, the Gain section was swept while both surrounding Pit sections (1&2) were maintained at set currents. All other sections remained unbiased. To obtain the LI of the slave, only the current of the slave section was swept, all other sections remaining unbiased. The results are shown in Fig. 2.




(a) SMSR map of master laser.



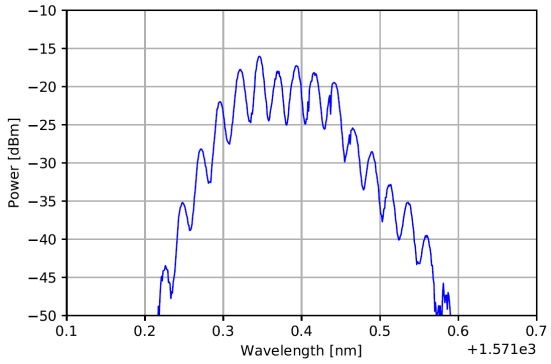

(b) Wavelength tuning map of master laser.

Figure 3: Tuning map of master laser under varying biases of sections Pit 1 and Pit 2. Gain was kept at 100 mA.

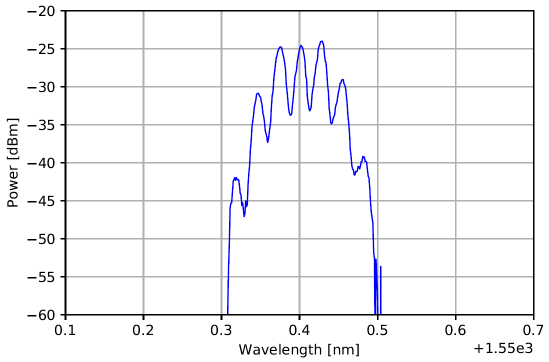
In order to suitably injection lock the slave lasers to the master laser, the light injected from the master laser was required to be single mode and sufficiently powerful. A tuning map of the peak wavelength and corresponding SMSR of the master laser was obtained by biasing the Gain section of the device with a current of 100 mA and sweeping the current through sections Pit 1 and Pit 2. Single mode behavior (>30 dB SMSR) was observed for an approximate wavelength tuning range of 10 nm as shown in Fig. 3.

### 3.2 Comb Generation

To generate the optical combs, the slave section was biased just above threshold current. The master laser was then powered and injected into the slave via biasing the MMI section to passivation with a current of 120 mA. The injection locked slave was then gain switched by applying a high power RF sinusoidal signal (> 20 dB) at frequencies near 3 GHz from a signal generator to directly modulate the current. The slave laser DC bias was then tuned to obtain the best combs, which were recorded using an OSA. The master section was tuned so as to obtain the best combs over multiple wavelengths. The optical combs obtained from some of these configurations are shown in Fig. 4.




(a) Slave 1 is set at 36 mA. Pit 1 and Pit 2 are set at 135 mA and 130 mA respectively. RF signal used was 2.905 GHz.




(b) Slave 1 is set at 27 mA. Pit 1 and Pit 2 are set at 50 mA and 97 mA respectively. RF signal used was 3.600 GHz.

Figure 4: Sample combs generated from device. Gain was set at 100 mA.

## 4 CONCLUSION

A dual output frequency comb has been demonstrated using the gain switching technique. Injection locking into two separate slave FP lasers was accomplished via a master laser, formed by pit-based sampled grating mirrors. This device has been shown to have a highly single mode output, suitable for gain switching. Multiple combs were obtained from each output ranging from 2.9 GHz - 3.6 GHz.

## ACKNOWLEDGMENT

This work was supported by the Enterprise Ireland commercialization fund CF-2017-0683A&B, and by Science Foundation Ireland under grants 12/RC/2276 (IPIC), SFI/13/IA/1960 and 14/TIDA/2415.

## REFERENCES

[1] G. Roelkens, U. Dave, S. Keyvaninia, F. Leo, S. Uvin, K. Van Gasse, Z. Wang, S. Latkowski, E. Bente, and B. Kuyken, "Frequency comb generation in III-V-on-silicon photonic integrated circuits," in Advanced Photonics 2016 (IPR, NOMA, Sensors, Networks, SPPCom, SOF), OSA technical Digest (online) (Optical Society of America, 2016), paper IM2A.5.

[2] I. Tomkos, S. Azodolmolky, J. Sole-Pareta, D. Careglio, and E. Palkopoulou, "A tutorial on the flexible optical networking paradigm: State of the art, trends, and research challenges," Proc. IEEE 102(9), 1317-1337 (2014).

[3] Anandarajah, P., Maher, R., Xu, Y., Latkowski, S., O'Carroll, J., Murdoch, S., Phelan, R., O'Gorman, J. and Barry, L. (2011). Generation of Coherent Multicarrier Signals by Gain Switching of Discrete Mode Lasers. IEEE Photonics Journal, 3(1), pp.112-122.

[4] Anandarajah, P., Duill, S., Rui Zhou and Barry, L. (2015). Enhanced Optical Comb Generation by Gain-Switching a Single-Mode Semiconductor Laser Close to Its Relaxation Oscillation Frequency. IEEE Journal of Selected Topics in Quantum Electronics, 21(6), pp.592-600.

[5] Weber, A., Ronghan, W., Bottcher, E., Schell, M. and Bimberg, D. (1992). Measurement and simulation of the turn-on delay time jitter in gain-switched semiconductor lasers. IEEE Journal of Quantum Electronics, 28(2), pp.441-446.

[6] Dernaika, M., Kelly, N., Caro, L., Shortiss, K. and Peters, F. (2017). Regrowth-free single-mode semiconductor laser suitable for monolithic integration based on pits mirror. Optical Engineering, 56(08), p.1.

# Perovskite Nanocrystals: an Active Material for Integrated Optics

*(Student Paper)*

**Juan Navarro-Arenas, [1] Andrés F. Gualdrón-Reyes,[2-3] Vladimir S. Chirvony, [1] Iván Mora-Seró,[2] Juan Martínez-Pastor[1] and Isaac Suárez [4]**

[1] Instituto de Ciencia de Materiales (ICMUV), Universidad de Valencia, C/ Catedrático José Beltrán, 2, 46980 Paterna, Spain.

[2] Institute of Advanced Materials (INAM), University Jaume I, Avenida de Vicent Sos Baynat, s/n, 12006 Castelló de la Plana, Castellón, Spain.

[3] Biofuels Lab-IBEAR, Faculty of Basic Sciences, University of Pamplona, Pamplona, Colombia. C. P. 543050.

[4] Escuela Técnica Superior de Ingeniería, Universidad de Valencia, C/Avenida de la Universidad s/n 46100 Burjassot, Valencia, Spain.

*e-mail: juan.navarro-arenas@uv.es*

**ABSTRACT**

Perovskite nanocrystals (PNCs) have demonstrated extraordinary capabilities to construct a new generation of optical sources and amplifiers. In this paper, we firstly analyze the optical gain properties of these materials, and then report our advances towards their integration in integrated optics devices.

**Keywords**: perovskite nanocrystals, optical amplification, nonlinear optical properties

## 1. INTRODUCTION

Traditionally, the implementation of integrated optical sources or optical amplifiers has been developed by using III-V semiconductors or glasses and ferroelectric materials doped by rare earth ions [1]. However, there is a cheaper alternative based on (nano)materials synthetized in colloidal solutions. The fabrication by chemical methods provide tailor-made optical properties (light emission, absorption, scattering) that can be engineered during the synthesis. In addition, the solution process nature allows a straightforward incorporation of the materials in optical architectures by coating techniques [2]. In this context, all-inorganic $CsPbX_3$ ($X_3 = Cl_3$, $Br_3$, $I_3$) perovskite nanocrystals (PNCs) have recently emerged as an outstanding material for integrated optics [3]. PNCs are synthetized under low cost chemical methods in cubic nanoparticles with sizes closed to the Bohr radius of the bulk material (10 nm) [4]. Their interesting optical properties include a high efficiency of absorption, a quantum yield of emission exceeding 90 % at room temperature, or a tunable band gap depending on chemical composition [4]. Consequently, during the last 3-4 years PNCs have been extensively studied as an active material, with demonstrated applications in light emitting diodes, lasers or optical amplifiers [5].

Here, we firstly analyze the formation of optical gain in $CsPbBr_3$ PNCs films and the conditions to minimize the threshold of stimulated emission. Then, PNCs films are integrated in a waveguide structure that efficiently exploits their promising light emitting properties. As a result, our waveguides demonstrate an enhancement factor of 3 for the emitted light that paves the road for future active integrated devices based on PNCs.

## 2. RESULTS

PNCs with three different bandgaps (see the PL spectra in Figure 1) were synthetized following the procedures explained elsewhere [4]. Then, PNCs where deposited on the appropriate substrate by a layer-by-layer technique based on a Doctor Blade applicator. This method provides the fabrication of smooth layers with an accurate thickness control (from ~10

nm to ~1 μm). First of all, the formation of ASE in these films was analyzed by pumping the active material with a pulsed (1 ns, 1 kHz) Nd:Yad laser tripled to 355 nm at cryogenic temperature in order to prevent the influence of nonradiative deactivation channels. In this way, ASE is demonstrated at 528, 600 and 705 nm by using PNC films with different halide compositions ($X_3$=$Br_3$, $X_3$=$Br_{1.5}I_{1.5}$, and $X_3$=$I_3$), as presented in Figure 1. Clearly, above a certain threshold the PL spectra collapse to a narrow peak (PL spectra in Figure 1) and the PL intensity grows superlinearly with the excitation fluency (insets in Figure 1), which are both signatures of optical gain. Among the possible physical mechanisms responsible for ASE (single excitions, biexcitons or free carriers) our characterization reveals that the optical gain in these materials is formed by the formation of single excitons (see a detailed explanation elsewhere [6]). In these conditions, inverted population can be reached under small thresholds (as low as 5 μJ/cm$^2$) only limited by the self absorption losses [6].

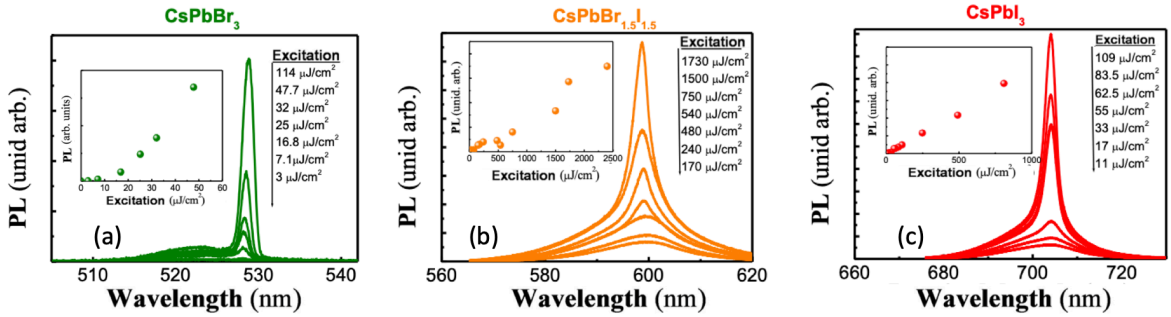



*Figure 1. PL spectra of $CsPbX_3$ films at cryogenic temperatures demonstrates the generation of ASE above a certain threshold. (a) $CsPbBr_3$ (b) $CsPb(BrI)_3$ (c)$CsPbI_3$*

Once the optical gain is demonstrated, PNC films are integrated in a waveguide which efficiently enhances the light. In particular, a 100 nm film of PNCs is sandwiched between two 0.5 μm thick layers of PMMA and deposited on a commercial $SiO_2$(2 μm)/Si substrate (see Figure 2(a)). The high refractive index contrast between the different materials results in the propagation of a fundamental $TE_0$ ($TM_0$) mode highly confined in the active layer. This strong overlap between the propagating mode and the active film enhances the reabsorption and reemission processes responsible for stimulated emission. In addition, the top and bottom claddings reduce the losses of the light travelling along the waveguide, hence allows the propagation of the light along the whole length of the structure [7]. Indeed, we showed an optical amplification in a similar configuration containing an organic compound as an active material [8]. Here, we evaluate the generation of photons emitted by the reabsoption of the light as the basis of optical amplification mechanism. For this purpose, the sample is illuminated with a stripe line at 450 nm. Then, PL collected at the output edge of the structure is analyzed as a function of the separation of the stripe and the edge of the sample (see Figure 2(b)). At these conditions, PL spectra red-shift for long separations (Figure 2(c)) due to the influence of the photons reemitted along the propagation path. Indeed, we evaluate by the Monte Carlo simulations that the generation of these secondary photons enhances the light emitted by the structure by a factor 3, indicating that this is a promising configuration for optical amplification. Future experiments will include the demonstration of optical amplification by stimulated emission or other nonlinear optical processes that can be enhanced by this configuration. For example, we recently demonstrated that a hollow-core optical fiber filled by $CsPbBr_3$ nanocrystals shows an amplification of 3 dB explained by the nonlinear properties of the nanocrystals [9].

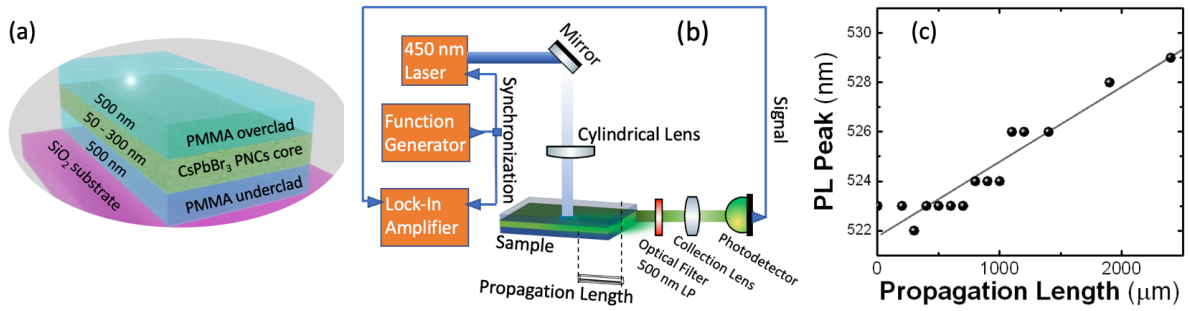



*Figure 2. (a) Waveguide structure. (b) Set-up (c) Red shift with the propagation length*

## 3. CONCLUSIONS

In this work the optical gain of perovskite nanocrystal films is thoroughly analyzed. Since these nanoparticles present a low threshold (5 μJ/cm$^2$ for the best film) of stimulated emission together with a straightforward integration in optical architectures, we believe that they are promising candidates for future integrated sources or amplifiers. In particular, we propose a waveguide configuration that enhances the absorption and generation of light by a high confinement of the propagating mode within the active layer. As a result, we demonstrate that the photons reemitted in the layer enhance the signal by a factor of 3 indicating that this is a promising approach for future active devices.


## ACKNOWLEDGEMENTS

The financial support by the Spanish MINECO through the PhD grant BES-2015-074014, the Spanish MINECO (Project No. TEC2017-86102-C2-1) and Generalitat Valenciana (Prometeo/2018/098) is gratefully acknowledged.


## REFERENCES


[1] Y. Hu *et al.*: "III/V-on-Si MQW lasers by using a novel photonic integration method of regrowth on a bonding template," *Light Sci. Appl.*, vol. 8, no. 1, p. 93, 2019.

[2] I. Suárez Alvarez: "Active photonic devices based on colloidal semiconductor nanocrystals and organometallic halide perovskites," *Eur. Phys. J. Appl. Phys.*, vol. 75, no. 3, p. 30001, Sep. 2016.

[3] M. V Kovalenko, L. Protesescu, and M. I. Bodnarchuk: "Properties and potential optoelectronic applications of lead halide perovskite nanocrystals," *Science (80-. ).*, vol. 358, no. 6364, pp. 745–750, 2017.

[4] L. Protesescu *et al.*: "Nanocrystals of Cesium Lead Halide Perovskites ($CsPbX_3$, X = Cl, Br, and I):," *Nano Lett.*, vol. 15, no. 6, pp. 3692–3696, 2015.

[5] Y.-F. Li, J. Feng, and H.-B. Sun: "Perovskite quantum dots for light-emitting devices," *Nanoscale*, vol. 11, no. 41, pp. 19119–19139, 2019.

[6] J. Navarro-Arenas *et al.*: "Single-Exciton Amplified Spontaneous Emission in Thin Films of CsPbX3 (X=Br, I) Perovskite Nanocrystals," *J. Phys. Chem. Lett.*, p. acs.jpclett.9b02369, Sep. 2019.

[7] I. Suárez Alvarez *et al.*: "Efficient excitation of photoluminescence in a two-dimensional waveguide consisting of a quantum dot-polymer sandwich-type structure," *Opt. Lett.*, vol. 39, no. 16, pp. 4962–4965, 2014.

[8] M. Signoretto *et al.*: "Efficient optical amplification in a sandwich-type active-passive polymer waveguide containing perylenediimides," *ACS Photonics*, vol. 4, no. 1, pp. 114–120, 2017.

[9] J. Navarro-Arenas *et al.*: "Optical Amplification in Hollow-Core Negative-Curvature Fibers Doped with Perovskite CsPbBr3 Nanocrystals," *Nanomaterials*, vol. 9, no. 6, p. 868, Jun. 2019.

# An Accurate Characterization Method for Polarization Converters on the Indium Phosphide Membrane on Silicon Platform

*(Student Paper)*

Sander Reniers [1], Kevin Williams [1], Jos van der Tol [1], Yuqing Jiao [1]
[1]*Institute for Photonic Integration (IPI), Eindhoven University of Technology*
*e-mail: s.f.g.reniers@tue.nl*

## ABSTRACT

In this paper, an accurate characterization method for characterization of the conversion efficiency of polarization converters on the InP-membrane-on-silicon (IMOS) platform is demonstrated. The method is insensitive to propagation losses, device insertion loss and grating coupler insertion loss. Circuits for demonstration of the method with polarization converters with various parameters are fabricated. A conversion efficiency as high as 97.5±0.7% is experimentally shown using the proposed method. The high-efficiency polarization converter is only 4.1 microns long.

**Keywords**: Indium phosphide, nanophotonics, polarization converter, membranes, characterization.

## 1 INTRODUCTION

The demand for higher bandwidths in optical fiber technologies is ever-increasing. To satisfy this demand, every degree of freedom in the communication technologies is being exploited. A commonly used technique is wavelength division multiplexing (WDM), enabling multiple data channels to be submitted over a single fiber using different wavelengths. Spatial division multiplexing (SDM) exploits the spatial modes in few-mode or multicore fibers to further increase the number of channels that can be submitted over a single fiber. The polarization state of the light can be exploited to increase the capacity of a single fiber with a factor two, by simply using the two orthogonal polarization states: the EH and the HE modes. Furthermore, polarization can be used to employ more complex modulation formats, e.g. Stokes vector modulation (SVM). SVM enables multilevel modulation formats without the requirement of increasing the optical power. To reduce the cost of the transceivers, it is desirable to have the full circuit integrated in one chip. To achieve on-chip polarization handling, components that can manipulate polarization are of key importance. It is crucial to be able to characterize these devices accurately. Reported performances are commonly obtained by direct measurement of the devices under test. The main disadvantage of this method is the sensitivity to calibration of the measurement with respect to the insertion losses and polarization dependent losses of the fiber coupling and other components in the measurement setup.

We demonstrate a characterization method to accurately measure the polarization conversion efficiency of an integrated polarization converter. The method is insensitive to device insertion losses and propagation losses.

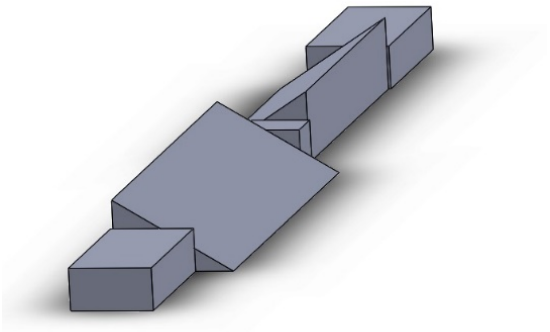


Figure 1. Cartoon of the polarization converter design.

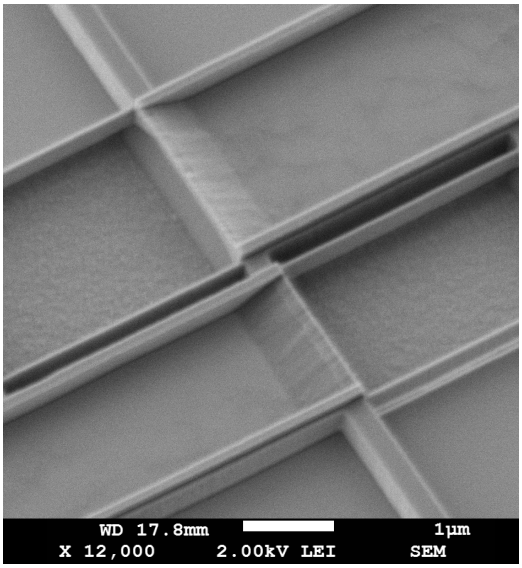



Figure 2. Scanning electron microscope picture of a polarization converter fabricated on the IMOS platform (before bonding).

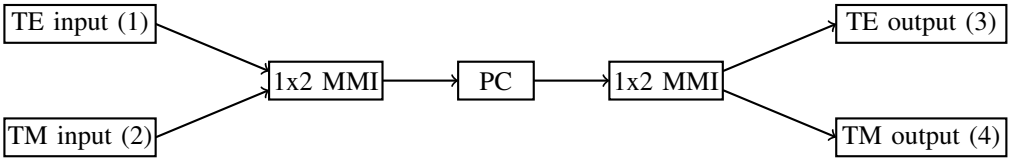



Figure 3. Schematic of characterization circuit for the characterization of polarization converters.

The fabrication of the investigated devices is carried out on the InP-membrane-on-silicon (IMOS) platform [1], which is a nanophotonic platform that provides tight optical confinement and miniaturization of components and waveguides. The tight optical confinement is achieved by adhesively bonding of the indium phosphide wafer to a silicon wafer with benzocyclobutene (BCB), and removing the substrate of the indium phosphide wafer. This results in an air cladding on one side and a BCB cladding on the other side. The core thickness of the photonic nanowires on the IMOS platform is 300 nm, and the typical waveguide width is 400 nm.

## 2 DEVICE DESIGN AND FABRICATION

The design of the polarization converter, shown in Fig. 1, is based on the design on a 250 nm thick InP membrane, reported in [2]. The current design is optimized for the 300 nm membrane thickness, enabling integration compatibility to the twin-guide active-passive integration scheme [3]. Furthermore, surface grating couplers capable of coupling both transverse electric (TE) and transverse magnetic (TM) polarized light are now available, which are required for directly measuring the polarization conversion. However, by doing this, one has to compensate for the polarization-dependent insertion losses of the surface grating couplers and other components, e.g. multi mode interference couplers (MMI), and the polarization-dependent propagation losses in the waveguides. In Section 3 we describe a 4-port measurement method which solves this issue.

The device was fabricated on the IMOS platform, and integrated with the standard process. To optimize the mode matching between the triangular sections and the rectangular waveguides, the triangles require a height of 460 nm. An extra quaternary etch-stop layer was introduced to provide the extra height for the triangular sections, as discussed in [3]. The vertical sidewalls of the triangular sections are patterned in the same step as the waveguide definition, while the slopes are created using a selective wet etch that stop on the (112) crystallographic plane of indium phosphide, providing a 35° slope with respect to the wafer surface. Since the tilt angle of the hybrid modes in the triangular sections is below 45°, two sections are required to obtain full polarization conversion. A scanning electron microscope (SEM) image of the fabricated device is shown in Fig. 2. All processing is performed prior to the wafer bonding, hence this image is taken before bonding the InP wafer to the silicon carrier wafer.

## 3 MEASUREMENT METHODOLOGY

The characterization circuit is schematically shown in Fig. 3. For further reference, the input and output ports have been numbered. We consider $P_{ij}$ the measured power at output $j$ when input $i$ is used, which, for all combinations of inputs and outputs results in

$$P_{13} = \alpha_1 \alpha_3 \alpha_{\text{MMI}}^2 (1-\eta) P_{\text{in}}, \tag{1}$$
$$P_{14} = \alpha_1 \alpha_4 \alpha_{\text{MMI}}^2 \eta P_{\text{in}}, \tag{2}$$
$$P_{23} = \alpha_2 \alpha_3 \alpha_{\text{MMI}}^2 \eta P_{\text{in}}, \tag{3}$$
$$P_{24} = \alpha_2 \alpha_4 \alpha_{\text{MMI}}^2 (1-\eta) P_{\text{in}}, \tag{4}$$

where $\alpha_k$ is the loss in input arm $k$, $\alpha_{\text{MMI}}$ is the insertion loss of the MMI, $\eta$ is the polarization conversion efficiency and $P_{\text{in}}$ is the input power. These losses are polarization dependent, but are compensated in the next step. We then introduce the paramater $C$ as

$$C = \frac{P_{13} P_{24}}{P_{14} P_{23}} = \frac{(1-\eta)^2}{\eta^2}. \tag{5}$$

From Eq. 5 it can be seen the parameter $C$ is independent of the insertion and propagation losses, and only depends on the polarization conversion efficiency $\eta$. Rewriting the equation gives

$$\eta = \frac{1}{1+\sqrt{C}} = \frac{1}{1+\sqrt{\frac{P_{13}P_{24}}{P_{14}P_{23}}}}. \tag{6}$$

The accuracy of a direct 2-port measurement method is limited by how accurately one can determine the insertion loss of the surface grating couplers, which typically gives an uncertainty of around 0.5 dB per grating coupler. This would already introduce an uncertainty of around 20% for this method, which diminishes the accuracy of the method.

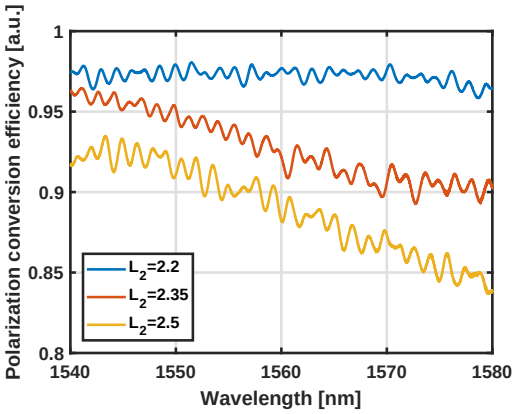



Figure 4. Measured polarization conversion efficiency versus wavelength for three lengths $L_2$. $L_1$ is fixed at 1.7 $\mu$m.

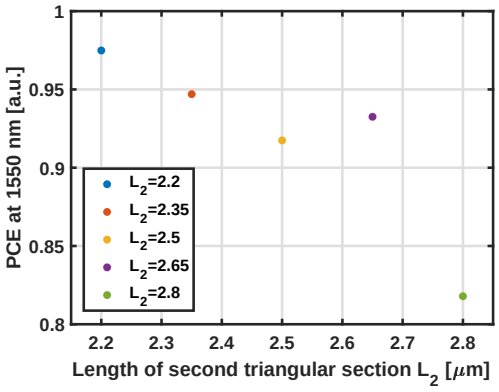



Figure 5. Measured PCE at 1550 nm for various lengths of the second triangular section. $L_1$ is fixed at 1.7 $\mu$m.

## 4 MEASUREMENT RESULTS

The proposed measurement method is applied to the previously introduced polarization converters. Converters with length variations for both sections have been measured over a wavelength range such that both TE and TM surface grating couplers have reasonable coupling efficiency, which is 1540-1580 nm for this fabrication run. In Fig. 4, the measured polarization conversion efficiency (PCE) is shown. Almost 98±0.7% PCE is achieved, which is comparable to the state-of-the-art in silicon photonics [4]–[6]. The ripple on the PCE is caused by reflections in the circuit. Reducing these reflections can improve the accuracy of the method further. The efficiency is above 96±0.7% for 1540-1580 nm for a total device length of 4.1 $\mu$m. In Fig. 5, the PCE at a wavelength of 1550 nm is shown for five devices with fixed $L_1$ and various $L_2$. A sinusoidal trend is expected, however, there is a limited amount and range of points available and there is an anomaly for $L_2 = 2.65\mu$m. After inspection of the structure, this is expected to be caused by residual InP after the wet etching of the triangular sections.

## 5 CONCLUSION

An accurate characterization method for the characterization of polarization converters has been experimentally demonstrated. Characterization circuits with polarization converts are fabricated on the IMOS platform, and the results are presented in this paper. A maximum conversion efficiency of 97.5±0.7% is achieved and over 96±0.7% is achieved over a wavelength range of 1540-1580 nm.

## REFERENCES

[1] J. J. van der Tol, Y. Jiao, L. Shen, A. Millan-Mejia, V. Pogoretskii, J. P. van Engelen, and M. K. Smit, "Indium Phosphide Integrated Photonics in Membranes," *IEEE Journal of Selected Topics in Quantum Electronics*, vol. 24, no. 1, pp. 1–9, 2018.

[2] J. Pello, J. van der Tol, S. Keyvaninia, R. van Veldhoven, H. Ambrosius, G. Roelkens, and M. Smit, "High-efficiency ultrasmall polarization converter in InP membrane," *Optics Letters*, vol. 37, no. 17, p. 3711, 2012.

[3] S. Reniers, V. Pogoretskiy, K. Williams, J. van der Tol, and Y. Jiao, "Towards the integration of an ultrashort polarization converter on the active-passive InP-membrane-on-silicon platform," *IEEE Photonics Benelux Symposium, Not Published*, 2019.

[4] Y. Zhang, Y. He, X. Jiang, B. Liu, C. Qiu, Y. Su, and R. A. Soref, "Ultra-compact and highly efficient silicon polarization splitter and rotator," *APL Photonics*, vol. 1, no. 9, 2016.

[5] D. Vermeulen, S. Selvaraja, P. Verheyen, W. Bogaerts, D. V. Thourhout, and G. Roelkens, "High Efficiency Broadband Polarization Rotator on," *Journal of the Optical Society of America*, pp. 42–44, 2010.

[6] A. Xie, L. Zhou, J. Chen, and X. Li, "Efficient silicon polarization rotator based on mode-hybridization in a double-stair waveguide," *Optics Express*, vol. 23, no. 4, p. 3960, 2015.

# Hybrid Integration of a Single-Frequency Ring Laser with a Microelectronic Driver

**Stanisław Stopiński, Krzysztof Siwiec, Witold Pleskacz,**
**Sławomir Szostak, Ryszard Kisiel and Ryszard Piramidowicz**
Warsaw University of Technology, Institute of Microelectronics and Optoelectronics,
Koszykowa 75, 00-662 Warsaw, Poland
*e-mail:stanislaw.stopinski@pw.edu.pl*

## ABSTRACT

In this work a concept of hybrid integration of a photonic integrated circuit with an integrated microelectronic driver is demonstrated. The idea is based on the flip-chip technique and is discussed using an example of a single frequency ring laser, realized in the framework of development of an optical gyroscope system. The laser is monolithically integrated with a detection circuit of the beating signal between two counter-propagating modes, resulting from the Sagnac shift. Initial characterization results of the fabricated laser confirm single frequency operation with the output power on the order of 1 mW within the cavity and side mode suppression ratio over 35 dB. The measured imbalance between the power level of the modes is ca. 10 dB, which can be compensated by optical amplifiers implemented in the detection circuit.

**Keywords**: application specific photonic integrated circuit, generic integration technology, application specific integrated circuit, hybrid integration, flip-chip technology, ring laser gyroscope.

## 1. INTRODUCTION

In recent years photonic integration technologies have been extensively developed with a specific attention given to telecom and sensing applications, where multiple channel operation is highly advantageous in comparison to traditional solutions based on discrete photonic devices. However, despite excellent performance in the laboratory environment, nowadays very few large-scale integrated devices are offered on a commercial basis. One of the major problems is lack of an efficient and scalable technique for integration of multiple high-speed active photonic components, i.e. lasers, modulators and detectors, with microelectronic drivers. A typical scheme of bonding, when the photonic chip is positioned next to the electronic circuits, may result in long bondwires and thus also high inductance of such an electrical connection. This, in turn, hampers the RF performance of complete optoelectronic systems. On the other hand, designing dedicated RF micro-strip lines or coplanar waveguides on the surface of the photonic chip sacrifices too much of its area. A hybrid integration scheme proposed in this work could be an efficient technique of connecting integrated microelectronic drivers with multiple high-speed active components of photonic integrated circuits.

The discussed concept is based on the flip-chip technique and will be presented using an example of a single-frequency ring laser, realized in the framework of development of a fully integrated optical gyroscope system. Up to date ring laser gyroscopes (RLGs) [1] are typically constructed using helium neon or solid state lasers, due to excellent spectral properties of the generated beams [2]. Such systems have proven excellent performance as rotation sensors in top-class inertial measurement units (IMUs) mounted in airplanes, spacecrafts and missiles. Integration of a gyroscope system remains a technological challenge, as it requires sufficiently good spectral properties (single frequency operation and a narrow laser line) combined with a relatively large ring perimeter (on the order of 10 mm). In this work we demonstrate a novel, proof-of-concept electronic-photonic hybrid system. It comprises an application specific photonic integrated circuit (ASPIC) providing combined functionality of a bi-directional single-frequency ring laser source and a detection circuit of the beating signal. The layout of the device is compatible with a dedicated microelectronic driver developed in parallel.

## 2. ASPIC DESIGN

Single-frequency integrated ring lasers in the indium phosphide technology can be realized using e.g. arrayed waveguide gratings (AWGs) or asymmetric Mach-Zehnder interferometers (AMZIs) as intra-cavity wavelength filters [3-7]. The latter solution provides tunability and precise control over the generated wavelength of the laser and thus also enable optimizing its output power by adjusting it to the maximum of the amplifier gain curve. An operational scheme of the designed photonic circuit is presented in Figure 1a.

A semiconductor optical amplifier (SOA 1) is the gain section of the laser. A cascade of three wavelength filters, each with a different value of free spectral range (70 nm, 5.8 nm and 0.56 nm) enables single frequency operation. The filters comprise two 1×2 multi-mode interference (MMI) splitters/combiners and two electro-optic phase modulator (EOPM) sections, which allow to accurately tune the maxima of the transmission bands of all

filters to the same wavelength. Thus, the output power and side mode suppression ratio of the laser line could be optimized. Figure 1b presents the effective power transmission characteristic of the cascade of all three filters connected in series.

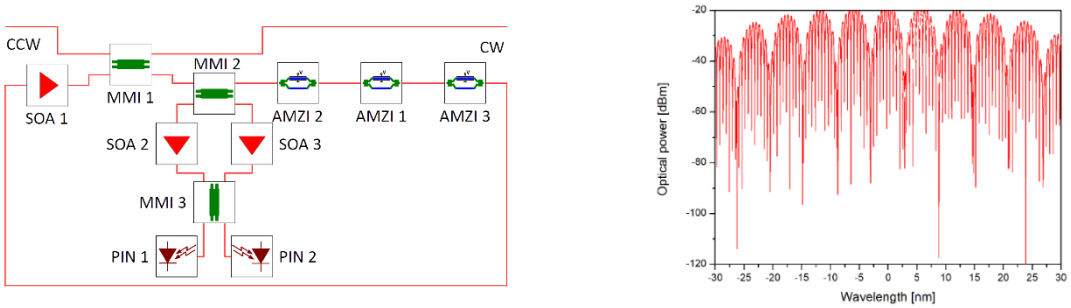



*Figure 1. a) Operational scheme of the single-frequency ring laser system;*
*b) Power transmission characteristic of a cascade of three asymmetric Mach-Zehnder interferometers.*

The laser design enables bi-directional operation, i.e. both clockwise (CW) and counter-clockwise (CCW) modes can be generated simultaneously. The Sagnac effect, occurring under rotation of the optical chip with the angular velocity $\Omega$, will cause a split of the CW and CCW resonant frequencies $v$ (which is the same at rest for both modes) by $\Delta v$, following equation (1): $\Delta v = (4av\Omega)/(pc)$, where $a$ is the area of the cavity and $p$ its perimeter. The frequency difference can be read out by monitoring the beating signal of the two laser modes. The CW and CCW signals are coupled out of the cavity using a 2×2 MMI (MMI 2) coupler and interfere at the output of a second 2×2 MMI (MMI 3). Since typically one mode has a higher power than the second one, two SOA sections are introduced to balance their power level. Two PIN photodiodes are connected to the outputs of MMI 3, which enables monitoring of the beating signal being a result of interference of CW and CCW laser mode.

## 3. ASIC DESIGN

The microelectronic driver of the RLG system was realized as an application specific integrated circuit (ASIC). The device is used to power the amplifiers of the ring laser and the detection circuit (forward bias applied by controlled current sources) and tune the phase shift introduced by electro-optic modulators of the AMZIs (reverse bias applied by controlled voltage sources).

Furthermore, the ASIC is used to read out the photocurrent of the PIN photodiodes and perform basic processing of the recorded signals. The readout circuit comprises a programmable transimpedance amplifier (TIA) and a comparator. The TIA converts and amplifies the current signal from the photodiodes. The TIA has a programmable gain from 300 V/A to 2.4 kV/A with a 6 dB step. Additionally the TIA can compensate input bias current within the range from 250 µA to 8 mA. The digital part of the ASIC comprises configuration registers and a frequency detector, which compares the frequency at the AFE output with a reference clock signal.

## 4. MASK LAYOUT

The ASPIC layout has been designed using the generic technology provided by SMART Photonics in the framework of multi-project wafer runs [8, 9], offering access to amplifiers, electro-optic phase modulators, PIN photodiodes and passive waveguides. The ASIC driver has been implemented and prototyped in the AMS 0.35 µm technology. Mask layout of both devices is presented in Figure 2.

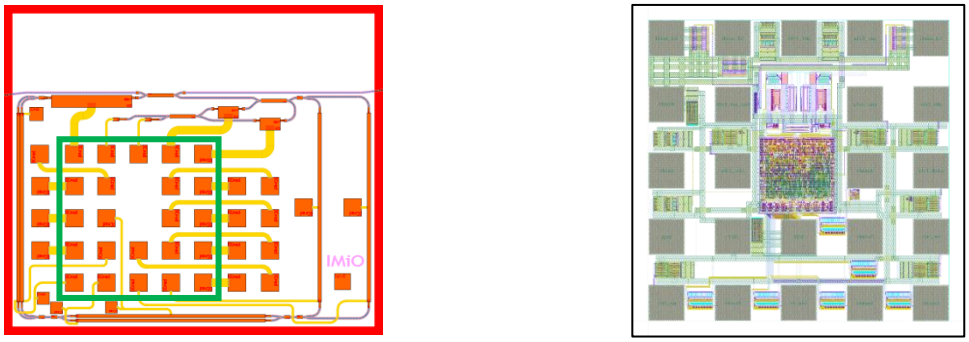


*Figure 2. a) Mask layout of the single-frequency ring laser integrated with a beating signal detection circuit;*
*b) Mask layout of the microelectronic driver.*

The laser gain section has the length of 1 mm. On the left-hand side it is connected to a cascade of three AMZI filters, with the length imbalance $\Delta l_2$ = 119 µm, $\Delta l_1$ = 12 µm and $\Delta l_3$ = 1252 µm, respectively. The output of the third AMZI is connected to the MMI 2, which couples the CW and CCW from of the laser cavity to the detection

circuit, which comprises the amplifiers SOA 2 and SOA 3 (both having the length of 250 μm), MMI 3 coupler and two PIN photodiodes. Furthermore, an additional 2×2 MMI (MMI 1 in Figure 1a) is introduced within the cavity, which enables performing optical characterization of the fabricated chip both for the CW and CCW mode. The total resonator length is around 14 mm, rectangular shape was chosen to maximize the area of laser and thus increase the gyroscope scale factor (see equation 1). The circuit size is 4.6 mm × 2.9 mm, it intentionally uses only a part of a standard SMART Photonics MPW cell.

Both devices have been designed taking into account further flip-chip bonding procedure. The green square in Figure 2a, with the dimensions of 2.0 mm × 2.0 mm equal to the ASIC size, indicates the area, where the driver will be flip-chip bonded. All of the bonding pads have the size of 220 μm × 220 μm. Eleven pads are used to connect the ASIC with the ASPIC active components (three SOAs, six EOPMs and two photodiodes). Furthermore, twelve pads are used to provide the ASIC with the power supply and control signals through electrical tracks on the ASPIC.

## 5. CHARACTERIZATION RESULTS

After the fabrication the ring laser circuit has been optically characterized. Figure 3a presents the emission spectra, recorded using a high-resolution optical spectrum analyser, for CW and CCW modes, obtained after careful adjusting the transmission of all three interferometers. The measured lasing wavelength is 1554.5 nm and the side mode suppression ratio over 35 dB for both modes, which confirms single-frequency operation. Figure 3b presents the recorded fiber-coupled power characteristic as a function of the SOA injection current. Since the signals within the cavity are ca. 3-4 dB higher, as they do not suffer from the chip-fiber coupling loss, it can be concluded that the obtained power levels on the order of 0.3-1.0 mW are sufficient for proper operation of a gyroscope system. The imbalance between the modes for the SOA driving current between 75 mA and 150 mA does not exceed 10 dB, which means that it can be easily compensated by the amplifiers in the detection circuit.

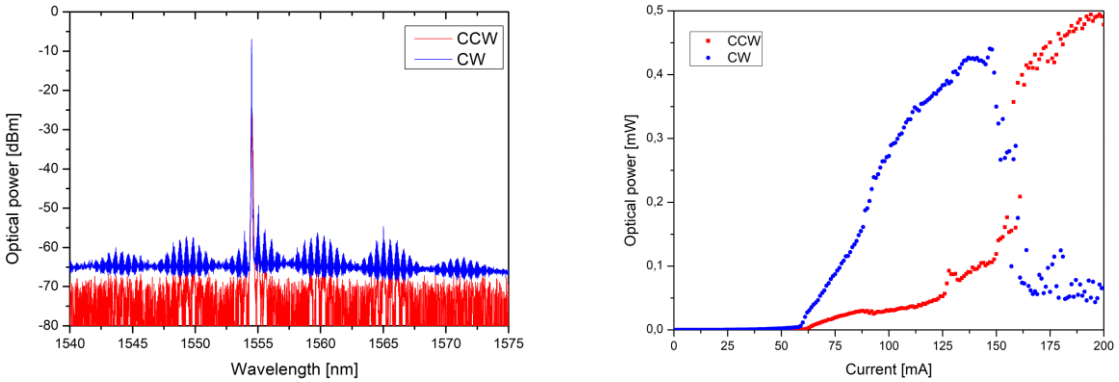



*Figure 3. a) Emission spectrum of the single frequency ring laser measured for both modes using high-resolution optical spectrum analyser; b) Measured LI characteristics of the laser for both modes.*

## 6. SUMMMARY

A concept of hybrid integration of a single-frequency ring laser system with a dedicated integrated microelectronic driver has been presented and discussed. The obtained results are promising with respect to application of such an approach in further development of a fully integrated optical gyroscope.

## ACKNOWLEDGEMENTS

The research leading to these results has received funding from the National Science Centre (decision DEC-2013/09/N/ST7/04430) and from the EU Horizon 2020 research and innovation programme under grant agreement No. 687777 (PICs4All).

## REFERENCES

[1] W. M. Macek, D. T. M. Davis, “Rotation rate sensing with traveling-wave ring lasers,” Appl. Phys. Lett., vol. 2, no. 3, pp. 67–68, 1963.
[2] M. N. Armenise, Advances in Gyroscope Technologies. Berlin, Germany: Springer-Verlag, 2010.
[3] S. Latkowski et al., “Monolithically integrated widely tunable laser source operating at 2 μm”, Optica 3, 1412-1417 (2016)
[4] J. H. den Besten et al., “A compact digitally tunable seven-channel ring laser,” IEEE Photon. Technol. Lett., vol. 14, no. 6, pp. 753–755, Jun. 2002.
[5] B. W. Tilma et al., “Integrated tunable quantum-dot laser for optical coherence tomography in the 1.7 μm wavelength region,” IEEE J. Quantum Electron., vol. 48, no. 2, pp. 87–98, Feb. 2012.
[6] S. Latkowski et al., “Novel widely tunable monolithically integrated laser source,” IEEE Photon. J., vol. 7, no. 6, pp. 1–9, Dec. 2015.
[7] S. Stopinski, L. Augustin and R. Piramidowicz, "Single-Frequency Integrated Ring Laser for Application in Optical Gyroscope Systems," IEEE Photonics Technology Letters, vol. 30, no. 9, pp. 781-784, 1 May1, 2018.
[8] M. Smit et al., “An introduction to InP-based generic integration technology,” Semicond. Sci. Technol., vol. 29, no. 8, p. 083001, 2014.
[9] SMART Photonics website, http://smartphotonics.nl/fsfsd

# Prospect for compact on-chip lasing with hybrid erbium-doped silicon integration

*(Student Paper)*

**Zhengrui Tu[1], Jianhao Zhang[1], John Rönn[2], Carlos Alonso-Ramos[1], Xavier Leroux[1], Laurent Vivien[1], Zhipei Sun[2], Éric Cassan[1]**

[1] Centre de Nanosciences et de Nanotechnologies (C2N), Université Paris Saclay, Université Paris Sud, CNRS, 91120 Palaiseau, France

[2] Department of Electronics and Nanoengineering, Aalto University, Tietotie 3, FI-00076 Espoo, Finland

*e-mail: zhengrui.tu@u-psud.fr*

## ABSTRACT

Taking advantage of our recently demonstrated erbium-doped $Al_2O_3/Er_2O_3$ thin film with large gain up to 52 dB/cm at 1533 nm, we investigate the feasibility for realizing compact on-chip lasers in the near infrared spectral region with the silicon on insulator photonic platform.

**Keywords**: Integrated silicon photonics, Erbium material, On-chip lasing.

## 1. INTRODUCTION

Silicon integration photonics has drawn a great interest in the past decades, and now it already plays an important role in modern photonics and optoelectronics [1,2]. Nevertheless, there are still a few key points to be resolved, including the issue of the light source. Due to the silicon's indirect band gap, one of the biggest challenges is indeed to realize compact, highly efficient, low power consumption and low cost on-chip lasers and amplifiers [3]. Several methods have been investigated to address the problem. Introducing hybrid integration of III/V based lasers on silicon can achieve highly efficient integrated lasing and is considered as the present dominant approach [4-6]. It nevertheless requires a heterogeneous integration, which is not COMS compatible with complex fabricating process and high cost. Any direct monolithic integration of materials deposited at temperatures compatible with a back-end CMOS process (<500°C) is therefore preferable. In this way, introducing rare-earth doped materials that were wildly employed in developments of optical fiber communications may be of interest [7]. Recently, progresses on the integration of rare-earth-doped amorphous aluminum oxides in silicon nitride waveguides have been reported by several research groups [8]. These works have opened up very interesting prospects by proposing integrated structures leading to laser emission in various configurations, the most interesting one is probably that of optically pumped integrated DFB lasers. However, the demonstrated obtained devices have typical lengths of more than 2 cm [8-9], which are significantly larger than the typical waveguides, micro-resonators, and active components. An effort to shrink erbium optical amplifiers and lasers is therefore required. Another limitation that is not addressed by the previous works is the choice of the pump wavelength. In previous works, the erbium-doped active matrix is pumped at 980nm. Although this pump wavelength is the most effective wavelength to get population inversion in the erbium-based medium, it is clearly not compatible with a light propagation in silicon in the near infra-red.

Our study is based on the active Erbium doped material we have recently developed [10-11]. With a 1470 nm pump source, up to 52.4 ± 13.8 dB/cm material gain per unit length at 1533 nm wavelength was realized, which, to the best of our knowledge, is among the highest gain achieved from erbium-based planar waveguides. Given such erbium-doped material properties, in order to get lasing, a proper optical cavity, which owns not only high mode confinement in the active material region but also low losses meanwhile, is worth being investigated. Inspired by the wise tiny multi-segment waveguide structure proposed before in Ref. [8] and taking advantage of our Erbium-doped material platform relying on the atomic layer deposition (ALD) technique, we investigate here the feasibility for realizing compact Erbium-doped on-chip lasers based on the SOI platform through the design of quarter-wave shifted (QWS) distributed feedback (DFB) cavities.

## 2. WAVEGUIDE STRUCTURE

Recently, based on silicon nitride platform, rare-earth doped material DFB lasers composed of several segment waveguides were explored [8]. This kind of structure presents a high light field confinement factor in the active material, which can perfectly meet our needs. As a result, we adopt here a similar waveguide structure, but after transposing it to SOI optical waveguides to target more compact designs. The waveguide structure cross section view is shown in Fig. 1(a). Based on a 220 nm thickness silicon core SOI wafer, fabrication can be carried out by etching five silicon segments, then planarizing the waveguide with depositing a thin SiO2 layer, and finally depositing a $Al_2O_3$:Er stack on top through an atomic-layer deposition (ALD) process. This thin $SiO_2$ layer can

reduce the impact of the high refractive index Si stripe on the optical mode distribution and improve wavelength insensitivity to get a higher overlap between the pump and signal mode fields. The 3D schematic diagram of the full waveguide structure is shown in Fig. 1(b), and Fig. 1(c) shows the front view.

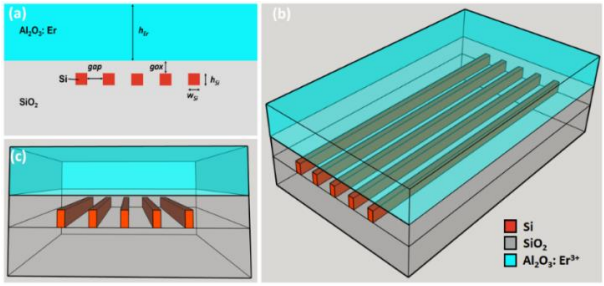



*Figure 1. (a) Waveguide structure cross section view.*
*(b) 3D schematic diagram of full waveguide structure. (c) Front view of waveguide structure.*

Mode analysis was conducted through *COMSOL Multiphysics*, with the parameters of the waveguide structure as follows: $h_{Er}$ = 500 nm, $w_{Si}$ = 100 nm, $h_{Si}$ =100 nm, *gap* = 300 nm, *gox* = 100 nm. Fig. 2(a) and Fig. 2(b) show the mode solution results of the pump and signal modes, respectively. Clearly, we can see that electric field distributes mainly inside the active material region, for both the pump and the signal. An ideal confinement factor of 0.05 is obtained in silicon, which makes it reasonable to neglect the Two Photon Absorption (TPA) effect.

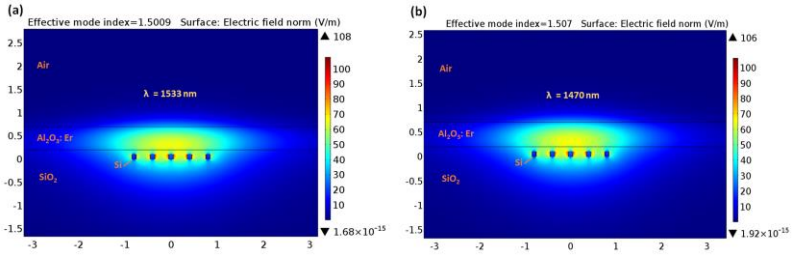



*Figure. 2. Mode analysis results when the parameters of the waveguide structure are as follows: $h_{Er}$ = 500 nm, $w_{Si}$ = 100 nm, $h_{Si}$ =100 nm, gap = 300 nm, gox = 100 nm. (a) Light electric field at the signal wavelength, λ = 1533 nm.*
*(b) Light electric field plot at the pump wavelength, λ = 1470 nm.*

## 3. COMPACT DFB LASERS

Based on the waveguide structure mentioned above, quarter-wave shifted (QWS) distributed feedback (DFB) lasers can be designed, as it contains several parallel rails and that patterning some of them with slits allows to realize Bragg mirrors with controlled and widely adjustable mirror strengths. A QWS-DFB laser structure is composed of two distributed Bragg reflectors (DBR), which are back to back with zero gap. The 3D schematic diagram of designed QWS-DFB structure is shown in Fig. 3(a), and Fig. 3(b) is the 2D counterpart diagram from the top view. Two rails of silicon segment structures next to the central strip is used as gratings. Through this way,

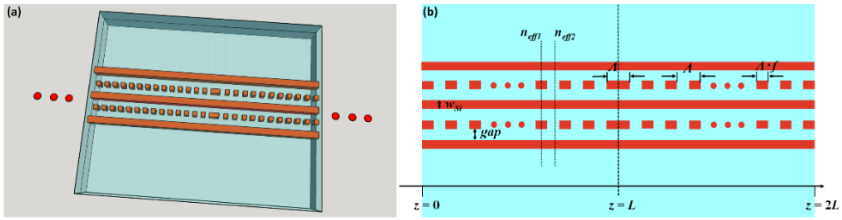



*Figure. 3. Designed QWS-DFB structure. (a) 3D schematic diagram. (b) 2D structure diagram from the top view.*

appreciable grating coupling coefficient (|κ|) can be obtained without huge effect on the target waveguide guided modes. The length of each DBR in each side is *L*. The grating period is *Λ*, and the filling factor *f* (defined as the ratio of single silicon grating length to the grating period) is 0.5, which provides the highest coupling coefficient [12].

To estimate the distribution level of the light electric field in the active material, the following confinement factor is considered. The confinement factor in active material is indicated by $\Gamma_a$, with its definition as: the ratio of the optical dielectric power confined in the active region to the total optical power flowing through the structure:

$$\Gamma_a = \frac{\iint_A \varepsilon |E|^2 \, dxdy}{\iint_\infty \varepsilon |E|^2 \, dxdy} \quad (1)$$

With this confinement factor, the threshold of the QWS-DFB laser can be further studied. The lasing threshold and mirror loss level (external loss)/ material absorption loss (cavity internal loss) are represented by $g_{th}$ and $\alpha_m/\alpha$, respectively. Mirror loss level ($\alpha_m$) is basically dominated by the grating coupling coefficient ($|\kappa|$) once the gain material is chosen and constrains the lasing through condition:

$$\Gamma_a g_{th} = \alpha_m + \alpha \quad (2)$$

In our case, the material absorption loss is $\alpha$ = 8.06 cm$^{-1}$ [10]. According to the simulation and analysis carried out by exploring the design space of the waveguide and active layer parameters, we find that only when the value of $\Gamma_a$ is larger than 0.714 (meanwhile for $|\kappa|L$ larger than 4) that lasing can be achieved. In other words, in the case of ensuring that $\Gamma_a$ > 0.714 and $|\kappa|$ > 8000 m$^{-1}$, a compact on-chip QWS-DFB laser with no longer than 1 mm footprint size can be obtained; even close to 0.5 mm long size when $|\kappa|$ > 16000 m$^{-1}$. Supported by numerous analysis, we can conclude that using our design, it is feasible to fulfil the requirement for a compact on-chip DFB laser. More information will be given during the conference.

## 4. CONCLUSION

In summary, we investigate the feasibility of realizing compact on-chip DFB lasers relying on composite silicon multiple-rail waveguides coated with a highly erbium doped concentration active $Al_2O_3/Er_2O_3$ materials. Supported by our proposed structure and good luminescent materials grown by the atomic layer deposition technique (ALD), sub-mm footprint size (even as short as 0.5mm) laser optically pumped at 1470nm wavelength can be achieved theoretically. This work opens up interesting prospects for integrating and combining these sources to create optical links or more complex on-chip functions.


## ACKNOWLEDGEMENTS

We thank the OpticAll ANR French national project as well as the China Scholarship Council for supporting this work.


## REFERENCES


[1] J. Bahrain, F. Sasan: Silicon photonics, J. Lig. Technol. 24(12), 4600-4615 (2006).
[2] S.Richard: The past, present, and future of silicon photonics, J. Sel. Top. Qua. Ele. 12(6), 1678-1687 (2006).
[3] D. Liang J. E. Bowers: Recent progress in lasers on silicon, Nat. Photonics 4(8), 511–517 (2010).
[4] Z. Fang, *et al.*: A review of recent progress in lasers on silicon, Opt. Laser Technol. 46, 103–110 (2013).
[5] K. Ohira, *et al.*: On-chip optical interconnection by using integrated III-V laser diode and photodetector with silicon waveguide, Opt. Express 18(15), 15440–15447 (2010).
[6] B. Ben Bakir, *et al.*: Electrically driven hybrid Si/III-V Fabry-Pérot lasers based on adiabatic mode transformers, Opt. Express 19(11), 10317–10325 (2011).
[7] J. D. B. Bradley, M. Pollnau: Erbium-doped integrated waveguide amplifiers and lasers, Laser Photonics Rev. 5(3), 368–403 (2011).
[8] M. Pollnau, J. D. B. Bradley: Optically pumped rare-earth-doped Al2O3 distributed-feedback lasers on silicon, Opt. Express 26(18), 24164-24189 (2018).
[9] M. Belt, D. J. Blumenthal: Erbium-doped waveguide DBR and DFB laser arrays integrated within an ultra-low-loss Si3N4 platform, Opt. Express 22(9), 10655-10660 (2014).
[10] J. Rönn, *et al.*: Ultra-high on-chip optical gain in erbium-based hybrid slot waveguides, Nat. Comm. 10(1), 432 (2019).
[11] J. Rönn, *et al.*: Atomic Layer Engineering of Er-Ion Distribution in Highly Doped Er:$Al_2O_3$ for Photoluminescence Enhancement, ACS Photonics 3(11), 2040-2048 (2016).
[12] T. E. Murphy: Design, fabrication and measurement of integrated Bragg grating optical filters, PhD thesis Massachusetts Institute of Technology (2001).

# Low-loss single-mode waveguides operating at UV/violet wavelengths and fabricated with contact optical lithography

*Student Paper*

**Chupao Lin [1, 2], David Schaubroeck [3], Gunther Roelkens[1, 2], Roel Baets[1, 2] and Nicolas Le Thomas[1, 2]**

[1] Photonics Research Group, INTEC Department, Ghent University-imec, Technologiepark-Zwijnaarde, 9052 Ghent, Belgium

[2] Center for Nano- and Biophotonics, Ghent University, Belgium

[3]Centre of Microsystems Technology (CMST), imec and Ghent University, Technologiepark 126, B-9052 Zwijnaarde, Belgium

*e-mail: Chupao.Lin@Ugent.be*

## ABSTRACT

We demonstrate air-cladding single-mode waveguides operating at ultraviolet (UV) wavelengths with propagation loss of 5 dB/cm at λ =402 nm. The waveguides are fabricated with atomic layer deposition (ALD) of aluminium oxide ($AlO_x$) on $SiO_2$/Si substrates and with contact optical lithography. This enables an efficient, cost-effective and fast processing. Our result paves the way for on-chip UV spectroscopy.

**Keywords**: UV, integrated photonic circuits, low-loss waveguides, $AlO_x$ waveguides, ALD

## 1. INTRODUCTION

Integrated photonics is an enabling technology in diverse fields of applications, including optical communications and biological sensing. In particular, on-chip bio-sensing arouses great interest, due to its potential in terms of low-cost, compactness and low detection limit. CMOS-compatible silicon nitride ($SiN_x$), which is currently playing an important role for on-chip spectroscopy, is the material of choice for visible/near infrared (NIR) platforms [1]. However, $SiN_x$ suffers from high absorption loss at blue/UV wavelengths [2]. Much effort has been devoted to investigate waveguides at UV wavelengths, yet the UV platform is still in its infancy. For an ideal photonic platform, both low-loss and single-mode operation are crucial to combine multiple optical components on chip. Recently, X. Liu et.al [3] reported a single crystal AlN platform. Benefiting from the excellent film quality, moderate waveguide-loss of 8 dB/cm at λ =390 nm was reached. Nevertheless, the large waveguide-dimension and high index (n) value of 2.2 lead to multi-mode guidance even using electron-beam lithography. In contrast, aluminium oxide ($AlO_x$) has a lower refractive index value and high transparency above 220 nm [4]. Using atomic layer deposition (ALD), the uniformity and thickness of $AlO_x$ film can be well controlled. G.N. West et al. demonstrated $AlO_x$ waveguides with an impressive low loss of ~3 dB/cm at λ =371 nm [5]. Stepper lithography was needed to pattern waveguides and then to achieve single mode operation. Besides, their platform implements silicon oxide ($SiO_x$) as hard mask which is kept as top-cladding afterward. Although this will efficiently decrease the index contrast between the core and cladding and then reduce the scattering loss, the $SiO_x$-cladding will inevitably inhibit the bio-sensing potentials of the platform. In this paper, we propose air-cladding single-mode $AlO_x$ waveguides fabricated by conventional contact photolithography (Karl Süss MA6 aligner). Prior to implement the expensive and time-consuming stepper lithography, this $AlO_x$ platform makes use of an efficient and cost-effective lithography tool to make research prototypes of devices in UV/violet spectrum. Propagation loss of 5 dB/cm is demonstrated at a wavelength of 402 nm.

## 2. DESIGN AND CHARACTERIZATION OF ALOX WAVEGUIDES

We have used the simulation tool COMSOL Multiphysics to investigate the range of single-mode operation of the $AlO_x$ waveguides. The $AlO_x$ layer is grown on 3-μm thermal $SiO_2$ on Si wafers. The thickness of $AlO_x$ layer is designed to be 120 nm for λ =402 nm, while 100 nm is adopted for λ =360 nm to inhibit high-order TE modes. To make sure that the designed waveguide supports only a TE-guided mode, we have simulated the evolution of the modal effective index with respect to the waveguide-width. The results are plotted in Fig. 1(a). With air top-cladding, the cut-off width of the single-mode operation is as large as 1190 nm and 1150 nm for λ=402 nm and 360 nm, respectively. The TE modal profiles of the simulated $AlO_x$ waveguide at λ =402 nm and 360 nm are shown in Fig. 1(b).

To precisely control the thickness and quality of the core layer, AlOx film is deposited on $SiO_2$/Si wafer via ALD using an Ultratech Savannah 200 instrument (Veeko). $AlO_x$ is deposited at 150°C using trimethylaluminum and water as precursors. Due to the poor etching selectivity between the photoresist and the $AlO_x$, a layer of $SiN_x$

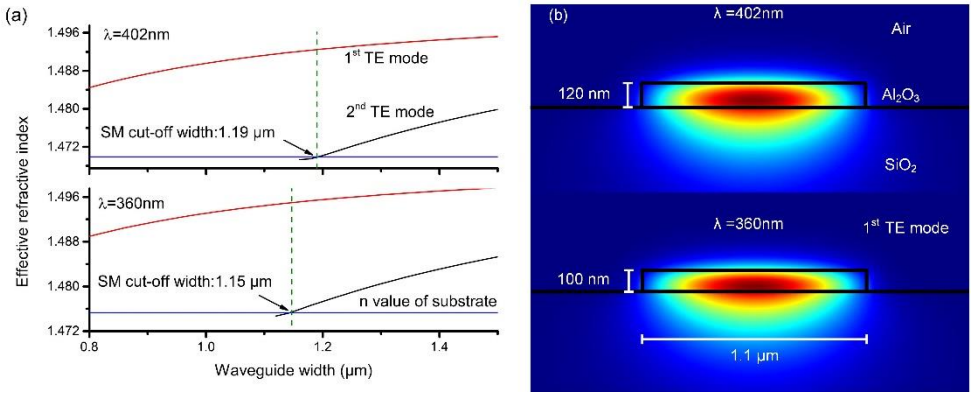



*Figure 1. (a) Evolution of 1st and 2nd TE mode effective index with respect to waveguide width at λ =402 nm and 360 nm, respectively. (b) Simulated modal profiles of the designed waveguide for λ=402 nm and 360 nm.*

grown by plasma enhanced chemical vapour deposition (PECVD) is used as hard mask to define the $AlO_x$ waveguides. We have used a conventional mercury lamp based contact photolithography system with a band pass filter selecting the 280-350 nm wavelength range to expose the photoresist. The patterns defined by the photoresist are transferred to the $SiN_x$ hard mask by using reactive ion etching (RIE). The $AlO_x$ layer is dry etched in an inductive coupled plasma (ICP)-RIE with a $BCl_3/Cl_2/Ar$ gas mixture. The anisotropy of the etching of both SiN and $AlO_x$ are well controlled, resulting in nearly vertical side walls. Finally, the SiN hard mask is removed by RIE. A typical cross-section of a waveguide is shown in Fig. 2(b). The fabricated waveguide with a width of 1100 nm and height of 120 nm is characterized using a 402 nm diode laser. The top image of the light scattered from a 1.6 cm-long spiral waveguide is shown in Fig. 2(a). The 200 μm bend radius is designed to minimize bend losses. The propagation loss is estimated to be ~5 dB/cm by analysing the intensity decay of scattered light. The intensities of scattering light at input and output are extracted and averaged by 20 lines of pixels, as shown in Fig. 2(c). The total waveguide loss is attributed to material absorption and scattering loss. With the higher deposition temperature of 300 ºC, the material absorption of ALD $AlO_x$ can be further decreased [4]. Meanwhile, waveguides designed to operate at $\lambda$ =360 nm are under processing.

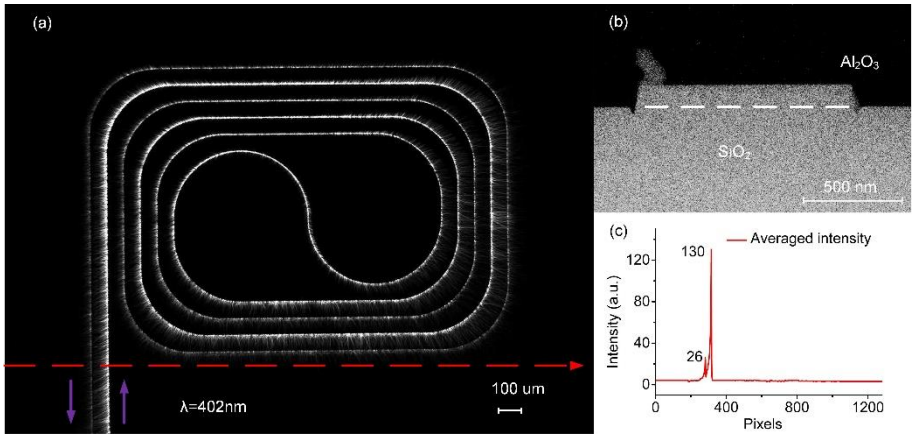



*Figure 2. (a) Microscopy images of the scattered light from a spiral waveguide at a wavelength of 402nm, (b) Cross-section of the corresponding $AlO_x$ waveguide imaged by a scanning electron microscope, (c) Averaged intensity profile of the scattered light at the input and output of the spiral. The total length of the spiral equals to 1.6 cm.*

## 3. CONCLUSIONS

This work paves the way for on-chip light-matter interaction in the UV/violet region, and in particular for on-chip UV spectroscopy. Furthermore, being compatible with contact optical lithography, the proposed $AlO_x$ platform exhibits the advantage of fast processing and low-cost. Finally, the achieved 5 dB/cm-loss single-mode waveguides are promising for developing a UV platform with complex on-chip optical components.

## REFERENCES

[1] Subramanian, A.Z., et al., "Silicon and silicon nitride photonic circuits for spectroscopic sensing on-a-chip", Photonics Res. **3**, B47-B58, 2015

[2] Sorace-Agaskar, C., et al., "Versatile Silicon Nitride and Alumina Integrated Photonic Platforms for the Ultraviolet to Short-Wave Infrared", IEEE Journal of Selected Topics in Quantum Electronics **25**, 1-15, 2019

[3] Liu, X., et al., “Ultra-high-Q UV microring resonators based on a single-crystalline AlN platform”, Optica **5**, 1279-1283, 2018
[4] Aslan, M.M., et al., “Low-Loss Optical Waveguides for the Near Ultra-Violet and Visible Spectral Regions with Al(2)O(3) Thin Films from Atomic Layer Deposition”, Thin Solid Films **518**, 4935-4940, 2010
[5] West, G.N., et al., “Low-loss integrated photonics for the blue and ultraviolet regime”, APL Photonics **4**, 026101-7,2019

# Ultra-wide band inter-mode four-wave mixing in sub-wavelength silicon waveguides

**Jianhao Zhang,[1] Carlos Alonso-Ramos,[1] Laurent Vivien,[1] Sailing He,[2] Eric Cassan**[1]
[1] Université Paris-Saclay, Univ. Paris-Sud, CNRS, Centre de Nanosciences et de Nanotechnologies, 91120, Palaiseau, France.
[2] State Key Laboratory for Modern Optical Instrumentation, Centre for Optical and Electromagnetic Research, Zijingang Campus, Zhejiang University, Hangzhou 310058, China
*e-mail: jianhao.zhang@universite-paris-saclay.fr*

## ABSTRACT

We propose an approach to provide wideband inter-mode four-wave mixing independently of the intrinsic dispersion of the involved waveguide modes. Sub-wavelength engineering is adopted to design an effective lateral confinement photonic well, i.e. with a graded potential along the waveguide cross section providing flexible control over the modes' confinement. The self-adaptive nature of the waveguide boundary allows different spatial modes with equi-spaced frequencies and shared propagation wavevector, thus automatically fulfilling both energy conservation and wavevector phase matching conditions. This strategy, which opens a design space for on-chip nonlinear applications, is applied here to silicon waveguides.

**Keywords**: Silicon photonics, nonlinear optics, four-wave mixing, sub-wavelength structures.

## INTRODUCTION

NONLINEAR processes like four-wave mixing (FWM) have a great interest in photonics due to their unique capabilities for on-chip light generation, with especially a large potential for the implementation of wideband sources for silicon photonics [1]-[4]. Harnessing third order nonlinear Kerr effect in silicon already allowed the demonstration of promising frequency combs [5]-[8], optical parametric amplification [9]-[12] and mid-infrared light sources in silicon [13]-[15]. A great effort has been devoted to compensate both the intrinsic material dispersion and the nonlinearity-induced dispersion that can spoil the needed phase matching condition to maximize the efficiency of FWM processes [2]. Nevertheless, achieving broadband phase-matching in fabrication-tolerant silicon waveguides remains a difficult task. The optimization of the transversal dimensions of conventional strip waveguides provided a successful phase-matching approach in relatively narrow wavelength ranges, thus compromising the bandwidth of the nonlinear wavelength conversion processes [9]-[15]. Here, we propose a new strategy to satisfy both phase matching and energy conservation conditions in an ultra-broad wavelength range. Rather than tuning the waveguide dimensions to yield anomalous dispersion, we shape the index profile of the waveguide to support directly different spatial modes with the same propagation constant and equal frequency spacings, ensuring the automatic phase matching and energy conservation rules.

## 1. PROPOSED APPROACH

In the conventional single-mode FWM approach, depicted in Fig. 1(a), energy is transferred from the pump into signal and idler propagating in the fundamental waveguide mode with different propagation constants. Thus, a precise control of dispersion is required to fulfill phase matching condition ($2k_{zP} = k_{zS} + k_{zI}$). In the proposed multi-mode FWM approach, see Fig.1(b), energy is transferred from the pump into signal and idler propagating in different waveguide modes with the same propagation constant ($k_{zP} = k_{zS} = k_{zI}$). Therefore, the phase matching condition is automatically satisfied. Concurrently, energy conservation requires equal frequency spacing. Then, the bandwidth of the proposed scheme does not depend on the exact dispersion of the waveguide, but on the relative slopes of the dispersion curves of the modes, determining the wavelength range where energy conservation is fulfilled, as illustrated in Fig. 1.

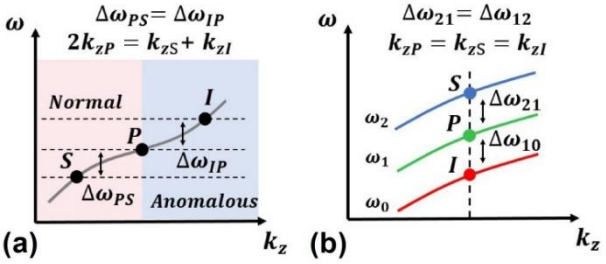



Fig. 1. Description of the degenerate four wave mixing process operated in a single-mode waveguide with anomalous dispersion (a) and operating within an inter-modal scheme regardless the absolute dispersion provided that all dispersion curves are obtained by translating the same curve with a constant frequency step (e.g. $\Delta\omega_{21}$=$\Delta\omega_{10}$ here).

## 2. OVERVIEW OF THE PROPOSED IMPLEMENTATION

Our concrete implementation of this idea is based on the use of multimode waveguides with a gradual transverse index profile. Our theoretical investigations have led us to identify a very important condition for obtaining multimode guides with constant frequency spacing. It turned out that the effective index of each guided mode of the waveguide should be higher than the index of its edges, so that each mode can freely occupy the desired lateral spacing. This condition, which we have noted Self-Adaptive Boundary (SAB) in Ref [16], combined with subwavelength engineering concepts for the realization of transverse optical index profiles, has allowed the design of various multimode waveguides dedicated to FWM processes.

Fig. 2 shows a typical example designed by considering a 340 nm silicon thick SOI optical wafer. Starting from the concept of a SAB graded index waveguide (3D picture) corresponding to an index profile of the form$(A + By)^p$ after a $2b$ wide central region, with $y$ the waveguide lateral dimension and $p$ a freely adjustable parameter, and thus a graded "potential-like" profile highlighted in Fig. 2 (a), we derived an analytical approach to describe the frequency mode spacing derivative against the mode number $m$ (see Fig. 2 (b)), and checked afterwards the obtained dispersion curves using 3D-FDTD simulation (see Fig. 2 (c)).

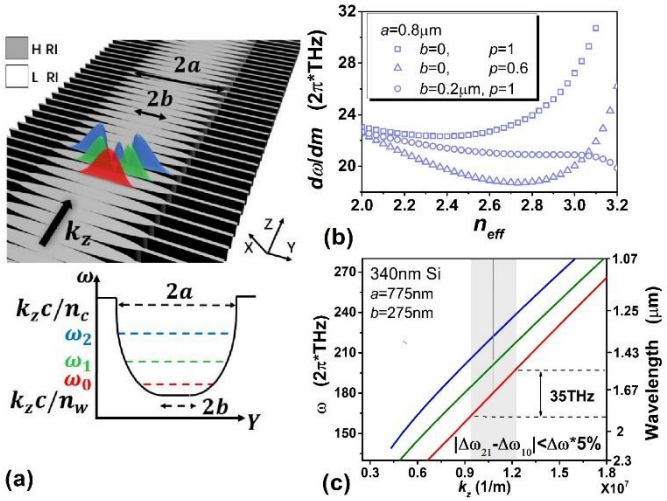



Fig. 2. (a) Sketches of a photonic well described by the cut-off frequency for photon propagating along $z$ axis with wavevector $k_z$. The unit cells of two types of graded-structure waveguides are presented as well. (b) Analytical Frequency spacings as a function of effective index $n_{eff}$, with different $order$s and $b$ values. The other parameters were adopted as: $n_{cent} = 3.48$, $n_b = n_c$=1.8. (c) Frequency spacings as a function of the effective index $n_{eff}$, using 3D FDTD calculation. The perfect matching point and the 5% tolerant range are labeled by grey line and grey region, respectively.

To take a step back from this whole study, we have studied a large number of waveguide structures, varying the main opto-geometrical parameters of the structures (in particular the thickness of the silicon film in the 200nm-600nm range). These investigations have led us to the conclusion that the proposed approach is quasi-universal, in that we have been able in each case, and without difficulty, to prepare multimode waveguides with very parallel dispersion curves, i.e. directly suited to FWM processes. Simultaneously, inter-modal electric-field overlaps were verified as well by calculating the 3D integral $\frac{\iiint E_{yS}\cdot E_{yP}\cdot E_{yP}^{*}\cdot E_{yI}^{*}dr^3}{\iiint |E_{yP}|^2dr^3\sqrt{\iiint |E_{yS}|^2dr^3}\cdot\sqrt{\iiint |E_{yI}|^2dr^3}}$, which gave values typically around 12%, $E_{yS}$, $E_{yP}$and $E_{yI}$ corresponding to the field of signal wave, pump wave and idler waves, respectively.

## 3. CONCLUSION

We report that waveguides with subwavelength-engineered graded index profiles can be designed to support the modes that adapt themselves to different effective boundaries according to their effective index values. This self-adaptive behavior provides a degree of freedom to achieve simultaneous both the energy conservation and phase matching regardless the intrinsic dispersion of the considered optical waveguide modes. This strategy, that can be adapted to different wavelength ranges and material platforms, opens a new design space for the application of FWM processes in multimode optical waveguides. The examples described in this summary will be developed at the conference and complemented by experimental results.

## REFERENCES


[1] G. P. Agrawal, *Nonl*inear *Fiber Optics*., 5th ed., Rochester, New York, USA, 2013, pp. 1–21.

[2] J. Hansryd, A. Andrekson, M. Westlund, J. Li, and P. Hedekvist, "Fiber-based optical parametric amplifiers and their applications," *IEEE J. Sel. Top. Quantum Electron.*, vol. 8, no. 3, pp. 506-520, 2002.

[3] J. Leuthold, C. Koos, and W. Freude, "Nonlinear silicon photonics," *Nat. Photon.*, vol. 4, no. 8, pp. 535-544, 2010.

[4] M. Borghi, C. Castellan, S. Signorini, A. Trenti, and L. Pavesi, "Nonlinear silicon photonics," *J. Opt.*, vol. 19, No. 9, pp. 093002, 2017.
[5] X. Xue, F. Leo, Y. Xuan, J. A. Jaramillo-Villegas, P. Wang, D. E. Leaird, M. Erkintalo, M. Qi, and A. M. Weiner, "Second-harmonic-assisted four-wave mixing in chip-based microresonator frequency comb generation," *Light: Science & Applications*, vol. 6, no. 4, pp. e16253, 2017.
[6] N. Singh, M. Xin, D. Vermeulen, K. Shtyrkova, N. Li, P. T. Callahan, E. S. Magden, A. Ruocco, N. Fahrenkopf, C. Baiocco, B. P. Kuo, S. Radic, E. Ippen, F. X. Kärtner, and M. R. Watts, "Octave-spanning coherent supercontinuum generation in silicon on insulator from 1.06 μ m to beyond 2.4 μ m," *Light: Science & Applications*, vol. 7, no. 1, pp. 17131, 2018.
[7] B. Stern, X. Ji, Y. Okawachi, A. L. Gaeta, and M. Lipson, "Battery-operated integrated frequency comb Generator," *Nature*, vol. 562, no. 7727, pp. 401-405, 2018.
[8] H. Guo, C. Herkommer, A. Billat, D. Grassani, C. Zhang, M. H. P. Pfeiffer, W. Weng, C. Brès and T. J. Kippenberg, "Mid-infrared frequency comb via coherent dispersive wave generation in silicon nitride nanophotonic waveguides," *Nat. Photon.*, vol. 12, no. 8, pp. 330-335, 2018.
[9] R. Salem, M. A. Foster, A. C. Turner, D. F. Geraghty, M. Lipson, and A. L. Gaeta, "Signal regeneration using low-power four-wave mixing on silicon chip," *Nat. Photon.*, vol. 2, no. 1, pp. 35-38, 2008.
[10] M. A. Foster, A. C. Turner, J. E. Sharping, B. S. Schmidt, M. Lipson, and A. L. Gaeta, "Broad-band optical parametric gain on a silicon photonic chip," *Nature*, vol. 441, no. 7096, pp. 960-963, 2006.
[11] M. A. Foster, A. C. Turner, R. Salem, M. Lipson, and A. L. Gaeta, "Broad-band continuous-wave parametric wavelength conversion in silicon nanowaveguides," *Opt. Exp.*, vol. 15, no. 20, pp. 12949-12958, 2007.
[12] A. C. Turner-Foster, M. A. Foster, R. Salem, A. L. Gaeta, and M. Lipson, "Frequency conversion over two-thirds of an octave in silicon nanowaveguides," *Opt. Exp.*, vo. 18, no. 3, pp. 1904-1908, 2010.
[13] X. Liu, R. M. O. Jr, Y. A. Vlasov, and W. M. J. Green, "Mid-infrared optical parametric amplifier using silicon nanophotonic waveguides," *Nat. Photon.*, vol. 4, no. 8, pp. 557-560. 2010.
[14] S. Zlatanovic, J. S. Park, S. Moro, J. M. C. Boggio, I. B. Divliansky, N. Alic, S. Mookherjea, and S. Radic, "Mid-infrared wavelength conversion in silicon waveguides using ultracompact telecom-band-derived pump source," *Nat. Photon.*, vo. 4, no. 8, pp. 561-564, 2010.
[15] X. Liu, B. Kuyken, G. Roelkens, R. Baets, R. M. O. Jr, and W. M. J. Green, "Bridging the mid-infrared-to-telecom gap with silicon nanophotonic spectral translation," *Nat. Photon.*, vol. 6, no. 10, pp. 667-671, 2012.
[16] J. Zhang, C. Alonso-Ramos, L. Vivien, S. He, E. Cassan, Eric, "Self-adaptive waveguide boundary for wideband multi-mode four-wave mixing", *IEEE Journal of Selected Topics in Quantum Electronics*, vo. 26, no. 2, pp. 5100108, 2019.

# Two-process frequency conversion under stimulated Raman adiabatic passage via a continuum of dark intermediate modes

**Pragati Aashna[1] and K Thyagarajan[2]**
[1]Department of Physics, Indian Institute of Technology Delhi, Delhi, 110016
[2]Department of Physics, School of Engineering and Applied Sciences, Bennett University, Greater Noida, UP, 201310
[1]pragatiaashna0812@gmail.com; [2]krishna.thyagarajan@bennett.edu.in

**ABSTRACT**
We study two-process frequency conversion using three wave mixing processes under stimulated Raman adiabatic passage in a planar-channel waveguide structure via an intermediate continuum of radiation modes with negligible power accumulation. The device is shown to have large bandwidth as well as high efficiency.
**Keywords**: Planar waveguides, Channel waveguides, Nonlinear Optics

## 1. INTRODUCTION

STIRAP is a simple, efficient and robust technique for population transfer under adiabatic interaction among two atomic levels via an intermediate level using two spatially overlapping laser beams referred to as pump and Stokes beams, arranged in a temporally counterintuitive fashion and during this process, the intermediate state remains unpopulated which is advantageous[1]. Recent analogy between quantum mechanical multilevel systems and optical systems has facilitated the application STIRAP into optical systems as well [2].

Three wave mixing (TWM) processes in second order nonlinear media exhibiting quasi phase matching has been widely used for optical frequency conversion to prepare new light sources. However, it is usually very difficult to generate new frequencies very near or very far from the input frequencies via a single TWM process and therefore, multistep TWM processes can be used. This generates a new problem of absorption losses at the intermediate frequency which causes degradation in efficiency for overall conversion. This problem can be resolved using the STIRAP process which prevents accumulation of any power at the intermediate frequencies.

Notwithstanding very high efficiency of the multiple TWM processes occurring simultaneously, the process is bandwidth limited because the phase matching can be satisfied for only a single set of frequencies under QPM with single period gratings. In bulk systems, in order to get the required power densities for TWM processes, large pump powers are required due to diffraction effects; however large bandwidths can be realized due to presence of continuum of propagating modes in both the transverse directions. In channel optical waveguides, light confinement in both the transverse directions leads to much lower power requirements but with the associated disadvantage of very small tunability with respect to input wavelength due to the discrete nature of the interacting modes. On the other hand, in the case of planar waveguides, the confinement is in one of the transverse directions while the light can diffract in other leading to lesser power requirement than bulk (due to the confinement) and higher tunability than channel waveguides (due to the presence of a continuum of modes in one transverse dimension). Here we propose a novel hybrid planar-channel waveguide structure to study a highly efficient as well as broadband two simultaneous TWM processes using STIRAP. The proposed waveguide geometry has a channel waveguide surrounded by a planar structure as shown in Figs. 1 (a) and (b).

## 2. THEORETICAL ANALYSIS

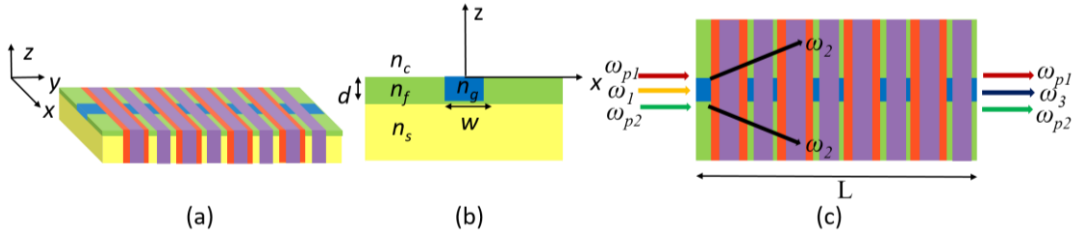



*Figure 1 (a) Schematic diagram of a hybrid planar-channel waveguide configuration for a two process TWM process under STIRAP via continuum (b) The cross sectional view (c) The top view of the structure. The two pumps, input and the output frequencies propagate within the channel waveguide region with the intermediate frequency radiating in the planar region.*

For the study we consider a *z*-cut and *y*-propagating periodically poled lithium niobate waveguide with channel waveguide surrounded by a planar waveguide region (see Fig. 1(a) and (b)). The two pump frequencies (pump1: $\omega_{p1}$ and pump2: $\omega_{p2}$ ), the incident input at $\omega_1$ and the output at $\omega_3$ are assumed to be guided modes of the channel waveguide while the intermediate frequency at $\omega_2$ is assumed to be a superposition of radiation modes of the planar waveguide. The frequency conversion efficiency depends upon the phase matching condition and it can be satisfied

for both the processes simultaneously using two independent gratings under QPM. The phase matching conditions for SFG ($\omega_2 = \omega_1 + \omega_{p_1}$) and DFG ($\omega_3 = \omega_2 - \omega_{p_2}$) respectively are $\Delta\beta_1 = \beta_2 - \beta_{p_1} - \beta_1 - K_1 = 0$ and $\Delta\beta_2 = \beta_2 - \beta_{p_2} - \beta_3 - K_2 = 0$ where $\beta_{p1}$, $\beta_{p2}$, $\beta_1$ and $\beta_3$ correspond to the propagation constants of the guided modes at frequencies $\omega_{p1}$, $\omega_{p2}$, $\omega_1$ and $\omega_3$ in the channel waveguide region, $\beta_2 = \beta_{2p}\cos\theta$ with $\beta_{2p}$ being the propagation constant for the mode at frequency $\omega_2$ in the planar region ($n_c < n_s < n_f$) and $K_1 = 2\pi/\Lambda_1$ and $K_2 = 2\pi/\Lambda_2$ with $\Lambda_1$ and $\Lambda_2$ being the poling period corresponding to the two gratings used for quasi phase matching SFG and DFG processes respectively. $\beta_2$ takes continuous values due to continuum of modes in *x*-direction in the planar region and therefore, if we chose one of the radiation modes for the intermediate frequency out of the continuum, we can fix the grating periods corresponding to that radiation mode which is exactly phase matched for both the TWM processes. This also fixes the angle $\theta$ at which the peak of the generated intermediate wave propagates. Now if the input wavelengths change, then due to the continuous spectrum of $\beta_2$, there would always be some radiation mode which will satisfy the required phase matching conditions. This results in an increase in the bandwidth of the conversion process.

The equations governing the interaction of the all the five fields can be obtained by the standard coupled mode theory approach and the coupled equations describing the evolution of the input, intermediate and the output frequency under undepleted pump approximation can be derived using the standard process and the equations can be written as

$$i\frac{dA_1}{dy} = \kappa_{12}\int A_2(y,\beta_2)\gamma_1(\beta_2)e^{-i\Delta\beta_1 y}d\beta_2; i\frac{dA_2}{dy} = \kappa_{21}A_1\gamma_1^*(\beta_2)e^{i\Delta\beta_1 y} + \kappa_{23}\gamma_2^*(\beta_2)e^{i\Delta\beta_2 y}; i\frac{dA_3}{dy} = \kappa_{32}\int A_2(y,\beta_2)\gamma_2(\beta_2)e^{-i\Delta\beta_2 y}d\beta_2 \quad (1)$$

where $A_{p1}$, $A_{p2}$, $A_1$ and $A_3$ correspond to the *y*-dependent amplitudes and $\psi_{p1}$, $\psi_{p2}$, $\psi_1$ ,and $\psi_3$ correspond to the transverse modal fields of the guided modes in the channel waveguide region at $\omega_{p1}$, $\omega_{p2}$, $\omega_1$ and $\omega_3$ respectively, $\psi_2$ corresponds to the transverse modal field of the planar waveguide mode with a propagation constant $\beta_2$ corresponding to the intermediate frequency in the planar waveguide region and $A_2(\beta_2, y)$ is the amplitude of the mode and is a function of $\beta_2$ because of continuum of modes (continuous $\beta_2$) in *x*-direction, $\gamma_1$ and $\gamma_2$ correspond to the overlap integrals and $\kappa_{12} = 2\omega_1^2 d_{33}A_{p_1}^*/\pi c^2\beta_1$, $\kappa_{21} = 2\omega_2^2 d_{33}A_{p_1}/\pi c^2\beta_2$, $\kappa_{23} = 2\omega_2^2 d_{33}A_{p_2}/\pi c^2\beta_2$ and $\kappa_{32} = 2\omega_3^2 d_{33}A_{p_2}^*/\pi c^2\beta_3$, where $d_{33}$ is the effective nonlinear coefficient and $c$ is the velocity of light in free space. The contribution from the continuum of modes can be eliminated by following a well-known standard procedure followed in quantum mechanical systems under Markovian approximation [3]. The condition for trapped state (dark state) can be obtained through a heuristic mathematical analysis of the coupled equations and the condition required for existence of trapped states is $\gamma_1 = \gamma_2$ and complete transfer of power from input frequency to output is possible without exciting the intermediate frequency requires $\kappa_{23} \gg \kappa_{21}$ at $y = 0$ and $\kappa_{21} \gg \kappa_{23}$ at $y = L$. We will show in the next section that in the proposed configuration, almost complete transfer of power from input frequency to the output frequency, under nearly trapped state i.e. $\gamma_1 \approx \gamma_2$, is possible.

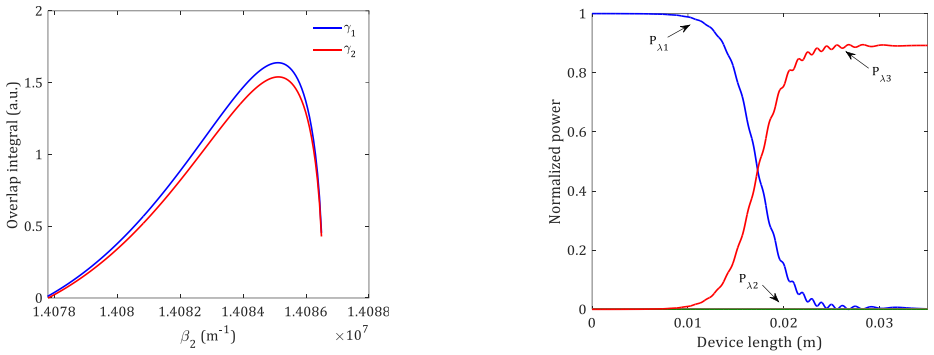
## 3. NUMERICAL RESULTS

In order to demonstrate the feasibility of the device structure for the two process frequency conversion under STIRAP via continuum, we have carried out the numerical simulations for a *z*-cut *y*-propagating titanium indiffused lithium niobate waveguide. For the intermediate frequency, we have used the separation of variable technique and have calculated the propagation constant for the guided modes along *z*-direction and taken the continuum of modes along *x*-direction with propagation constant value being continuous and satisfying the condition $0 < \beta_2^x < k_0 n_f$. Here $\beta_2^x$ correspond to the propagation constant in *x*-direction corresponding to the continuous radiation modes in that direction in the planar region. Since $\beta_2^x$ is continuous, this in turn results into continuous $\beta_2$.

For numerical simulation we have chosen the various wavelengths to be $\lambda_{p_1} = 3000$ nm, $\lambda_{p_2} = 2800$ nm, $\lambda_1 = 1500$ nm and $\lambda_3 = 1667$ nm. This results in an intermediate wavelength of $\lambda_2 = 1000$ nm. In order to optimize the device we first obtain the variation of both the overlap integrals with respect to $\beta_2$ which are shown in Fig. 2 (a). It can be seen that the two overlap integrals are very close to each other. To maximize efficiency we fix $\beta_2$ corresponding to the maximum overlap as the perfect phase matching intermediate mode.

Figure 2(b) shows the variation of power in the three generated frequencies along the length of propagation. It may be observed from Fig. 2(b) that at the output end the ratio of output power $P_3$ at $\omega_3$ to the input power $P_1$ at $\omega_1$ is 0.892 which is very close to the maximum conversion ratio of 0.9 for the two frequencies (equal to the ratio of the

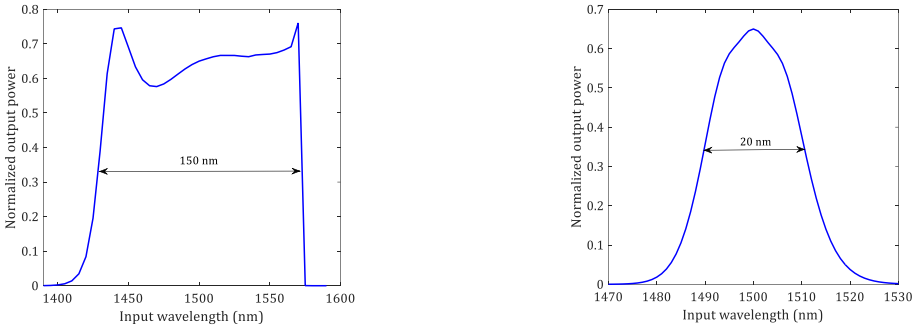
output frequency $\omega_3$ to input frequency $\omega_1$). The figure also shows that there is almost no power in the continuum modes at frequency $\omega_2$ over the entire length of interaction. Therefore, we can say that even if we deviate slightly from the completely trapped condition, almost complete conversion from input to output frequency via an intermediate is possible under STIRAP with the intermediate forming a continuum.




(a) (b)

*Figure 2 (a)Variation of the two overlap integrals, $\gamma_1$ and $\gamma_2$ , corresponding to SFG and DFG processes respectively with $\beta_2$ (b) Almost complete transfer of power from input frequency to output frequency is possible for almost trapped state case.*

The intermediate wave propagating in the planar region forms a continuum and therefore, the two process frequency conversion under STIRAP in the proposed structure has a large tolerance with respect to the variation in the input wavelength unlike in the case of all guided configuration where all the frequencies lie within the channel waveguide. In order to demonstrate this aspect, we have simulated the variation of normalized power at the output frequency with respect to the input wavelength for our proposed hybrid planar-channel waveguide configuration in Fig. 3(a) and for the all guided configuration in Fig. 3(b). We can see from the figures that the bandwidth corresponding to the all guide wave configuration is 20 nm while for the proposed configuration it is 150 nm which is much larger.




(a) (b)

*Figure 3 Variation of normalized output power with the input wavelength for the SFG-DFG process under STIRAP (a) for all guided configuration with 3 dB bandwidth of 20 nm (b) for our proposed hybrid planar-channel waveguide structure with 3 dB bandwidth of 150 nm*

## 4. CONCLUSIONS

In conclusion, we have proposed a novel device structure with a hybrid planar-channel waveguide configuration and used the STIRAP process with the input waves and the generated frequency being guided modes and the intermediate frequency being a continuum of modes in the planar waveguide. We have shown that the proposed device has a broad bandwidth as well as high efficiency in comparison to the all guided configuration. The proposed idea can be used for the generation of new frequencies with high efficiency and large bandwidth using multiple nonlinear processes.

## REFERENCES


[1] K. Bergmann and B. W. Shore, “Coherent population transfer,” in Molecular Dynamics and Spectroscopy by Stimulated Emission Pumping, edited by H. C. Dai and R.W. Field (World Scientific, Singapore, 1995), Chap. 9

[2] Klaas Bergmann, Nikolay V. Vitanov and Bruce W. Shore, Perspective: Stimulated Raman adiabatic passage: The status after 25 years, *J. Chem. Phys.*, vol. 142, 170901(1-20), 2015

[3] S. Longhi, *et al.*: Transfer of light waves in optical waveguides via a continuum, *Phy. Rev. A.*, vol. 78. pp. 013815(1-10), 2008.

# Characterization of an $Er^{3+}/Yb^{3+}$ Codoped Two Core Integrated Waveguide Femtosecond Laser written in a Phosphate Glass

## European Conference on Integrated Optics (ECIO 2020)


D. Benedicto[1], A. Días[2], J. C. Martín[1], J. A. Vallés[1], J. Solís[2].

1. Department of Applied Physics, University of Zaragoza, 50009 Zaragoza, Spain.
2. Laser Processing Group, Institute of Optics, IO-CSIC, Madrid, Spain.

Tel. +34-876 55 34 48, e-mail: dbenedicto@unizar.es


## Introduction


Integrated dual core waveguides have been fabricated in $Er^{3+}/Yb^{3+}$ co-doped phosphate glasses by femtosecond laser writing. A technique is proposed to determine their dimensions and core-substrate refractive index differences, based on asymmetric excitation of the dual core waveguide and mesurements of its output distribution. On the other hand, also a single core waveguide has been written for characterization purposes: gain measurements carried out with it have allowed determination of the glass active properties. Then, enhancement measurements with the two-core waveguides for different signal and pump powers have been carried out, together with simulations of the experiments with the parameters determined in the previous characterization. A good agreement between measurements and simulations has been found, which supports validity of the characterization methods employed.


## Fabrication

### Fs-laser writting

Irradiation of phosphate glasses with femtosecond laser pulses allows the inscription of 3D integrated waveguides with high refractive index contrast by ion migration mechanisms [1]. Waveguides written in phosphate glasses with high $La_2O_3$ content present high refractive index differences in the guiding region mainly due to the incoming migration of La accompanied by the out-diffusion of K.

### Sample

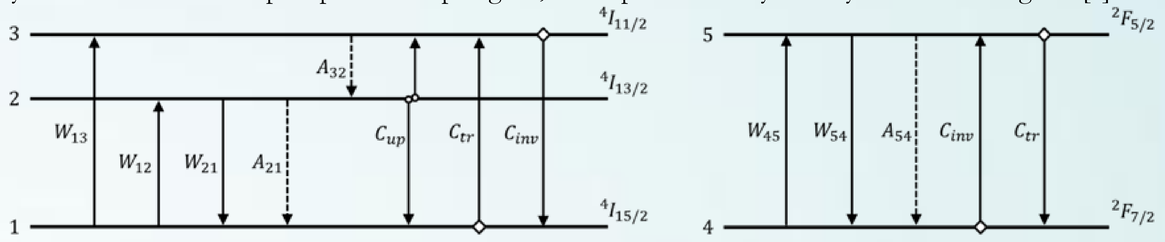
The sample under study, fabricated by the Laser Processing Group of the Institute of Optics in Madrid, has several two-core waveguides with different core-to-core separations. Dimensions of each isolated core would make them single mode for third telecommunication window wavelengths. For characterization purposes, also a single core waveguide has been written.

| Composition (%) | |
|---|---|
| $P_2O_5$ | 58.72 |
| $La_2O_3$ | 18.4 |
| $Al_2O_3$ | 5.82 |
| $Yb_2O_3$ | 5.42 |
| $K_2O$ | 4.89 |
| $SiO_2$ | 4.24 |
| $Er_2O_3$ | 2.53 |

Wavelength 1030 nm
Repetition rate 350 kHz
Pulse energy 520 nJ
Pulse duration 320 fs

## Theoretical Model

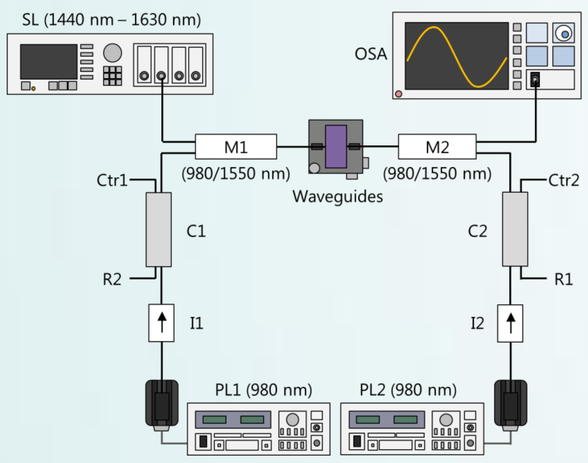
In order to model the amplification of an optical signal along a rare earth doped waveguide, both the **rate equations** system (describing the time evolution of the population densities of the involved active ions energy levels) and the coupled **optical power equations** system (describing the propagation of the optical powers), are required. We follow the conventional diagram of cooperative energy transfer from ytterbium to erbium in phosphate codoped glass, and represent the system by a five-level diagram [2]:




being $W_{ij}$ the stimulated transition rates and $A_{ij}$ the relaxation rates between *ith* and *jth* levels, $C_{tr}$ and $C_{inv}$ the direct and inverse energy transfer rates and Cup the homogeneous upconversion coefficient. Some of the parameters needed in the theoretical model must be obtained experimentally. In order to do that, we first characterize an isolated waveguide written in the same bulk glass.

## Characterization

### Experimental setup

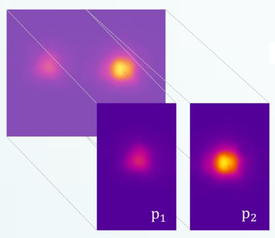


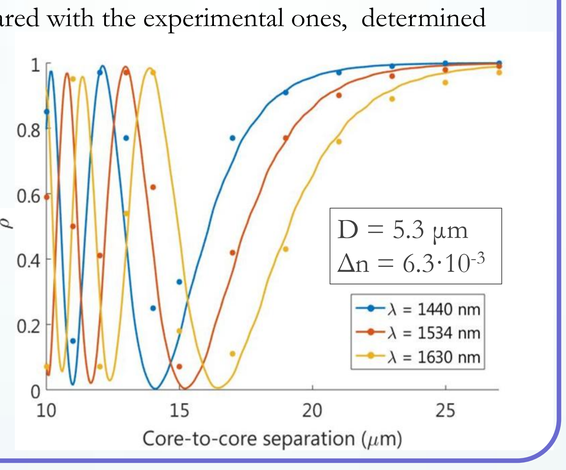

PL: Pump Laser, I: Isolator, R: Residual Pump, C: Coupler, Ctr: Pump Control, M: Multiplexer, SL: Signal Laser, OSA: Optical Spectrum Analyzer.

### Guiding parameters

The parameter ϱ is numerically calculated for each double waveguide, by means of the BeamPROP tool from the RSoft CAD software. Different combinations of core diameter and refractive index difference are tried and the results are compared with the experimental ones, determined through the output intensity distribution

$$\varrho = P_1/(P_1+P_2)$$

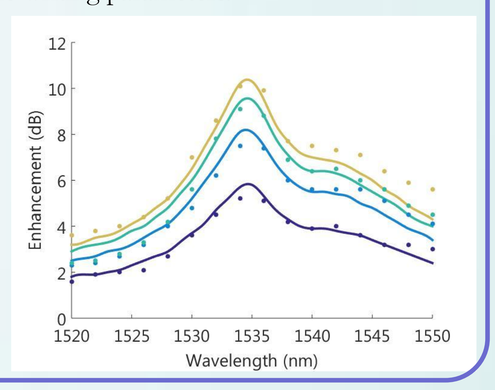



### Active parameters

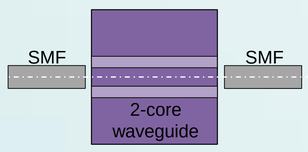
The parameters have been determined by fitting the model results with the absorption spectrum and signal enhancement of the monomode, single core waveguide. We assume that the parameters determined in this stage for the single core are also valid for the rest of cores. This single core is similar to the others composing the double core waveguides, as all of them have been inscribed with the same writing parameters.

| Propagation losses ($m^{-1}$) | |
|---|---|
| Signal (1534 nm) | 30 |
| Pump (980 nm) | 215 |
| **Cross section ($m^2$)** | |
| $^4I_{15/2} \rightarrow {}^4I_{13/2}$ | $9.70\cdot10^{-25}$ |
| $^2F_{7/2} \rightarrow {}^2F_{5/2}$ | $1.25\cdot10^{-24}$ |
| **Energy transfer rates ($m^3/s$)** | |
| Direct | $5.0\cdot10^{-24}$ |
| Inverse | $1.5\cdot10^{-23}$ |
| Upconversion Coef. | $5.5\cdot10^{-24}$ |

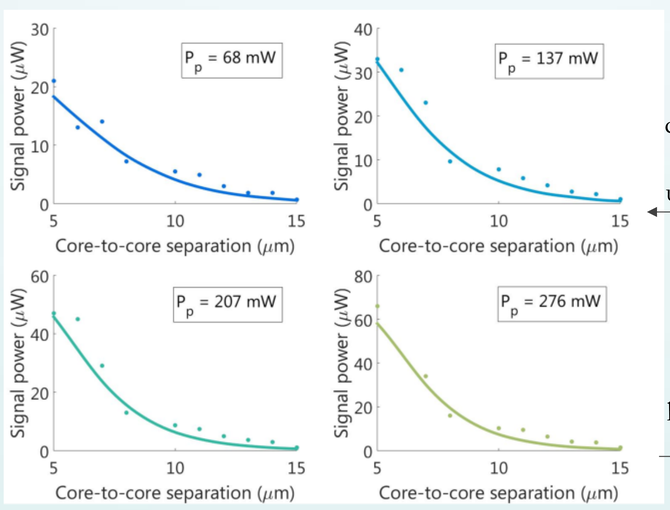



## Results

In order to check the characterization procedure usefulness, experimental and numerical output signal results on pumped double core waveguides have been compared. For each double core waveguide, both adjacent SMFs are aligned symmetrically:

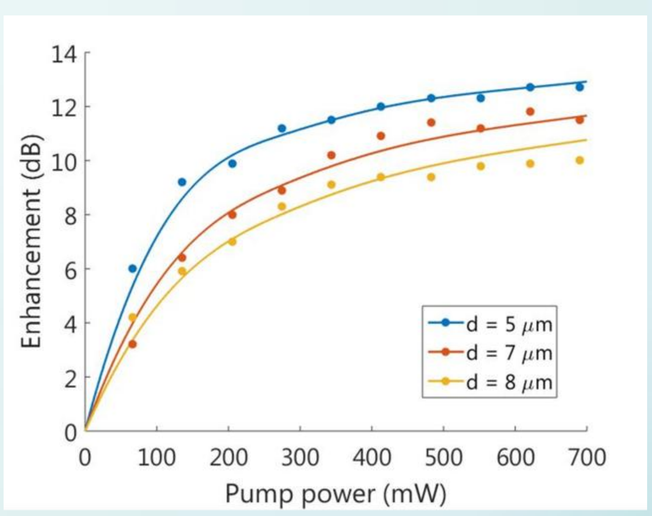



Series of measurements are carried out with 100 μW input signal power at λ=1534 and different pump powers. The same way, numerical calculations have been carried out, with characterization parameters employed as the model parameters. Following figure shows several comparisons between measurements and calculations.




Output signal power dependence on core-to-core separation, for different unidirectional pump powers

Enhancement dependence on bidirectional pump power, for different core-to-core separations




## Conclusions

A complete analysis on dual-core active waveguides including fabrication and characterization has been carried out. Inscription of a single core waveguide together with a set of dual core ones, with different core-to-core distances, has been essential for the procedure. Parameters concerning the active ions have been determined with measurements on the single core waveguide. Their good performance in the prediction of the double-core experimental results shows that the model chosen is suitable for propagation calculations in double-core active waveguides and that the designed characterization procedure allows one to obtain all the parameters necessary to perform calculations with this model, with sufficient precision. Besides, the whole analysis is based on accuracy of the writing technique, which should guarantee enough control on the writing conditions, so that all the cores engraved present similar features. The agreement obtained also confirms trustworthiness of the waveguide fabrication technique employed.


**Referencias:**

[1] Toney TEDDY FERNANDEZ, et al., "*Ion migration assisted inscription of high refractive index contrast waveguides by femtosecond laser pulses in phosphate glass,*" OL, 38, 24, 2013.

[2] Juan A. VALLÉS et al., "*Performance of ultrafast laser written active waveguides by rigorous modeling of optical gain measurements*," OME, 1, 4, 2011.



**Acknowledgments:** This work was partially supported by the Spanish Ministry of Economy and Competitiveness under the TEC2014-52642-C2 project, by the Diputación General de Aragón (DGA) and by the Fondo Social Europeo.

# Amorphous chalcogenide thin films for nonlinear integrated optics in mid-infrared

**J.-B. Dory[1,2], J.-Y. Raty[1,3], M. Ibnoussina[2], J.-B. Jager[4], A. Verdy[1], F. d'Acapito[5], M. Tessaire[1], M. Bernard[1], P. Colman[2], A. Coillet[2], B. Cluzel[2] and P. Noé[1]**

[1] Univ. Grenoble Alpes, CEA, LETI, F-38000 Grenoble, France.
[2] ICB, UMR CNRS 5209, Université de Bourgogne Franche Comté, 21078 Dijon cedex, France
[3] CESAM-Physics of Solids Interfaces and Nanostructures, B5, Université de Liège, Belgium.
[4] Univ. Grenoble Alpes, CEA, INAC, F-38000 Grenoble, France.
[5] CNR-IOM-OGG c/o ESRF – The European Synchrotron, F-38043 Grenoble, France.
*e-mail: jean-baptiste.dory@hotmail.fr; pierre.noe@cea.fr; Benoit.Cluzel@u-bourgogne.fr*

## ABSTRACT

Some chalcogenide glasses (ChGs) are showing a large transparency window in the infrared coupled with outstanding optical nonlinearities offering tremendous opportunities for achievement of innovative mid-infrared (MIR) on-chip components. By means of industrial co-sputtering deposition technique, we study the amorphous structure and the nonlinear optical properties of As-free amorphous $GeSb_wS_xSe_yTe_z$ chalcogenide thin films. The nonlinear refractive Kerr index ($n_2$) of the films were evaluated by means of modelling of spectroscopic ellipsometry data validated experimentally for some compositions by means of advanced nonlinear optical characterizations in waveguides. State-of-the-art and higher $n_2$ values were obtained. Depending on the composition of the $GeSb_wS_xSe_yTe_z$, $n_2$ can vary of more than one order of magnitude. Finally, Fourier-Transform Infrared (FTIR), Raman and X-ray Absorption (XAS) spectroscopies analysis of the amorphous structure of some ChGs prototypical compositions in relation with their nonlinear optical properties was used as a basis for *ab initio* molecular dynamics (AIMD) simulations. Thus, the intimal link between local atomic configurations and optical nonlinearities is proposed giving unique clues to control optical nonlinearities of chalcogenide materials.

**Keywords**: chalcogenide glasses; mid infrared; nonlinear optics; co-sputtering; AIMD; photonics.

## 1. INTRODUCTION

Among their unique portfolio of properties, some chalcogenide glasses (ChGs) offer also unique opportunities for innovative mid-infrared (MIR) components thanks to their outstanding trade-off between a high transparency window and large optical nonlinearities in the infrared range. However, the REACH European recommendation and the World Health Organization have both identified Arsenic as one of the ten most harmful chemicals for human health. In that context, we study here how to tailor the linear and nonlinear optical properties of As-free amorphous $GeSb_wS_xSe_yTe_z$ chalcogenide thin films with a particular emphasis on their compatibility with CMOS technologies for future realization of on-chip MIR components.

## 2. EXPERIMENTS

The $GeSb_wS_xSe_yTe_z$ thin films were obtained by means of magnetron co-sputtering in an industrial 200 mm deposition cluster tool. Modelling of spectroscopic ellipsometry data acquired on the as-deposited films allowed to determine their optical constants (refractive index n, extinction coefficient k and optical bandgap $E_g^{opt}$) using Cody-Lorentz model as well as evaluating their nonlinear refractive Kerr indices ($n_2$). Experimental nonlinear coefficient ($\gamma$) link to Kerr index are obtained by analysing the nonlinear phase shift of waveguides using heterodyne detection setup. The good agreement between experimental and calculated Kerr indices of chosen prototypical ChGs allows to validate modelling of 3$^{rd}$ order nonlinear refractive indices. The link between amorphous structure and enhanced optical nonlinearities was probed by means of FTIR, Raman and XAS spectroscopies on some chosen compositions. On the basis of all experimental data, AIMD simulations permitted to calculate the local electronic polarizability depending on the local structural motifs in the different prototypical glasses evidencing the non-obvious link between some peculiar structural motifs and the material's enhanced macroscopic optical nonlinearity.

## 3. RESULTS & DISCUSSION

### 3.1 Experimental evaluation of Kerr index

In Fig. 1 are plotted the nonlinear coefficient $\gamma$ of 4 $GeSb_wS_xSe_yTe_z$ chalcogenides and $SiN_x$ reference material measured in waveguides using an experimental heterodyne detection setup at 1550 nm. The experimental $n_2$ Kerr refractive indices of the samples are derived from the nonlinear coefficient $\gamma$ and compared to those calculated with the Sheik-Bahae model [1] using linear refractive index and optical band gap values evaluated in thin films.

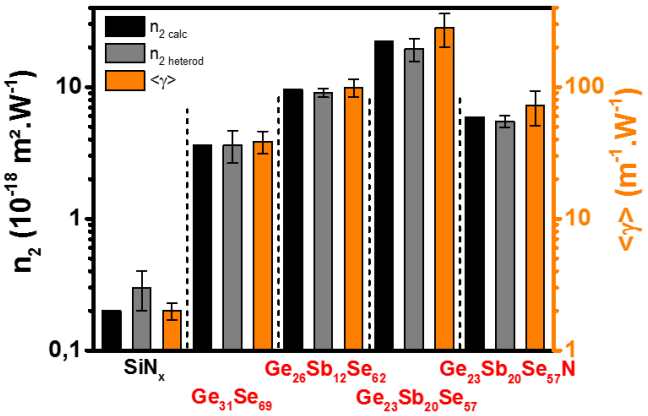



*Figure 1: Experimental nonlinear coefficient γ of some chalcogenide thin films and $SiN_x$ measured in waveguides at 1550 nm. The $n_{2\ heterod}$ Kerr index is deduced from nonlinear coefficient and compared to $n_{2\ calc}$ the Kerr index calculated using the Sheik-Bahae model.*

One can note a good agreement between experimental and calculated Kerr indices of chalcogenide films. The obtained values are of one to two orders of magnitude higher than that of $SiN_x$ samples. A huge variation of 3rd order nonlinearity is also observed depending on the composition of the chalcogenide film. The dramatic change of Kerr index depending on the chalcogenide composition can be related to modifications of the amorphous structure.

### 3.2 Study of the link between optical properties and local amorphous structure

In Fig. 2a are plotted the $n_2$ Kerr refractive indices as a function of the bandgap of the studied $GeSb_wS_xSe_yTe_z$ thin films. Depending on the composition, the amorphous $GeSb_wS_xSe_yTe_z$ films exhibit a wide range of $n_2$ values reaching up to 500 times that of silicon dioxide. We emphasize that these results are well supported by previous study of similar $GeSb_xSe_y$ compounds in the literature [2]. Kerr index shows strong dependence on the ChG's composition [3]. In order to relate optical nonlinearities and structure, four prototypical compositions differing by their $n_2$ values were selected and studied experimentally by means of optical and advanced structural characterization to be used as a basis to robust AIMD models for atomistic simulations.

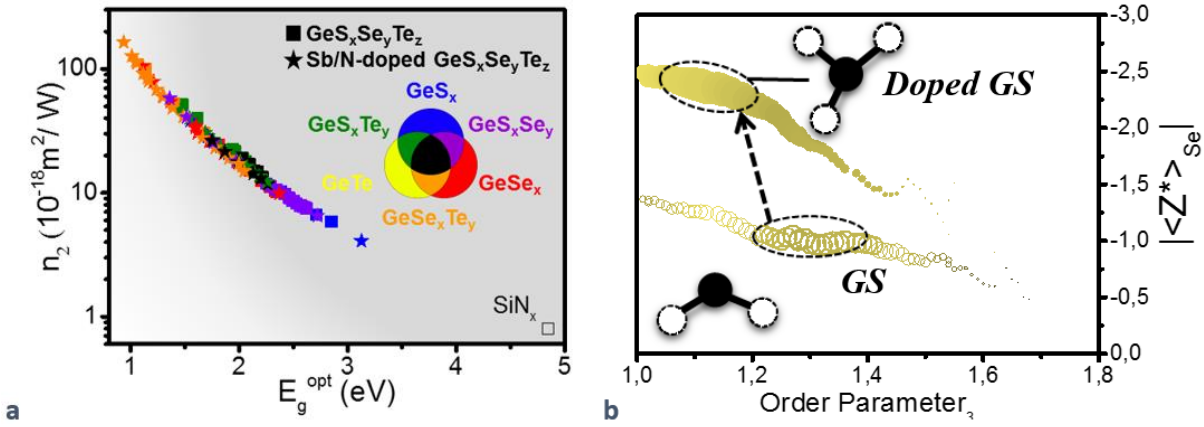



*Figure 2: (a) calculated 3rd order nonlinear refractive indices at 0,534 x $E_g^{opt}$ depending on optical band gap energy of (co-)sputtered $GeSb_wS_xSe_yTe_z$ films. (b) Born effective charges $Z^*$ extracted from AIMD calculations for $Ge_{72}Se_{168}$ (GS) and $Ge_{66}Se_{127}Sb_{48}N_{12}$ (doped GS) materials (open and close symbols). Dots' size is proportional to number of Se-based structural motifs distinguished by means of the order parameter. A significant increase of Z* and thus electronic polarizability is observed for GS upon doping.*

From the calculation of the atomic Born effective charges in Fig. 2b, one could relate the origin of the local very high electronic polarizability related to highly polarizable structural motifs in the amorphous network to the enhanced optical nonlinearities of the material. We show that these highly polarizable motifs result from a unique bonding configuration that is somehow reminiscent to the so called metavalent bonding (MVB), a unique bonding mechanism that is behind the huge optical and electrical contrast between amorphous and crystalline state of phase-change materials [4,5].

## 4. CONCLUSIONS

The outstanding linear and nonlinear optical properties of some chalcogenide glasses at origin of their promising potential of applications for MIR on-chip components is shown to result from formation of peculiar structural motifs leading to specific bonding mechanism at origin of their huge polarizability. In particular, some element increases dramatically the local electronic polarizability by inducing structural motifs supporting bonds similar to the newly introduced metavalent bonding mechanism arising in some local crystal-like motifs [6]. These results pave the way to control and improve further the unique optical properties of chalcogenide glasses in thin films.

## REFERENCES


[1] M. Sheik-Bahae, *et al.*: Dispersion of Bound Electronic Nonlinear Refraction in Solids. *J. Quantum Electron.* 27, 1991.

[2] T. Kuriakose *et al.*: Measurement of ultrafast optical Kerr effect of Ge–Sb–Se chalcogenide slab waveguides by the beam self-trapping technique. *Opt. Commun.* **403**,352-357, 2017.

[3] J.-B. Dory, *et al.*: Ge-Sb-S-Se-Te amorphous chalcogenide thin films towards on-chip nonlinear photonic devices. *Under revision for publication* in *Scientific Reports* 2020.

[4] M. Wuttig *et al.*: Incipient Metals: Functional Materials with a Unique Bonding Mechanism. *Adv. Mater.* 30, 1803777, 2018.

[5] J.-Y. Raty *et al.*: A Quantum-Mechanical Map for Bonding and Properties in Solids. *Adv. Mater.* 31, 1806280, 2019.

[6] J.-B. Dory, J.-Y. Raty *et al.*: Revealing the role of amorphous structural motifs on the huge optical nonlinearities of chalcogenide glasses. *To be published* 2020.

# Polarization-selective defect mode suppression in a deterministic aperiodic photonic crystal through plasmon excitation in an embedded array of metallic nanoparticles


**I.A. Glukhov[1,2], Y.S. Dadoenkova[1,2], F.F.L. Bentivegna[1], S.G. Moiseev[2]**

[1] Lab-STICC, UMR CNRS 6285, ENIB, Brest, France

[2] Ulyanovsk State University, Ulyanovsk, Russia

*glukhov@enib.fr*


## Introduction

Dichroic filters separate spectral bands in a broad spectrum of light. Heat / UV control, color separation, and fluorescence microscopy are a few of the most common uses of dichroic filters.

In this work, the operating principle of a polarization-sensitive dichroic filter based on a multilayered deterministic aperiodic photonic crystal (PC) including a two-dimensional (2D) array of spheroidal metallic nanoparticles is described.

The structure is designed in such a way that two separate narrow passbands can be suppressed for two mutually orthogonal polarizations of light, thus achieving the required behavior.

## Heterostructure with an embedded plasmonic nanoparticle array

### DETERMINISTIC APERIODIC PC

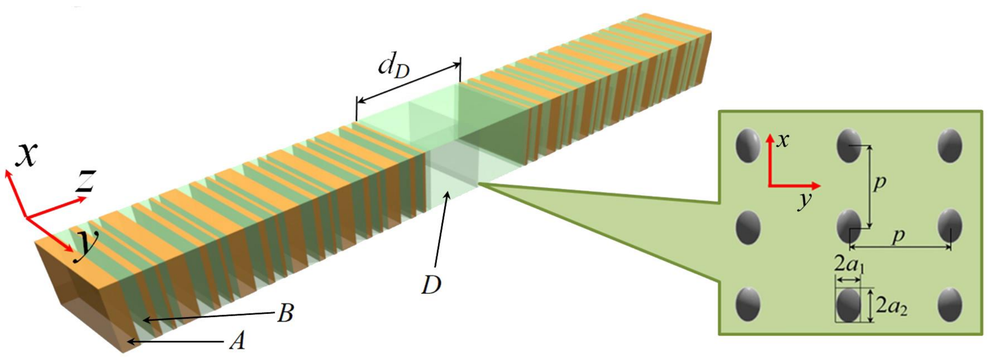



**Fig. 1: Schematic of the composite photonic structure.** Two symmetrical deterministic aperiodic multilayered reflectors are separated by a composite layer *D* at the center of which a 2D array of spheroidal metallic nanoparticles is located (*A* layers are made of $ZrO_2$, *B* and *D* layers of $SiO_2$).

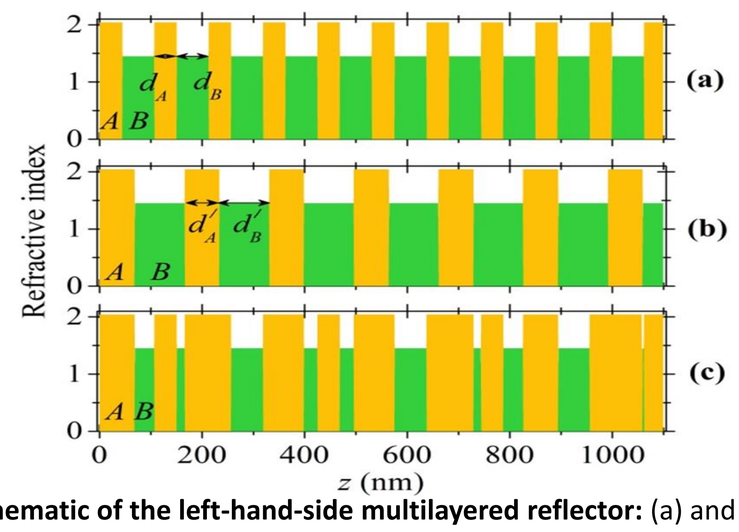



**Fig. 2: Schematic of the left-hand-side multilayered reflector:** (a) and (b) represent the two periodic DBRs that are combined in order to obtain a deterministic aperiodic reflector shown in (c). The right-hand-side reflector of the structure is the mirror image of the left-hand-side one.

### 2D ARRAY OF NANOPARTICLES

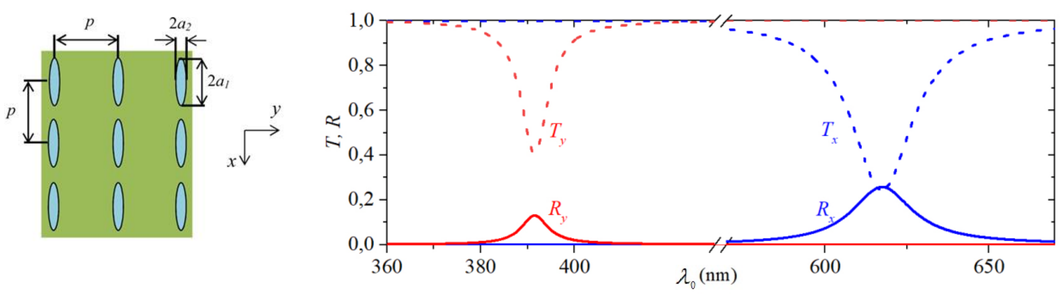



**Fig. 3: Transmittivity ($T_{x,y}$) and reflectivity ($R_{x,y}$) spectra of a 2D array** of silver NPs embedded in a $SiO_2$ matrix for the longitudinal (*x*-) and transverse (*y*-) polarization states of the incoming light wave.

**The anisotropic 2D array exhibits strongly polarization dependent transmittivity and reflectivity spectra.**

## Modelization

### COUPLED-DIPOLE METHOD

**Reflection coefficient of an array of NPs** with dielectric permittivity $\varepsilon_p$ embedded into a medium with permittivity $\varepsilon_m$

$$r_{x,y}^{\mathrm{NP}} \approx i\frac{k_0\sqrt{\varepsilon_m}\,\alpha_{x,y}}{2p^2 - 0.72\alpha_{x,y}/p - ik_0\sqrt{\varepsilon_m}\,\alpha_{x,y}}$$

$$\alpha_{x,y} = V\frac{\varepsilon_p - \varepsilon_m}{g_{x,y}(\varepsilon_p - \varepsilon_m) + \varepsilon_m}$$

polarizability of a single spheroidal NP of volume *V*

$$g_x = \frac{1}{1-\xi^2}\left(1 - \xi\frac{\arcsin\sqrt{1-\xi^2}}{\sqrt{1-\xi^2}}\right), \quad g_y = \frac{1}{2}(1 - g_x)$$

geometric shape factors of a NP

## TRANSFER MATRIX METHOD

**Interface and propagation matrices**

$$r_j^F = \frac{\sqrt{\varepsilon_{j-1}} - \sqrt{\varepsilon_j}}{\sqrt{\varepsilon_{j-1}} + \sqrt{\varepsilon_j}}$$

Fresnel reflection coefficient at the interface *j* between layers with dielectric permittivities $\varepsilon_{j-1}$ and $\varepsilon_j$

$$\hat{I}_j^{\mathrm{F}} = \frac{1}{t_j^{\mathrm{F}}}\begin{pmatrix} 1 & r_j^{\mathrm{F}} \\ r_j^{\mathrm{F}} & 1 \end{pmatrix}$$

Interface matrix of a dielectric/dielectric interface

$$\hat{P}_j = \begin{pmatrix} \exp(-ik_0\sqrt{\varepsilon_j}\,d_j) & 0 \\ 0 & \exp(ik_0\sqrt{\varepsilon_j}\,d_j) \end{pmatrix}$$

Propagation matrix through a dielectric layer of thickness $d_j$

$$\hat{I}_{x,y}^{NP} = \frac{1}{1 + r_{x,y}^{NP}}\begin{pmatrix} 1 & -r_{x,y}^{NP} \\ r_{x,y}^{NP} & 1 + 2r_{x,y}^{NP} \end{pmatrix}$$

Interface matrix of a NP array

**Transfer matrix of the structure**

$$\hat{G}_{x,y} = \left(\prod_{j=1}^{2N+2}\hat{I}_j^{\mathrm{F}}\hat{P}_j\right)\hat{I}_{x,y}^{\mathrm{NP}}\left(\prod_{j=2N+3}^{4N+4}\hat{P}_j\hat{I}_{j+1}^{\mathrm{F}}\right)$$

**Reflectivity and transmittivity of the structure**

$$R_{x,y} = \left|\frac{(\hat{G}_{x,y})_{21}}{(\hat{G}_{x,y})_{11}}\right|^2, \quad T_{x,y} = \left|\frac{1}{(\hat{G}_{x,y})_{11}}\right|^2$$

## Spectra and field distribution

### DEFECT MODE SEPARATION

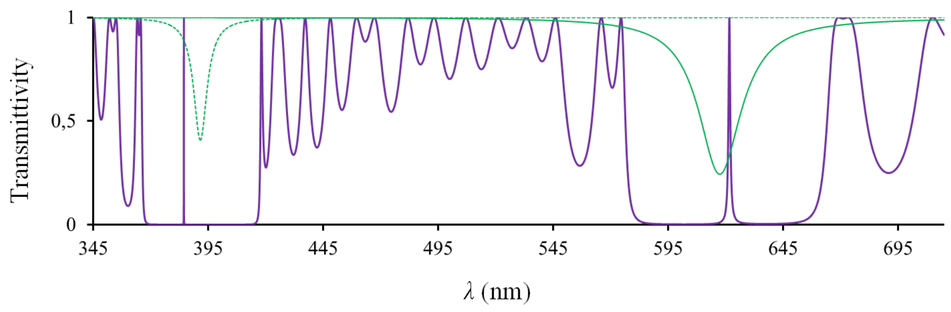
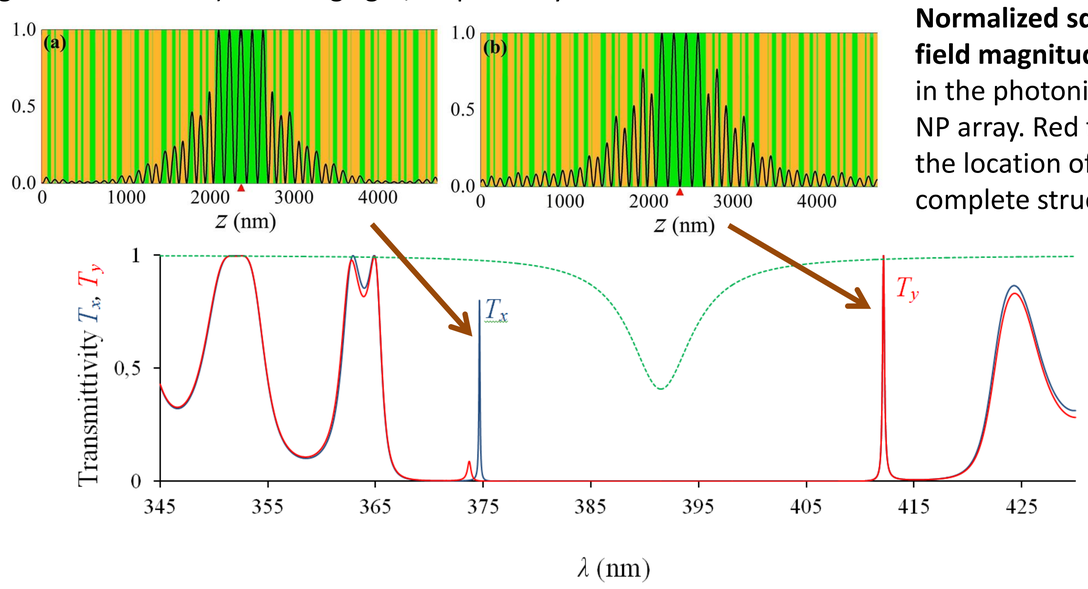



**Fig. 4: Transmittivity spectrum of the photonic structure without NPs** *(purple line)*

The green curves superimposed to the spectrum show the transmittivity dips due to surface plasmon resonances in the sole 2D NP array embedded in a $SiO_2$ layer for *x*-polarized (green solid line) and *y*-polarized (green dashed line) incoming light, respectively.




**Normalized square of the optical field magnitude** along the *z*-axis in the photonic structure without NP array. Red triangles indicate the location of the NP array in the complete structure.

**Fig. 5: Transmittivity spectra of the photonic structure with two defect modes in one bandgap** for *x*-polarized (blue solid line) and *y*-polarized (red solid line) incoming light. Top insets show the optical field distribution at the wavelengths of the defect modes.

**The suppression of a defect mode is achieved when the NP array is embedded at a location of maximal optical field localization and the defect mode wavelength coincides with a plasmon resonance in the NP array.**

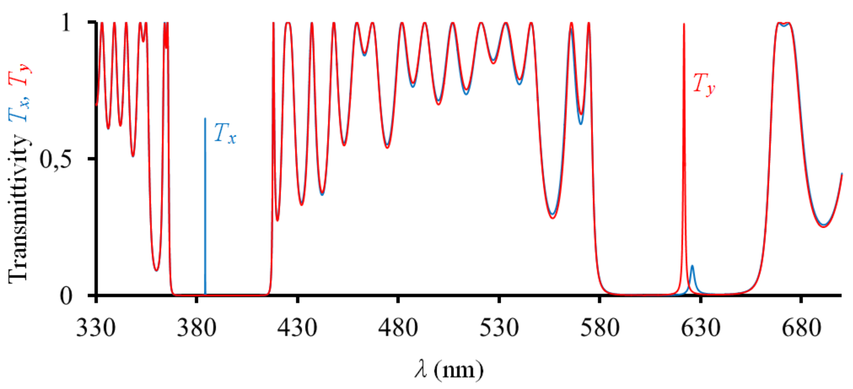



**Fig. 6: Transmittivity spectra of the photonic structure** for *x*-polarized (blue solid line) and *y*-polarized (red solid line) incoming light.

## Summary

- The use of a deterministic aperiodic photonic crystal makes it possible to tailor the spectral position of the bandgaps and defect modes.
- Two distinct localized surface plasmon resonances can be excited in the nanoparticles by mutually orthogonal linear polarization states of light.
- For well-chosen values of the structural parameters of both the photonic crystal and the nanoparticle array, these resonances can be made to coincide with two defect modes located in neighboring bandgaps.
- The non-simultaneous polarization-dependent suppression of two narrow transmittivity peaks can thus be achieved in the structure. Photonic defect mode suppression is possible when the NP array is embedded at a location of maximal optical field localization.

## Acknowledgements


École Nationale d'Ingénieurs de Brest, France (HF-CCCP); Regional Council of Brittany, France (PhotoMag); the Ministry of Science and Higher Education of the Russian Federation; the Russian Foundation for Basic Research (18-42-730007, 19-42-730008).

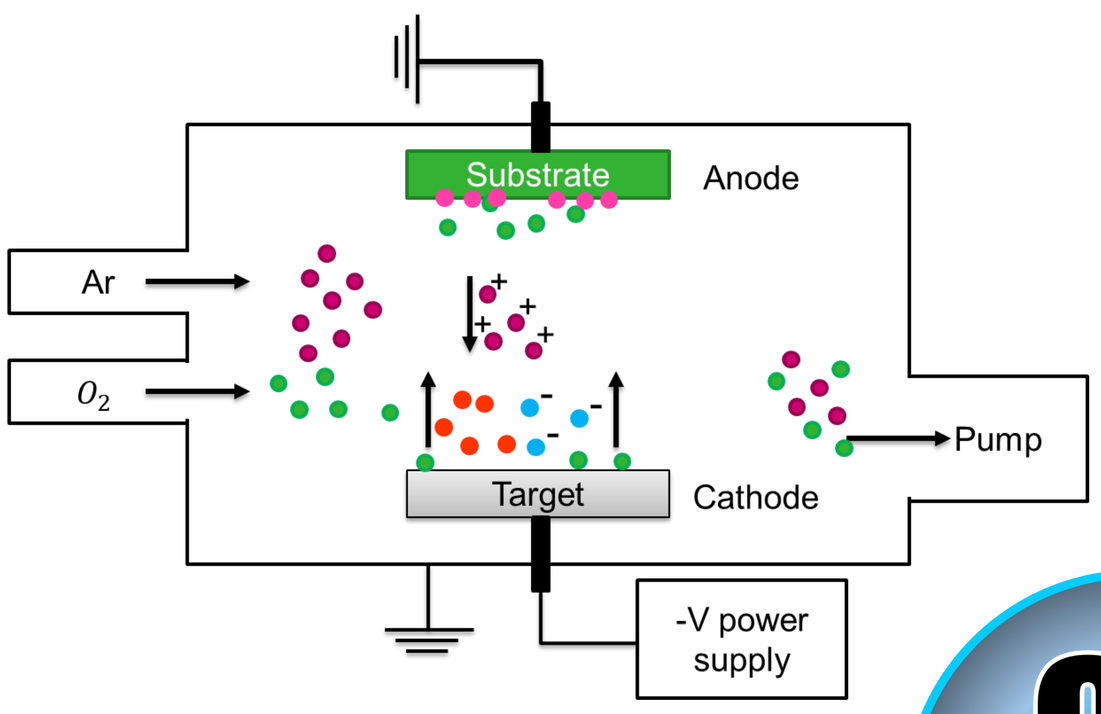
# High refractive index low-loss aluminium oxide waveguides

W.A.P.M. Hendriks, M. Dijkstra, C.I. van Emmerik, I. Hegeman S.M. García-Blanco
MESA+ Institute, University of Twente, P.O. Box 217, 7550 AE, Enschede, The Netherlands
e-mail: w.a.p.m.hendriks@utwente.nl

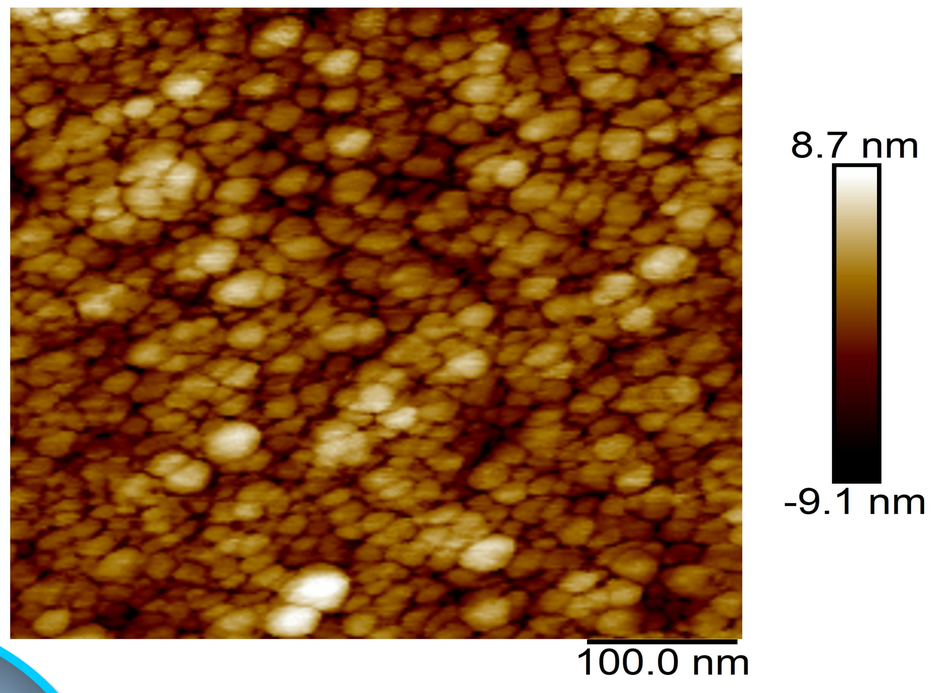
## Abstract

A high refractive index (n~1.715 at 633 nm of wavelength) aluminium oxide slab waveguide has been developed, which exhibits very low losses from the near-UV to the near infrared wavelength range. Slab waveguide losses as low as 2 dB/cm at 407 nm and less than 0.1 dB/cm at 1550 nm of wavelength have been experimentally characterized. Such low losses are limited by surface scattering. The layer was deposited by reactive sputter coating with an aluminium target, with a set substrate temperature of 700 C and oxidation state of the target of 5 %. The very high optical quality of this material, in combination with rare-earth ion doping, could pave the way towards high-gain on-chip amplifiers in different wavelength ranges, on-chip lasers and non-linear applications.

## Reactive sputter deposition



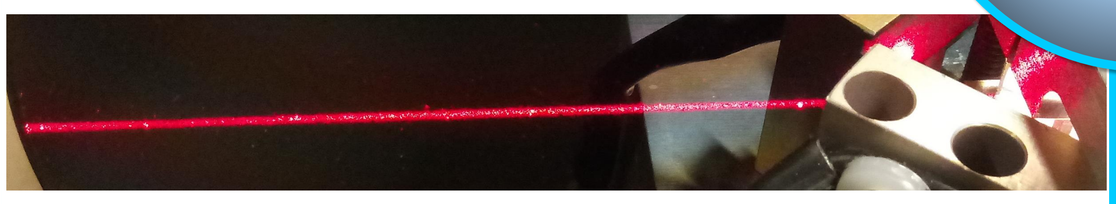

## Surface roughness

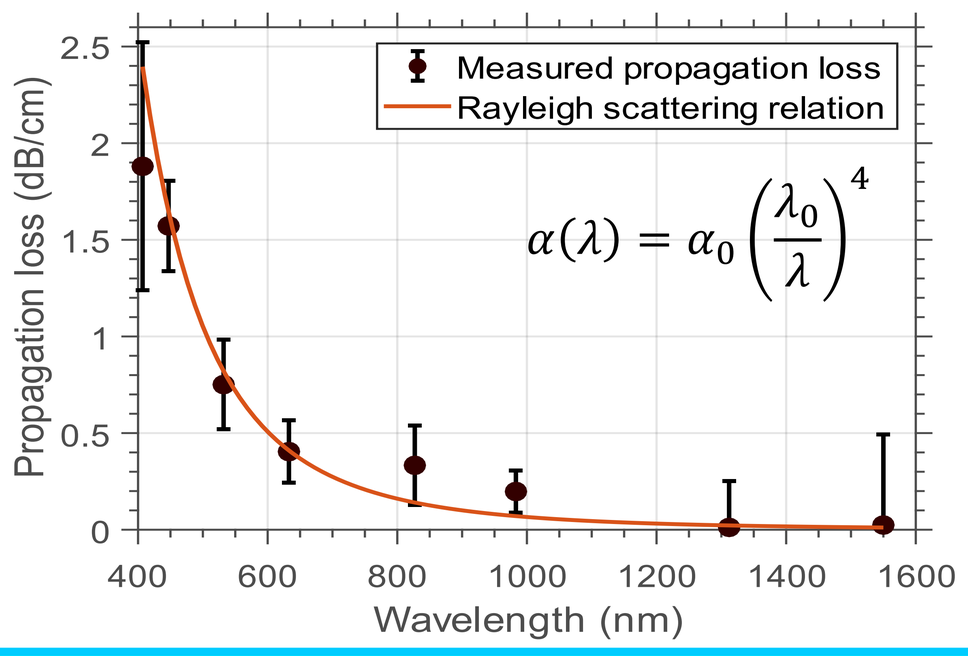



**Surface roughness**
**2.4 nm rms**

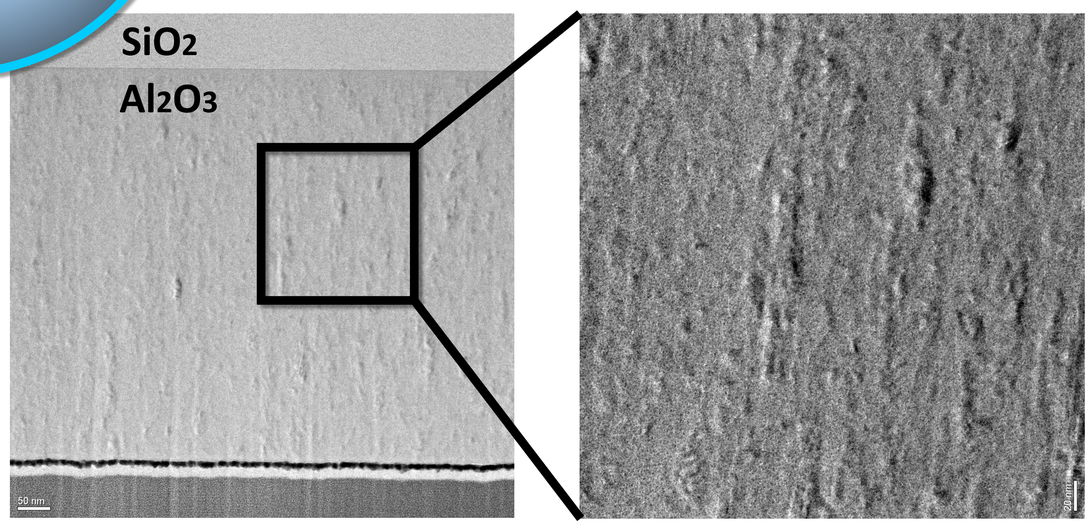
Optical Sciences

## Propagation losses






## Polycrystalline




## Conclusion

- **High refractive index**
- **Low propagation loss (2.5 dB/m @1550nm)**
- **Polycrystalline**

**References**

Van Emmerik, C. I., Hendriks, W. A. P. M., Stok, M. L., De Goede, M., Chang, L., Dijkstra, M., ... García-Blanco, S. M. (2020). Relative oxidation state of the target as guideline for depositing optical quality RF reactive magnetron sputtered Al2O3 layers. Optical materials express, 10(6), 1451-1462.

MESA+ INSTITUTE FOR NANOTECHNOLOGY

UNIVERSITY OF TWENTE.

NWO



# Quantum Well Intermixing of InP-Based AlInGaAs Quantum Wells Using IFVD Technique and the Mask Boundary Effect


**Zhengkai Jia[1], Hua Yang[2], Hui Wang[1], Xing Dai[1], Alison H. Perrott[1,2], Frank H. Peters[1,3]**

*1* Integrated Photonics Groups, Tyndall National Institute, Cork, Ireland

*2* Rockley Photonics Ireland, Cork, Ireland

*3* Department of Physics, University College Cork, Cork, Ireland


## Introduction

- Quantum Well Intermixing (QWI) is a post-growth technique that allows the energy band gap of a quantum well (QW) to be modified without any regrowth and thus can be used in the fabrication of PICs to reduce or eliminate epitaxial regrowth.
- During the QWI process, the diffusion of different atoms into the QW changes the material composition of the well. The band gap of the QW typically increases (thus blue-shift) as a result of the QWI.
- IFVD results in little or no damage to the surface of the epitaxial wafer and requires no extra treatment to the epitaxial wafer, such as a sacrificial layer.
- This paper proposed on the effect of QWI's mask boundary on the laser wavelength shift. This QWI technique and the boundary effect will be a useful reference for further photonic integration design and fabrication.

## QWI Using IFVD

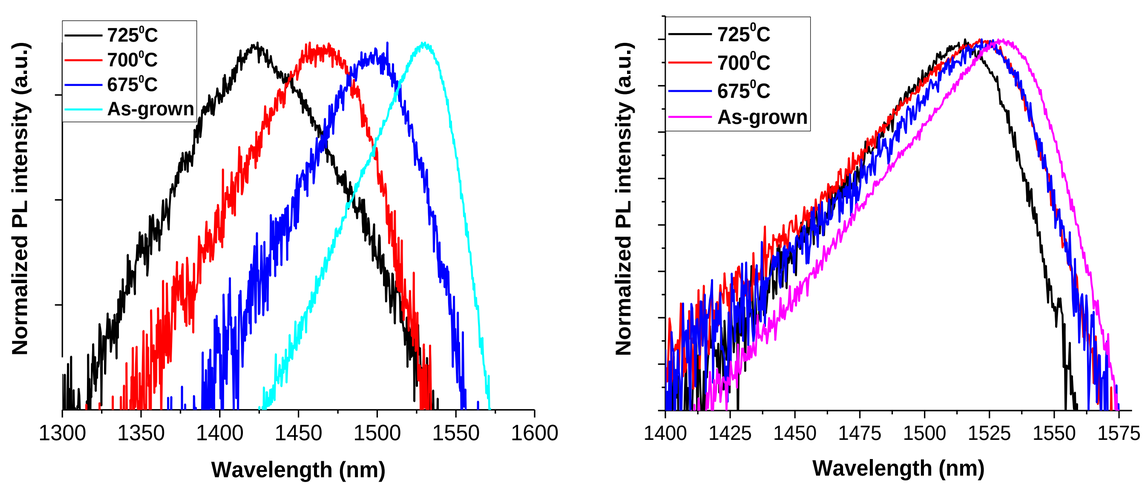



Figure 1(a). PL spectra of the samples capped with $SiN_x$ (left) and Figure 1(b). $SiO_2$ films by PECVD and annealed under different temperature (right).

**Experiments show that the $SiN_x$ deposited by PECVD works as the promotor while the $SiO_2$ by PECVD acts as inhibitor in our QWI technique.**

## Mask Boundary Effect

- 12 FP lasers are designed with a 40μm wide $SiN_x$ mask but with different distances between the centre of the ridge waveguide of the FP laser to the edge of the mask from: -20μm (negative numbers mean that the ridge is fully covered with the mask) to 21.25μm. All the lasers were 500μm long with 2.5μm wide ridges, using one deep etched facet and one cleaved facet.
- The fabrication process is a typical Fabry-Perot semiconductor laser process using conventional photolithography and etching techniques.
- The FP lasers with the ridge waveguide non-fully covered or several microns (0 to around 7.5μm) away from the edge of the SiNx mask also show a blue-shift of the lasing peak wavelength, but shows less blue shift as the distance increases. When the distance is more than 7.5μm, the QWI effect is no longer observed to affect the lasing performance.




Figure 2. 12 lasers with different distances (the numbers on the chip design represent the distance from edge of the mask to the edge of the ridge) on the QWI boundary

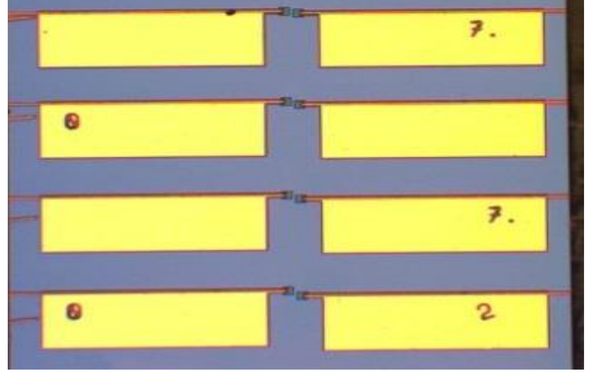



Figure 3. Microscopic picture of the fabricated FP lasers array.

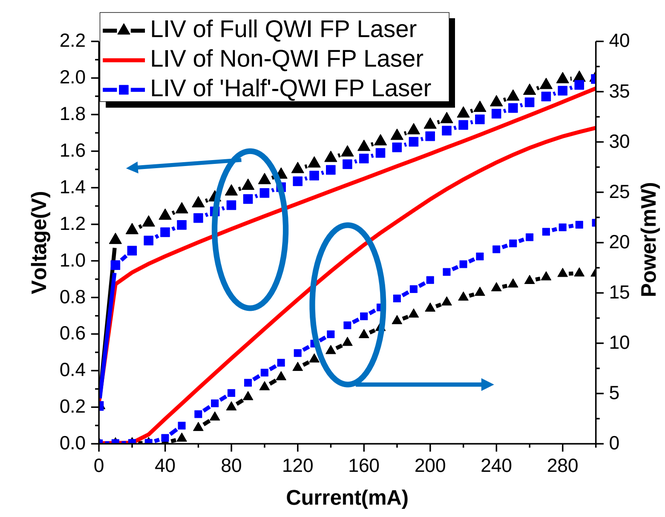



Figure 4. Characteristics of current--voltage and output power--current at 20˚C of non-QWI FP laser, 'Half'-QWI FP laser and Full-QWI FP laser

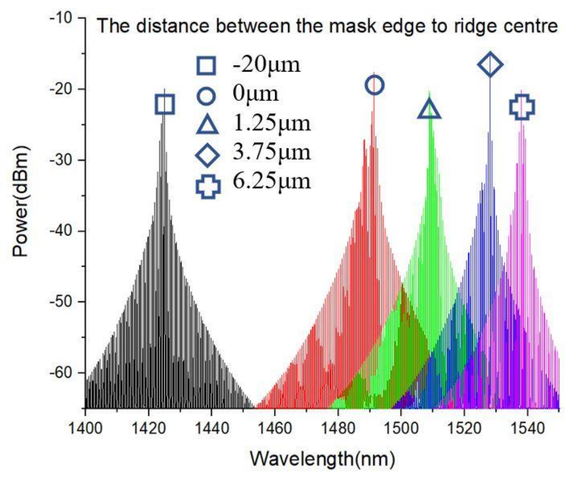



Figure 5. The lasing spectra of the FP laser annealed at 725˚C with different distance between the ridge centre to the edge of the QWI mask

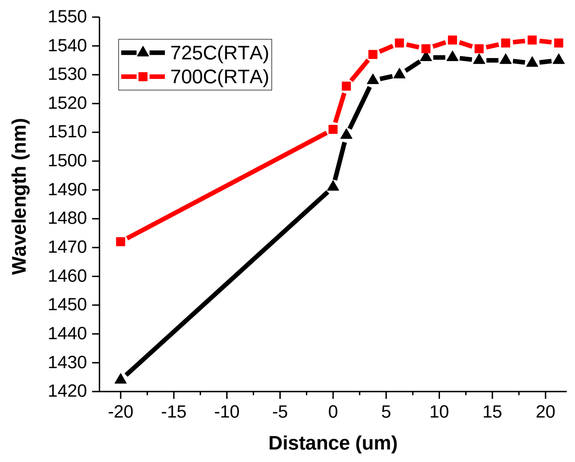



Figure 6. The lasing peak wavelength vs the distance between the ridge centre to the edge of the QWI area mask (all the FP lasers are tested under 40mA and the same other condition). Here, "-20" and "0" represent the ridge is in the centre of the mask and half covered by the mask (right).

## Conclusion

- We have successfully demonstrated a QWI technique using IFVD method with SiNx by PECVD as promoter and SiO2 by PECVD as inhibitor and protector. A 120nm blue shift was obtained using InP-based AlInGaAs/AlInGaAs multiple quantum wells, further proved by Fabry-Perot ridge waveguide lasers fabricated with this technique. The QWI mask boundary effect was investigated, which shows the QWI mask edge needs to be more than 7.5μm away from the area where the intermixing is not desired. This QWI technique and the mask boundary effect result will be beneficial for the monolithic integration of photonic devices using AlInGaAs quantum well material.


Thanks to Science Foundation Ireland under Grant SFI 12/RC/2276 and Grant SFI 13/IA/1960.

# Robust Architecture for Programmable Universal Unitaries

I.V. Kondratyev, I.V. Dyakonov, M. Yu. Saygin, S. S. Straupe, S. P. Kulik

Quantum Technology Centre, Faculty of Physics, Lomonosov Moscow State University, Leninskie gory 1, building 35, 119991, Moscow, Russia.

This work has been published in Physical Review Letters
Scan the QR to view:

# Background

## Previous Universal Designs

For realization of linear optical quantum computation, it is of high importance to be capable of manufacturing device, that could implement arbitrary unitary transformation upon input photonic states. Such devices are emerging as a powerful tool for fields such as microwave photonics [1], optical networking [2], and quantum optics [3], [4].

The seminal work by Reck et al. demonstrated that a specific triangular mesh of 2*2 tunable beamsplitters (Mach-Zehnder interferometers) and phaseshifting elements could implement any unitary transformation between a set of optical channels [3].

Later, another design for universal multiport interferometers based on an alternative arrangement of 2*2 beamsplitters and phase shifters was demonstrated by Clements et al [4]. That design due to its symmetry occupies half the physical footprint of the Reck design.

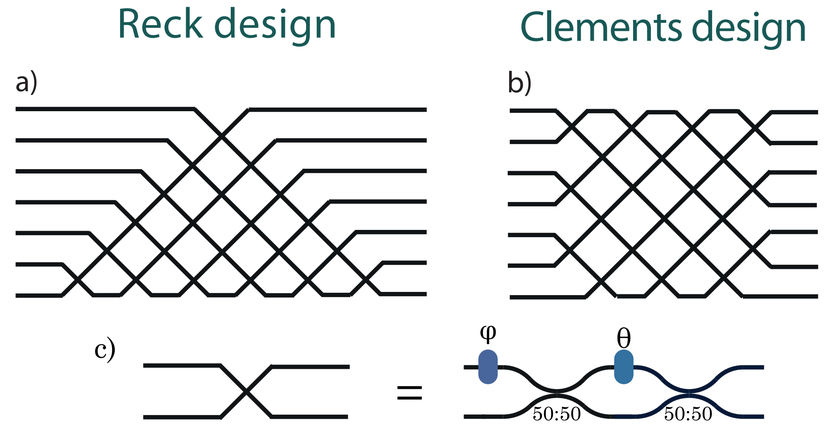



Figure 1. A universal N-mode multiport interferometer (shown here for N = 7) can be implemented using a mesh of N(N−1)/2 tunable beamsplitters such as a) the one proposed by Reck [3] or b) the one proposed by Clements [4]. c) a line corresponds to an optical mode, and crossings between two modes correspond to a tunable beamsplitter, which can be implemented by a Mach-Zehnder interferometer consisting of two 50:50 directional couplers, preceded by a phase shift at one input port. [4]

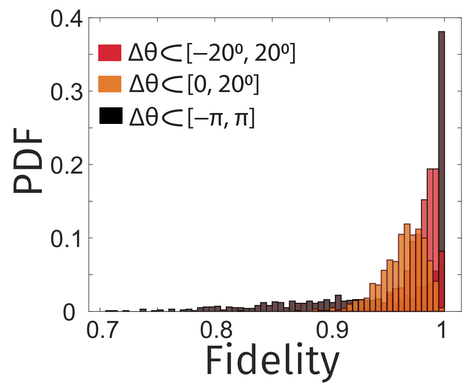



Figure 2. Optimization results for the Clements architecture circuit with different beamsplitter imbalance models. [7]

However, both architectures have strong requirements on the manufacturing quality of its comprising components - beam splitters - to be strongly 50:50 balanced. Even slight deviation in the splitting ratio leads to noticeable decreasing in the overall fidelity of the transformation [5].

We have numerically tested the performance of Clements interferometric circuit to different beamsplitter imperfections, which might occur in the experimental setting. The results are shown in Fig. 2. The numerical optimization algorithm couldn't fit the interferometer parameters to reproduce randomly sampled unitaries perfectly. Our results are in good agreement with those of [5], where similar tests were performed.

# The Unitary Composer

## Overview of the proposed design

Here we propose a novel multimode interferometer structure, consisting of multipath beamsplitters and phaseshifters, implementing universal unitary transformation.

Here we propose an optical circuit architecture which is extremely robust even to quite large fabrication errors.

The overall structure of the proposed unitary composer is:

$$U = P_{K+1} V^{(K)} P_K V^{(K-1)} \dots P_2 V^{(1)} P_1 \qquad (1)$$
$$P_k = \mathrm{diag}\left(e^{i\phi_{k1}}, e^{i\phi_{k2}}, \dots, e^{i\phi_{kN-1}}, 1\right)$$

where $V^{(K)}$ is a mode mixing element, for example Fourier mixing gate, $P_K$ is a phaseshifters.

We conducted a series of numerical experiments providing strong evidence for the universality of the proposed scheme (Fig. 4).

The procedure of the numerical tests was the following: large number (1000 samples) of random unitary matrices of particular dimension $N$ was sampled from a Haar uniform distribution - $U_S(N)$ - and the infidelity function $1-F(U_S,U)$:

$$F(U_s, U) = \frac{1}{N^2} \left| Tr(U^\dagger U_s) \right|^2 \qquad (2)$$

between sample matrix $U_s$ and our arbitrary composer U was minimized. Where scalar product defined as $\langle U|U_S\rangle = Tr(U^\dagger U_S)$.

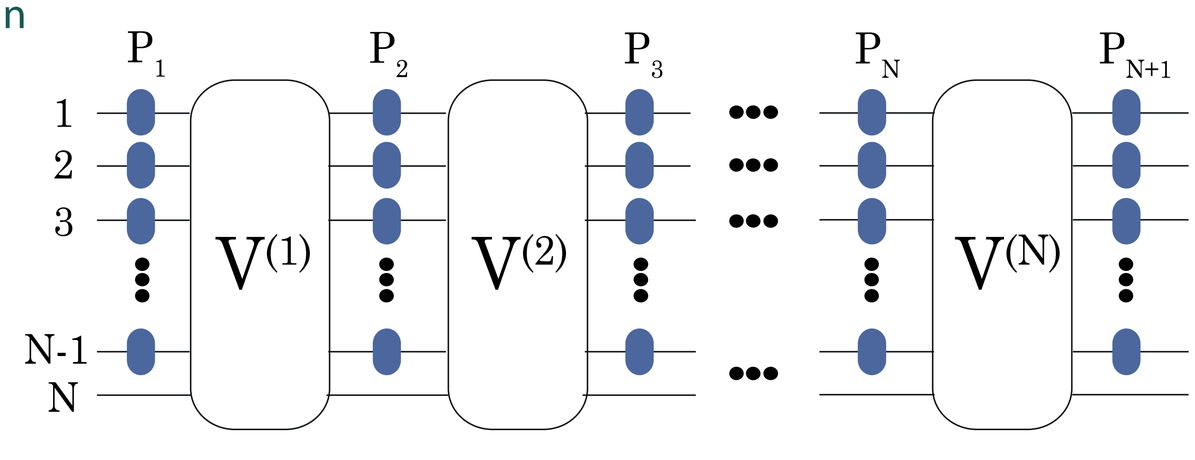



Figure 3. An overview of a general layout of a multimode unitary composer. N input modes are mixed N times in the consecutive mixing layers followed by layers of tunable phaseshifters (blue ovals). The relative phases are tuned to achieve the required unitary transformation.

Integrated photonic technologies provide all the necessary instruments to develop multiport beamsplitters which can be employed in the proposed unitary composer circuit [6]. For instance, one of the simplest possible mode mixing layer configuration that can be easily exploited in linear optics is a linear array of adjacent waveguides, which is schematically illustrated in Fig. 6 (a).

The numerical simulation testifies that from certain interaction length L ~ 0.62 mm average fidelity of the composer's operation reaches it's maximum possible value F = 1 with the computational accuracy $10^{-6}$. Calculations were performed for N = 5 equally coupled waveguides with coupling constant C = 0.5 $mm^{-1}$ (which is a value achievable in the experiment), each point is a mean fidelity over 40 sample random unitary matrices approximation.

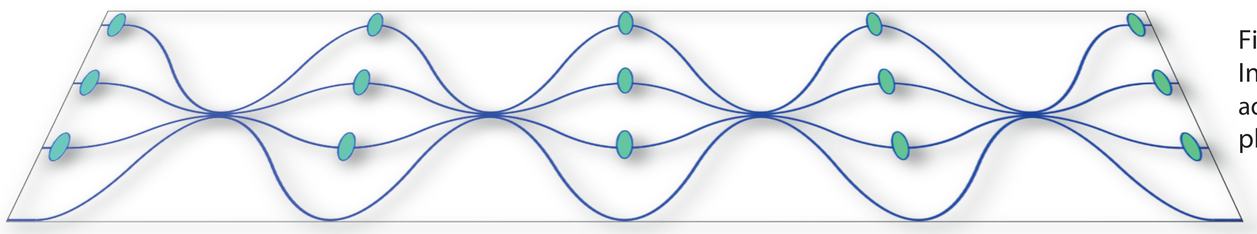


Figure 4. Optical chip structure for N = 4 input modes. Input modes are mixed N = 4 times in linear arrays of adjacent waveguides followed by layers of tunable phaseshifters (blue ovals).

# Results and discussion

## Numerical test of the composer performance

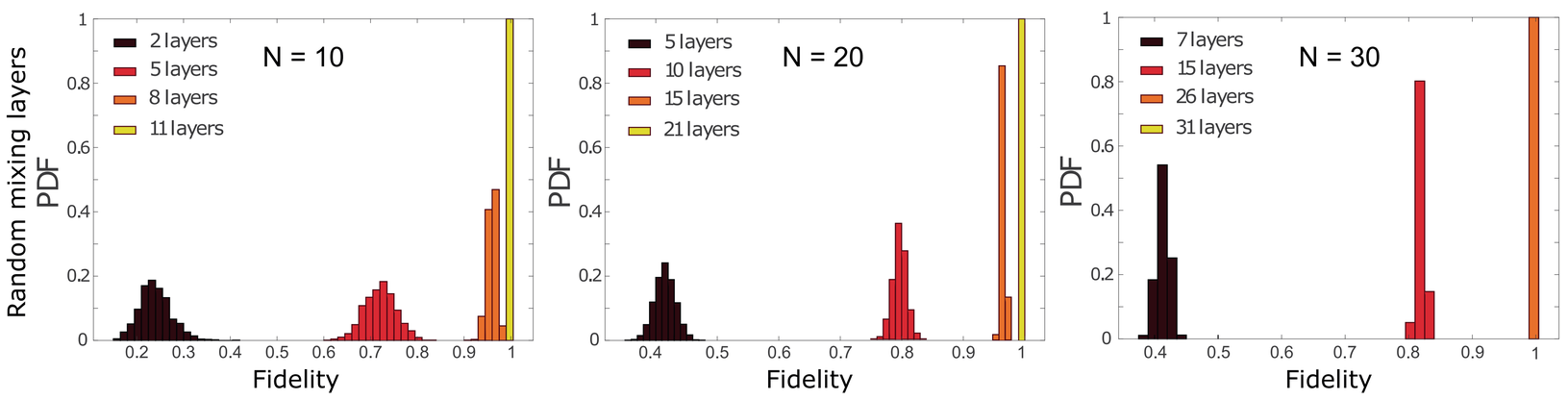



Figure 5. Numerical test of the composer performance

Results of the numerical experiments are presented on the Fig. 5. Each histogram represents the probability density function of optimizing a chosen random N×N unitary, drawn from a Haar uniform distribution, using a composer with a specified number of phase layers.

All tests include a numerical search of the optimal phase setting $P_l$ for 1000 random unitary samples. The result for the full configuration clearly shows that the proposed circuit (Fig. 3) may approximate any arbitrary unitary.

It turns out that the unitary composer constructed with completely *random mixing gates* demonstrates perfect performance. This result demonstrates superior robustness of the proposed composer architecture to any fabrication defects altering the mixing layer, as opposed to the previously reported implementations of Reck and Clements [5].

However, recent work [8] has claimed existence of some matrices which cannot be implemented via composer (1) in dimensions 3 and 4, unless one more pair of static mode-mixing layer and phaseshifting layer is added to the end of the scheme. We are currently investigating this case, and for dimensions of N > 4 we haven't found any deviations from universality of the proposed composer (1).

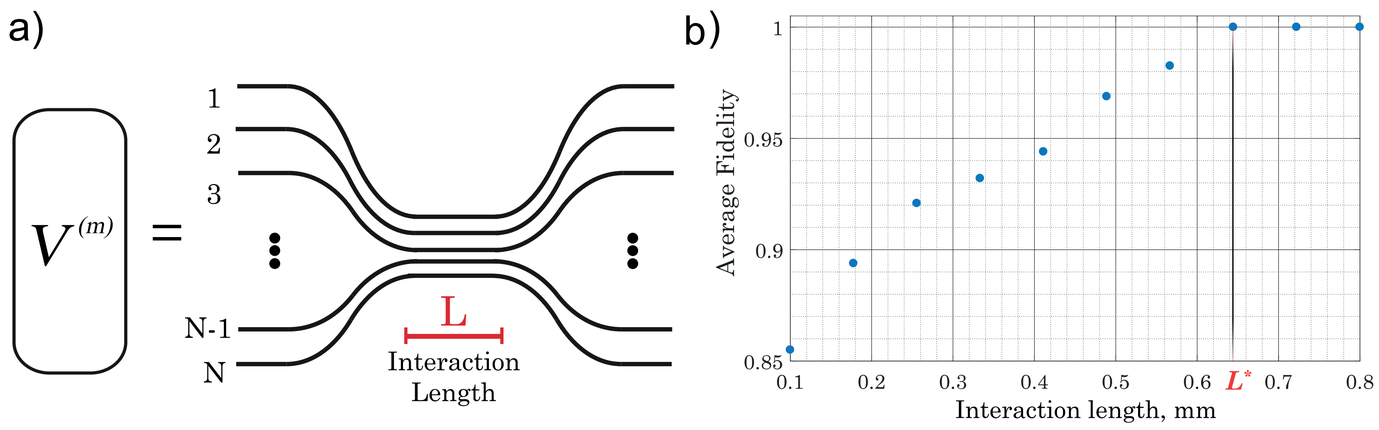



Figure 6 a) Schematic illustration of a linear array of adjacent waveguides used as a mode mixing layer in decomposition (1), b) Average fidelity dependence from the mode mixing interaction area length L.

We have proposed novel multimode interferometer design capable of realizing an arbitrary unitary operator.
The circuit in our architecture is composed of interchanging mode mixing layers, which may be almost arbitrary, and layers of variable phaseshifters, allowing to program the device to approximate any desired unitary transformation.

Our architecture finds a straightforward application in linear-optical computing, however its generality may allow it to be used in much wider context.

## References

1. D. Marpaung, J. Yao, J. Capmany, https:// arxiv.org/abs/1810.02585v1 (2018)
2. C. Sun, Y. Yu, G. Chen, and X. Zhang, Opt. Lett. **41**, 3257 (2016)
3. M. Reck et al., PRL **73**, 58 (1994)
4. W. R. Clements et al., Optica **3**, 1460 (2016)
5. R. Burgwal et al., Opt. Expr. **25**, 28236 (2017)
6. J. Wang et al., https://arxiv.org/abs/2005.01948 (2020)
7. M. Saygin et al., PRL **124**, 1 (2020)
8. L. Pereira et al., https://arxiv.org/abs/2002.01371 (2020)

Quantum Optical Technologies laboratory

Quantum Technologies Center

# Ultrafast Laser Plasma Doping(ULPD) enabled $Er^{3+}$ doped Silica-on-Silicon for Integrated Waveguide Amplifier Platforms

PARAMITA PAL, E. KUMI BARIMAH, BENJAMIN DAWSON and GIN JOSE
Applied Photon Science, School of Chemical and Process Engineering, University of Leeds, LS2 9JT, UK
Email: pmppa@leeds.ac.uk and g.jose@leeds.ac.uk

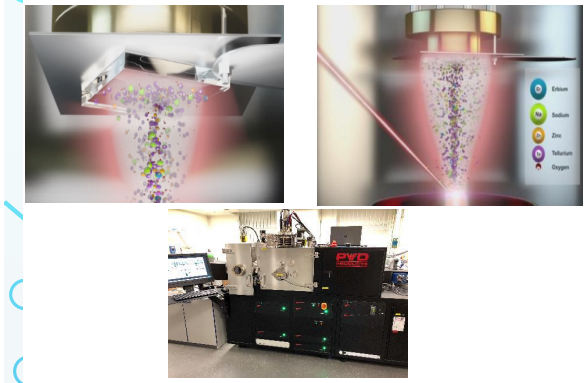
UNIVERSITY OF LEEDS

## WHAT IS ULPD?

➢The fabrication of doped or undoped planar waveguides on glass or silica on silicon using femtosecond laser induced plasma[1,2].

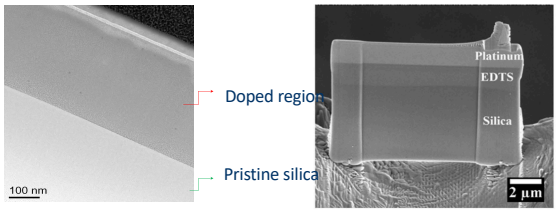
➢ULPD provides **high index contrast waveguide with higher doping concentrations[3,4].**

## THE DOPING PROCESS

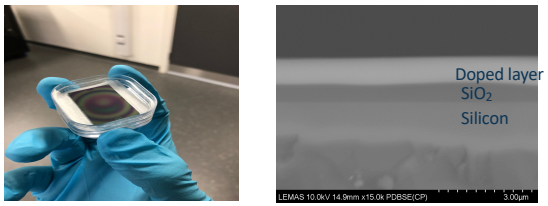


- **Substrate:** Silica on Silicon
- **Target (source of dopants):** $Er^{3+}$doped Zinc sodium tellurite glass (TZN)
- **Laser:** Amplified Ti-sapphire fs laser with high repetition rate (**10 kHz**) and pulse duration of 45 fs
- **Laser fluences used:** (S1= 0.44 J/cm$^2$, S2= 0.53 J/cm$^2$, S3= 0.66 J/cm$^2$).
- **Substrate temperature and duration:** 600° C for 4 hours.

## PREVIOUS WORK




➢ The TEM cross-sectional images of doped silica shows the depth profile[1].
➢ SEM images shows the erbium doped tellurite silica layer (EDTS) [2]which will act as planer optical waveguiding region[2].



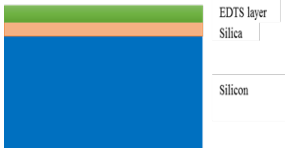

➢ Films with very lower surface roughness can be doped on silica-on silica-on silicon [3]. The cross-section is shown.

## REFERENCES

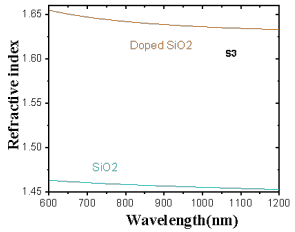
[1] G. Jose, et al: "Multi-ion diffusion in silica glass using femtosecond pulsed laser deposition," in Conference on Lasers and Electro-Optics 2012, OSA Technical Digest (online) (Optical Society of America, 2012), paper CM3L.6.
[2] S.A. Kamil, et al: Ultrafast laser plasma doping of Er3+ ions in silica-on-silicon for optical waveguiding applications, Optics Letters, Vol. 41, No. 20 October 15 (2016).
[3] J. Chandrappan, et al: Target dependent femtosecond laser plasma implantation dynamics in enabling silica for high density erbium doping, Sci. Rep. 5, 14037; doi: 10.1038/srep14037 (2015).
[4] J. Chandrappan et.al: Doping silica beyond limits with laser plasma for active photonic materials, **Opt.** Mater. Exp. 5 (2015) 2849-2861.

## PLANAR WAVEGUIDE ON SOS WITH ULPD

➢The $Er^{3+}$doped SOS fabricated in the present work can form the laser/amplifier region for Silicon PIC. The EDTS can patterned to form integrated waveguide laser or amplifier.

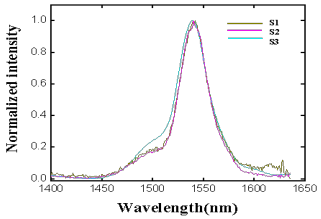



## REFRACTIVE INDEX AND THICKNESS




➢ The refractive index plot of the planar waveguide formed for sample S3.
➢The waveguide thicknesses obtained for different samples S1, S2 and S3 were 571nm, 480 nm and 1317 nm respectively.
➢The measured effective indexes of the guided modes of S3 were **TE0(1.6405), TE1 (1.6003) and TE2(1.5364)** respectively at 633 nm.

## PHOTOLUMINOSCENCE(PL) AND LIFETIME COMPARISON




| Sample ID | Laser fluences (J/cm$^2$) | FWHM(nm) | Lifetime (ms) |
|---|---|---|---|
| S1 | 0.44 | 36.53 | 13.38 |
| S2 | 0.53 | 33.38 | 13.40 |
| S3 | 0.66 | 33.05 | 10.52 |

Here the radiative transition of $Er^{3+}$ ions from $^4I_{13/2}$ -$^4I_{15/2}$ results in PL emission- peaked around **1540 nm.**

## CONCLUSIONS

High refractive index, high photoluminescence and lifetime properties are measured for planar slab waveguides with three guided modes at 633 nm for the EDTS waveguide with thickness 1.32µm. We have increased the rate of growth of the waveguides using a high repetition rate repetition rate (10 kHz) fs-laser comparing to those reported previously using 1 kHz fs-laser. Further work towards channel waveguide amplifier is in progress.

EPSRC SEAMATICS Seamless Integration of Materials for Photonics www.seamatics.org

# Aperiodic DM-FFF compared to the A-FMM: A Rigorous Method for the Modeling of Guided Optical Structures


**HABIB MOHAMAD[1], ALAIN MORAND[1] , SYLVAIN BLAIZE[2] and PIERRE BENECH[1]**

[1] IMEP-LAHC, Univ. Grenoble Alpes, CNRS, Grenoble INP, 38000 Grenoble , France

[2] L2n, 12 rue Marie Curie CS 42060 10004 Troyes Cedex , France

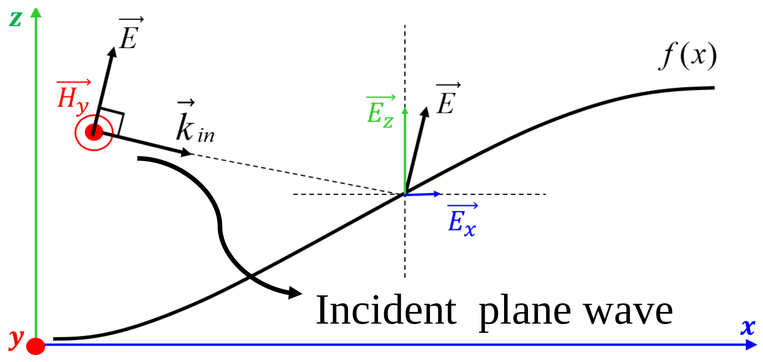
E-mail: habib.mohamad@grenoble-inp.fr

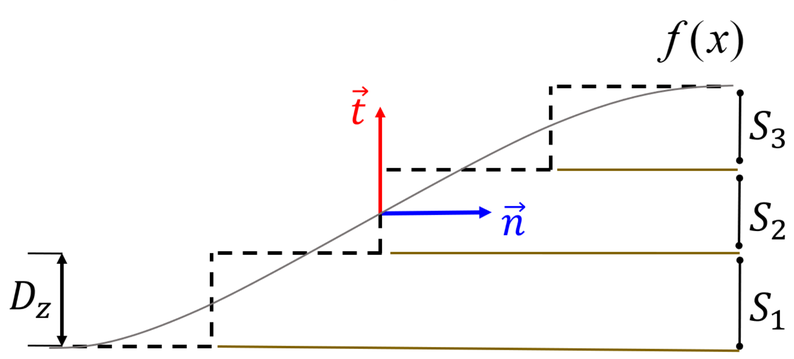

## Introduction:

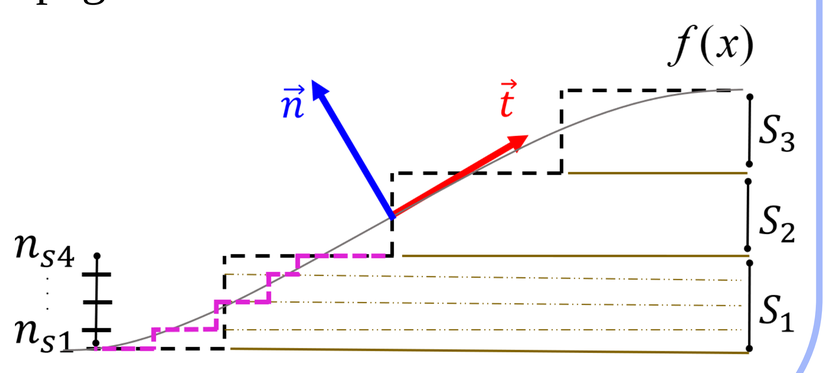
- DM associated with Fast Fourier Factorization (FFF) has demonstrated its effectiveness with the modeling of metallic periodic diffractive structures [1].
- A complex coordinate transformation acting as Perfectly Matched Layer (PML) has been used for the modelization of aperiodic structures with the RCWA [2].
- We will exploit the possibility of simulating aperiodic guided structures by associating the PML to the DM-FFF.

## I. Fast Fourier Factorization applied on diffractive structures [1]

- For TM polarization, the Electric Fields ( $\boldsymbol{E_x}$ and $\boldsymbol{E_z}$ ) at the boundary of arbitrary structure are never continuous.
- FFF takes into consideration the evolution of the profile $\boldsymbol{f(x)}$ by expressing $\boldsymbol{E_x}$ and $\boldsymbol{E_z}$ in terms of their tangential ( $\boldsymbol{E_t}$ ) and normal ($\boldsymbol{E_n}$ ) components. Li's rule is applied on $\boldsymbol{E_n}$ components.
- RCWA and DM-FFF are Fourier methods depending on N harmonics that discretize the structure with a constant step $D_z$.
- RCWA uses the Eigen-values and Eigen vectors algorithm.
- The DM-FFF is based on the Runge-Kutta numerical integration to perform the propagation.

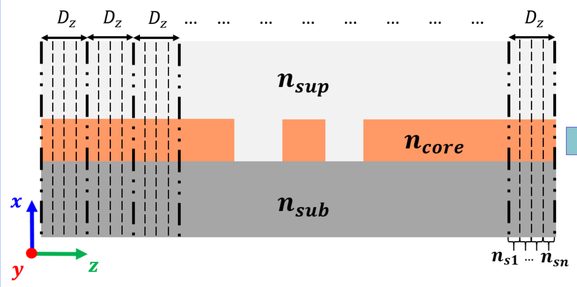


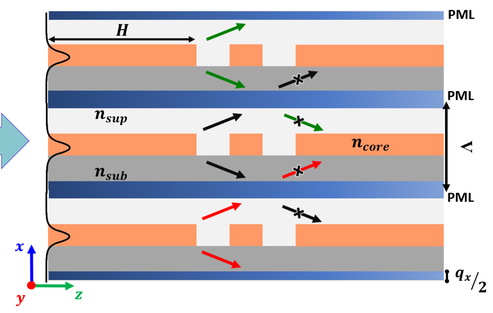




## II. DM-FFF and PML

### Goal



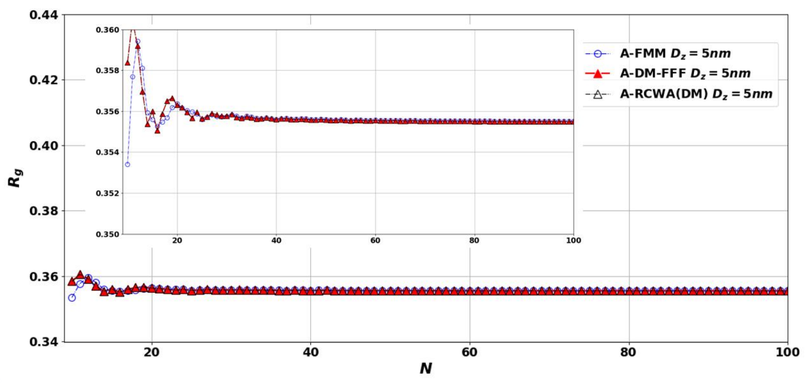

### Execution



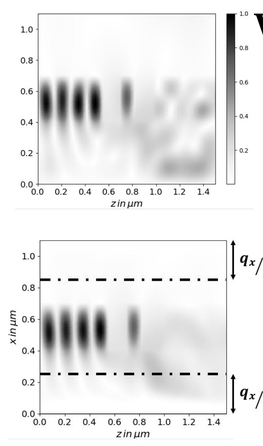

- Performing complex coordinate transformation type Hugonin-Lalanne to the propagation Equation.
- Polarized guided mode excitation (TE or TM).

## III. Validation by a Lamellar structure

- Reference structure studied by P. Lalanne using the A-FMM [2].
- Convergence Test of the reflection '$R_g$' following N.
- $|H_y|$ with and without PML.

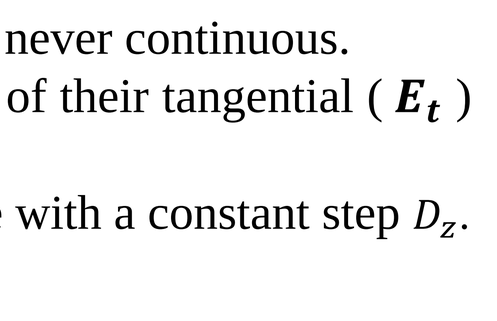



**A-DM-FFF**



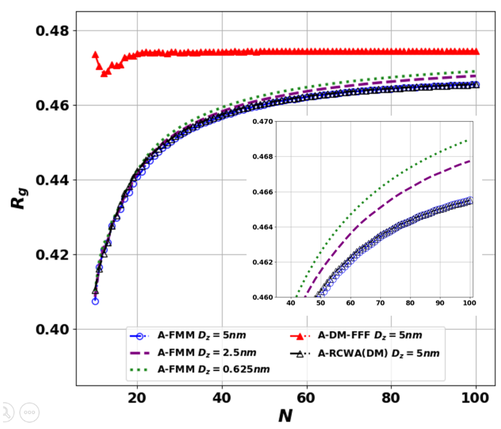

## IV. Curvilinear Structure[3]

- Cylindrical Pillar reflector of refractive index $n_d$.
- $\Lambda = 1.1\ \mu m$ , $q_x = 0.4875 \mu m$.
- Excitation with $TM_{01}$ mode @ $\lambda = 1.5\ \mu m$.

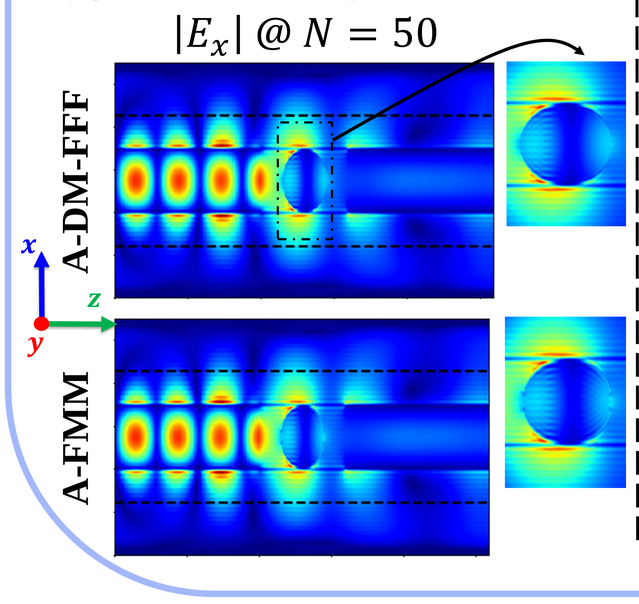



**High Contrast dielectric structure**

$n_{ext} = 1.0$ , $n_d = n_{core} = 3.5$

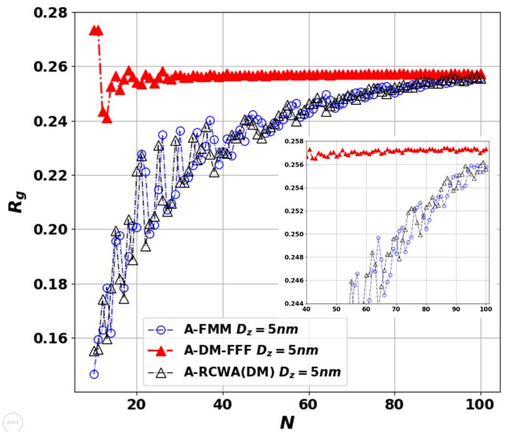



$|E_x|$ @ $N = 50$

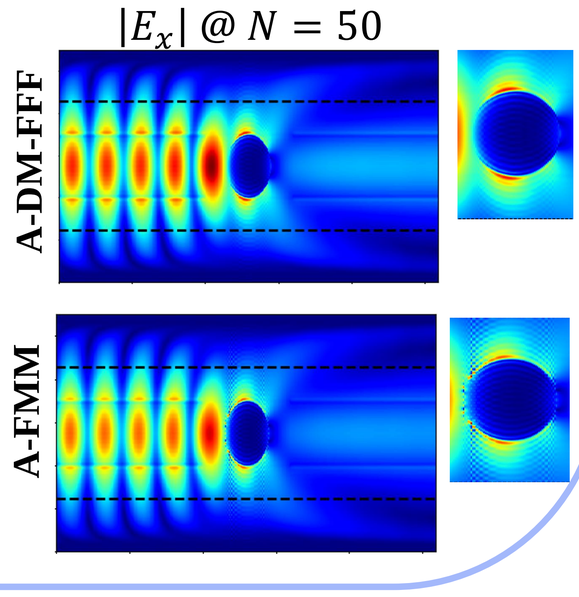



**Metallic Pillar Structure**

$n_{ext} = 2.9$ , $n_d = 1.0 + j7.0$ $n_{core} = 3.5$




$|E_x|$ @ $N = 50$





[1] E. Popov et al, JOSA A, vol. 17, no. 10,pp. 1773–1784, 2000.

[2] J. Hugonin et al, JOSA A, vol. 22, no. 9, pp.1844–1849, 2005.

[3] H. Mohamad et al, JOSA A, vol.37, no.6, pp. 1014-1024,2020.



L2n Lumière, Nanomatériaux, Nanotechnologies

AGENCE NATIONALE DE LA RECHERCHE ANR

ODISSEA Project ANR-16-CE39-0016-01

# Ultrafast Laser Plasma Doping(ULPD) enabled $Er^{3+}$ doped Silica-on-Silicon for Integrated Waveguide Amplifier Platforms

PARAMITA PAL, E. KUMI BARIMAH, BENJAMIN DAWSON and GIN JOSE
Applied Photon Science, School of Chemical and Process Engineering, University of Leeds, LS2 9JT, UK
Email: pmppa@leeds.ac.uk and g.jose@leeds.ac.uk

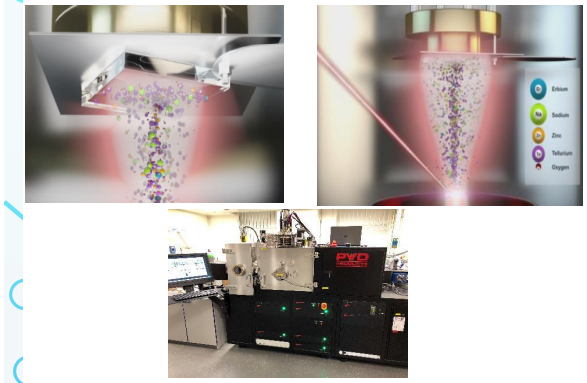
UNIVERSITY OF LEEDS

## WHAT IS ULPD?

➢The fabrication of doped or undoped planar waveguides on glass or silica on silicon using femtosecond laser induced plasma[1,2].

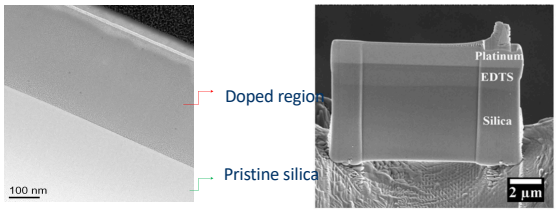
➢ULPD provides **high index contrast waveguide with higher doping concentrations[3,4].**

## THE DOPING PROCESS

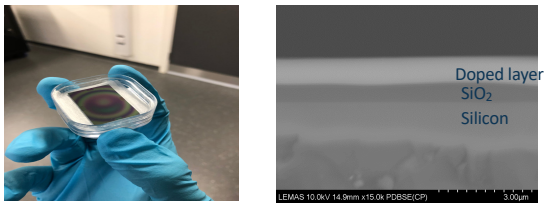


- **Substrate:** Silica on Silicon
- **Target (source of dopants):** $Er^{3+}$doped Zinc sodium tellurite glass (TZN)
- **Laser:** Amplified Ti-sapphire fs laser with high repetition rate (**10 kHz**) and pulse duration of 45 fs
- **Laser fluences used:** (S1= 0.44 J/cm$^2$, S2= 0.53 J/cm$^2$, S3= 0.66 J/cm$^2$).
- **Substrate temperature and duration:** 600° C for 4 hours.

## PREVIOUS WORK




➢ The TEM cross-sectional images of doped silica shows the depth profile[1].
➢ SEM images shows the erbium doped tellurite silica layer (EDTS) [2]which will act as planer optical waveguiding region[2].



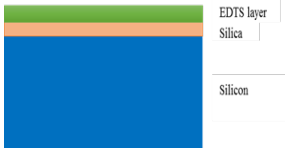

➢ Films with very lower surface roughness can be doped on silica-on silica-on silicon [3]. The cross-section is shown.

## REFERENCES

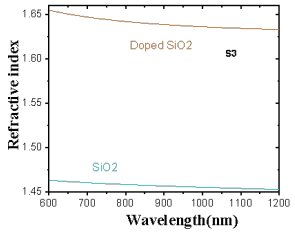
[1] G. Jose, et al: "Multi-ion diffusion in silica glass using femtosecond pulsed laser deposition," in Conference on Lasers and Electro-Optics 2012, OSA Technical Digest (online) (Optical Society of America, 2012), paper CM3L.6.
[2] S.A. Kamil, et al: Ultrafast laser plasma doping of Er3+ ions in silica-on-silicon for optical waveguiding applications, Optics Letters, Vol. 41, No. 20 October 15 (2016).
[3] J. Chandrappan, et al: Target dependent femtosecond laser plasma implantation dynamics in enabling silica for high density erbium doping, Sci. Rep. 5, 14037; doi: 10.1038/srep14037 (2015).
[4] J. Chandrappan et.al: Doping silica beyond limits with laser plasma for active photonic materials, **Opt.** Mater. Exp. 5 (2015) 2849-2861.

## PLANAR WAVEGUIDE ON SOS WITH ULPD

➢The $Er^{3+}$doped SOS fabricated in the present work can form the laser/amplifier region for Silicon PIC. The EDTS can patterned to form integrated waveguide laser or amplifier.

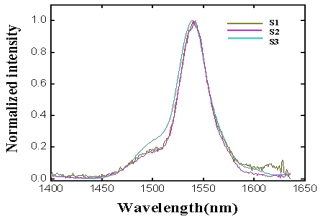



## REFRACTIVE INDEX AND THICKNESS




➢ The refractive index plot of the planar waveguide formed for sample S3.
➢The waveguide thicknesses obtained for different samples S1, S2 and S3 were 571nm, 480 nm and 1317 nm respectively.
➢The measured effective indexes of the guided modes of S3 were **TE0(1.6405), TE1 (1.6003) and TE2(1.5364)** respectively at 633 nm.

## PHOTOLUMINOSCENCE(PL) AND LIFETIME COMPARISON




| Sample ID | Laser fluences (J/cm$^2$) | FWHM(nm) | Lifetime (ms) |
|---|---|---|---|
| S1 | 0.44 | 36.53 | 13.38 |
| S2 | 0.53 | 33.38 | 13.40 |
| S3 | 0.66 | 33.05 | 10.52 |

Here the radiative transition of $Er^{3+}$ ions from $^4I_{13/2}$ -$^4I_{15/2}$ results in PL emission- peaked around **1540 nm.**

## CONCLUSIONS

High refractive index, high photoluminescence and lifetime properties are measured for planar slab waveguides with three guided modes at 633 nm for the EDTS waveguide with thickness 1.32µm. We have increased the rate of growth of the waveguides using a high repetition rate repetition rate (10 kHz) fs-laser comparing to those reported previously using 1 kHz fs-laser. Further work towards channel waveguide amplifier is in progress.

EPSRC SEAMATICS Seamless Integration of Materials for Photonics www.seamatics.org

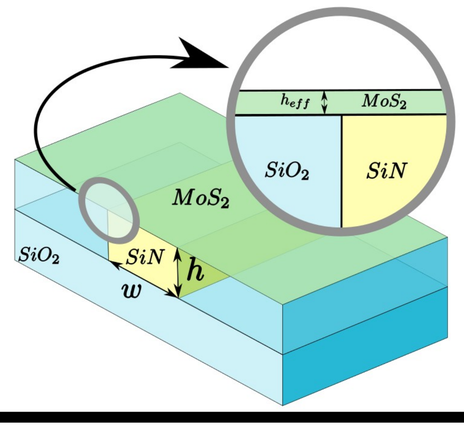
# Kerr effect enhancement through hybrid integration of 2D materials on the silicon platform

Vincent Pelgrin[1,2], Yuchen Wang[2], Carlos Ramos[1], Laurent Vivien[1], Zhipei Sun[2], Eric Cassan[1]

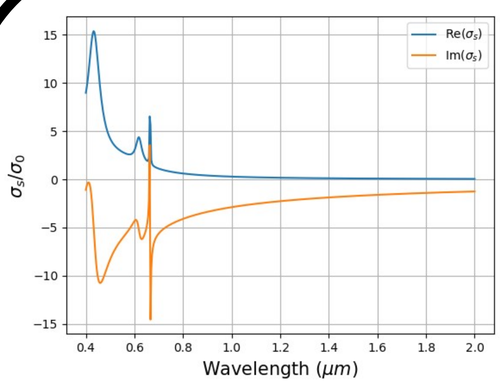
[1] Centre for Nanoscience and Nanotechnology, CNRS, Univ. Paris-Sud, Univ. Paris-Saclay, C2N – Palaiseau, France .
[2] Department of Electronics and Nanoengineering, Aalto University, P.O. Box 13500, FI-00076 Aalto, Finland
e-mail: vincent.pelgrin@universite-paris-saclay.fr

## Context

- Third order nonlinear optics on the Silicon platform offers a wide array of promising application (supercontinuum, frequency comb generation,...)
- The silicon platform lacks of good options for nonlinear optics around 1,5 µm due to the rather weak SiN performances and the TPA in Si.
- 2D materials such as Transition Metal Dichalcogenide for nonlinear optics may offer a solution since high nonlinearities have been rapported
- We propose here a new approach for designing highly nonlinear waveguides using hybrid integration as a mean of improvement



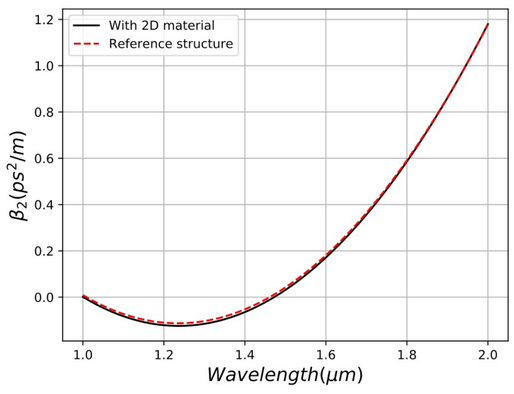

## Modelling a 2D material




$$\epsilon_r = \frac{\epsilon(\omega)}{\epsilon_0} = 1 + \sum_{k=1}^{N} \frac{f_k}{\omega_k^2 - \omega^2 - i\omega\gamma_k}$$

$$\epsilon(\omega) = \epsilon_0\left(1 + \frac{i\sigma_b}{\epsilon_0\omega}\right) = \epsilon_0\left(1 + \frac{i\sigma_s}{\epsilon_0\omega h_{eff}}\right)$$

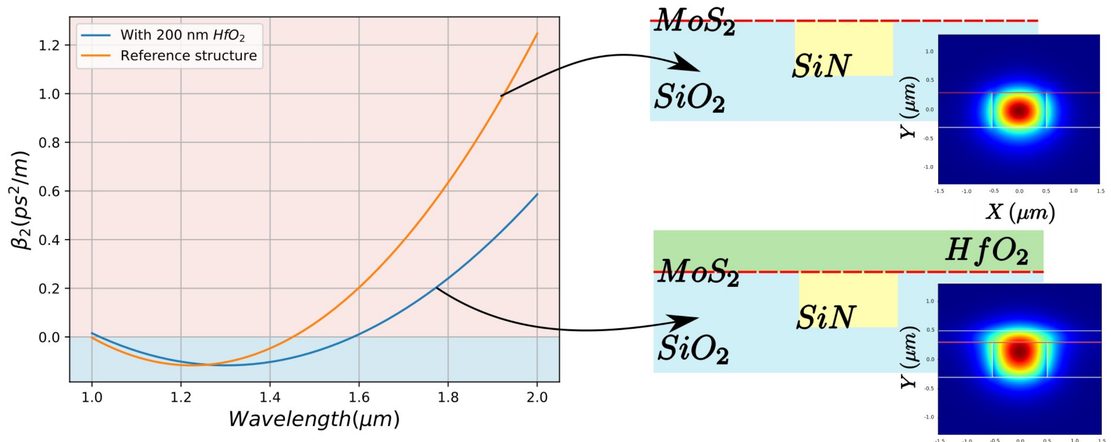
- We use FDE simulations (Finite Difference Eigenmodes).
- 2D materials are modelized thanks to their surface conductivity $\sigma_s$.
- The surface conductivity $\sigma_s$ can be expressed using the permittivity of the material (sum of N lorentzian).
- No difference has been noted in the group velocity profile after addition of the 2D layer of $MoS_2$




## Structure improvements

Multiple parameters of the waveguide can be improved using ALD deposited oxydes ($Al_2O_3$, $HfO_2$, ...) after deposition of the 2D material.

- The GVD profile can be improved usind high index oxydes on top of the 2D material.
- This oxyde layer provides protection for the 2D material.
- It has other beneficial effects like shifting the transverse mode more towards the 2D material (see bottom panels).




## Effective nonlinearity

$$\gamma = \frac{3\omega\Gamma}{4\epsilon_0 A_0 v_g^2}$$

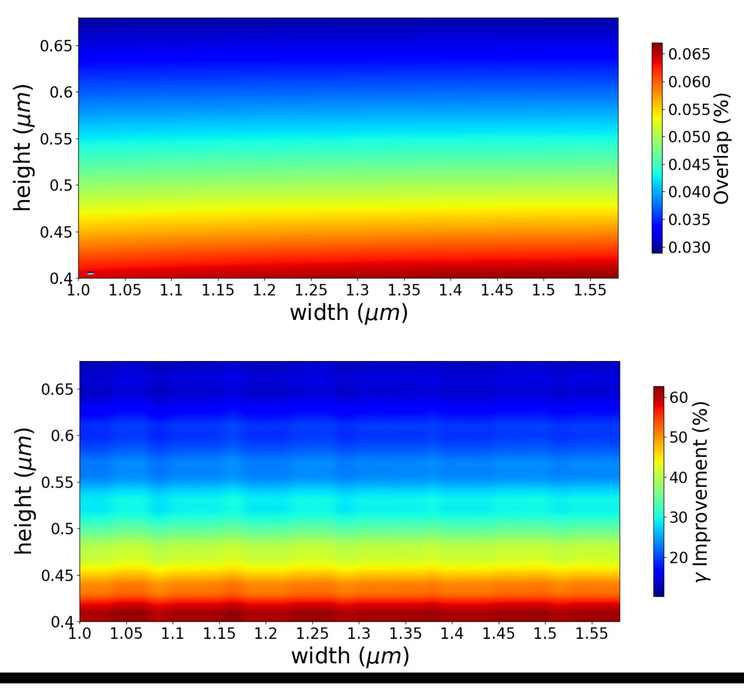
**Overlap:**

$$S = E \times H$$

$$\langle P \rangle = \left\langle \iint S.u_z\, ds \right\rangle$$

$$Overlap = \frac{\langle P \rangle_{2D}}{\langle P \rangle_{tot}}$$

- With the effective susceptibility Γ (which takes into account the nonlinearities of each component of the waveguide) we derive the effective nonlinear coefficient γ
- Direct link between the overlap and the improvement factor attributed to the 2D material.

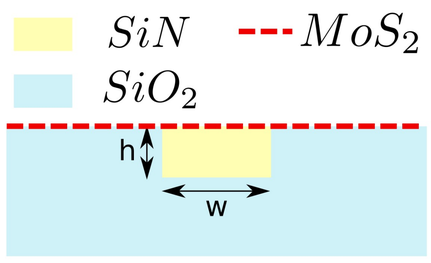


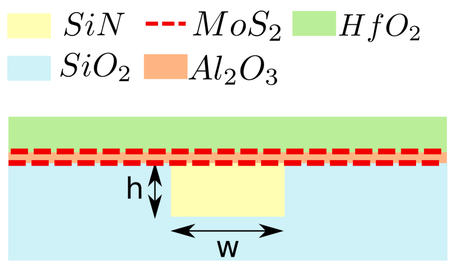

Results from the simulation of SiN burried strips on $SiO_2$ compared with the same waveguides covered with a monolayer of $MoS_2$ ►

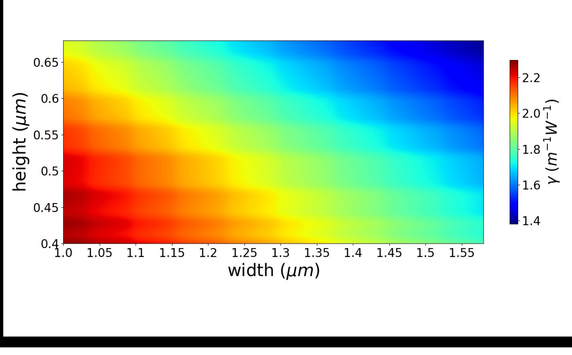
## Optimized structure

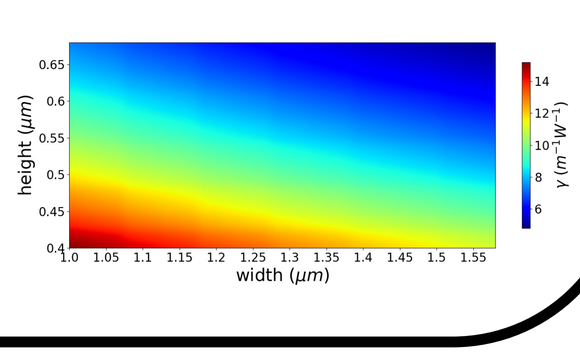
Optimization of the structure using the gathered information.

- Addition of an oxyde layer for GVD profile improvement and overlap increase (the shift of the mode toward the oxyde makes the overlap more important)
- Use of multiple single layers for maximizing this overlap.




## Conclusion

- Adding 2D materials to existing stucture can in itself improve the performances (up to 60 % improvement for a planarized burried with added $MoS_2$ on top).
- The use of other process such as ALD deposition of oxydes allows us to improve further the designs (better GVD profile, protective layer on top of the 2D material, deposition of multiple single layers, shifting of the transverse mode)
- Achieving a structure using all those tools can bring huge improvements (up to 500 % with an optimized 2 layer structure).
- From a practical point of view, we will need to study further the introduction of propagation losses which will require experimental data (work in progress)

# MMI plus Simplified Coherent Coupling to design a small footprint SOI power splitter

Roberto Peyton[1,2,*], Damian Presti[1,2], Fabian Videla[1] and Gustavo A Torchia[1,2,**]

[1]Photonics Integrated Group, Centro de Investigaciones Ópticas (CONICET-CICBA-UNLP), Camino Centenario y 506 s/n. M.B. Gonnet (1897), Buenos Aires, Argentina.

[2]Depto. de Ciencia y Tecnología, Universidad Nacional de Quilmes, Rodriguez Peña 352, Bernal (1876), Argentina.

[*]**robertop@ciop.unlp.edu.ar**; [**]**gustavot@ciop.unlp.edu.ar**

## 1. Introduction

Nowadays, silicon photonic technology has a relevant importance in optical communications systems mainly due to some fabrication and functionality advantages, these are:small footprint devices, CMOS process compatibility and high integration level. In particular in this contribution we focus on silicon-on-insulator (SOI) which is the most popular platform within silicon photonics [1]. The high refractive index contrast between silicon and silica layers makes possible submicron waveguides and tight bends, also state-of-the-art electronics industry foundry processes can be performed for optical goals [2]. However, unlike electronic circuits where electrical routing can be accomplished flexibly, optical routing is limited either for optical conditions or technological limitation. In this contribution we present a new approach to fabricate under SOI platform very small footprint power splitter. The design strategy is based on the well-known simplified coherent coupling combining to a multimode interferometer (MMI) structure [3, 4]. Along this paper, the sensibility of design parameters are analyzed and discussed. By this new approach which includes a MMI to spatially split the optical modes, can be constructed a very compact device. This opens a new avenue to improve and enhance the performance of integrated devices developed under SOI scheme and with high integration.

## 2. Splitter design model

The designed power splitter device consists of a 340-nm-thick crystalline silicon core on top of a buried oxide layer with a thickness of 2 $\mu$m on a silicon substrate and a silicon dioxide deposition of 1 $\mu$m as final cladding. Standard single mode strip waveguide width for $\lambda_0$=1.55 nm is 450 nm. In order to validate the optical design we have conducted computational simulations. These simulations were performed by using varFDTD and Bidirectional Eigenmode Expansion Propagation.

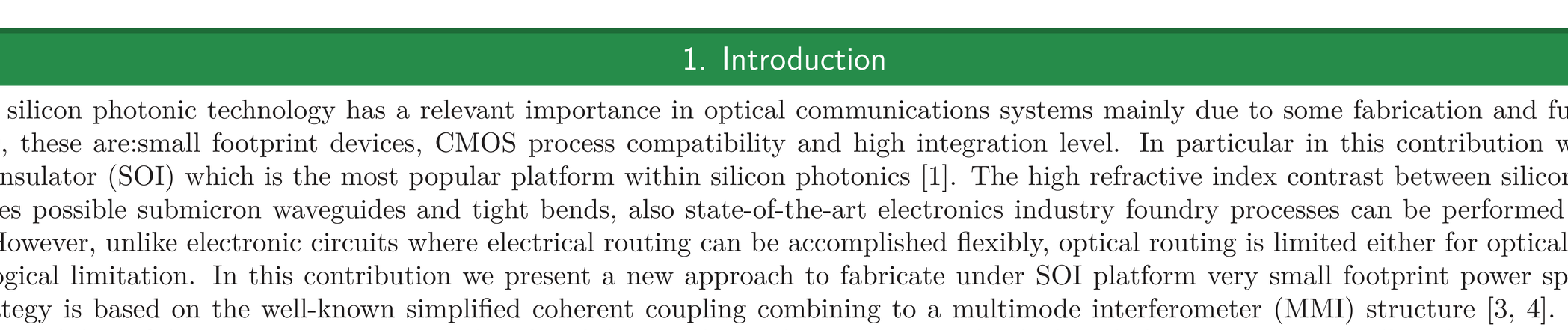



**Figure 1**: Splitter design. **(a)** Tuning the MMI parameters. **(b)** Schematic of the proposed power slitter. The mode TE is coupled to the designed power splitter. **(c)** Transmission sensitivity in a coherent coupling period with respect to the angle $\theta$. **(d)** Transmission in the coherent coupling zone by sweeping the length $L_1$, with $L_2 = L_1$ and $\theta = 10^o$.

## 3. Results

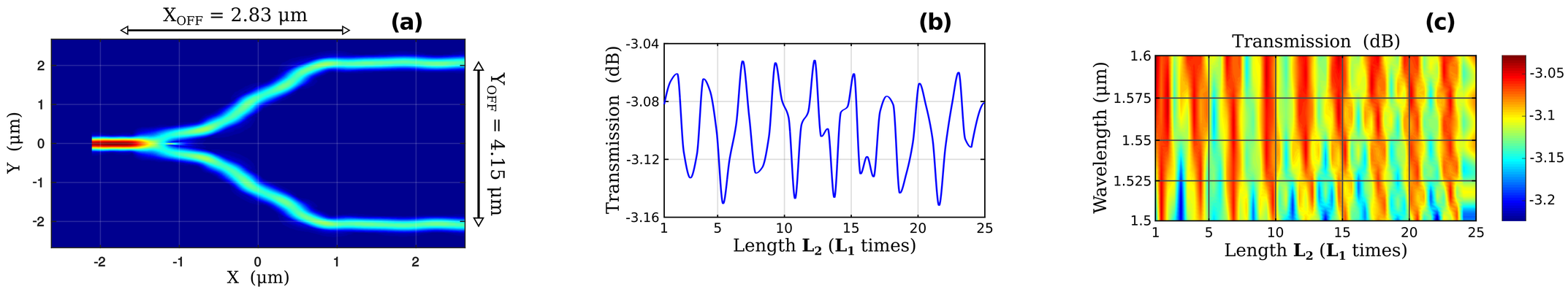



**Figure 2**: **(a)** Power map of an optimized power splitter. Transmission on a branch by sweeping the free parameter $L_2$ between 1 and 25 of $L_1$ times; **(b)** total power transmission, and **(c)** power map with respect to wavelength.

## 4. Conclusions

In summary, we have proposed and demonstrated an ultra-compact, nicely adaptable and highly efficient Y-branch power splitter on silicon-on-insulator. We combine two techniques for that, the simplified coherent coupling and the multimode interference structure to bent and split the light, respectively. The design parameters were optimized to reduce the footprint and maximize the transmission. All the results were conducted by using three steps of computational simulation, according to the consuming time: EME, varFDTD and full 3D-FDTD. Besides, a free design parameter to be adjusted according to the application is provided. We have achieved a transmitted power between -3.05dB and -3.15dB, depending on the free design parameter $L_2$. Finally, our design proved to be almost 9 times smaller than one other commonly used device with similar performance.

## Acknowledgments

This work was partially supported by the Agencia Nacional de Promoción Científica y Tecnológica (Argentina) under the projects PICT-2016-4086 and PICT 2017-0017; and by Universidad Nacional de Quilmes (Argentina) under project PPROF-2019.

## References

[1] Lionel C Kimerling. Silicon photonics and interconnects: Roadmap for implementation. In *2012 Optical Interconnects Conference*, pages 24–24. IEEE, 2012.

[2] Yi Zhang and et. al. A compact and low loss y-junction for submicron silicon waveguide. *Optics express*, 21(1):1310–1316, 2013.

[3] Henry F Taylor. Power loss at directional change in dielectric waveguides. *Applied optics*, 13(3):642–647, 1974.

[4] LM Johnson and FJ Leonberger. Low-loss linbo3 waveguide bends with coherent coupling. *Optics letters*, 8(2):111–113, 1983.

EUROPEAN CONFERENCE ON INTEGRATED OPTICS

# Polarization splitters based on form birefringence for micron-scale silicon photonics

Dura Shahwar, Matteo Cherchi, Mikko Harjanne, Timo Aalto
VTT Technical Research Centre of Finland

## Introduction

The polarization handling has significant benefits for photonic integrated systems targeting coherent receivers, polarization multiplexed transmission systems, and sensing applications. For polarization handling, on-chip polarization management which includes polarization splitters and rotators is important. Indeed, VTT silicon photonics platform has low polarization dependency, which is an advantage when both polarization should be handled the same way. The polarization splitters along with rotators can be used to develop on-chip polarization manipulation devices including all-silicon optical isolators and circulators. In this work we investigated how to achieve on-chip polarization splitters based on interferometer design, utilizing the tunable birefringence of our waveguides.

## Mach-Zehnder Interferometric (MZI) polarization splitters

In the polarization splitter based on interferometric design shown in Fig.1, polarization-dependent phase shifts are achieved by introducing birefringence in the waveguide arms of a MZI, by varying the waveguide dimensions, which in practice means width variations. An analytical model is developed for these MZI based polarization splitters, which takes in account waveguide width variation and physical path length change.

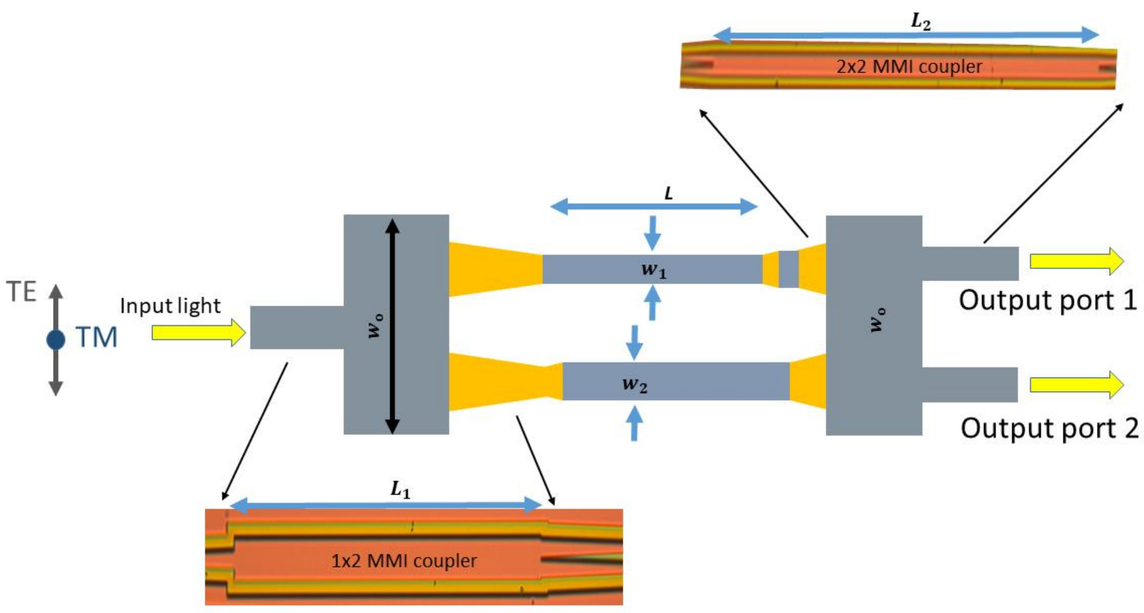



*Figure 1. Schematic and microscopic pictures of polarization splitter based on Mach-Zehnder interferometer design.*

The length and the width of the 1×2 MMI is $L_1$ and $w_o$, respectively, the width of the upper arm waveguide is $w_1$ whereas the width of lower arm waveguide is $w_2$. The length of the 2×2 MMI is $L_2$ and width is $w_o$. L presents the length of birefringent section.

## Simulation results for an ideal polarization splitter

Simulation results for ideal device are presented in Fig.2. Extinction ratio (ER) >20 dB is achieved for both polarizations in the wavelength range 1511-1551 nm, and ER >40 dB is observed around 1540 nm wavelength.

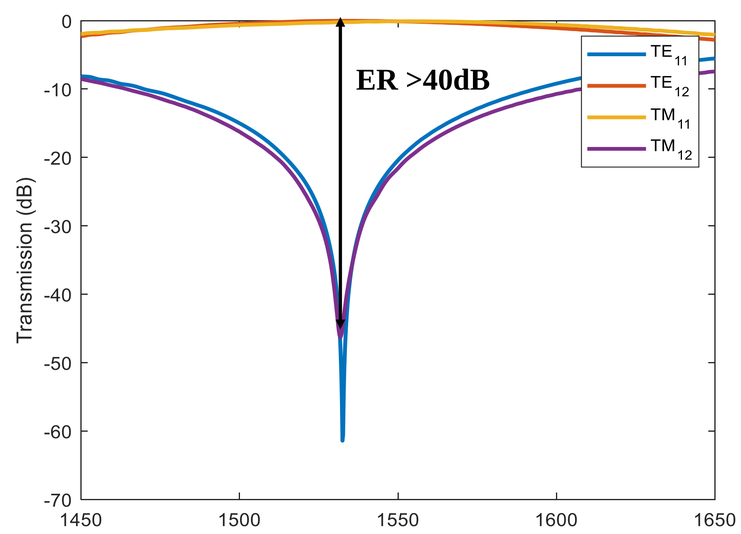



*Figure 2. Simulation of ideal polarization splitter. $w_1 = 1.58\ \mu m$, $w_2 = 2.5\ \mu m$, $L_1 = 236.5\ \mu m$, $L_2$ = 793.6 µm, $w_o$ = 13.5 µm, and $L$ = 216 µm is used for simulation.*

## Experimental results

Measurement results from passive wafer are presented in Fig.3 with solid lines. Dotted lines show the simulation results which are in good agreement with measurement. The measured insertion losses are less than 1 dB. When input light is TE-polarized, ER >20 dB is achieved in the wavelength range of 1550 - 1580 nm, and >14 dB ER is observed on 40 nm bandwidth. In case of TM-polarized light, ER is approximately 14 dB in the wavelength range of 1475 - 1515 nm.

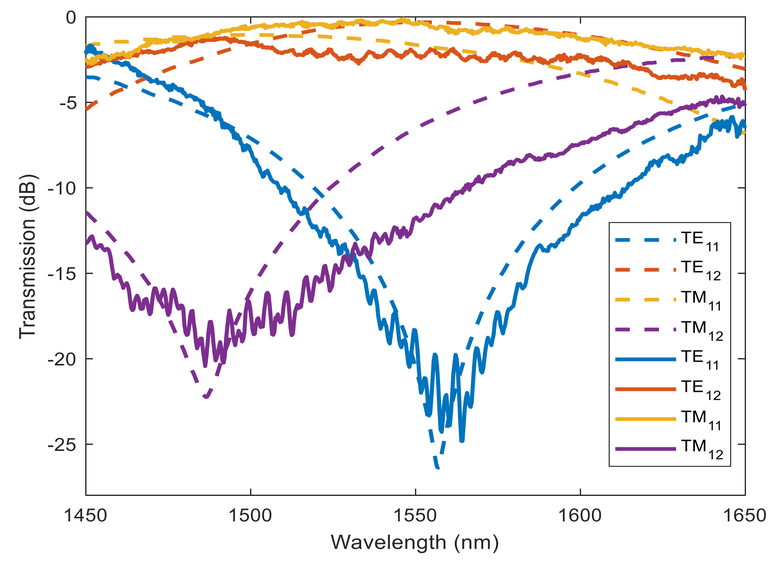



*Figure 3. Analytical model results compared with measurement results.*

## Conclusion and future outlook

Up to 14 dB ER has been achieved for both polarizations on a bandwidth of 40 nm. The device can be optimized with active tuning and we can expect upto 20 dB ER on same wavelength range.

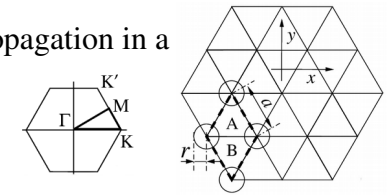


**Contact**
**Dura Shahwar,**
Tel. +358 405008152,
dura.shahwar@vtt.fi

# Valley-polarized beam propagation in metallic photonic graphene

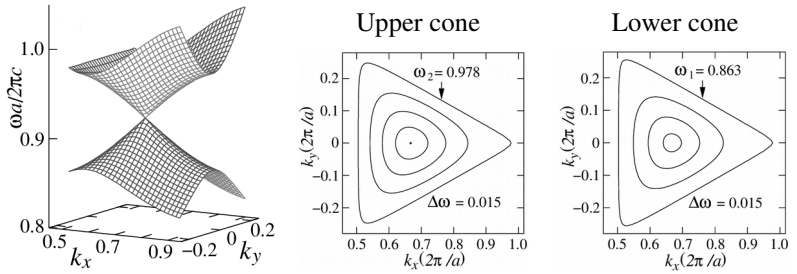
Kang Wang
Universite Paris-Saclay, CNRS, Laboratoire de Physique des Solides, 91405, Orsay, France
kang.wang@universite-paris-saclay.fr

– Electromagnetic wave propagation in a triangular metallic photonic graphene structure



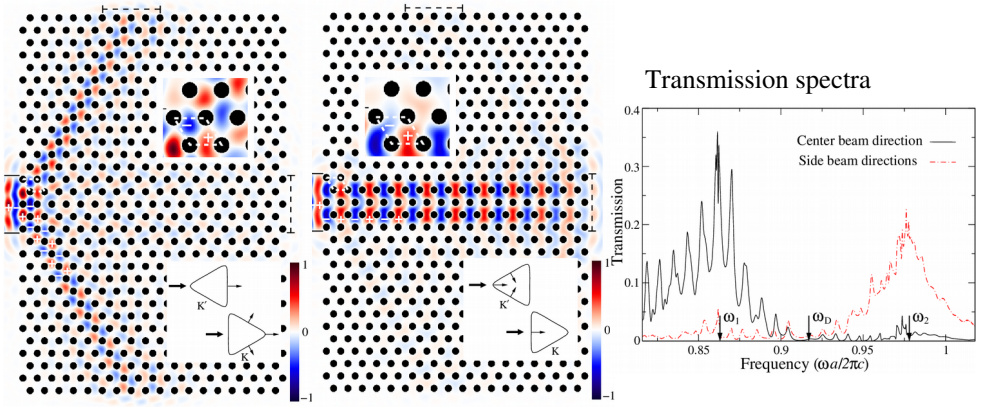

– Transport properties from the armchair edge, associated to trigonally warped Dirac cones, display drastically different behaviors as compared to the results obtained for analogous systems

– Dirac cone at K (4π/3a, 0) and its isofrequency contours (FDTD solutions)




– The incident beam associated to the upper Direc cone is split into two beams with a 2π/3 angle

– The incident beam associated to the lower Dirac cone is collimated to one center beam

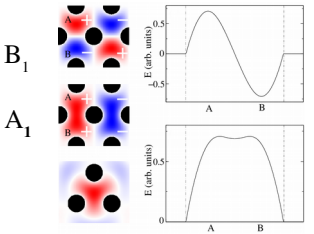



– The other expected propagating beams (the center and side beams associated to the upper and lower cones, resp.) are all strongly inhibited

– Symmetry of the wave function along Γ-K (tight binding model)

$$|\Psi_{\mathbf{k}}(\mathbf{r})\rangle = \sum_m \frac{e^{i\mathbf{k}\mathbf{R}_m}}{\sqrt{2N}}[|\phi_A(\mathbf{r}-\mathbf{R}_m-\mathbf{d}_A)\rangle \pm |\phi_B(\mathbf{r}-\mathbf{R}_m-\mathbf{d}_B)\rangle]$$

– Mirror or mirror inversion symmetry with respect to Γ-K line and $z$ axis




$A_1$ and $B_1$ representations of the $C_{2V}$ group, associated to the lower and the upper cone

– The incident beam is characterized by a mirror symmetry plane defined by the Γ-K line and the z axis

– Coupling with an $A_1$ beam, not with a $B_1$ beam

– Excitation of the center $A_1$ beam, inhibition of the central $B_1$ beam

– Strong inhibition of the side $A_1$ beams due to the destructive coupling along the π/3 direction (see inset)

– Better beam self-collimation associated to the lower Dirac cone

– Large angle beam splitting associated to the upper cone at one Dirac point, allowing addressing directly and separately each valley

Applications in valley photonics
– high efficiency beam collimators to convey information associated to both valleys
– large angle splitters for the beam carrying information associated to a single specific valley

# Microwave model for optimizing electro-optical modulation response of the Mach-Zehnder modulator

Arezou Meighan*, W. Yao, M. Wale, and K.A. Williams

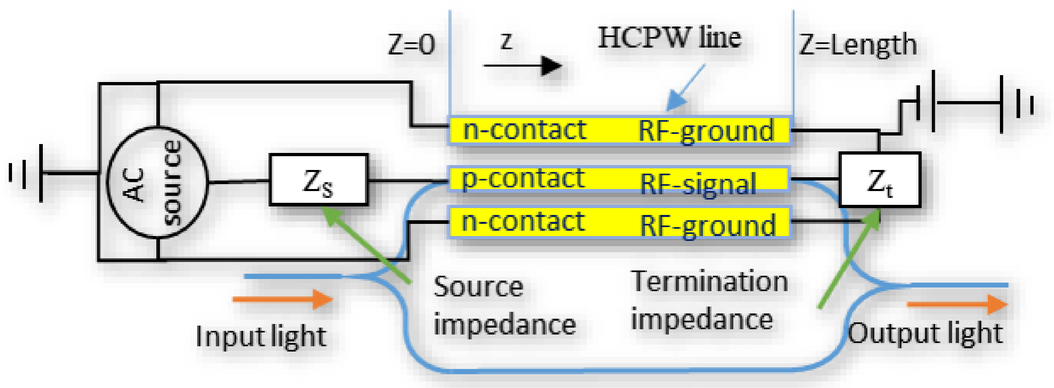
Institute of Photonic Integration, Eindhoven University of Technology, P.O. Box 513, 5600 MB, the Netherlands

*E-mail: a.meighan@tue.nl

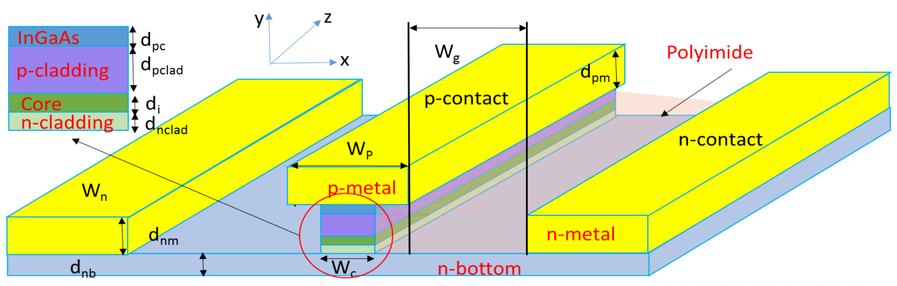
## Introduction

**Non-iterative electro-optical combined model of the MZM to calculate:**

- The frequency-dependent characteristic impedance
- The frequency-dependent propagation constant
- Electro optical frequency response
- The role of impedance matching




## Combined Model




Elevated view cross-section of the reference HCPW-MZM

CST Microwave Studio is used to calculate:

- Frequency-dependent electrical complex Propagation constant ($\gamma_m$)
- Characteristic impedance of the MZM ($Z_m$)

small-signal normalized modulation index:

$$M(\omega) = \left|\frac{\Delta\phi(\omega)}{\Delta\phi(0)}\right| = \frac{R_t + R_s}{R_t}\left|\frac{Z_{in}}{Z_{in}+Z_s}\right|\left|\frac{(Z_t+Z_m)F(u_+)+(Z_t-Z_m)F(u_-)}{(Z_t+Z_m)e^{\gamma_m L}-(Z_t-Z_m)e^{-\gamma_m L}}\right|$$

Where:

$$F(u)=\frac{1-exp(u)}{u}, \gamma_m = \alpha_m + j\frac{\omega n_m}{c_0}, u_\pm(\omega) = \pm\alpha_m L + j\frac{\omega}{c_0}(\pm n_m - n_0)L \quad (3)$$

$$Z_{in} = Z_0\frac{Z_t + Z_m tanh(\gamma_m L)}{Z_m + Z_t tanh(\gamma_m L)}$$

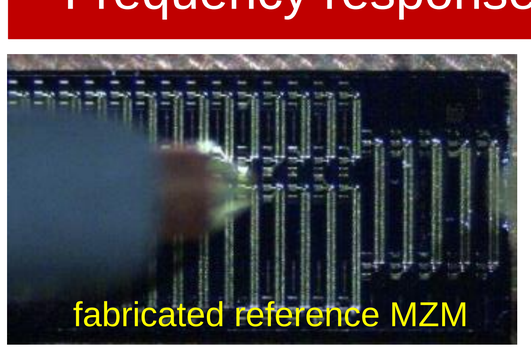
- $\Delta\phi(\omega)$: Frequency dependent cumulative phase modulation over the interaction length L
- $Z_s$: Source impedance with the real part of $R_s$
- $Z_t$: Termination impedance with the real part of $R_t$
- no: Optical refractive index
- $c_0$: Speed of light in vacuum
- $\omega$: Angular frequency

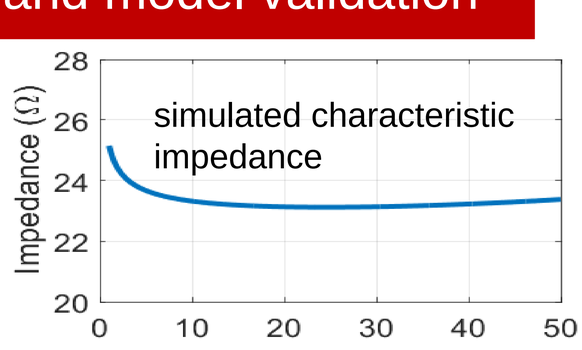
*G. Ghione: Semiconductor devices for high-speed optoelectronics, Cambridge University Press, 382-386 2009

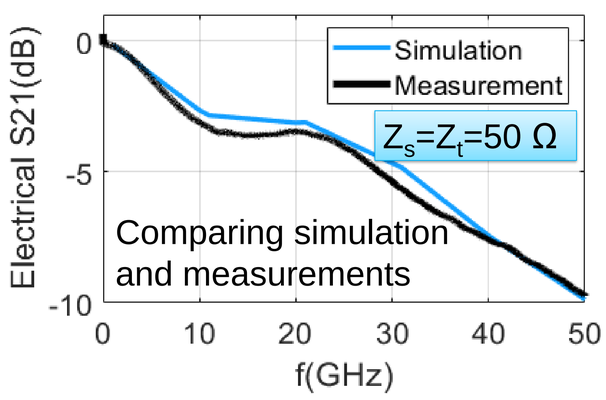
**PARAMETERIZATION OF THE REFERENCE HCPW-MZM**

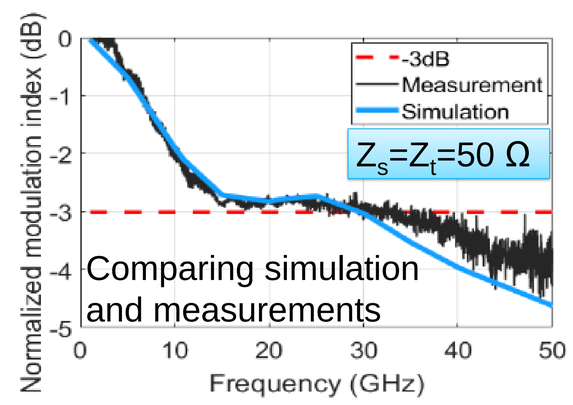
| Layer | Doping ($cm^{-3}$) | Thickness (μm) | Width (μm) | Resistivity (Ω.m) |
|---|---|---|---|---|
| **n-metal** | | $d_{mn}$=2 | $w_n$=20 | $\rho_{mn}$= 2.5x10$^{-8}$ |
| **p-metal** | | $d_{mp}$=2 | $w_p$=9 | $\rho_{mp}$= 2.5x10$^{-8}$ |
| **p-contact** | 1x10$^{19}$ | $d_{pc}$=0.28 | $w_c$= 1.4 | $\rho_{cp}$= 4.34x10$^{-5}$ |
| **p-cladding** | 1x10$^{18}$ | $d_{pclad}$=1.35 | $w_c$=1.4 | $\rho_{pclad}$=10$^{-3}$ |
| **Intrinsic** | n.i.d | $d_i$=0.21 | $w_c$=1.4 | Infinite |
| **n-cladding** | 6x10$^{16}$ | $d_{i2}$=0.31 | $w_c$=1.4 | $\rho_{nclad}$=6.097x10$^{-5}$ |
| **n-bottom** | 5x10$^{17}$ | $d_{nb}$=1.5 | | $\rho_{nb}$= 3.62x10$^{-5}$ |

## Frequency response and model validation



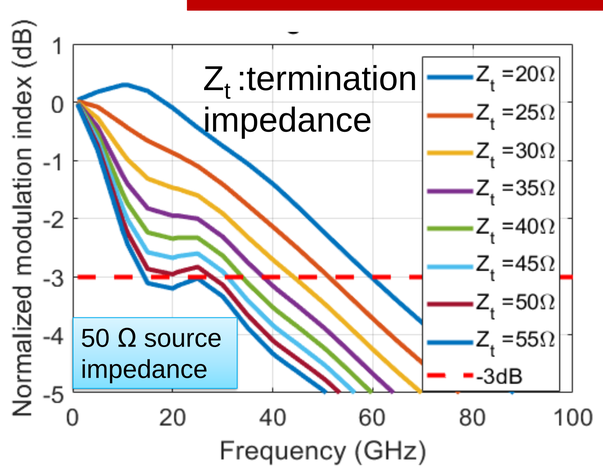



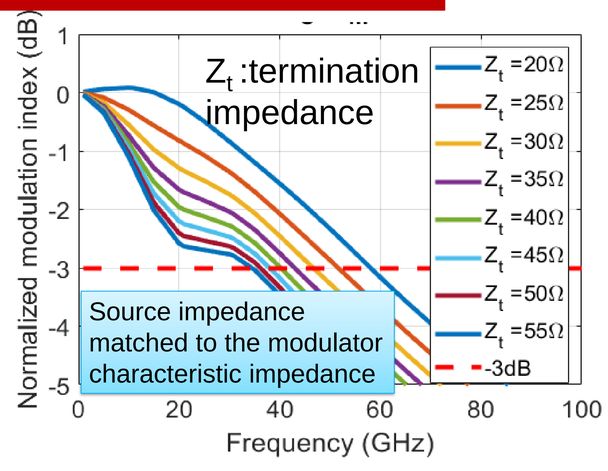




- The measured and 3D-simulated electrical S21 transfer functions are presented with good agreement
- The 3D-simulated characteristic impedance of the reference modulator design is between 23 to 25Ω in the simulated frequency range, indicating a significant mismatch between modulator, source, and termination
- Measured electro-optical-frequency response is overlaps with the calculated modulation index M(ω) of the reference HCPW-MZM when both source and termination impedances are 50 Ω.

## The role of impedance mismatch




- Matching termination impedance ($Z_t$~25Ω) to the characteristic impedance of the HCPW-line, instead of having 50Ω termination, doubles the -3dB EO-bandwidth of the reference MZM
- When the termination is not matched to the modulator impedance ($Z_t$ 50 =Ω), the source impedance matching plays a role, increasing the 3dB bandwidth from 30 GHz to 38 GHz.
- load impedance has a higher impact on the electro-optical bandwidth than the source impedance.

## Conclusion

- We have developed a simple and accurate model that combines analytical expressions with line parameters obtained from 3D EM simulators, have shown that it can effectively predict device performance and have validated its output with experimental data
- Matching the termination and source impedances can increase the EO-bandwidth from 30 GHz to 60 GHz

This research was carried out within the HTSM Photronics project, supported by the Dutch Technology foundation NWO.

# Modeling of plasmonic organic hybrid E/O modulators: towards a comprehensive 3D simulation framework

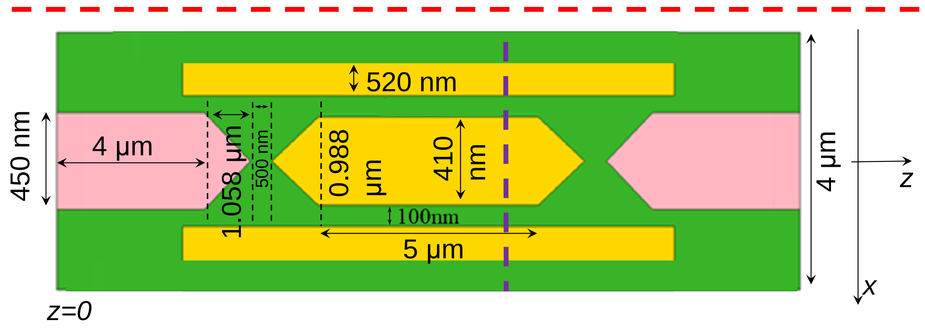

**A. Tibaldi[1,2,*], M. Ghomashi[1], F. Bertazzi[1,2], M. Vallone[1], A. Palmieri[1], M. Goano[1,2] , and G. Ghione[1]**

(1) Dipartimento di Elettronica e Telecomunicazioni, Politecnico di Torino, Corso Duca degli Abruzzi 24, 10129 Torino, Italia
(2) IEIIT-CNR c/o Politecnico di Torino, Corso Duca degli Abruzzi 24, 10129 Torino, Italia
(*) alberto.tibaldi@polito.it

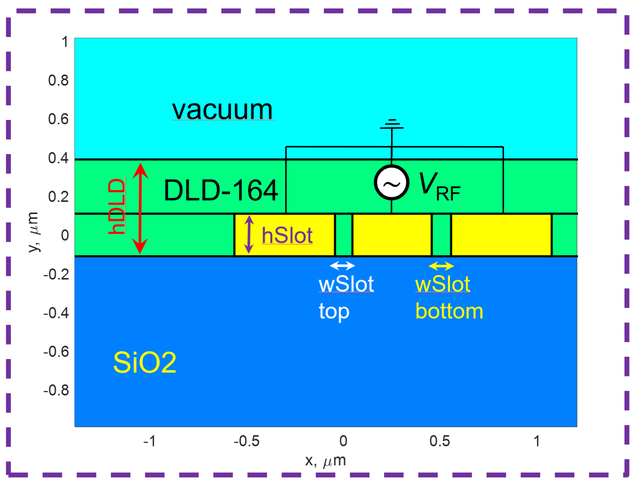


***The work focuses on the simulation of plasmonic organic hybrid electro/optic modulators. Preliminary multiphysics-augmented simulations of the slot waveguide are presented. Instead of applying them in system-level models, they are combined with the results of 3D finite-difference time-domain (FDTD) simulations to achieve realistic physics simulations at moderate computational costs. The model is demonstrated on a device from the literature and validated through a comparison with 3D-FDTD simulations of the entire device.***

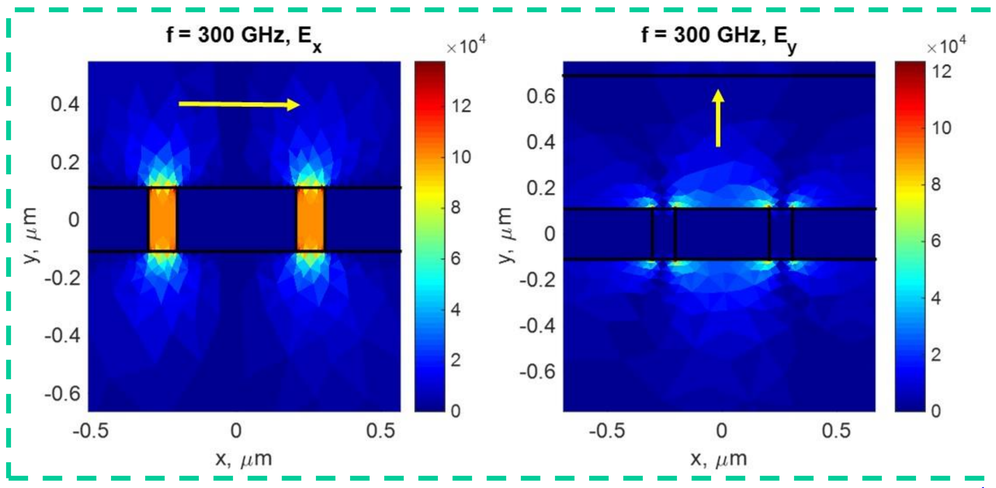

## Multiphysics-augmented slot waveguide simulation




Top view of the device under investigation from Haffner et al., Nature Photon., vol. 9, pp. 525–528, July 2015

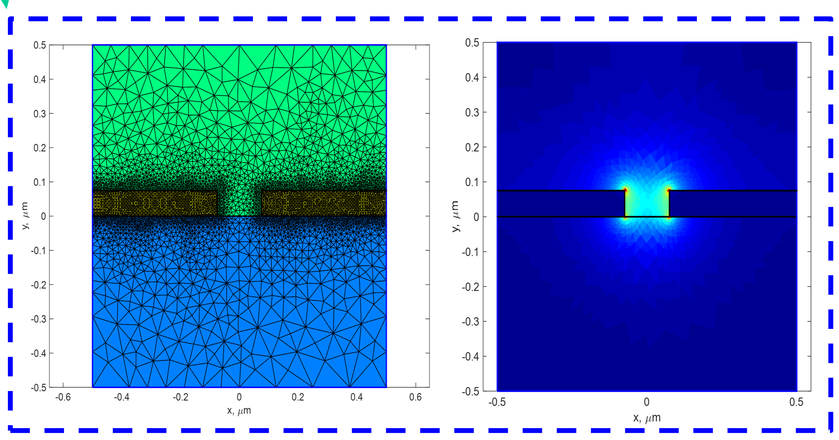



The cross-section indicated in the top view as a vertical purple line is shown here. DLD-164 is the E/O polymer, reacting to the RF field applied to the two slot waveguides realizing the phase modulator.




The RF field exhibits both *x*-directed and *y*-directed components, both contributing to the electro/optic effect. From this field profile, a map of refractive index change, $\Delta n_{mat}(x,y)$, is obtained as

$$\Delta n_{\text{mat}} = \frac{1}{2} r_{33} n_{\text{NLO}}^3 \sqrt{E_x^2 + E_y^2}$$



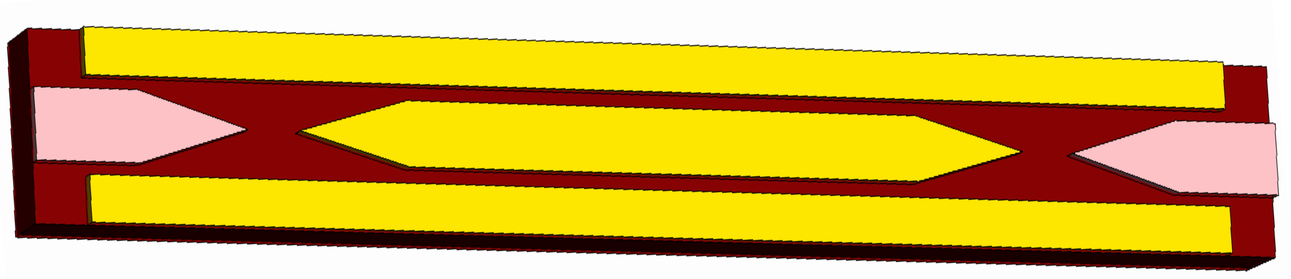
The refractive index change is used as input of the optical waveguide simulator, which estimates the mode features of the waveguides. E/O effect is enhanced by the strongly-localized plasmonic mode (left, optical mesh; right, fundamental plasmonic mode)

## Divide-et-impera simulation strategy

Waveguide simulations are usually adopted in system-level models. Even providing a rough idea of the modulator response, such models are not sufficient to achieve realistic estimates of the main figures of merit, *e.g.,* extinction ratio (ER), insertion loss (IL).

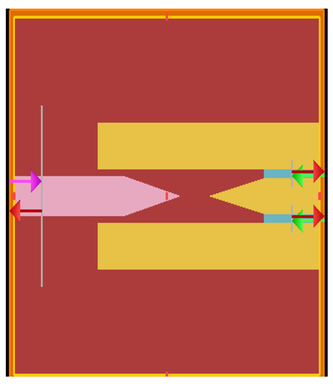
Better realism can be achieved from 3D-FDTD simulations of the entire device, which are very computationally-intensive.

An intermediate approach between *all-in-one* 3D-FDTD simulations and system-level models can be achieved by identifying the POH E/O Mach-Zehnder modulator with a bimodal Fabry-Pérot interferometer.



In this approach, the only component requiring 3D-FDTD simulation (only at 0 V!) is the splitter.

The FDTD solver returns scattering matrices of the splitter, including a piece of transmission line, to be de-embedded analytically.

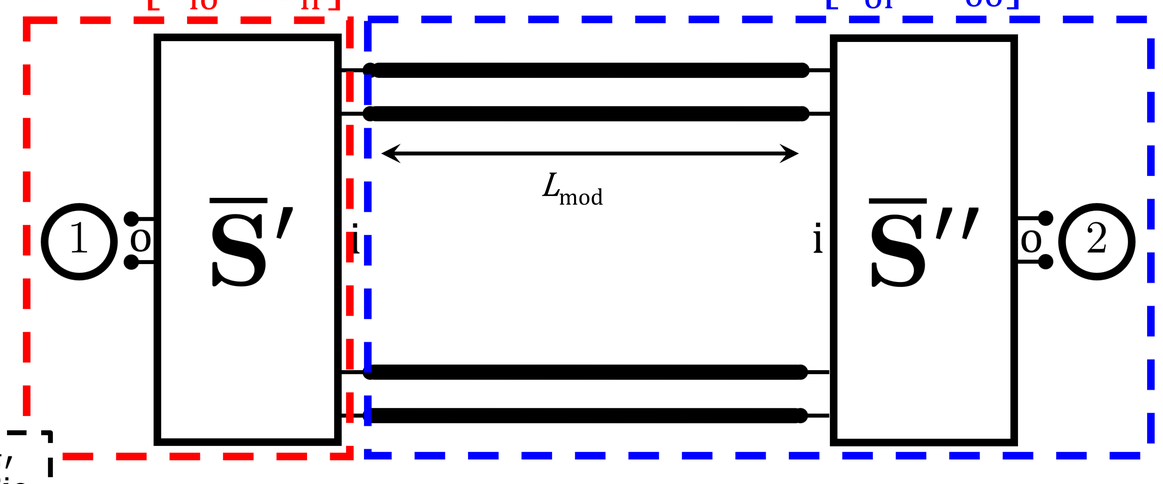


$$\mathbf{E}_{\text{port}} = \begin{bmatrix} \exp\left(\mathrm{j}k_0 n_{\text{eff,i,1}} L_{\text{port}}\right) & 0 \\ 0 & \exp\left(\mathrm{j}k_0 n_{\text{eff,i,2}} L_{\text{port}}\right) \end{bmatrix}$$

$$\bar{\mathbf{S}}'_{\text{ii}} = \mathbf{E}_{\text{port}}^{-1} \bar{\mathbf{S}}^{\text{L}}_{\text{ii}} \mathbf{E}_{\text{port}}^{-1}$$
$$\bar{\mathbf{S}}'_{\text{io}} = \mathbf{E}_{\text{port}}^{-1} \bar{\mathbf{S}}^{\text{L}}_{\text{io}}$$
$$\bar{\mathbf{S}}'_{\text{oi}} = \bar{\mathbf{S}}^{\text{L}}_{\text{oi}} \mathbf{E}_{\text{port}}^{-1}$$
$$\bar{\mathbf{S}}'_{\text{oo}} = \bar{S}^{\text{L}}_{\text{oo}}$$

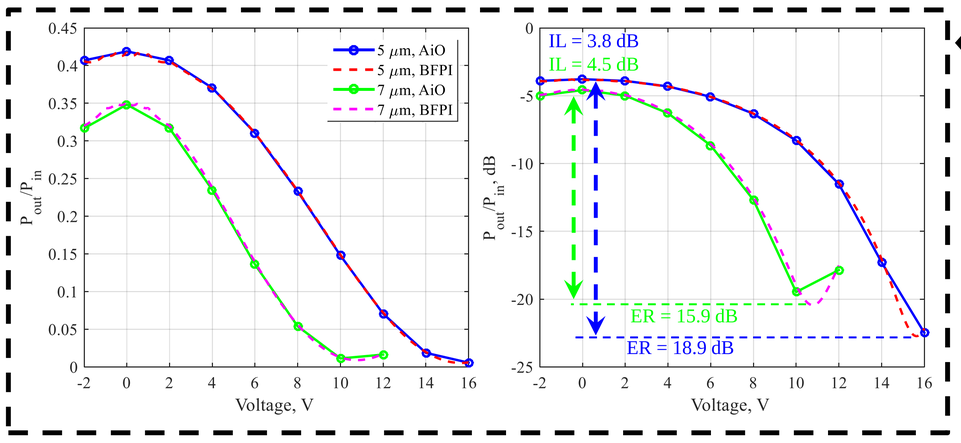
$$\mathrm{S}_{11} = \bar{\mathrm{S}}'_{\text{oo}} + \bar{\mathbf{S}}'_{\text{oi}} \bar{\mathbf{S}}''_{\text{ii}} [\mathbf{I} - \bar{\mathbf{S}}'_{\text{ii}} \bar{\mathbf{S}}''_{\text{ii}}]^{-1} \bar{\mathbf{S}}'_{\text{io}}$$
$$\mathrm{S}_{12} = \bar{\mathbf{S}}'_{\text{oi}} [\mathbf{I} - \bar{\mathbf{S}}''_{\text{ii}} \bar{\mathbf{S}}'_{\text{ii}}]^{-1} \bar{\mathbf{S}}''_{\text{io}}$$
$$\mathrm{S}_{21} = \bar{\mathbf{S}}''_{\text{oi}} [\mathbf{I} - \bar{\mathbf{S}}'_{\text{ii}} \bar{\mathbf{S}}''_{\text{ii}}]^{-1} \bar{\mathbf{S}}'_{\text{io}}$$
$$\mathrm{S}_{22} = \bar{\mathrm{S}}''_{\text{oo}} + \bar{\mathbf{S}}''_{\text{oi}} [\mathbf{I} - \bar{\mathbf{S}}'_{\text{ii}} \bar{\mathbf{S}}''_{\text{ii}}]^{-1} \bar{\mathbf{S}}''_{\text{ii}} \bar{\mathbf{S}}''_{\text{io}}$$

$$\bar{\mathbf{S}}' = \begin{bmatrix} \bar{S}'_{\text{oo}} & \bar{\mathbf{S}}'_{\text{oi}} \\ \bar{\mathbf{S}}'_{\text{io}} & \bar{\mathbf{S}}'_{\text{ii}} \end{bmatrix} \qquad \bar{\mathbf{S}}'' = \begin{bmatrix} \bar{\mathbf{S}}''_{\text{ii}} & \bar{\mathbf{S}}''_{\text{io}} \\ \bar{\mathbf{S}}''_{\text{oi}} & \bar{S}''_{\text{oo}} \end{bmatrix}$$




$$\mathbf{E}_{\text{mod}} = \begin{bmatrix} \exp\left(\mathrm{j}k_0 n_{\text{eff,i,1}}(V) L_{\text{mod}}\right) & 0 \\ 0 & \exp\left(\mathrm{j}k_0 n_{\text{eff,i,2}}(V) L_{\text{mod}}\right) \end{bmatrix}$$

$$\bar{\mathbf{S}}''_{\text{ii}} = \mathbf{E}_{\text{mod}} \bar{\mathbf{S}}'_{\text{ii}} \mathbf{E}_{\text{mod}}$$
$$\bar{\mathbf{S}}''_{\text{io}} = \mathbf{E}_{\text{mod}} \bar{\mathbf{S}}'_{\text{io}}$$
$$\bar{\mathbf{S}}''_{\text{oi}} = \bar{\mathbf{S}}'_{\text{oi}} \mathbf{E}_{\text{mod}}$$
$$\bar{\mathrm{S}}''_{\text{oo}} = \bar{S}'_{\text{oo}}$$




The results obtained with all-in-one 3D-FDTD simulations (AiO) are compared to those achieved with the bimodal Fabry-Pérot interferometer model (BFPI) for two devices having 5 μm (blue/red curves) and 7 μm modulator length (green/magenta curves).

The multiphysics waveguide simulations presented in the top part can be used to define the matrix **S''** as equal to **S'**, but with reference planes changed accordingly to the voltage-dependent phase-shift:

# InP-based integrated OLT and ONU with cyclic AWG for WDM-PON

*Student Paper*

**Aleksandra Paśnikowska, Stanisław Stopiński, Andrzej Kaźmierczak, Ryszard Piramidowicz**
Warsaw University of Technology, Institute of Microelectronics and Optoelectronics,
Koszykowa 75, 00-662 Warszawa, Poland
*e-mail: aleksandra.pasnikowska.dokt@pw.edu.pl*

**ABSTRACT**

In this work we demonstrate integrated multichannel transceivers dedicated to cost-optimized, fiber-optic communication systems. Two different transceivers are discussed - Optical Line Termination (OLT) and Optical Network Unit (ONU), designed for an application in the WDM-PON access system. The application of cyclic arrayed waveguide gratings (AWGs) is tested in order to achieve better performance of integrated transmitters. Open eye diagrams and an error-free operation at -17 dBm prove the applicability of developed circuits to access systems with wavelength multiplexing.

**Keywords**: photonic integrated circuit, InP, multichannel transmitter, arrayed waveguide grating, optical access network, cyclic AWG

## 1. INTRODUCTION

Modern transmission systems exploited today, all-optical and optically transparent at the level of core and metropolitan network, enable extremely high speeds of data transmission of the order of Tb/s. The main bottleneck limiting the bandwidth is still in the access networks, which are partially still based on copper lines, utilized previously for telephone networks, limiting the possibilities of fast data transmission [1]. Consequently, the development towards the optical access networks is a must. Nowadays passive optical networks (PON) are the most popular solution offering advantages of broad-band transmission, simplicity and low cost of equipment. In order to provide a high-speed, all-optical, symmetric transmission of digital signals, the passive optical networks with the wavelength division multiplexing technique (WDM-PON) [2] are considered as one of attractive approaches. WDM-PONs might offer higher bandwidth per optical network unit (ONU), lower splitting losses and higher link reach?? [3]. A typical WDM-PON uses a single Optical Line Termination (OLT) and several Optical Network Units (ONUs). Generally, OLT is located at a service provider's signal office and ONUs are located at end users' premises.

The InP-based PICs offer advantages of low cost, small size and limited power consumption and provide impressively high reliability. This has resulted in extensive research of PICs applications in the optical telecommunication, addressing topics such as access networks, metro and core networks as well as data communication [4]-5].

In this work, we present and discuss the design of a transmitter with a cyclic arrayed waveguide gratings (AWG) for application in access systems. Application of cyclic AWGs is a solution for compensating technological problems with appropriate matching the wavelengths of integrated lasers with the bandwidth transmission of AWG channels, reported in our previous works [6-7].

## 2. DESIGN

The schematic of the proposed WDM-PON system based on PICs is presented in Fig 1. The OLT Tx PIC was designed for operating as an OLT transmitter. It has six channels connected to an 8×8 AWG. Each of these channels contains a DBR laser and an electro-absorption modulator. Each laser comprises a 150 μm-long semiconductor amplifier (SOA), two Bragg gratings and two isolation sections. The emission wavelengths of the lasers are matched to the AWG passbands. Two channels are connected to the photodiodes, which allows testing the spectral characteristic of the AWG. The AWG has the following parameters: channel spacing $\Delta\lambda$ = 0.8 nm, FSR = 6.4 nm and central wavelength $\lambda C$ = 1572.8 nm. The choice of the spectral parameters was dictated by the wavelength range of modulators (1570-1580 nm). All outputs of the AWG are connected to the outputs of the chip. The OLT Rx was designed as the receiving part of the OLT. It consists of an array of eight photodiodes connected to a cyclic AWG (with the same parameters as in the previous chip). The last of the designed chips was intended for operating as two ONU circuits. It contains two transmitters and two photodiodes. The OLT Rx and ONU TxRx have also test structures of lasers with modulators and photodiodes.

The downstream signal is generated by OLT Tx and with one of the outputs of AWG connected through a circulator to the fiber-optic link. This signal is received by one of the photodiodes in ONU. The upstream signal is generated in the ONU TxRx and with circulators and (de)multiplexer addressed to the OLT Rx.

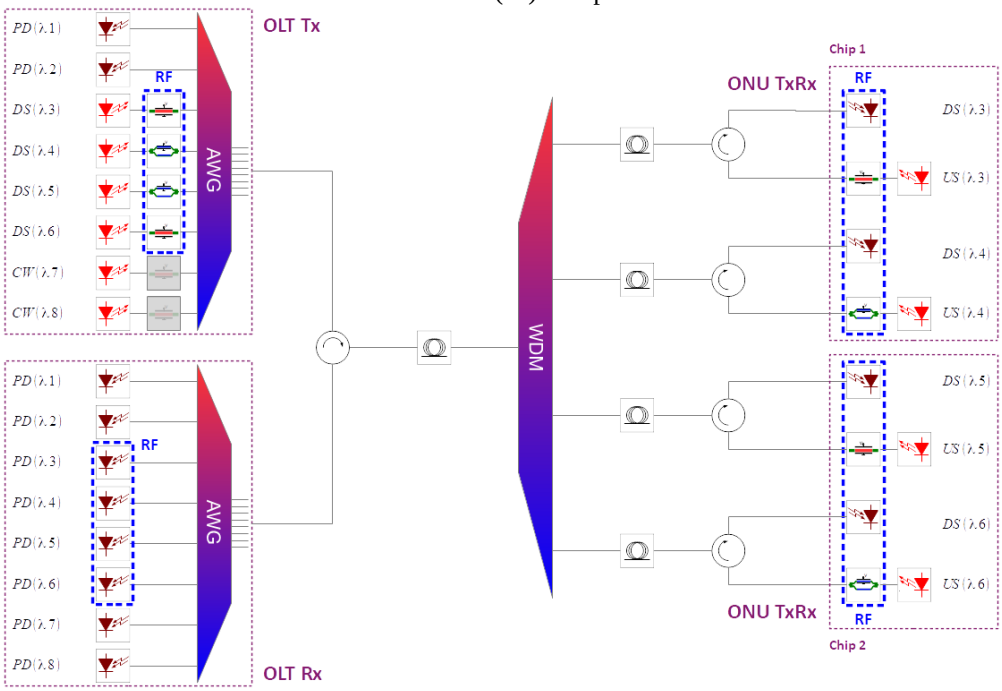



*Figure 1. Schematic of proposed WDM-PON based on InP transmitters and receivers.*

All chips, realizing the above described functionalities were designed using generic approach and fabricated in a generic foundry process [8-9]. Fig 2. presents microscope photographs of designed and manufactured circuits.

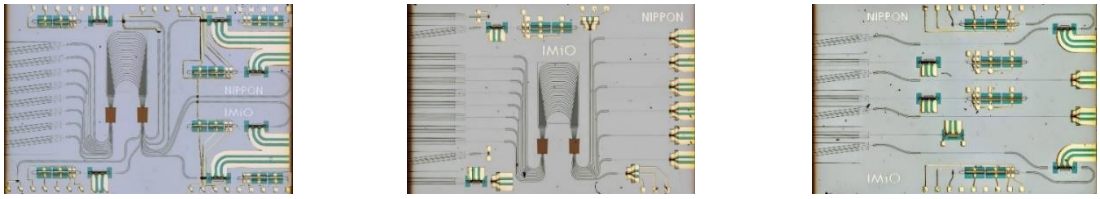


*Figure 2. Microscope photographs of designed PICs from left: OLT Tx, OLT Rx, ONU TxRx*

## 3. CHARACTERIZATION

For experimental evaluation all the chips were mounted on copper blocks and thermally stabilized at 20°C. The output signal was collected from SSCs with SMF fibres. Measured thresholds of all lasers were in the range from 30 mA to 40 mA. The output power of both transmitters reaches about 0.5 mW (-3 dBm). The single-mode operation was observed with side-mode suppression ratios above 30 dB. The static extinction ratio above 15 dB was recorded.

The dynamic measurements of both transmitters were also performed. The 10 Gb/s PRBS signal was applied to the modulators together with DC voltage. The signal from the PRBS was amplified by a broadband amplifier (SHF 100APP) to amplify the RF signal. A digital sampling oscilloscope was used to capture the eye diagrams, which were measured in a back-to-back configuration (B-t-B). The biasing parameters were adjusted to achieve the most open eye diagram. The SOA of a laser was biased 154 mA /180 mA, the DC modulator bias were 1.64 V/1.5 V and $V_{pp}$ 1 V/0.5 V for the OLT Tx/ONU Tx Rx. A sample measured eye diagram is presented in Fig. 3. The dynamic extinction ratios were 6.3 dB (OLT Tx) and 7.2 dB (ONU TxRx). The eye diagram is more open in ONU TxRx than in OLT Tx, due to the absence of AWG in the latter.

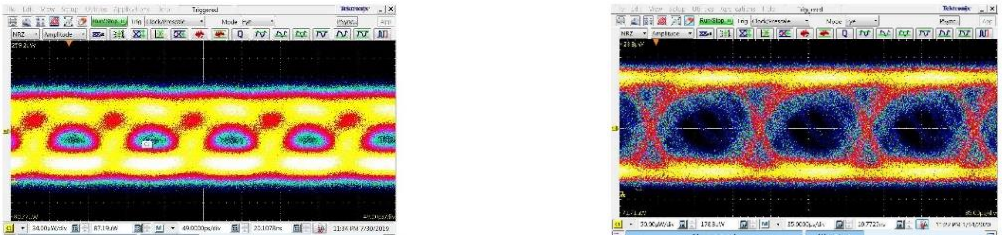


*Figure 3. Recorded 10 Gb/s eye diagrams of OLT Tx (left) and ONU TxRx (right) transmitters.*

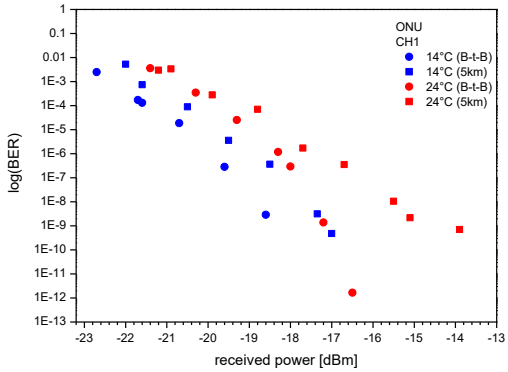



*Figure 4. Bit error for ONU transmission in back-to-back configuration and 5 km in 14 °C and 24° C.*

The bit error ratio (BER) measurements were performed using a BER tester. Figure 4. shows measured BER curves of the channel CH1 of the ONU TxRx chip, recorded for two different temperatures (14°C and 24°C). The transmitter in the lower temperature shows better performance with an error-free operation of -17 dBm compared to -14 dBm for 24°C.

## 4. CONCLUSIONS

In conclusion, we have demonstrated the WDM-PON link based on PICs equipped with a cyclic AWG. The output power of the transmitters was around 0.5 mW, extinction ratio was above 15 dB, side mode suppression ratio was above 30 dB. Open eye diagrams and error-free operation at -17 dBm prove that photonic integration technology can be efficiently applied to develop a new type of transmitters for access systems.

## ACKNOWLEDGEMENTS

This work was supported by the National Centre for Research and Development (project NIPPON of the 3rd Applied Research Programme, grant agreement PBS3/A3/21/2015).

## REFERENCES

[1] "Fixed and mobile broadband subscriptions by technology," 2017. [Online]. Available: http://www.oecd.org/sti/broadband/broadband-statistics/. [Accessed: 08-Nov-2018].

[2] Y. Chung and Y. Takushima, "Wavelength-Division-Multiplexed Passive Optical Networks (WDM PONs)," *Opt. Fiber Telecommun. V1B*, pp. 927–984, 2013.

[3] L. G. Kazovsky, W. T. Shaw, D. Gutierrez, N. Cheng, and S. W. Wong, "Next-generation optical access networks," *J. Light. Technol.*, vol. 25, no. 11, pp. 3428–3442, Nov. 2007.

[4] D. F. Welch *et al.*, "Large-scale InP photonic integrated circuits: Enabling efficient scaling of optical transport networks," *IEEE J. Sel. Top. Quantum Electron.*, vol. 13, no. 1, pp. 22–29, Jan. 2007.

[5] B. Wohlfeil, "Photonic Integrated Circuits for Data Center Interconnects," pp. 2–3, 2017.

[6] A. Paśnikowska, K. Anders, A. Kaźmierczak, R. Piramidowicz, M. Tomkiewicz, and S. Stopiński, "Development of InP-based multichannel transmitters for application in WDM access systems," 2018, p. 79.

[7] A. Pasnikowska, S. Stopinski, K. Anders, A. Jusza, R. Piramidowicz, and M. Tomkiewicz, "Integrated transceivers for WDM-PON access systems," *URSI 2018 - Balt. URSI Symp.*, pp. 31–32, 2018.

[8] M. Smit *et al.*, "An introduction to InP-based generic integration technology," *Semicond. Sci. Technol.*, vol. 29, no. 8, p. 083001, 2014.

[9] L. M. Augustin *et al.*, "InP-Based Generic Foundry Platform for Photonic Integrated Circuits," *IEEE J. Sel. Top. Quantum Electron.*, vol. 24, no. 1, pp. 1–10, Jan. 2018.

# Fast Silicon-Photonics Wavelength-Selective Phase Shifter

**C. Porzi[1], F. Falconi[2], L. Ansalone[3], P. Ghelfi[2], A. Bogoni[1,2]**

1: Scuola Superiore Sant'Anna, TeCIP Institute, 56124 Pisa, Italy

2: CNIT - National Inter-University Consortium for Telecommunications, 56124 Pisa, Italy

3: ASI-Italian Space Agency, Via del Politecnico, snc 00133 Roma

***Abstract**: A fast wavelength-selective phase shifter in silicon-on-insulator technology based on carrier-depletion effect in a microring resonator is designed and experimentally verified. Phase variation of 250°, bandwidth of 10GHz and insertion loss of 3.5dB have been demostrated*

## INTRODUCTION

Microring resonators (MRRs) in all-pass configuration have long been proposed and demonstrated as an effective mean for controlling the phase of radio-frequency (RF) signals [1].

Strong thermo optic effect of silicon by heating the ring waveguide has been widely used [2], [3] to design devices with high efficiency and phase tuning range but with response time limited to few us

To overcome bandwidth limitation the use of fast plasma dispersion effect using carrier injection in a doped MRR has also been reported [4] but with limited phase shift range <180°

For the first time an optimized design of a MRR embedding pn-doped waveguides to exploit carrier-depletion mechanism to obtain a fast phase shifter (10Ghz bandwidth) with a wide phase range: >250° has been proposed

## MRR DESIGN AND OPTIMIZATION

An analytical model describing the pn-doped waveguide behavior as a function of the applied reverse voltage has been employed to take in account relatively weak index change associated with modulation of depletion region and the optical losses due to free-carriers in the doped waveguide.

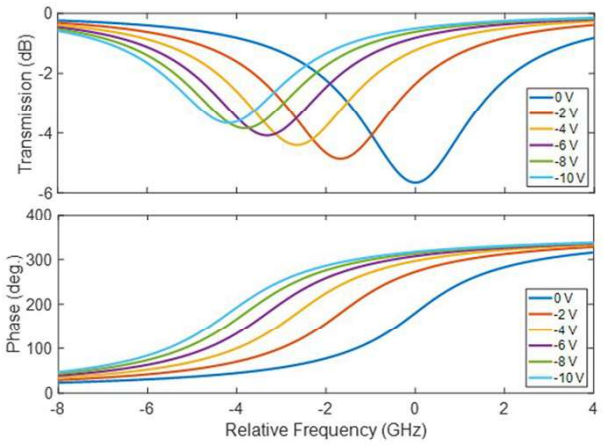
Available doping concentrations for the selected foundry in a multi-project wafer (MPW) run has been estimated based on the provided values for the sheet resistance of the implanted waveguide with p- an n-type dopant

The doped waveguide length, Lpn and the cross-coupling power coefficient $\kappa$ of the directional coupler (DC) between the ring and input-output access bus waveguide have been optimized to:

- Maximize the phase shift for a maximum applied voltage below the inverse breakdown threshold
- to keep low as low as possible the Q-factor of the resonator for minimizing the residual amplitude modulation

Transmission and phase response for different reverse voltage bias are shown for Lpn=200 $\mu$m, and $\kappa$=0.2

Model results




## Experimental setup and results

The fast selective PS has been fabricated using a SiP MPW run [6].

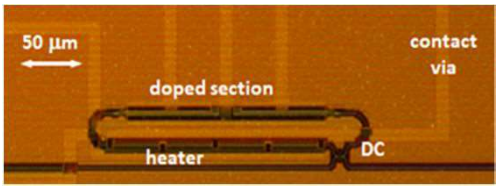
A resistive heater is placed in proximity to a portion of the MRR undoped waveguide to provide an additional broad tuning mechanism, as required for precise resonance alignment when multiple MRRs are cascaded to achieve full 360° phase shift control.

The group-delay characteristics of the MRR for different levels of Vbias have then been measured using a standard phase shift method [7].

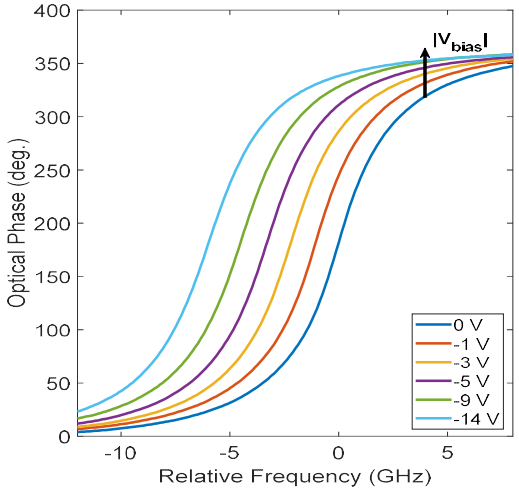
The optical phase variation and insertion loss over the full considered voltage swing at a detuning of 3 GHz in respect to the unbiased resonant frequency are plotted

the high-speed operation of the selective PS has been assessed by measuring the electro-optical bandwidth of the device under small-signal regime using a Network Analyser

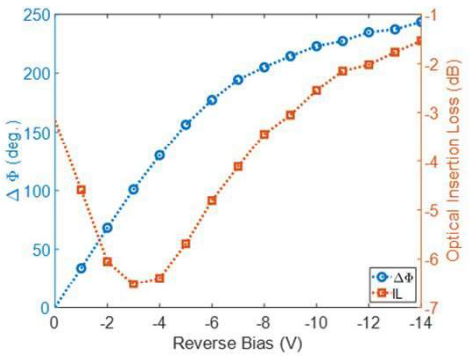
Device micrograph



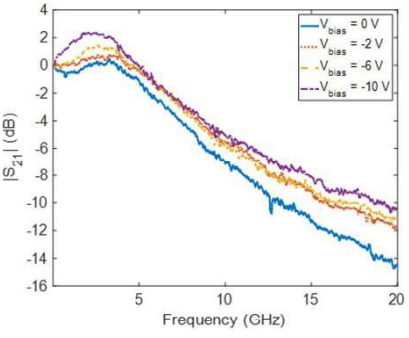

Measured




Phase and loss measure




Bandwidth measure




## Final remarks

- A silicon-photonics microring resonator embedding a pn-doped waveguide designed for implementing a novel fast wavelength-selective phase shifter through carrier-depletion mechanism has been presented
- The MRR has been dimensioned for optimizing its performances in terms of optical phase variation, amplitude modulation and insertion loss
- Experimental characterization confirms phase shift range >200° , residual amplitude modulation <3dB and response time <1ns

**References**

[1] D. B. Adams, and C. K. Madsen, J. Light. Technol., vol. 26, pp. 2712-2717, Aug. 2008.

[2] M Pu, et al.Photon. Technol. Lett., vol. 22, pp. 869-871, June 2010.

[3] G. Choo, et al, J. Lightw. Technol., vol. 36, pp. 5263-5275, Nov. 2018.

[4] J. Tang, et al, in Proc. WOCC 2016, Chengdu, China, May 2016, pp.1-3.

[5] L. Chrostowski, and M. Hochberg, Silicon photonics design: from devices to systems, Cambridge University Press, 2015.

[6] https://europractice-ic.com/mpw-prototyping/siphotonics/imec/

[7]S. Ryu, Y. Horiuchi, K., J. Lightw. Technol., vol. 7, pp. 1177-1180, Aug. 1989.

# Strain-induced electro-optical effect in silicon Mach-Zehnder modulators

Christian LAFFORGUE[1], Mathias BERCIANO[1], Guillaume MARCAUD[1], Xavier LE ROUX[1], Carlos ALONSO-RAMOS[1], Daniel BENEDIKOVIC, Vladyslav VAKARIN, Alicia RUIZ-CARIDAD, Paul CROZAT, Delphine MARRIS-MORINI[1], Eric CASSAN[1], and Laurent VIVIEN[1]

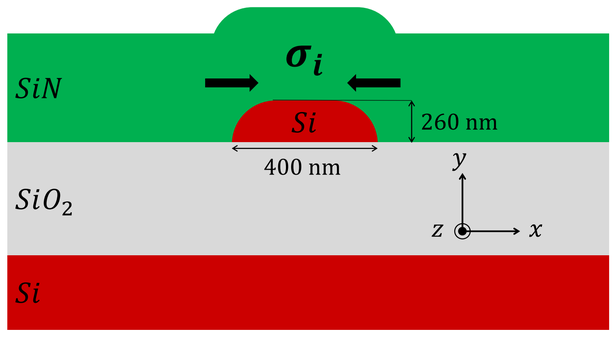
[1] Centre de Nanosciences et de Nanotechnologies, CNRS, Univ. Paris-Sud, Univ. Paris-Saclay, C2N – Palaiseau, France .

ERC POPSTAR

## Context

Todays electro-optic modulators do not address the issues of energy consumption and mass production at the same time. Taking advantage of second order nonlinear optical effects, such as Pockels effect, in silicon would answer both challenges. Indeed, Pockels effect is an ultra-fast linear electro-optic effect and silicon is fully compatible with CMOS industrial fabrication lines. However, due to its centrosymmetry, silicon does not naturally provide Pockels. A stressing layer is used to break this symmetry, enabling the existence of second order nonlinearities in silicon.

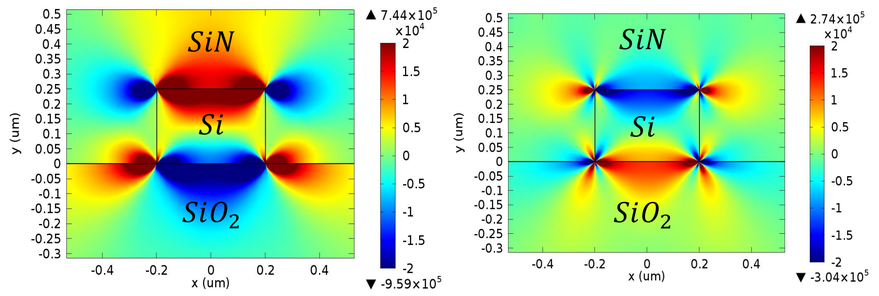
## How to strain silicon?




Silicon waveguide strained by a silicon nitride layer (SiN)

A highly stressed SiN layer is deposited on the silicon waveguide (PECVD)

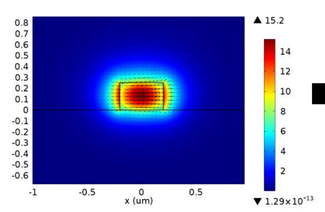
$$\chi^{(2)}_{ijk}(\vec{r}) = \sum_{mnl} \Gamma^{ijk}_{mnl}\, \eta_{mnl}(\vec{r}) \neq 0$$



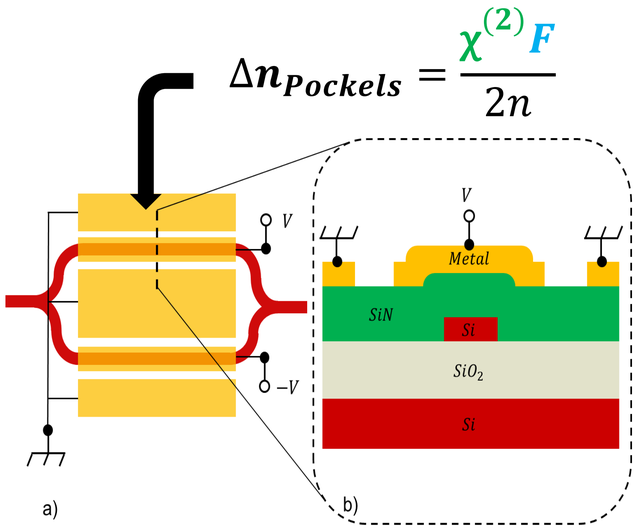

**Distribution profiles of strain gradients** $\eta_{xxy}$ and $\eta_{yyy}$ in the waveguide

## Experimental characterization: electro-optic modulation[1]

$$\Delta n_{Pockels} = \frac{\chi^{(2)} F}{2n}$$

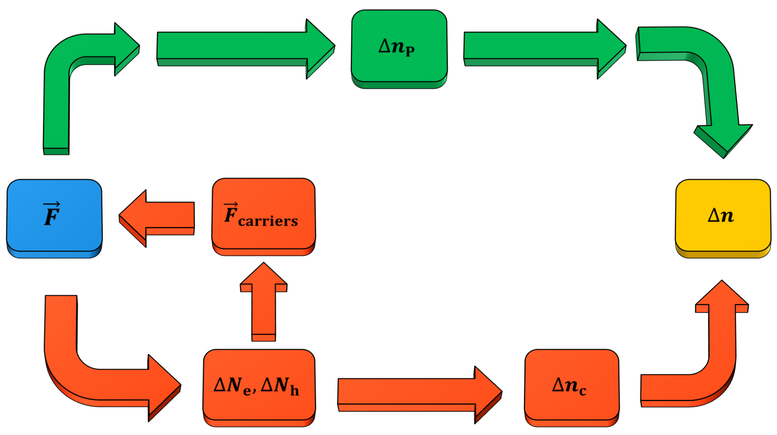



Single mode waveguide (TE)




Schematic vue of the modulator

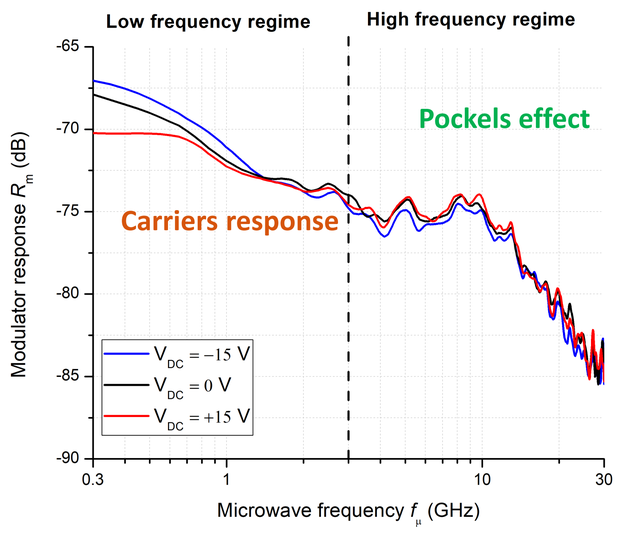
**Strain-induces Pockels effect**




**Free carriers plasma dispersion effect**

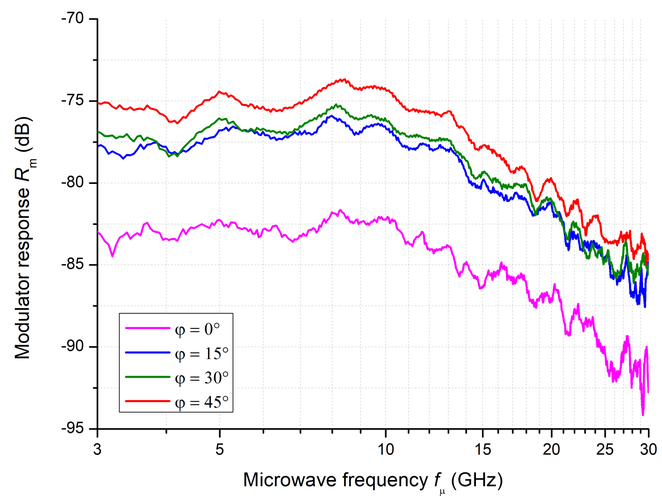
Problem: interplay between Pockels effect and free carriers effect. How to separate them?

## Speed

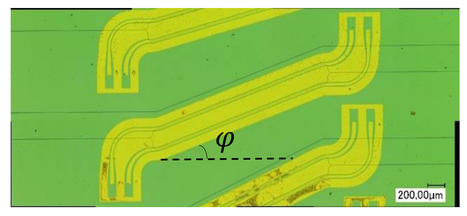



At high frequencies, free carriers are not fast enough to play on the modulation response

## Angular dependence




Pockels effect depends on the crystal orientation, while carriers are not.




## Conclusion

We demonstrate the possibility to unlock second order nonlinear effects in silicon, a centrosymmetric material, by depositing a stressing layer on top of the device. Experimental results highlight Pockels effect signatures by playing on the modulation frequency and the crystal orientation. A theoretical model developed in our team permits to study the effect of strain on the electro-optic response of the modulator. These studies are promising for the future of the strained silicon platform. Further investigations are currently under study to improve the strain-induced Pockels effect.

[1] M. Berciano *et al.* , « Fast linear electro-optic effect in a centrosymmetric semiconductor », Communication physics, 2018

# $LiNbO_3$ V-Groove Fabrication for Optical Fibre Pigtailing

*(Student Paper)*

**Ercan Karagöz[1,2], Evren Öztekin[1,2], Mutlu Gökkavas[1], Şadan Özcan[2,3], Ekmel Özbay[1,4]**

[1]*Nanotechnology Research Center-NANOTAM, Bilkent University, Ankara, Turkey*
[2]*Department of Nanotechnology and Nanomedicine, Hacettepe University, Ankara, Turkey*
[3]*Department of Physics Engineering, Hacettepe University, Ankara, Turkey*
[4]*Department of Electrical and Electronics Engineering, Bilkent University, Ankara, Turkey*
e-mail: ercan.karagoz@bilkent.edu.tr

## INTRODUCTION

Due to its unique electro-optical properties, lithium niobate has an important role in telecommunication and inertial navigation systems. Proper packaging of lithium niobate devices is essential for mechanical and thermal stability. Fibre carriers are commonly used for better mechanical stability of pigtailed lithium niobate devices [1],[2],[3].

This study aims fabrication of V-grooves in lithium niobate (LiNbO3) crystals for producing optical fibre carrier pigtails. Due to anisotropic thermal expansion of lithium niobate, it is important to use the lithium niobate based fibre optic carriers for pigtailing lithium niobate devices to achieve better thermal stability.

V-shaped grooves are generally used as precise fibre mounts for fibre carriers [4]. Unlike silicon or glass, lithium niobate is not suitable for V-groove wet etching or moulding process [5],[6],[7],[8]. In this study, lithium niobate based V-grooves are machined with a V-shaped diamond wheel by using a computer controlled dicing saw.

**Keywords**: $LiNbO_3$, V-groove, fibre pigtailing, packaging.

## METHOD AND ANALYSIS

1mm thick X-cut lithium niobate wafers from Delmar Photonics are used as fibre carrier material. With the help of a Disco DAD3220 dicing saw, lithium niobate pieces are grooved using a V-shaped diamond wheel. To obtain a set of controlled variation of V-groove depths, multiple groove cuts in parallel order are done. This set of V-grooves are analysed for optimum depth and shape. In order to determine optimum machining parameters, a dummy fibre is placed in machined set of parametrically varying V-groove samples, and the position of the fibre core is checked under an optical microscope.

Figure 1 shows illustration of the diamond wheel and different depth V-grooves on lithium niobate sample. Figure 2 shows SEM image of two parallel 45° V-grooves with same depth.

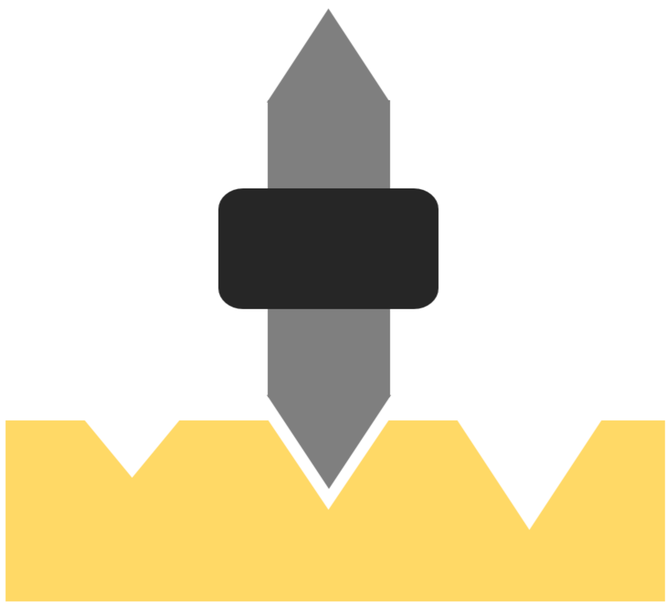


Figure 1. Illustration of V-shaped wheel and different depth V-groove cuts on lithium niobate sample.

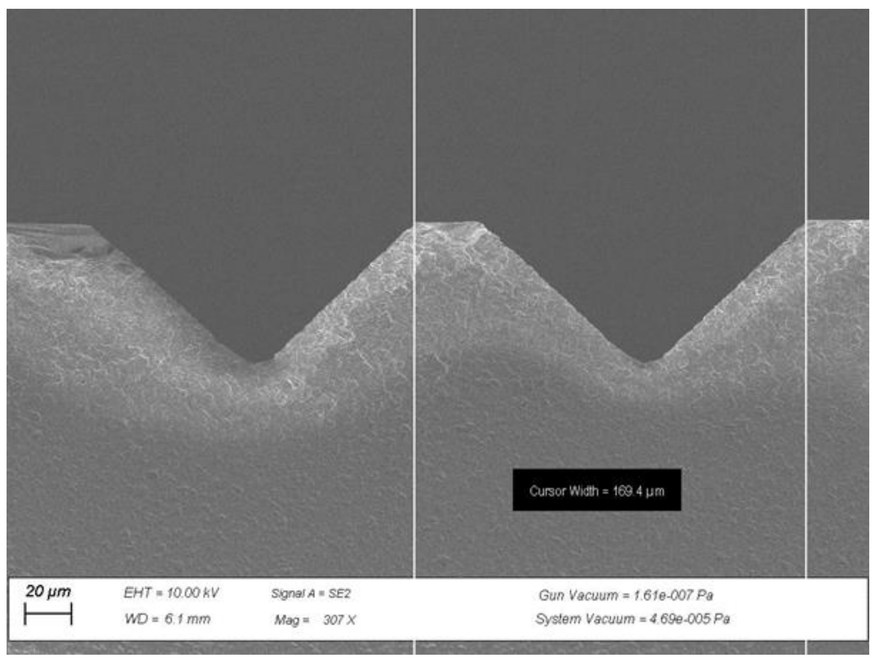



Figure 2. SEM image of LiNbO3 V-grooves.

Fibres are placed in these V-groove mounts using an optical microscope. To fix the fibres, a UV curable epoxy is applied on top of the fibres and compressed with a separate lithium niobate lid. The sample is cured using a UV source and the sample surface with fibre-end is chemical-mechanical polished. Figure 3 shows an optical microscope image of the polished surface of a complete lithium niobate fibre carrier with an 80µm polarization-maintaining (PM) optical fibre.

## RESULTS AND DISCUSSION

Figure 3 shows an optical microscope image of the polished surface of a complete lithium niobate fibre carrier with an 80µm polarization-maintaining (PM) optical fibre. The position of the PM fiber was confirmed using an optical measurement setup with a nanopositioning stage, a powermeter and a polarizer.

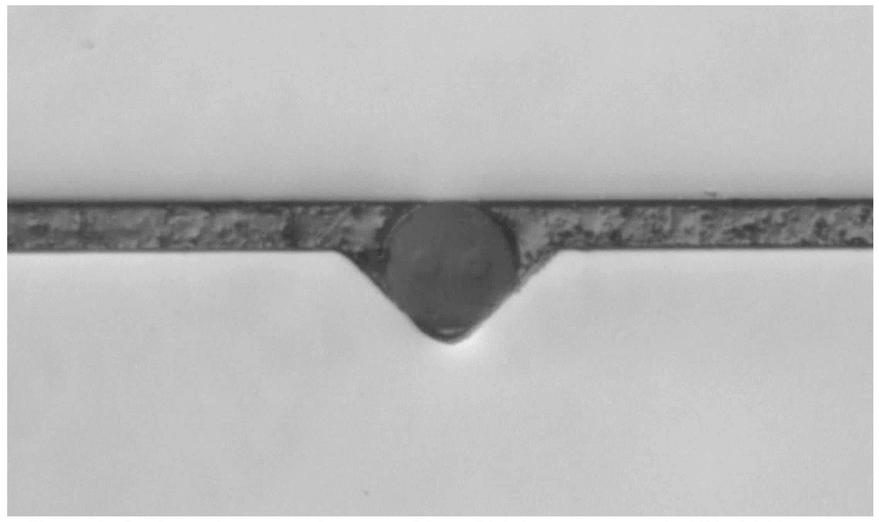


Figure 3. Optical microscope image of 80µm PM fibre mounted in LiNbO3 V-groove.

## REFERENCES

[1] R. S. Weis and T. K. Gaylord, “Lithium niobate: Summary of physical properties and crystal structure,” Appl. Phys. A, vol. 37, no. 4, pp. 191–203, 1985, doi: 10.1007/BF00614817.
[2] A. S. Greenblatt, C. H. Bulmer, R. P. Moeller, and W. K. Burns, “Thermal stability of bias point of packaged linear modulators in lithium niobate,” J. Light. Technol., vol. 13, no. 12, pp. 2314–2319, 1995.
[3] Y. S. Kim and R. T. Smith, “Thermal expansion of lithium tantalate and lithium niobate single crystals,” J. Appl. Phys., vol. 40, no. 11, pp. 4637–4641, 1969.
[4] M. A. Uddin, M. Y. Ali, H. P. Chan, and others, “Materials and fabrication issues of optical fiber array,” Rev. Adv. Mater. Sci, vol. 21, no. 2, pp. 155–164, 2009.
[5] C. Strandman, L. Rosengren, H. G. A. Elderstig, and Y. Backlund, “Fabrication of 45/spl deg/mirrors together with well-defined v-grooves using wet anisotropic etching of silicon,” J. microelectromechanical Syst., vol. 4, no. 4, pp. 213–219, 1995.
[6] T. Zhou, X. Liu, Z. Liang, Y. Liu, J. Xie, and X. Wang, “Recent advancements in optical microstructure fabrication through glass molding process,” Front. Mech. Eng., vol. 12, no. 1, pp. 46–65, 2017.
[7] R. W. Eason, I. E. Barry, G. W. Ross, and P. G. R. Smith, “Fabrication of alignment grooves in LiNbO3 substrates for simplified optical fibre pigtailing,” Electron. Lett., vol. 35, no. 4, pp. 328–329, 1999.
[8] I. E. Barry, G. W. Ross, P. G. R. Smith, R. W. Eason, and G. Cook, “Microstructuring of lithium niobate using differential etch-rate between inverted and non-inverted ferroelectric domains,” Mater. Lett., vol. 37, no. 4–5, pp. 246–254, 1998.
[9] J. Guo, J. Zhang, H. Wang, K. Liu, and A. S. Kumar, “Surface quality characterisation of diamond cut V-groove structures made of rapidly solidified aluminium RSA-905,” Precis. Eng., vol. 53, pp. 120–133, 2018.

BİLKENT ÜNİVERSİTESİ NANOTAM nanoteknoloji araştırma merkezi

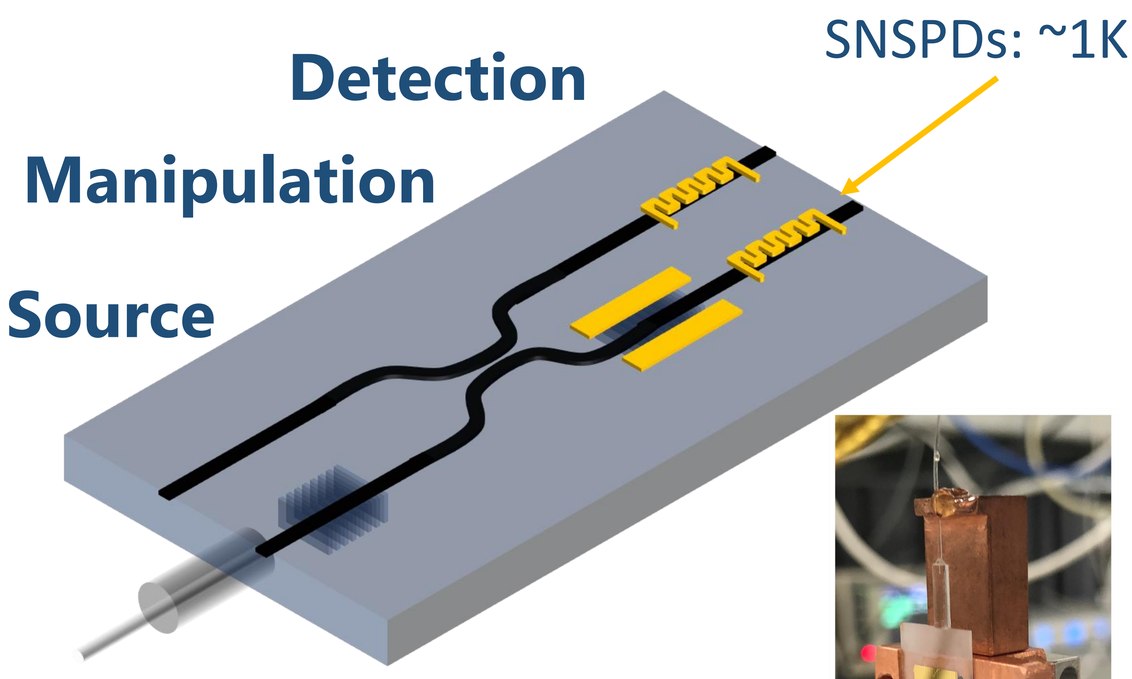
Bilkent 06800, Ankara, Türkiye
T: +90-312-290 1966 F: +90-312-266 4042
nanotam@bilkent.edu.tr

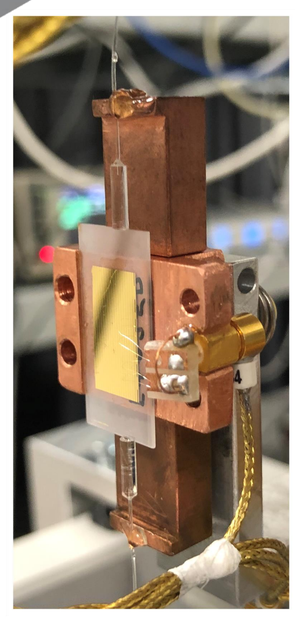
# Cryogenic operation of a polarisation converter and directional coupler in $LiNbO_3$ for quantum circuits

**Frederik Thiele[1], Jan Philipp Höpker[1], Felix vom Bruch[2], Harald Herrmann[2], Raimund Ricken[2], Viktor Quiring[2], Christof Eigner[2], Christine Silberhorn[2], Tim Bartley[1]**

[1] Mesoscopic Quantum Optics, Department of Physics, Warburger Str. 100, 33098 Paderborn, Germany
[2] Integrated Quantum Optics, Department of Physics, Warburger Str. 100, 33098 Paderborn, Germany

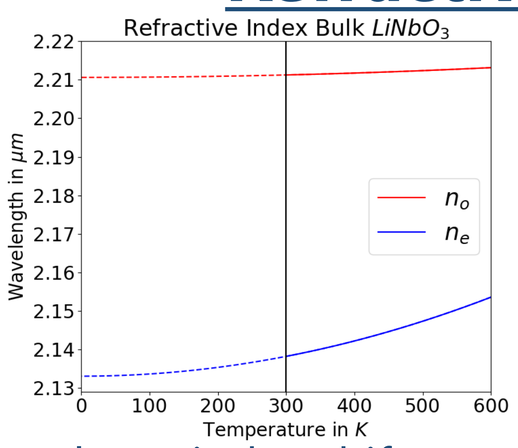
## 1) Quantum Photonic Chip

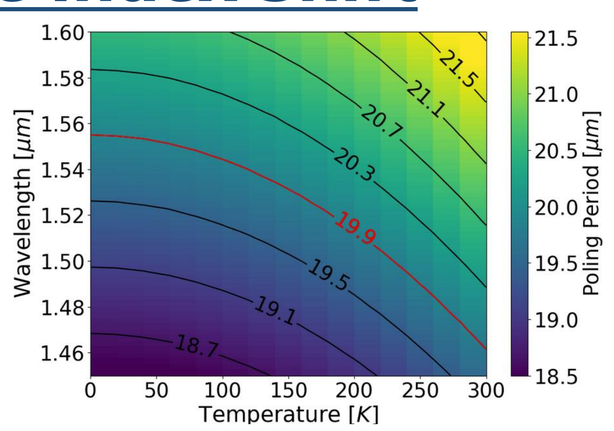


z-cut Lithium Niobate :
- Ti waveguides loss: 0.1dB/cm
- 90% fibre overlap
- large $\chi^2$-nonlinearity
- electro-optical effect [1,2]

## 2) Temperature Dependent Refractive Index Shift

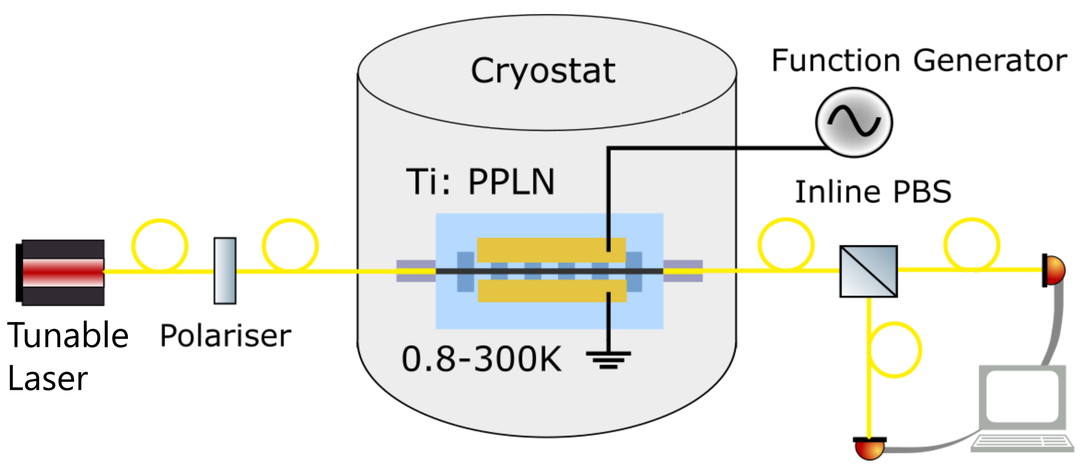


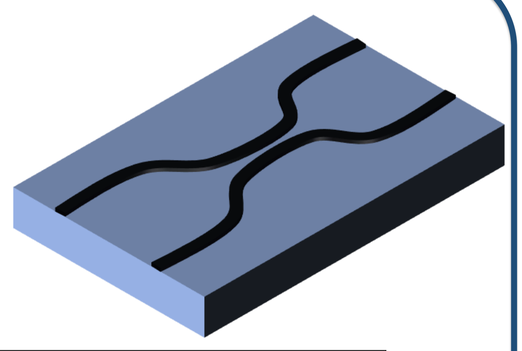

a large index shift is expected [3]

phasematched wavelength shift for polarisation converter

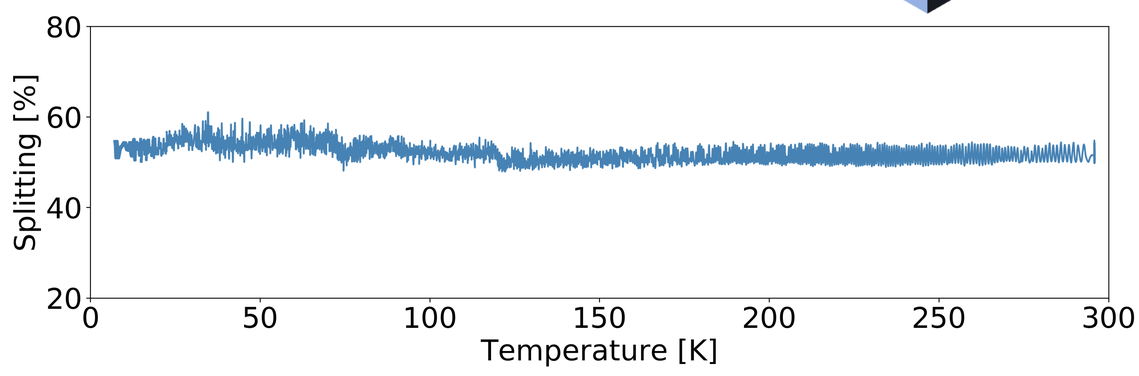
## 3) Experimental Setup



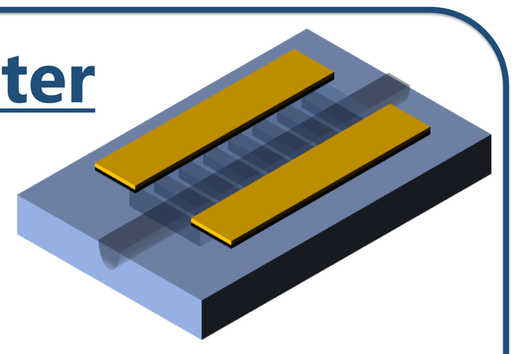

## 4) Directional Coupler



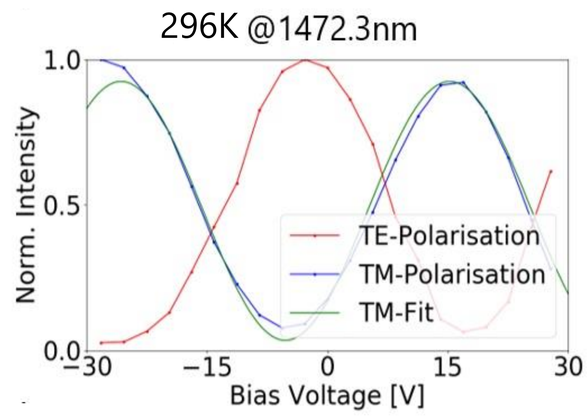
splitting ratio:
- 52±2.5% @300K
- 55±2.5 % @22K

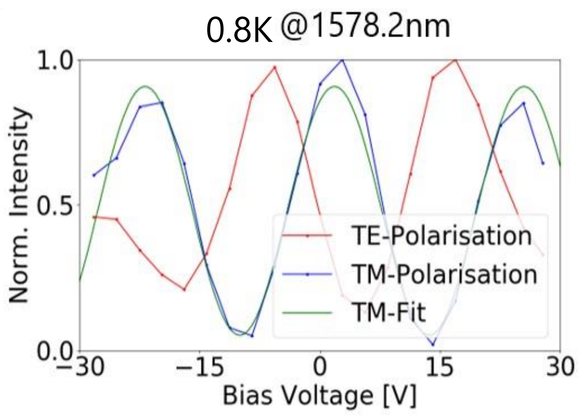


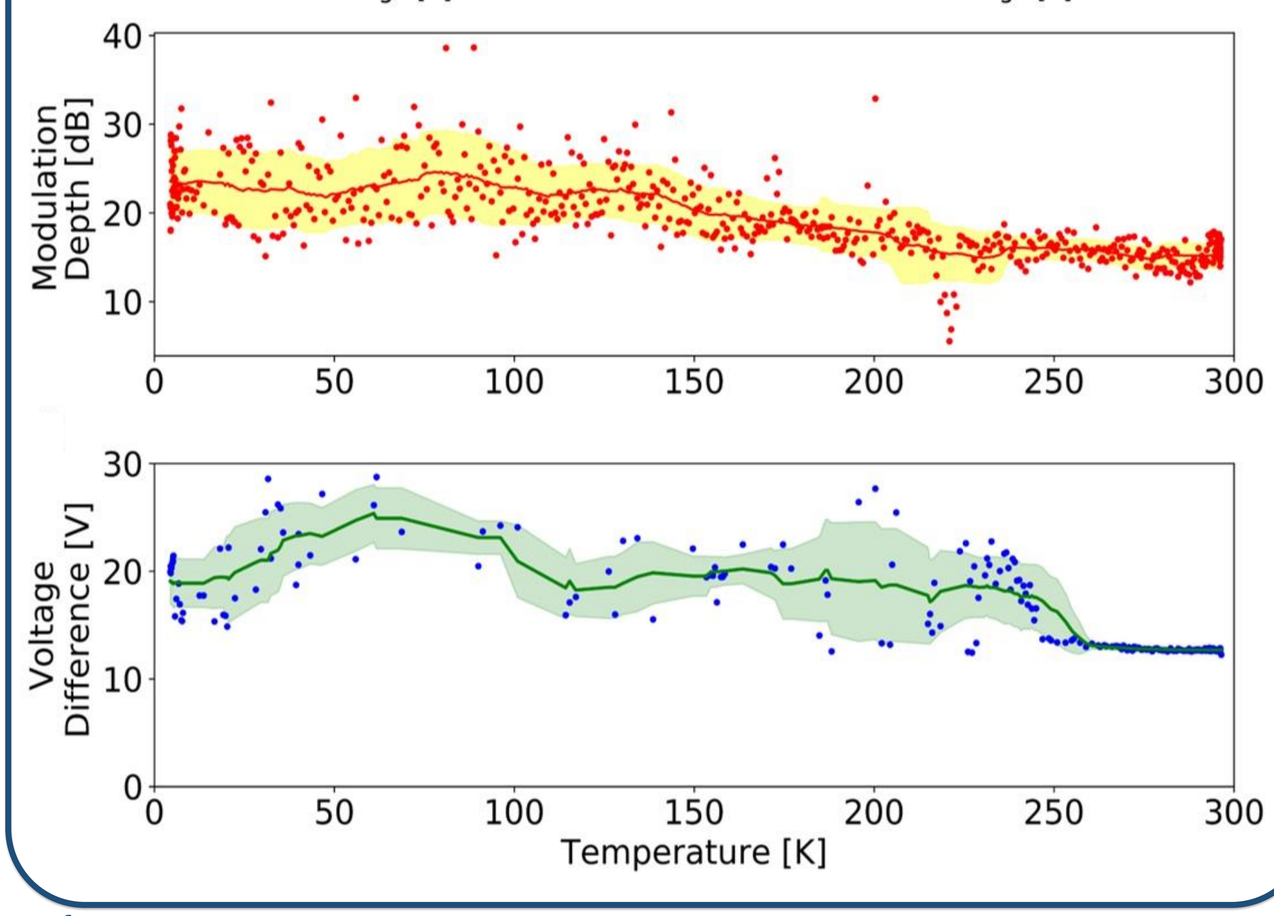

## 5) Polarisation Converter



- 23dB modulation depth
- 43% fibre-to-fibre transmission




References

1. P. Sharapova et al, New J. Phys. **19**, 123009 (2017)
2. J.P. Höpker et al, APL Photonics **4,** (2019)
3. S. C. Abrahams, The Institution of Electrical Engineers, London, (1989)

Bundesministerium für Bildung und Forschung

German Federal Ministry of Education and Research, funding program Photonics Research Germany, contract number 13N14911

# Design of an Integrated Optical Circuit for Generation of Optical Vortex

**Mihai Kusko, Rebeca Tudor, Stefan Caramizoiu, Cristian Kusko**
National Institute for R&D in Microtechnologies IMT-Bucharest, 126A Erou Iancu Nicolae Str., Voluntari, 077190, Romania e-mail: mihai.kusko@imt.ro

**ABSTRACT**

**We present the results of design studies on an integrated optical circuit able to generate optical vortex by superposition of the two first order modes on the horizontal and vertical direction, respectively. The vertical first order mode has been excited by a discontinuity on the vertical direction, the separation of this mode by the remaining fundamental mode has been obtained via a directional coupler. Another very short directional coupler has been employed to transfer the fundamental mode into a first order mode of a larger waveguide. The vertical and horizontal first order modes has been recombined in order to produce an optical vortex.**

## LAYOUT

**The configuration of the integrated optical circuit illustrated in Fig 1 is generated by the OptiBPM software 3D viewer. There are three distinctive zones. We consider silicon nitride waveguides (n = 2) embedded in silicon dioxide (n= 1.46). In zone A, there is the input waveguide having a rectangular shape 400 nm thick and 400 nm wide such that it allows only three modes to operate at 635 nm wavelength - the fundamental mode, the first order mode on the vertical direction and the first order mode on the horizontal direction. One can notice that the input waveguide presents a a height discontinuity of 220 nm in order to excite the first order mode on the vertical direction.**

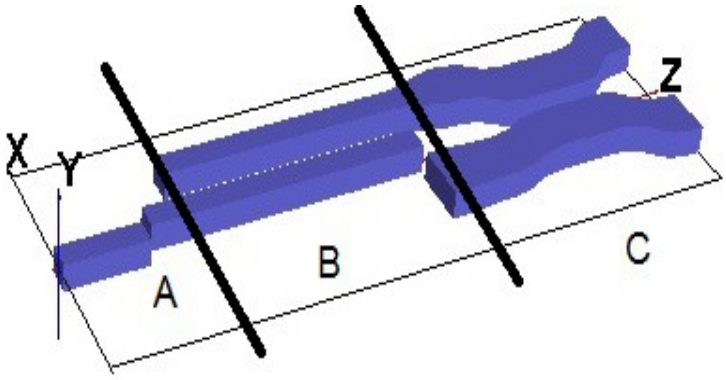



**Fig.1**

## RESULTS

**The radiation propagating in the input waveguide as the fundamental mode is equally split into the vertical mode and the fundamental mode by the discontinuity 220 nm. The two modes generated in zone "A" are separated in the zone "B" via a symmetrical directional coupler with its length and separation distance adjusted such the vertical order is completely transferred in the lateral left waveguide, while the fundamental mode remains in the input waveguide. The fundamental mode remained in the input waveguide is laterally coupled in a large waveguide as the horizontal first order using matching of fundamental mode of the input waveguide with horizontal first order mode of the larger waveguide. Once the two first order modes are generated at the end of "B" zone, they are recombined in another directional coupler ("C" zone). At the end of the simulation layout one can notice the generation of the optical vortex. The radiation propagation through the circuit is represented in Fig. 2, and the field configuration at the end of the computational domain showing an optical vortex is represented in Fig. 3.**

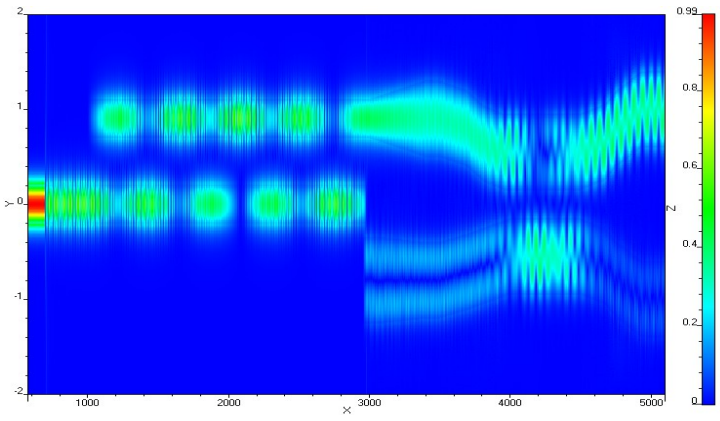


**Fig .2**

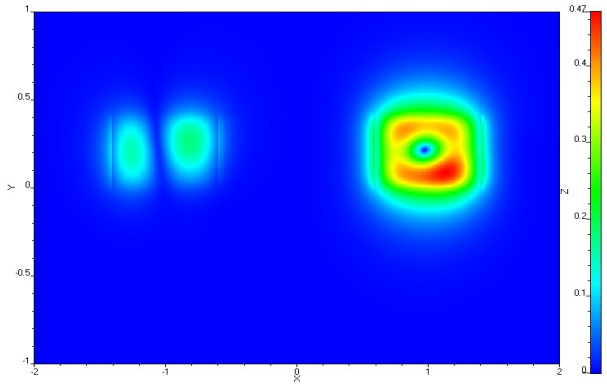


**Fig. 3**

**ACKNOWLEDGEMENTS**

The authors acknowledge support from a grant of the Romanian Ministry of Research and Innovation, PCCDI UEFISCDI, project number PN-III-P1-1.2-PCCDI-2017-0338/79PCCDI/2018, within PNCDI III.

EUROPEAN CONFERENCE ON INTEGRATED OPTICS June 2020

**PASSION:** Photonics technologies for ProgrAmmable transmission and switching modular systems based on Scalable Spectrum/space aggregation for future agIle high capacity metrO Networks

TU/e EINDHOVEN UNIVERSITY OF TECHNOLOGY

# Compact InP Wavelength Blocker based on a Single AWG and SOA gates for Metro Networks

Netsanet Tessema, Kristif Prifti, Aref Rasoulzadehzali, Ripalta Stabile, Nicola Calabretta

Institute for Photonic Integration, Eindhoven University of Technology, The Netherlands

Institute for Photonic Integration
Materials • Devices • Systems

PASSION

HORIZON 2020

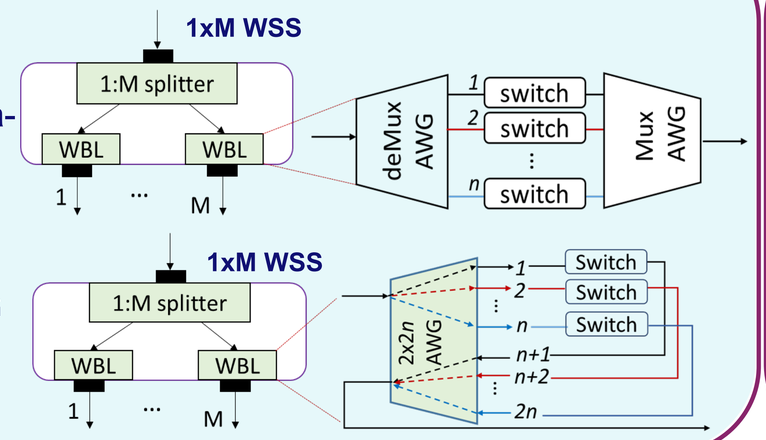
## I . Introduction

### Traditional Wavelength blocker (WBL)

- Based on two AWGs and soa-gates
- Centeral wavelength mismatch

### Proposed novel WBL

- Folded: based on a single AWG
- Scalable:
  - Modular and compactness



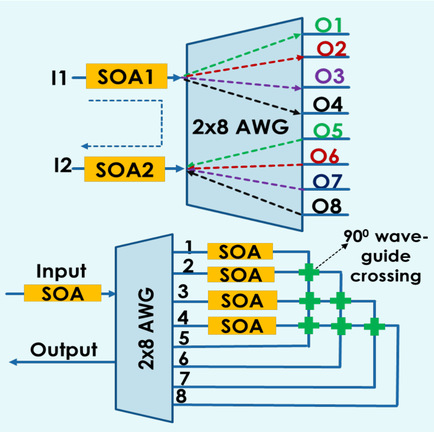

## II. Proof of concept PIC implementation : folded WBL

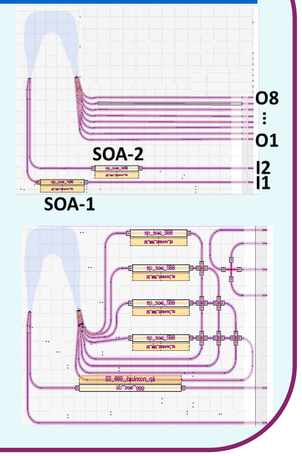
### 2x8 AWG

- Ch1 (O1,O5)
- Ch2 (O2,O6)
- Ch3 (O3,O7)
- Ch4 (O4,O8)

### Folded WBL

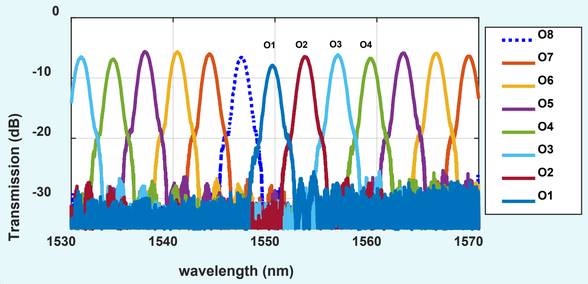
- 4 –SOA gates
- waveguide crossing



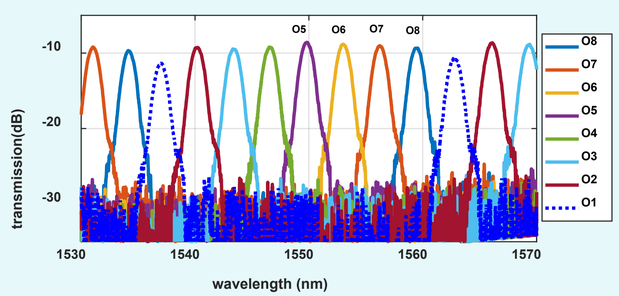




## III. PIC characterization

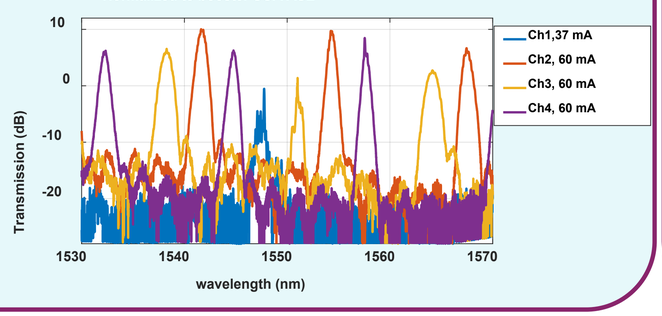
### 2x8 AWG, I1




### 2x8 AWG, I2



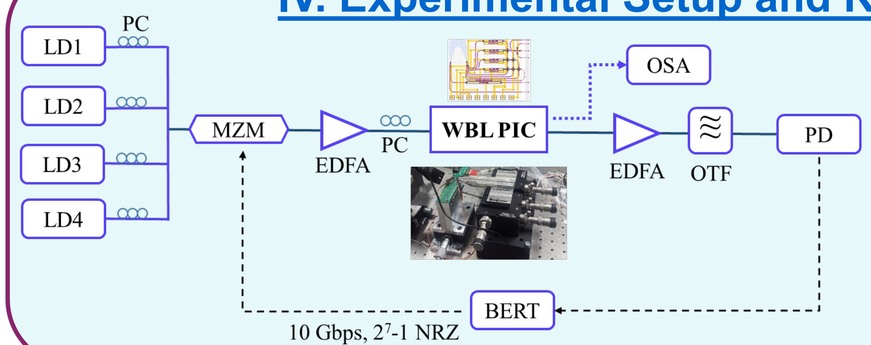

### Folded WBL

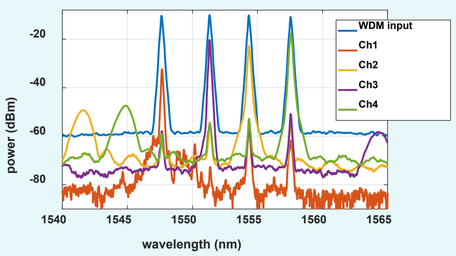



## V. Conclusion

- Experimental verification of a novel WSS design
- supports scalability by reducing footprint
- Low-loss operation enabled by booster SOAs

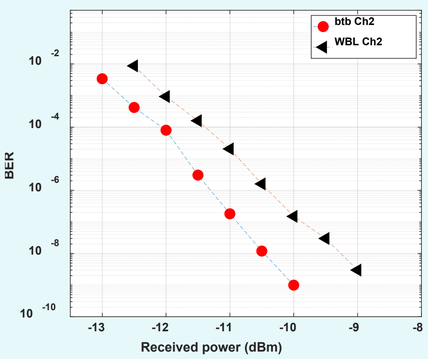
## IV. Experimental Setup and Results

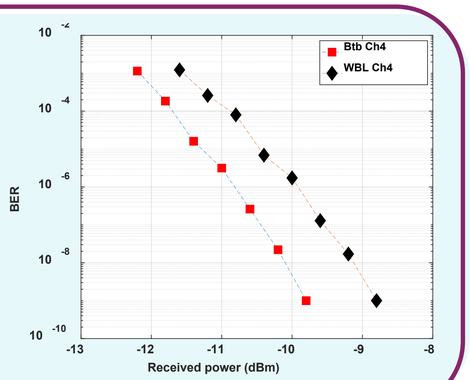



### 10 Gbps OOK transmission

- Error free operation
- Penalty 1 dB for Ch2 and 1.3 dB for Ch4



# Enhanced Optical Readout in Resistive Memory Through Plasmonic Amplification

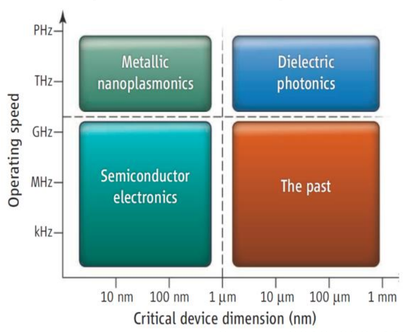
Lalit Singh[1], Rahul D. Mishra[1], Swati Rajput[1], Sourabh Jain[1], and Mukesh Kumar[1,2]

[1]Optoelectronic Nanodevice Research Laboratory, Electrical Engineering, Indian Institute of Technology Indore, India

[2]Centre of Advanced Electronics,

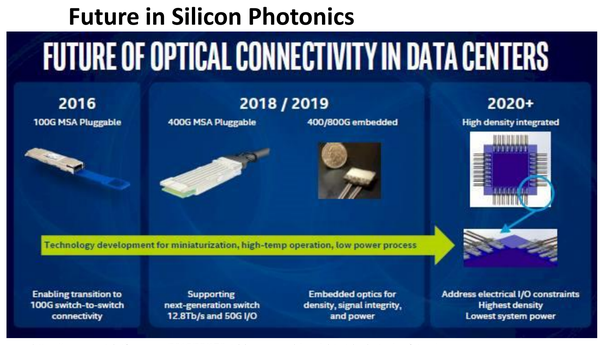
**Abstract:** An electrically writable resistive switch with optical readout capability is proposed with a high extinction ratio of 16 dB utilizing plasmonic amplification in InGaP. The proposed device operating at 1550 nm wavelength shows an optical gain of 2.4 dB. The optical readout is less error prone and has low energy consumption then it's electrical counterpart. The high index layer, bottom electrode material, provide dual benefits: low loss waveguiding of light and electrical rectification. The device can find applications in optical interconnects, optical modulation, memory and neuromorphic computations

**Importance of nanophotonics**




*Science, 2010, 328, 440*

**Future in Silicon Photonics**




https://www.nextplatform.com/2016/08/17/intel-leverages-chip-might-etch-photonics-future/

## Requirement of Optical Processors

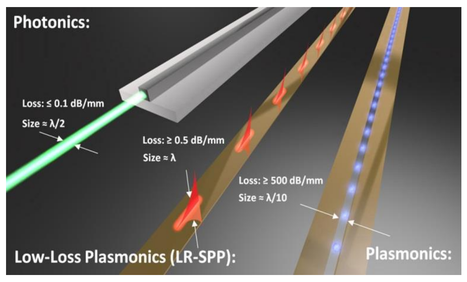
- Optical Interconnects
- Large-scale photonic integration
- Compact on-chip devices
- Nanophotonics

## Compact Devices with Tuning

- Electrical control
- Tunable delay
- Low power tuning

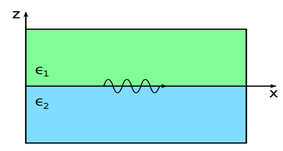
***Control and Manipulation of light at nanoscale remains an important requirement***

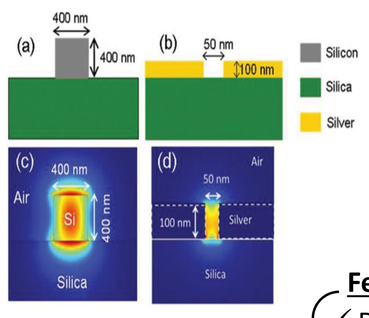
## Plasmonics Waveguide




*N. Kinset et. al. http://spie.org/newsroom/5462-a-platform-for-practical-plasmonics.*

- Surface Plasmon Polaritons (SPP) are electromagnetic excitations
- Propagating at the interface between a dielectric and a conductor




M. Z. Alam, J. S. Aitchison and M. Mojahedi, Laser & Photonics Reviews, 8, 394-408, 2014.

### Issues with Plasmonic Devices

- Short-life to serve as a basis for computer chips
- Large propagation loss & weak confinement
- Small Coupling efficiency

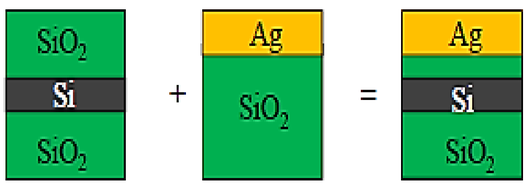
### Major concern:

- Diffraction limited Device size
- Complex Tuning scheme

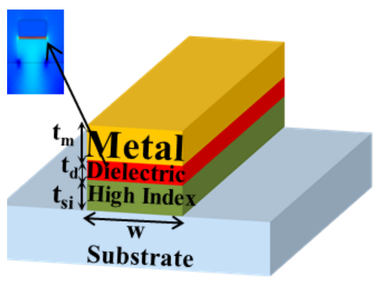
### Features/Applications

- ✓ Devices for Optical Communications
- ✓ Tight Control on Optical properties
- ✓ Slow-light Devices
- ✓ Bio-chemical Sensors

## Hybridization of photonic and plasmonic mode



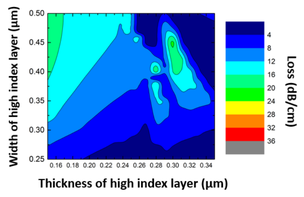

*Oulton et al., 2008,Nature Photonics*




- ❑ Optical mode + SPP mode => Hybrid plasmonic waveguide
- ❑ Dragging SPP mode deep into Dielectric/Semiconductor

### Hybridization controlling elements

- ➢ Thickness and width of high index layer where leaky optical mode resides
- ➢ Thickness of dielectric layer
- ➢ Optimized thickness found out to be 10-nm for dielectric layer.

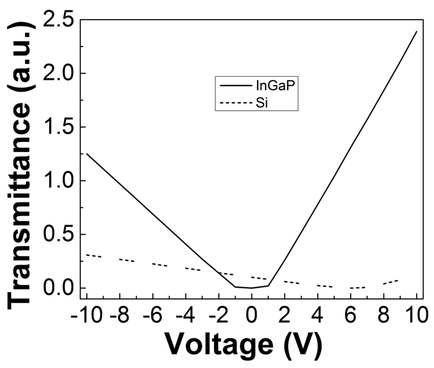



### Findings

- ➢ Good Fabrication tolerance
- ➢ Smaller mode area ($\lambda^2/270$)
- ➢ Subwavelength dimensions
- ➢ Longer propagation

## Loss Compensation using material again and Electron Injection

- ➢ Due to large metallic losses amplification is required
- ➢ To reduce losses
  - ✓ Pushing electrons away from metal surface
  - ✓ Increase number of electrons in dielectric layer
  - ✓ Increasing number of electrons near semiconductor dielectric interface
  - ✓ Using of gain material

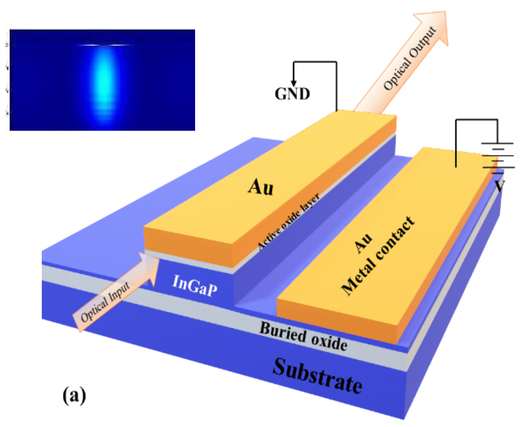


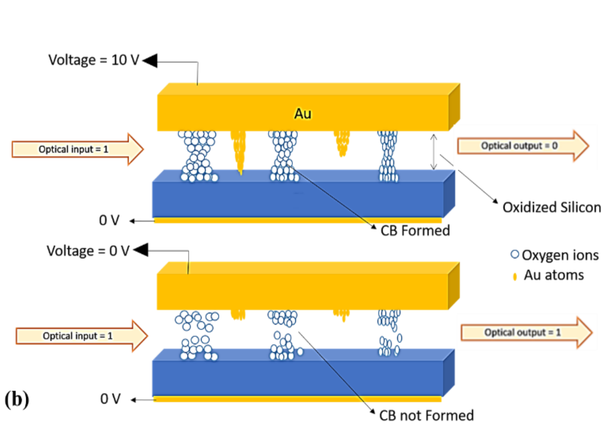

***Material gain + electrons Injection = amplified SPP***

Features & Applications:

- ❑ Phase modulation provides 670-µm of π shift
- ❑ Optical gain of 2.39 dB/cm of intensity
- ❑ With silicon gain is less than 0.5

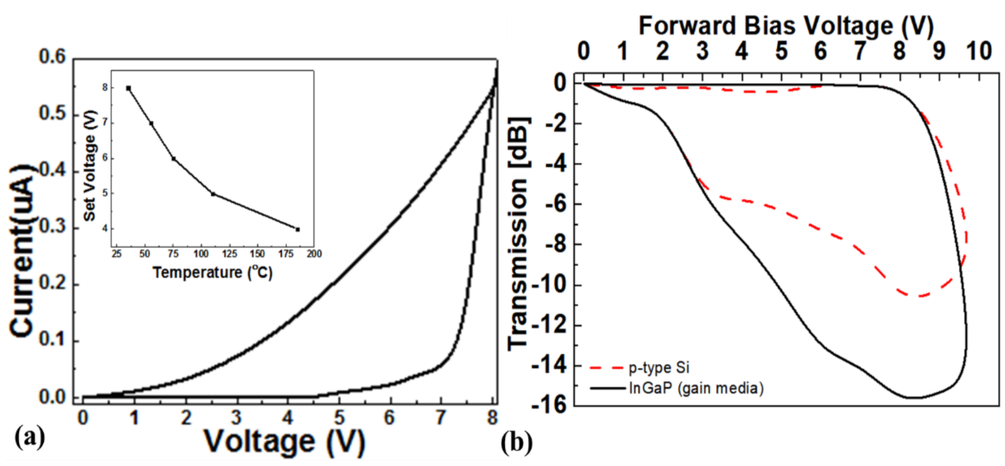
## Optical Readout in Resistive Memory




### Features

1. Optical readout of resistive switch
2. High endurance (comparing to other optical readout based devices)
3. Self rectifying (enables low leakage current high density fabrication)
4. Application in neuromorphic computation
5. 16 dB optical extinction ratio (6dB better then no amplification)
6. Low power consumption: 0.15pJ (over one readwrite cycle)
7. Frequency checked 2MHz
8. Two techniques for work: Valency change effect + Electrochemical Metallisation




## References

1. M. A. Zidan, J. P. Strachan, and W. D. Lu: The future of electronics based on memristive systems, Nat. Electron. Vol. 1, pp. 22, 2018.
2. R. F. Oulton, V. J. Sorger, D. Genov, D. Pile, and X. Zhang: A hybrid plasmonic waveguide for subwavelength confinement and long-range propagation, Nat. Photonics vol. 2, pp 496, 2008.
3. L. Singh, T. Sharma, and M. Kumar: Controlled hybridization of plasmonic and optical modes for low-loss nano-scale optical confinement with ultralow dispersion, IEEE J. Quantum Electron., vol. 54, pp 1–5, 2018.
4. Emboras, I. Goykhman, B. Desiatov, N. Mazurski, L. Stern, J. Shappir, and U. Levy: Nanoscale plasmonic memristor with optical readout functionality, Nano letters vol. 13, pp. 6151–6155, 2013.
5. L. Singh, S. Jain and M. Kumar, "Electrically Writable Silicon Nanophotonic Resistive Memory with Inherent Stochasticity, Optics Letters, Vol. 44, Issue 16, pp. 4020-4023, 2019.

## Summary

- ➢ Confinement at real nano-scales
- ➢ Optical readout of resistive memory
- ➢ SPP amplification is possible with material gain and population inversion
- ➢ Application in on chip optical modulation at nanoscale

## Acknowledgment:

The author acknowledge the financial support by DST Nano Mission DST/NM/NT/1009/2017(G) and Council of Scientific and Industrial Research CSIR(22/814/19/EMR-II).

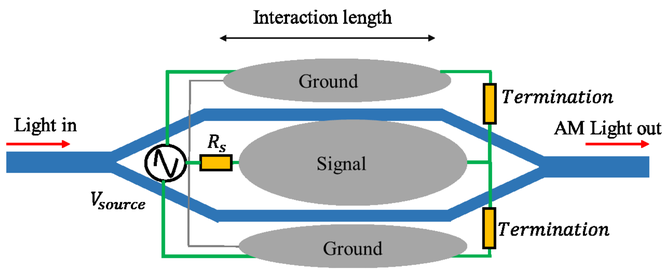
# Side Mode Suppression Ratio Reduction in Mach-Zehnder Modulators Using Slow-Light Waveguides

Reza Hosseini[1,3], Shahryar Sabouri[1], Arijit Misra[2], Stefan Preußler[2], Thomas Schneider[2], and Kambiz Jamshidi[1,*]
[1] Integrated Photonic Devices Lab, Chair of RF, Technische Universität Dresden, 01062 Dresden, Germany
[2] Terahertz-Photonics Group, Institut für Hochfrequenztechnik, TU Braunschweig, Schleinitzstraße 22, 38106 Braunschweig, Germany
[3] SIMULIA Solution Consultant at Dassault Systemes Deutschland GmbH
* kambiz.jamshidi@tu-dresden.de

- To generate high-frequency micro- or millimeter wave signals, higher harmonics of an intensity modulator can be superimposed in a photodiode. Usually, this requires very high RF input powers.
- Slow-light waveguides are investigated to reduce the side mode suppression ratio (SMSR) of reverse-biased silicon Mach-Zehnder modulators (MZM) in simulation and experiment.
- It is reported that the SMSR of single arm-biased modulators can be decreased by more than one order of magnitude at a slow-down factor of 5. This enables the reduction of SMSR without the need for high RF powers.

## Side Mode Suppression Ratio in MZMs

The optical output of an MZM can be written as:




$$E_o = A(t)e^{j2\pi f_{opt}t}\left[e^{-\alpha_1 L_1}e^{j\pi\frac{V_{ap1}}{V_{\pi 1}}} + e^{-\alpha_2 L_2}e^{j\pi\frac{V_{ap2}}{V_{\pi 2}}}\right]$$

where *A(t)* is the time-domain shape of the input optical signal, $V_{ap} = V_{dc} + V_{ac}$ is applied voltage, $f_{opt}$ is the optical frequency, $L_i$ and $\alpha_i$ is the length and loss coefficient of the modulator at arm *i*, respectively. Due to simplicity, we assume $\alpha_1 = \alpha_2 = \alpha$, $L_1 = L_2 = L$, $V_{ap1} = V_{dc} + V_m\sin(2\pi f_{RF}t)$, and $V_{ap2} = V_{dc}$. After Jacobi Anger expansion, the detected signal at the photodiode can be found as:

$$I(t) = E_o(t)E_o(t)^* =$$

$$2A(t)^2 e^{-2\alpha L}[1 + B\,\mathrm{J}_0(C) + 2B\sum_{n=1}^{\infty}J_{2n}(C)\cos(2n\omega_m t) - 2D\sum_{n=1}^{\infty}J_{2n-1}(C)\sin((2n-1)\omega_m t)]$$

In which:

$$B = \cos\left(\pi V_{DC}\left(\frac{1}{V_{\pi 1}} - \frac{1}{V_{\pi 2}}\right)\right) \quad C = \left(\frac{\pi V_m}{V_{\pi 1}}\right) \quad D = \sin\left(\pi V_{DC}\left(\frac{1}{V_{\pi 1}} - \frac{1}{V_{\pi 2}}\right)\right)$$

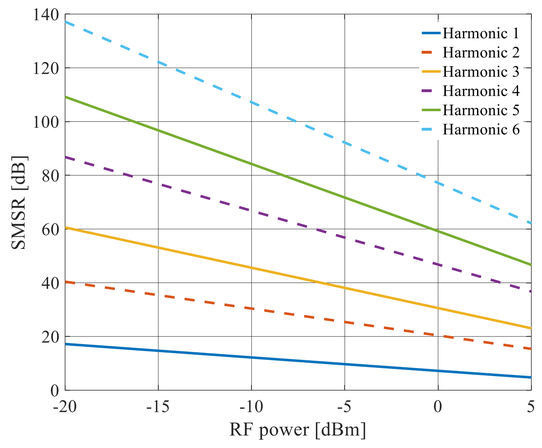
and $J_n(x)$ is the Bessel function of the first kind.

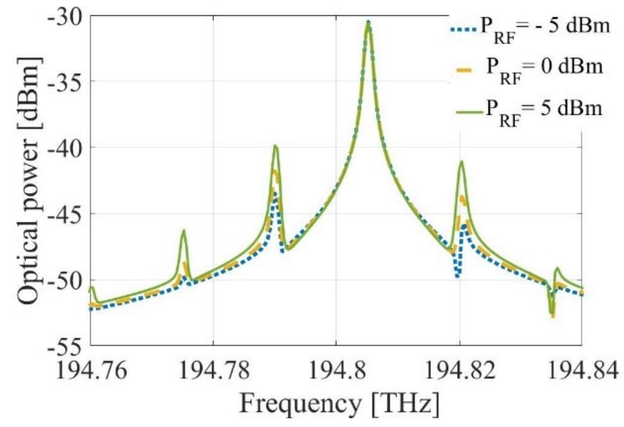
SMSR is defined as the ratio of the DC component to even and odd components of the output current of the photodiode.

$$SMSR|_{even} = \frac{1 + BJ_0(C)}{2BJ_{2n}(C)} \qquad SMSR|_{odd} = -\frac{1 + BJ_0(C)}{2\sqrt{1-B^2}\,J_{2n-1}(C)}$$

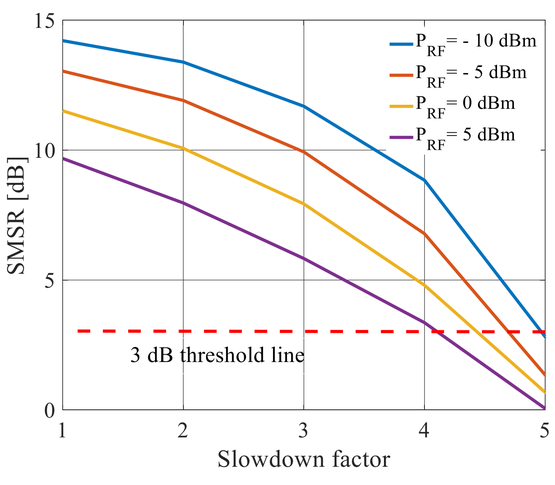
## Simulation and Experimental Results

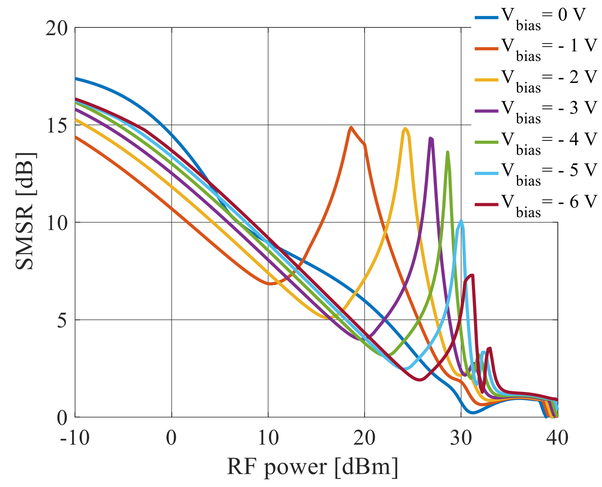
The parameters of the modulator used in the simulations are $N_A$=$N_D$=$5 \times 10^{17}\ cm^{-3}$ as acceptor and donor doping, $L_1$=$L_2$=1 mm and a DC bias voltage of $V_{DC}$=-2 V. The modulation frequency is $f_{RF}$ =15 GHz.




SMSR of different harmonics versus RF power on the left, and simulation and measurement results for the generation of the first two harmonics on the right.




Enhancement of the SMSR using the slow-light effect, quantified by the slow-down factor on the left and the required RF power for reducing the SMSR of a standard MZM on the right.

## Conclusion

- Slow-light modulators can decrease the required voltage for a π radian phase shift by increasing the slow-down factor.
- The SMSR decreases by an order of magnitude if the modulator is employed at a slow-down factor of 4 by using 15 dB less RF power at the same time.

Acknowledgements
This work is funded by the Deutsche Forschungsgemeinschaft (DFG, German Research Foundation) - JAM2401/11-2; SCHN716/15-2.

References
1. T. Schneider *et al.*: Investigation of Brillouin Scattering in Optical Fibers for the Generation of Millimeter Waves, *Journal of Lightwave Technology*, Vol. 24, pp. 295-304, 2006.
2. R. Hosseini *et al.*: Compact, High Extinction Ratio Silicon Mach-Zehnder Modulator with Corrugated Waveguides, in Proc. CLEO: Science and Innovations, Optical Society of America, 2018, paper SM3B-6.
3. R. Hosseini *et al.*: Energy Consumption Enhancement of Reverse-Biased Silicon-Based Mach–Zehnder Modulators Using Corrugated Slow Light Waveguides, *IEEE Photonics Journal*, vol. 10, no. 1, pp. 1-7, 2018.
4. M. Passoni *et al.*: Slow light with interleaved pn junction to enhance performance of integrated Mach-Zehnder silicon modulators, *Nanophotonics*, vol. 8, pp. 1485-1494, 2019.
5. J. Witzens: High-speed silicon photonics modulators, *Proceedings of the IEEE*, vol. 106, no. 12, pp. 2158-2182, 2018.

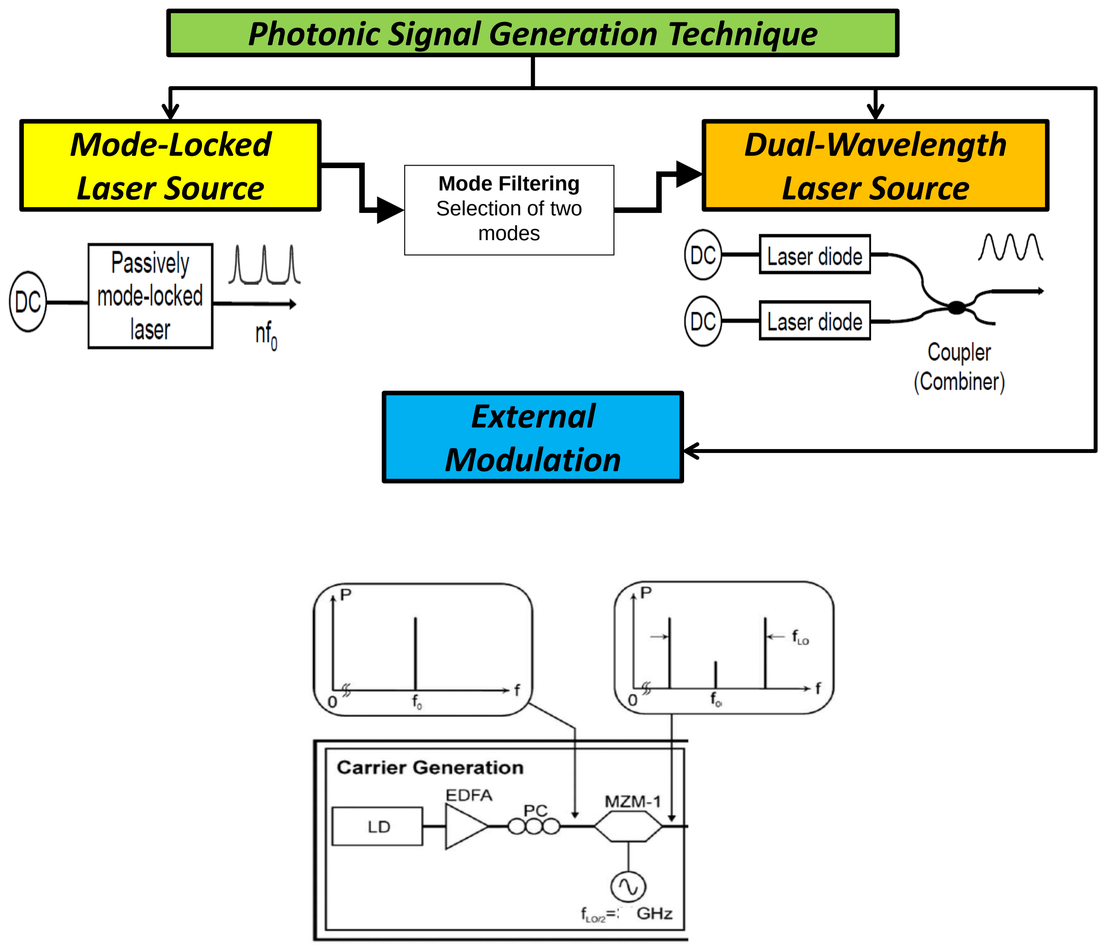
# Integrated Microwave Photonic Signal Generation System based on the External Modulation Technique

R. C. Guzmán, Alberto Zarxuelo, Jessica César, Mushin Alí, Jean Raphael Fernandez*, Oscar Valles*, Miguel Virseda*, Fernando Martín*, Luc Agustin** and G. Carpintero.
Universidad Carlos III de Madrid, *SENER, **SMART Photonics

## Introduction

**Microwave Photonics (MWP)** has evolved from the combination of photonics and radiofrequency engineering, to exploit the best of both in the generation, transmission and signal processing of high frequency signals, starting at the **microwave range (3 GHz to 30 GHz)**, which has evolved to include the **millimeter (30 GHz to 300 GHz)** and above

Some of the Photonic Technique for microwave signal generation are



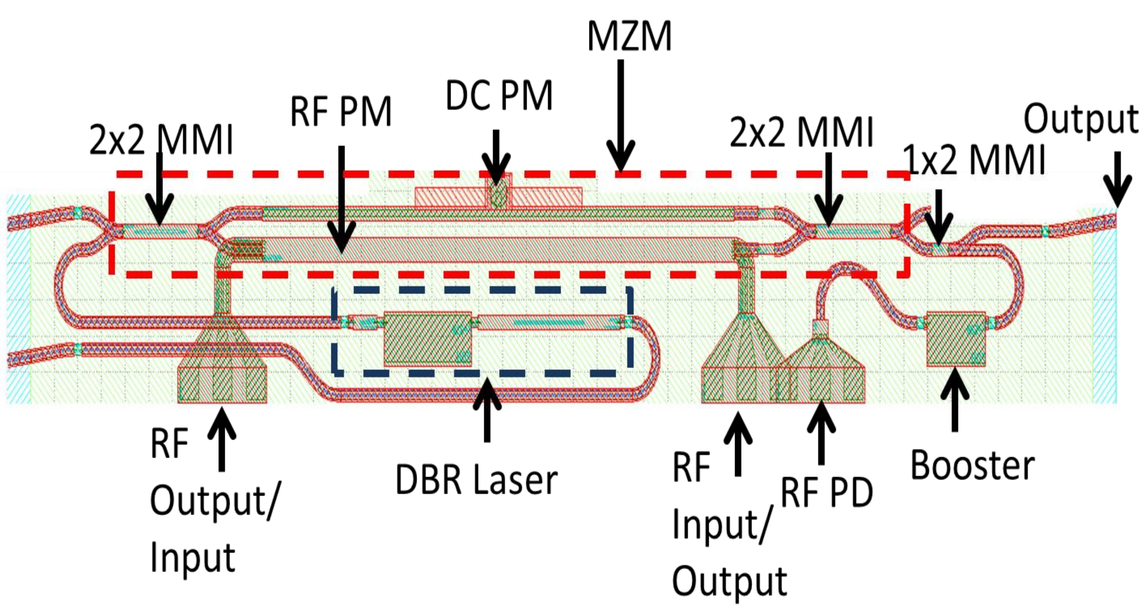

We present a **Photonic Technique** for the **Microwave Wave Signal (MMW)** generation based on external modulation using **Photonic Integrated Circuits (PIC)**, addressing size, cost, reliability and performance issues

## The Photonic Integrated Circuit

The **PIC is designed using a generic approach for InP-based PICs** and fabricated within a multi-project wafer (MPW) run by SMART Photonics, where standardized building blocks are provided for the selection of the optical components which form photonic transmitter source structure.

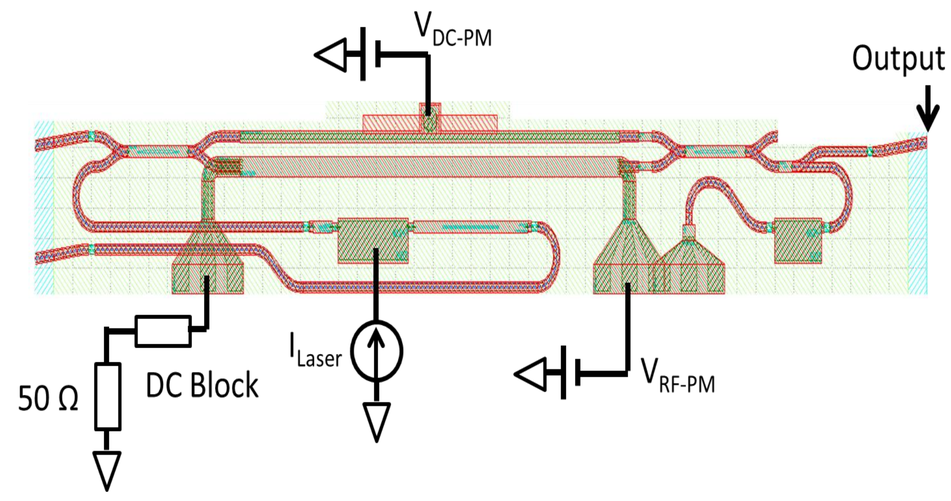
The PIC is composed of **DBR laser**, **Mach-Zehnder interferometer (MZM), boost amplifier, multimode interference (MMI) couplers, RF photodiode (PD)**, RF access tracks and straight/bent passive waveguides. The DBR laser structure is formed by a gain section and two mirrors located at the front and rear part of laser,

The **MZM interferometer structure has two arms** in which one of the arms has a DC phase modulator (PM) whilst the other arm has an RF PM. The RF PM arm allows us to inject an RF signal for the modulation of the optical signal supplied by the DBR laser. As for the DC PM is used for the setting of the MZM's biasing point, performing one of the four working points of the MZM's transfer function – **Null point, Maximum point, and +Q/-Q point.**

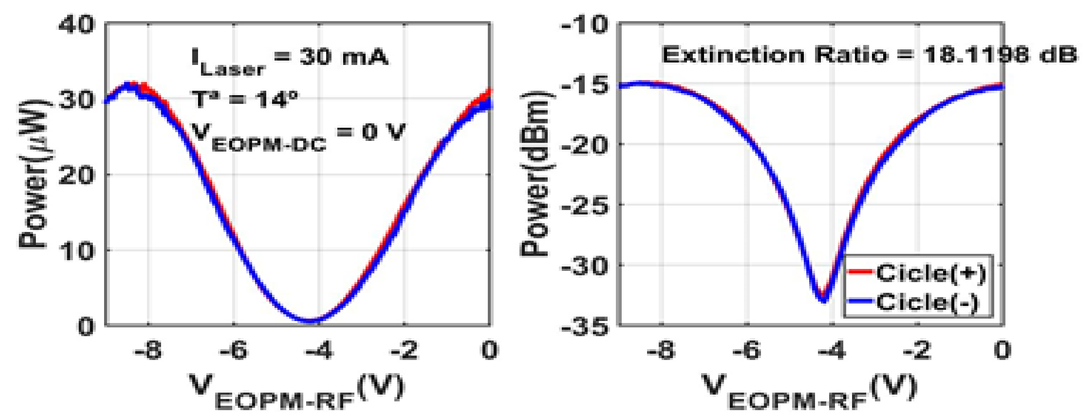



## Experimental Results

**Characterization of the MZM, transfer function.**

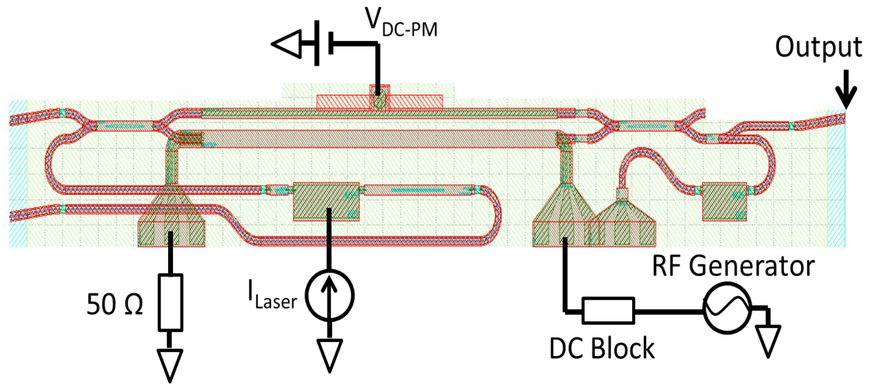


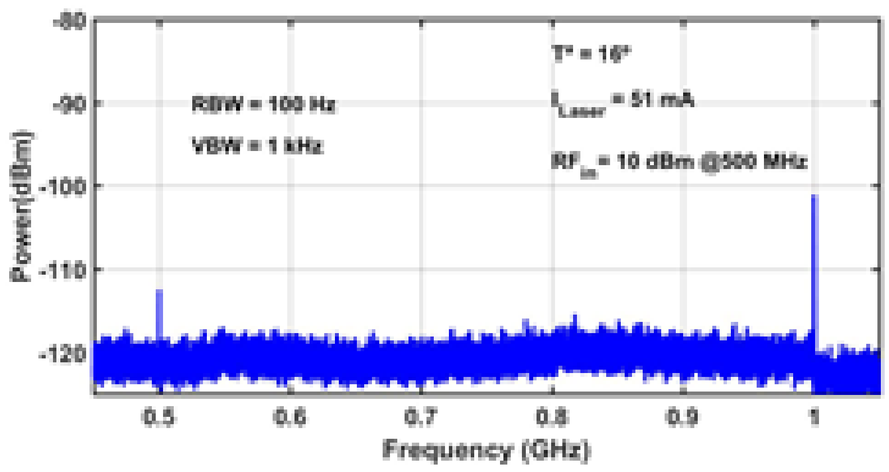

**MZM's Transfer function response** sweeping $V_{RF-PM}$ from 0 to -9 Vand fixing $V_{DC-PM}$ to 0 V.




### Microwave Signal Generation

The RF input of the RF-PM is connected to a DC block and followed by an external RF signal generator. An SMD 50 Ω resistor for matching of the RF signal is connected to the other end of the RF-PM. In order to achieve the second harmonic generation of the external RF signal injected into the RF-PM input, the DC_PM must be biased at null point mode (minimum transmission point). .




Electrical Response biasing the DC-PM at the Null Point

## Conclusions

**We show for the first time a photonic integrated circuit for signal generation, based on the external modulation technique,** including a semiconductor laser, optical modulator and photodiode on a single chip. We demonstrate that optical carrier suppress double sideband modulation allows us to multiply the RF signal injected into the device, doubling the output frequency. Due to low frequency probe accesses, this demonstration is limited to 500 MHz RF input. The 1 GHz signal on the photodiode inherits the quality of the signal from this reference oscillator and the power level can be furtherly improve with propertly RF probes.

## Acknowledgements

This work has been supported by **Spanish Ministerio de Economia y Competitividad** through Programa Estatal de Investigación, Desarrollo e Inovación Orientada a los Retos de la Sociedad (**grant iTWIT, TEC2016-76997-C3-3-R**), and by Comunidad de Madrid through Ayuda para la realización de doctorados Industriales ref. IND 2018/TIC-9617.

# Optical fiber-to-chip assembly process for ultra-low loss photonic devices based on silicon nitride for space applications

**A. Brimont[1], D. Zurita[1], V. C. Duarte[2], T. Mengual[2], B. Chmielak[3], S. Suckow[3], A. Giesecke[3], M. A. Piqueras[2], P. Sanchis[1]**

[1]Nanophotonics Technology Center, Universitat Politècnica de València, Camino de Vera s/n, 46022 Valencia, Spain

[2]DAS Photonics, Camino de Vera s/n, 46022 Valencia, Spain

[3]AMO GmbH, Otto-Blumenthal-Str. 25, 52074 Aachen, Germany

*e-mail: pabsanki@ntc.upv.es*

## ABSTRACT

In this work, we demonstrate an efficient fiber array-to-chip assembly process with a high number of input/output ports. The proposed approach is based on using a pre-alignment coupling structure to separately align the input and output ports. The assembling process has been experimentally validated in photonic integrated circuits fabricated with an ultra-low-loss waveguide technology based on silicon nitride, which features propagation losses as low as 9.5 dB/m. The developed technology is expected to extend the use of integrated photonics for space applications.

**Keywords**: silicon nitride, fiber-to-chip coupling, assembling, packaging.

## 1. INTRODUCTION

Photonic technologies may become key enablers to satisfy the flexibility, size, weight and power performance requirements for space applications [1]. The ability of photonics to handle high data rates, high frequencies and fast reconfigurability is critical for applications such as synthetic aperture radar space systems for next generation earth observation missions [2,3]. Photonics is a promising option for implementing beamforming networks based on true time-delay switching matrices [4,5]. When implementing true-time delay beamformers the signals are delayed instead of being phase shifted. This allows to have the correct phase shift for each frequency, and therefore, avoiding beam squinting and showing a broadband operation [6]. This type of beamforming also has the capability of performing multi-beam operation [7]. However, the use of photonics is currently restricted to a few demonstrations in non-critical equipment, due to their perceived immaturity compared to RF. One of the critical points is the mandatory need of an ultra-low loss photonic platform for minimizing the optical power budget and an efficient assembling process for optical fiber interconnection. In this work, an efficient fiber array-to-chip assembly process is proposed and demonstrated for interfacing ultra-loss photonic integrated circuits (PICs). The ultra-low loss PIC platform based on silicon nitride is firstly detailed. Then, the proposed assembly process is described and experimentally validated.

## 2. ULTRA-LOW LOSS PIC PLATFORM

The proposed PIC platform is based on the ultra-low loss photonic waveguide shown in Fig. 1(a). The core consists on a 2.8 µm wide and 100 nm high silicon nitride ($Si_3N_4$) waveguide, located on top of a 6 µm thick silicon dioxide ($SiO_2$) buffer layer that separates it from the silicon (Si) substrate. The waveguide core is covered by a 1.6 µm thick low temperature oxide (LTO) cladding layer. The simulated mode profile for TE polarization is shown in Fig. 1(b).

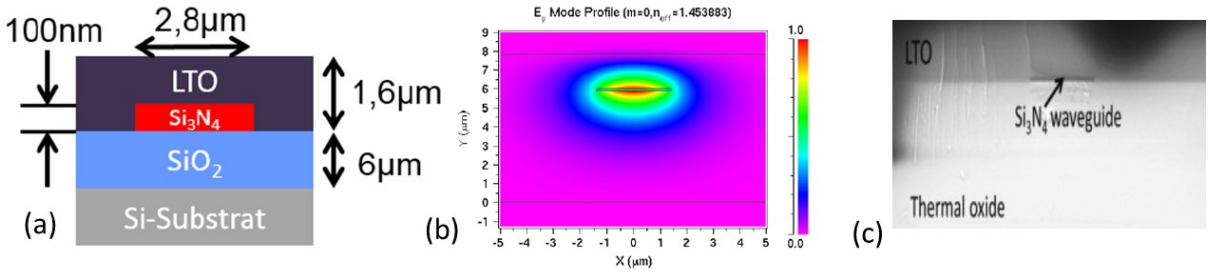



*Figure 1.(a) Ultra-low loss photonic waveguide cross-section, (b) simulated mode profile for TE polarization and (c) fabricated waveguide.*

The $Si_3N_4$ waveguide core was fabricated by low pressure chemical vapour deposition (LPCVD). The waveguide layer is defined via optical projection lithography with an i-line stepper tool and patterned via reactive ion etching

(RIE). An optimized RIE process is used, which yields steep and smooth sidewalls that are essential for low loss operation. After the etching step, the photoresist mask is removed using oxygen plasma and subsequently the LTO cladding material is deposited via LPCVD. Finally, the wafer is annealed at 1000°C for several hours, which is critical to improve the quality of the LTO layer and so ensuring low-loss operation. Fig. 1(c) shows a scanning electron microscope (SEM) image of the fabricated waveguide. The cut-back method was used to experimentally characterize the propagation losses. To achieve a good statistic, a full wafer featuring photonic waveguides with varying lengths from $1.5\,\mathrm{cm}$ to $109\,\mathrm{cm}$ was fabricated and characterized thoroughly, yielding ultra-low propagation losses of $9.5\,\mathrm{dB/m}$.

## 3. OPTIMIZATION OF FIBER-TO-CHIP ASSEMBLY PROCESS

### 2.1 Design of pre-alignment photonic structure for seamless fiber array coupling

A high number of input/output ports are usually required for supporting advanced multi-beam operation for space applications. Therefore, an efficient fiber-to-chip assembly process is necessary. A photonic structure, shown in Fig. 2(a), is proposed to carry out the pre-alignment procedure of the fiber array, which is then slightly moved to the functional ports of the photonic device. Grating couplers optimized for both positive and negative coupling angles ($\pm\,\theta$) are necessary. In such a way, the alignment of the fiber array at the input and output ports can be optimized separately. A configuration of 32 input/output ports is targeted. The proposed photonic structure is based on the interconnection of several ports by using directional couplers featuring a 1:99 splitting ratio. A low coupling ratio is desirable to achieve a similar optical power in all ports, which makes the optimization of the alignment process much more robust. Figure 2(b) shows the normalized output power by considering that the input signal is injected into port number #0 and considering that the optical power at the output ports is extracted by using a directional coupler with a coupling ratio of 1% and 10%. It can be seen that the power is lower for the smallest coupling ratio but turns out to be much more balanced (around $-20\,\mathrm{dBm}$) across each single output ports.

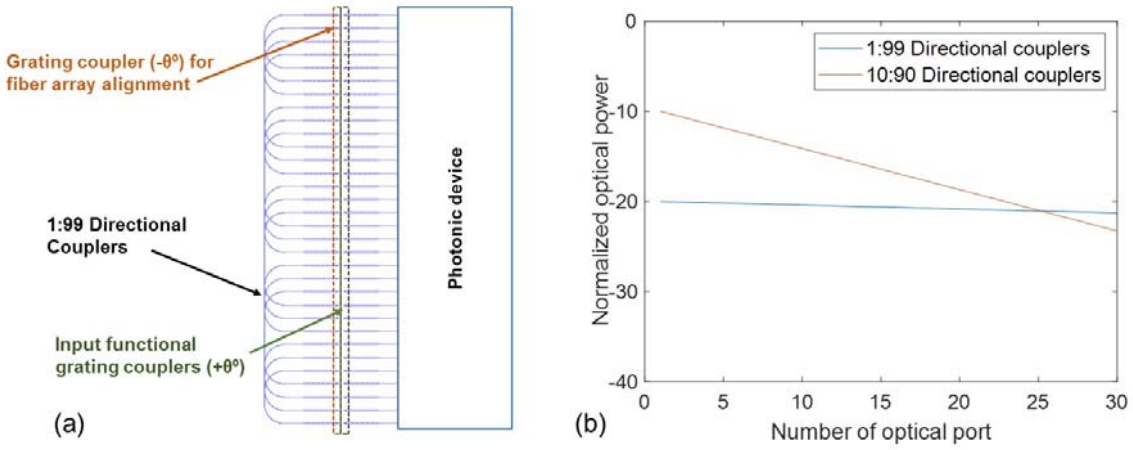



*Figure 2.(a) Proposed photonic structure for fiber array pre-alignment. (b) Extracted normalized output power at each optical port by using directional couplers with a* 1% *and* 10% *coupling ratio.*

### 2.2 Experimental demonstration of the assembly process

In the proposed approach of an efficient fiber assembly, low-loss grating couplers are a key building block to minimize the overall insertion loss of the assembled PIC. In the original grating coupler structure, coupling losses were as high as 10 dB [2]. Therefore, a new design was developed to reduce coupling losses by about a factor of two (in dB). A more detailed description of the final structure will be reported elsewhere.

An early photonic multiport waveguiding structure was fabricated to experimentally demonstrate the assembly process. The layout consisted of straight waveguides connected with the optimized grating couplers together with the proposed pre-alignment photonic structure. The fiber array is firstly aligned with the row of grating couplers, which couple light with a negative angle. Once aligned, each grating coupler become optically connected to the other ones via the 1:99 directional couplers, allowing us to measure an almost constant $-20\,\mathrm{dBm}$ output power across the grating couplers and seamlessly monitor the alignment process in situ. Once aligned, the fiber array is moved towards the functional grating couplers by a single translation.

Figure 3(a) shows an optical microscope image of the fabricated PIC. The measured spectra fiber-to-fiber at different ports are depicted in Fig. 3(b). Total fiber-to-fiber insertion losses of around 11.9 dB and 13.2 dB were measured, yielding $\approx$ 5.85 to 6.6 dB coupling losses per grating coupler (input/output ports 1-32, 20-13 and 32-1, $\theta > 0$). Grating couplers with a negative coupling angle ($\theta < 0$) were also designed by optimizing the grating period and filling factor. Similar coupling losses around 5.9 dB were experimentally validated. Fig 3(c) and Fig 3(d) show, respectively, the side and perspective views of the setup once the alignment procedure is completed.

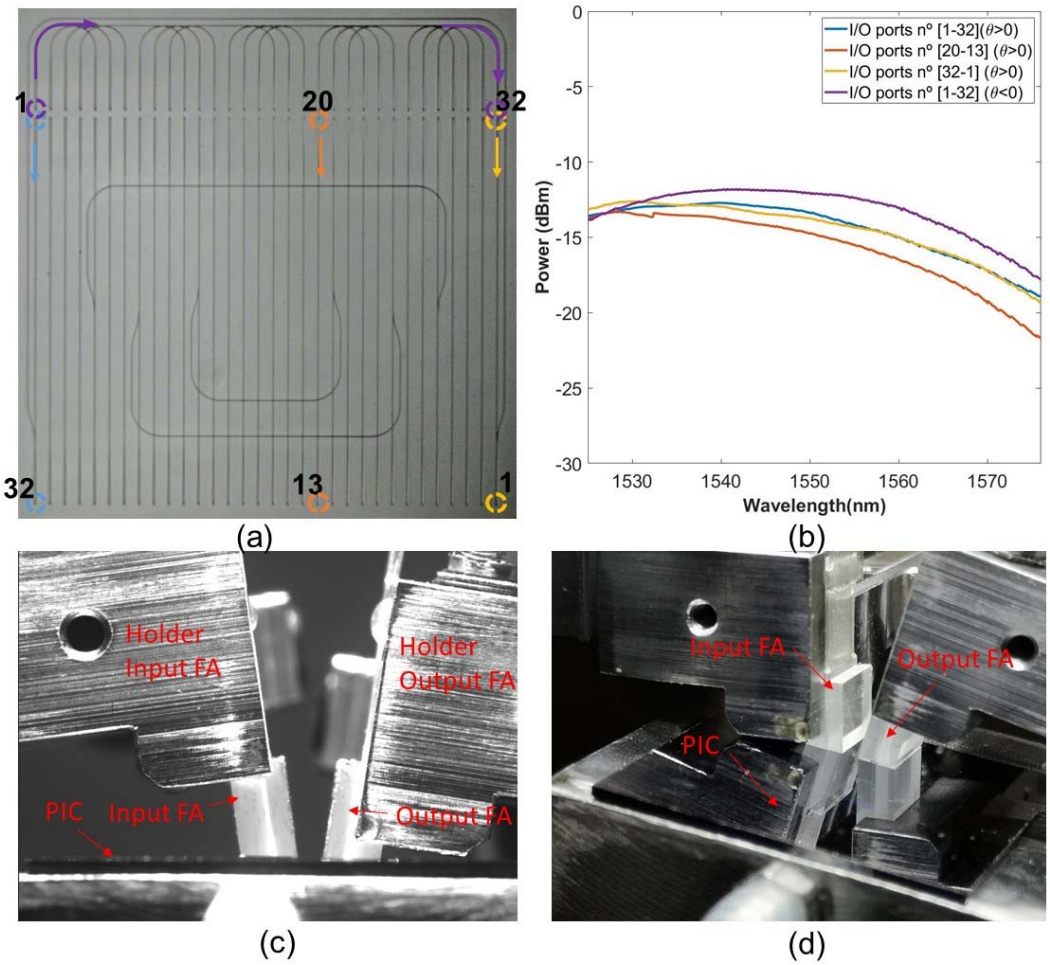



*Figure 3. (a) Optical microscope image of the PIC, (b) measured fiber-to-fiber spectra once aligned at different I/O ports, (c) side-view of the I/O fiber arrays and their respective holders and (d) perspective view the I/O fiber arrays and their respective holders.*

## 3. CONCLUSIONS

A fiber array-to-chip assembly process to optically interconnect ultra-low loss photonic integrated circuits with a high number of input/output ports has been demonstrated. The proposed approach is based on using pre-alignment photonic structures to ease the alignment process, hence allowing us to reduce the assembly time and cost. Low loss grating couplers have also been developed and demonstrated. The obtained results are a significant step forward towards the integration of photonic technologies for space applications.


## ACKNOWLEDGEMENTS

This work was supported by EU-funded H2020 project RETINA under grant agreement n° 821943.


## REFERENCES


[1] C. Ciminelli, F. Dell'Olio and M. N. Armenise: Photonics in Space: Advanced Photonic Devices and Systems, World Scientific, 2016.

[2] M. A. Piqueras, *et al.*: Photonic Front-End for the next-generation of space SAR applications, pp. 1152-1155, *in Proc. 45th European Microwave Conference (EuMC)*, Paris, France, Sep. 2015.

[3] http://www.retinah2020.eu/

[4] M. A. Piqueras, *et al.*: Optically beamformed beam-switched adaptive antennas for fixed and mobile broad-band wireless access networks, *IEEE Trans. Microw. Theory Tech.*, vol. 54, pp. 887–899, 2006.

[5] Y. Liu, *et al.*: Ultra-Low-Loss Silicon Nitride Optical Beamforming Network for Wideband Wireless Applications, *IEEE Journal of Selected Topics in Quantum Electronics*, vol. 24. pp. 1-10, 2018

[6] V. C. Duarte, M. V. Drummond and R. N. Nogueira: Photonic true-time delay beamforming system for a phased array antenna receiver, pp. 1-5, *SBMO/IEEE MTT-S International Microwave and Optoelectronics Conference (IMOC)*, Porto de Galinhas, 2015.

[7] V.C. Duarte, J. G. Prata, C. F. Ribeiro, *et al.*: Modular coherent photonic-aided payload receiver for communications satellites, *Nat. Commun.*, vol. 10, pp. 1984, 2019.

# First results on an electro-optic visible multi-telescope beam combiner for next generation FIRST/SUBARU instruments

G. Martin[a], M. Foin[a], F. Gardillou[b], C. Cassagnettes[b], G. Ulliac[c], N. Courjal[c], K. Barjot[d], S.Vievard[d], N. Cvetojevic[d], E. Huby[d], S. Lacour[d]
[a] Univ. Grenoble Alpes, CNRS, IPAG, F-38000 Grenoble, France
[b] Teem Photonics, F-38240, Meylan, France
[c] FEMTO-ST, Univ. Franche-Comté, Besançon, F-25030, France
[d] LESIA/CNRS, F-92195, Meudon, France

## ABSTRACT

Integrated optic devices are nowadays achieving extremely high performances in the field of astronomical interferometry, as shown by the PIONIER and GRAVITY instruments. Progress remains to be made in order to increase the number of apertures/beams/channels to be combined (up to 9) and eventually ensure on-chip phase modulation (for fringe temporal scanning). We present a novel generation of beam combiners, based on the hybridization of two integrated optic devices: (i) one producing glass waveguides, that can ensure very sharp bend radius, high confinement and low propagation losses, with (ii) a lithium niobate device providing phase modulators and channel waveguides that can achieve on-chip, fast (>100kHz) phase modulation. The aim of this work is to show our results on a hybrid device where splitting and phase modulation are achieved in the lithium niobate chip, coupled to a glass passive chip where all recombinations are done, to obtain interference fringes between the different inputs (i.e. telescopes or sub-apertures).

**Keywords:** integrated optics, visible interferometry, electro-optic modulation, Lithium Niobate, glass waveguides, Subaru Telescope, FIRST Instrument.

*guillermo.martin@univ-grenoble-alpes.fr; phone +33 4 76 63 52 76; www. ipag.osug.fr

## 1. INTRODUCTION

Integrated optic devices are nowadays achieving extremely high performances in the field of astronomical interferometry, as shown by the PIONIER [1] and GRAVITY [2] silica/silicon-based instruments, already installed at VLTI. Progress remains to be made in order to address other wavelengths (e.g. visible range), increase the number of apertures/beams/channels to be combined (up to 9) and eventually ensure on-chip phase modulation (for fringe temporal scanning). For that purpose, we have been working on a novel generation of beam combiners, based on the hybridization of two integrated optic devices: (i) one producing glass waveguides, that can ensure very sharp bend radius, high confinement and low propagation losses, with (ii) a lithium niobate device providing phase modulators and channel waveguides that can achieve on-chip, fast (>100kHz) phase modulation.

In this presentation we will report on our results for the transmission and modulation obtained with a beam combiner that has been developed in the context of FIRST/SUBARU 9T [3]. The prototype is based on a configuration where the phase modulation is obtained in a first-stage electro-optical modulator [4] prior to injection into the passive glass, where all the beams are recombined.

## 2. HYBRID BEAM COMBINER

This concept can be addressed by using an electro-optical waveguide [2]. We therefore studied a preliminary concept, where global phase modulation after splitting the input (each of the 9 inputs, split into 8), and subsequently phase modulated:

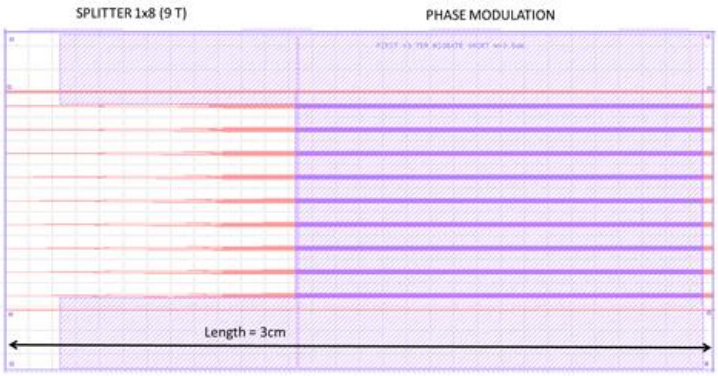



Fig. 1: Layout of the all electro-optical beam combiner. On the left, splitting each of the 9 inputs, followed by push-pull phase modulation (only a GND-Vapp signal is needed to control simultaneously all the phases).

The second stage is the passive beam combination:

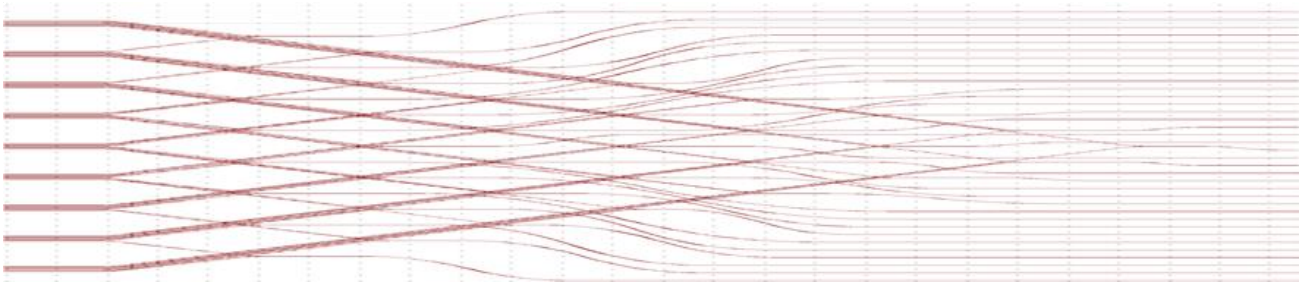


Fig. 2: Layout of the beam combination, achieved in a passive glass. On the left, the splitted 9 inputs, that will receive the phase modulated signal of stage 1 (Fig. 1), and recombine by pairs to obtain a final output of 36 signals.

The preliminary results on mode adaptation, transmission on each stage and global transmission of the hybrid device (after assembling the active and passive part) will be presented. Discussion on the efficiency of phase modulation and eventual crosstalk will be also presented. Some alternatives on reduced number of inputs (5 instead of 9) and other concepts (3D Laser Written beam combiners, in order to avoid in-plane crossings) will be discussed.

## 3. CONCLUSION & PERSPECTIVES

We have conceived, realized and characterized a hybrid 9T beam combiners allowing to simultaneously obtain the interference fringes of nine sub-apertures for future integration in the SUBARU/FIRST instrument. A hybrid device is for the moment the most promising instrument, that is currently being tested in the FIRST/SUBARU simulator at LESIA.

## 4. ACKNOWLEDGMENTS

Authors acknowledge the funding from ASHRA (Action Specifique Haute Resolution Angulaire) from INSU-CNRS, AGIR PEPS and ERC LITHIUM for funding the technological developments and realizations.

## 5. REFERENCES

[1] R. Abuter el al. “First light for GRAVITY: Phase referencing optical interferometry for the Very Large Telescope Interferometer”, Astronomy & Astrophysics, 602, A94, (2017).

[2] J.-P. Berger, et al., "PIONIER a visitor instrument for VLTI," Proc. SPIE 7734-114 (2010).

[3] E. Huby, G. Duchêne, F. Marchis, S. Lacour, G. Perrin, T. Kotani, É. Choquet, E. L. Gates, O. Lai and F. Allard “FIRST, a fibered aperture masking instrument”Astronomy & Astrophysics 560, A113 (2013).

[4] Martin, G., Heidmann, S.; Rauch, J.-Y., Jocou, L., Courjal, N. “Electro-optic fringe locking and photometric tuning using a two-stage Mach-Zehnder lithium niobate waveguide for high-contrast mid-infrared interferometry”. Opt. Eng. 53 (3), 034101 (2014).

# Guided-Wave, Electro-Optic Electric-Field Sensors Utilizing Ti Diffused Lithium-Niobate (Ti:$LiNbO_3$) Channel Waveguides

**Hongsik Jung**[1]
[1] Hongik University
*e-mail:* hsjung@hongik.ac.kr

**ABSTRACT**

This paper comprehensively reviews and compares Ti:$LiNbO_3$ integrated optic electric-field sensors, including the asymmetric Mach-Zehnder interferometer (MZI), 1 × 2 directional coupler (DC), and Y-fed balanced-bridge Mach-Zehnder interferometer (YBB-MZI), based on the operating principles, the dc/ac electrical and optical characteristics, and electric-field measurements for each fabricated device, respectively.

**Keywords**: integrated-optics, electric-field sensor, electro-optic effect, Ti:$LiNbO_3$ channel waveguide,

## 1. INTRODUCTION

Electro-optic electric-field sensors utilizing Ti:$LiNbO_3$ channel waveguides, being all-dielectric, present several intrinsic advantages compared to their electronic counterparts, such as noise immunity, compact size (a few millimeters), large bandwidth, feasibility of electrode-free operation, and consequently the possibility of operating even in harsh or dangerous environments. The optical fibers and dielectric electro-optic materials also produce minimal field distortion. In this paper we review and compare Ti:$LiNbO_3$ E-field sensors based on the electro-optic effect of lithium-niobate. Three types of E-field sensors were reviewed according to configurations, operating principles, fabrication, dc/ac characteristics, and various experimental results including E-field–sensed RF spectra, and frequency responses. [1]

## 2. FABRICATION and DEVICE THEORY and STRUCTURES

### 2.1 Fabrication of Ti:$LiNbO_3$ channel waveguide

The integrated-optic sensors were fabricated on X- or Z-cut $LiNbO_3$ substrate using standard photolithographic technique. Channel waveguides were formed by diffusing a 1050-Å-thick, 7.5μm-wide stripe of titanium film at 1050℃ in wet ambient. The substrate edges were optically polished to allow butt coupling and pig-tailing. A $SiO_2$ buffer layer ~3000 Å thick was deposited using e-beam evaporation and 99.99% pure $SiO_2$ pellets to prevent propagation loss caused by the optical absorption of the antenna metal. An aluminium dipole antenna electrode ~5000 Å thick was fabricated to allow sensing of the electric field. [1] Polarization maintaining single-mode and multi-mode optical fibers were attached to the input and output waveguides, respectively.

### 2.2 Asymmetric Mach-Zehnder Interferometer

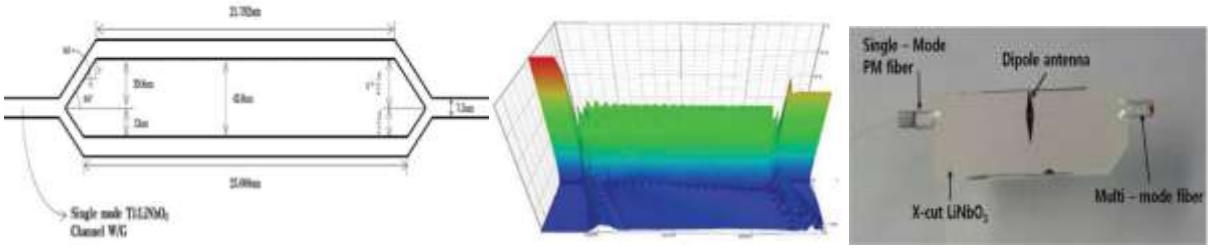



Fig. 1 (a) Schematic diagrams and dimensions, (b) BPM-CAD simulations, and (c) fabricated sensor module of Ti:$LiNbO_3$ asymmetric Mach-Zehnder interferometer.

A configuration of an asymmetric Ti:$LiNbO_3$ Mach-Zehnder interferometer and optical propagation BPM-CAD simulations are shown in Fig. 1. [2] The device was designed to have π/2 phase difference between its two arms through adjusting the path length difference, which makes the sensor have better linearity and sensitivity without a need for external bias to be applied. The device has a 3-dB input splitter and output combiner. The sensed E-field produces phase shifts in the light beam propagating in one of the parallel channel waveguide arms, thereby leading to a net phase shift between two light beams through each channel. When the two light beams recombine

at the output combiner, the phase modulation is converted to an amplitude-modulated signal at the same frequency as the sensed E-field. Therefore the light signal amplitude is proportional to the E-field strength.

### 2.3 1×2 Directional Coupler

A 1 × 2 directional coupler consists of a single-mode Y-junction splitter and a co-directional coupler with two parallel and symmetric waveguide channels. [3] The schematic diagram and its dimensions are shown in Fig. 2. Light is fed in and split into the two symmetric waveguides equally through the Y-junction region. The co-directional coupler guides the two single-mode light beams traveling along the two channels. With no modulating voltage applied, the coupler is set to the 3-dB operating point automatically due to the symmetric structure of the 1 × 2 directional coupler. While a driving voltage is applied through the electrodes over the coupler region, however, light can be coupled from one channel into the other. The 1 × 2 directional coupler modulator has two complementary optical outputs and, in general, is characterized by its interaction length (L), coupling conversion length (lc), and the phase mismatch of the propagation constant (Δβ) between the two arms.

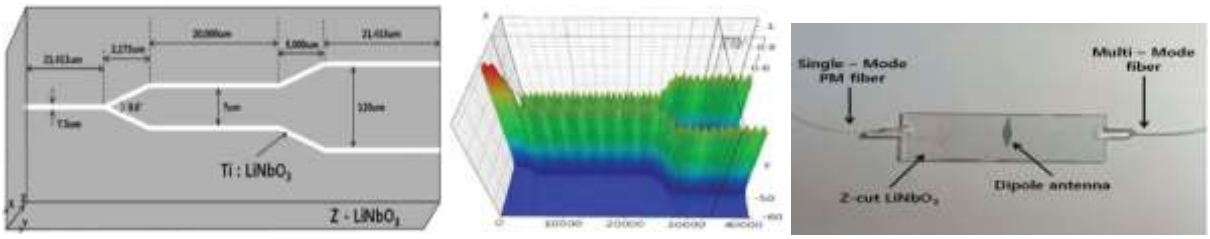



Fig. 2. (a) Schematic diagrams and dimensions, (b) BPM-CAD simulations, and (c) fabricated sensor module of Ti:$LiNbO_3$ 1×2 directional coupler.

### 2.4 1×2 Y-fed balanced bridge Mach-Zehnder interferometer

The YBB-MZI modulator consists of a 3-dB directional coupler at the output and has two complementary output waveguide as shown in Fig. 3. [4] This type of modulator provides a well-defined transfer function for the output optical power versus the detected electric-field intensity and can be automatically biased at the optimum 3 dB operating point due to its symmetrical structure, which offers a more tolerant design in the fabrication process than Mach–Zehnder interferometric modulators or 1 × 2 directional couplers, which are asymmetrical.

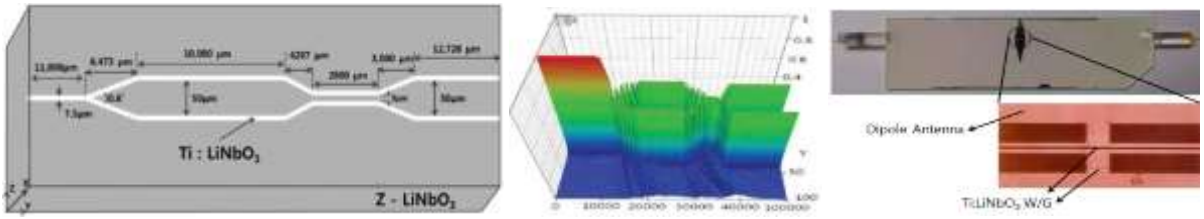



Fig. 3. (a) Schematic diagrams and dimensions, (b) BPM-CAD simulations, and (c) fabricated sensor module of Ti:$LiNbO_3$ 1×2 YBB-MZI interferometer.

## 3. DC/AC CHARACTERISTICS and E-FIELD SENSING

### 3.1 DC Characteristic Curve

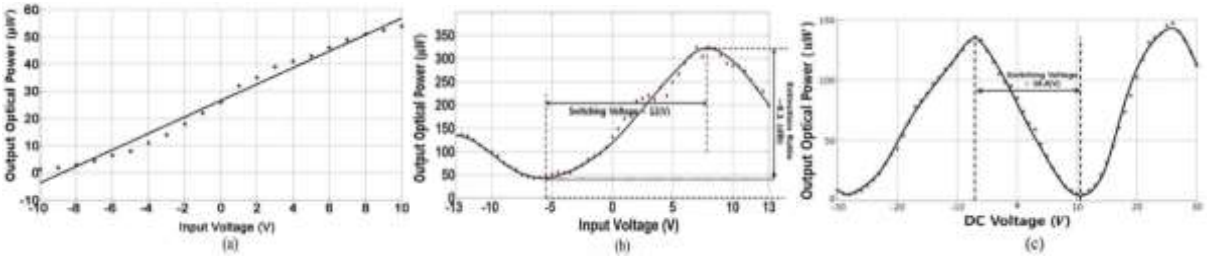



Fig. 5. Measured optical output power intensities versus applied dc voltage of (a) asymmetric Mach-Zehnder interferometer, (b) 1 × 2 directional coupler, and (c) 1 × 2 YBB-MZI interferometer.

### 3.2 AC Characteristics

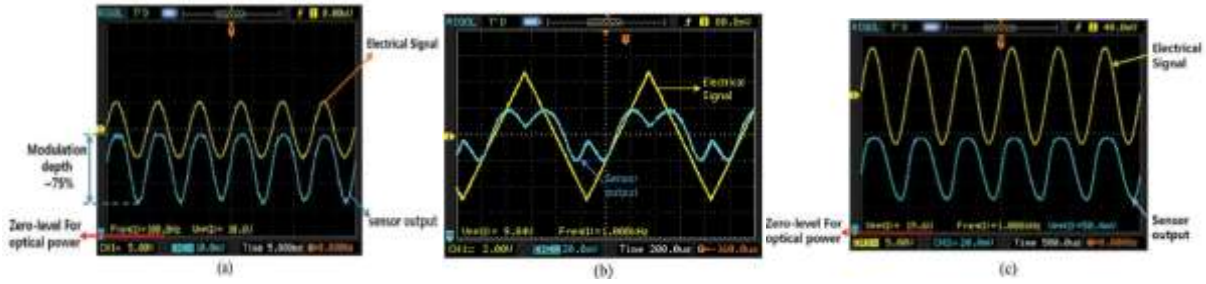



Fig. 6. The 1-kHz ac modulation responses of (a) asymmetric Mach-Zehnder interferometer, (b) 1 × 2 directional coupler, and (c) 1 × 2 YBB-MZI interferometer.

### 3.3 RF Sensing

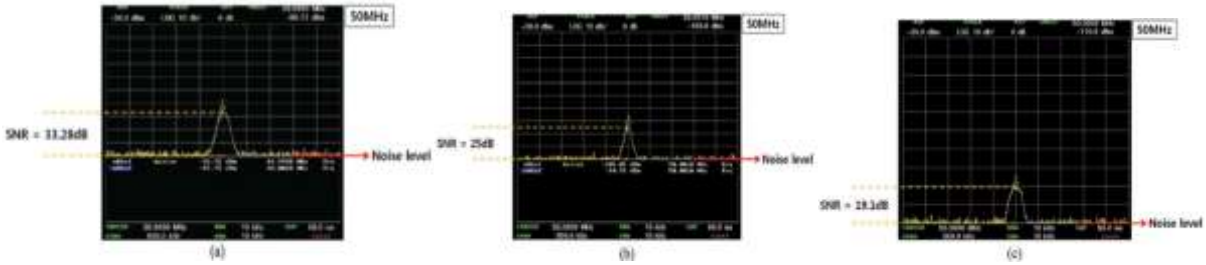



Fig. 7. The RF spectra of 50 MHz RF input signal into the TEM cell with a power level of 100 mW: (a) asymmetric Mach-Zehnder interferometer, (b) 1 × 2 directional coupler, and (c) 1 × 2 YBB-MZI interferometer.

.

## 4. CONCLUSIONS

The ac output characteristics of the asymmetric MZI interferometer show a modulation depth of ~75% at Vπ voltage of ~5.3 V. The minimum detectable electric fields are ~0.28 V/m and ~0.646 V/m, corresponding to a dynamic range of about ~32 dB and ~26 dB at frequencies of 20 MHz and 50 MHz, respectively. A dc switching voltage of ~12 V and an extinction ratio of ~8.1 dB were observed with the 1 × 2 directional coupler. The minimum detectable electric fields are ~0.99 V/m and ~1.67 V/m, corresponding to a dynamic range of about ~29.5 dB and ~25 dB at frequencies of 20 MHz and 50 MHz, respectively. A dc switching voltage of ~16.6 V and an extinction ratio of ~14.7 dB were observed on the 1 × 2 YBB-MZI interferometer. The minimum detectable electric fields are ~1.12 V/m and ~3.3 V/m, corresponding to a dynamic range of about ~22 dB and ~18dB at frequencies of 10MHz and 50 MHz, respectively.


## ACKNOWLEDGEMENTS

This research was supported by the Basic Science Research Program through the national Research Foundation of Korea (NRF: 2018049908) and funded by the Ministry of Education, Science and Technology.


## REFERENCES


[1] H. S. Jung: Ti:$LiNbO_3$ Integrated Optic Electric-Field Sensors based on Electro-Optic Effect, *Fiber and Integrated Optics*, vol. 35(3) pp. 161-180, Jun. 2016.

[2] H. S. Jung: Photonic electric-field sensor utilizing an asymmetric Ti: $LiNbO_3$ Mach-Zehnder interferometer with a dipole antenna, *Fiber and Integrated Optics*, vol. 31(6) pp. 343–354, Dec.2012.

[3] H. S. Jung: Electro-optic electric-field sensors utilizing Ti: $LiNbO_3$ 1 × 2 directional coupler with dipole antennas, *Optical Engineering*, vol. 52(6) pp. 064402.1–064402.6, June 2013.

[4] H. S. Jung: An Integrated Photonic Electric-Field Sensor Utilizing a 1 × 2 YBB Mach-Zehnder Interferometric Modulator with a Titanium-Diffused Lithium Niobate Waveguide and a Dipole Patch Antenna, *Crystals*, vol. 9(9) pp. 459(1-11), Sep. 2019.

# Optimized silicon-nitride Y-branch splitter and directional coupler elements

**I. A. Krutov[1], M. Yu. Saygin[1], I. V. Dyakonov[1], A. S. Baburin[2,3], E. V. Sergeev[2,3], S. S. Avdeev[2,3] I. A. Rodionov[2,3], and S. P. Kulik[1]**

[1]Quantum technologies center, Faculty of physics, Lomonosov Moscow State University, Leninskiye Gory 1-2, Moscow 119991, Russia

[2] Bauman Moscow State Technical University, Rubtsovskaya emb. 2/18, Moscow 105082, Russia

[3] Dukhov Research Institute of Automatics (VNIIA), st. Sushchevskaya 22, Moscow 127055, Russia

## Motivation

We present results of numerical optimization, fabrication and measurement of Y-branch spliter and directional couplers (DC) in integrated silicon-nitride photonic structures. Silicon nitride platform enables further miniaturization of the circuits we produce in the lab using femtosecond laser writing technology [1].

Our goal is to develop the integrated photonic technology suitable for linear optical quantum computing [2].

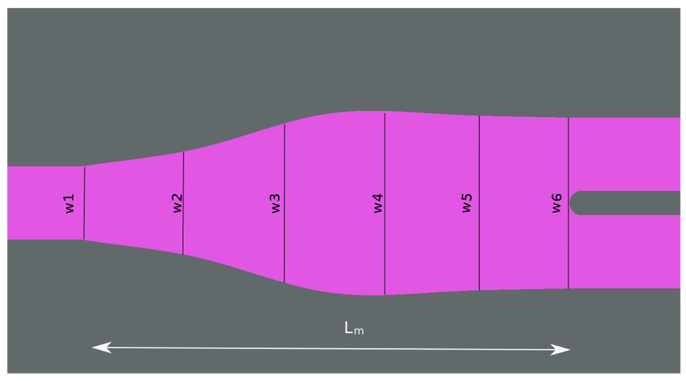
The aim of this research is to optimize the geometry of balanced Y-branch junction for 925 nm wavelength and investigate directional coupler performance.

## Y-branch optimization

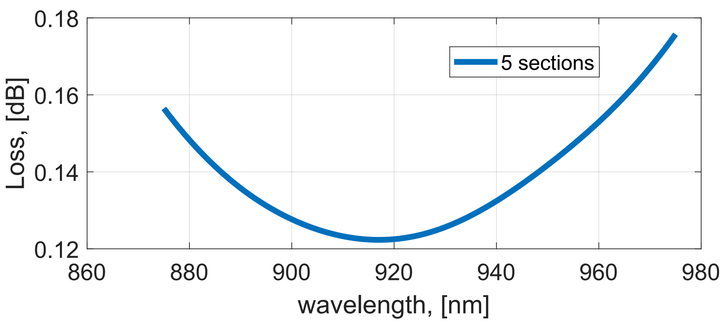
The integrated element design was optimized for 220 nm thick $Si_3N_4$ wafers and 925 nm wavelength. The optimization of Y-branch spliter was carried out with the use of the particle swarm optimization [3] according [4]. The Fig. 1 a) schematically depicts the design of Y-branch. The taper was first divided into 5 segments of equal length and different width w1, w2, w3 ... w6. The particle swarm method was applied to optimize the number of sections into which the Y-junction was divided, their widths and the length $L_m$ of the splitter. Result of the optimization is presented in following table:

**Table:** Optimized parameters. Units of the width are in microns, loss in dB.

| w1 | w2 | w3 | w4 | w5 | w6 | Lm | Loss @ 925 nm |
|---|---|---|---|---|---|---|---|
| 0.55 | 0.611 | 0.86 | 1.6 | 1.5 | 1.3 | 6 | 0.13 |




a)




b)

**Figure:** 1. a) Schematic view of the layout with 5 section. The branch geometry is defined by the spline interpolation of w1 to w6. b) Loss in Y-branch with 5 section.

## Directional coupler

The directional coupler is depicted on the Fig. 2. According to the coupled mode theory the fraction of the power coupled from one waveguide to the other can be expressed as:

$$T_{cross}(L_{int}) = \sin^2\left(\frac{\pi L_{int}\Delta n}{\lambda_0} + C_0\right) = \sin^2(C \times L_{int} + C_0),$$

$$T_{through}(L_{int}) = \cos^2\left(\frac{\pi L_{int}\Delta n}{\lambda_0} + C_0\right) = \cos^2(C \times L_{int} + C_0),$$

where $C_0$ corresponds to coupling between bent waveguide sections, provided that the $L_{int} = 0$.

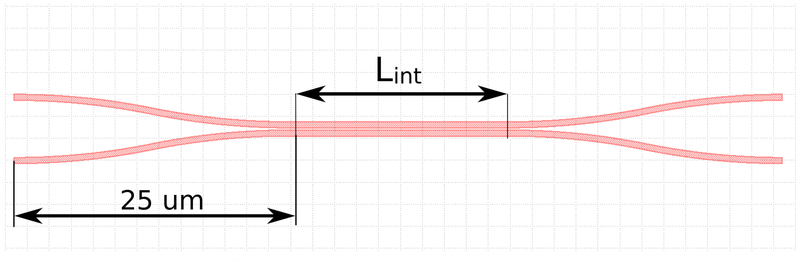
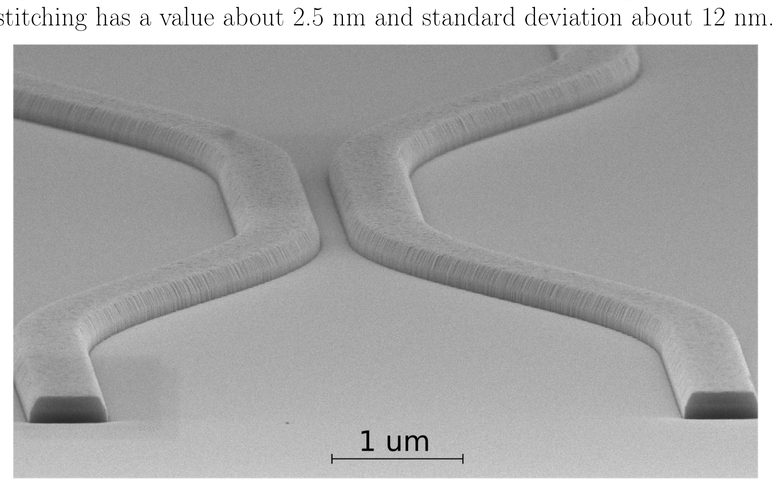


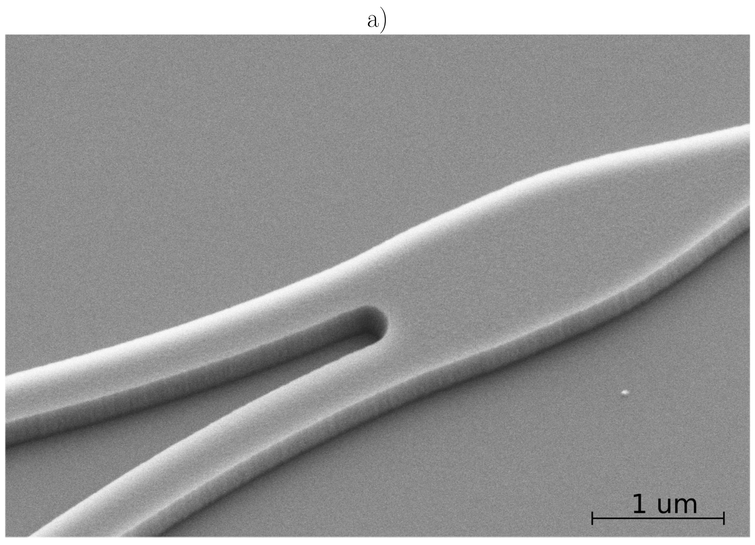

**Figure:** 2. GDS layout of directional coupler.

## Fabrication in BMSTU

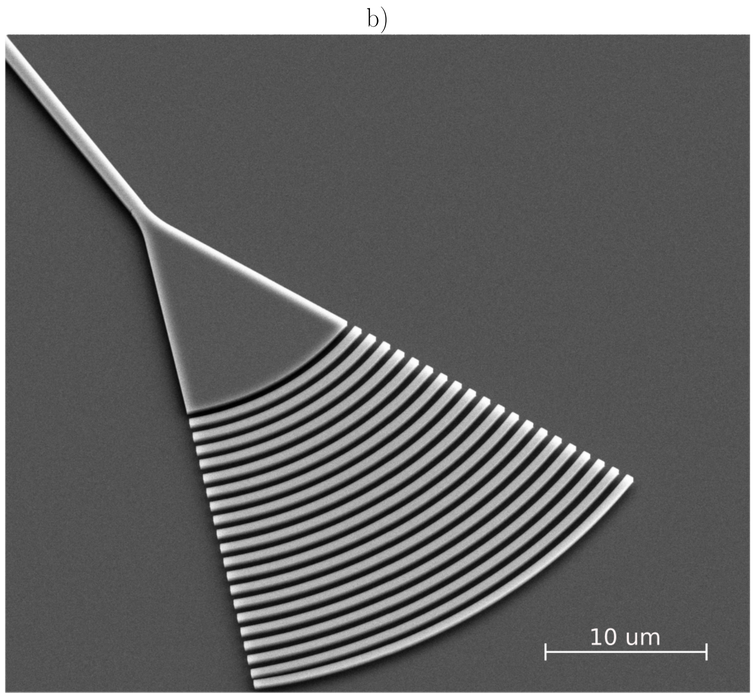
All integrated elements (DC, Y-branch splitter and grating couplers Fig.3) were fabricated by ultra-high resolution electron-beam lithography system with 50 kV accelerating voltage. We chose ma-N 2405 negative resist with polymer conductive layer for our design. For 220 nm thick $Si_3N_4$ the resist layer was estimated as 330 nm and 30 nm of conductive layer to prevent charging of dielectric layers stack during e-beam exposure process. The multiple-pass lithography technique reduces the exposure statistical errors by averaging so the final working fields stitching has a value about 2.5 nm and standard deviation about 12 nm.




a)




b)




c)

**Figure:** 3. The SEM image of a) Directional coupler, b) Y-branch and c) grating coupler.

## Optical I/O

To couple light into integrated structures, several approaches are used: with grating coupler and edge coupling. Grating coupler were numerically optimized at wavelength 925 nm using the particle swarm method. The optimization was carried out according to three parameters (filling factor, period, fiber position above the grating) and yielded the following results: at $ff = 0.465$ and $period = 606$ nm, the loss is 3.77 dB. In the experiment, losses of about 8 dB per grating were obtained. In some gratings, losses close to 7 dB were observed.

## Y-branch. Experimental results

To measure the loss on Y-junctions, a different number of consecutive pairs of dividers were manufactured. Each pair consisted of two dividers interconnected as shown in the Fig. 4.

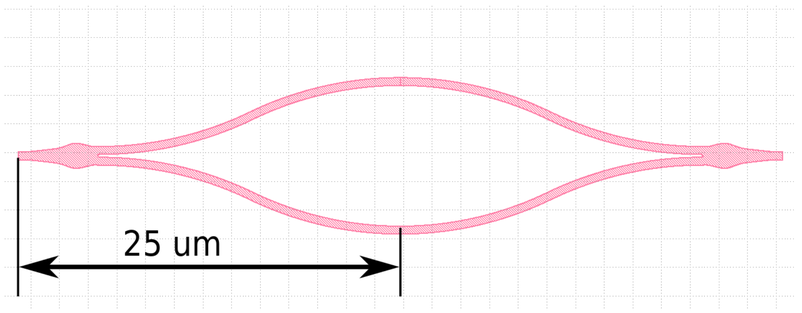



**Figure:** 4 GDS layout view of pair of spliting y-branches.

The dependence of losses on the number of pairs of Y-dividers is shown in Fig.5. According to data fit the loss per Y-junction is about $0.36 \pm 0.14$ dB.

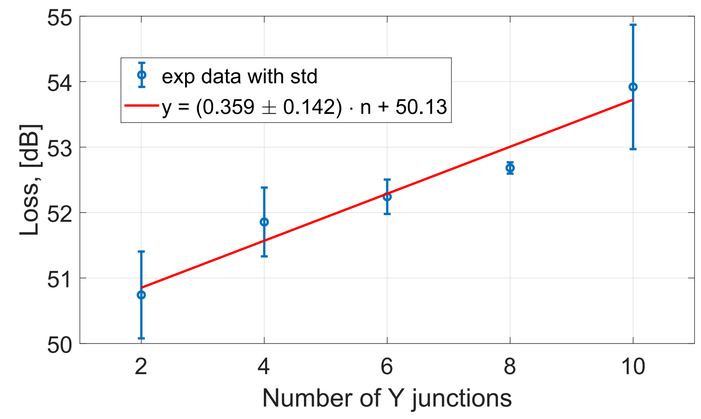



**Figure:** 5 Dependence of losses on the number of y-branches.

## DC. Experimental results

The characteristics of the directional coupler were analyzed for two polarizations in a wide range of interaction lengths ($L_{int}$) from 0 to 42 $\mu m$.

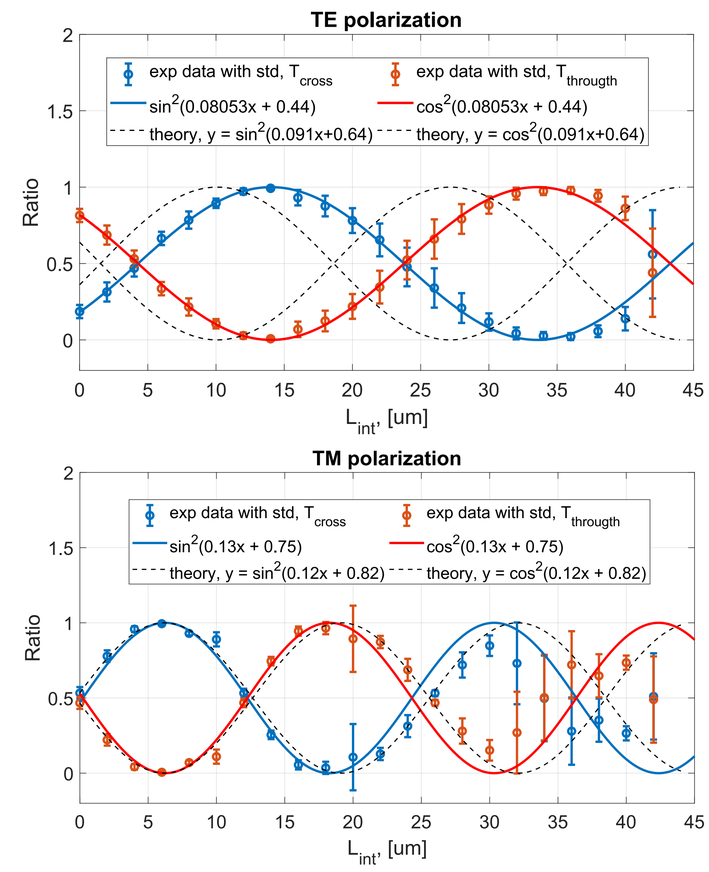



**Figure:** 6. DC. a) TE polarization b) TM polarization . The graph shows the experimental points and standard deviations corresponding to them. Each experimental point represents an average value of 20 measurements. Solid red and blue lines - results fit. The dashed black lines correspond to numerical calculations in 3D FDTD.

The numerical calculations in 3D FDTD were done as follows: the coefficient $C_0$ was found corresponding to the case when the interaction length $L_{int}$ was zero . The coupling coefficient $C$ was found from equation $C = \frac{\pi\Delta n}{\lambda_0}$, where $\Delta n = n_1 - n_2$ – difference in index between the 2 coupled modes of 2 waveguides that are separated by a gap of 200 nm.

Quantum Technologies Center

FMN Laboratory

**Contacts: Design and measurement - Ivan Krutov, research fellow, Quantum technology centre, krutov13@physics.msu.ru;**
**Fabrication - Ilya Rodionov, director of FMN laboratory irodionov@bmstu.ru;**
**qotlabs.org; quantum.msu.ru, fmn.bmstu.ru**

**References:**

[1] **I. Dyakonov et al. "Reconfigurable photonics on a glass chip".** In: *Physical Review Applied* 10.4 (2018), p. 044048.

[2] **X. Qiang et al. "Large-scale silicon quantum photonics implementing arbitrary two-qubit processing".** In: *Nature photonics* 12.9 (2018), p. 534.

[3] **R. Eberhart and J. Kennedy. "A new optimizer using particle swarm theory".** In: *MHS'95. Proceedings of the Sixth International Symposium on Micro Machine and Human Science*. Ieee. 1995, pp. 39–43.

[4] **Y. Zhang et al. "A compact and low loss Y-junction for submicron silicon waveguide".** In: *Optics express* 21.1 (2013), pp. 1310–1316.

1. For the Y-splitter, the optimal geometry was calculated and the series of prototype devices has been fabricated and measured. In the calculations of such an element, the loss is 0.13 dB per splitter,experimentally measured loss $0.36 \pm 0.14$ dB per splitter.
2. For a directional coupler there are noticeable deviations of the experiment from calculation. This may be due to production uncertainty characteristic of lithographic processes. These uncertainties can lead to small variations in the width of the waveguides and as a consequence to a change in the gap.

# Chiroptical Applications Enabled by Integrated Photonic Waveguides

*(Student Paper)*

J. Enrique Vázquez-Lozano, Alejandro Martínez
*Nanophotonics Technology Center, Universitat Politècnica de València, Camino de Vera s/n, 46022 Valencia, Spain*
*e-mail: juavazlo@ntc.upv.es*

## ABSTRACT

Chiral spectroscopy is a routine technique for identifying the chirality of matter through optical means. So far, all the approaches to analyze the chirality of chemical analytes or artificial nanostructures consider arrangements in which the input light propagates through free space. A similar conception for chiral sensing and spectroscopy may also be applicable in integrated photonic platforms. This would bring about numerous practical benefits such as miniaturization, massive parallel detection, low-cost and large-volume production, repeatability, portability, or integration with electronics, among others. Here we show that all-dielectric integrated photonic waveguides can support chiral modes under proper combination of fundamental eigenmodes. Specifically, we analyze numerically two different scenarios in which such waveguides could be used for chiroptical applications: waveguides as near-field probes for excitation and read-out of chiral light-matter interaction (in-gap configuration), and evanescent-induced chiral interaction (on-top configuration). For simplicity, a metallic nanohelix modeled as a PEC is regarded as a chiral probe, though it would be extensible to other geometries and materials more relevant. Our results may open up new perspectives towards chiroptical applications, such as sensing or spectroscopy, in silicon-based integrated photonic platforms compatible with standard CMOS technology.

**Keywords**: optical chirality, circular dichroism, chiral sensing, chiroptical spectroscopy, integrated photonics.

## 1 INTRODUCTION

Chirality is the geometrical property by which an object cannot be superimposed on its mirror image. At the molecular level it plays a key role from a practical point of view, since enantiomers, i.e., pairs of stereoisomers having opposite handedness or chirality, may have well different pharmacological effects [1]. Besides in the geometrical aspects of molecules or structures, chirality is also present in some elementary particles such as photons, leading up to the optical chirality, which, has been recognized as a fundamental property of light characterizing the local handedness of the electromagnetic (EM) field in free-space [2]. Recently, it has been put forward a general and closed expression for the optical chirality, extending the original definition so as to include field propagation through dispersive and even lossy media [3]:

$$C = \frac{\omega}{4c^2}\mathrm{Im}[(\varepsilon(\omega)\mu_{\mathrm{eff}}(\omega) + \varepsilon_{\mathrm{eff}}(\omega)\mu^*(\omega))\,\mathbf{E}\cdot\mathbf{H}^*], \tag{1}$$

where $c$ is the speed of light in free space, $\mathbf{E}$ and $\mathbf{H}$ are, respectively, the electric and magnetic complex field amplitudes, with the asterisk denoting complex conjugation, and $\varepsilon$ and $\mu$ stand for the material parameters.

Information about the chirality of matter at the micro or even molecular scale can be directly retrieved just by making it interact with chiral light. In this regard, notice that circularly polarized light (CPL) is typically considered as the paradigmatic example of chiral light [2]. There are a number of techniques to discriminate enantiomers, but the most commonly performed is the so-called circular dichroism (CD) spectroscopy, which consists in determining the differential absorption rate of left (L) and right (R) CPL when propagating through a chiral medium [4]. The efficiency of this asymmetric chiroptical response is generally expressed in terms of the dissymmetry factor:

$$g = 2\left[\frac{A^+ - A^-}{A^+ + A^-}\right], \tag{2}$$

where $A^{\pm}$ is the absorption rate of L-CPL (+) and R-CPL (-). This establishes a standard metric to quantify the enantioselectivity and its possible enhancement with respect to CPL. Importantly, in the dipolar approximation, it has been proved that this dissymmetry factor [Eq. (2)] is, in turn, proportional to the optical chirality density [Eq. (1)], thereby providing an enlightening manner to manage the enhanced chiroptical response via an all-optical approach, namely, regardless of the geometric characteristics of the chiral analyte [5].

In recent years there have been many efforts to implement sensing and spectroscopy applications in photonic integrated platforms. In all these cases, light is guided on a circuit through lossless dielectric nanowires, wherein some integrated elements are included to perform the required optical processing. Motivated by this current trend towards full-integrated devices, we explore the existence of (enhanced) optical chirality in integrated dielectric waveguides for its potential application in conventional chiroptical functionalities such as sensing or spectroscopy [6]. While keeping the same working principle, the integrated approach yields many practical advantages, mainly if realized onto silicon-based platforms compatible with standard CMOS technology.

## 2 CHIRAL RESPONSE IN STRIP WAVEGUIDES: NORMAL INCIDENCE (IN-GAP CONFIGURATION) AND EVANESCENT-INDUCED CHIRAL INTERACTION (ON-TOP CONFIGURATION)

We start by considering a guiding system consisting of a silicon nitride ($Si_3N_4$) strip waveguide with square cross-section that, for simplicity, is surrounded by vacuum. The fundamental eigenmodes of these structures, typically referred to as transverse electric (TE) and transverse magnetic (TM), yield no chirality. Still, it can be shown that a net optical chirality of opposite signs can arise from the adequate superposition of two orthogonally polarized guided modes [6], thus giving rise to left- and right-handed circularly polarized guided modes (CPGMs), analogously to the conventional case of L- and R-CPL. Building on this analysis, we first show that such waveguides can be used as near-field tips and probes for excitation and read-out of chiral nanostructures in arrangements equivalent to that routinely performed in CD measurements. To this aim, we investigate a chiral metallic scatterer embedded in a narrow gap separating two silicon nitride waveguides with square cross-section ($w = t = 450$ nm). The chiral nanostructure consists of a 4-turns single helix placed in between the waveguides, being centered and orientated along the propagation axis in the $z$-direction [see Fig. 1(a)]. To understand the chiral behavior of the helix on account of its geometry itself, i.e., dismissing any potential influence of dispersion or absorption effects, the metal is simply modeled as a PEC. Regardless of the number of turns, a full geometrical description of this complex object is determined by the following set of structural parameters: helix radius ($R_{\mathrm{helix}}$), pitch ($p$), and helix wire radius ($r_{\mathrm{helix}}$), apart from the handedness, given by a relative phase shift between the $x$ and $y$ coordinates. By properly engineering each of these parameters one can gain control over the main spectral features, tuning the resonance position and depth, as well as the optical activity of the metallic chiral structure. In this case, we consider a right-handed helix with geometrical parameters fixed to $p = 50$ nm, $r_{\mathrm{helix}} = 20$ nm, and $R_{\mathrm{helix}}$ set as the control parameter, varying from 100 to 114 nm. Notice that this choice is done so that we can keep constant the gap width, in this case to 240 nm.

We excite either L- and R-CPGM in the input waveguide by controlling the relative phase shift between the TE and TM modes. The light exiting the input waveguide will excite the chiral structure in the near-field, here acting as a probe. The output waveguide will collect the light both scattered by the structure and transmitted from waveguide to waveguide, thus enabling the read-out of the chiroptical interaction. To account for the chiral spectral response, we numerically obtain the transmission and mode conversion spectra for L- and R-CPGM [Fig. 1(b)]. From this, it can be seen that, while L-CPGM is nearly transparent to the presence of the helix, R-CPGM exhibit a narrow transmission dip depending on $R_{\mathrm{helix}}$, thereby providing clear evidence of the underlying optical activity brought about when the handedness of the CPGM coincides with that of the chiral structure. These signals directly translate into an asymmetric response on the transmission spectra, whose strength is characterized by the chiral dissymmetry factor [see Fig. 1(c)].

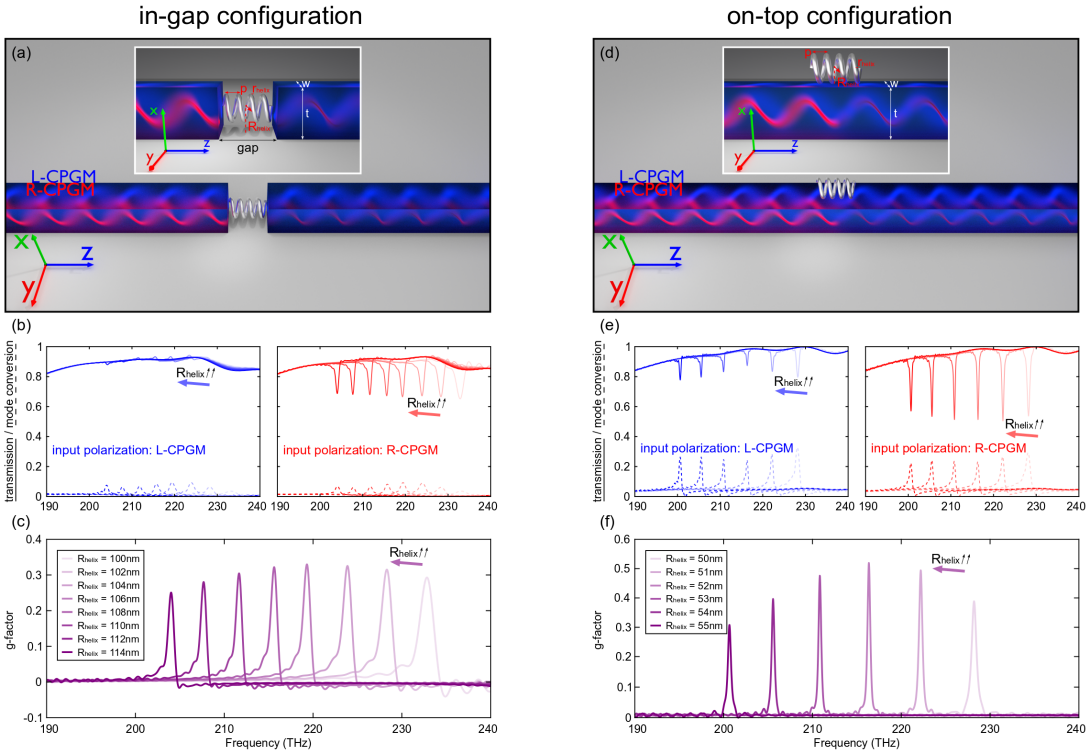



Figure 1. For each configuration: (a,d) Scheme of the arrangement for chiral sensing and spectroscopy enabled by a dielectric strip waveguide; (b,e) numerical simulation of transmission and mode conversion spectra for different values of $R_{\mathrm{helix}}$; (c,f) calculated dissymmetry factor.

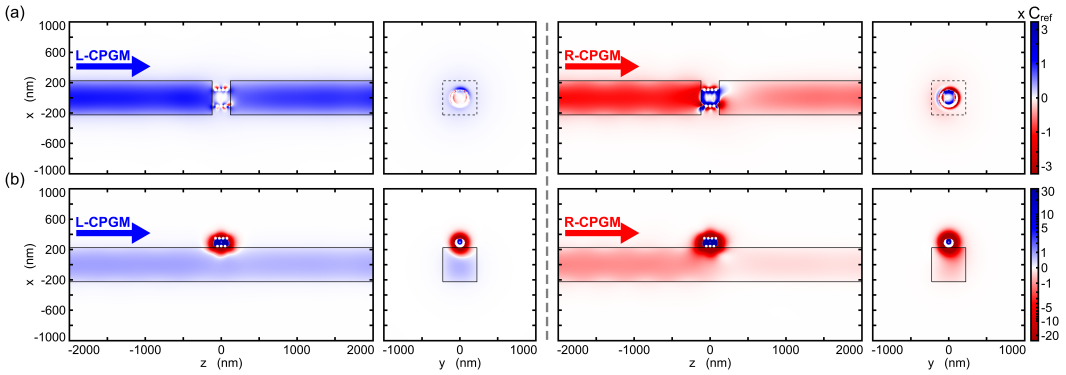



Figure 2. Cross-sectional maps of the optical chirality density for L- and R-CPGM in silicon nitride strip waveguides for (a) the in-gap configuration [Fig. 1(a)] and (b) the on-top configuration [Fig. 1(d)]. In both cases we consider the working frequency $f_{\mathrm{res}} \approx 216$ THz.

A similar analysis holds for the near-field chirality induced by the evanescent field neighboring the silicon nitride square waveguide over which a metallic chiral nanostructure is placed. The scheme of this approach is depicted in Fig. 1(d). Again, maintaining the same geometrical parameters for the nanohelix and modeling it as a PEC, we obtain, via numerical simulations, the spectral behavior of the transmission of L- and R-CPGM for different radii of the helix [Fig. 1(e)]. From these results we can directly calculate the dissymmetry factor $g$ [Fig. 1(f)]. It can be seen that the peaks of $g$ become narrower and higher in comparison with the previous case. This is quite striking since the fields in the evanescent region are much weaker than in the gap spacing two waveguides, wherein they are essentially similar to those in the waveguide core. Yet, this configuration still retain common features with respect to the previous case, in particular, the peak position (or resonance frequency) dependent on the helix radius, and the intermodal conversion between L- and R-CPGM, and vice versa, as a result of the interaction between the CPGMs and the chiral structure.

For a more intuitive description, in Fig. 2 we plot the cross-sectional map of optical chirality density from the corresponding EM field distributions, which are obtained via numerical simulations with the aid of the commercial 3D full-wave solver CST Microwave Studio. This map brings about complementary information to be accounted for. In particular, it provides a clear visualization of the resonant behavior of the nanohelix. Indeed, as shown in Fig. 2, most of the optical chirality density is tightly localized and strongly enhanced in the surroundings of the chiral structure, reaching a value of up to 30 times $C_{\mathrm{ref}}$, i.e., the maximum chirality attainable when the chiral particle is ignored. Remarkably, both the enhancement and the localization are even larger when the input mode possesses the same handedness as the chiral nanohelix, namely, for R-CPGM. This translates into a higher absorption by the particle (or a lower transmission at the output port), thus exhibiting a true chiroptical effect. Regardless of the input mode, the sign of chirality remains uniform in both the outer and the inner region of nanohelix. In this regard, it is worth observing that, inside the helix, the chiral sign is always opposed to that of its handedness. This fact becomes even more evident for the on-top configuration.

## 3 CONCLUSION AND OUTLOOK

Our results suggest that chiral applications such as sensing and spectroscopy, as well as enantioselectivity, would be feasible using all-dielectric integrated photonic waveguides. Far from providing fully optimized geometries, we only sought to show the viability of this working approach enabled by integrated photonic waveguides. Further considerations should be accounted for a more realistic scenario of chiroptical applications in integrated platforms [6]. In particular, going beyond the ideal PEC model, including dispersion and absorption losses, analyzing the effect of adding a substrate, or investigating the enhancement caused in slotted configurations. At any rate, next steps should be aimed at simplifying both the chiroptical measurement and enhancement schemes.

## ACKNOWLEDGMENT

This work was supported by funding from the European Comission Project THOR H2020-EU-829067.

## REFERENCES

[1] S. W. Smith, “Chiral toxicology: It’s the same thing...only different,” Toxicol. Sci., vol. 110, pp. 4–30, 2009.

[2] Y. Tang and A. E. Cohen, “Optical chirality and its interaction with matter,” Phys. Rev. Lett., vol. 104, p. 163901, 2010.

[3] J. E. Vázquez-Lozano and A. Martínez, “Optical chirality in dispersive and lossy media,” Phys. Rev. Lett., vol. 121, p. 043901, 2018.

[4] L. D. Barron, Molecular Light Scattering and Optical Activity, Cambridge Univ. Press, Cambridge, 2004.

[5] E. Hendry et al., “Ultrasensitive detection and characterization of biomolecules using superchiral fields,” Nat. Nanotechnol., vol. 5, pp. 783–787, 2010.

[6] J. E. Vázquez-Lozano and A. Martínez, “Towards chiral sensing and spectroscopy enabled by all-dielectric integrated photonic waveguides,” arXiv:1911.11106, 2019.

# Light-Intensity Distributions in Distributed-Feedback Resonators

Jerry Yeung and Markus Pollnau

Advanced Technology Institute, Department of Electrical and Electronic Engineering, University of Surrey, Guildford GU2 7XH, United Kingdom

## Introduction

Numerous models have been developed to model the performance of Bragg gratings and distributed-feedback (DFB). The coupled-mode theory [1] is an approximated formalism that has been extended in various ways to better approximate specific configurations. Alternatively, the characteristic-matrix approach [2] provides exact solutions, at the expense of larger computing efforts. Equally exact, but avoiding the matrix formalism, is the impedance method [3]. By use of these theories, frequently reflection and transmission curves of Bragg gratings and DFB resonators without propagation losses have been calculated. In some cases, either propagation losses have been included or light-intensity distributions at the Bragg wavelength have been modelled. These theories, though accurate, often prove cumbersome to implement.

Using a recursive method based on the circulating-field approach [4] we calculate the exact reflection and transmission curves and light-intensity distributions in DFB resonators with propagation losses.

## Recursive circulating field approach

The circulating-field approach has previously been applied to single Fabry-Pérot resonators [5]. It can straight-forwardly be extended to the situation of a multiple Fabry-Pérot-resonator structure. The relationships between the electric fields in the double-Fabry-Pérot resonator of Figure 1 are

$$E_{circ,1} = it_1E_{inc} + r_1e^{-i\phi_1}e^{-\alpha_{loss}/2}E_{b-circ,1}, E_{b-circ,1} = r_2e^{-i\phi_1}e^{-\alpha_{loss}/2}E_{circ,1} + it_2e^{-i\phi_2}e^{-\alpha_{loss}/2}E_{b-circ,2}$$

$$E_{circ,2} = it_2e^{-i\phi_1}e^{-\alpha_{loss}/2}E_{circ,1} + r_2e^{-i\phi_2}e^{-\alpha_{loss}/2}E_{b-circ,2}, E_{b-circ,2} = r_3e^{-i\phi_2}e^{-\alpha_{loss}/2}E_{circ,2}$$

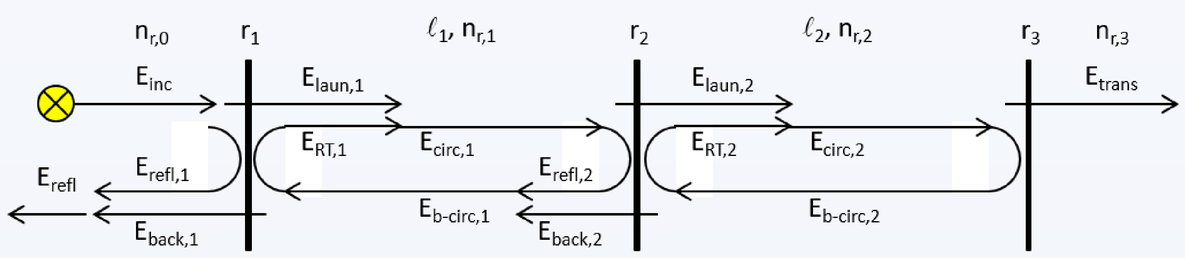



Figure 1. Double Fabry-Pérot resonator with relevant electric fields E; inc: incident; refl: reflected; laun: launched; circ: forward-circulating; b-circ: backward-circulating; RT: round-trip; trans: transmitted.

These equations can be exploited to describe the electric-field distributions of a structure with N consecutive Fabry-Pérot resonators. As long as there is no light launched from the other end of the multi-resonator structure, the electric fields for all resonators are given by

$$\frac{E_{circ,j}}{E_{circ,j-1}} = \frac{it_je^{-i\phi_{j-1}}e^{-\alpha_{loss}/2}}{1 - r_jr_{j+1}e^{-i2\phi_j}e^{-\alpha_{loss}} - r_jit_{j+1}e^{-i\phi_j}e^{-i\phi_{j+1}}e^{-\alpha_{loss}}\frac{E_{b-circ,j+1}}{E_{circ,j}}}$$

$$\frac{E_{b-circ,j}}{E_{circ,j-1}} = \left(r_{j+1}e^{-i\phi_j}e^{-\alpha_{loss}/2} + it_{j+1}e^{-i\phi_{j+1}}e^{-\alpha_{loss}/2}\frac{E_{b-circ,j+1}}{E_{circ,j}}\right)\frac{E_{circ,j}}{E_{circ,j-1}}$$

By applying these equations recursively, the exact electric-field distribution along the grating can be found.

| | | | |
|---|---|---|---|
| Number of films | 4485 | Low eff. refractive index | 1.6049715 |
| Bragg wavelength | 1.5500e-06 m | Grating length | 1.0818413 cm |
| High eff. refractive index | 1.6079535 | Phase-shift position | 0.5409207 cm |

Table 1:DFB grating parameters

## Results

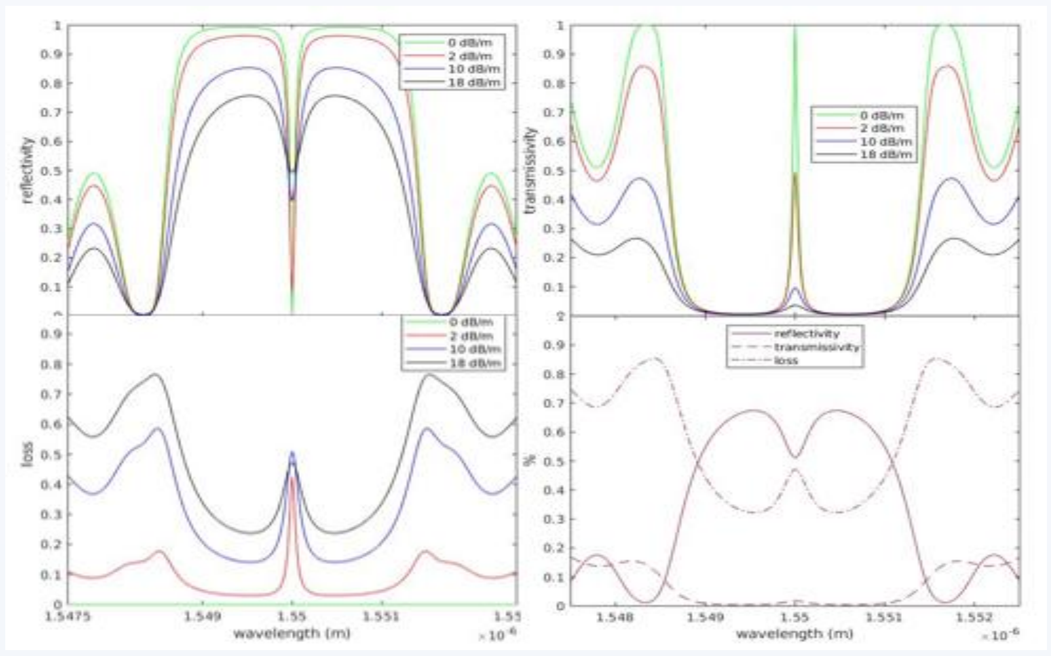



Figure 2. (Top left) Reflectivity, (top right) transmissivity, and (bottom left) loss curves for different propagation losses (legend). (Bottom right) Reflectivity, transmissivity, and loss curves for a propagation loss of $a_{loss}$ = 26 dB/m

The output curves of a DFB grating with the design parameters of Table 1 are shown in Figure 2. At the resonant wavelength, the reflectivity increases and the transmissivity decreases significantly with increasing losses, indicating a loss of resonance. At low propagation losses, the highest loss occurs at the Bragg wavelength, but as the propagation losses increase, the highest loss now occur at either end of the stopband.

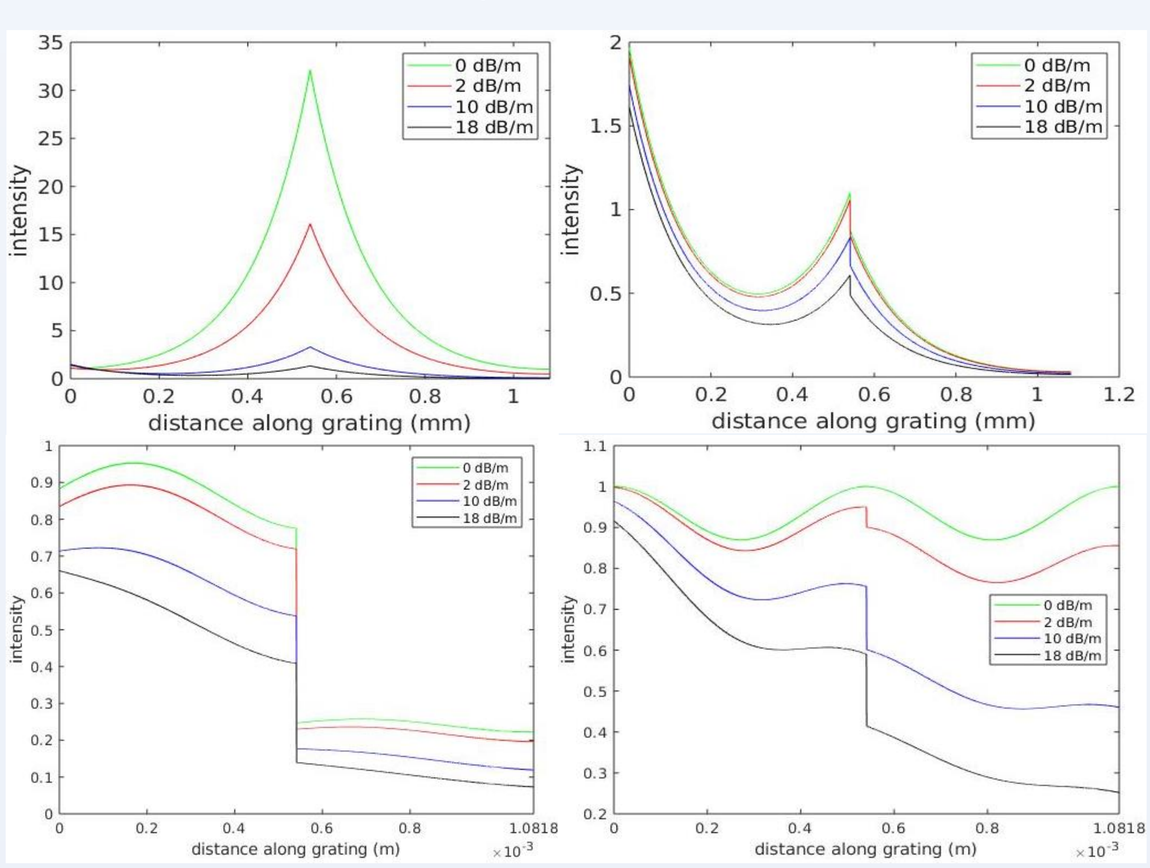



Figure 3. Intensity distribution versus grating position for different wavelengths: (top left) λ = 1.5000×10$^{-6}$ m (= Bragg wavelength), (top right) λ = 1.5498×10$^{-6}$ m (bottom left) λ = 1.5487×10$^{-6}$ m, and (bottom right) λ = 1.5484e×10$^{-6}$ m (= wavelength of first zero reflection), for different propagation losses (legend).

The intensity distribution exhibits an intensity jump as we move further away from the Bragg wavelength and displays oscillatory behavior at wavelengths far away from the Bragg wavelength, as can be seen in Figure 3.

## Conclusion

We have presented a simple, straight-forward method, based on the recursive calculation of single Fabry-Pérot resonators, to calculate the exact intensity distributions within a DFB resonator. Uniform propagation losses have been considered. The resulting output and loss curves, as well as the intensity distribution along the resonator axis have been calculated and their behavior studied. These results will help predict the performance of DFB lasers.

## References

1. H. Kogelnik, C.V. Shank: Coupled-wave theory of distributed feedback lasers, J. Appl. Phys., vol. 43, pp. 2327-2335, 1972.
2. C.C. Kores, N. Ismail, D. Geskus, M. Dijkstra, E.H. Bernhardi, M. Pollnau: Temperature dependence of the spectral characteristics of distributed-feedback resonators, Opt. Express, vol. 26, pp. 4892-4905, 2018.
3. N.M. Kondratiev, A.G. Gurkovsky, M.L. Gorodetsky: Thermal noise and coating optimization in multilayer dielectric mirrors, Phys. Rev. D, vol. 84, art. 022001, 2011.
4. A.E. Siegman: Lasers, University Science Books, Mill Valley, CA, 1986, ch. 11.3, pp. 413-428.
5. N. Ismail, C.C. Kores, D. Geskus, M. Pollnau, Fabry-Pérot resonator: Spectral line shapes, generic and related Airy distributions, linewidths, finesses, and performance at low or frequency-dependent reflectivity, Opt. Express, vol. 24, pp. 16366-16389, 2016.

The authors acknowledge funding by the European Research Council (ERC) Advanced Grant “Optical Ultra-Sensor” No. 341206.

H POSTER

# Silicon nitride passive photonic platform for applications at visible wavelengths: design, fabrication and characterization

*Marcin Lelit*[1,2], Mateusz Słowikowski[1,2], Andrzej Kaźmierczak[1], Stanisław Stopiński[1], Krzysztof Anders[1], Maciej Filipiak[2], Marcin Juchniewicz[2], Bartłomiej Stonio[1,2], Bartosz Michalak[2], Krystian Pavłov[2], Piotr Wiśniewski[1,2], Romuald B. Beck[1,2] and Ryszard Piramidowicz[1]*

[1]Warsaw University of Technology, Institute of Microelectronics and Optoelectronics, Koszykowa 75, 00-662 Warsaw, Poland

[2]Warsaw University of Technology, Centre for Advanced Materials and Technologies CEZAMAT, Poleczki 19, 02-822 Warsaw, Poland

**e-mail:* ***marcin.lelit@pw.edu.pl***

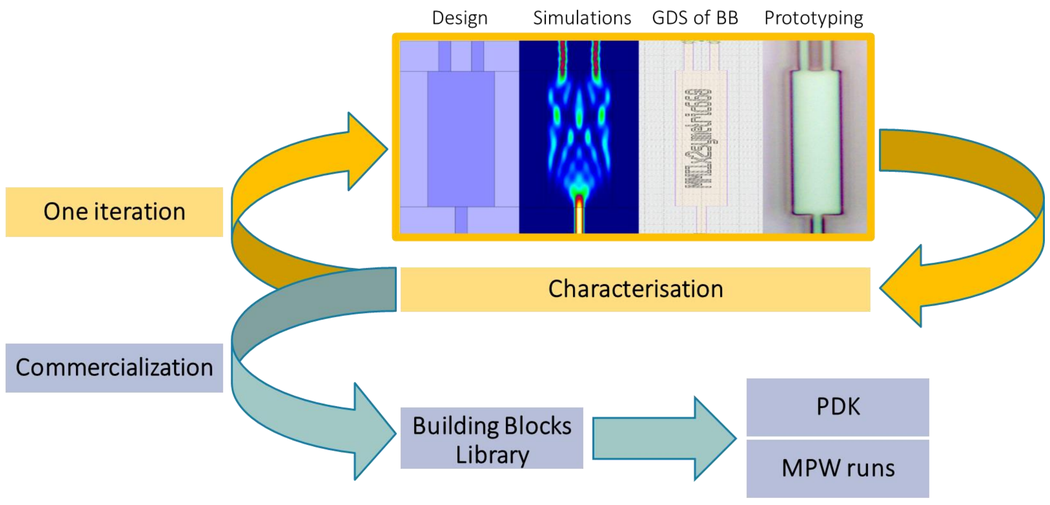
## Introduction

Recent pursuit in replacing electronic devices with photonic integrated circuits in a growing number of applications resulted in silicon nitride ($Si_3N_4$) as a material of choice for development of versatile photonic platform due to:

- Wide transparency window ranging from visible to mid-infrared range
- Low thermo-optic coefficient
- CMOS-compatibility
- Low loss and compactness of the devices

Despite commercial $Si_3N_4$-based platforms available, multiple applications like biophotonics, telecom, datacom and sensing applications and usage in hybrid photonic devices [2] leaves room further improvement and introduction of next platforms to the market.

**In this work we report recent results of development of $Si_3N_4$-based photonic devices as an initial step to establish flexible generic technology photonic platform and to offer multi-project wafer (MPW) production runs. Three sets of test devices have been developed: waveguides (WGs) including tapers and bends, symmetrical multimode interferometer (MMIs) couplers and arrayed waveguide gratings (AWGs)**



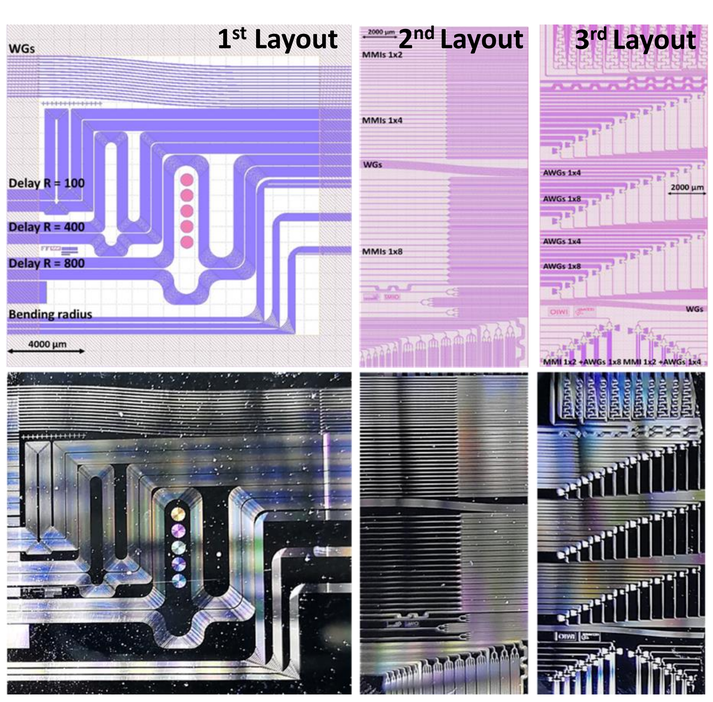

## Simulation and design

Numerical methods implemented in commercial software packages have been utilized for waveguides (WGs) cross-section optimization and later for devices simulations. Film Mode-Matching (FMM) method has been used for investigation of electromagnetic field distribution for modes in WGs and bends. For MMIs and AWGs simulations, a Finite Difference (FD) method has been used.

**1st Layout:**
- WGs of widths from 0.3 µm to 2.9 µm with 0.2 µm step
- Three complex series of delay lines
- waveguides for testing exclusively bending radius influence on losses

**2nd Layout:**
- MMIs 1x2, 1x4, 1x8 and symmetrical cascades comprising MMIs optimized for 380, 470, 550, 590, 610, 660 nm

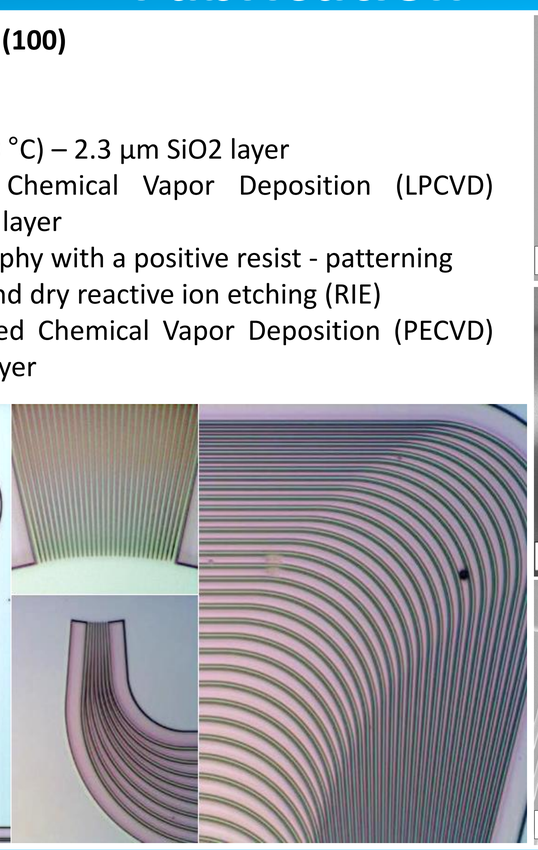
**3rd Layout:**
- WGs 90 deg. delay lines
- 3 series of AWGs 1x4 and 1x8 optimized for: 380, 470, 550, 590, 610, 660 nm
- MMIs 1x2 + 2xAWG 1x4 and 1x8 symmetrical cascades optimized for: 380, 470, 550, 590, 610, 660 nm




## Fabrication

- **4-inch silicon wafers (100)**
- **Processing:**
  - Cleaning
  - Oxidation (1200 °C) – 2.3 µm SiO2 layer
  - Low Pressure Chemical Vapor Deposition (LPCVD) – 0.32 µm $Si_3N_4$ layer
  - E-beam lithography with a positive resist - patterning
  - Development and dry reactive ion etching (RIE)
  - Plasma Enhanced Chemical Vapor Deposition (PECVD) – 2.3 µm $SiO_2$ layer







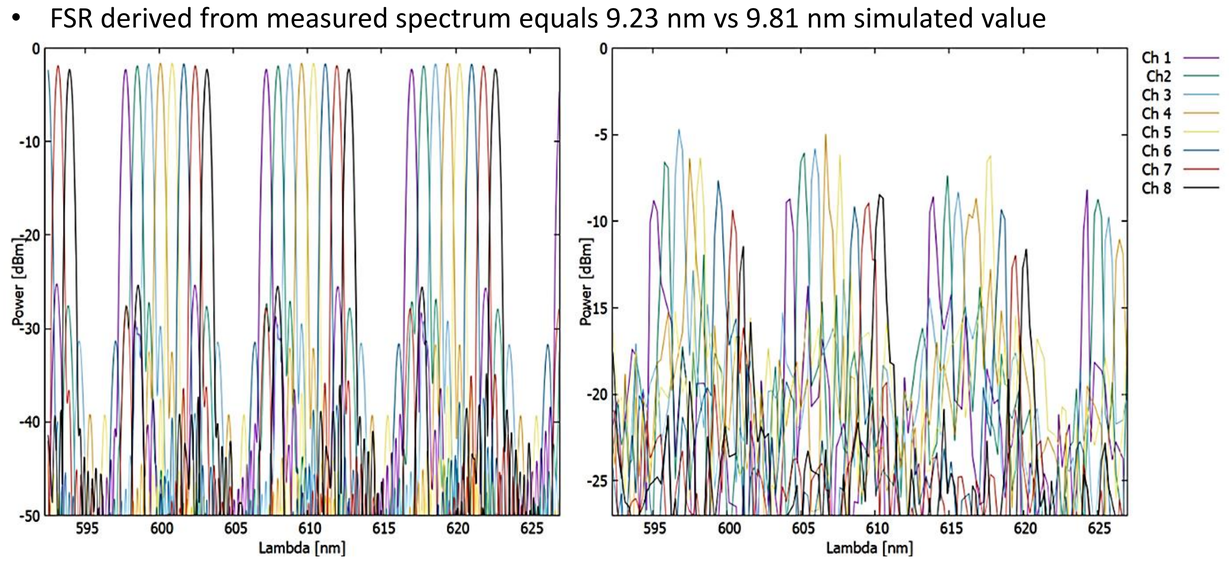

## Characterization

**Characterization setups:**
- 1st: Laser diode – 660 nm and fiber to chip and chip to fiber coupling/decoupling for fixed-wavelength measurements
- 2nd: Ti:Sapphire laser and dye laser for wavelength tuning (570 to 630 nm). Light was free space coupling to chip with 50x objective and decoupling with fiber

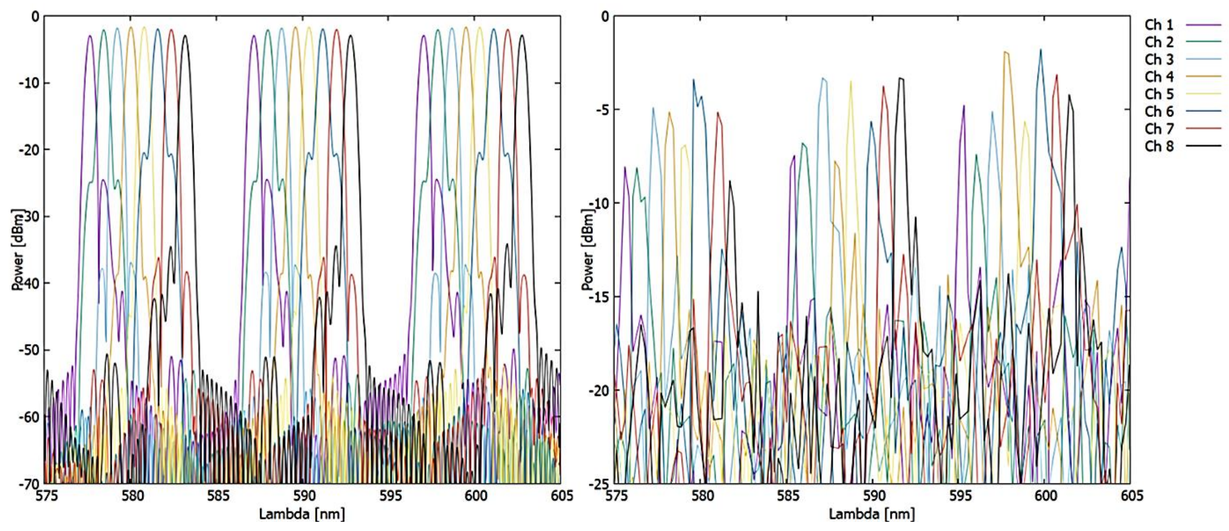
**WGs average loss:**
- Straight WG 1000x320 nm at 660 nm is 1.71 ± 0.50 dB/cm
- 90 deg, 100 µm bend WG 1000x320 nm at 660 nm is 0.21 ± 0.01 dB

**MMIs average loss:**
- 1x2 MMI (λ = 660 nm) 0.49 ± 0.04 dB
- 1x4 MMI (λ = 660 nm): 5.53 ± 0.43 dB
- 1x4 MMI (λ = 610 nm – design, λ = 660 nm – coupled): 9.31 ± 1.55 dB

**AWG 1x8 $\lambda_c$ = 610 nm characterization – design vs measurement:**
- Wavelength range from 590 to 630 nm with resolution of 0.275 nm
- 2.85 nm shift in central wavelength in respect to design parameters
- Channel spacing value of 0.79 nm is consistent with simulations
- FSR derived from measured spectrum equals 9.23 nm vs 9.81 nm simulated value




**AWG 1x8 $\lambda_c$ = 590 nm characterization – design vs measurement:**
- Wavelength range from 575 to 605 nm with resolution of 0.275 nm
- 1.67 nm shift in central wavelength in respect to design parameters
- Channel spacing value of 0.81 nm is consistent with simulations
- FSR derived from measured spectrum equals 10.23 nm vs 9.81 nm simulated value




## Conclusions

- **Working devices of all designed types have been developed within a single production run.**
- **Fast initialization of photonic platform development with current state of technology**
- **Identified sources of inconsistences between simulated and measured characteristics:**
  - Difference between structure temperature chosen for simulations (25°C) and actual temperature of measured structures due to high power coupled into the chip
  - Geometrical offsets between design and fabricated structures
  - Refractive index in simulations not equal to actual one
- **Identified sources of additional losses:**
  - Material chemical and structural nonuniformity
  - Coupling efficiency
  - Edges quality
  - Defects and impurities

## References

*[1] Q. Wilmart et al., "A Versatile Silicon-Silicon Nitride Photonics Platform for Enhanced Functionalities and Applications," Applied Sciences, vol. 9, no. 2, p. 255, Jan. 2019.*

*[2] P. Muñoz et al., "Silicon Nitride Photonic Integration Platforms for Visible, Near-Infrared and Mid-Infrared Applications," Sensors (Basel), vol. 17, no. 9, Sep. 2017.*

# Fabrication of Silicon Nitride PIC by Laser Direct Writing

**M. Tosi[1], J. H. Martínez[2], R. Peyton[2], A. Fasciszewki[1], G. Torchia[2,3], N. Abadía[4], J. Parra[5], P. Sanchis[5], L. A. Bulus-Rossini[1,3,6] and P. A. Costanzo Caso[1,3,6]**

*[1] Comisión Nacional de Energía Atómica (CNEA), Argentina*
*[3] Centro de Investigaciones Ópticas – CIOp (CONICET – CICPBA – UNLP), La Plata (BA), Argentina*
*[3] Consejo Nacional de Investigaciones Científicas y Técnicas (CONICET), Argentina*
*[4] Institute for Compound Semiconductors, Cardiff University, Queen's Building, The Parade, Cardiff, CF24 3AA, UK*
*[5] Nanophotonics Technology Center, Universitat Politècnica de València, Cam. de Vera, 46022 Valencia, Spain*
*[6] Instituto Balseiro, UNCuyo-CNEA, Av. Bustillo 9500, Bariloche (RN), Argentina*

*mauricio.tosi@cnea.gov.ar; pcostanzo@ib.edu.ar*

## Introduction

The main advantage of laser direct-writing (LDW) lithography is the possibility of obtaining sub-micrometer resolution inscription of a pattern by means of an inexpensive procedure. Maskless lithography provides an alternative for rapid PIC prototype fabrication without the mask manufacturing extra cost of standard lithography.
In this work, we present our first results of UV LDW waveguide designs written in a silicon nitride platform. The general outline of this project is to explore the feasibility of developing a standard procedure for UV LDW of photonic waveguides in a $Si_3N_4$ platform using the available cleanroom facilities.

## Fabrication process in SiN platform

- The wafers were composed of three-layers: a silicon substrate, a buried layer of $SiO_2$, and a top layer of $Si_3N_4$.
- LDW lithography was applied to define a photoresist (PR) mask layer over the silicon nitride without the need of a physical mask.

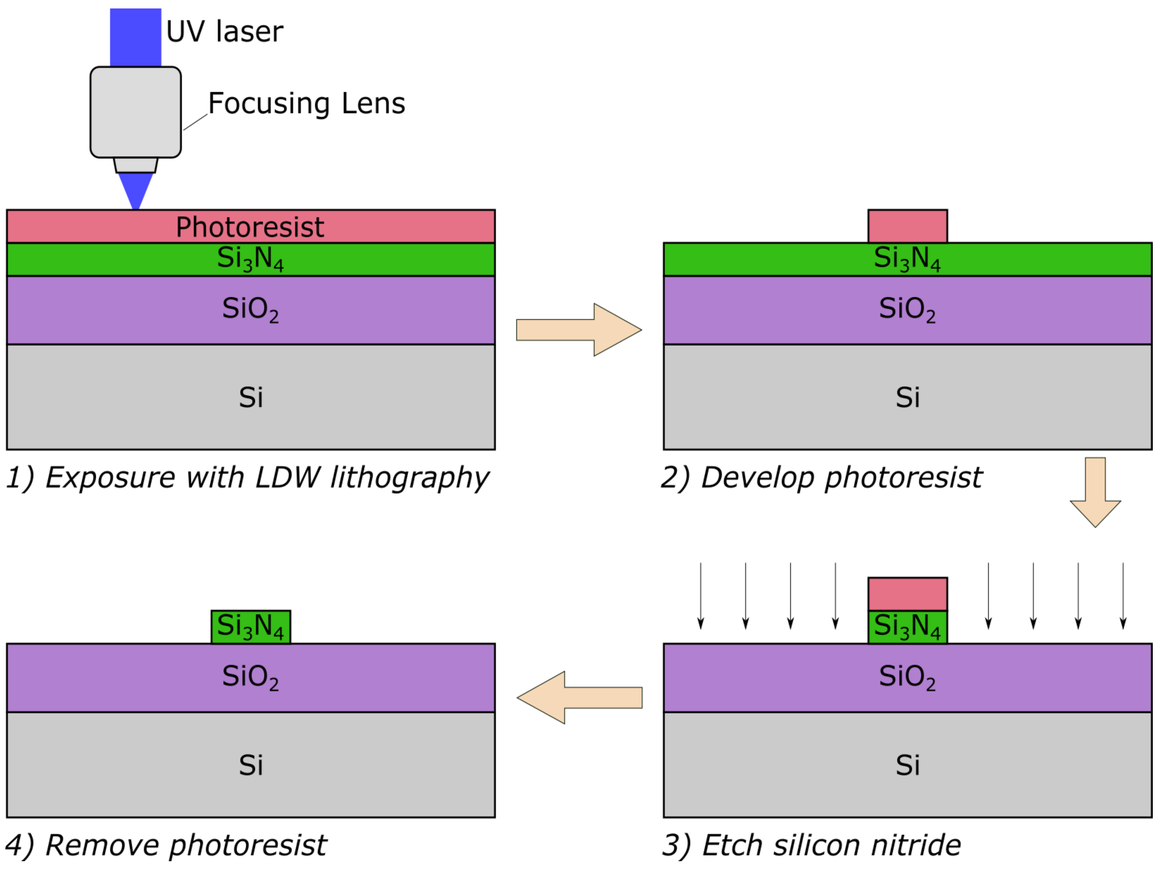



*Fig. 1 – Schematic of the fabrication process in silicon nitride platform. 1) Exposure the PR with LDW lithography; 2) develop the PR; 3) Etch silicon nitride with RIE attack; 4) Remove PR.*

## Lithography

- The PR was exposed employing laser direct-writing lithography using a commercial Heidelberg machine:
- It was used positive photoresist AZ 1518:
- Calibration structures were exposed repeatedly over the wafer with different setups of the exposition parameters:
  - Energy (set in terms of the percentage of the maximum energy)
  - DeFOC (focus deviation from the default lens position)

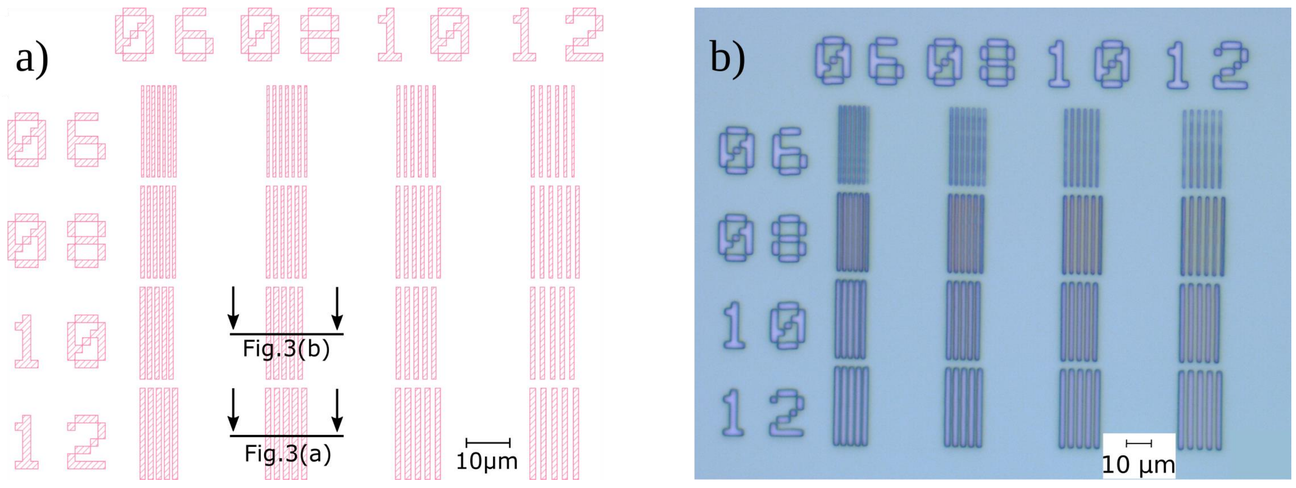



*Fig. 2 – Calibration structures. (a) Layout in GDSII format (vertical lines). The black lines with arrows corresponds to the SEM cuts illustrated in Fig. 3. (b) Vertical lines after exposing and developing the PR.*

## Etching

The selective SiN etching process was performed with the Oxford Plasmalab 80plus reactive-ion etching (RIE) equipment:

- The samples were etched for 90 seconds (SiN attack rate of 4.5 nm/s)

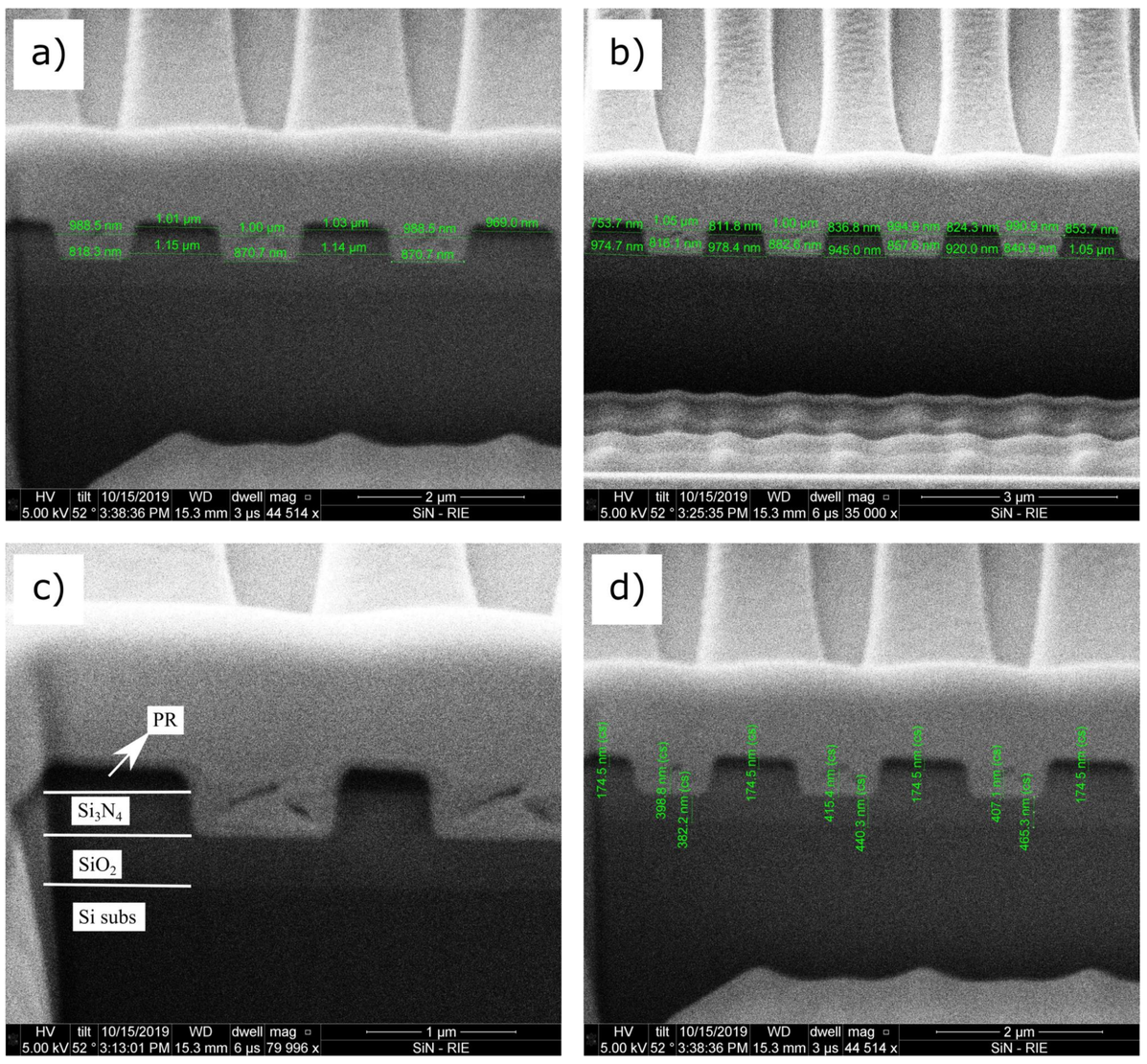



*Figure 3: SEM images of the fabricated silicon nitride structures. Designed lines of (a) 1.2 µm separated by 800nm and (b) 1 µm separated by 800 nm. (c-d) Cross-section of the waveguides and the three layers stack plus PR.*

## Results and Discussions

- The fabricated waveguide has trapezoidal section with an angle of (80 ± 3)° measured from the horizontal surface.
- The width of the waveguide is approximately 50 nm less than the design value at the waveguide base, while at the top the difference increases to 200 nm.
- These inaccuracies become the opposite when the gap values between waveguides are considered.
- This effect can be compensated using a spot correction when the digital designs are transferred to the equipment.

Photonic circuits were designed and fabricated using the three-layer wafer. Y-branch splitters were designed and fabricated with 1500 nm wide waveguides and Bezier-type bends with a gradual curvature variation and a minimum radius of 80 µm.

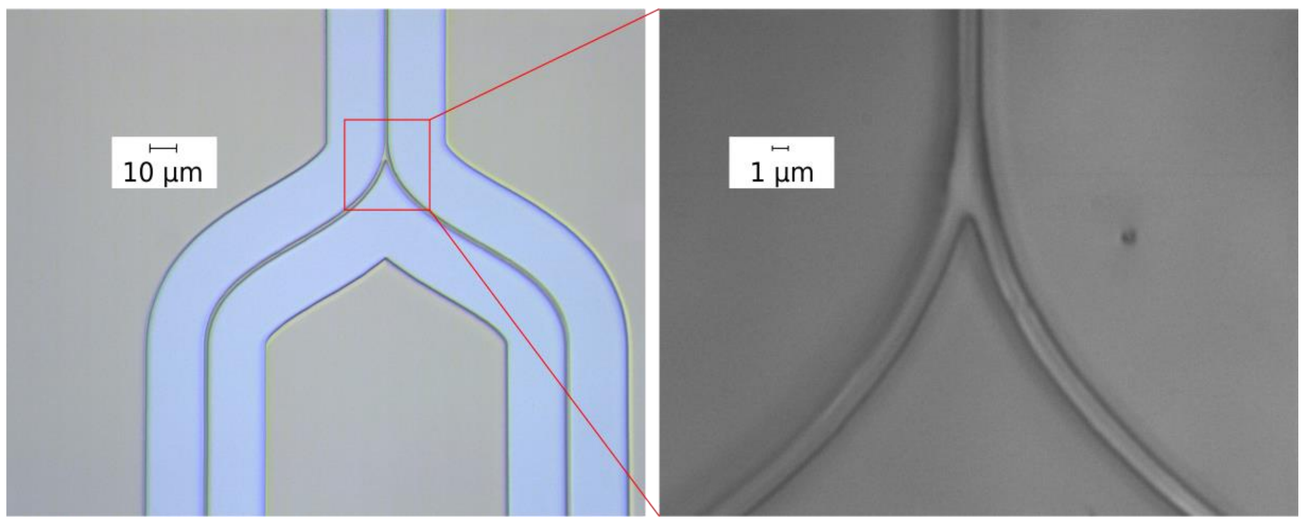



*Figure 4: Optical micrograph of the fabricated Y-branch splitter base on silicon nitride platform. The inset shows an optical zoom of the split zone.*

## Conclusions

- We presented a manufacturing procedure and fabrication results of UV laser direct-writing photonic waveguides in Si3N4 platform, achieving submicrometer resolution.
- A power splitter was shown with a clean and well defined pattern, having dimensions according to the expected values that the fabrication method allows.
- The presented results demonstrate the possibility of prototype passive PICs based on silicon nitride platform by UV LDW lithography.

## References & Acknowledgements

- P. Muñoz, et al. *Sensors*, 17(9), pp. 2088, 2017.
- M. Tosi, et. al. *IET Optoelectronics*, 14(3), pp. 120-124, 2020.
- D. B. Bonneville, et. al. *Opt. Mater. Express*, 9, pp. 1728-1737, 2019.

The authors would like to thank the support of CONICET (PIP 2017 1035CO), CNEA, CIOp, Universidad Nacional de Cuyo (SIIP 06/C560 and SIIP 06/C555), ANPCyT (PICT 2017-4581), Subsidio Milstein 2017 and 2019, NTC - Universitat Politècnica de València, BC Higher Education Links Programme 2019, and Future Compound Semiconductor Manufacturing Hub (EPSRC EP/P006973/1).

# FSR free coupled microring resonator filter on extended C-band in silicon photonics

*(Student Paper)*

**Maziyar Milanizadeh, Matteo Petrini, Francesco Morichetti and Andrea Melloni**
Dipartimento di Elettronica, Informazione e Bioingegneria - Politecnico di Milano,
Milano, 20133 Italy

*e-mail: maziyar.milanizadeh@polimi.it*

## ABSTRACT

In this work we present a modified Vernier scheme which allows the realization of FSR free filters based on coupled micro ring resonators overcoming the limits induced by the constraints on the physical dimensions of the cavities. We present a two stage optimization procedure to design a tunable filter with no FSR. Through experimental trials we demonstrate the design procedure on a 4 ring filter operating FSR-free over 60 nm.

**Keywords**: Photonic Integrated Circuits, Silicon Photonics, Ring Resonators, Optical Add Drop, Hitless Filters.

## 1. INTRODUCTION

High-order microring resonator (MRR) filters, typically with more than two series-coupled resonators, can leverage both the compact footprint sizes and the resonant characteristics of MRR to offer attractive spectral features such as wide passbands, steep roll-offs, and large extinction ratios that are desirable for a wide range of applications in telecommunication and computing systems. Silicon on insulator (SOI) MRR are good candidates for such filters because they can achieve the high bandwidth requirements while having compact footprints. Furthermore, by coupling resonators with different lengths and utilizing the Vernier scheme [1] we can extend the free-spectral-ranges (FSRs), leading to devices that can also operate over wide wavelength ranges. Extending individual FSR of resonators in Vernier scheme to achieve larger overall FSR of filter leads to excess bending loss in MRR which reduce the performance of the device. Not to mention smaller footprint of MRR limits the efficiency of thermo-optic actuators thus limiting the tunability of the device along the band. Considering a fair constraint on bending radius of MRR in SOI (about 7μm) the FSR of filter can barely reach 4.6THz for example 32nm in [2] and 36.7nm in [3].

In this work we propose a modified Vernier scheme, using non-integer ratio between MRR size, resulting to larger wavelength distances for alignment of all resonators which means wider FSR. Neglecting the dependent of couplers on wavelength, we can achieve 120THz of FSR with the same constraint on MRR bending radius (see simulation results in Fig.1(a) for a 4$^{th}$ order coupled MRR filter using this approach). In the next section we describe the optimization technique used to design a filter tuneable on 1520-1570 nm (well above the telecom extended C-band) using this modified Vernier scheme.

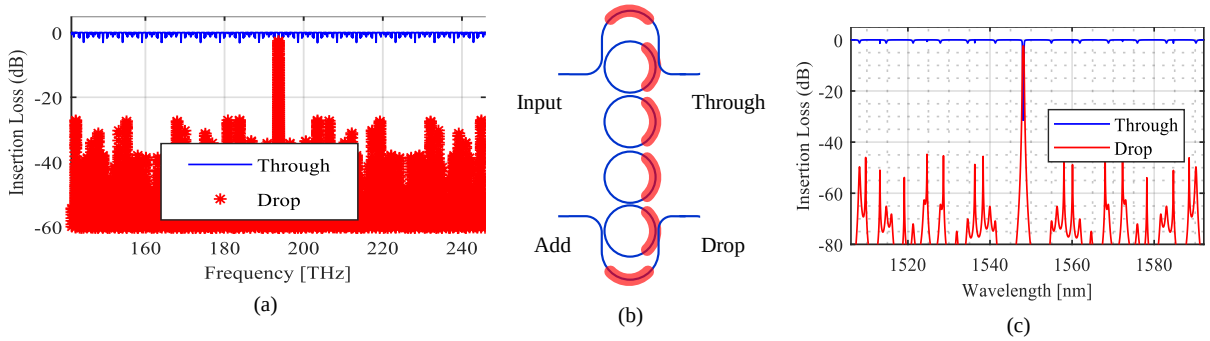



Figure 1: (a) Through and Drop port simulation of filter designed based on non-integer Vernier scheme neglecting the dependence of coupler on wavelength presenting more than 120THz of FSR. (b) schematic of 4$^{th}$ order Vernier filter with two tunable couplers connecting it to input/output bus waveguide. (c) Frequency response of 4$^{th}$ order filter with 40GHz bandwidth and more than 70nm of FSR.

## 2. Design of filter and simulation

A 4$^{th}$ order coupled MRR filter was designed with 40GHz of 3dB bandwidth along a 10 THz band (80nm). The Through port of the filter shows spurious out of band notches less than 1.2dB deep corresponding to out of band peaks on Drop port frequency response lower than 40dB. Two tuneable couplers are connecting this filter to the bus input/output waveguide allowing wavelength compensation for dependence of couplers along the band. The filter has a Butterworth spectral response. Schematic of this filter is presented in Fig.1(b). Design procedure consists of two stages, **I**: finding the best configuration of the non-integer Vernier scheme to have acceptable depth of notches (less than 1.5dB) and high of peaks (less than 20dB) in Through and Drop port frequency response along the wide operating wavelength range; **II**: optimizing the couplers between MRRs to satisfy requirements on filter performance along the wide spectral range. This requirement includes 40GHz of 3dB bandwidth, 18 dB of in-band isolation and 20dB of off band isolation in 50GHz distance from the centre of the filter. An optical simulator is developed capable of simulating different configuration of Vernier filter with appropriate coupler values. This simulator considers the dispersion of the waveguide and dependence of couplers on wavelength along the band. It can shift the simulated filter along the band while evaluating its performance which is used as merits in optimization procedure.

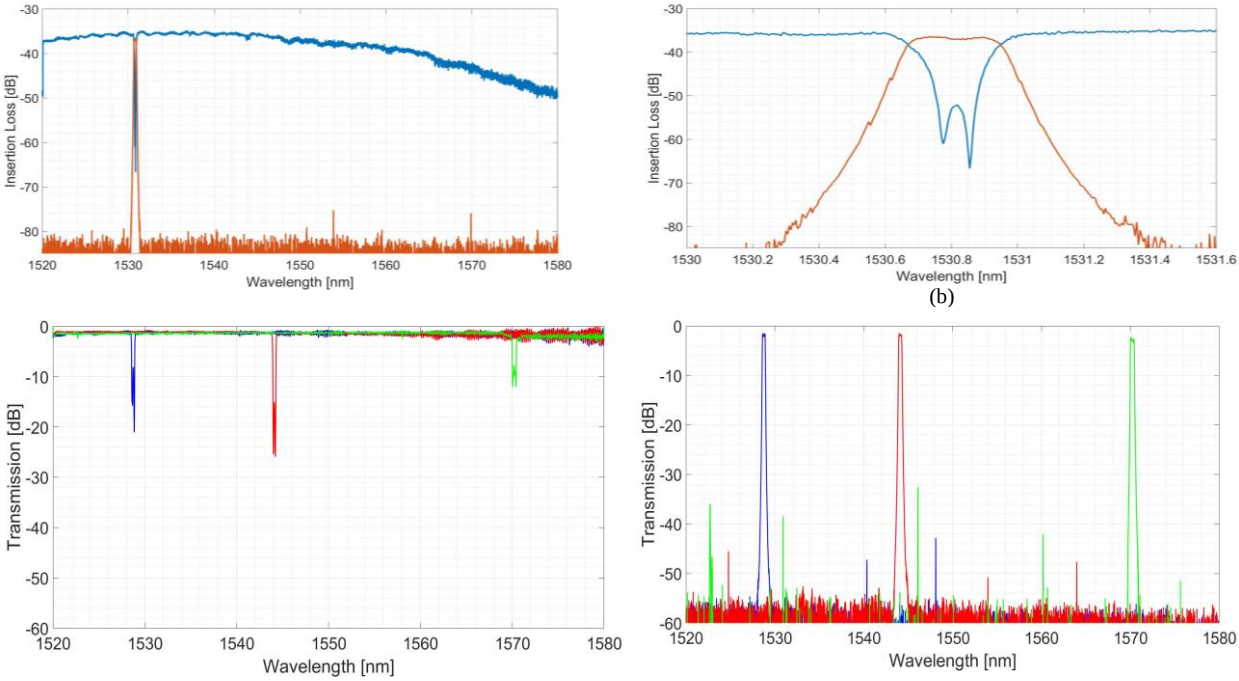
Design procedure starts from the best integer configuration (conventional Vernier scheme) of the Vernier filter (with 4.6THz of FSR) and introduce random coarse perturbations in the configurations to find a one with larger FSR equal to 10THz. In the winner candidates, finer perturbations are introduced to find the cases that satisfy two criteria's **A**: depth of notches out of band in Through port lower than 1.5dB; **B**: height of peaks out of band in Drop port lower than 20dB. Performance of device, in terms of bandwidth and isolation, is evaluated on chosen filters from previous steps. These filters are shifted along the band to the min wavelength at 1520nm and end of band at 1570nm (considering the variation of couplers and effective refractive index) and their performance is evaluated. Second part of design continues by optimizing values of couplers between MRR to satisfy the requirements along the band on chosen cases from previous optimization step. At the end of this procedure winner cases are filters capable of satisfying requirements along the extended C-band. To encounter fabrication tolerances, expected variations are simulated in these filters to understand the standard deviation of performance along the band and the best candidate is chosen. This tolerance analysis is done for coupler values and waveguide width (in form of variation of MRR radius and effective refractive index). Frequency response of this filter (with MRR ratio of [5.73 3.3 4 4.8]) for Through and Drop port is presented in Fig.1(c) and performance of filter along the extended C-band is presented in table below.

| Vernier Filter | **3dB Bandwidth** | **50GHz Channel Isolation** | **100GHz Channel Isolation** | **Max Port Isolation** | **MAX Out of Band Notch Depth** |
|---|---|---|---|---|---|
| @ 1545 nm | 43.9 [GHz] | -22.5 [dB] | -51 [dB] | -28 [dB] | -1.2 [dB] |
| @ 1570 nm | 47.9 [GHz] | -20.1 [dB] | -50 [dB] | -20.5 [dB] | -1.2 [dB] |
| @ 1520 nm | 39.5 [GHz] | -25.2 [dB] | -53.2 [dB] | -25 [dB] | -1.2 [dB] |
| Specification | 40 [GHz] | 20 [dB] | 30 [dB] | 18 [dB] | -1.1 [dB] |

## 3. Experimental Results

In this section we show experimental results of this 4th MRRs filter fabricated in silicon photonic platform. More specifically we demonstrate automatic tunability across the wavelength range 1520-1570nm (larger than the extended C band). Automatic tuning of this filter is done using gradient descent technique while cancelling the effect of thermal cross talk by thermal eigenmode decomposition (TED) in [4]. A tuneable signal with 40GHz bandwidth (to match with filter design) is used to find the optimum response of filter along the band.

Figure 2(a) shows the measured transmission at Drop (orange) and Through (blue) ports of the filter, when the passband is tuned at a wavelength of 1530.8 nm. Since the design of filter is based on non-integer Vernier scheme, the filter is FSR free well above the extended C band and indeed no other passbands are visible in the measured wavelength range. At the Through port, only a couple of off-band notches are visible which are within the specification limits. Most significant one has a depth of less than 1.5 dB at 1545 nm. At the drop port, off band peaks are more than 45 dB below the in-band transmission.
Figure 2(b) shows zoomed of filter response at the tuned wavelength. We can observe that the in-band loss and the in-band ripple at the drop port is less than 0.5 dB. The 3dB bandwidth is about 43 GHz, which is in line with what has been defined during the design phase. Channel isolation at 50 GHz is about 22 dB, and more than 45 dB at 100 GHz for non-adjacent channels.




(b)

(c)

(d)

Figure 2: (a) Spectral response of the 4th order MRR filter (blue, through port, orange, drop port). (b) Zoom around the wavelength of interest. (c) Measured transmission at Through port of the filter tuned at three different channels over the entire extended C band. (d) Measured transmission at Drop port of the filter tuned at three different channels over the entire extended C band.

In band isolation at the Through port is about 16 dB (worst case in a passband of 20GHz), but we expect that this parameter can be improved by finely tuning the input/output MZI coupler to optimize the impedance matching of the filter to the bus waveguides.

The filter has been tuned at three different channels close to the lower limit (1528.5 nm), the center (1544.4 nm) and the upper limit (1570 nm) of the extended C-band. Results shown in Figure 2(c) for Through port and 2(d) for Drop port proves the feasibility of covering a very wide wavelength range with a thermally tunable MRR filter. We want to underline that the filter has been tuned at these three new channels using the automated algorithm mentioned before. Spectral parameters are significantly varying along the frequency domain due to non-negligible impact of the coupler variation with wavelength. Nonetheless, the filter appears FSR free in each tuning condition.

## 4. Conclusion

In this work we present a modified Vernier scheme design for coupled microring resonator filters presenting extremely large FSR. We demonstrated a 4th order filter with more than 60nm FSR, well above the extended C-band. Through presented optimization techniques this filter demonstrates 40GHz of bandwidth alongside 20dB of isolation off band at 50GHz over the considered spectral range.

## 5. Bibliography

[1] G. Griffel, "Vernier Effect in Asymmetrical Ring Resonator," *PHOTONICS TECHNOLOGY LETTERS,* vol. 12, no. 12, 2000.

[2] Y. Ren, D. Perron, F. Aurangozeb , Z. Jiang, M. Hossain and V. Van, "Silicon Photonic Vernier Cascaded Microring," *PHOTONICS TECHNOLOGY LETTERS,* vol. 31, no. 18, 2019.

[3] H. Jayatilleka, R. Boeck, M. AlTaha, J. Flueckiger, N. A. F. Jaeger, S. Shekhar and L. Chrostowski, "Automatic Tuning and Temperature Stabilization of High-Order Silicon Vernier Microring Filters," in *OFC,* 2017.

[4] M. Milanizadeh, D. Aguiar, A. Melloni and F. Morichetti, "Canceling Thermal Cross-Talk Effects in Photonic Integrated Circuits," *Journal of Lightwave Technology,* vol. 37, no. 4, pp. 1325-1332, 2019.

# Self-referenced Sensing in Microring Resonators

Nirmalendu Acharyya[1], Mohamed Maher[2] and Gregory Kozyreff[2]

[1]*Max-Born-Institut für Nichtlineare Optik und Kurzzeitspektroskopie, D-12489 Berlin, Germany*

[2]*Université libre de Bruxelles, Optique Nonlinéaire Théorique, Campus Plaine, C.P. 231, 1050 Bruxelles, Belgium*

Nirmalendu.Acharyya@mbi-berlin.de gkozyref@ulb.ac.be

## Introduction

With advances in medical diagnostics, there is a growing demand for biosensors to detect low concentrations ($\sim$ few nM) of specific analytes in a complex biological sample.

An **ideal biosensor** should have **high sensitivity, low limit of detection (LOD) and high selectivity.** Further, it should be **cheap, portable and easy to use.**

A **whispering gallery mode (WGM) resonator** is an ideal candidate for high performance sensor: WGM have high $Q$ and occupies small mode volume $V$. Owing to the high $Q/V$, photons with **locally large electric field recirculates with long lifetime.** This allows enhanced interaction with analyses, ensuring **an ultra-high sensitivity of detection.**

The conventional sensing using WGM resonators are based on measuring shift in resonances, rosonance broadening or mode splitting. Indeed, in all these schemes, very **high sensitivity is achieved** [1].

The figure of merit of biosensing is the LOD, which is remarkably low for WGM detectors sensing via linear and non-linear processes. Subsequently, there have been several recent developments, which include

- multiplexed arrays, with each microresonator functionalized to respond to a specific molecule developed
- biosensing in real complex biological samples like undiluted human urine [2]

**Hurdle in commercial use:** Despite these remarkable advances, WGM sensors are largely confined to academic labs. Their operations require tunable laser sources or high precision spectrometers. As a result, these are expensive, bulky and require special training to use. This is the main obstacle in their commercial use.

**Heterodyne sensing** using a sensing and a reference cavities **does not require spectrometer or tunable laser source**. However, these are impractical as minute fabrication uncertainties can lead to unacceptable uncertainties in the reference resonances. This means, each fabricated device would have to be calibrated individually, which is not viable commercially.

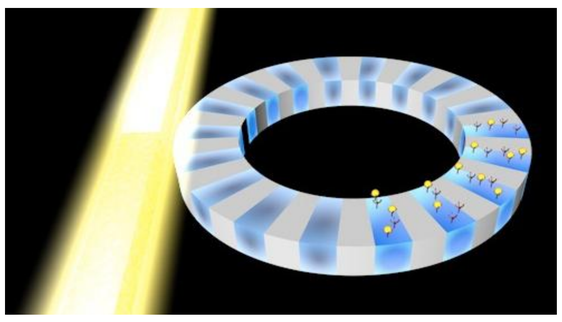
**Self-heterodyne detection** using a single resonator proposed in [3] is promising: single particle binding event can lead to detectable resonance splitting. The resulting low frequency beat signal can be measured by conventional electronics. However, in this case, the beat signal does not have a monotonic dependence on the number of analyte particles. Consequently, the scheme is not suitable to measure of analyte concentrations.

### New Self-heterodyne Sensing Scheme:

We propose a new self-heterodyne sensing scheme based on mode splitting which varies monotonically with analyte concentration [4]. The proposed scheme has following features:

- The proposed architecture consists of a bragg grating imprinted on a microring resonator and only a fraction of the ring is functionalized for molecular attachment.
- In absence of the analyte, the cavity supports doubly degenerate modes on either side of the edge of the Brillouin zone.
- **As analyte molecules bind, the degeneracy lifted and leads to mode splitting.**
- When the split modes are simultaneously excited, **low frequency beat signal is produced, which can be recorded by off-the-shelf electronics.**

Schematically, the situation is depicted below:



## Theory

We consider a microring resonator with a Bragg grating imprinted on it. The grating, of period $d$, comprises of periodic step variation of refractive index between $n_1$ and $n_2$. The eigenmodes of the cavity are $\psi_\ell(r,\theta,z)$. For TE modes $\psi_\ell(r,\theta,z) = E_z^\ell(r,\theta,z)$ and for TM modes $\psi_\ell(r,\theta,z) = H_z^\ell(r,\theta,z)$.

For the ring with Bragg grating, **there is a gap $\Delta\omega$ in the frequency spectrum, with modes on two branches.**

**Near the edge of a Brillouin zone**, $\ell_c = \pi/d$, the eigenmodes on the two branches can written as

$$\psi_\ell^\pm(r,\theta,z) \approx \Phi_{\ell_c}(r,z)\left(e^{i\ell\theta} \pm e^{i(\ell-2\ell_c)\theta}\right) \quad (1)$$

$\Phi_\ell(r,z)$ is the transverse spatial dependence, which is same (leading order) for all $\ell$ in the vicinity of $\ell_c$.

Note that the modes $\psi^\pm_{\ell_c+p}$ and $\psi^\pm_{\ell_c-p}$ have the same frequency for any $p \in \mathbb{Z}$. Consequently, there is a **two-fold degeneracy in the spectra.**

To illustrate the sensing scheme, let us focus on the modes

$$\chi_1 = \psi^\pm_{\ell_c+1} + \psi^\pm_{\ell_c-1} \approx 4\Phi_{\ell_c}(r,z)\cos(\ell_c\theta)\cos\theta, \qquad \chi_2 = \psi^\pm_{\ell_c+1} - \psi^\pm_{\ell_c-1} \approx 4i\Phi_{\ell_c}(r,z)\cos(\ell_c\theta)\sin\theta \quad (2)$$

which have **identical frequency**.

**When analytes bind on a fraction of the ring (say, $-\theta_0 \le \theta \le \theta_0$):**

- In the exposed region, the refractive index changes: $n_1 \to n_1 + \Delta n'$ and $n_2 \to n_2 + \Delta n'$
- The change in the refractive index induces a polarization $\mathbf{P} = \alpha\mathbf{E}$, where $\alpha \propto \Delta n'$
- This leads to a **differential shift** of the wavelengths $\delta\lambda_1$ and $\delta\lambda_2$ of the modes $\chi_1$ and $\chi_2$

In the spectrum, **the degeneracy is lifted in the presence of the analytes and the mode splitting is given by $\Delta\lambda = \delta\lambda_1 - \delta\lambda_2$:**

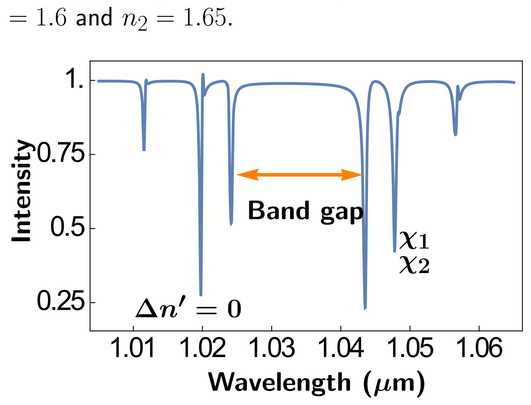
$$\frac{\Delta\lambda}{\lambda} = \frac{\delta\lambda_1 - \delta\lambda_2}{\lambda} = \frac{2\iint \mathbf{E}^*_{\ell_c}\cdot\alpha\mathbf{E}_{\ell_c} r dr dz}{\pi\iint |\mathbf{E}_{\ell_c}|^2 r dr dz}\int_{-\theta_0}^{\theta_0}\cos^2(\ell_c\theta)(\cos^2\theta - \sin^2\theta)d\theta, \quad (3)$$

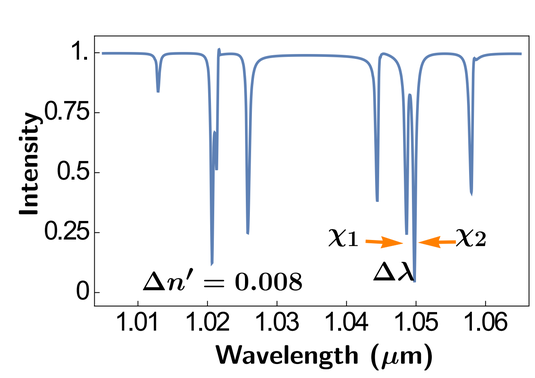
## Simulations and Results

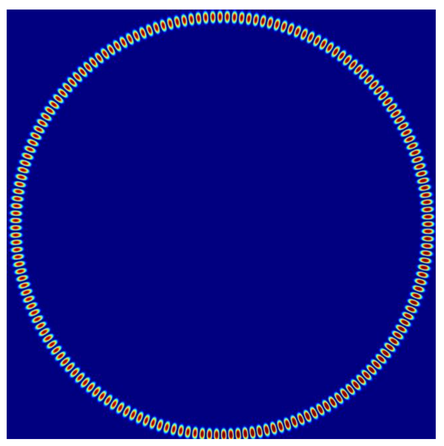
To verify the above theory, we have simulated a $Al_2O_3$ microring resonator using **COMSOL**.

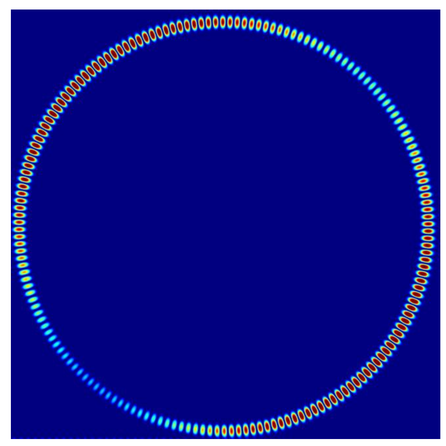
In the simulations, we used a ring with inner and outer radii $9.75\mu$m and $10.25\mu$m, respectively.

The Bragg grating of period $d = \pi/\ell_c$ with $\ell_c = 90$ comprise of periodic variation of refractive index between $n_1 = 1.6$ and $n_2 = 1.65$.





## Results:

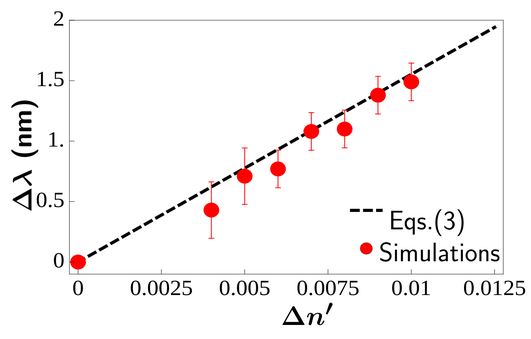
- **Our simulations confirm that when analyte is present ($\Delta n' > 0$), the modes of the cavity on either side of the band gap splits.**
- **For a fixed $\Delta n'$, we found that the splitting is maximum when two opposite quarters of the ring are functionalized.**
- Further, the splitting $\Delta\lambda$ **monotonically increases with $\Delta n'$.**
- There is an **excellent agreement between** our simulations and the estimates from Eqs.(3).

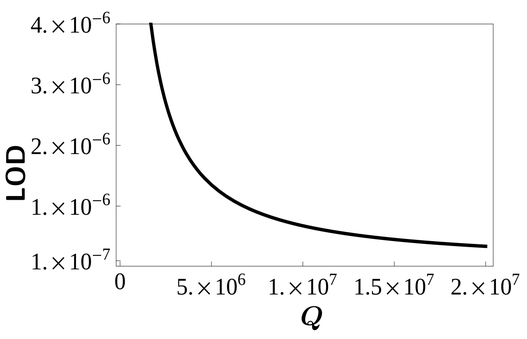
### Sensitivity and Limit of detection:

The sensitivity of the detection is given by $S = \Delta\lambda/\Delta n$. For our simulations, $S \approx 150$**nm/RIU** (bulk Refractive Index Unit).

The smallest detectable change $\Delta n'$ gives the LOD $\sim \lambda/(QS)$ where $Q$ is the quality factor. For $Q \sim 10^6 - 10^7$, our simulations yield **LOD** $\sim 10^{-6} - 10^{-7}$ .

The value of $S$ and LOD are comparable with the best reported values in the literature.




## Conclusion

- We have proposed a new design that can be **implemented with state of the art fabrication techniques.**
- With the new scheme an ultra-sensitive self-referenced detection of analyte was demonstrated both analytically and through an extensive set of numerical simulations.
- This could pave the way to a **portable and inexpensive** microring-based sensor, which improves the performance of point-of-care and other on-field detections.

## References

[1] F. Vollmer and S. Arnold, Nat Methods, 5, 591–596 (2008).

[2] M. de Goede, M. Dijkstra, R. Obregón, J. Ramón-Azcón, E. Martínez, L. Padilla, F. Mitjans, and S. M. Garcia-Blanco, Opt. Express, 27, 18508 (2019).

[3] L. He, Ş. K. Özdemir, J. Zhu, W. Kim, and L. Yang, Nat. Nanotech. 6, 428–432 (2011).

[4] N. Acharyya, M. Maher, and G. Kozyreff, Opt. Express, 27, 34997 (2019).

## Acknowledgments

G.K. is a Research Associate of the Fonds de la Recherche Scientifique - FNRS (Belgium.) This research has received funding from the European Union's Seventh Programme for research, technological development and demonstration under grant agreement No 634928 (GLAM project, http://www.glam-project.eu/).

# ENABLING HIGH-RESOLUTION FLUORESCENCE IMAGING AND DETECTION USING INTEGRATED PHOTONICS

**O. Arisev[1,2], Q. Deng[1,2], D. Kouznetsov[1,2], K. de Wijs[1,2], S. Libbrecht[1], Md. Mahmud ul Hasan[1], M. Ferreira Cao[1], B. Du Bois[1], P. Neutens, Z. Luo[1,2], S. Ha[1,2], K. Covens[1], R. Vos[1], L. Lagae[1,2], P. Van Dorpe[1,2] and N. Verellen[1,*]**

[1]imec, Kapeldreef 75, Leuven, Belgium; [2]KU Leuven, Dept. of Physics and Astronomy, Leuven, Belgium; *corresponding author: niels.verellen@imec.be

## Introduction

The ultimate resolution in microscopy is set by the diffraction limit. Various super resolution (SR) techniques have been developed in the recent years to surpass this limit. Among these techniques the one that gained the most traction is structured illumination microscopy (SIM) owing to the following advantages [1]:

- Efficient use of photon budget / least photo-toxic
- Relatively high imaging speed among other SR techniques
- Compatibility with conventional fluorophores used

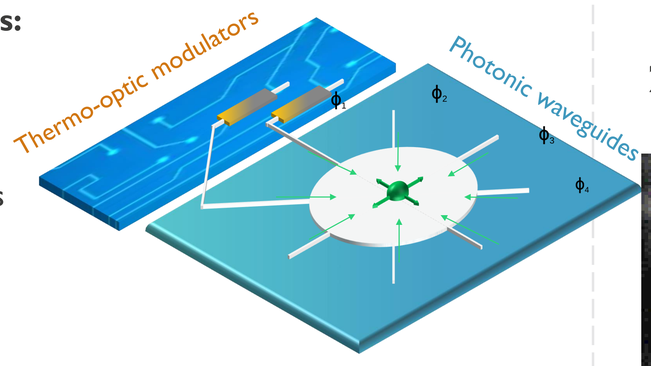
However, all the SR techniques including SIM suffer from common drawbacks: low throughput, bulky and expensive equipment. High throughput imaging excitation can be realized by means of waveguide excitation in a photonics integrated circuit (PIC) chip together with a large field-of-view (FOV) objective. It has recently been demonstrated that high throughput is achieved with such a configuration [2]. PIC can be integrated on top of a CMOS imager as the next step. This is possible by using the plasma enhanced chemical vapor deposition (PE-CVD) developed at imec [3].

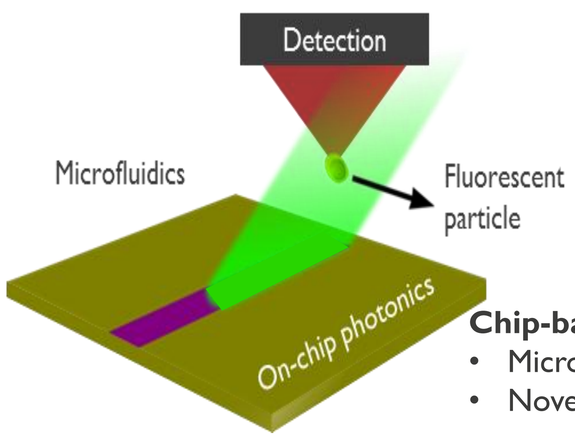
Furthermore, together with integrated microfluidics PICs holds promise for miniaturization of flow cytometry. Sorting cells based on fluorescent labels is an essential step in various research and clinical applications [4, 5].

**Here we demonstrate two devices:**

**SIM PIC chip**:

- Cost-effective and portable
- On-chip thermo-optic modulators
- CMOS compatible



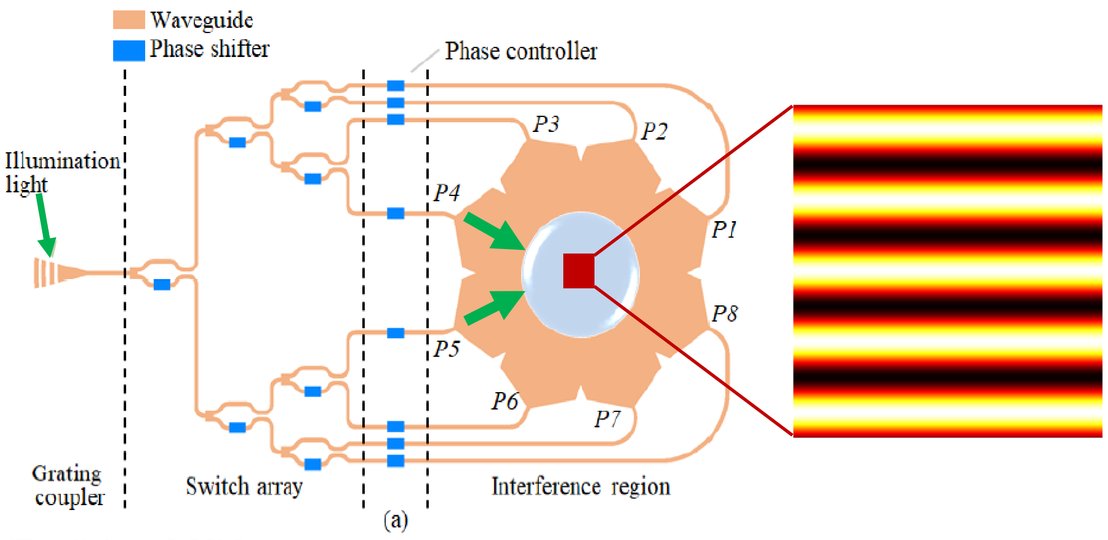

**Chip-based flow cytometer**:

- Microfluidics integrated on a PIC
- Novel grating design -> uniform illumination

## Method

On-chip SIM works as follows:

1. Couple illumination light into the PIC through a grating coupler
2. Tune thermo-optic phase modulators by applying voltage
3. Generate the desired structured illumination pattern
4. Capture raw images looping through steps 2-3
5. Reconstruct super-resolution image




**Traditional SIM:**

- Illumination and detection through the same microscope objective
- Modulation frequency of the illumination pattern bounded by objective
- Lower number of raw images

**On-chip SIM:**

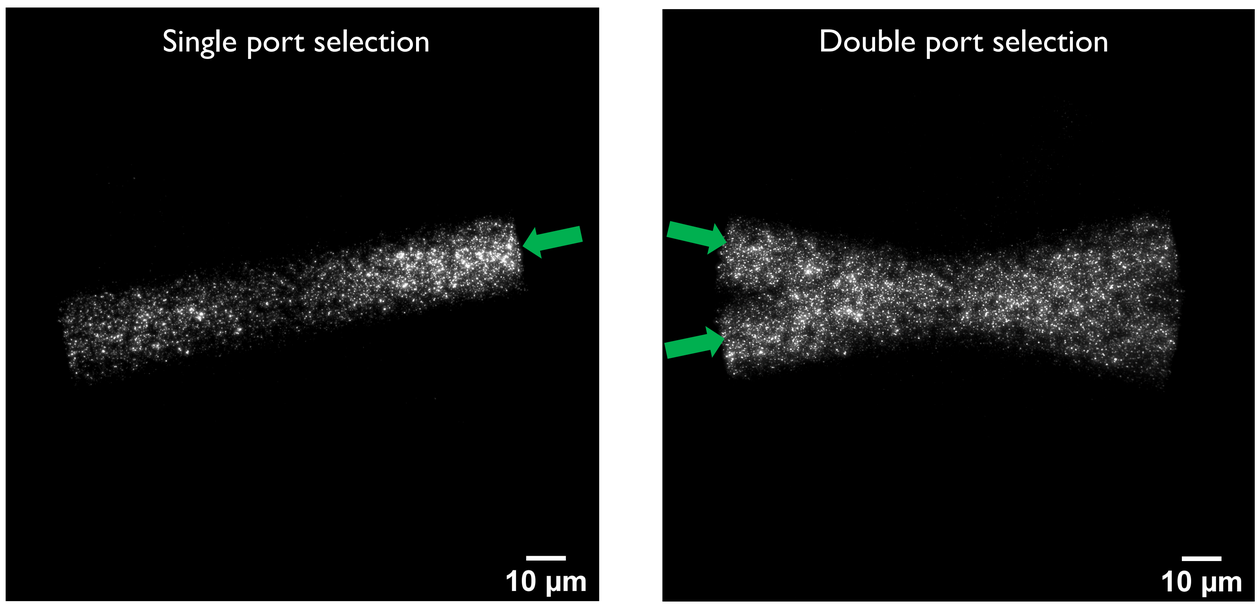
- TIRF illumination through photonic waveguides
- High throughput imaging with a large FOV objective
- Increased number of raw images

**References**:

1. Heintzmann, R. & Huser, T. Chem. Rev. **117** (2017) 13890–13908.
2. Helle, Ø. I. *et al*. Nature Photonics (2020).
3. A. Z. Subramanian et al., IEEE Photonics Journal **5** (2013) 6.
4. K. de Wijs et al., Lab Chip **17** (2017) 1287-1296.
5. D. Vercruysse et al., Lab Chip **15** (2015) 1123-1132.

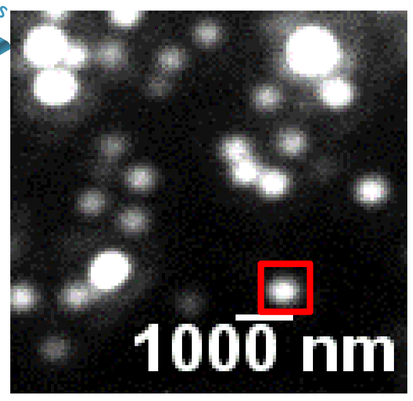
## Results of on-chip SIM

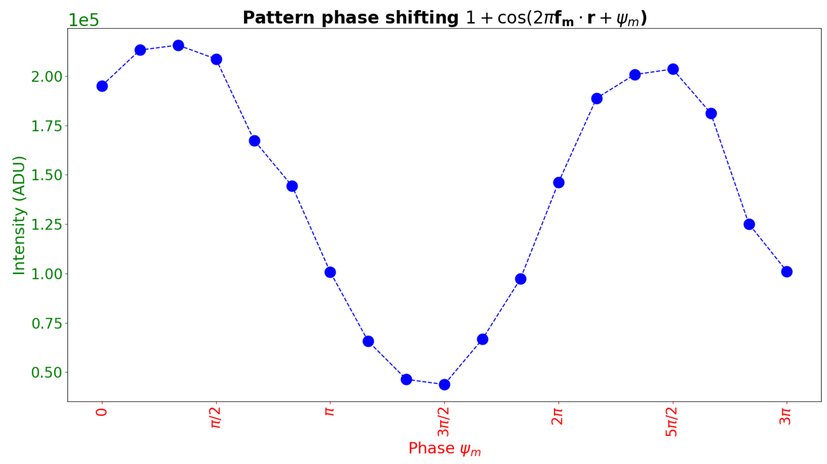
### 1. Selection of different ports for SI




The imaging area is deposited with 100 nm fluorescent beads. These results confirm that single/multiple ports can be selected with high accuracy via electrical actuation of the thermo-optic modulators.

### 2. Phase shift of sinusoidal illumination pattern

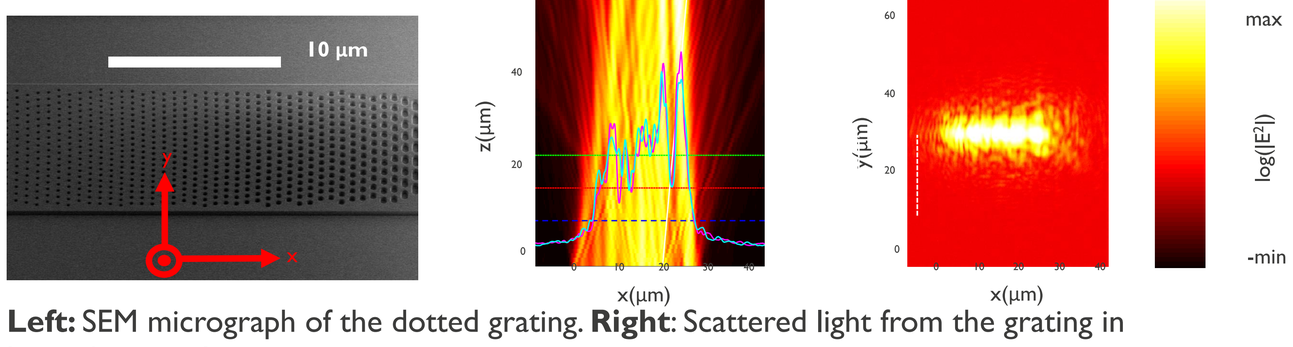



**Left:** Micrograph of fluorescence emission from 100 nm fluorescent bead clusters, show in red box is the region of interest **Right**: Sweeping the phase of the sinusoidal illumination pattern

## Results of chip-based flow cytometer

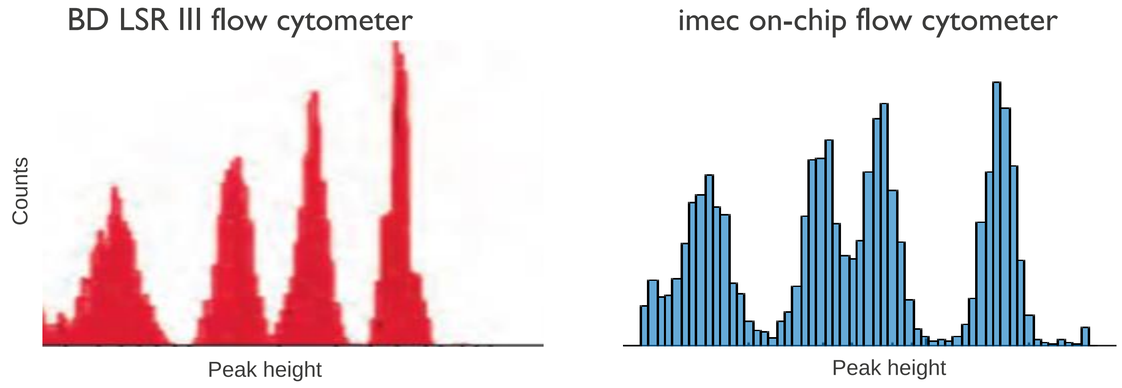
### 1. Uniform illumination




**Left:** SEM micrograph of the dotted grating. **Right**: Scattered light from the grating in logarithmic scale.

### 2. Calibration beads test

Peak height histogram for a mixture of calibration beads with different number of fluorescent markers imitating a cell-sorting scenario.




## Conclusion

A portable, PIC based SIM device that generates structured illumination patterns with thermo-optic phase modulators is demonstrated. The same concept can be expanded to achieve other functionality through monolithic integration of PIC chip on a CMOS imager. This also eliminates the need for a host optical setup and alignment. Furthermore, the on-chip flow cytometer achieves uniform illumination and shows comparable sorting performance with commercial cytometers. The device design allows for dense parallelization yielding high throughput.

# CMOS Compatible Thermal Management for Silicon Photonic Optical Phased Arrays

A. Krochin[1,2]; Dr. U. Scholz[1] ; Prof. Dr. A. Zimemrmann[2,3]
[1]Robert Bosch GmbH – Advanced Technologies and Micro Systems (CR/ATM)
[2]Institute for Microintegration (IFM) - University of Stuttgart
[3]Hahn-Schickard

## Motivation

Silicon photonic **optical phased arrays** (OPAs) are strongly **temperature dependent**:

- **Temperature** fluctuations, gradients and offsets **influence** functionality of **OPAs** [1].
- Novel **thermal management** solutions are **required** to guarantee proper functionality of silicon OPAs [2,3].

## Background

- **Optical phased arrays** are **phase sensitive**, solid-state **beam steering devices**

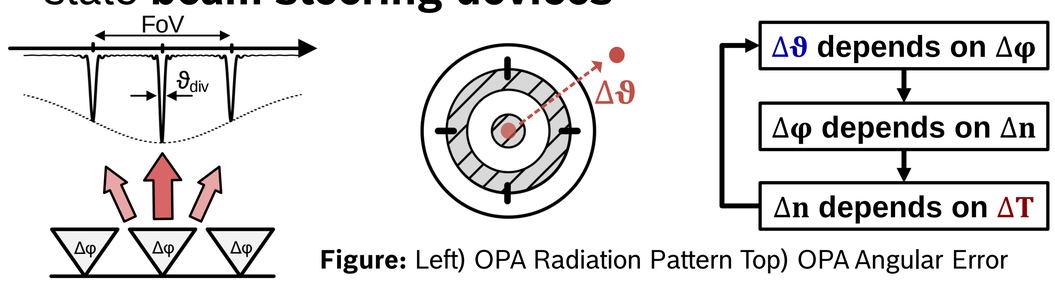


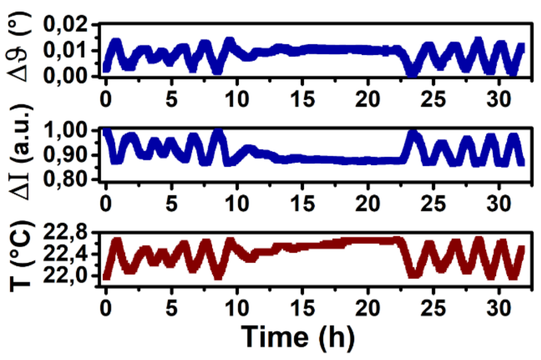

**Figure:** Left) OPA Radiation Pattern Top) OPA Angular Error

- **Strength** of the temperature influence **depends on** OPA **implementation**[1] and **α depends** on OPA initial **calibration**.

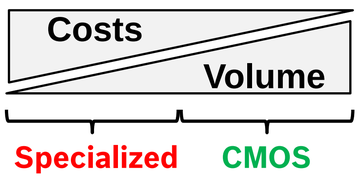
$$\Delta\vartheta \approx \frac{L}{d} \cdot \frac{\partial n}{\partial T} \cdot \Delta T_{diff} + \alpha \cdot \Delta T_{off}$$

**L:** Component Length
**d:** Component Pitch
**∂n/∂T:** Thermo-optic coefficient
**α:** Offset / Calibration factor

**Figure:** Response of a prototype OPA towards room temperature fluctuations.




- **CMOS** compatible **thermal management** solutions are **required.**



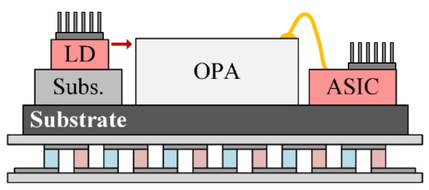




**Figure:** OPA system with specialized thermal management solutions

## Approach

- Perform **structural modifications** within the photonic IC to **change** the preferred **heat paths.**

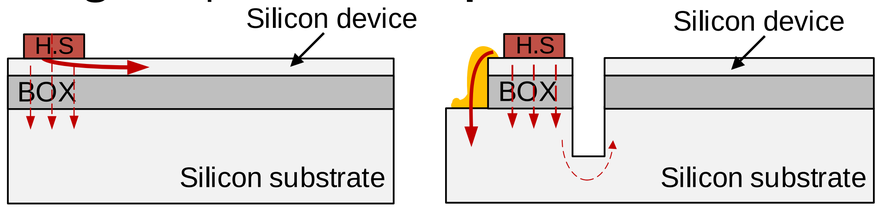



**Figure:** Left) Conventional Photonic IC. Right) Photonic IC with Heat Shunts and Trenches.

- Alternate **CMOS processes** (e.g. PVD, CVD, IBE, DRIE, Lithography) for **fabrication** of thermal **demonstrators**.

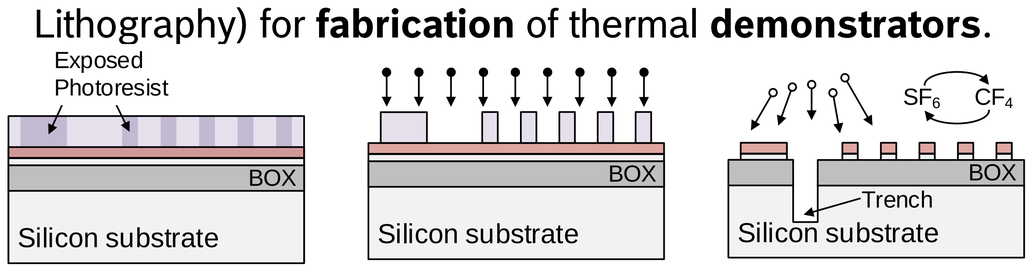



**Figure:** Left) Lithography Step. Center) IBE Step. Right) DRIE Step.

## Results

- **Confirmed** concept **feasibility** by fabrication and characterization of **thermal demonstrators.**

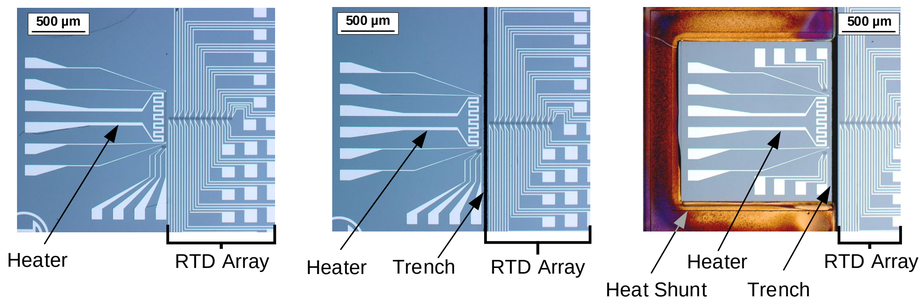



**Figure:** Left) Reference thermal demonstrator. Center) Thermal demonstrator with trench. Right) Thermal demonstrator with trench and heat shunts. Figure adapted from [2]

- **Trenches reduce safe distances ($x_{safe}$) at the cost of an increased heat source temperature.**

| width → / ↓ depth | Safe distance $x_{safe}$ 25 µm | 50 µm | 100 µm | Heat source temperature 25 µm | 50 µm | 100 µm |
|---|---|---|---|---|---|---|
| 0 µm | | 1393 µm | | | 74.7 °C | |
| 119 µm | 913 µm | 777 µm | 768 µm | 81.0 °C | 88.1 °C | 92.7 °C |
| 254 µm | 259 µm | 273 µm | 473 µm | 95.3 °C | 92.0 °C | 96.1 °C |
| 330 µm | 217 µm | 234 µm | 279 µm | 103.1 °C | 105.0 °C | 111.2 °C |

**Table:** Comparison of the calculated safe distance $x_{safe}$ and the heat source temperature for different trench widths and trench depths.

- **Heat shunts** provide a **high thermal conductivity connection** between heat source region and silicon substrate
  → **preferred path** for heat dissipation
  → **reduction of thermal resistance**

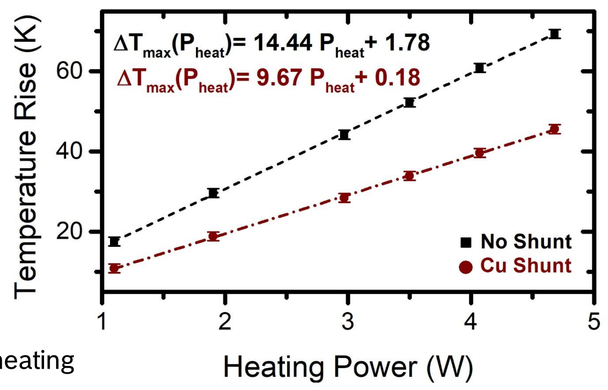



**Figure:** Temperature rise for different heating powers with and without heat shunts.

- **Combination** of trenches and heat shunts provide a **convenient solution** to **reduce** on-chip temperature **gradients** and **improve** heat **dissipation**

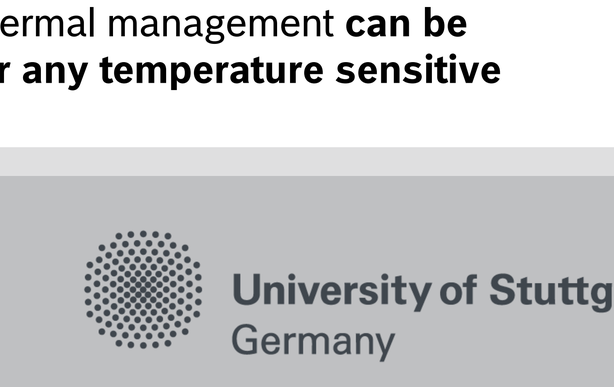



**Figure:** Temperature profile on thermal demonstrator.

## Conclusions

- **CMOS compatible solutions** for thermal management of silicon photonic OPAs were **successfully demonstrated.**
- **Trenches reduce $x_{safe}$** by over 80 %
  → **Trade-offs** between trench width, depth and reduction of temperature gradients were **identified**.
- **Heat Shunts reduce thermal resistance** by over 30 %.
- **Modular solutions** for thermal management **can be applied** beyond OPAs **for any temperature sensitive photonic IC.**

**1: Krochin et al. , IEEE Photonics Journal, Vol. 12 No. 2 (2020)**
**2: Krochin et al. , MDPI Photonics, Vol. 7 No. 1 (2020)**
**3: Krochin et al. , IEEE Photonics Journal, Vol. 11 No. 4 (2019)**

**Contact: Andrei Krochin, Robert Bosch GmbH**
**PedroAndrei.KrochinYepez@de.bosch.com**

University of Stuttgart
Germany

# PECVD SiN photonic integrated circuit for swept source OCT at 840 nm

*(Student Paper)*

Nevlacsil S.[1], Muellner P.[1], Maese-Novo A.[1], Sagmeister M.[2], Kraft J.[2],
Rank E.[3], Drexler W.[3], Hainberger R.[1]
[1]*AIT Austrian Institute of Technology GmbH, Giefinggasse 4, 1210, Vienna, Austria*
[2]*ams AG, Tobelbader Straße 30, 8141 Premstätten, Austria*
[3]*Medical University of Vienna, Währinger Gürtel 18-20, 1090 Vienna, Austria*
*e-mail: stefan.nevlacsil.fl@ait.ac.at*

## ABSTRACT

Optical coherence tomography (OCT) is an imaging technique widely used for retinal diagnostics, typically operating in the wavelength region around 840 nm. Current state of the art systems use a combination of bulk and/or fiber optical components, which limits their utilization due to high cost and large dimensions. With photonic integrated circuits (PICs) both aspects can be reduced allowing for a more widespread use, especially for point of care applications. In this paper, we present the design of a prototype PIC for a swept source (SS) OCT system operating in the 840 nm wavelength region with a bandwidth of up to 100 nm. Due to the operation wavelength silicon nitride (SiN) is used as the waveguiding material. The SiN fabrication is done with a low-temperature plasma enhanced chemical vapor deposition (PECVD) process to ensure CMOS-compatibility. This enables the subsequent monolithic co-integration of opto-electronic and electronic components for on-chip signal detection and analogue to digital conversion. With the fabricated SiN waveguide chip, we show for the first time a PIC based SS-OCT system capable of in-vivo retinal imaging.

**Keywords**: photonic integrated circuit, optical coherence tomography, silicon nitride, PECVD

## 1 INTRODUCTION

Optical coherence tomography is a non-invasive interferometric technique used for cross sectional imaging [1]. The OCT image is created by interfering light reflected at different positions in a sample with light from a reference optical path, both originating from a common light source. In contrast to conventional microscopy, the axial resolution provided by OCT is independent of the numerical aperture, which makes it especially useful for retinal imaging due to the limited opening of the pupil. While OCT is already an established method in ophthalmology for retinal diagnostics, current state-of-the-art systems are expensive and bulky. This limits the widespread use in particular for point of care applications, which require cheap, light-weight and compact probes. Photonic integrated circuits (PICs) hold the promise of providing the same functionality as bulk/fiber optical systems with much smaller dimensions and unit manufacturing costs. Further, PICs can be monolithically co-integrated with opto-electronic and electronic components, further reducing the cost and size. Additionally, this would allow novel OCT designs that are challenging to implement with bulk/fiber optical components, e.g. functional multiplexing as demonstrated by Wang et al. with an integrated receiver [2].

There are two imaging modalities in OCT which can provide the cross sectional information of the sample, time domain and Fourier domain with the latter having an inherent sensitivity advantage [3]. In Fourier domain OCT the sample cross section is encoded in the spectral response of the interference and accessed with an inverse Fourier transformation. This spectral response can either be obtained with a broadband light source and a spectrometer for spectral domain (SD) OCT or with a wavelength swept light source and a photodiode recording different wavelengths at different time steps for swept source (SS) OCT. Similar performance to state-of-the-art systems is easier to achieve with a PIC based SS-OCT system, which does not require the implementation of a spectrometer. In the following section, the design of a PIC based SS-OCT system intended for retinal diagnostic is described, which includes the full functionality of a conventional optical OCT system.

## 2 DESIGN OF A PIC FOR SWEPT SOURCE OCT

Light probing the retina has to pass through the vitreous body, mainly consisting of water. Therefore, light with wavelengths above 1100 nm is unsuitable for this application due to the high absorption in water at these wavelengths. Consequently, the well established SOI waveguide platform cannot be used because silicon is not transparent for wavelengths below 1100 nm. OCT systems for retinal diagnostics operate in the wavelength regions around 840 nm and 1050 nm. The wavelength region around 840 nm is chosen for the PIC design in this work. This has the advantage of better axial resolution, which is proportional to $\lambda_0^2/\Delta\lambda$ with $\lambda_0$ being the central wavelength and $\Delta\lambda$ the wavelength bandwidth. To allow low loss propagation of light with a wavelength

This research has received funding from the European Union's Horizon 2020 research and innovation program under grant agreement No 688173 (OCTCHIP).

of 840 nm silicon nitride (SiN) as core material and silicon dioxide (SiO2) as cladding material are chosen for the waveguide platform. Low-temperature plasma enhanced chemical vapor deposition (PECVD) is used to fabricate these waveguide layers because it opens up the highly attractive possibility of a monolithic back-end-of-line co-integration of SiN waveguides on CMOS opto-electronic chips. Low pressure chemical vapor deposition (LPCVD) would result in lower propagation losses but render this co-integration impossible.

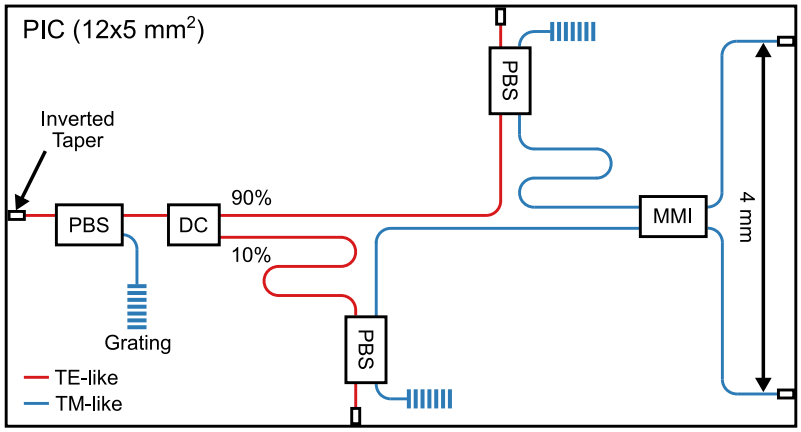



Figure 1. Schematic of the PIC design for SS-OCT. The input is on the west side and the outputs towards the balanced photodiodes on the east side. The light is coupled from the input single mode (SM) fiber to the PIC with a low-loss inverted taper. A polarization beam splitter (PBS) suppresses the orthogonal polarization and allows optimizing the input polarization by using the light emission of the grating as feedback signal. A directional coupler (DC) splits the optical power into the sample and the reference path. Before emission towards the sample and the reference mirror another PBS is passed. This allows redirecting the reflected light towards the detector by introducing a 90 degree rotation of the polarization before reentering the PIC. The returning light is brought to interference with light from the reference path at the multimode interferometer (MMI). The optical signals of both MMI output ports are guided to the east side facet of the chip.

A schematic of the PIC based SS-OCT system can be seen in Fig. 1. Typically, in OCT setups the light returning from the sample and reference mirror is diverted to the detector either by means of an optical power splitter or by an fiber optical circulator. In the optical power splitter approach, a significant portion of the source light is sacrificed to maximize the amount of reflected sample light returning to the detector. In many cases, a 90/10 splitter is used such that only 10% of the source light hits the sample while 90% of the reflected light is redirected to the detector. This power loss can be avoided by using a fiber optical circulator. However, it is difficult to implement the functionality of an optical circulator as a waveguide component in a photonic integrated circuit. To avoid excessive loss of optical power we therefore exploit the polarization characteristic of light. By rotating the polarization of the light returning from the sample by 90 degrees with respect to the light illuminating the sample, an almost lossless splitting of the forward and returning sample light paths can be achieved on chip. The 90 degree polarization rotation can be realized by means of a polarization controller acting as quarter wave plate in the off-chip sample path between chip and sample. An on-chip polarization beam splitter (PBS) acts as a nearly lossless optical path separating element.

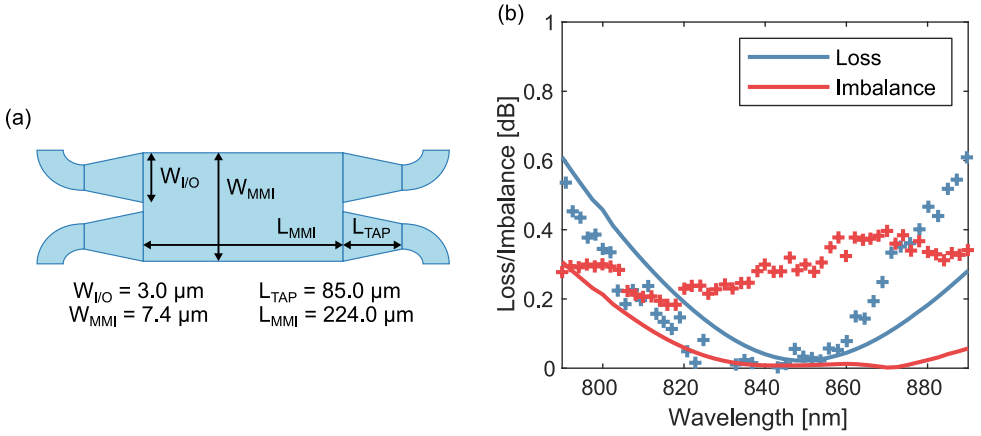



Figure 2. (a) The MMI design used as interferometer. (b) Simulation (lines) and measurement results (crosses) for the loss and imbalance of the fabricated device for TM-like polarization.

To implement the PIC design we use SiN wire waveguides with a core dimension of $700 \times 160\,\mathrm{nm}^2$ surrounded by a SiO2 cladding. The thickness of the SiO2 bottom cladding is 3 µm to avoid coupling to the silicon substrate. This waveguide cross section only supports the fundamental TE-like and TM-like polarization modes for the relevant wavelength range. Measurements of the propagation losses for these PECVD SiN waveguides in the wavelength range of 790 nm to 890 nm show values below 1 dB and 0.5 dB for TE-like and TM-like polarization, respectively [4]. Light was coupled to and from the chip by means of optical fibers. Inverted tapers were designed to better match the mode field of the optical fibers for maximizing the coupling efficiency. Coupling losses below 1.4 dB in the full wavelength range have been achieved by using high-NA fibers in combination with index matching fluid [4]. For this PIC we use the design of the broadband 90/10 directional coupler (DC) for TE-like polarization shown in our previous work [5]. Measurements of the PBS show that in the operational wavelength range the polarization extinction ratio can be kept above 10 dB [6]. The multimode interferometer (MMI) design was optimized for TM-like polarization. The simulation as well as measurement results can be seen in Fig. 2.

The PIC was fabricated at ams AG using PECVD, deep UV lithography, and reactive ion etching [7]. With the fabricated PIC in-vivo measurements were carried out at the Medical University of Vienna. Figure 3 shows the in-vivo optical coherence tomogram of a human retina obtained with the above described SiN waveguide PIC based SS-OCT system. These first measurements demonstrate that losses in the PIC can be kept sufficiently low to perform in-vivo retina OCT measurements without exceeding a power limit of 0.75 mW for the single beam entering the human eye.

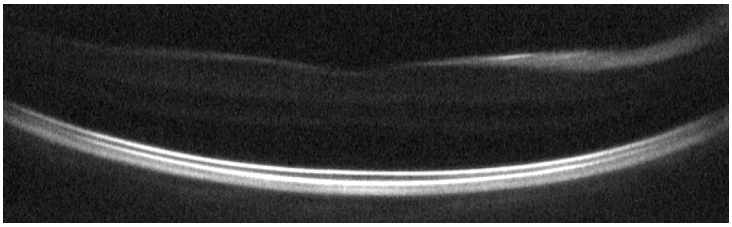


Figure 3. In-vivo optical coherence tomogram of a human retina obtained with the fabricated PIC.

## 3 CONCLUSIONS

In conclusion, we have shown the design of a PIC based SS-OCT system operating at 840 nm. The first measurements using the fabricated PIC show that in-vivo measurements of the human retina can be achieved even with the limited amount of sample light in accordance with laser light safety regulations. The use of a CMOS-compatible PECVD SiN waveguide layer deposition process opens up the possibility for the co-integration of photodiodes and read-out electronics, which would significantly increase the PIC functionality.

## ACKNOWLEDGMENT

This research has received funding from the European Union's Horizon 2020 research and innovation program under grant agreement No 688173 (OCTCHIP).

## REFERENCES

[1] W. Drexler and J. G. Fujimoto, *Optical Coherence Tomography*. Springer International Publishing, 2015.

[2] Z. Wang, H.-C. Lee, D. Vermeulen, L. Chen, T. Nielsen, S. Y. Park, A. Ghaemi, E. Swanson, C. Doerr, and J. Fujimoto, "Silicon photonic integrated circuit swept-source optical coherence tomography receiver with dual polarization, dual balanced, in-phase and quadrature detection," *Biomed. Opt. Express*, vol. 6, pp. 2562–2574, Jul 2015.

[3] R. Leitgeb, C. K. Hitzenberger, and A. F. Fercher, "Performance of fourier domain vs. time domain optical coherence tomography," *Opt. Express*, vol. 11, pp. 889–894, Apr 2003.

[4] R. Hainberger, P. Muellner, S. Nevlacsil, A. Maese-Novo, F. Vogelbacher, M. Eggeling, J. Schotter, M. Sagmeister, G. Koppitsch, and J. Kraft, "Silicon-nitride waveguide-based integrated photonic circuits for medical diagnostic and other sensing applications," in *Smart Photonic and Optoelectronic Integrated Circuits XXI*, vol. 10922, pp. 10 – 18, SPIE, 2019.

[5] S. Nevlacsil, M. Eggeling, P. Muellner, G. Koppitsch, M. Sagmeister, J. Kraft, and R. Hainberger, "Broadband SiN asymmetric directional coupler for 840 nm operation," *OSA Continuum*, vol. 1, pp. 1324–1331, Dec 2018.

[6] R. Hainberger, P. Muellner, S. Nevlacsil, F. Vogelbacher, M. Eggeling, A. Maese-Novo, M. Sagmeister, G. Koppitsch, J. Kraft, X. Zhou, J. Huang, M. Li, K.-J. Jiang, and Y. Song, "PECVD silicon nitride optical waveguide devices for sensing applications in the visible and $<$1µm near infrared wavelength region," in *Integrated Optics: Design, Devices, Systems, and Applications V*, vol. 11031, pp. 40 – 47, SPIE, 2019.

[7] M. Sagmeister, G. Koppitsch, P. Muellner, S. Nevlacsil, A. MaeseNovo, R. Hainberger, D. Seyringer, and J. Kraft, "Monolithically integrated, CMOS-compatible SiN photonics for sensing applications," *Proceedings*, vol. 2, p. 1023, Nov 2018.